DOE/MC/23075 -- 5031
(DE9600 2217
Vol. III

Measurement and Modeling of Advanced Coal Conversion Processes Volume III

User's Manual FBED-1: Fixed Bed Coal Combustion and Gasification Model with a Generalized Coal Devolatilization Submodel (FG-DVC)

M. Usman Ghani
Michael L. Hobbs
David G. Hamblen

L. Douglas Smoot
Yuxin Zhao
Predrag T. Radulovic

August 1993

Work Performed Under Contract No.: DE-AC21-86MC23075

For
U.S. Department of Energy
Office of Fossil Energy
Morgantown Energy Technology Center
Morgantown, West Virginia

By
Advanced Fuel Research, Inc.
East Hartford, Connecticut
and
Brigham Young University
Provo, Utah

DISCLAIMER

DOE/MC/23075 -- 5031
(DE96002217
Vol. III
Distribution Category UC-109

Measurement and Modeling of Advanced Coal Conversion Processes Volume III

User's Manual FBED-1: Fixed Bed Coal Combustion and Gasification Model with a Generalized Coal Devolatilization Submodel (FG-DVC)

M. Usman Ghani
L. Douglas Smoot
Michael L. Hobbs
Yuxin Zhao
David G. Hamblen
Predrag T. Radulovic

Work Performed Under Contract No.: DE-AC21-86MC23075

For
U.S. Department of Energy
Office of Fossil Energy
Morgantown Energy Technology Center
P.O. Box 880
Morgantown, West Virginia 26507-0880

By
Advanced Fuel Research, Inc.
87 Church Street
East Hartford, Connecticut 06108
and
Brigham Young University
Provo, Utah 84602

August 1993

Abstract

A generalized, one-dimensional, heterogeneous, steady-state, fixed-bed model for gasification and combustion of coal is presented. The model, referred to as FBED-1, is a design and analysis tool that can be used to simulate a variety of fixed or moving bed gasification, combustion, and devolatilization processes. The model considers separate gas and solid temperatures, axially variable solid and gas flow rates, variable bed void fraction, coal drying, devolatilization based on chemical functional group composition, depolymerization, vaporization and crosslinking, oxidation and gasification of char, and partial equilibrium in the gas phase. The conservation equations and boundary conditions are formulated for gas and solid overall continuity, gas and solid energy equations, and gas and solid species or elemental continuity equations. Plug flow is assumed in both the solid and the gas phase with variable axial velocities. Gas phase pressure drop is calculated with the Ergun equation for packed beds. Large coal particle devolatilization is allowed to occur simultaneously with char oxidation and gasification. A generalized, coal devolatilization submodel, FG-DVC, is an important part of the model. Shell progressive or ash segregation, shrinking core char submodel describes oxidation and gasification. Turbulence is not treated formally in the slowly moving bed with low gas velocity, but is included implicitly through model correlations such as the effective heat transfer coefficient. A split, back-and-forth iteration and a Livermore solver for ordinary differential equations, LSODE, are used to solve a highly non-linear, stiff system of differential governing equations. Model formulation and solution method are presented, along with user and implementation guides and a sample problem.

Preface

To expand the utilization of coal, it is necessary to reduce the technical and economic risks inherent in using a feed stock which is highly variable and which sometimes exhibits unexpected and unwanted behavior. Reducing these risks can be best achieved by developing technology for predicting coal's behavior in various processes. One such process is combustion and gasification of coal in fixed or slowly moving beds. Combustion and gasification of coal in fixed beds or slowly moving beds is of great commercial interest, since these systems can be conveniently integrated into combined cycle processes. In addition, these systems are reliable, require minimal pretreatment of feed coal, offer high thermal efficiencies, and generate easily disposable wastes. This manual presents a one-dimensional, steady-state, fixed-bed model FBED-1, for simulating combustion and gasification of coal in fixed or slowly moving beds. The FBED-1 model incorporates a functional group - depolymerization, vaporization, and crosslinking devolatilization submodel, FG-DVC.

The manual is divided in two parts. The first part presents model formulation and solution method for the system of governing equations. The second part presents user's and implementation guides and a sample problem for the code. As the sample problem, a simulation for an atmospheric, air-blown, dry-ash Wellman-Galusha gasifier fired with Jetson bituminous coal is presented.

The complex nature of the physical and chemical processes being modeled results in a computer code that is sensitive to input parameters. Several input parameters, needed for FBED-1 simulations, are not known with certainty. The manual provides guidelines for selection of such parameters. Users are cautioned that an arbitrary set of input parameters will not necessarily produce a converged solution. A thorough understanding of the model equations and the numerical solution technique will give the user a better understanding of how to select appropriate input parameters and to adjust numerical parameters to obtain a converged solution. FBED-1 is thus considered a "user specialist" code.

Acknowledgments

The development of this code and user's manual was sponsored by The U.S. Department of Energy, Morgantown Energy Technology Center (Contract Number DE-AC21-86MC23075), under subcontract from Advanced Fuel Research, Inc. with cost sharing by the Advanced Combustion Engineering Research Center (ACERC) at Brigham Young University. Funds for this center are provided by the U.S. National Science Foundation, the State of Utah, the U.S. Department of Energy, industrial participants, Brigham Young University and the University of Utah. Mr. Justin L. Beeson, Dr. Richard A. Johnson, and Dr. Norman T. Holcomb served as the DOE contracting Officer's Technical Representatives (COTRs). The financial support of these institutions, as well as the technical guidance of the DOE COTRs, are gratefully acknowledged.

At BYU, aside from the BYU authors of this manual, other contributors to the development of this code were Drs. B. Scott Brewster and Sung-Chul Yi. At AFR, aside from the AFR authors of this manual, major contributors to the development of the FG-DVC code were Drs. Peter R. Solomon and Michael A. Serio. Other contributors at AFR were Dr. Zhen Zhong Yu, Ms. Sylvie Charpenay, and Dr. Phillip E. Best. Professor Don E. Norton, of BYU Department of English, reviewed and edited the manual. The contributions of these individuals are greatly appreciated.

Finally, sincere appreciation is expressed to Ms. Nicole Banks and Ms. Melissa Wright for carefully typing and coordinating this document; to Mr. Mack R. Lund, ACERC computer system manger, for computer support; and to Mr. Michael R. King, ACERC manager, for administrative support.

Table of Contents

List of Tables

List of Figures

PART ONE: MODEL FORMULATION AND SOLUTION

CHAPTER 1

INTRODUCTION

Fixed-bed systems are simple, reliable, have high thermal efficiency, and require minimal pretreatment of feed coal. Combustion and gasification of coal in fixed or slowly moving beds of packed coal particles are of substantial commercial interest. Eighty-nine percent of the coal gasified in the world is gasified by the fixed-bed, ten percent by the entrained-bed, and only one percent by the fluidized bed process. Fixed beds can be operated at high pressure, providing opportunity for increased power generation efficiency through combined cycle processes. Fixed beds are also a popular choice for mild gasification since, by their countercurrent nature, the liquids can be quickly removed before being altered by substantial reaction. Fixed bed gasification and combustion processes are classified according to the flow pattern of coal and gas as countercurrent, cocurrent, and crosscurrent processes. The countercurrent process is the most common fixed bed combustion and gasification process.

Figure 1.1 shows a schematic of a large-scale, atmospheric pressure, air-blown, dry-bottom, fixed-bed gasifier. Coal is fed to the top of the gasifier and moves downward under gravity, countercurrent to the rising gas stream. The dry ash is removed at the bottom of the gasifier. The feed gas is commonly composed of air or oxygen and steam. Excess steam is supplied to the gasifier to control the ash temperature. Figure 1.1 also shows the reactor divided into four overlapping zones: drying, devolatilization, gasification and combustion. As the coal slowly

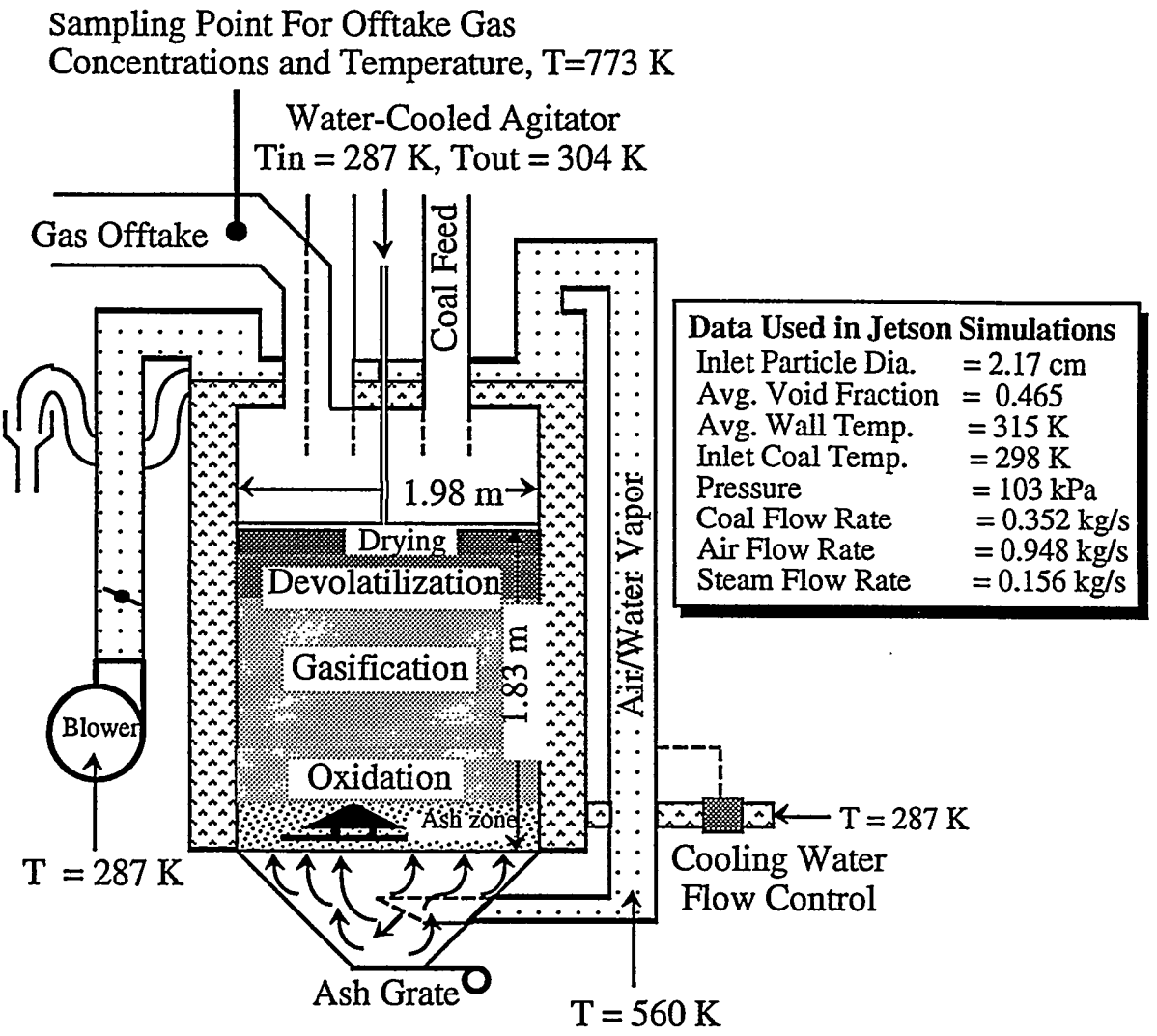

Figure 1.1. Typical atmospheric-pressure, fixed-bed gasifier (Wellman-Galusha), with input data for Jetson simulation (Thimsen et al., 1984).

descends, the hot gases produced in the gasification and combustion zones exchange energy with the colder solid. Water and subsequently volatile matter are released when the solid reaches sufficiently high temperatures. After drying and

devolatilization, the char enters the gasification zone where carbon reacts with steam, carbon dioxide and hydrogen. Endothermic reactions in this section produce carbon monoxide and hydrogen. The slightly exothermic reaction of hydrogen with carbon produces methane. Differentiation between the "gasification zone" and "combustion zone" is based on the presence or absence of free oxygen. Combustion and gasification reactions occur simultaneously in the "combustion zone." The combustible gases such as carbon monoxide and hydrogen may react with oxygen. The exothermic combustion reactions provide the necessary energy for the endothermic gasification reactions and drying. Blast gas, which is composed of steam and oxidant (air or oxygen), is preheated by the hot ash. Part of the process steam is produced by a water jacket surrounding the gasification chamber.

Solid residence times in the drying, gasification and oxidation zones may be on the order of several hours. Residence time in the ash layer may be even higher depending on the thickness of this zone. Gas residence times are on the order of seconds. Solid and gas temperature gradients are highest in the devolatilization and oxidation zones. In the fixed bed gasifiers, as opposed to the entrained and the fluidized bed gasifiers, the devolatilization products are released in the region of relatively low temperature and lack of free oxygen. Thus, tars, oils, and heavier hydrocarbon gases are neither cracked nor oxidized, but added to the product gas. This may be a disadvantage but it may also be used to advantage as in the mild gasification process.

The fixed bed systems have been the focus of significant modeling efforts (Desai and Wen, 1978; Yoon et al., 1978; Amundson and Arri, 1978; Thorness and Kang, 1986; Bhattacharya et al, 1986). Most of these models make simplifying assumptions such as equal gas and solid temperatures, plug flow, constant bed porosity, instantaneous devolatilization and simplified gas phase chemistry. This manual presents a one-dimensional fixed-bed model, FBED-1, in which most of these assumptions are relaxed. The major advances achieved by the FBED-1 model are: (1) A coal general devolatilization submodel which is based on a rigorous functional group, depolymerization, vaporization, and crosslinking submodel (FG-DVC) proposed by Solomon et al., (1988); (2) Generalized gas chemistry to predict the composition of gas phase; (3) Finite, overlapping, drying, devolatilization,

gasification and oxidation zones; (4) Axially variable bed porosity and velocities to properly predict the pressure profile; (5) Ash layer effects; (6) A split back-and-forth shooting method to satisfy the conditions at both boundaries. Furthermore, the FBED-1 model is the first fixed-bed combustion and gasification model which has been extensively validated by comparisons with measured temperature and pressure profiles.

Code Description

This manual presents the details of an advanced, comprehensive, one-dimensional computer code, referred to as FBED-1 (Fixed-BED, 1-dimensional), which describes drying, devolatilization, combustion, and gasification of large coal particles in countercurrent flow. FBED-1 can be used to simulate dry-ash gasifiers, such as the atmospheric pressure Wellman-Galusha gasifier, the medium pressure, METC gasifier, and the high pressure Lurgi gasifier. FBED-1 is a one-dimensional steady-state model that simulates the major conversion processes during coal gasification, namely drying, devolatilization, oxidation and gasification of char with an ash layer, and tar decomposition in the gas phase. It considers separate gas and solid temperatures, axially variable solid and gas velocities, and variable bed void fraction. Coal devolatilization is based on the functional group, depolymerization, vaporization and crosslinking (FG-DVC) submodel (Solomon et al., 1988). A simpler devolatilization submodel, FG-SET, based on functional group composition (Solomon et al., 1988) and tar evolution using a semiempirical correlation (Ko et al., 1988), is also provided as an option. The gas composition is determined by considering either total or partial equilibrium in the gas phase. The input data include reactor dimensions, operating conditions, inlet solid and gas temperatures, pressure, composition, flow rates and wall temperature. The additional input data needed for the devolatilization submodel include the initial functional group composition, and kinetic parameters. For the FG-DVC submodel, bond population and kinetics, cross-link efficiency for each functional group, and probabilities for tar mass distribution are also needed. The predicted quantities include axial solid and gas temperatures, gas phase species concentration, pressure, char conversion, particle size and number density, gas and solid phase flow rates,

residence times, heating rates, velocities, film, ash and chemical resistances, gas phase transport properties, and wall heat loss.

The FBED-1 code is based on a set of 191 coupled, first order ordinary differential equations. These equations simulate the chemical and physical processes taking place in both the gas and the solid phase during the coal conversion in a fixed-bed. The system of differential equations is composed mainly of the overall continuity and energy equations for the gas and solid phases, the solid and gas species and elemental continuity equations, and equations for the functional groups composition in the gas, tar and char. In the FBED-1 model, plug flow is assumed for both solid and gas phase; gas phase pressure drop is determined with Ergun's equation (Ergun, 1952). In addition, an attempt has been made to formulate a general reaction scheme that can accommodate results of future measurements and improved kinetic parameters.

The model presented in this manual applies to countercurrent fixed-bed processes for large particles (>1 mm), where solid heating rates are small (<10 K/s) and gas heating rates are moderate ($<10^4$ K/s). This model is not applicable without modification to cocurrent fixed-bed, entrained-flow or fluidized-bed processes.

Code Development

The formulation and the numerical solution of FBED-1 are based on a previous model, MBED-1, developed by Hobbs et al., (1992). FBED-1 provides the following improvements over MBED-1: 1) improved predictions of product gas composition and temperature; 2) improved prediction of tar flow rate; 3) integration of the devolatilization submodel, FG-DVC; 4) modifications in the iteration scheme to satisfy the gas phase boundary conditions at the bottom of the gasifier; 5) improved modularity, code structure and user friendliness; and 6) improved graphics output. To evaluate and validate FBED-1, several practical cases have been simulated and comparisons have been made with the available experimental data. The appropriate use of this comprehensive code requires a thorough

understanding of its foundations and operation. A person with a strong technical background may require several months to understand and effectively use the code. Results can be obtained faster with the guidance of more experienced users.

Limitations

The assumptions employed in the development of FBED-1 are discussed in detail in Chapters 2 and 3. The input data also require several model parameters which may be difficult to determine from the available experimental data. These parameters include the bed void fraction distribution, the adjustable factor for reacting solid-to-gas heat transfer, and the effective ash diffusivity. Guidelines for specifying these parameters are provided in Chapter 3. The kinetic parameters for devolatilization are assumed to be a function of coal rank. However, the kinetic parameters for the oxidation and gasification reactions are provided by the user and may be either rank dependent or rank independent. The kinetic parameters used herein were obtained from small particle data and may not apply to large particles. However, due to the dominant mass transport effects in large particles, these kinetic parameters are expected to give reasonable predictions.

Document Format

This manual is organized in two parts. Part One documents the theory (Chapters 2-4) and the solution method for the governing equations (Chapter 4-5). An understanding of the theoretical foundations of the code is essential for its correct application, and potential users should study this material carefully. Part Two describes the use of the code (Chapter 6), gives suggestions regarding its implementation on different computer systems (Chapter 7), and presents a sample simulation of the atmospheric pressure Wellman-Galusha gasifier (Chapter 8).

CHAPTER 2

ZERO-DIMENSIONAL SUBMODEL

The core of the fixed-bed model, FBED-1, is a set of 191 coupled, first order ordinary differential equations. These equations simulate the chemical and physical processes taking place in both the gas and the solid phase during the coal conversion in a fixed-bed. Due to the countercurrent flows of gas and solids, these equations constitute a split boundary value problem. The input conditions for the solid phase are known at the top of the gasifier, whereas the input conditions for the gas phase are known at the bottom of gasifier. This system of equations can be converted to an initial value problem and integrated from the top to the bottom of the gasifier, provided the initial estimates for the gas phase quantities are made available at the top of the gasifier. In order to provide these estimates, a zero-dimensional submodel, FBED-0, is proposed and described in this chapter.

FBED-0 is a two-zone, well mixed, partial equilibrium model. Its primary use is to provide estimates for the product gas enthalpy, composition and species flow rates, as well as the product tar composition and flow rate. The zero-dimensional submodel, FBED-0, considers drying and devolatilization on one side, and gasification and oxidation on the other to take place in separate zones. It uses an advanced devolatilization submodel, FG-DVC, which is based on the chemical structure of the coal. It provides an option to use a simpler devolatilization submodel, FG-SET, and a provision to consider tar recycle. FBED-0 can also be used as a stand-alone model to predict the temperature and composition of the effluent gas and tar streams.

Foundations and Assumptions

The basic assumption of the zero-dimensional submodel, FBED-0, is that oxidation and gasification on one hand, and drying and devolatilization on the other occur at different temperatures in separate zones. The rationale behind this assumption is that oxidation and gasification of char take place at relatively high temperatures, as compared to the devolatilization and drying of coal. This temperature difference provides a natural division of the process into two zones -- a higher temperature oxidation and gasification zone, and a lower temperature drying and devolatilization zone. Higher temperatures in the oxidation and gasification region favor total chemical and thermal equilibrium. Lower temperatures in the devolatilization zone may favor partial chemical equilibrium while maintaining thermal equilibrium. In the subsequent discussions, these two zones are referred to as "equilibrium zone" and "drying and devolatilization zone."

In FBED-0, the equilibrium, and the drying and devolatilization zones are assigned different temperatures, $T_{equilibrium}$ and T_{exit}, respectively. All gases are assumed to be in thermal equilibrium in both zones. The gases produced in the equilibrium zone are assumed to be in chemical equilibrium in this zone, but can be considered to be either reactive or nonreactive in the drying and devolatilization zone. The volatile gases and the water vapor produced in the drying and devolatilization zone can also be assumed to be either reactive or nonreactive. Coal is assumed to be composed of various chemical functional groups (Solomon et al., 1988), which evolve to form light gases and tar. The input data for the zero-dimensional model include the gasifier dimensions, operational variables such as pressure, coal and gas flow rates and temperatures, ultimate and proximate analysis of coal, composition of the feed gas, water jacket temperature, wall heat loss or overall heat transfer coefficient, and coal burnout. When the recycled tar is considered, its fraction must also be specified. The computations are based on an overall mass and energy balance. The output of FBED-0 includes the temperatures and compositions of the product gas, product tar and residual solid streams.

Mass and Energy Balance

The two-zone, zero-dimensional submodel has evolved from simpler one-zone total equilibrium and partial equilibrium submodels. In the one-zone submodels, the complete conversion of coal is assumed to take place at a uniform temperature. The gases, however, may be taken to be in total or partial chemical equilibrium. The control volumes for these three submodels are shown in Figure 2.1. The one-zone submodels shown in Figures 2.1.A and 2.1.B are included for comparison only and show the evolution of the two-zone submodel. The mass and energy balances around any control volume shown in Figure 2.1 are given by

$$\dot{m}_{s,in} + \dot{m}_{g,in} - \dot{m}_{s,out} - \dot{m}_{g,out} = 0 \tag{2.1}$$

$$\dot{m}_{s,in}h_{s,in} + \dot{m}_{g,in}h_{g,in} - \dot{m}_{s,out}h_{s,out} - \dot{m}_{g,out}h_{g,out} - Q = 0 \tag{2.2}$$

where $\dot{m}(kg/s)$, $h(J/kg)$, and Q (*watts*) refer to mass flow rate, total enthalpy, and heat loss, respectively. The subscripts *s, g, in* and *out* refer to solid, gas, control volume inlet, and control volume outlet, respectively. The total equilibrium submodel shown in Figure 2.1.A assumes complete reaction of the dry, ash-free coal by either devolatilization, gasification or oxidation. This submodel, however, does not differentiate among mechanisms for these chemical processes as do the one- and two-zone partial equilibrium submodels. The only difference between the one- and two-zone partial equilibrium submodels is the treatment of drying and devolatilization processes. The one-zone submodel assumes that drying and devolatilization occur in the same zone as oxidation and gasification. This assumption is relaxed in the two-zone partial equilibrium submodel.

The total enthalpy of a substance is computed from the enthalpy of formation and the sensible enthalpy:

$$h = h_f^o + h^s \tag{2.3}$$

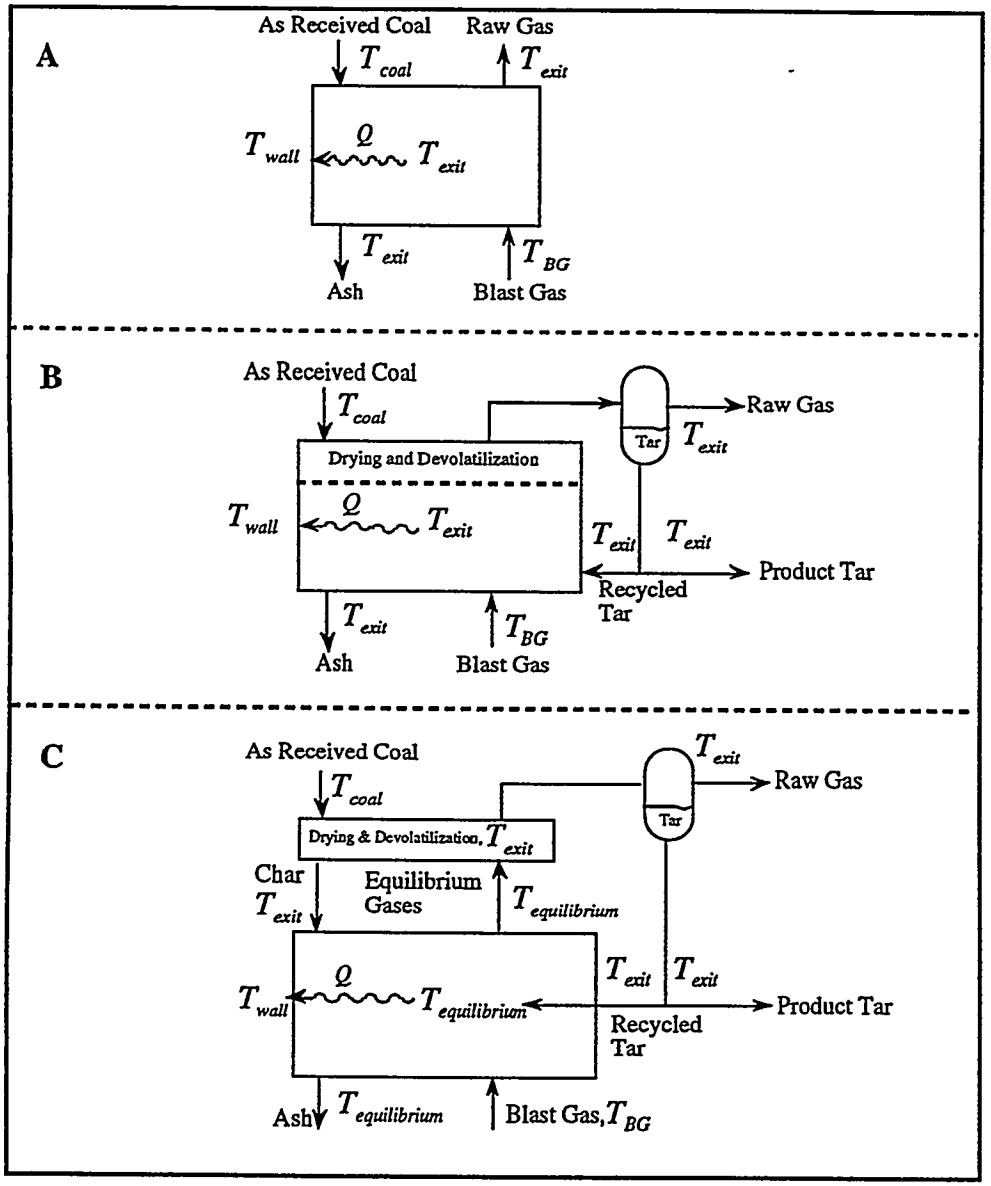

Figure 2.1. Control volume for A) 1-zone total equilibrium submodel, B) 1-zone partial equilibrium submodel, and C) 2-zone partial equilibrium submodel.

where the superscripts o and s refer to the reference temperature (298.15 K) and sensible enthalpy from the reference temperature to the stream temperature.

The heat of formation of the coal can be obtained from its higher heating value, $HHV(J/kg)$, which is the negative of the heat of reaction (i.e., $HHV = -\Delta h_{reaction}$). The higher heating value of coal can be measured or estimated from the ultimate analysis using the Dulong's formula (Perry and Chilton, 1973). Ash effects are included via the experimentally determined HHV. The heat of formation of the coal, $h^o_{f,c}$, is then determined as the sum of the heats of formation of the products from the following reaction:

$$C_nH_mO_hS_jN_k + \left(n + \frac{m}{4} - \frac{h}{2} + j\right)O_2 \rightarrow nCO_2 + \frac{m}{2}H_2O + \frac{k}{2}N_2 + jSO_2 \qquad (2.4)$$

and the higher heating value of the coal:

$$h^o_{f,c} = \sum_{i=1}^{4} \upsilon_i h^o_{f,i} + HHV \qquad (2.5)$$

where i represents the formation of CO_2, $H_2O(l)$, N_2, and SO_2, respectively and υ_i represents the stoichiometric coefficient for the *i-th* product given in Equation 2.4. Since both terms in Equation 2.5 are of similar magnitude and of limited accuracy, error may result in determining the heat of formation of coal, which is a relatively small number, when computed as the difference of these two numbers (Johnson, 1981).

The sensible enthalpy for the coal or char, $h^s_c(J/kg)$, can be determined using the Merrick's (1983) correlation evaluated at 298.15 K and the coal temperature:

$$h^s_c = \left(\frac{R}{a}\right)\left[380g_o\left(\frac{380}{T}\right) + 3600g_o\left(\frac{1800}{T}\right)\right] \qquad (2.6)$$

$$g_o(z) = \frac{1}{exp(z) - 1} \tag{2.7}$$

where R (8314.4 $J/kmol \cdot K$) is the universal gas constant, T (K) is solid temperature, 380 and 1800 (K) are characteristic Einstein temperatures, and z is a dummy variable representing the ratio of the Einstein temperature and T. The mean atomic weight, a, is defined (Merrick, 1983) as

$$\frac{1}{a} = \sum_{i=1}^{5} \frac{\Omega_i}{\mu_i} \tag{2.8}$$

where μ_i and Ω_i represent the atomic weights and dry-ash free mass fraction of carbon, hydrogen, oxygen, nitrogen and sulfur respectively.

The specific heat of the ash, Cp_a ($J/kg \cdot K$), can be determined from Kirov's correlation (Merrick, 1983), given by:

$$Cp_a = 754 + 0.586\,t \tag{2.9}$$

where t ($°C$) is the ash temperature. The Kopp-Neumann rule (Mills and Rhine, 1989) can also be used to obtain reliable estimates of the ash heat capacity, provided various constituents of the ash are known:

$$C_{p_a} = 1000 \left(\frac{\sum_{i=1}^{n} x_i C_{p_i}}{\overline{M}_w} \right) \tag{2.10}$$

where x_i, $C_{p_i}(J/mol \cdot K)$, and $\overline{M}_w$ represent the mole fraction of the i-th ash constituent, partial molar heat capacity of the pure i-th component, and the average molecular weight of the ash or slag. The temperature dependence of ash heat capacity, C_p, is expressed as $C_p = a + bT - cT^{-2}$. The values of the coefficients a, b, and c for ash constituents used in the present formulation are given in Table 2.1. Equation 2.10 can

Table 2.1. Partial molar heat capacity of slag components used in Kopp-Neumann rule.§

Ash	M_w	$C_{p_i}(J/molK) = a + bT - CT^{-2}$ (solid)			C_p (liquid)
Component	*kg/kmol*	*a*	*b*	*c*	*J/molK*
SiO_2	60.09	53.591	1.8715×10^{-2}	1.2644×10^{6}	87.0
CaO	56.08	41.868	2.0264×10^{-2}	4.5217×10^{5}	80.8
Al_2O_3	101.96	92.445	3.7560×10^{-2}	2.1876×10^{6}	146.4
MgO	40.31	45.469	5.0116×10^{-3}	8.7379×10^{5}	90.4
K_2O‡	94.2	65.700	2.2600×10^{-2}	0.0	74.0
Na_2O‡	61.98	65.700	2.2600×10^{-2}	0.0	92.0
TiO_2	79.9	49.446	3.1568×10^{-2}	1.7543×10^{5}	111.7
MnO	70.94	31.108	4.3459×10^{-2}	5.5156×10^{-5}	79.9
FeO	71.85	52.84	6.2470×10^{-3}	3.1903×10^{5}	76.6
Fe_2O_3	159.7	103.50	6.7156×10^{-2}	1.7727×10^{6}	191.2
Fe‡	55.85	12.72	3.1710×10^{-2}	-2.5100×10^{5}	43.9
P_2O_5‡	141.91	182.5	4.6400×10^{-2}	4.5440×10^{6}	242.7
CaF_2‡	78.08	59.83	3.045×10^{-2}	-1.9600×10^{5}	96.2
SO_3‡	80.06	70.2	9.774×10^{-2}	0.0	175.7

§ All solid heat capacity coefficients obtained from Perry's Handbook (1973, page 3-119) except as noted. All liquid heat capacity values are obtained from Mills and Rhine (1989).

‡ Solid heat capacity coefficients obtained from Mills and Rhine correcting b and c by 10^{-3} and 10^{5}, respectively.

also be used to determine the heat capacity of the liquid slag. In that case, melting is assumed to occur at the measured ash fluid temperature, and the associated enthalpy of fusion is taken to be $230\ J/g$ following Mills and Rhine (1989). The predicted temperatures of the solid phase were found to be insensitive to the enthalpy of fusion; therefore a single value for enthalpy of fusion is used for coals of all ranks.

The total enthalpies of the feed gases are found with the polynomial expressions obtained by the regression analysis of the thermochemical data given in the JANAF tables (Stull and Prophet, 1971).

The final term in Equation 2.2 represents the heat loss through the reactor wall, Q (*watts*). This quantity can be estimated provided the jacket steam flow rate is known. Otherwise, the heat loss through the wall can be calculated using the following expression, which requires that the overall heat transfer coefficient, U ($watts/m^2K$), be known:

$$Q = UA(T_e - T_w) \tag{2.11}$$

where A, T_e, and T_w represent the surface area of steam jacket, the equilibrium zone temperature, and the wall temperature, respectively. The values of the overall heat transfer coefficient, U, are usually in the range from 50 to 200 $watts/m^2K$, which represent the forced convection regime.

Gas Phase Chemistry

Most of the currently available fixed-bed models compute the gas phase composition by assuming the major gaseous species (CO, CO_2, H_2, and H_2O) to be in equilibrium, following the water-gas-shift reaction. Furthermore, these models do not account for the minor species in the equilibrium calculations. In FBED-0, all gaseous species are fully taken into account, and the gas composition can be determined based on either total or partial equilibrium in the gas phase. A mixture is said to be in partial equilibrium if at least one of its constituent species is considered to be out of chemical equilibrium. The "out of equilibrium" species may be chemically frozen or undergo changes following certain reactions with finite rate kinetics.

In FBED-0, minor species such as higher hydrocarbons (C_2H_2, C_2H_4, C_2H_6, C_3H_6, C_3H_8, C_4H_{10}, etc.), and nitrogenous species (HCN, NO, and NH_3) are fully treated. The gas phase in the equilibrium zone is assumed to be in total

chemical and thermal equilibrium. The composition and temperature are determined, using a generalized chemical equilibrium code, CREE (Pratt, 1979), by minimizing the Gibbs free energy, given the total static enthalpy, pressure and elemental composition of the gas phase. In the drying and devolatilization zone, thermal equilibrium is assumed, but the gas phase composition is determined using one of the following two options: 1) total chemical equilibrium is assumed for the gas phase; 2) the gases generated in the oxidation and gasification zone as well as the devolatilized gases and moisture released in the drying and devolatilization zone are assumed to be nonreactive. In both of these options, the tar evolved from the coal is taken to be in thermal equilibrium but kept out of chemical equilibrium. In countercurrent, fixed-bed gasifiers, the assumptions regarding nonreacting species may be justified due to the low temperature in the drying and devolatilization zone, which prevents further reactions of the volatile gases and moisture with the gases produced in the equilibrium zone.

Devolatilization

During the devolatilization process, as much as 40-60 percent of the dry-ash free mass of feed coal is evolved as light gases and tar. A precise treatment of devolatilization is, therefore, essential to predict accurately the yield of volatiles and the composition of residual char and volatiles. In FBED-0, two devolatilization submodels FG-DVC and FG-SET are provided. In both submodels, char is assumed to be composed of various functional groups, which evolve to yield both light gases and tar. The main difference between these two models is in the treatment of tar evolution from the char matrix. The FG-DVC submodel computes the tar evolution from the char, based on the coal structure. The simpler FG-SET model uses a semiempirical correlation to determine the potential tar forming fraction, x^o, and tar evolution is assumed to follow a first order decay of x^o. It also provides an option to allow for user specified tar-forming fraction. The functional group composition is only available for a select group of standard coals, such as Argonne Premium Coals. In order to use the available data, the functional group composition of the standard coal, which is closest to the feed coal, must be adjusted to match the ultimate composition of the feed coal. The guidelines to adjust the

functional group composition are presented in Appendix A. The FG-DVC submodel is presented and discussed in Chapter 4; the simpler FG-SET submodel is presented in Appendix B.

Ultimate Yields and Compositions

In the zero-dimensional submodel, the ultimate char, tar, and gas yields and composition are determined by integrating the set of differential equations, from time zero to infinity (taken as a suitably large value). After the integration, the ultimate yields, ω_c^∞, ω_t^∞, and ω_g^∞, are readily obtained using the following expressions:

$$\omega_t^\infty = \sum_{i=1}^{nfg} W_{Tar,i}^\infty \tag{2.12}$$

$$\omega_g^\infty = \sum_{i=1}^{nfg} W_{gas,i}^\infty \tag{2.13}$$

$$\omega_c^\infty = \sum_{i=1}^{nfg} y_i^\infty \tag{2.14}$$

The ultimate volatiles yield, ω_v^∞, is by definition sum of the tar and the gas ultimate yields, ω_t^∞ and ω_g^∞, and thus from Eqns. 2.12 and 2.13:

$$\omega_v^\infty = \sum_{i=1}^{nfg} \left(W_{gas,i}^\infty + W_{Tar,i}^\infty \right) \tag{2.15}$$

The compositions of the devolatilized tar, gas and residual char are then determined by the following expressions:

$$\chi_{gas,j} = \sum_{i=1}^{nfg} W^{\infty}_{gas,i} \chi_{FG,i,j} \tag{2.16}$$

$$\chi_{Tar,j} = \sum_{i=1}^{nfg} W^{\infty}_{Tar,i} \chi_{FG,i,j} \tag{2.17}$$

$$\chi_{char,j} = \sum_{i=1}^{nfg} y_i^{\infty} \chi_{FG,i,j} \tag{2.18}$$

where $\chi_{FG,i,j}$ is the mass fraction of the *j-th* element in the *i-th* functional group.

Oxidation and Gasification

Oxidation and gasification in FBED-0 are treated by specifying the total burnout and accounting for devolatilization. The elemental mass from the residual char (i.e., after devolatilization) is released to the gas phase, and the composition and temperature are then determined assuming total equilibrium. The sensitivity of temperature and composition to specified burnout is discussed further by Hobbs et al., (1992b). The paper by Hobbs et al., (1992b) is included in this manual as Appendix C. If no estimate is available for burnout, a value of unity (i.e., 100% burnout) is recommended. Long solid residence times and high oxygen concentrations and temperatures in the equilibrium zone justify this assumption for fixed-beds.

Freeboard

The freeboard is the void space directly above the coal bed. The two-zone submodel predicts the temperature at the top of the coal bed, which is greater than

the temperature at the sampling point due to heat loss in the water-cooled freeboard. The freeboard temperature, T_{fb} (K), can be determined by doing an energy balance around the freeboard zone and accounting for heat loss in this section, Q_{fb} (watts), as follows:

$$T_{fb} = T_{exit} + \frac{Q_{fb}}{\dot{m}_{gas} Cp_{gas}} \tag{2.19}$$

where T_{exit} (K), $\dot{m}_{gas}(kg/s)$, and $Cp_{gas}(J/kgK)$ are the exit temperature, exit gas mass flow rate, and exit gas heat capacity, respectively. The gas heat capacity is computed at the freeboard temperature and requires an iterative procedure. The freeboard temperature is the temperature usually reported in the literature. For the air-blown, Wellman-Galusha gasifier, the temperature drop from the bed top to the sampling point is on the order of 10-20 K. Quantitative agreement between measured exit temperature and predicted exit temperature is not expected, since the zero-dimensional assumption gives an average temperature in the drying and devolatilization zone that is significantly higher than the exit temperature. However qualitative comparisons are possible and have been discussed by Hobbs et al., (1992b).

Summary

A zero-dimensional submodel, FBED-0, has been developed and discussed. The motivation for developing the two-zone fixed-bed submodel was to provide an initial estimate of effluent compositions and temperatures for the one-dimensional, fixed-bed model, which is discussed in detail in chapter 3. This two-zone, partial equilibrium submodel uses an advanced devolatilization submodel and a partial equilibrium gas phase submodel to predict effluent temperature and composition. Effluent composition is determined for all the major species and a number of minor species. Tar recycle is taken into account. The key assumption for the two-zone submodel is that oxidation and gasification occur at relatively high temperature compared to the colder drying and devolatilization zone. The temperature difference provides a natural division of the process into two zones. High temperature in the

oxidation and gasification zone favors total equilibrium in the gas phase. Lower temperature in the drying and devolatilization zone favors partial equilibrium. The limitations to the two-zone submodel are a need to specify burnout and uncertainty in wall heat loss estimates. The solution method to solve the equations for FBED-0 is discussed in Chapter 5.

CHAPTER 3

ONE-DIMENSIONAL FIXED-BED MODEL

The zero-dimensional submodel described in Chapter 2 can be used to estimate the temperature and composition of the product gas and the product tar. However, in order to design a gasifier or analyze the performance of an existing gasifier, additional information, such as temperature and composition profiles in the gasifier bed, is needed. Information such as peak solid temperature may also be needed to design a specific type of gasifier, e.g., dry-ash gasifier or a slagging gasifier. In order to predict these desired quantities, a one-dimensional fixed-bed model, FBED-1, is presented and discussed in this chapter. FBED-1 can predict axial solid and gas temperatures, species concentrations, pressure, char consumption rate, particle size and number density, gas and solid flow rates, residence times, heating rates, velocities, and wall heat loss. These predictive capabilities of FBED-1 make it a potentially important tool for design and analysis of coal gasification units. FBED-1 is a one-dimensional, steady-state model that considers separate gas and solid temperatures, axially variable solid and gas velocities, variable bed void fraction, devolatilization based on FG-DVC submodel, coal drying, oxidation and gasification of char with an ash layer, and gas composition based on either total or partial equilibrium in the gas phase. Input data include reactor dimensions, operating conditions, inlet solid and gas temperatures, pressure, concentrations, flow rates and wall temperature. The output data, in addition to the quantities listed above, include auxiliary quantities such as film, diffusion and chemical resistances, gas phase transport properties, and heat and mass transfer coefficients. The FBED-1 model is described by a system of 191 coupled, ordinary differential equations. These equations are integrated using the LSODE (Livermore Solver for Ordinary Differential Equations) package. The zero-dimensional submodel presented in Chapter 2 is used to provide the initial effluent

gas properties needed to perform the integration of the system of equations for the one-dimensional model.

Foundations and Assumptions

The conservation equations for mass and energy form the foundation of the FBED-1 model. The gas and solid phase equations are coupled through the source terms. These source terms account for the release of mass from the solid phase to the gas phase, and energy exchange between the two phases. The source terms in the continuity and energy equations are described by various physical and chemical submodels. Plug flow is assumed in both the solid and the gas phase with variable axial velocities. Gas phase pressure drop is calculated with the Ergun equation for packed beds (Ergun, 1952). An effective heat transfer coefficient is used for heat loss to the wall, including both stagnant and dynamic contributions, as well as conduction and diffusive radiation. Drying and devolatilization are allowed to occur simultaneously with char oxidation and gasification. Oxidation and gasification of char are described by either shell progressive or a shrinking core ash segregation submodel. Chemical equilibrium is assumed to calculate gas concentrations and temperature. Turbulence is not treated formally in the slowly moving bed with low gas velocities, but is included implicitly through correlations such as for the effective heat transfer coefficient. Primary assumptions employed in the development of the one-dimensional fixed-bed model (FBED-1) are listed in Table 3.1.

The basis and justifications of these assumptions are now discussed. The one-dimensional assumption can be justified by following the development of Yoon et al., (1978). The fixed-bed reactor may consist of an adiabatic core and a boundary layer. The boundary layer thickness, ℓ (m), can be calculated from the following equation (Carslaw and Jaeger, 1959):

$$\ell = \sqrt{\frac{k_e \tau}{\rho C_p}} \tag{3.1}$$

Table 3.1 Primary assumptions for the one-dimensional, fixed-bed model (FBED-1)

1. The moving-bed is one-dimensional.
2. Interdiffusion (diffusional transport of kinetic energy and enthalpy) is small compared to chemical reactions.
3. Both particles and gases are treated as a continuum.
4. Pressure is uniform at control surfaces surrounding particles.
5. Viscous heating is negligible.
6. Aerodynamic drag is negligible.
7. Conduction, radiation and convection to the wall are combined in an effective bulk heat transfer term.
8. Work performed by moving particles is negligible.
9. Work due to body forces is small compared to chemical reaction terms.
10. Work associated with particle volume changes is small.
11. Soret and Dufour effects are negligible.
12. Axial diffusion is negligible.
13. The ideal gas law is valid.
14. PV-work is negligible.
15. Viscous dissipation is negligible.
16. Turbulence effects are implicitly included in the effective heat transfer correlation.
17. The solid phase internal energy is equal to the solid phase enthalpy.
18. Particles are isothermal.
19. Feed coal is represented by a single type, and particles are assumed to be of uniform size.

where k_e, τ, ρ, and Cp represent the effective radial thermal conductivity ($w/m\,K$), residence time of the coal in the gasifier (s), apparent density of the coal (kg/m^3), and heat capacity of the coal ($J/kg\,K$), respectively. Hobbs (1990) estimated the boundary layer thickness in a Wellman-Galusha gasifier to be approximately 0.07 m, which when compared to the reactor diameter (2 m), justifies the one-dimensional assumption. However, two-dimensional models may be necessary to investigate wall effects or details near the grate.

The ideal gas assumption is justified because of relatively low pressure operation and high temperatures. The compressibility factor is essentially unity for conditions applying to both the Lurgi and Wellman-Galusha gasifiers; this justifies the use of the ideal gas law in the fixed-bed model.

Yu (1981) discusses the steady-state operation of a fixed-bed gasifier at partial load. As the coal feed rate is reduced, the relative importance of convection to dispersion is lessened. Yu's calculation with and without axial dispersion indicates that when the coal feed rate is less than ten percent of full load, axial dispersion of heat is important and should be considered. However, mass dispersion is small for all conditions and can be neglected. Axial dispersion at low coal flow rates affects the predicted temperature profile by moving the profile axially and decreasing the temperature peak slightly. Young and Finlayson (1976) give the following criteria for neglecting axial diffusion:

$$\frac{d_p M_w}{Pe_m^a \rho_g u_z} \sum_i \sum_j r_j \alpha_{ij} << 1 \tag{3.2}$$

$$\frac{d_p}{Pe_h^a \left(H_g - H_s\right)} \sum_j \left(-\Delta H_j\right) r_j << 1 \tag{3.3}$$

where d_p, M_w, Pe_a^m, Pe_h^a, ρ_g, u_z, r_j, α_{ij}, H_g, H_s, and ΔH_j represent the particle diameter, particle molecular weight, axial mass Peclet number, axial thermal Peclet number, gas density, gas velocity, reaction rate, stoichiometric coefficient for the *j-th* reaction, convective heat flux of gas and solid, and the *j-th* reaction enthalpy, respectively. Denn et al., (1982) give the magnitude of the expressions in Equations 3.2 and 3.3 as 0.0001 for fixed-bed reactors operating under full load. Denn et al., (1982) also show that axial thermal dispersion is equal to axial thermal convection at a flow rate of 1% of the normal load. Denn further states that axial mass dispersion is not important even at 1% of normal load. However, axial dispersion of heat is significant when the coal feed rate is less than 10% of full load (Yu, 1981). Negligible axial diffusion also implies negligible Dufour and Soret effects.

The importance of pressure-volume work (PV-work) can be shown by comparing the term $v_z \frac{\partial P}{\partial z}$ with its counterpart $\rho_g C p_g v_z \frac{\partial T}{\partial z}$ (Khanna and Seinfeld, 1987):

$$\frac{v_z \frac{\partial P}{\partial z}}{\rho_g Cp_g v_z \frac{\partial T}{\partial z}} \approx \frac{\Delta P}{\rho_g Cp_g \Delta T} << 1 \qquad (3.4)$$

PV-work can be neglected if Equation (3.4) is satisfied. For a dry-ash Lurgi gasifier at typical operating conditions, the quantity $\frac{\Delta P}{\rho_g Cp_g \Delta T}$ is approximately 0.0001, which justifies neglecting PV-work (Hobbs, 1990).

In FBED-1, multidimensional effects such as viscous dissipation and turbulence are included implicitly via correlations such as for the heat transfer and mass transfer coefficients.

Conservation Equations

The conservation equations for the one-dimensional, fixed-bed model are listed in Table 3.2. These equations are classified as gas and solid overall continuity, gas and solid energy equations, and gas and solid species or elemental continuity equations. The constitutive relations for solid flow have been only proposed recently, and no solution for these equations has been attempted (Gray and Stiles, 1988). Thus, only differential equations for continuity and energy are treated in the model described herein. Table 3.2 shows only the conservation equations for gas and solid phase. Remaining equations are related to the devolatilization and tar cracking submodels and will be discussed later.

The derivation of the two phase conservation equations can be found in Crowe and Smoot (1979). The conservation equations in Table 3.2 show reaction source terms that represent drying, devolatilization, char oxidation and gasification. These chemical and physical processes are shown in Figure 3.1, which depicts a conceptual coal particle divided into various functional groups, including moisture and ash. Drying is assumed to be diffusion-limited, and devolatilization is

Table 3.2 Conservation Equations for FBED-1

Overall Gas Continuity	$\frac{dW_g}{dz} = A\sum_{i=1}^{6} r_i$	(1)
Overall Solid Continuity	$\frac{dW_s}{dz} = -A\sum_{i=1}^{6} r_i$	(2)
Gas Phase Energy	$\frac{dW_g h_g}{dz} = A(Q_{sg} - Q_{gw} + \sum_{i=1}^{6} r_i h_{g,i})$	(3)
Solid Phase Energy	$\frac{dW_s h_s}{dz} = A(-Q_{sg} - Q_{sw} - \sum_{i=1}^{6} r_i h_{g,i})$	(4)
Gas Phase Species Continuity	$\frac{dW_{g,\ell}}{dz} = A\sum_{i=1}^{6} r_{i,\ell}^{gas}$	(5-26)
Gas Phase Elemental Continuity	$\frac{dW_{g,j}}{dz} = A\sum_{i=1}^{6} r_{i,j}^{gas}$	(27-31)
Overall Tar Continuity	$\frac{dW_{tar}}{dz} = Ar_d^{tar}$	(32)
Tar Elemental Continuity	$\frac{dW_{tar,j}}{dz} = Ar_{d,j}^{tar}$	(33-37)
Moisture Continuity	$\frac{dW_{moisture}}{dz} = -Ar_{drying}$	(38)

1. Equations 39-164 describe the FG-DVC devolatilization submodel presented in Chapter 4.
2. Equations 165-191 describe the lower bound of the distribution function for the gas phase tar cracking reactions and follow the FG-DVC formulation.
3. Equations 5-26 are solved only when the gas phase is not considered to be in chemical equilibrium.
4. i=1-6 represents drying, devolatilization, CO_2, H_2, H_2O gasification, and oxidation reactions respectively.
5. j=1-5 represents elements C, H, O, N, and S respectively.
6. l=1-22 represents 22 gaseous species considered in FBED-1.

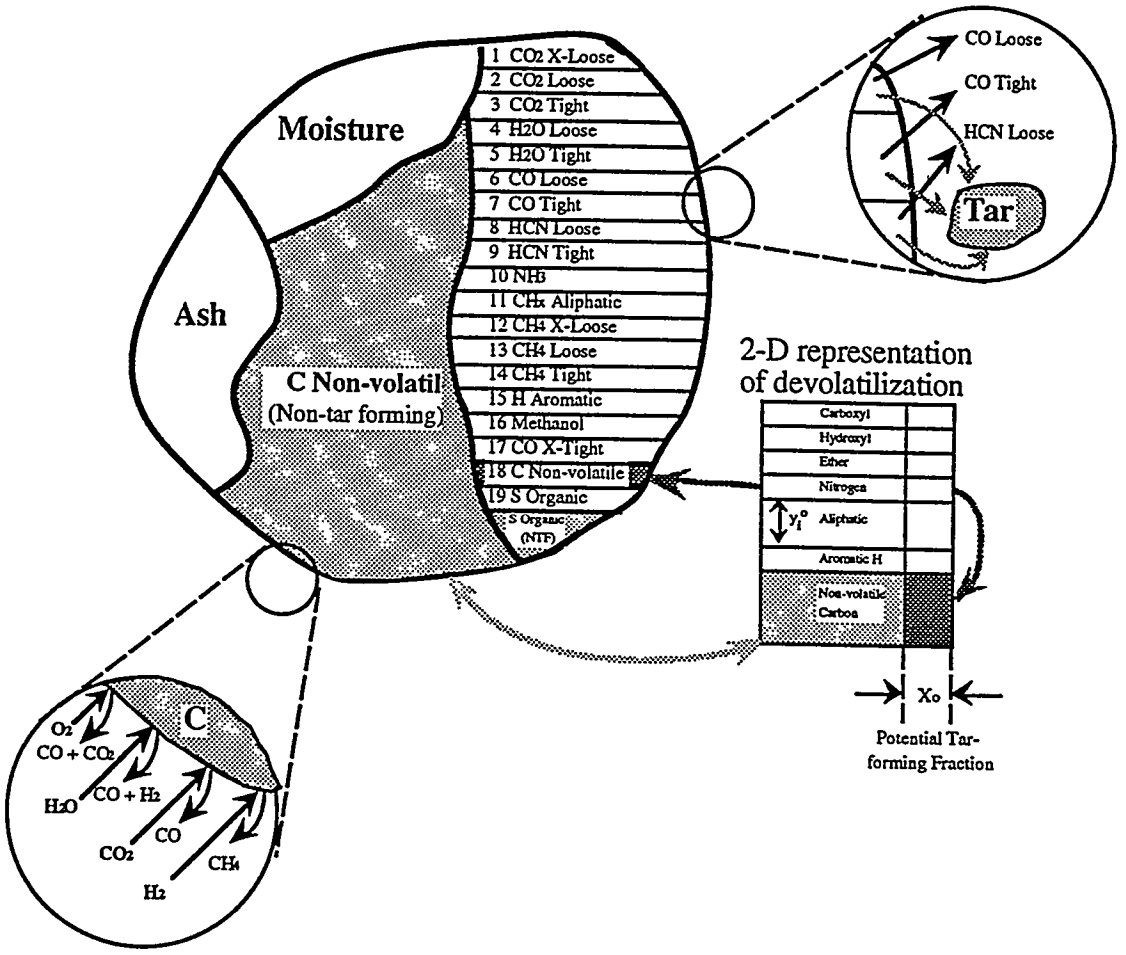

Figure 3.1. Schematic of a coal particle with FG-SET devolatilization model based on chemical functional groups (Solomon et al., 1988).

described by assuming that the organic portion of the coal particle is composed of various functional groups such as carboxyl, hydroxyl, ether, nitrogen, etc. A functional group model (FG model) has been used to describe the evolution of light gases from the char, and the evolution of tar is based on DVC submodel (Solomon and Hamblen, 1985; Serio et al., 1987; and Solomon et al., 1988). The coal

dependent kinetics is used for the FG-DVC submodel, which is discussed in Chapter 4. A simpler devolatilization submodel, FG-SET, also provided as an option, is discussed in Appendix B.

Oxidation and gasification reactions act on all functional groups. As shown in Figure 3.1, three gasification agents are considered: steam, carbon dioxide, and hydrogen. The volatile functional groups can competitively evolve as either light gases or tar. In FBED-1, tar and char are treated as single species which have a variable composition, depending on the location in the reactor.

Gas temperature is determined by assuming all gas species to be in thermal equilibrium. Gas phase composition is determined by Gibbs free energy minimization. Solid temperature is determined from the solid enthalpy and the elemental composition of the char. All gas phase transport properties (conductivity, viscosity, diffusivity, etc.) are considered to be functions of both temperature and composition.

Overall Gas and Solid Continuity Equations

The overall gas and solid species continuity equations are given by Equations 1 and 2 in Table 3.2. The gas and solid flow rates are represented by W_g (kg/s) and W_s (kg/s), respectively. The axial distance and cross sectional areas are represented by z (m) and A (m^2), respectively. The volumetric reaction rate is represented by r_i (kg/m^3s), where i depicts the different processes and heterogeneous reactions, such as drying, devolatilization, char gasification, and char oxidation. Summation of Equations 1 and 2 in Table 3.2 results in the overall continuity equation, with a zero source term that represents conservation of mass. Reaction rates are written as the volumetric rate of mass addition to the gas phase; thus a positive rate signifies a source of mass for the gas phase and a sink for the particle phase. The submodels used to determine these source terms are discussed later in this chapter.

Gas and Solid Energy Equations

The gas and solid energy equations are given by Equations 3 and 4 in Table 3.2. The total gas and solid enthalpies are represented by h_g (J/kg) and h_s (J/kg).

The energy exchange between solid and gas is represented by Q_{sg} (w/m^3). The heat losses to the wall from the gas and solid phases are represented by Q_{gw} (w/m^3) and Q_{sw} (w/m^3), respectively. Calculation of Q_{sg}, Q_{gw}, and Q_{sw} will be discussed later. The last term in the energy equations represents the energy exchange due to the coal decomposition processes i.e., drying, devolatilization, and heterogeneous reactions of char with CO_2, H_2, H_2O and O_2. A discussion of these equations is presented in later sections.

Heat of Vaporization - The heat of vaporization accounts for the energy exchange due to drying of the feed coal. This term is calculated as

$$h_{total}^{vap} = h_f^o + h_{vap}(T_s) + h_s(T_s) \tag{3.5}$$

where h_f^o is heat of formation of H_2O, $h_{vap}(T_s)$ is the heat of vaporization of water at the solid temperature, and $h_s(T_s)$ is the sensible heat from the reference temperature to the solid temperature.

Heat of Devolatilization - The energy exchange due to devolatilization is computed following the model proposed by Merrick (1983). The Merrick's model, which considers 9 species, including tar, was extended to accommodate 27 functional groups of the FG-DVC devolatilization submodel. The resulting equations are

$$\frac{dh_{devel}}{dt} = \sum_{k=1}^{nfg+1} \frac{\partial q}{\partial m_k} \frac{dm_k}{dt} \qquad (W/kg) \tag{3.6}$$

where

$$\frac{\partial q}{\partial m_k} = \sum_{j=1}^{5} A_{jk} \left(\lambda_j - \Phi_j + \frac{f(\overline{T})}{\mu_i} \right) - h_k \tag{3.7}$$

$$\frac{dm_k}{dt} = r_{d,k}^{gas} \qquad (k = 1, \ldots, nfg) \tag{3.8}$$

$$\frac{dm_{nfg+1}}{dt} = \sum_{k=1}^{nfg} r_{d,k}^{tar} \tag{3.9}$$

Heat of Reactions - The heat of reaction for the gasification and oxidation reactions of char can be calculated by performing an energy balance around the particle/gas interface. The location within the particle and the temperature at which the reaction occurs must be assumed. The energy exchange at the solid-to-gas interface due to transport of mass between the two phases during heterogeneous oxidation is shown in Figure 3.2. Solid conduction and solid-to-gas energy exchange are not shown. Since the products of heterogeneous reactions leave at the solid temperature, the energy exchange due to these reactions can be viewed as a nonisothermal heat of reaction. The enthalpy terms shown in Figure 3.2 are total enthalpies at the indicated temperature. Furthermore, the reaction rates are based on the given species and stoichiometry of the given reaction. A sample calculation of the enthalpy associated with the term $r_i h_{g,i}$ for the oxidation reaction is given in Table 3.3. The heats of reactions for the gasification reactions can be calculated in a similar manner.

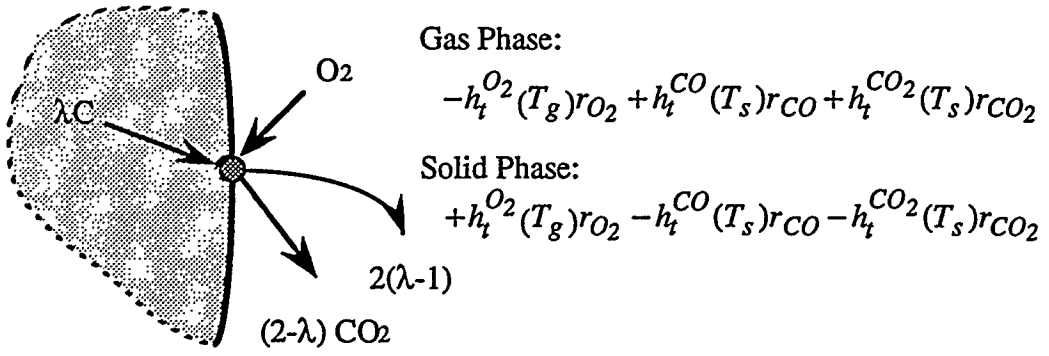

Figure 3.2. Energy exchange due to the transport of mass between solid and gas phase due to oxidation.

Table 3.3 Enthalpy exchange associated with the oxidation reaction .

Oxidation Reaction:

$$\lambda C + O_2 \rightarrow 2(\lambda - 1)CO + (2 - \lambda)CO_2$$

Formation Enthalpies:§

$$h_f^{CO}, \frac{J}{kg(carbon)} = -9.203 \times 10^6 \frac{2(\lambda - 1)}{\lambda}$$

$$h_f^{CO_2}, \frac{J}{kg(carbon)} = -3.276 \times 10^7 \frac{(2 - \lambda)}{\lambda}$$

$$h_f^{O_2}, \frac{J}{kg(carbon)} = 0.000$$

Sensible Enthalpies:‡

$$h_s^{CO}(T_s), \frac{J}{kg(carbon)} =$$

$$83.25\left[\frac{2(\lambda - 1)}{\lambda}\right]\left[28.41(T_s - 298) + 0.0041\left(T_s^2 - 298^2\right) + 4.6 \times 10^4\left(\frac{1}{T_s} - \frac{1}{298}\right)\right]$$

$$h_s^{CO_2}(T_s), \frac{J}{kg(carbon)} =$$

$$83.25\frac{2 - \lambda}{\lambda}\left[44.22(T_s - 298) + 0.00879\left(T_s^2 - 298^2\right) + 8.62 \times 10^5\left(\frac{1}{T_s} - \frac{1}{298}\right)\right]$$

$$h_s^{O_2}(T_g), \frac{J}{kg(carbon)} =$$

$$\frac{83.25}{\lambda}\left[29.96(T_g - 298) + 0.00418\left(T_g^2 - 298^2\right) + 1.67 \times 10^5\left(\frac{1}{T_g} - \frac{1}{298}\right)\right]$$

Table 3.3 Enthalpy exchange associated with the oxidation reaction (continued).

Enthalpy Exchange due to oxidation:

$$r_i h_{g,i}, \frac{J}{m^3 s} = r_{O_2}[(h_f^{CO} + h_s^{CO}) + (h_f^{CO_2} + h_s^{CO_2}) - (h_f^{O_2} + h_s^{O_2})], \quad i = oxidation$$

§ Formation enthalpies are from Laidler and Meiser (1982, page 66). Units for the heat of formation are on carbon basis. For example, the heat of formation for CO can be calculated as follows:

$$-9.203 \times 10^6 \frac{2(\lambda - 1)}{\lambda} = \left(-110.54 \frac{KJ}{molCO}\right)\left(\frac{1000J}{KJ}\right)\left[\frac{2(\lambda - 1)molCO}{\lambda molC}\right]\left(\frac{molC}{12.01115g\ C}\right)\left(\frac{1000g\ C}{kgC}\right)$$

‡ Sensible enthalpies are taken from Laidler and Meiser (1982, page 63) by integration of gas heat capacity.

Gas Phase Elemental Continuity Equations

The mass rate of change of each reactive element in the gas phase is given by Equations 27-31 in Table 3.2. These elements include C, H, O, N, and S. Elements related to inert species such as argon do not take part in any reaction, thus eliminating the need for a differential equation. The term $r_{i,j}$ represent the volumetric evolution rate of the *j-th* element contributed by the *i-th* reaction. These reactions include drying, devolatilization, and heterogeneous oxidation and gasification reactions of char; these are discussed later in this chapter. The gas phase elemental continuity equations include the contribution of tar.

Overall and Elemental Continuity Equations for Tar

Tar, which is part of the gas phase, is treated as a pseudospecies in FBED-1. The use of the advanced devolatilization submodel makes tracking of tar throughout the reactor bed possible. Tar can be either assumed to be nonreactive in the gas phase, which would classify the one-dimensional model as a partial equilibrium model, or assumed to react to completion in the gas phase. The evolution of tar is based on either FG-DVC or FG-SET submodel; these are presented in Chapter 4 and Appendix B respectively. The overall tar continuity is

given by Equation 32; its elemental continuity is given by Equations 33-37 of Table 3.2.

Solid Species Continuity Equations

The solid particle is represented as being composed of moisture, ash, and organic functional groups, as depicted in Figure 3.1. Ash is considered inert and does not require a differential equation. Moisture is released during the drying of the coal particles; the equations governing the drying process have been discussed previously. The composition of the char is updated from the instantaneous functional group composition of the char. It should be noted that the functional groups are depleted by devolatilization and gasification, as well as by oxidation reactions.

Pressure Drop

The pressure drop in the reactor is calculated from the Ergun's equation (Ergun, 1952):

$$-\Delta P_t = \frac{fLG^2}{g\rho_g d_p} \tag{3.10}$$

$$f = \frac{1-\varepsilon}{\varepsilon^3}\left(1.75 + 150\frac{1-\varepsilon}{Re}\right) \quad for \frac{RE}{1-\varepsilon} < 500 \tag{3.11}$$

where P_t, g, ρ_g, d_p, L, G, and f represent total pressure ($kg\,force/m^2$), acceleration due to gravity (9.81 m/s^2), gas density (kg/m^3), particle diameter (m), reactor length (m), superficial gas mass flux (kg/m^2s), and friction factor, respectively. Ergun's equation is used to determine pressure drop, since Reynolds numbers are typically less than 500 in fixed-bed coal gasifiers. Although the pressure drop in a fixed-bed reactor is relatively small, it is sensitive to the bed void fraction, ε, as

shown in Equations 3.10 and 3.11, and can be used to determine if the bed void fraction distribution is appropriate.

Gas Phase Chemistry

The composition and temperature of the gas phase are determined by total or partial equilibrium submodels. In the total equilibrium submodel, all gaseous species, including tar, are assumed to be in chemical and thermal equilibrium. For the partial equilibrium option, tar is held out of chemical equilibrium. In this case, the remaining gaseous species are taken to be in equilibrium. However, an option is provided to prevent the gases from reacting to equilibrium below a user specified temperature. This option is mainly exercised during drying and devolatilization when the gas phase temperature is low. Gas phase kinetics would be required to hold certain gas species out of equilibrium in the high temperature region. For all these options, all species, including tar, are considered to be in thermal equilibrium. Equations 5-26 (Table 3.2) are solved only when the gas phase is assumed to be out of chemical equilibrium. Otherwise, the gas phase species concentrations are computed from the equilibrium submodel.

Heat and Mass Transport

Mass and heat transfer processes in fixed-bed gasifiers are affected by complex solid flow and chemical reactions. Coarsely crushed coal settles while undergoing heating, drying, devolatilization, gasification and combustion. Coal particles change in diameter, shape and porosity. Nonideal behavior may result from coal bridges, gas bubbles and channels. Variable bed void fraction may also change heat and mass transport properties. Steep temperature gradients, typical to fixed-bed gasification and oxidation of coal, make the use of correlations for solid-to-gas heat transfer coefficients uncertain, since these are typically obtained under ideal conditions. Mass transfer occurs by diffusion and convection. The modes of heat transfer are conduction, convection and radiation for both the gas and solid phases.

Transport and Thermodynamic Properties

Several physical properties for the gas and particle phases are required to obtain mass and heat transfer coefficients needed to solve the system of differential equation set given in Table 3.2. Chapman-Enskog theory has been used to calculate multicomponent gas mixture viscosity and diffusivity (Bird et al., 1960). The equations used to determine the gas species and mixture conductivity, viscosity, and diffusivity are given in Table 3.4. The particle is assumed to swell linearly with the extent of devolatilization as given by Equation 9 of Table 3.4. The particle diameter and number density are discussed later in this chapter.

Euken's formula is used to calculate the conductivity of individual gaseous species, as given by Equation 1, Table 3.4. The multicomponent gas viscosity is calculated from Equation 2, as given in Table 3.4. The gas species viscosity given by Equation 3 of Table 3.4 is based on the viscosity of a pure monatomic gas. The Stockmayer collision diameter, σ, and the collision integral for viscosity which describes the deviation from rigid sphere behavior, Ω_m, are computed from the relations of Neufield with Brokaw's correction (1969). The interaction parameter is obtained from Equation 5 of Table 3.4.

The effective mass diffusivity for a single gaseous species *i* through the gas mixture is given by Equation 8 of Table 3.4. This formulation assumes that each species in the mixture moves with the same velocity. The species mass diffusivities are calculated using the Chapman-Enskog formula given by Equation 6 of Table 3.4. The collision integral for diffusion, Ω_d, is a dimensionless function of the temperature and of the intermolecular potential field for species *i* and *k*. This function can be approximated by the Lennard-Jones function (Bird et al., 1960). This requires a suitable estimate of the Lennard-Jones parameters σ_{ik} and ε_{ik} from the individual species parameters σ_i and ε_i. These interspecies parameters are computed as $\sigma_{ik} = 0.5(\sigma_i + \sigma_k)$ and $\varepsilon_{ik} = \sqrt{\varepsilon_i \varepsilon_k}$. Furthermore, the diffusivity of gaseous tar is assumed to be 0.1 cm^2/s at standard temperature and pressure following Suuberg et al., (1979). The pressure and temperature dependencies for

Table 3.4 Physical property equations used in the one-dimensional fixed-bed model.§

Gas species conductivity	$k_i = \left(Cp_i + \frac{5R}{4Mw_i} \right) \mu_i$	(1)
Gas mixture conductivity	$k_g = \sum_{i=1}^{n} \frac{x_i k_i}{\sum_{j=1}^{n} x_j \Phi_{ij}}$	(2)
Gas species viscosity	$\mu_i = 2.6693 \times 10^{-5} \frac{\sqrt{Mw_i T_g}}{\sigma_i^2 \Omega_m^2}$	(3)
Gas mixture viscosity	$\mu_g = \sum_{i=1}^{n} \frac{x_i \mu_i}{\sum_{j=1}^{n} \chi_j \Phi_{ij}}$	(4)
Interaction parameter	$\Phi_{ij} = \frac{1}{\sqrt{8}} \left(1 + \frac{Mw_i}{Mw_j} \right)^{-\frac{1}{2}} \left[1 + \left(\frac{\mu_i}{\mu_j} \right)^{\frac{1}{2}} \left(\frac{Mw_j}{Mw_i} \right)^{\frac{1}{4}} \right]^2$	(5)
Species diffusivity	$D_{ij} = 0.0018583 \frac{\sqrt{T_g^3 \left(\frac{1}{Mw_i} + \frac{1}{Mw_j} \right)}}{P \sigma_{ij}^2 \Omega_{d,ij}}$	(6)
Tar diffusivity	$D_{tar} = 0.1 \left(\frac{T}{273} \right)^{1.5} \left(\frac{1}{P} \right)$	(7)
Effective species diffusivity	$D_{im} = \frac{1 - x_i}{\sum_{j \neq i} \frac{x_j}{D_{ij}}}$	(8)
Particle diameter	$d = d^o \left[1 + \gamma \left(\frac{v^\infty - v}{v^\infty} \right) \right]$	(9)
Particle surface area	$A_p = \pi d^2$	(10)

§The physical property equations for all gases except tar are from Bird et al., (1960). The tar diffusivity is calculated following Suuberg et al. (1979). The particle diameter is assumed to swell during devolatilization; and the particle surface area is dependent on the instantaneous particle diameter.

the tar diffusivity are assumed to be the same as predicted by Chapman-Enskog theory, as shown by Equation 7 of Table 3.4.

The thermodynamic properties of gaseous species are determined from the widely used polynomial expression (Kee et al., 1991) obtained from the regression analysis of the thermochemical data from JANAF tables (Stull and Prophet, 1971). These expressions for the dimensionless heat capacity, enthalpy, and entropy are given below:

$$\frac{C_p}{R} = a_1 + a_2 T + a_3 T^2 + a_4 T^3 + a_5 T^4 \tag{3.12}$$

$$\frac{H^o}{RT} = a_1 + \frac{a_2}{2} T + \frac{a_3}{3} T^2 + \frac{a_4}{4} T^3 + \frac{a_5}{5} T^4 + \frac{a_6}{T} \tag{3.13}$$

$$\frac{S^o}{R} = a_1 \ln T + a_2 T + \frac{a_3}{2} T^2 + \frac{a_4}{3} T^3 + \frac{a_5}{4} T^4 + a_7 \tag{3.14}$$

where T = gas temperature (K).

The enthalpies and heat capacities of char and ash are determined as discussed in chapter 2 and summarized below. Dulong's formula (Perry and Chilton, 1973) is used for the heating value of the char. The correlations proposed by Merrick (1983) for char enthalpy and heat capacity are used for computing the enthalpy of char. Finally, either Kirov (Merrick, 1983) or Kopp-Neumann (Mills and Rhine, 1989) relation is used to calculate the heat capacity of ash.

Heat and Mass Transfer Correlations

The correlations used for the calculation of the heat and mass transport coefficients used in the one-dimensional model are presented in Table 3.5. The

Table 3.5 Heat and mass transport correlations used in FBED-1.

Bed-to-wall heat transfer coefficient	$h_w = \frac{2.44k_r^o}{D^{4/3}} + \frac{0.033k_g PrRe}{d_p}$	(1)
Gas-to-wall heat transfer coefficient	$h_w^g = \frac{k_{rg}}{k_{rg}+k_{rs}} h_w$	(2)
Solid-to-wall heat transfer coefficient	$h_w^s = \frac{k_{rs}}{k_{rg}+k_{rs}} h_w$	(3)
Static effective radial conductivity	$k_r^o = k_g\varepsilon\left(1+\frac{\beta d_p h_{rv}}{k_g}\right) + \frac{\beta k_g(1-\varepsilon)}{\left(\frac{1}{\phi}+\frac{h_{rs}d_p}{k_g}\right)^{-1}+\frac{2}{3\kappa}}$	(4)
Gas effective radial conductivity	$k_{rg} = k_g\left\{\varepsilon\left(1+\frac{\beta d_p h_{rv}}{k_g}\right) + PrRe\left[\frac{0.14}{1+46\left(\frac{d_p}{D}\right)^2}\right]\right\}$	(5)
Solid effective radial conductivity	$k_{rs} = \frac{\beta k_g(1-\varepsilon)}{\left(\frac{1}{\phi}+\frac{h_{rs}d_p}{k_g}\right)^{-1}+\frac{2}{3\kappa}}$	(6)
Solid conductivity	$k_s = \left(\frac{\rho_s^t}{4511}\right)^{3.5}\sqrt{T_s}$	(7)
Void-to-void radiation coefficient	$h_{rv} = \frac{2.27\times10^{-7}T_g^3}{1+\frac{\varepsilon}{2(1-\varepsilon)}\left(\frac{1-\varepsilon'}{\varepsilon'}\right)}$	(8)
Solid radiation coefficient	$h_{rs} = 2.27\times10^{-7}\left(\frac{\varepsilon'}{2-\varepsilon'}\right)T_s^3$	(9)

Table 3.5 Heat and mass transport correlations used in FBED-1 (continued).

Packing parameter

$$\phi = \begin{cases} \phi_2 + (\phi_1 - \phi_2)\dfrac{\varepsilon - 0.260}{0.476 - 0.260} & if\ \varepsilon_1 \geq \varepsilon \geq \varepsilon_2 \\ \phi_1 & if\ \varepsilon > \varepsilon_1 = 0.476 \\ \phi_2 & if\ \varepsilon > \varepsilon_2 = 0.260 \end{cases} \quad (10)$$

Loose packing parameter (for ε_1)

$$\phi_1 = \frac{0.3525\left(\dfrac{\kappa - 1}{\kappa}\right)^2}{ln[\kappa - 0.5431(\kappa - 1)] - \dfrac{0.4569(\kappa - 1)}{\kappa}} - \frac{2}{3\kappa} \quad (11)$$

Dense packing parameter (for ε_2)

$$\phi_2 = \frac{0.07217\left(\dfrac{\kappa - 1}{\kappa}\right)^2}{ln[\kappa - 0.9250(\kappa - 1)] - \dfrac{0.07498(\kappa - 1)}{\kappa}} - \frac{2}{3\kappa} \quad (12)$$

Solid-to-gas heat transfer coefficient $$h_{sg} = \frac{2.06 Cp_g G}{\varepsilon} Re^{-0.575}\, Pr^{-2/3} \quad (13)$$

Mass transfer coefficient $$k_m = \frac{2.06 G}{\varepsilon \rho_g} Re^{-0.575}\, Sc^{-2/3} \quad (14)$$

Reynolds number $$Re = d_p G/\mu_g = \rho_g d_p v_g/\mu_g \quad (15)$$

Prandtl number $$Pr = Cp_g \mu_g / k_g \quad (16)$$

Schmidt number $$Sc_i = \mu_g/\rho_g D_{im} \quad (17)$$

Conductivity ratio $$\kappa = k_s/k_g \quad (18)$$

Table 3.5 Heat and mass transport correlations used in FBED-1 (continued).

Bed void fraction	ε = void volume/bed volume	(19)
Emissivity	$\varepsilon' = 0.85$	(20)

Units for Table 3.5

h_{rs}, h_{rv}, h_{sg}, h_w, h_w^g, and h_w^s	$J/s\,m^2K$
k_g, k_{rg}, k_{rs}, k_r^o, and k_s	$J/s\,m\,K$
k_m	m/s
D (reactor diameter) and d_p (particle diameter)	m

References for Table 3.5

Equations (1)-(6), (8,9)	Froment and Bischoff (1979)
Equations (7)	Merrick (1983)
Equations (10)-(12)	Kunii and Smith (1960)
Equations (13)-(14)	Gupta and Thodos (1963)
Equations (15)-(19)	Definitions
Equation (20)	Estimated for coal

effective axial and radial conductivities have been correlated by Yagi et al., (1960) and Bischoff (1962), and by Froment and Bischoff (1979), respectively. Both the axial and radial effective conductivities take into account molecular as well as turbulent contributions. The effective radial conductivities of the gas and solid phases also account for radiation and have been correlated by DeWasch and Froment (1971).

No direct experimental data are available on the gas and the solid phase contributions to the bed-to-wall heat transfer. Therefore, the effective bed-to-wall heat transfer coefficient as well as the gas and solid phase contributions are determined by the correlations suggested by DeWasch and Froment (1971). The heat transfer to the wall is treated following Yagi and Wakao (1959) and Yagi and

Kunii (1960). The reader is referred to Rohsenow et. al., (1985) for additional information.

The volumetric heat transfer rate from solid-to-gas, $Q_{sg}\left(J/m^3 s\right)$, is computed as

$$Q_{sg} = \zeta\, h_{sg} \pi\, d_p^2 \eta_p \left(T_s - T_g\right) \tag{3.15}$$

where ζ, $h_{sg}\left(J/s\, m^2\, K\right)$, and $\eta_p\left(1/m^3\right)$ represent deviation from nonreactive solid-to-gas heat transfer (ranges from 0.02 to 1.0), the nonreactive solid-to-gas heat transfer coefficient (Equation 13, Table 3.5), and the particle number density, respectively. The volumetric wall heat loss from the solid and gas phase, Q_{gw} and $Q_{sw}\left(J/m^3 s\right)$, can be calculated as follows:

$$Q_{gw} = \frac{4h_w^g}{D}\left(T_g - T_{wall}\right) \tag{3.16}$$

$$Q_{sw} = \frac{4h_w^s}{D}\left(T_s - T_{wall}\right) \tag{3.17}$$

where h_w^g, h_w^s, T_g, T_s, T_{wall}, and D represent the gas-to-wall heat transfer coefficient, solid-to-wall heat transfer coefficient, gas temperature, solid temperature, wall temperature and reactor diameter, respectively. The wall temperature can be varied from the bottom to the top of the reactor.

The mass transport coefficient given in Table 3.5 is used to calculate the film resistance and the effective particle resistance to mass transport.

Drying

The chemical submodels are composed of coal drying, devolatilization, char oxidation and gasification, and gas phase chemistry. The drying of coal is based on the diffusion-limited vaporization of moisture from the coal particle, as described by Smoot and Smith (1979):

$$r_w = k_{wm}\left(\rho_{wp} - \rho_{wg}\right) \tag{3.18}$$

where k_{wm}, ρ_{wp} and ρ_{wg} represent the moisture mass transfer coefficient, surface moisture concentration, and bulk water concentrations, respectively. Blowing or transpiration effects influence the rates by less than 5% for large particles at typical operating conditions in fixed-bed coal gasifiers and therefore are assumed negligible (Hobbs et al., 1992a, see Appendix D).

Devolatilization

In FBED-1 model, devolatilization is based on either the FG-DVC submodel, or the simpler FG-SET submodel. These submodels provide the rates of evolution of light gases, tar, and char. These rates are per unit mass of initial char and can then be converted to the overall coal devolatilization rates using the following expression:

$$r_i = \pm\rho^o_{sm}\left(1-\varepsilon^o\right)\left(1-\Omega^o_{ash}-\Omega^o_{moisture}\right)\frac{d\omega_{i,\ (char,\ tar,\ or\ gas)}}{dt} \tag{3.19}$$

where ρ^o_{sm} is the measured apparent density of the feed coal, ε^o is the bed void fraction at the gasifier top, Ω^o_{ash} and $\Omega^o_{moisture}$ are the proximate ash and moisture

fractions of the feed coal, and $\omega_{i,\,(char,\,tar,\,or\,gas)}$ is the weight fraction of the *i-th* functional group in the char, tar, or gas.

Oxidation and Gasification

The two most common char oxidation submodels used in the currently available fixed-bed models are the Shell Progressive model (SP model) and the Ash Segregation model (AS model). The difference between the two models is in the treatment of the ash layer. In the SP model, the ash remains intact and the oxidant is required to diffuse through the film boundary layer and the ash layer. In the AS model, ash is assumed to crumble slowly and fall away from the char particle; the oxidant is required to diffuse through the film boundary layer only. Both these submodels assume global reactions and depend on the external surface area of the particle.

The SP or AS submodel is used to obtain the rates of oxidation and gasification reactions. The rate equation for a single particle is given by Hobbs et al., (1992a):

$$r_i^{o,g} = \frac{A_p v_s M w_p C_{ig}}{\frac{1}{k_r \zeta} + \frac{1}{k_m} + \frac{1}{k_{eff}}} \tag{3.20}$$

where the resistances in the denominator represent surface reaction, molecular diffusion through the gaseous film, and diffusion through the ash layer. Equation 3.20 neglects the effects of diffusion-induced convective transport and assumes that the reactions are first order in oxidizer concentration. It also explicitly neglects pore diffusion, in which case, these effects are implicitly lumped into k_{eff}. The diffusional resistance through the ash layer is set to zero if the AS model is used. The quantities A_p, v_s, M_p, C_{ig}, k_r, ζ, k_m, and k_{eff} represent the external surface area of the particle, the stoichiometric coefficient to identify the number of moles of product gas per mole of oxidant, char molecular weight, molar concentration of

oxidizer or gasification agent in the bulk gas phase, Arrhenius chemical reaction rate constant, particle area factor to account for internal surface burning, bulk mass transfer coefficient, and ash layer mass transfer coefficient, respectively. Oxidation and gasification kinetic rate constants are given in Table 3.6. Baxter (1987) used nonlinear analysis to correlate the Arrhenius parameters listed in Table 3.6. The results of the original investigators obtained by linear analysis are also listed.

Oxidation and gasification kinetics data for large particle are limited and not readily available in the open literature. Essenhigh (1981) listed various publications regarding fixed-bed experimental methods used in obtaining kinetic data. Unfortunately, the experimental programs for which data were available primarily involved small particles (Essenhigh, 1981). Although the kinetic parameters given in Table 3.6 were derived from small particle experimentation, they are assumed to be applicable to the oxidation and gasification of large particles.

It is pointed out that several studies were done on large spherical carbon particles (Froberg, 1967; Kurylko, 1969) and might not be directly applicable to coal. However, mass transport may dominate the oxidation and gasification processes for large coal particles, thereby justifying the use of the available kinetic data. Hobbs (1990) reported an order of magnitude analysis showing the film resistance to be ten orders of magnitude higher than the chemical resistance for the oxidation reaction. It is, therefore, concluded that shrinking core models using effective internal diffusion may be adequate for comprehensive fixed-bed modeling.

The last resistance in the denominator of Equation 3.20 can be determined using an effective mass transfer coefficient (Thorsness and Kang, 1984):

$$\frac{1}{k_{eff}} = \frac{(1-F)d_p}{2D_{eff}} \tag{3.21}$$

where F, d_p, and D_{eff} represent the fraction of original carbon, particle diameter, and effective diffusivity, respectively. Walker et al., (1959) and Laurendeau (1978) discuss methods for calculating effective diffusivities. Park and Edgar (1987) show the effect of a developing ash layer on the burning rate of a sample core of coal. The core burning rate can be predicted by using an effective

Table 3.6 Oxidation and gasification kinetic rate constants (after Hedman et al., 1987).

$$k = A\,T\,exp\left(\frac{-E}{RT}\right),\ \frac{m}{s}$$

Reaction	$A\left(\frac{m}{sK}\right)$	$\frac{E}{R}(K)$	Source of Correlation	Source of Data
$C + 0.5O_2 \rightarrow CO$				
All ranks[a]	2.30 x 10^0	1.11 x 10^4	Baxter (1987)[b]	Field et al., (1967)
HVBA	1.03 x 10^0	9.01 x 10^3	Baxter (1987)	Goetz et al., (1982)
HVBC	5.00 x 10^{-1}	6.31 x 10^3	Baxter (1987)	Goetz et al., (1982)
SUBC	1.04 x 10^1	1.12 x 10^4	Baxter (1987)	Goetz et al., (1982)
Lignite A	1.22 x 10^0	1.03 x 10^4	Nsakala et al., (1985)	Nsakala et al., (1985)
HVBA	2.26 x 10^0	1.02 x 10^4	Goetz et al., (1982)	Goetz et al., (1982)
HVBC	2.05 x 10^0	8.63 x 10^3	Goetz et al., (1982)	Goetz et al., (1982)
SUBC	4.96 x 10^0	1.00 x 10^4	Goetz et al., (1982)	Goetz et al., (1982)
$C + CO_2 \rightarrow 2CO$				
All ranks[a]	5.89 x 10^2	2.68 x 10^4	Hobbs et al., (1992a)[c]	Goetz et al., (1982)
HVBA	1.16 x 10^3	3.12 x 10^4	Baxter (1987)	Goetz et al., (1982)
HVBC	4.89 x 10^3	3.13 x 10^4	Baxter (1987)	Goetz et al., (1982)
SUBC	6.19 x 10^3	2.89 x 10^4	Baxter (1987)	Goetz et al., (1982)
Lignite A	3.42 x 10^0	1.56 x 10^4	Baxter (1987)	Goetz et al., (1982)
HVBA	9.51 x 10^1	2.70 x 10^4	Goetz et al., (1982)	Goetz et al., (1982)
HVBC	8.86 x 10^2	2.84 x 10^4	Goetz et al., (1982)	Goetz et al., (1982)
SUBC	7.11 x 10^1	2.14 x 10^4	Goetz et al., (1982)	Goetz et al., (1982)
Lignite A	4.51 x 10^1	1.99 x 10^4	Goetz et al., (1982)	Goetz et al., (1982)

[a] Base case parameters used in sensitivity analysis.
[b] Baxter's (1987) rate constants were obtained by nonlinear analysis of Fields's et al., (1967) and Goetz' et al., (1982) data.
[c] Hobb's et al., (1992a) rate constants for all ranks were obtained by averaging Baxter's (1987) rate constants for four coal ranks.

diffusivity based on the molecular diffusivity multiplied by a constant, i.e., $D_{eff} = \phi D_m$. The constant, ϕ, is based on the porosity of the developing ash layer.

Thorsness and Kang (1985) have used 0.35 for ϕ . Wang and Wen (1972) measured the porosity of a fire clay ash which varied from 0.4 to 0.8. Laurendeau (1978) shows that ϕ can be estimated by the ash porosity divided by the tortuosity squared, which is estimated to be 2.0. Using Wang and Wen's values for the ash porosity (0.4 to 0.8), ϕ should range between 0.2 and 0.4. However, lower values of ash porosity (0.06 - 0.60) were determined for ash originating from the Lurgi and Wellman-Galusha gasifiers, indicating a lower range of 0.03 to 0.3 for the constant ϕ for the fixed-bed gasifiers.

The single particle model can be related to the bed by use of the particle number density and unreacted core particle surface area. Assuming spherical particles, Hobbs et al., (1992a) presented the expressions for the particle diameter, unreacted core diameter and particle number density for the SP submodel. These expressions are given by

$$d_p = \left[\left(1-\Omega_{ash}^o\right)d_u^3 + \Omega_{ash}^o d_o^3\right]^{1/3} \tag{3.22}$$

$$d_u = F^{1/3} d_o \tag{3.23}$$

$$\eta_p = \frac{6(1-\varepsilon)}{\pi d_p^3} \tag{3.24}$$

where the subscripts o and u represent initial and unreacted core, respectively.

The heterogeneous oxidation of carbon produces both CO and CO_2 as primary products as shown by the following reaction:

$$\lambda C + O_2 \rightarrow 2(\lambda-1)CO + (2-\lambda)CO_2, \quad 1 \le \lambda \le 2 \tag{3.25}$$

Carbon monoxide may be favored at higher temperatures if CO is formed at carbon edges and CO_2 is formed at inorganic sites. Lower temperatures may favor CO_2

due to catalytic activity. The CO/CO_2 ratio has been correlated by Laurendeau (1978):

$$\frac{CO}{CO_2} = A\,exp\left(-\frac{E}{RT}\right) = \frac{2(\lambda - 1)}{(2-\lambda)} \tag{3.26}$$

where $A \approx 10^{2.5}$, $E \approx 6-9 kcal/mol$ for low pressures and $A \approx 10^{3.5}$, $E \approx 12-9 kcal/mol$ at high pressures. The stoichiometric coefficient for Equation 3.25 can be determined as a function of temperature from Equation 3.26:

$$\lambda = \frac{2\left[A\,exp\left(-\frac{E}{RT}\right)+1\right]}{A\,exp\left(-\frac{E}{RT}\right)+2} \tag{3.27}$$

The values for λ at 500, 1000, 1500, and 2000 K are 1.08, 1.78, 1.93, and 1.96 using Equation 3.27 with the low pressure parameters and 1.00, 1.06, 1.47, and 1.76 using the high pressure parameters. This indicates that CO is favored at higher temperatures.

Summary of Model Equations, Model Parameters and Options

A summary of the one-dimensional fixed-bed model equations is given in Table 3.7. The system of ordinary differential equations listed in Table 3.2 is solved simultaneously from the top to the bottom of the reactor with LSODE (Livermore Solver for Ordinary Differential Equations, Hindmarsh, 1983). The equations for drying, devolatilization, combustion and gasification are described by Equations 3.18, 3.19, and 3.20. The volumetric heat transfer rate from solid-to-gas, solid-to-wall, and gas-to-wall are described by Equations 3.15, 3.16 and 3.17.

Table 3.7 Summary of the one-dimensional fixed-bed model equations.

Basic Equations and Boundary Conditions	Reference
Overall gas species continuity	Table 3.2
Overall solid species continuity	Table 3.2
Gas phase energy	Table 3.2
Solid phase energy	Table 3.2
Gas species continuity	Table 3.2
Solid species continuity	Table 3.2
Gas phase elemental	Table 3.2
Gas phase tar species continuity	Table 3.2
Gas phase tar elemental continuity	Table 3.2
Auxiliary Equations	**Reference**
Total enthalpies	Eq. (2.3)
Enthalpies of formation	Eq. (2.5) and Table 3.3
Sensible enthalpies	Eqs. (2.6) and Table 3.3
Enthalpy exchange due to reaction	Table 3.3
Ash heat capacity	Eq. (2.9, 2.10) and Table 2.1
Pressure drop	Eq. (3.11)
Gas conductivity, viscosity, and diffusivity	Table 3.4
Particle diameter and surface area	Table 3.4, Eq. (3.22)
Particle number density	Eq. (3.24)
Volumetric solid-to-gas heat transfer rate	Eq. (3.15)
Volumetric wall heat loss from solid	Eq. (3.16)
Volumetric wall heat loss from gas	Eq. (3.17)
Gas-to-wall heat transfer coefficient	Table 3.5
Solid-to-wall heat transfer coefficient	Table 3.5
Effective gas and solid conductivities	Table 3.5
Solid conductivity	Table 3.5
Diffusive radiation coefficients	Table 3.5
Solid-to-gas heat transfer coefficient	Table 3.5
Mass transfer coefficient	Table 3.5
Reynolds, Prandtl, and Schmidt numbers	Table 3.5
Drying rate	Eq. (3.18)
Devolatilization rates	Eq. (3.19)
Oxidation and gasification rates	Eq. (3.20)

The heat and mass transfer correlations are described in detail in Table 3.5. Elemental reaction rates can be determined from reaction stoichiometry. The tar reaction rates can be determined from Equation 3.19.

Table 3.8 provides a summary of the parameters and options for the one-dimensional fixed-bed model. Parameters that are difficult to obtain and are highly uncertain are the solid-to-gas heat transfer coefficient, effective diffusivity, and bed void fraction. Most of these parameters can be determined independently, as shown in Table 3.9. However, if experimental values are unavailable, Table 3.9 can be used as a guide to select the optimum value of bed void fraction, ε, solid-to-gas heat transfer correction factor, ζ, and the ash porosity, ϕ, which can be used to determine the effective diffusivity. The solid-to-gas heat transfer correction factor ranges between 0.02 and 1.0 and is discussed by Hobbs et al., (1992a). Bed void fraction for the feed coal can be determined experimentally. However, the bed void fraction is not constant throughout the reactor. Values at the top and bottom of the reactor can be specified in the one-dimensional model. The bed void fraction is assumed to vary linearly from the specified values at the reactor top and bottom.

The choice of either the SP or AS char model options is difficult to determine *a priori*. The SP model option seems to give temperature profiles closer to experimental results (Hobbs et al., 1992a). Other model options include the gas phase tar reaction equilibrium option and volatiles mass transport option. Also, the combustion product distribution can be considered a model option. However, this option is not listed in Table 3.8, since the distribution is assumed to be sufficiently correlated to experimental data.

Table 3.8 Summary of the one-dimensional fixed-bed model parameters and options.

PARAMETER	TYPICAL VALUE	DESCRIPTION
Devolatilization		
x^o	0.16 (Table B.1)	Potential tar-forming fraction
$k_i^o, 1/s$	5.0×10^{12} (CO_2 extra loose, Table A.6)	Functional group frequency factor
$\overline{E}_i/R,\ K$	20,850 (CO_2 extra loose, Table A.6)	Functional group activation energy
$\sigma_i/R,\ K$	3600 (CO_2 extra loose, Table A.6)	Standard deviation for distribution function
χ_i	2048 (CO_2 extra loose, Table A.6)	Cross-link efficiency
$k_x^o, 1/s$	27,500 (Tar, Table B.1)	Tar frequency factor
$\overline{E}_x/R,\ K$	0.86×10^{15} (Tar, Table B.1)	Tar activation energy
Oxidation/Gasification		
$k_{CO_2}^o, 1/s$	589 (Table 3.6)	Frequency factor for CO_2 gasification reaction
$E_{CO_2}/R,\ K$	26,800 (Table 3.6)	Activation energy for CO_2 gasification reaction
$k_{H_2}^o, 1/s$	0.589	Frequency factor for CO_2 gasification reaction
$E_{H_2}/R,\ K$	26,800	Activation energy for CO_2 gasification reaction
$k_{H_2O}^o, 1/s$	589	Frequency factor for CO_2 gasification reaction
$E_{H_2O}/R,\ K$	26,800	Activation energy for CO_2 gasification reaction
$k_{O_2}^o, 1/s$	2.3 (Table 3.6)	Frequency factor for CO_2 gasification reaction
$E_{O_2}/R,\ K$	11,100 (Table 3.6)	Activation energy for CO_2 gasification reaction
Flow, Heat and Mass Transport		
ε'	0.85 (Table 3.5)	Coal emissivity
ε_{top}	0.33 (Thimson et al., 1984)	Bed void and bed top
ε_{bottom}	0.6 (Thimson et al., 1984)	Bed void at bed bottom
ζ	0.05 (Lowry, 1963)	Reactive/nonreactive heat transfer coeff.
ϕ/τ	0.5 (Laurendeau, 1978)	Ash porosity divided by tortuosity squared

Table 3.8 Summary of the one-dimensional fixed-bed model parameters and options. (continued)

Operating Parameters

Prox. & ultimate comp.		Proximate and ultimate analysis
d_p, *cm*	2.2 (Thimson et al., 1984)	Particle diameter
D, *m*		Reactor diameter
L, *m*		Reactor length
T_{coal}, *K*	298	Feed coal temperature
T_{BG}, *K*	560	Feed gas temperature
T_{wall}, *K*	325 (Thimsen et al., 1984)	Wall temperature
$\dot{m}_c$, *kg/s*	0.35 (Thimsen et al., 1984)	Coal mass flow rate
$\dot{m}_O$, *kg/s*	0.95 (Thimsen et al., 1984)	Oxidizer mass flow rate
$\dot{m}_S$, *kg/s*	0.16	Steam mass flow rate

Model Options: AS or SP char submodel, gas phase tar reaction equilibrium option, and volatiles mass transport option for FG-SET submodel.

Table 3.9 Guidelines for the selection of some critical model parameter.

Parameter	Independent Calculation	Selection Procedure
Bed void fraction at gasifier top, ε_c, and gasifier bottom, ε_a	Void fractions can be measured or estimated from coal and ash properties. Typical values may range between 0.2 and 0.8 depending on particle distribution, sphericity and particle roughness§.	Bed void fraction is selected to match measured pressure profile. Initially, ε_c and ε_a are adjusted in equal increments; however, the top or bottom void fractions are adjusted independently if the measured profile indicates a larger or smaller void fraction.
Solid-to-gas heat transfer correction factor, ζ.	ζ ranges from 0.02 to 1.0 based on reacting solid-to-gas heat transfer (Hobbs et al., 1992a). A value of 0.05 is recommended if no other data are available.	ζ is selected to match the location of the maximum measured temperature.
Effective diffusivity parameter, $\phi = \frac{\phi_a}{\tau^2} \approx \frac{\phi_a}{2}$	ϕ can be measured or estimated from the ash porosity, ϕ_a. Ash porosities range from 0.06 to 0.60 for ash obtained from fixed-bed gasifiers (Hobbs, 1990). An acceptable range for ϕ might be 0.02 to 0.5. A value of 0.5 is recommended if no other data are available.	ϕ can be selected to match the location of the maximum measured temperature. ϕ is usually adjusted after ζ is chosen. In other words, if adjusting ζ is insufficient to adjust the location of the maximum temperature, adjust ϕ.
SP or AS model option	The SP model option is recommended if no other data are available as discussed by Hobbs et al., (1992a).	The AS model option can be chosen if a discontinuity is observed in the measured pressure profile, or if the oxidation zone is very small with a corresponding steep temperature gradient, or if burnout is high simultaneously with a large drying zone as is common for lignites with high moisture contents.

§ MeFayed (1984) discusses bed void fraction. For spherical particles, bed void fraction for close random packing ranges from 0.359 to 0.375; for hexagonal close packing, bed void fraction is 0.26. The effect of sphericity is to increase bed void fraction. For example, for a sphere with a sphericity of 1.0, it is 0.4; for a cube with sphericity 0.8, it is 0.5; and for a particle with sphericity of 0.2 it is 0.85.

CHAPTER 4

FG-DVC DEVOLATILIZATION SUBMODEL

FG-DVC Model Basis

FG-DVC is a general model for coal pyrolysis that predicts the decomposition of coal into tar, char, and gas, given the ambient pressure and the temperature history of an isothermal coal particle. The model predicts the amount, functional group composition, elemental composition, and molecular weight distribution of tar and char and the amount and composition of the gas. The model is described in more detail in Appendices E, F, and G.

The letters FG stand for Functional Group, and DVC for Depolymerization, Vaporization and Crosslinking. The FG model considers certain functional groups in the coal which decompose to form the light gas species. At the same time, the DVC model describes the overall depolymerization of the macromolecular network which combines bridge breaking and crosslinking to produce fragments of the coal macromolecule. These fragments are then subjected to transport behavior, specifically the vaporization of the lightest fragments to form tar. The tar fragmentation process provides a second mechanism for the removal of functional groups from the coal. The model, whose parameters are determined in the laboratory at moderate temperatures and one atmosphere, can then be used to

extrapolate away from the laboratory conditions to predict pyrolysis and combustion in high temperature reactions, or liquefaction at high pressure.

The model for coal thermal decomposition has six basic concepts.

- Functional Groups (decompose to produce light gases),
- Macromolecular Network (decomposes to produce tar and metaplast),
- Network Coordination Number (possible number of attachments per cluster),
- Bridge Breaking (limited by hydrogen availability),
- Crosslinking (related to gas evolution),
- Mass Transport of Tar (evaporation of light network fragments into light gases).

The first concept is that light gases are formed by the decomposition of certain functional groups in the coal. For example, methyl groups can lead to the formation of methane, carboxyl groups can lead to the formation of CO_2, etc. The second concept is that coal consists of a macromolecular network. This network is made up of fused aromatic ring clusters (which are described by their molecular weight) linked by bridges, some of which are relatively weak. There are some unattached parts of the network which can be extracted. Sometimes, there is also a second component of high polymethylene content. When heated, this network decomposes to produce smaller fragments. The lightest of the fragments evaporate to produce tar; the heavier fragments form the metaplast. These heavier molecules are the primary liquid fragments in liquefaction or the fragments that make coal fluid.

The third concept is that one of the most important properties of the network is its coordination number. The coordination number describes the geometry of the network, and specifies how many possible attachments there are per aromatic ring cluster. For example, a linear polymer chain has a coordination number of 2, because each fused aromatic ring has two possible attachments to link it in the chain. On the other hand, a square "fish net" has a coordination number of 4, because there are four possible attachments at each ring cluster. The coordination number controls the molecular weight distribution of the network fragments at a

given extent of decomposition. The extent of decomposition is specified by the probability that the possible attachments are made. For example, for 20% of broken bridges, a linear chain is totally fragmented, while a "fish net" will have some holes but is almost totally connected. In describing the network, a crosslink is defined to occur at a branch point where there are more than two attachments on a ring cluster. The coordination number is thus related to the crosslink density. With no possible crosslinks, the coordination number is two. With increasing crosslink density, the coordination number increases.

The second important property of the network is the fraction of possible attachments, p, which are actually present. During thermal decomposition, this fraction is determined by the rates of bridge breaking. The factors that control how many of the weak links can break are the rate constant and the amount of hydrogen that can be donated from the coal to stabilize the free radicals which form when the links break.

A competitive process with the bond breaking is the retrogressive process of crosslinking. Crosslinking reactions appear to be related to the evolution of certain gases. Specifically, for low rank coals, crosslinking at low temperature (prior to bridge breaking) seems to be related to the evolution of carbon dioxide. For coals of all rank, a higher temperature crosslinking event (following bridge breaking) seems to be related to the evolution of methane. At high temperatures, the evolution of hydrogen should be related to crosslinking, but this is not currently done.

The final concept is that the tar evolution is controlled by mass transport. Bridge breaking and crosslinking produce a set of fragments with a molecular weight distribution. The lightest fragments can leave the coal melt by evaporation into the light gas species. The heavier fragments remain, forming the metaplast that controls the coal's fluidity.

In the following sections, the descriptions of DVC and FG submodels are given. More details can be found in Appendices E, F, and G.

Depolymerization-Vaporization-Crosslinking (DVC) Formulation

The DVC model predicts the yield and molecular weight distribution of the tar, and the yield and molecular weight distribution, extract yield, and the crosslink density of the char. The theory describes the combined effects of: 1) **depolymerization and hydrogen consumption**; 2) **cross-linking**; and 3) **transport**. These processes, described below, are incorporated into a computer code that employs a percolation theory method for performing the statistical analysis (Grant et al., 1989; Fisher and Essam, 1961).

Process 1. Depolymerization and Hydrogen Consumption. Bond cleavage in coal is likely to be very complicated, including homolytic cleavage, ipso substitution, and hydrogen-transfer-induced bond-scission reactions for a variety of bond types. However, it has been observed that tar evolution is consistent with a narrow distribution of activation energies; this allows consideration in the model of a single representative bridge (while acknowledging that other types may be present). Also, the rate for tar formation from coal, k_{tar}, is in good agreement with the rate determined for the breaking of ethylene bridges between naphthalene rings, k_B. This kinetic rate, k_B, employs an activation energy that is in agreement with resonance-stabilization calculations and an overall rate that agrees with previous measurements on model compounds. In view of these observations, a single type of bond (ethylene) undergoing homolytic cleavage is assumed for coal as a simple approximation of a complex behavior.

Bond cleavage is accompanied by the consumption of donatable hydrogens, H(al), to cap free radicals, along with corresponding carbon-carbon double bond formation at the donor site. For simplicity, the DVC model assumes that all the coal's donatable hydrogens, whether in bridges or in hydroaromatic rings, are in bridges, i.e., H(al) = (2/28)W_B, where H(al) is the weight fraction of donatable hydrogen and W_B is the weight fraction of labile bridges. This approximation will produce some error in tar yield, since a broken bond in a hydroaromatic ring will not be as effective as a broken bond in a bridge in fragmenting the coal. But this effect will be compensated for, since H(al) is a parameter that is determined for each coal from a selected pyrolysis experiment. H(al) could, in principle, be determined by FT-IR or NMR, but not with sufficient accuracy.

The equation describing the disappearance of labile bridges in the char, W_B (char), due to bridge breaking and hydrogen donation is

$$\frac{dW_B}{dt} = -2k_B W_B \tag{4.1}$$

or

$$\frac{dp_L}{dt} = -2k_B p_L \tag{4.2}$$

where p_L is the fraction of occupied bridges. The value for k_B is the same as for tar formation, k_{tar}. The rate of decrease of labile bridges is twice the rate of bridge breaking, since for each broken bridge, an additional labile bridge is converted to a nonlabile bridge with the donation of hydrogen. By assuming that all the donatable hydrogen is in the labile bridges, the consumption of labile bridges and donatable hydrogen occurs simultaneously. The redistribution of hydrogen creates source and loss terms, $dW_i(DVC)/dt$, in the equations for the char functional groups $W_i(char)$.

Equation 4.1 describes only the loss due to bridge breaking and hydrogen donation. The loss of labile bridges due to evolution with the tar is computed by using the transport equations (Eq. 4.6) discussed below.

Process 2. Crosslinking. Crosslinking reactions are important in describing the rank and heating rate dependence of the tar molecular weight distributions and yields. A correlation between gas evolution and crosslinking permits the rates for crosslinking and the number of crosslink sites to be related to rates and yields for gas evolution. The model assumes the following expression for the rate of increase of the fraction of crosslinks in the coal, q:

$$\frac{dq}{dt} \alpha \sum_{CH_4, CO_2} \left[\frac{dW_i(gas)}{dt}\right] \cdot \left[\frac{\#\,crosslinks\ \ formed}{unit\ \ of\ \ gas\ \ i}\right] \tag{4.3}$$

where the rates, dW_i/dt, of evolution per gram of coal of CO_2 and CH_4 are calculated in the FG submodel.

We caution that the assumed reactions must be a gross simplification of a very complicated set of chemical reactions. This is especially true for the crosslinks occurring during methane formation, during which time extensive bond breaking and crosslinking accompany tar formation.

Process 3. Transport. The external transport of tar components from the particle surface to the bulk gas by vaporization and diffusion through a gas boundary layer is described by simply assuming a constant pressure drop from the interior to the exterior of the coal particle. This assumption is plausible for a swelling coal.

In the DVC model, we assume that the tars achieve their equilibrium vapor pressure, P_j, in the evolving gases, which can be computed with a few assumptions. The rate of transport, per gram of coal dn_j/dt, for tar component j is proportional to the volume of gases evolved, dV/dt. That is,

$$\frac{dn_j}{dt} = P_j \chi_j \left(\frac{dV}{dt}\right)\left(\frac{1}{RT}\right) \tag{4.4}$$

where χ_j is the mole fraction of tar species j in the metaplast (using Raoult's Law). The volume flow rate of gases is given by the ideal gas law: proportional to the molar gas flow rate and the temperature, and inversely proportional to the pressure within the particle, $P_0 + \Delta P$, where P_0 is the ambient pressure and ΔP is the average pressure difference between the surface and the particle's interior. That is,

$$\frac{dV}{dt} = \sum_i \left(\frac{dn_i}{dt}\right)_{gas\ \&\ light\ tar} \left(\frac{RT}{P_0 + \Delta P}\right) \tag{4.5}$$

where $\sum_i (dn_i/dt)_{gas\ \&\ light\ tar}$ is the rate of production per gram of coal of gas components i summed over all gas and light tar species. For gas molecules, dn_i/dt is taken as the rate of production given by the FG model. For tar molecules, dn_i/dt

is computed using Eqs. 4.4 and 4.5 simultaneously. Summing Eq. 4.4 over the light tar species, adding to it the sum over gas species, and substituting into Eq. 4.5, we obtain an expression for dV/dt in terms of the gas evolution rates and the tar vapor concentrations from Raoult's Law, which leads to

$$\frac{dn_j}{dt} = P_j \chi_j \sum_{FG\ gases\ only} \left(\frac{dn_i}{dt}\right) \left(\frac{1}{P_0 + \Delta P - \sum_{light\ tars} P_j \chi_j}\right) \qquad (4.6)$$

ΔP is used as an adjustable parameter that varies with the coal and experimental conditions.

While $\Delta P = 0$ appears to be a good approximation for fluid coals at one atmosphere or more, $\Delta P > 0$ is expected for some coals and situations. ΔP is proportional to the coal's viscosity and so will become important for less fluid coals. ΔP is also important when P_0 is small, for large particles, and when the heating rates are very high. For nonfluid coals, ΔP is very large due to the limited gas transport ability of these coals, while the highly fluid coals have a small ΔP. We have found that reasonable results can be obtained with ΔP equal 10 atm for nonfluid coals and 0.2 atm for fluid coals. The quantities needed to evaluate Eq. 4.6 are discussed under Solution Technique later in this chapter.

Functional Group (FG) Model Formulation

The Functional Group (FG) model permits the detailed prediction of the composition of volatile species (gas yield, tar yield and tar functional group and elemental composition) and of char (elemental and functional group composition). It employs coal dependent rates for the decomposition of individual assumed functional groups in the coal and char to produce gas species. The ultimate yields of each gas species are related to the coal's functional group composition. Tar evolution is a parallel process that competes for all the functional groups in the coal. There are three additional processes in the FG submodel.

Process 4. Gas Formation. The evolution of each gas species is assumed to be a first order reaction,

$$\frac{dW_i(gas)}{dt} = k_i[W_i(char) + W_i(tar)\cdot\begin{bmatrix}0\\1\end{bmatrix}] \qquad (4.7)$$

where, $dW_i(gas)/dt$ is the rate of evolution of species i into the gas phase, k_i is a distributed rate for species i, and $W_i(char)$, $W_i(tar)$ are the functional group sources remaining in the char and tar. The [0,1] distinguish between the cases where tar does or does not continue to pyrolyze.

We employ the concept of the distributed rate where k_i is given by an Arrhenius expression $k_i(E) = k_i exp[-(E \pm \sigma_i)/RT]$, where $\pm\sigma_i$ indicates that a Gaussian distribution is employed to describe the source pools, $dW_i(E)$, as a function of the activation energies E about the initial average activation energy E_i.

$$dW_i(E) = \frac{W_i^0}{\sqrt{2\pi\sigma_i}}\exp\left(\frac{-(E-E_i)^2}{2\sigma_i^2}\right)dE \qquad (4.8)$$

where σ_i is the standard deviation of the Gaussian distribution.

Process 5. Tar Formation. The tar composition is tracked by summing the functional group contributions evolved with the tar. The rate of evolution of each contribution is

$$\frac{dW_i(tar)}{dt} = \left(\frac{dW(tar)}{dt}\right)_{DVC}\cdot\left(\frac{W_i(char)}{\sum_i W_i(char)}\right) - k_i\cdot W_i(tar)\cdot\begin{bmatrix}0\\1\end{bmatrix} \qquad (4.9)$$

where $dW_i(tar)/dt$ is the rate of evolution of each functional group component with the tar; $[dW(tar)/dt]_{DVC}$, the rate of tar production from the char, is discussed later in this chapter under DVC submodel Solution Technique.

Process 6. Char Formation. The change in the *i-th* char pool, $W_i(char)$, is computed by summing the losses to the gas and tar, and the redistributions determined in the DVC submodel,

$$\frac{dW_i(char)}{dt} = -\left(\frac{dW_i(gas)}{dt}\right) - \left(\frac{dW(tar)}{dt}\right) + \left(\frac{dW_i(DVC)}{dt}\right) \quad (4.10)$$

Percolation Theory

The coal macromolecular network can be represented using several methods. This model uses the percolation theory, which predicts analytically the probability that a bond will be occupied, given the coordination number and the starting bond occupation probability (Appendix E).

The DVC model predicts, and experiments confirm, that there are more than one kind of bond bridges and crosslinks which have different coordination numbers, and independent probabilities of being broken. To take advantage of the benefits of percolation theory, we have extended percolation theory on a Bethe lattice (one with no loops) to use two independent subnetworks, as illustrated in Fig. 4.1. In the figure, double lines represent one of the bond types, while single lines represent the other. As can be seen by comparing Fig. 4.1a and 4.2b, this lattice has the desired feature of modeling a transition from chain-like structures (a) to fishnet structures (b). The mathematics of this two-bond percolation theory follows closely that of the standard theory. The mathematics are presented in Appendix E.

Four parameters describe the network: p, q, σ_1 and σ_2. p and q are the occupation probabilities of bridges and crosslinks, respectively, while σ_1+1 and σ_2+1 are the coordination numbers for bridge linkage and crosslink linkage, respectively. σ_1 and σ_2 are model constants. p_L is the number fraction of occupied labile bridges; the evolution in time is given by Eq. 4.2. Similarly, q is the number fraction of crosslinks, computed using Eq. 4.3. p and q, are the state variables computed at each time step, and are set equal to the input parameters p_o, q_o, at time equal 0. p_o, q_o vary with each coal.

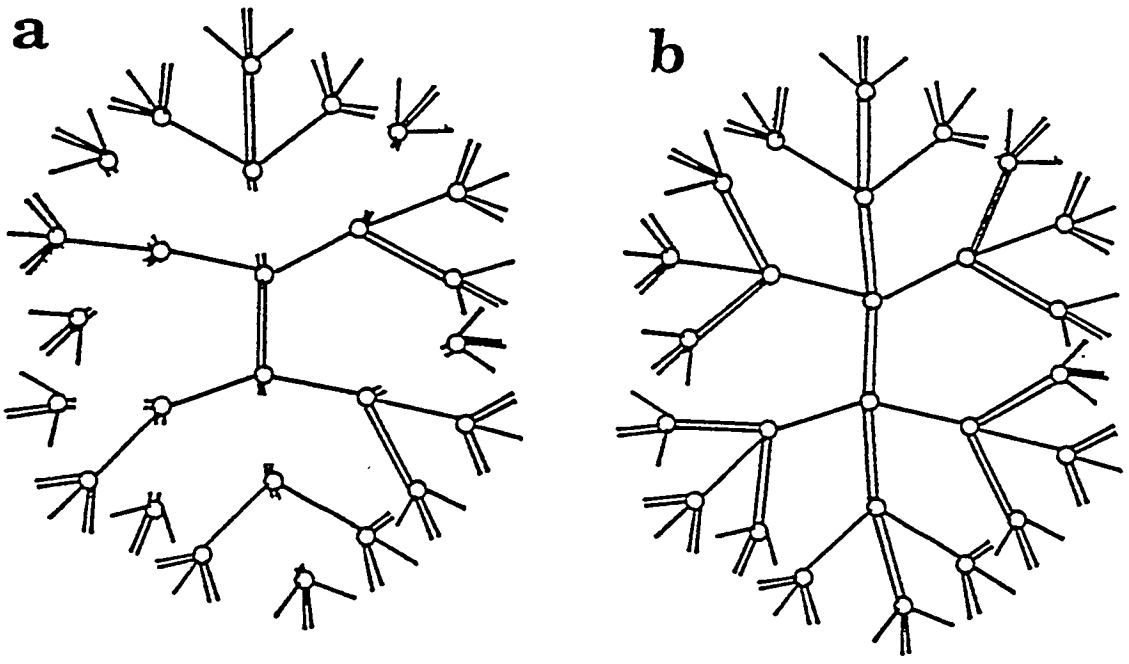

Figure 4.1 Bethe Lattice for two-σ model with $\sigma_1 = \sigma_2 = 1$ (shown as single bonds). a) With most double bonds representing the crosslinks not yet formed to represent the starting coal, the lattice is like one-σ model with $\sigma = 1$, linear chains. b) Fully linked case ($p = q = 1$) is like one-σ model with $\sigma = 3$.

FG-DVC Solution Technique

The "standard version" of the FG-DVC model implements the distributed rate kinetics by subdividing each functional group pool into 21 subpools, each with fixed rate parameters. This essentially decouples all the equations and allows us to integrate all 27*21 equations analytically, thereby allowing us to have large time increments. For the fixed bed model presented in this manual, this approach cannot be used: we must use the actual differential equations, and we have therefore treated the distributed rate kinetics differently. We start out with a Gaussian distribution for each functional group, as indicated by Eq 4.8. In the "standard" FG-DVC, model this distribution evolves away from the Gaussian as the subpools with lower activation energies are consumed. In this version, we retain the Gaussian shape of the distribution for all time (or more accurately, we retain the error function shape), and allow only the lower energy limit on the error function to change with time. This implies **one** extra differential equation (for the lower energy limit) per functional group instead of 21.

FG Submodel

As described in the previous Section, the model determines the weight loss of char to form tar and gas, where the initial char is a raw coal. The basic equations are Eqs. 4.7, 4.9, and 4.10. We start by defining a set of char fraction variables f as follows:

$$W_i(char,t) = W^0(char) \cdot f_i(t) \tag{4.11}$$

where

W^0 = the whole starting char (constant = 1.0)
$f_i(t)$ = the mass fraction of the starting char (coal) which can form gas species i at time t,

In order to implement the distributed activation energy reaction kinetics, each of these mass fraction functions, f_i, is described as a distribution function of activation energy, E:

$f_i(E,t)dE$ = the mass fraction of the starting char which, at time t, can evolve gas species i, with Arrhenius parameters given by frequency factor $A(i)$ [sec^{-1}], and activation energy between E and $E+dE$.

The integrals of these $f_i(E,t)$'s over all E are equal to the corresponding $f_i(t)$'s in Equation 4.11. In the discussion which follows, we usually leave out the time variable, t. Note that $f_i(E)$ is zero for $E < E^{min}$.

To this definition, we add the following definitions:

$$W_i(char,E) = W^0 \cdot f_i(E) \tag{4.12}$$

$$W_i(char,E) = W^0 \cdot \int_{-\infty}^{\infty} f_i(E)dE \tag{4.13}$$

and

$$k_i(E) = A_i \ exp\left(-\frac{E}{RT}\right) \tag{4.14}$$

Eqs. 4.12 and 4.13 imply that

$$W_i(char,E) = W^0(char) \cdot \frac{f_i(E)}{\int_{-\infty}^{\infty} f_i(E)dE} \tag{4.15}$$

For cases where the tar also pyrolyzes to form gases, we **assume** the same form (since the tar is functionally similar to the parent char).

$$W_i(tar,E) = W^0(tar) \cdot \frac{f_i(E)}{\int_{-\infty}^{\infty} f_i(E)dE} \qquad (4.16)$$

With these definitions, Eq 4.7 becomes

$$\frac{dW_i(gas)}{dt} = \int_{-\infty}^{\infty} k_i(E) \cdot [W_i(char,E) + W_i(tar,E)\begin{bmatrix}0\\1\end{bmatrix}]dE \qquad (4.17)$$

Eqs. 4.9 and 4.10 are unchanged.

If we define average kinetic rate constants as follows,

$$\langle k_i \rangle = \frac{\int_{-\infty}^{\infty} k_i(E) f_i(E)dE}{\int_{-\infty}^{\infty} f_i(E)dE} \qquad (4.18)$$

then Eq. 4.17 becomes

$$\frac{dW_i(gas)}{dt} = \langle k_i \rangle \cdot [W_i(char) + W_i(tar) \cdot \begin{bmatrix}0\\1\end{bmatrix}] \qquad (4.19)$$

Eqns. 4.9, 4.10, and 4.19, together with equations describing the time dependence of the distribution functions, are the basic differential equations needed for the FG submodel.

Distributed Rate Submodel (the f's)

As pointed out above, in the original versions of the FG and FG-DVC models, the $f(E)dE$ were approximated by initializing them to a Gaussian distribution and subdividing the range covering ±3 standard deviations into 21 equal energy increments. This approach gives 21 differential equations for each functional group and bridge (each subdivision decreases with the first order kinetics

given by the rate constants determined by Equation 4.18. This means that the shape of the *f(E)* changes with time. More recently, we have approximated this model by assuming that the shape remains fixed in time, but that the lower cutoff point changes in such a way as to give the same area under the *f(E)dE* curve as before. This gives a single differential equation for each distribution instead of 21. In this section, we derive this equation. For simplicity we assume that tar does not pyrolyze.

We start with the observation that

$$\frac{dW_i(gas)}{dt} = -\left(\frac{dW_i(char)}{dt}\right)_{tar,\ other\ held\ fixed} \tag{4.20}$$

and require that the distribution function is zero for the energies less than the minimum, and thus we differentiate Equation 4.13 with respect to time. Since only the lower bound of the integral, E_i^m, varies with time, the result is

$$\frac{dW_i(gas)}{dt} = W^0 \cdot f_i(E_i^m(t)) \cdot \frac{dE_i^m(t)}{dt} \tag{4.21}$$

Using Eqs. 4.15 and 4.19,

$$\frac{dW_i(gas)}{dt} = \langle k_i \rangle \cdot W_i(char) = \frac{W_i(char) \cdot f_i(E_i^m(t)) \cdot \dfrac{dE_i^m(t)}{dt}}{\displaystyle\int_{E_i^m(t)}^{\infty} f_i(E)dE} \tag{4.22}$$

Solving for *dE/dt*,

$$\frac{dE_i^m(t)}{dt} = \langle k_i \rangle \cdot \frac{\int_{E_i^m(t)}^{\infty} f_i(E)dE}{f_i(E_i^m(t))} \tag{4.23}$$

For simplicity, we use a truncated Gaussian, so that

$$\int_{E_i^m(t)}^{\infty} f_i(E)dE = erfc(z_i(t)) \tag{4.24}$$

$$z_i(t) = \frac{E_i^m(t) - E_i}{\sqrt{2}\sigma_i} \tag{4.25}$$

where E_i and σ_i are the parameters of the Gaussian distribution. We observe that the f_i's occur only in Eqns. 4.18 and 4.23, and only in normalized form, so the proportionality constant is not needed.

If there are source redistribution terms, then we must make suitable assumptions as to how these terms affect the distribution functions. For the cases considered to date, we have assumed that material removed from a given functional group, by mechanisms other than the bond breaking associated with freeing up the functional group, is removed from each activation energy subpool in proportion to its current quantity.

DVC Submodel

The DVC submodel is described fully in the General Model Paper (Solomon et al., 1988, see Appendix F). To implement this using the two coordination number percolation theory, as described in the Network Paper (Solomon et al., 1990, see Appendix E), we define two bond types (referred to as bridges and cross-links), each bond type having its own coordination number and probability of occupation. The bridges with probability of occupation, *p(t)* are broken with a distributed kinetic rate (in much the same manner as the gas functional groups

above). The cross-links (with probability of occupation, $q(t)$) are formed in conjunction with the evolution of CO_2 and CH_4. To cope with the problem of cross-linking tar to char, the cross-linking rate for dq/dt is divided by $W_i(char)$, i.e., the percolation is done on the whole coal basis. The current version of the model assumes that bridges are only broken (never formed), and that crosslinks are only formed (never broken). To model the hydrogen abstraction, the population of bridges is subdivided into labile and nonlabile (unbreakable) bridges, so that each time a labile bridge is broken, an additional labile bridge is converted into a non-labile bridge. Thus the differential equations needed for the percolation part of the model are

$$\frac{dp_L}{dt} = -2 \cdot \langle k_B \rangle \cdot p_L \tag{4.26}$$

$$\frac{dp}{dt} = -\langle k_B \rangle \cdot p_L \tag{4.27}$$

$$\frac{dp}{dt} = \sum_{CO_2, CH_4} \frac{dW_i(gas)}{dt} \cdot \frac{X_i}{M_i \cdot \Sigma W_i(char)} \tag{4.28}$$

where

p_L	=	the number fraction of bridge sites containing labile bridges
p	=	the number fraction of bridge sites containing either labile or nonlabile bridges
q	=	the number fraction of occupied crosslink sites.
X_i	=	the number of crosslinks formed for each molecule of gas i evolved [moles x-link/mole gas i)*(gm coal/crosslink site]
M_i	=	the molecular weight of gas species i [gm/mole]

and

$$\langle k_B \rangle = \frac{\int_{-\infty}^{\infty} k_B(E) f_B(E) dE}{\int_{-\infty}^{\infty} f_B(E) dE} \tag{4.29}$$

with

$$k_B(E) = A_B \cdot \exp\left(\frac{-E}{RT}\right) \tag{4.30}$$

where

$f_B(E)$ = the fraction of the starting bridges which can break at time t, with Arrhenius parameters given by frequency factor $A(B)[sec^{-1}]$, and activation energy between E and $E+dE$.

The $p(t)$ and $q(t)$ computed from these three differential equations are then used to compute the molecular weight distribution function, $F_j(p,q)$, from percolation theory. $F_j(p,q)$ is the weight fraction of *j-mers* in the char, and is a function only of p,q and the two coordination numbers.

This $F_j(p,q)$ is converted to the mass distribution function needed for the tar submodel by using a molecular weight distribution of monomers.

$$n_i(char) = \sum_j \frac{G_{ij} \cdot F_j(p,q)}{MT_i} \tag{4.31}$$

$$\chi_i = \frac{n_i(char) - n_i(tar)}{\sum_i [n_i(char) - n_i(tar)]} \tag{4.32}$$

where

$F_j(p,q)$ = mass fraction of coal in *j-mers* [gm j-mer/gm coal]

$n_i(char)$	=	fraction of coal in the *i-th* mass bin [mole *i*/gm coal]
$n_i(tar)$	=	fraction of tar in the *i-th* mass bin [mole *i*/gm coal]
G_{ij}	=	fraction of *j-mers* in the *i-th* mass bin [gm *i*/gm *j-mer*]
MT_i	=	Effective Molecular weight of the *i-th* mass bin [gm *i*/mole *i*]
χ_i	=	the mole fraction of material in the *i-th* mass bin [mole *i*/mole coal]

To allow for the fact that some of the tar has already evolved from the char, we use for tar evolution only the difference $n_i(char)$-$n_i(tar)$, (or zero if the difference is negative). Finally, we have

$$\left(\frac{dW(tar)}{dt}\right)_{DVC} = \sum_j \left(\frac{dn_j}{dt}\right) \cdot M_j \qquad (4.33)$$

Thus, from the differential equations for the p's and q, we compute (using Eqs. 4.13, 4.17 to 4.32) the quantities needed to evaluate the differential equation 4.6.

Calculation of $F_j(p,q)$ and $F(p,q)$

The probability $F_{s,u}(p,q)$, that a site is a member of a cluster of n sites with s bridges and u crosslinks, is given by

$$F_{s,u}(p,q) = a_{s,u} p^s (1-p)^\tau q^u (1-q)^\nu \qquad (4.34)$$

where

$$n = u + s + 1 \qquad (4.35)$$

$$\tau = (\sigma_i + 1)n - 2s \qquad (4.36)$$

$$\nu = (\sigma_2 + 1)n - 2u \qquad (4.37)$$

and τ, v are the number of broken bridges and crosslinks, respectively, on the perimeter of the cluster, and $a_{s,u}$ is the number of different ways to form such a cluster. To derive an expression for $a_{s,u}$, we note that $\Sigma_{all\ s,u}\ F_{s,u}\ (p,\ q)$ ---> 1.0 as both p and q go to 0; i.e., in the limit of no bonds, all sites are monomers with probability unity.

Second, define Z, W such that

$$Z = p(1-p)^{(\sigma_1-1)}(1-q)^{(\sigma_2+1)} \tag{4.38}$$

and

$$W = q(1-q)^{(\sigma_2-1)}(1-p)^{(\sigma_1+1)} \tag{4.39}$$

then we have, after some rearrangement,

$$\sum_{a,s} a_{s,u} Z^s W^u = \frac{1}{(1-p)^{\sigma_1+1}\cdot(1-q)^{\sigma_2+1}} \tag{4.40}$$

Then, following Fisher and Essam (1961), this can be evaluated using a two variable version of Cauchy's theorem as

$$a_{s,u} = \frac{1}{(2\pi i)^2}\oint\frac{dZ}{Z^{s+1}}\cdot\oint\frac{dW}{W^{u+1}}\frac{1}{(1-p)^{\sigma_1+1}\cdot(1-q)^{\sigma_2+1}} \tag{4.41}$$

to change variables in this double integral:

$$dW\,/\,dZ = \frac{\partial(W,Z)}{\partial(p,q)}dpdq = \left[\frac{\partial W}{\partial p}\cdot\frac{\partial Z}{\partial q} - \frac{\partial W}{\partial q}\cdot\frac{\partial Z}{\partial p}\right]\cdot dpdq \tag{4.42}$$

This can be evaluated from the definitions of W, Z; and we obtain the following integral for $a_{s,u}$:

$$a_{s,u} = \frac{1}{(2\pi i)^2} \oint dp \oint dq \frac{(1-\sigma_1 p)\cdot(1-\sigma_2 q) - pq(\sigma_2+1)}{p^{s+1} q^{u+1} (1-p)^{\tau+1} (1-q)^{\nu+1}} \quad (4.43)$$

This is easily factored into integrals of the form given by Fisher and Essam (1961), leading to the following expression:

$$a_{s,u} = \frac{(\sigma_1+1)(\sigma_2+1)}{(s+\tau)(u+\nu)} \binom{s+\tau}{s} \binom{u+\nu}{u} (u+s+1) \quad (4.44)$$

Note that for $u = 0$ (no cross-links), this reduces to the quantity nb_n in Grant et al., (1989) and Fisher and Essam (1961). To determine the probability, $F_n(p,q)$, that a given site is a member of a cluster of n sites, i.e., the fraction of *n-mers*, we must sum Eq. 4.34 over all possible values of s and u that give an n-site cluster:

$$F_n(p,q) = \sum_{s=0}^{n-1} a_{s,u} p^s (1-p)^\tau q^u (1-q)^\nu; \quad u = n-s-1 \quad (4.45)$$

The total fraction of sites, $F(p,q)$, in finite clusters is the sum over all s and u

$$F(p,q) = \sum_{s=0}^{\infty} \sum_{u=0}^{\infty} F_{s,u}(p,q) = \left(\frac{1-p}{1-p^*}\right)^{\sigma_1+1} \left(\frac{1-q}{1-q^*}\right)^{\sigma_2+1} \quad (4.46)$$

where p^* and q^* are obtained by finding the smallest roots of

$$p^* \cdot (1-p^*)^{\sigma_1-1} \cdot (1-q^*)^{\sigma_2+1} - p \cdot (1-p)^{\sigma_1-1} \cdot (1-q)^{\sigma_2+1} = 0 \quad (4.47)$$

$$q^* \cdot (1-q^*)^{\sigma_2-1} \cdot (1-p^*)^{\sigma_1+1} - q \cdot (1-q)^{\sigma_2-1} \cdot (1-p)^{\sigma_1+1} = 0 \quad (4.48)$$

The quantity $F(p,q)$ is used as the fluid fraction in the full DVC model, which is not currently used in the fixed bed submodel. The critical point, where an infinite lattice begins to form (i.e., $F(p,q)$ begins to decrease), becomes a critical curve that divides the p-q plane into two regions. Note that for $q = 0$, all the equations reduce to the single σ case given in Grant et al., (1989) and Fisher and Essam (1961).

Summary of Active Differential Equations

The Equation set that must be integrated for the FG-DVC submodel in the fixed bed code is thus

$$\frac{dW_i(tar)}{dt} = \left(\frac{dW(tar)}{dt}\right)_{DVC} \cdot \left(\frac{W_i(char)}{\sum_i W_i(char)}\right) - k_i \cdot W_i(tar) \cdot \begin{bmatrix} 0 \\ 1 \end{bmatrix} \quad (4.49)$$

$$\frac{dW_i(char)}{dt} = \frac{dW_i(gas)}{dt} - \frac{dW_i(tar)}{dt} + \frac{dW_i(DVC)}{dt} \quad (4.50)$$

$$\frac{dW_i(gas)}{dt} = \langle k_i \rangle \cdot \left[W_i(char) + W_i(tar) \cdot \begin{bmatrix} 0 \\ 1 \end{bmatrix}\right] \quad (4.51)$$

$$\frac{dp_L}{dt} = -2 \cdot \langle k_B \rangle \cdot p_L \quad (4.52)$$

$$\frac{dp}{dt} = -\langle k_B \rangle \cdot p_L \quad (4.53)$$

$$\frac{dq}{dt} = \sum_{CO_2 CH_4} \frac{dW_i(gas)}{dt} \cdot \frac{X_i}{M_i \cdot \Sigma W_i(char)} \quad (4.54)$$

$$\frac{dn_j}{dt} = P_j \chi_j \left(\frac{dn_i}{dt}\right)_{gas\ \ only} \left(\frac{1}{P_0 + \Delta P - \sum_{all\ tars} P_j \chi_j}\right) \quad (4.55)$$

$$\frac{dE_i^m(t)}{dt} = \langle k_i \rangle \cdot \frac{\int_{E_i^m(t)}^{\infty} f_i(E)dE}{f_i(E_i^m(t))} \quad (4.56)$$

CHAPTER 5

SOLUTION METHOD

The set of differential equations presented in Table 3.2, along with the auxiliary equations summarized in Tables 3.4 and 3.5, form the core of the FBED-1 model. These equations constitute a split boundary value problem, because the boundary conditions for all the dependent variables are not known at the same boundary. For the solid stream the boundary conditions are known at the top of the gasifier, whereas the boundary conditions for the gas stream are known at the bottom of the gasifier. Split boundary value problems can be solved by a shooting technique in which the unknown conditions at either boundary are guessed and then the system of equations is integrated to the other boundary. This requires iteration on the guessed conditions in order to satisfy the known boundary conditions.

In FBED-1, the two-zone, zero-dimensional submodel, FBED-0, as discussed in Chapter 2 is used to convert the split boundary value problem into an initial value problem by providing an initial estimate of the effluent gas composition and temperature. However, the gas exit temperature predicted by the two-zone submodel is always high due to the assumption that the devolatilization zone is at a single temperature. Likewise, the exit solid temperature may be high due to the uniform temperature and well-mixed assumption in the equilibrium zone. Thus after integrating from the top to the bottom of the reactor, the calculated temperature and compositions may be different from the input feed gas temperature and compositions. Therefore, a new guess for the product gas temperature and compositions must be obtained. This guess is obtained by integrating the gas phase quantities from the bottom to the top of the gasifier. This procedure can be repeated in an iterative manner until the calculated temperature and composition of the feed

gas satisfy the input feed gas conditions within the specified tolerances. The details on this iterative solution method are discussed in the next section.

Computational Algorithm

The computational algorithm for the one-dimensional model, using the two-zone submodel to obtain the initial guess for the gas phase quantities, is shown in Figures 5.1A to 5.1D. Subroutine names are shown in italics. The two-zone submodel solves overall energy and mass balances around the devolatilization and drying zone as well as the equilibrium (combustion and gasification) zone.

The initial conditions for the differential equations given in Table 3.2 are determined from the known values for the solid phase quantities and the values predicted by FBED-0 for the gas phase quantities. The integration of the system of equations is performed by LSODE (Hindmarsh, 1983). The derivatives of the dependent variables are evaluated by computing all the needed physical and thermodynamic quantities as given by the auxiliary equations listed in Table 3.7. The dependent variables are converted to the quantities of interest; e.g., total gas enthalpy is converted to gas temperature. The particle diameter and number density are calculated from Equations 3.22, and 3.24, respectively. Transport properties are calculated at the solid and gas temperatures and the corresponding particle diameter. Next, drying, devolatilization, oxidation and gasification rates are calculated.

The directions of the solid and gas flows are important. Flow in the positive axial direction, taken to be in the upward direction from the bottom to the top of the reactor, is considered positive, e. g., the gas flow rate. The flow rate of the solids is taken to be negative because the solid phase flows in the negative axial direction.

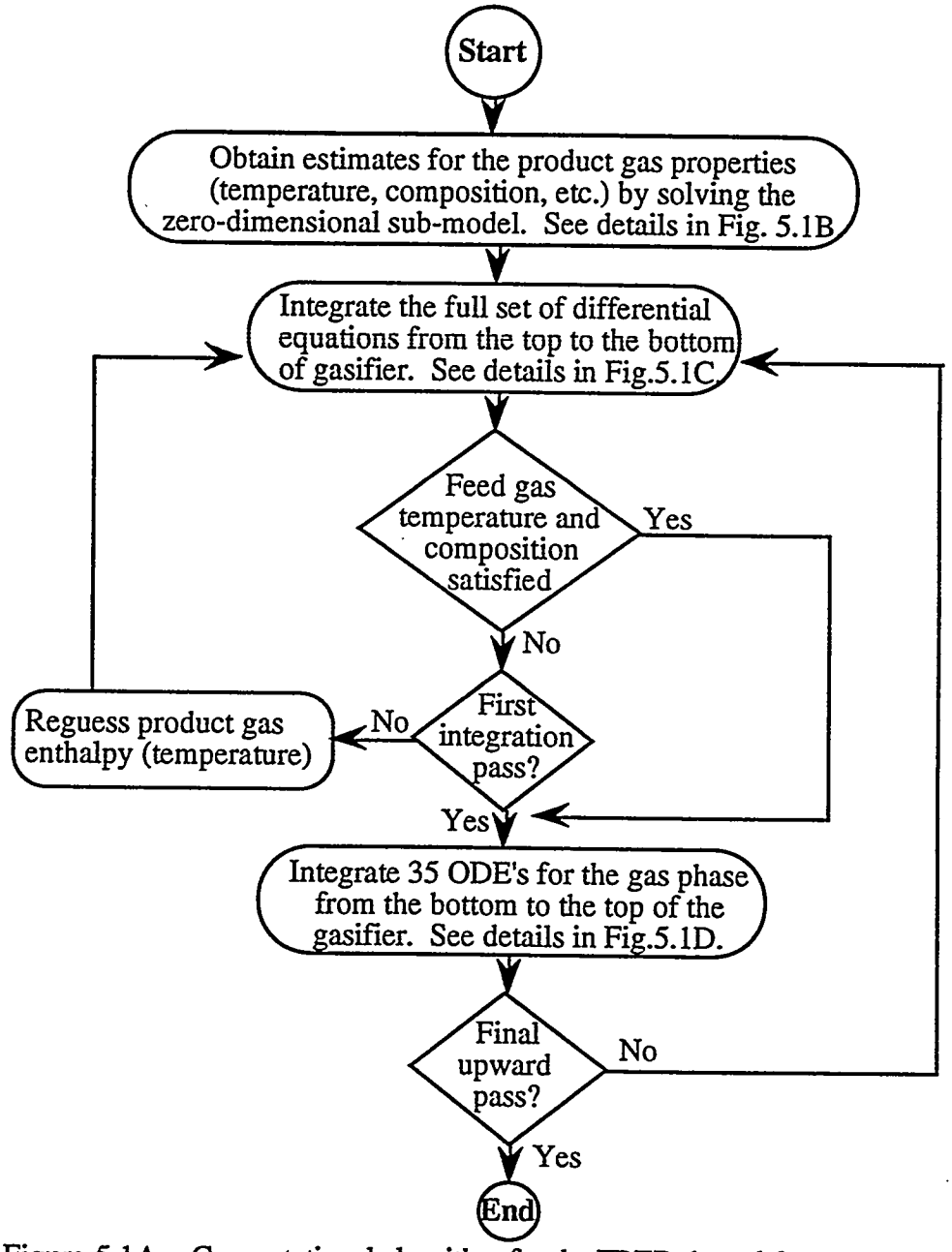

Figure 5.1A. Computational algorithm for the FBED-1 model.

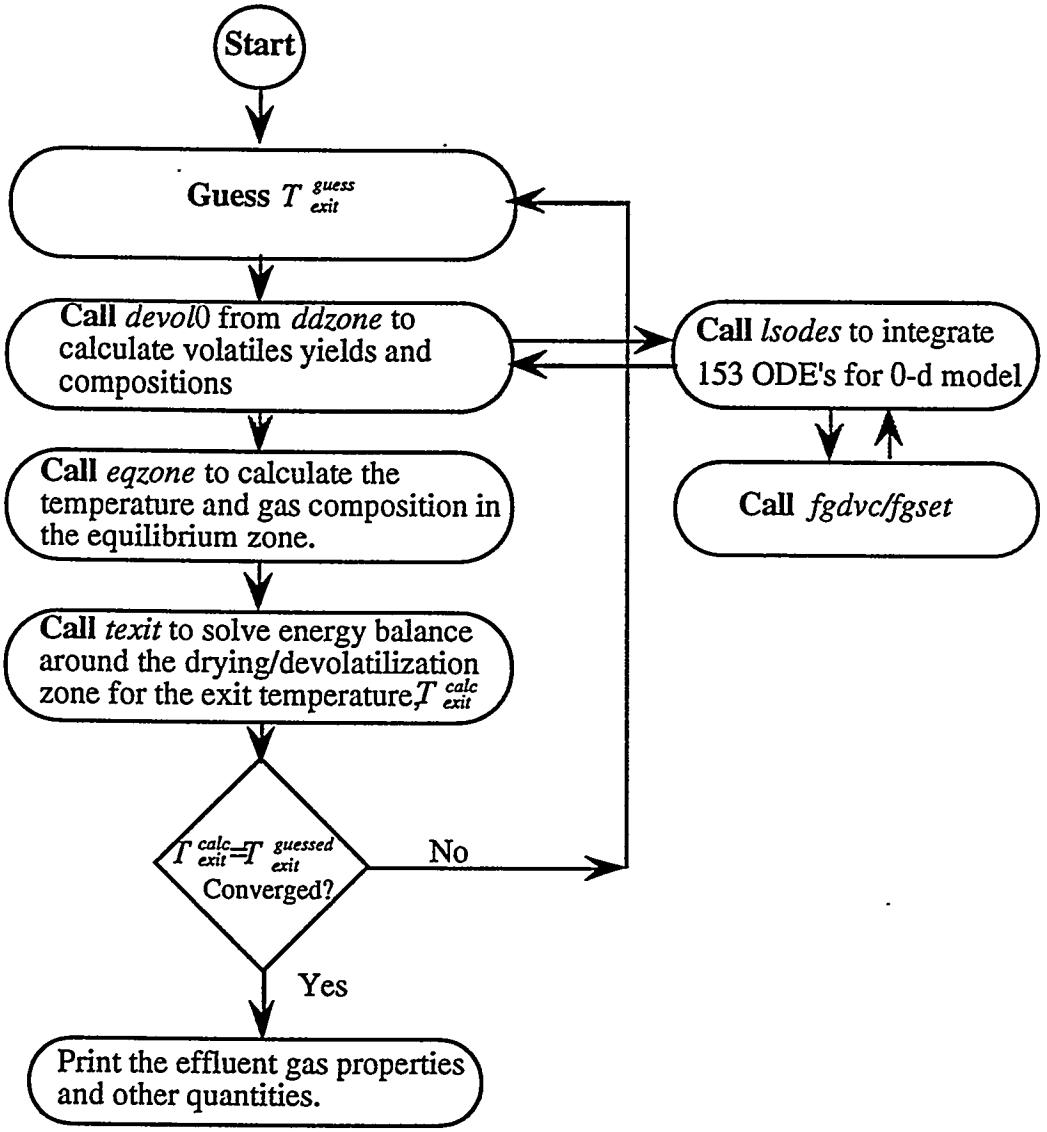

Figure 5.1B. Details of computational algorithm for the zero-dimensional submodel, FBED0D.

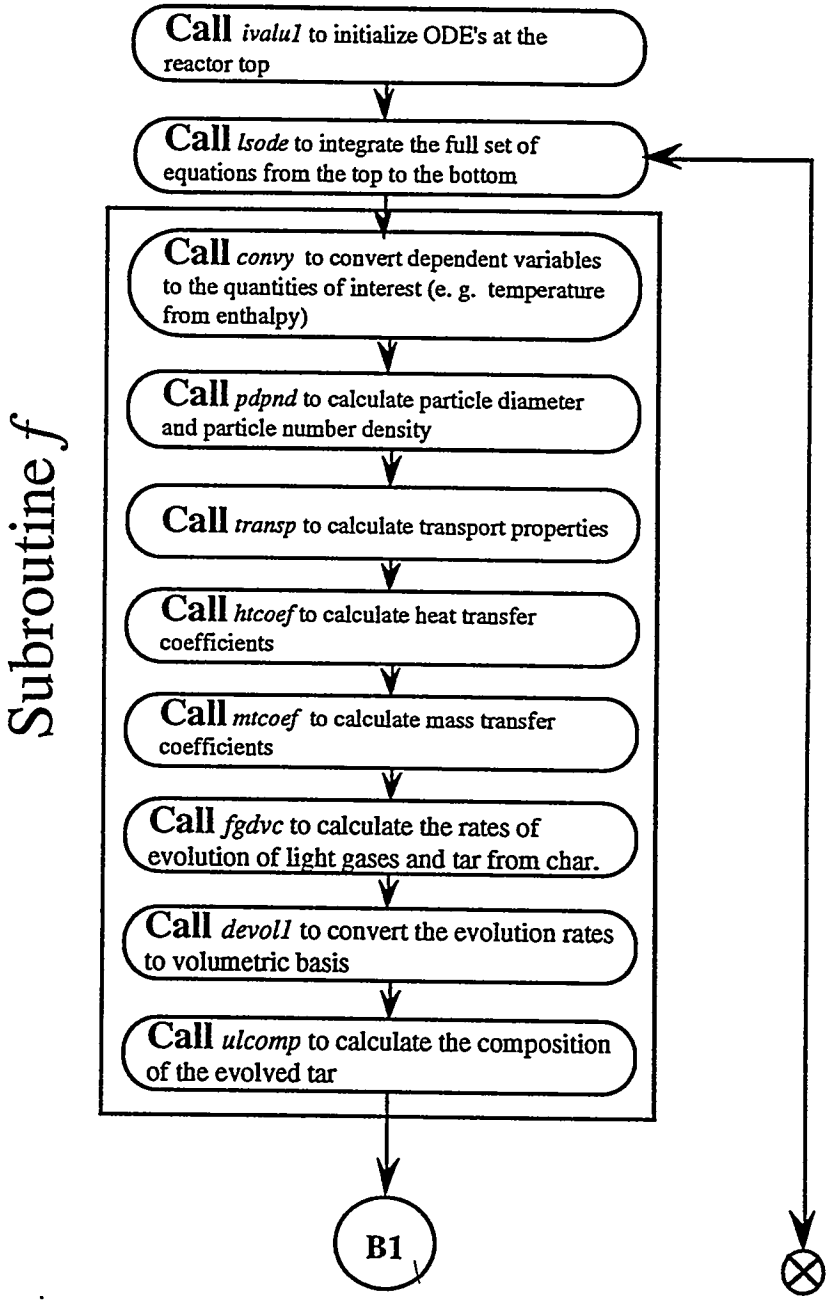
Call ivalu1 to initialize ODE's at the reactor top
Call lsode to integrate the full set of equations from the top to the bottom
Subroutine f
Call convy to convert dependent variables to the quantities of interest (e. g. temperature from enthalpy)
Call pdpnd to calculate particle diameter and particle number density
Call transp to calculate transport properties
Call htcoef to calculate heat transfer coefficients
Call mtcoef to calculate mass transfer coefficients
Call fgdvc to calculate the rates of evolution of light gases and tar from char.
Call devol1 to convert the evolution rates to volumetric basis
Call ulcomp to calculate the composition of the evolved tar
B1

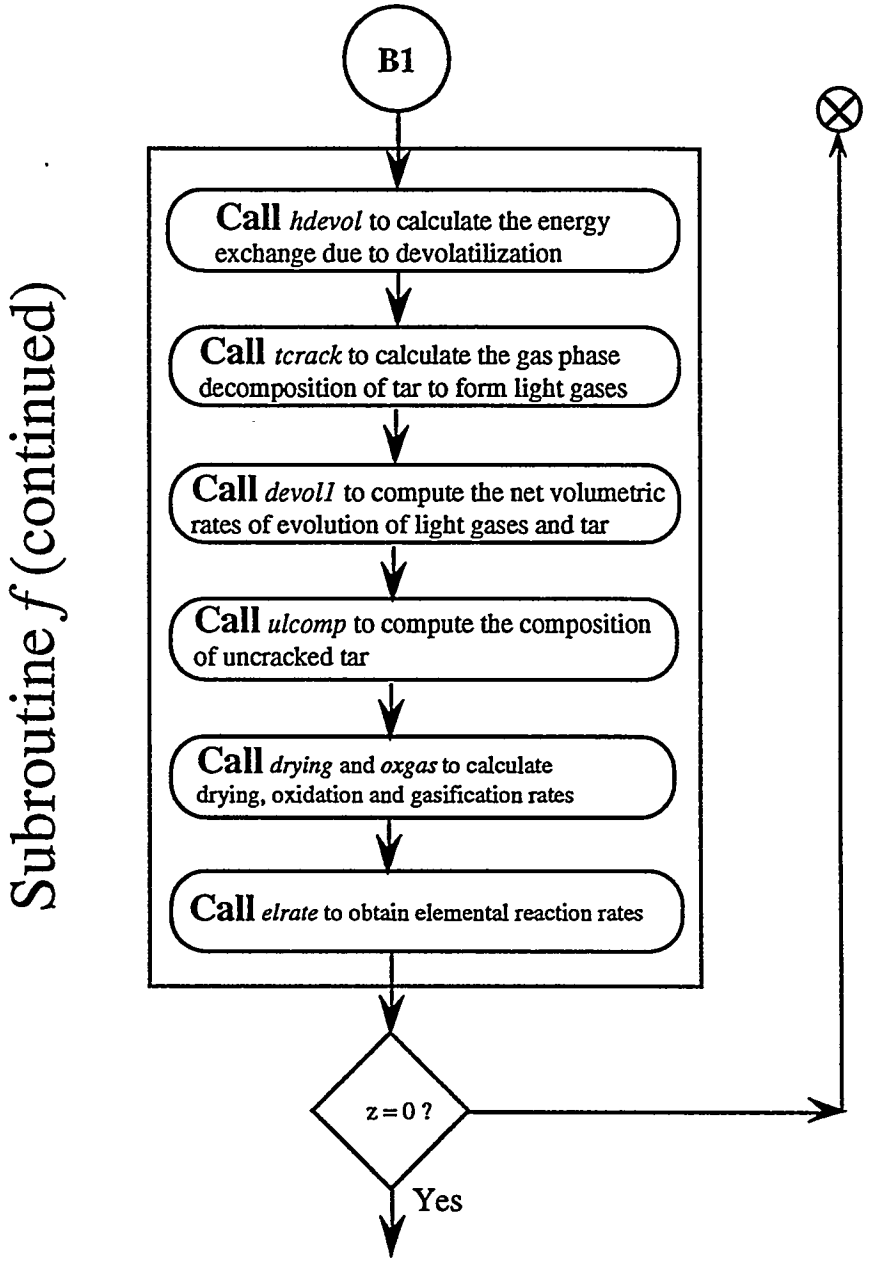

Figure 5.1C. Details of computational algorithm for the downward integration pass.

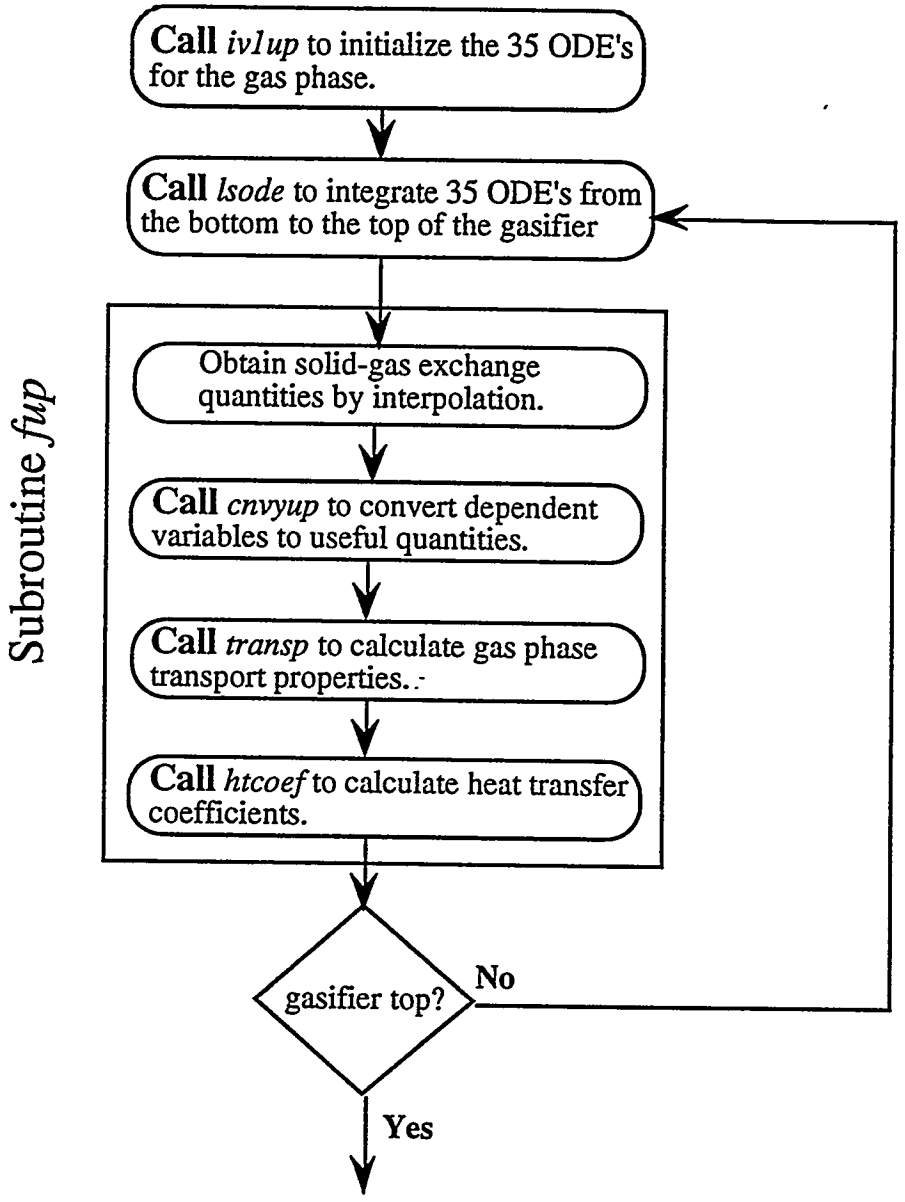

Figure 5.1D. Details of computational algorithm for the upward integration pass.

After integrating from the top to the bottom of the reactor, the calculated feed gas temperature and composition are compared to the input feed gas temperature and composition. If the values do not agree within the specified tolerances, the temperature and composition of the product gases must be guessed again and the procedure repeated in an iterative manner. In order to obtain a new estimate for the product gas temperature and composition, 35 differential equations for the gas phase, which are a subset of the full system of governing equations, are integrated from the bottom to the top of the gasifier. In the upward integration pass, the solid phase variables are held constant, and the solid-gas exchange quantities are calculated from the values predicted during the downward integration pass. This yields a new guess for the gas phase quantities at the top of the gasifier; this guess is then used for the next downward integration pass. This procedure, called split back-and-forth integration, may be repeated untill all the boundary conditions have been satisfied. Simulations with consecutive back-and-forth integrations did not show much change in the composition of the product gas. The predicted feed gas composition was also found to be close to the input feed gas composition and did not show much change in subsequent iterations. However, this procedure did not yield a converged feed gas temperature. In order to satisfy the feed gas temperature, the split back-and-forth integration was coupled with the shooting method with the product gas enthalpy as the iteration variable. In this scheme, the product gas enthalpy is varied, while all other gas phase quantities are held constant, and the complete set of equations is integrated from the top to the bottom of the gasifier. Once the feed gas temperature is converged within the specified tolerance, an upward pass is taken to compute the final product gas composition and temperature.

In general, burnout should also be used as an iteration variable. The predicted burnout from the one-dimensional model should be used in the zero-dimensioanl model to obtain new estimates for the product gas properties. However, burnout is typically high in fixed-bed gasifiers and is, therefore, assumed to be unity in our formulation. Iterations may be done both in an interactive mode and in an automatic mode. In the interactive mode, iterations are performed by adjusting the product gas temperature through the product gas enthalpy. A positive factor will increase the product gas temperature; a negative factor will lead to a lower product gas temperature. It is pointed out that a good set

of input parameters is essential for this procedure to work properly. The code will successfully execute in a noninteractive mode, provided the predicted value of the feed gas temperature obtained in the first iterative pass is close to the input feed gas temperature. Convergence is typically obtained in 8-10 iterations; CPU time is typically around one hour on a CONVEX 220 computer, and around two hours on a SUN 4/310 computer.

PART TWO: CODE USER'S INSTRUCTIONS

CHAPTER 6

USER'S GUIDE

FBED-1 was developed on a SUN 4/310 running under the UNIX operating system. The code is written in FORTRAN 77 and should be portable to machines with compatible compilers. Two plotting routines written for the DISSPLA graphics package are also distributed with the code and are discussed later. The source code occupies approximately 1.2 Megabytes of disk space. The executable and object code requires an additional 2 Megabytes of disk space. A total of 10 Megabytes may be needed for the additional graphics and output files.

The structure of the FBED-1 code and a description of the subroutines is presented in the next section. The functions performed by the subroutines used in the FBED-1 code are given in Appendix H. All input data to FBED-1 are in SI units. The input files are discussed later in this Chapter. All working variables within the program are either dimensionless or in SI units. Units associated with all variables are either given in the nomenclature or can be found in Appendix I.

CPU run time depends on the particular hardware on which the code has been implemented, as well as on the degree of compiler optimization. Typical CPU time on a CONVEX 220 is around one hour. The same simulation on a SUN 4/310 requires around two hours of CPU time.

Description of Subroutines

The computational algorithm for FBED-1 was shown in Figure 5.1. A tree diagram of the structure of the program showing most of the actual subroutines is given in Figures 6.1 and 6.2. The differential equation solver LSODE or LSODES is represented by it's main routine, shown as a black box in Figures 6.1 and 6.2.

The main program is named FBED1D; its structure and the various routines called by it are shown in Figure 6.1. The routine CPUTIM is called to track the execution time. The first function performed by the main program FBED1D is the reading of the input data. This is accomplished through the subroutine READIN. The subroutine READIN reads the input data from the data file FB1IN. It also invokes the reading of the input data file FB1THM from the subroutine CREE0 and COAL0.ARGX from the subroutine COALIN. The X in the COAL0.ARGX corresponds to an appropriate value as input by the user. The subroutine COALIN also adjusts the input functional group composition, which is read from the data file COAL0.ARGX, to match the ultimate composition of the feed coal. This is achieved by a call to the subroutine ADJSTY0. In addition, subroutine READIN also computes the coefficients for the polynomial expression of ash heat capacity through a call to the module ASHCP and the input properties of the feed gas through a call to the module GASIN. The input files, which are read in the module READIN, are discussed further in the next section. Then the subroutine ECHOIN is called to echo the input data, as well as a number of computed quantities to the output file, FB1OUT, which is discussed in more detail in the next section. Then the main program FBED1D calls the routine FBED0D, which provides the initial estimates of the effluent gas properties. The structure and the routines associated with subprogram FBED0D, shown in Figure 6.2, are discussed later in this section. To compute the CPU time for the zero-dimensional portion of the code, another call is made to the routine CPUTIM. Next, the dependent variables are initialized through a call to either IVALU1 or IV1UP, depending on the direction of integration. The routine IVALU1 also calls the routine IVALU0 to initialize the dependent variables that relate to the zero-dimensional portion of the code, i.e., for the devolatilization submodel. In order to initialize the derivatives of all the dependent variables at the start of the integration, a call is made to the subroutine F.

The subroutine F calls a number of other subroutines, which are discussed later. The integration of the system of differential equations is performed by the LSODE integration package. The main integration routine LSODE also calls the subroutine F, as needed, to compute the derivatives. The control is transferred back to the main program FBED1D when the independent variable attains the final value **tout**, as specified in the main program. At this stage, another call is made, from the main program FBED1D, to either F or FUP, to compute the derivatives of the dependent variables at **tout**. The results are printed in the output files at each output location. A machine dependent routine FLUSH is used to write the buffer to the output files. This procedure is repeated iteratively following the logic discussed in the Chapter 5. Finally, after a converged solution is obtained, the mass and energy balance calculations are performed by calling the subroutine BALANC.

The subroutine F is the most important of all because it computes the derivatives of the dependent variables, which is done through calls to a number of other routines. First, the routine CONVY is called, which converts the dependent variables to the quantities of interest such as temperature from enthalpy. This routine also calculates the equilibrium composition and temperature of the gas, and the temperature of the solid stream, by calling the equilibrium code CREE and the subroutine PTEMP. When the gas phase is kept out of chemical equilibrium, the gas temperature is determined by a call to the subroutine GTEMP. The routine PDPND is called to update the particle diameter as well as particle number density. Next, transport properties of the gas phase are computed by calling the routine TRANSP.

The next step is the calculations of the heat and mass transfer coefficients, accomplished through calls to the routines HTCOEF and MTCOEF respectively. Now the derivatives of the dependent variables related to the devolatilization model are computed by calling either the routine FGDVC or FGSET. Next, the volumetric rates of devolatilization are calculated by calling the routine DEVOL1. The ultimate composition of the evolved tar is computed by the routine ULCOMP. The heat of devolatilization is computed by the routine HDEVOL. The decomposition of tar to the gas is calculated by the subroutine TCRACK. The subroutines DEVOL1 and ULCOMP are called again to update the volumetric rates

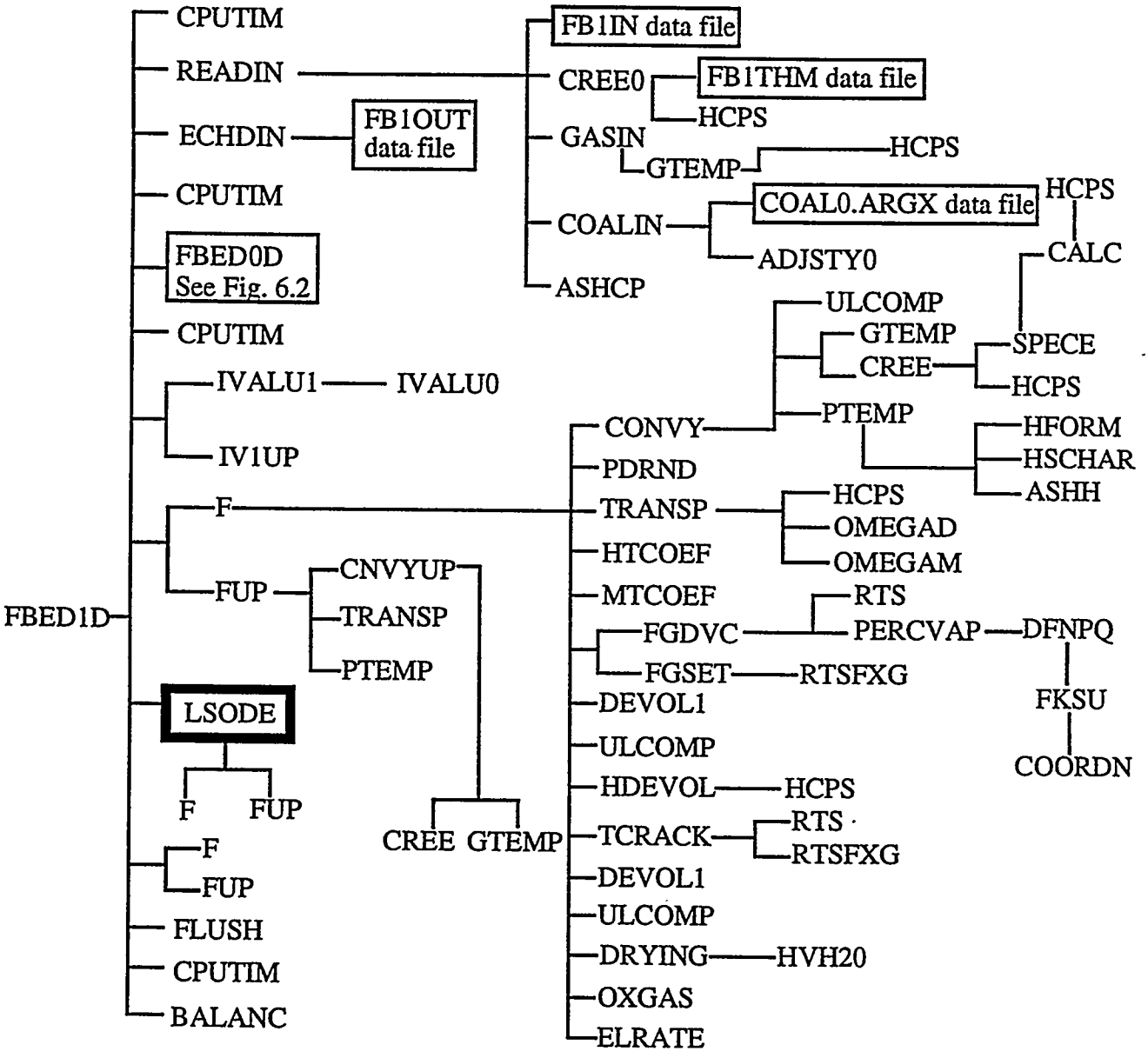

Figure 6.1. Structure of the main program FBED1D.

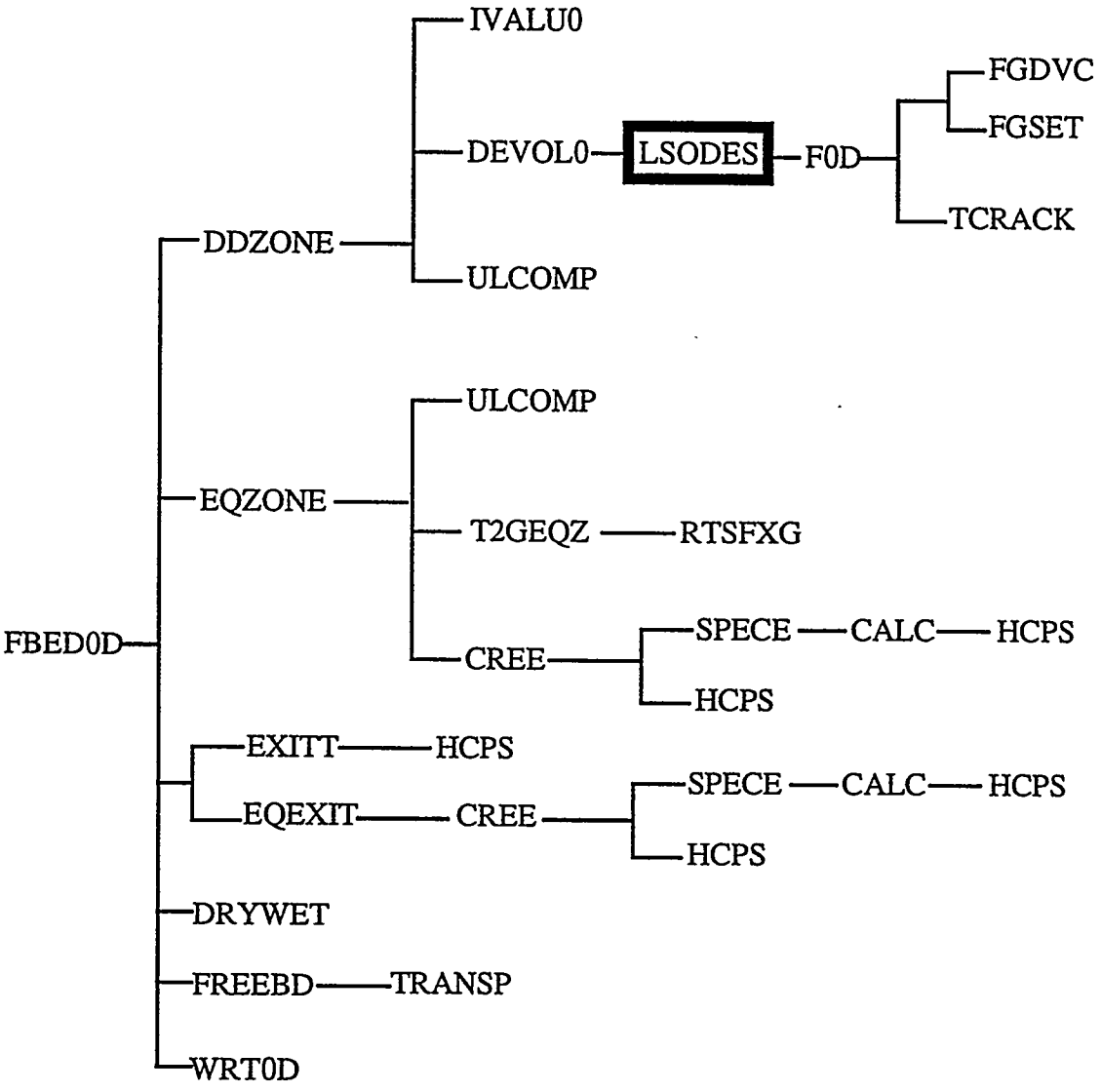

Figure 6.2. Structure of the subprogram FBED0D.

of tar and gas evolution and the ultimate composition of the tar. Then volumetric rates of drying, oxidation and gasification are calculated by calling the routines DRYING and OXGAS. Finally, the subroutine ELRATE converts the volumetric rates to elemental basis. These computed quantities are then used to compute the derivatives of the quantities related to the one-dimensional model.

During the upward integration pass, a subset of the full differential equation set is integrated. The number of equations for the upward pass is 35; these are related to the gas and tar quantities. The corresponding routines for initialization, computations of the derivatives, and conversion of the dependent variables to the quantities of interest are IV1UP, FUP, and CNVYUP.

The subroutine FBED0D calculates the effluent gas temperature and composition according to the two-zone submodel discussed in chapter 2. The program structure for the FBED0D is shown in Figure 6.2. First, it calls the subroutine DDZONE, which in turn calls the subroutines IVALU0, DEVOL0, and ULCOMP. The routine IVALU0 initializes the variables for the zero-dimensional model. The subroutine DEVOL0 calculates the ultimate volatiles yield and composition based on the selected devolatilization submodel. This is accomplished through the integration of the system of equations for the zero-dimensional submodel. The differential equations for this submodel are integrated using the sparse version of the integrator, i.e., LSODES, which is called from DEVOL0. The subroutine DDZONE also computes the ultimate composition of tar and char. Next, the subroutine EQZONE is called, which computes the composition and temperature of the gases leaving the equilibrium zone and entering the drying and devolatilization zone. Then the temperature of the gases leaving the drying and devolatilization zone is computed either by assuming all gases to be in thermal and chemical equilibrium, or by keeping the moisture and the gases released in the drying and devolatilization zone to be out of chemical equilibrium. This is accomplished by calls to the subroutines EQEXIT and EXITT respectively. This procedure is repeated iteratively following the logic explained in Figure 5.1B. Finally, the effluent gas composition is determined on both dry and wet basis, heat loss in the freeboard is calculated, and the results are written to the output file FB1OUT by calling the subroutines DRYWET, FREEBD, and WRT0D respectively.

Program Input

Three input data files are needed for the execution of FBED-1. These files are text files and can be generated or modified using any text editor. The first input data file, FB1IN, provides the essential input data, which include the operational parameters, e.g., gasifier dimensions, temperatures, flow rates and compositions of the gas and solid streams, flags for submodel selection, etc. In addition, values for parameters needed for integration routines, such as tolerances and operation mode (single-step/multi-step), are provided. All variables are fully explained in the input file. The second data file, FB1THM, provides the elemental and species data for thermodynamic calculations and parameters for the calculation of transport properties. The third data file provides the input data for the devolatilization submodel; data include the number of functional groups, the initial functional group composition, the kinetic parameters for rate coefficients based on the distributed activation energy model, and cross-linking efficiency for each functional group. In addition, input values for the DVC portion (percolation submodel) are provided. An optional input file EXPT.DAT is also needed when the experimental data for the effluent gas properties are available. A description of these data files is given in the next section.

Main Input Data File, FB1IN

A typical input data file (FB1IN) is shown in Table 6.1.

Table 6.1 Main data file, FB1IN.

```
5,                              !nsay..(say(i),i=1,nsay) follows:
*****************************************************************  FBED1D
***************  BRIGHAM YOUNG UNIVERSITY SIMULATION OF  *******  Vol. 2
*****************  WELLMAN GALUSHA 10/30/82 TEST USING   ******* Page 68
***********************  JETSON BITUMINOUS COAL  ************************
***************************************************************** 12/10/92
-----------------------------------------------------------------------
ESSENTIAL INPUT PARAMETERS TO RUN ZERO-DIMENSIONAL MODEL:
-----------------------------------------------------------------------
    f       * l0d     (T--> do 0-d calculation only)
    t       * lgaseq  (T--> all exit gases\but tar in equilibrium)
    f       * lfreeb  (T--> do FREEBoard calculation using qfreeb)
    f       * ljkstm  (T--> calculate heat loss with flowjs latent heat)
```

```
     f       * lashcp (T--> use ASH composition to calculate CP)
     f       * lx0    (T--> use usrx0 for x0 rather than SET model x0)
     t       * lecho  (T--> echo input parameters to mb1out)
     t       * ldvc   (T--> use FG-DVC submodel for devolatilization)
     f       * lfixg  (T--> use FIXd Gaussian to compute tar crack. rates)
     t       * lexpt  (T--> Experimental values available for comparison)
1.9812d0     * diach  (DIAmeter of reactor CHamber, m)
2.0828d0     * chlgh  (reactor CHamber axial LenGtH, m)
1.02259d5    * pres   (reactor PRESsure at bed top, Pa, GUESS)
342.89d0     * twtop  (Temperature of Wall at reactor TOP, K)
287.31d0     * twbot  (Temperature of Wall at reactor BOTtom, K)
298.0d0      * tcoal  (Temperature of feed COAL, K)
0.0d0        * qfreeb (heat loss in FREEBoard, watts)
0.3524d0     * flowc  (FLOW rate of feed Coal, kg/s)
0.9481d0     * flowo  (FLOW rate of Oxidizer in feed, air or oxygen, kg/s)
0.1562d0     * flows  (FLOW rate of Steam in feed, kg/s)
0.13390      * flowjs (FLOW rate of Jacket Steam, kg/s)
0.80d6       * qwall  (overall wall heat loss, W)
0.0d0        * trf    (Recycled Tar fraction)
0.0d0        * trctar (Temperature of ReCycled TAR, K)
0.0490d0     * prxash (PRoXimate ASH fraction)
0.4908d0     * prxfc  (PRoXimate Fixed Carbon fraction)
0.0671d0     * prxh2o (PRoXimate moisture fraction)
0.3931d0     * prxvm  (PRoXimate Volatile fraction))
0.8125d0     * udaffc(1) (ultimate Carbon fraction, Dry Ash-Free basis)
0.0505d0     * udaffc(2) (ultimate Hydrogen fraction, Dry Ash-Free basis)
0.1037d0     * udaffc(3) (ultimate Oxygen fraction, Dry Ash-Free basis)
0.0170d0     * udaffc(4) (ultimate Nitrogen fraction, Dry Ash-Free basis)
0.0163d0     * udaffc(5) (ultimate Sulfur fraction, Dry Ash-Free basis)
1704.2d0     * tmash     (Melting Temperature of ASH, K)
0.4204d0     * wtash(1)  (mass fraction SIO2 in Ash)
0.0091d0     * wtash(2)  (mass fraction CAO in Ash)
0.1985d0     * wtash(3)  (mass fraction AL2CO3 in Ash)
0.0066d0     * wtash(4)  (mass fraction MGO in Ash)
0.0127d0     * wtash(5)  (mass fraction K2O in Ash)
0.0023d0     * wtash(6)  (mass fraction NA2O in Ash)
0.0109d0     * wtash(7)  (mass fraction TIO2 in Ash)
0.0d0        * wtash(8)  (mass fraction MNO in Ash)
0.0852d0     * wtash(9)  (mass fraction FEO in Ash)
0.2434d0     * wtash(10) (mass fraction FE2O3 in Ash)
0.0d0        * wtash(11) (mass fraction free iron, FE, in Ash)
0.0002d0     * wtash(12) (mass fraction P2O5 in Ash)
0.0d0        * wtash(13) (mass fraction CAF2 in Ash)
0.0108d0     * wtash(14) (mass fraction SO3 in Ash)
1.0d0        * bout0d (BurnOUT for 0-Dimensional part)
0            * idcoal (IDentification flag for coal data file)
0.1560       * usrx0  (USeR supplied X0, used when lx0 is set to t)
elements     * elem   (flag to read ELEMent data in cree0)
thermo       * ther   (flag to read species data in cree0)
```

```
reactant    * reac    (flag to read REACtant feed stream 1, steam)
560.0d0     * tf1     (Temperature of Feed stream 1 or steam feed, K)
 h2.0      O1.0       0.0       0.0     h2o       1.00000m
                                                              (blank Line)
reactant    * reac    (flag to read REACtant feed stream 0, oxidizer)
560.0d0     * tf0     (Temperature of Feed stream 0 or oxidizer feed, K)
 o2.0       0.0       0.0       0.0     o2        0.20990m
ar1.0       0.0       0.0       0.0     ar        0.00980m
 n2.0       0.0       0.0       0.0     n2        0.78030m
                                                              (blank Line)
-------------------------------------------------------------------------
ADDITIONAL INPUT PARAMETERS TO RUN ONE-DIMENSIONAL MODEL:
-------------------------------------------------------------------------
    t       * lsp     (T--> Shell Progressive rather than ash segregation)
    f       * ltareq  (T--> let TAR go to equilibrium in the gas phase)
    f       * lstiff  (T--> use STIFF LSODE solver)
    t       * lstop   (T--> STOP calculation when bottom of reactor reached)
    t       * louta   (T--> print output file OUTA
    t       * loutb   (T--> print output file OUTB
    t       * loutc   (T--> print output file OUTC
    t       * loutd   (T--> print output file OUTD
    t       * loute   (T--> print output file OUTE
    t       * loutf   (T--> print output file OUTF
    t       * loutg   (T--> print output file OUTG
    t       * louth   (T--> print output file OUTH
    t       * louti   (T--> print output file OUTI
    t       * loutj   (T--> print output file OUTJ
1           * itask   (LSODE parameter used to specify output)
0.01d0      * deltaz  (step size for output, m)
1.0d-8      * abstol  (ABSolute TOLerance)
1.0d-4      * reltol  (RELative TOLerance)
2.17d-2     * pd0     (initial Particle Diameter, m)
0.10d0      * gamma   (swelling parameter, fraction)
1.0d0       * zi      (heat of rxn partition, if zi = 1, rxn heat to solid)
0.60d0      * vfash   (Void Fraction in ASH zone, volume void/total volume)
0.33d0      * vfcoal  (Void Fraction in COAL zone at reactor solid feed port)
1.192d3     * rhosm   (apparent coal density, kg/m^3)
0.1359d0    * poros   (POROSity of coal)
0.589d3     * ffco2   (Frequency Factor for CO2 gasification, m/K_s)
0.589d0     * ffh2    (Frequency Factor for H2 gasification, m/K_s)
0.589d3     * ffh2o   (Frequency Factor for H2O gasification, m/K_s)
2.3d0       * ffo2    (Frequency Factor for O2 oxidation, m/K_s)
2.2282d8    * eco2    (activation Energy for CO2 gasification, J/kmol)
2.2282d8    * eh2     (activation Energy for H2 gasification, J/kmol)
2.2282d8    * eh2o    (activation Energy for H2O gasification, J/kmol)
9.2285d7    * eo2     (activation Energy for O2 oxidation, J/kmol)
1.0d0       * zeta    (particle area factor to account for internal burning)
0.5d0       * apdivt  (developing Ash Porosity DIVided by Tortuosity)
0.05d0      * adfhsg  (ADjstable Factor for Solid to Gas Heat transfer coef.)
```

```
1.0d0       * adfdev (ADjustable Factor for DEVolatilization)
1.0d0       * adfco2 (ADjustable Factor for co2 gasification reaction)
1.0d0       * adfh2  (ADjustable Factor for h2 gasification reaction)
1.0d0       * adfh2o (ADjustable Factor for h2o gasification reaction)
1.0d0       * adfo2  (ADjustable Factor for oxidation reaction)
1.0d0       * adfhgw (ADjustable Factor for Gas-to-Wall Heat transfer coef.)
1.0d0       * adfhsw (ADjustable Factor for Solid-to-Wall Heat transfer coef.)
1200.0d0    * tswtch (Temperature at which to SWiTCH to non-reactive gases)
1.03567d5   * pbotom (Presure at the BOTtOM of the bed, Pa)
0.0d0       * zbotom (Boundary Axial Position for integration purpose, m )
1.0d0       * deltat (Tolerance for temperature convergence, K)
1.0d-3      * hmax   (MAXimum step size allowed for LSODE)
    f       * intrac (T --> Run the code INTeRACtively)
1           * itratn (Number of back & forth sweeps before starting ITeRATioNs)
```

When setting up a new problem for simulation, it is easiest to start by editing the input files from a previous simulation, since much of the information remains unchanged. The main input file, FB1IN, is divided into two major sections. The first section contains the required data to run the two-zone, zero-dimensional submodel; the second section contains the additional data required to run the one-dimensional model.

Most of the input data in FB1IN are single line, format free entries. After the data value, a comment statement is provided to describe the input variable. The variable is given in lower case, followed by its description and units, if required. Upper case is used in description to indicate the selection of the variable name (e.g., **diach** **DIA**meter of reactor **CH**amber, m).

The first entry in the file FB1IN is the integer **nsay**, which indicates the number of header statements that are printed at the top of the main output file FB1OUT. Any number of comment statements may be included in the header. In the sample file shown in Table 6.1, five comment lines are used to describe the simulation. Following the five comment lines, three more lines are used to differentiate the zero-dimensional input parameters from the one-dimensional input parameters. **These three lines are required and must be included in the input file.**

The next nine entries provide logical input parameters for the zero-dimensional model in an L5 format: **l0d, lgaseq, lfreeb, ljkstm, lashcp,**

lx0, lecho, ldvc, and lfixg. These options are discussed in more detail later in this chapter. The next entry is the value of the logical variable **lexpt** in L5 format. If this variable is set to .true., then the optional input file EXPT.DAT must be provided. The next fourteen entries following the logical inputs are format free and describe the reactor geometry (**diach** and **chlgh**), reactor pressure at the bed top (**pres**), temperature of the wall at the top of the reactor (**twtop**), temperature of the wall at the bottom of the reactor (**twbot**), the feed coal temperature (**tcoal**), the freeboard heat loss (**qfreeb**), the flow rate of the feed coal (**flowc**), the flow rate of the oxidizer in the feed (**flowo**), the flow rate of the steam in the feed (**flows**), the flow rate of jacket steam (**flowjs**), the 0-D overall wall heat loss (**qwall**), the recycled tar fraction (**trf**), and the temperature of the tar recycle fraction (**trctar**). All of these fourteen parameters are not used in the zero-dimensional calculation. The recycled tar fraction and temperature are used only when the recycle stream is provided; otherwise these are set to zero. Similarly, the jacket steam flow rate is used to calculate the wall heat loss based on the heat of vaporization of steam, provided the logical variable **ljkstm** is set to .true.. When the wall heat loss is calculated based on the jacket steam flow rate, the estimated wall heat loss is set to zero.

The next nine entries provide the proximate and the ultimate analysis of feed coal. These are followed by the melting temperature and the composition of the mineral constituents of the ash. The next entry, **bout0d**, specifies the burnout of char for the zero-dimensional portion . The next two entries essential to run the zero-dimensional portion of the code are related to devolatilization. The integer variable, **idcoal**, governs the selection of input data file for the FG-DVC submodel; it is discussed later. The next variable, **usrx0**, is used to specify the potential tar-forming fraction when the flags **lx0** is set to .true. and the flag **ldvc** is set to .false..

The next two entries, **elem** and **ther**, invoke the reading of the data from the thermodynamic input data file FB1THM. The keyword **reac** invokes the reading of feed gas streams temperature and composition. In FBED-1 formulation, only two gaseous reactant streams are allowed; steam and oxidant. The oxidant stream may be either air or oxygen. **A blank line signifies the end of data for a particular reactant stream and must be included.** Following the

keyword **reac**, the temperature of the stream is input in a format free manner. This is followed by the species atomic composition. A separate line is used for each species. The atomic composition of each species is provided by formatted input, 4(a2,f7.5). The character string, in a2 format, describes the element. For example, " h" is used for hydrogen as shown in Table 5.1. Note the blank before the "h" is required for the a2 format. The real value following the element character string, in f7.5 format, describes the number of atoms. For example, in Table 6.1, " h2.0 " indicates two hydrogen atoms per water molecule. The four blanks following the 2.0 are consistent with the f7.5 format specification. Following the description of the atomic composition of the species, the species name is described in a 2a4 format. Finally, the composition of the species in the reactant stream is provided with a format specification of (1x,f7.5,1a). For example, pure steam is specified as " 1.00000m" in Table 6.1. **A blank must precede the concentration fraction as required by the format specification.** The character "m" following the concentration fraction specifies the fraction as a mole fraction. Weight fractions can be specified by using a "w" instead of an "m" after the species concentration fraction. The complete format specification for the species definition is (4(a2,f7.5),2a4,1x,f7.5,a1).

The second half of the input file FB1IN is used to provide the additional input data that are necessary to run the one-dimensional fixed-bed model, as described in chapter 3. The additional one-dimensional parameters are separated from the essential zero-dimensional input parameters by the **required** three comment lines, which are followed by fifteen lines of logical input parameters: **lsp, ltareq, lstiff, lstop, louta, loutb, loutc, loutd, loute, loutf, loutg, louth, louti, and loutj.** Parameters essential to the differential equation solver then follow. The differential equation solver, LSODE, requires **itask** and **deltaz** to specify the mode of operation (single-step or multi-step) and output. Tolerances are specified with the variables **abstol** and **reltol.** For more information on the differential equation solver LSODE, the reader is referred to Hindmarsh (1983).

The diameter of the feed coal particles is then specified as **pd0.** In FBED-1, multiple particle sizes in the feed coal are not treated. Particle swelling is assumed to be proportional to the extent of devolatilization. The swelling parameter

is input as **gamma**. The next entry, **zi**, specifies the heat of reaction partition, which assigns part of the heat of reaction to solid phase and remainder to the gas phase. The void fractions at the top and bottom of the bed are represented by **vfcoal** and **vfash**, respectively. Next, the format free apparent coal density and coal porosity are represented by **rhosm** and **poros** respectively. Likewise, the gasification and oxidation kinetics are also provided in format free manner. The frequency factors are provided first, followed by the activation energies: **ffco2, ffh2, ffh2o, ffo2, eco2, eh2, eh2o,** and **eo2.** The remaining parameters required to run FBED-1 are used to study the sensitivities of various parameters. Some of these values represent the observed physical phenomena. The remaining format free parameters are the particle area factor, used to account for internal particle burning (**zeta**), the developing ash porosity divided by tortuosity squared (**apdivt**), the adjustable factor for the solid-to-gas heat transfer (**adfhsg**), the adjustable factor for devolatilization mass transfer (**adfdev**), the adjustable factor for CO_2 gasification kinetics (**adfco2**), the adjustable factor for H_2 gasification kinetics (**adfh2**), the adjustable factor for H_2O gasification kinetics (**adfh2o**), the adjustable factor for oxidation kinetics (**adfo2**), the adjustable factor for gas-to-wall heat transfer (**adfhgw**), and the adjustable factor for solid-to-wall heat transfer (**adfhsw**). The next entries are **tswtch**, the temperature below which the gases are assumed to be nonreactive; **pbotom**, the pressure at the bottom of the gasifier bed; **zbotom**, which specifies the axial position at the bottom of the gasifier; **deltat**, the tolerance for the feed gas temperature; **hmax**, which specifies the maximum step size allowed in integration routines; and **intrac**, a logical variable. When the flag **intrac** is set to .true., the code can be executed in an interactive mode. The final entry in this file is **itratn**, which species the number of back and forth integration sweeps before the iteration on the feed gas temperature is started.

Thermodynamic Data File, FB1THM

The second input data file, FB1THM, provides the data needed to calculate the thermodynamic and the transport properties of the gaseous species. A typical data file is shown in Table 6.2. In FBED-1, a maximum of twenty five gaseous species may be treated. This number, however, may be increased by changing the value of parameter **maxsp** in all the subroutines where it is used. In our

formulation, twenty two species are actually treated, as shown in Table 6.2. This file does not change unless a new species or element is needed. The thermodynamic properties data file is read from the subroutine CREE0. The keywords **elem** and **ther** in the main data file FB1IN are used to invoke the reading of data from the thermodynamic input data file FB1THM.

The input file FB1THM is divided into three major sections: element data, species thermodynamic data, and species transport data. The elemental data are read in by specifying the species name, molecular weight, and valence. The elemental data use the following format specification: a2,8x,2f10.6. **The order in which the elements are listed must be C, H, O, N, S, and Ar.** A blank line is **required** between the elemental data and the species thermodynamic data, as shown in Table 6.2.

The thermodynamic data for each species are entered on three separate lines. The first line is used to specify the species name and the elemental composition. The second and third lines are used to specify the polynomial coefficients for the calculation of the thermodynamic properties (heat capacity, enthalpy and entropy) of the species. The format for specifying the species name and elemental composition is 3a4,12x, 4(a2,f3.0). Following the species name, the source and date of the data are also provided, as shown in Table 5.2 (e. g., j 9/65) The "j" indicates the source of the data as being the JANAF thermochemical tables (Stull and Prophet, 1971). Also, the entry "g 300.000 5000.000" indicates that the species is a gas over the temperature range 300 to 5000 K. FBED-1 does not use the literature source and date, species physical state, and valid temperature range. This information, however, is available in Table 6.2 for reference.

A blank line is **required** between the species thermodynamic data and the species transport data. The format free input for the species transport data is read in by the subroutine READIN. The species transport data include the Stockmeyer collision diameter (**s**), Lennard-Jones temperature parameter (**ek**), and the nonpolar correction factor for the Lennard-Jones parameter (**delta**).

Table 6.2 Thermodynamic Input Data File, FB1THM.

```
c          12.01115       4.0
h          1.00797        1.0
o          15.9994       -2.0
n          14.0067        0.0
s          32.06          4.0
ar         39.9480        0.0

ar                 1 5/66ar 1.00 0.00 0.00 0.g   300.000  5000.000
 0.25000000d+01 0.0d0           0.0d0           0.0d0           0.0d0
-0.74537500d+03 0.43660002d+01 0.25000000d+01 0.0d0           0.0d0
 0.0d0          0.0d0          -0.74537476d+03 0.43660002d+01
co                 j 9/65c  1.o  1.00 0.00 0.g   300.000  5000.000
 0.29840689d+01 0.14891387d-02-0.57899678d-06 0.10364576d-09-0.69353499d-14
-0.14245227d+05 0.63479147d+01 0.37100916d+01-0.16190964d-02 0.36923584d-05
-0.20319673d-08 0.23953344d-12-0.14356309d+05 0.29555340d+01
co2                j 9/65c  1.o  2.00 0.00 0.g   300.000  5000.000
 0.44608040d+01 0.30981717d-02-0.12392566d-05 0.22741323d-09-0.15525948d-13
-0.48961438d+05-0.98635978d+00 0.24007788d+01 0.87350905d-02-0.66070861d-05
 0.20021860d-08 0.63274039d-15-0.48377520d+05 0.96951447d+01
ch4                j 3/61c  1.h  4.00 0.00 0.g   300.000  5000.000
 0.15027056d+01 0.10416795d-01-0.39181514d-05 0.67777872d-09-0.44283706d-13
-0.99787031d+04 0.10707143d+02 0.38261929d+01-0.39794557d-02 0.24558321d-04
-0.22732920d-07 0.69626952d-11-0.10144945d+05 0.86690062d+00
c2h6                cr2178c   2h   60   00   0g   300.000  5000.000
 1.67107058d+00 1.88078150d-02-6.98943156d-06 1.16385735d-09-7.17707692d-14
-1.14683543d+04 1.26317347d+01 1.92453270d+00 1.68224303d-02-2.24906498d-06
-3.40875417d-09 1.49239675d-12-1.14789269d+04 1.16292438d+01
h2                 j 3/61h  2.0  0.0  0.0  0.g   300.000  5000.000
 0.31001883d+01 0.51119458d-03 0.52644204d-07-0.34909964d-10 0.36945341d-14
-0.87738013d+03-0.19629412d+01 0.30574446d+01 0.26765198d-02-0.58099149d-05
 0.55210343d-08-0.18122726d-11-0.98890430d+03-0.22997046d+01
hcn                000000h  1.c  1.n  1.0  0.g   300.000  5000.000
 0.37068110d+01 0.33382799d-02-0.11913307d-05 0.19992916d-09-0.12826451d-13
 0.14962633d+05 0.20794888d+01 0.24513550d+01 0.87208301d-02-0.10094202d-04
 0.67255677d-08-0.17626959d-11 0.15213000d+05 0.80830069d+01
h2o                j 3/61h  2.o  1.00 0.00 0.g   300.000  5000.000
 0.27167616d+01 0.29451370d-02-0.80224368d-06 0.10226681d-09-0.48472104d-14
-0.29905820d+05 0.66305666d+01 0.40701275d+01-0.11084499d-02 0.41521180d-05
-0.29637404d-08 0.80702101d-12-0.30279719d+05-0.32270038d+00
h2s                j12/65h  2.s  1.00 0.00 0.g   300.000  5000.000
 0.28479090d+01 0.38415990d-02-0.14099360d-05 0.24278735d-09-0.15783280d-13
-0.34469788d+04 0.74781399d+01 0.38811293d+01-0.13211856d-03 0.36517713d-05
-0.21820441d-08 0.28783779d-12-0.36350916d+04 0.25161505d+01
n2                 j 9/65n  2.0  0.0  0.0  0.g   300.000  5000.000
 0.28963194d+01 0.15154863d-02-0.57235275d-06 0.99807385d-10-0.65223536d-14
-0.90586182d+03 0.61615143d+01 0.36748257d+01-0.12081496d-02 0.23240100d-05
-0.63217520d-09-0.22577253d-12-0.10611587d+04 0.23580418d+01
```

```
nh3               j 9/65n  1.h  3.00 0.00 0.g   300.000  5000.000
 0.24165173d+01 0.61871186d-02-0.21785136d-05 0.37599057d-09-0.24448854d-13
-0.64747109d+04 0.77043467d+01 0.35912762d+01 0.49388665d-03 0.83449304d-05
-0.83833385d-08 0.27299092d-11-0.66717070d+04 0.22520962d+01
no                j 6/63n  1.o  1.00 0.00 0.g   300.000  5000.000
 0.31889992d+01 0.13382279d-02-0.52899316d-06 0.95919314d-10-0.64847928d-14
 0.98283242d+04 0.67458115d+01 0.40459509d+01-0.34181783d-02 0.79819174d-05
-0.61139254d-08 0.15919072d-11 0.97453867d+04 0.29974976d+01
o2                j 9/65o  2.0  0.0  0.0  0.g   300.000  5000.000
 0.36219521d+01 0.73618256d-03-0.19652219d-06 0.36201556d-10-0.28945623d-14
-0.12019822d+04 0.36150942d+01 0.36255980d+01-0.18782183d-02 0.70554543d-05
-0.67635071d-08 0.21555977d-11-0.10475225d+04 0.43052769d+01
oh                j 3/66o  1.h  1.00 0.00 0.g   300.000  5000.000
 0.29106417d+01 0.95931627d-03-0.19441700d-06 0.13756646d-10 0.14224542d-15
 0.39353811d+04 0.54423428d+01 0.38375931d+01-0.10778855d-02 0.96830354d-06
 0.18713971d-09-0.22571089d-12 0.36412820d+04 0.49370009d+00
so2               j 6/61s  1.o  2.00 0.00 0.g   300.000  5000.000
 0.52451363d+01 0.19704204d-02-0.80375759d-06 0.15149969d-09-0.10557998d-13
-0.37558227d+05-0.10873518d+01 0.32665329d+01 0.53237863d-02 0.68437544d-06
-0.52809987d-08 0.25590450d-11-0.36908145d+05 0.96513472d+01
CH3OH             L 4/80c  1.h  4.o  1.0  0.G   300.000  5000.000
 0.40334730D+01 0.93680508D-02-0.30449373D-05 0.43456994D-09-0.22136329D-13
-0.26159859D+05 0.23539820D+01 0.26587849D+01 0.73515214D-02 0.71443337D-05
-0.87661114D-08 0.23805116D-11-0.25353684D+05 0.11238121D+02
C2H4              L 4/80c  2.h  4.0   00   0G   300.000  5000.000
 0.43843679D+01 0.96509494D-02-0.31845530D-05 0.46213655D-09-0.24069342D-13
 0.41205039D+04-0.23853559D+01 0.11654673D+01 0.13374992D-01 0.25754771D-05
-0.10187399D-07 0.43603341D-11 0.53428867D+04 0.15699718D+02
C3H6              120186c  3.h  6.0   00   0G   300.000  5000.000
 0.06732257D+02 0.14908336D-01-0.04949899D-04 0.07212022D-08-0.03766204D-12
-0.09235703D+04-0.13313348D+02 0.14933071D+01 0.02092517D+00 0.04486794D-04
-0.16689121D-07 0.07158146D-10 0.10748264D+04 0.16145340D+02
C4H8              120186c  4.h  8.0   00   0G   300.000  5000.000
 0.02053584D+02 0.03435050D+00-0.15883196D-04 0.03308966D-07-0.02536104D-11
-0.02139723D+05 0.15543201D+02 0.11811380D+01 0.03085338D+00 0.05086524D-04
-0.02465488D-06 0.11110192D-10-0.01790400D+05 0.02106247D+03
C3H8              L 4/80c  3.h  8.0   00   0G   300.000  5000.000
 0.75252171D+01 0.18890340D-01-0.62839244D-05 0.91793728D-09-0.48124099D-13
-0.16464547D+05-0.17843903D+02 0.89692080D+00 0.26689861D-01 0.54314251D-05
-0.21260007D-07 0.92433301D-11-0.13954918D+05 0.19355331D+02
I-C4H10         I-L 5/80c  4.h 10.00  00   0G   300.000  5000.000
 0.10845599D+02 0.23333851D-01-0.77793875D-05 0.11375818D-08-0.59640660D-13
-0.21725719D+05-0.35869400D+02 0.50704670D+00 0.38149782D-01 0.46916175D-05
-0.29491598D-07 0.13621288D-10-0.18030996D+05 0.21284882D+02
C2H2              J 3/61c  2.h  2.0   00   0G   300.000  5000.000
 0.45751083D+01 0.51238358D-02-0.17452354D-05 0.28673065D-09-0.17951426D-13
 0.25607428D+05-0.35737940D+01 0.14102768D+01 0.19057275D-01-0.24501390D-04
 0.16390872D-07-0.41345447D-11 0.26188208D+05 0.11393827D+02
```

```
3.418d0,124.0d0,0.0d0,    * ar       s(i), dk(i), delta(i) (BSL)
3.590d0,110.0d0,0.0d0,    * co       (BSL)
3.996d0,190.0d0,0.0d0,    * co2      (BSL)
3.822d0,137.0d0,0.0d0,    * ch4      (BSL)
4.418d0,230.0d0,0.0d0,    * c2h6     (BSL)
2.915d0, 38.0d0,0.0d0,    * h2       (BSL)
3.630d0,569.0d0,0.0d0,    * hcn      (Chemkin Data Base)
2.520d0,775.0d0,1.0d0,    * h2o      (Reid, Prausnitz and Sherwood, 3rd Ed.)
3.490d0,343.0d0,0.21d0,   * h2s      (Reid, Prausnitz and Sherwood, 3rd Ed.)
3.681d0, 91.5d0,0.0d0,    * n2       (BSL)
3.150d0,358.0d0,0.7d0,    * nh3      (Reid, Prausnitz and Sherwood, 3rd Ed.)
3.470d0,119.0d0,0.0d0,    * no       (BSL)
3.433d0,113.0d0,0.0d0,    * o2       (BSL)
2.750d0, 80.0d0,0.0d0,    * oh       (Chemkin Data Base)
4.040d0,347.0d0,0.42d0,   * so2      (Reid, Prausnitz and Sherwood, 3rd Ed.)
3.690d0,417.0d0,0.5d0,    * ch3oh    (Reid, Prausnitz and Sherwood, 3rd Ed.)
4.232d0,205.0d0,0.0d0,    * c2h4     (BSL)
4.982d0,266.8d0,0.0d0,    * c3h6     (Chemkin Data Base)
5.176d0,357.0d0,0.0d0,    * c4h8     (Chemkin Data Base)
5.061d0,254.0d0,0.0d0,    * c3h8     (BSL)
5.341d0,313.0d0,0.0d0,    * i-c4h10  (BSL)
4.221d0,185.0d0,0.0d0,    * c2h2     (BSL)
```

FG-DVC Input Data File

The input data for the FG-DVC submodel include the initial functional group composition of the coal, the rank dependent kinetic parameters, percolation submodel data for bond population, and probability distribution for the tar mass bins. Eight data files, COAL0.ARG1 to COAL0.ARG8, with the input values for the standard Argonne premium coals, are provided in Appendix A. Three options are provided in the code to select or provide an appropriate data file for the coal dependent parameters for the devolatilization submodel. These options are implemented through the integer variable idcoal, which is read from the main input data file FB1IN. The variable **idcoal** can take a value from 0-9. The first option is implemented when the value of the variable, **idcoal**, is 0. This option allows the program to select the standard coal which is closest, on a oxygen/carbon-hydrogen/carbon plot, to the feed coal. The second option allows the user to specify a standard coal based on specific considerations, e.g., the geographical origin of the feed coal. This option requires that the user specify the value of the

variable **idcoal** from 1 to 8. As an example, a value of 1 will invoke the reading of FG-DVC input data to be read form the file coal0.arg1 for the standard Argonne Premium coal 1. The third option allows the user to provide the data for the feed coal. **The user must provide the data file as COAL0.USER, and the value of the variable idcoal must be specified as 9.** A typical input data file for the FG-DVC devolatilization submodel is shown in Table 6.3.

Input Data File EXPT.DAT

The final input data file for the FBED-1 code is an optional file EXPT.DAT This file must be provided when the logical variable **lexpt**, which is read from the input file FB1IN, is set to .true.. This file contains the experimental composition of CO, CO_2, CH_4, H_2, H_2O and N_2 in the product gas specified as percents. In addition, product gas temperature, product tar flow rate, experimental wall heat loss and burnout are specified. A sample data file is shown in Table 6.4.

Table 6.4 Sample Data file EXPT.DAT

22.62d0	CO in the product gas (%v)
5.19d0	CO_2 in the product gas (%v)
1.47d0	CH_4 in the product gas (%v)
15.75d0	H_2 in the product gas (%v)
8.44d0	H_2O in the product gas (%v)
45.43d0	N_2 in the product gas (%v)
773.15d0	Product gas temperature (K)
0.0452d0	Product tar flow rate (Kg/s)
0.4159d0	Wall heat loss (MW)
0.9610d0	Burnout

Program Output

The output of FBED-1 is available both in tabular and graphical form. The output data files provide the values for important variables, e.g., gas and solid

TABLE 6.3 Sample Input File for FG-DVC Devolatilization Submodel

```
27                                                                          <--- nfg (Number of Functional Groups)
0.10000D-02 0.29240D+02 0.20855D+05 0.36000D+04 0.20480D+03                 <--- y0, a, b, sigmaa, and xeff for fg #  1 = CO2XL
0.25000D-02 0.29240D+02 0.25705D+05 0.30000D+04 0.20480D+03                 <--- y0, a, b, sigmaa, and xeff for fg #  2 = CO2L
0.65000D-02 0.29646D+02 0.31040D+05 0.25000D+04 0.20480D+03                 <--- y0, a, b, sigmaa, and xeff for fg #  3 = CO2T
0.23040D-01 0.29240D+02 0.25220D+05 0.12500D+04 0.00000D+00                 <--- y0, a, b, sigmaa, and xeff for fg #  4 = H2OL
0.42789D-01 0.32929D+02 0.31040D+05 0.25000D+04 0.00000D+00                 <--- y0, a, b, sigmaa, and xeff for fg #  5 = H2OT
0.25000D-02 0.29240D+02 0.25220D+05 0.12500D+04 0.00000D+00                 <--- y0, a, b, sigmaa, and xeff for fg #  6 = COL
0.15231D-01 0.29240D+02 0.29828D+05 0.19000D+04 0.00000D+00                 <--- y0, a, b, sigmaa, and xeff for fg #  7 = COT
0.39087D-02 0.31369D+02 0.29100D+05 0.15000D+04 0.00000D+00                 <--- y0, a, b, sigmaa, and xeff for fg #  8 = HCNL
0.26963D-01 0.30482D+02 0.41225D+05 0.47500D+04 0.00000D+00                 <--- y0, a, b, sigmaa, and xeff for fg #  9 = HCNT
0.00000D+00 0.28730D+02 0.26481D+05 0.30000D+04 0.00000D+00                 <--- y0, a, b, sigmaa, and xeff for fg # 10 = NH3
0.15687D+00 0.00000D+00 0.00000D+00 0.00000D+00 0.00000D+00                 <--- y0, a, b, sigmaa, and xeff for fg # 11 = CAL
0.00000D+00 0.00000D+00 0.00000D+00 0.00000D+00 0.00000D+00                 <--- y0, a, b, sigmaa, and xeff for fg # 12 = CH4XL
0.18000D-01 0.31032D+02 0.27160D+05 0.13000D+04 0.10240D+03                 <--- y0, a, b, sigmaa, and xeff for fg # 13 = CH4L
0.32000D-01 0.31725D+02 0.31040D+05 0.22000D+04 0.10240D+03                 <--- y0, a, b, sigmaa, and xeff for fg # 14 = CH4T
0.11587D-01 0.33152D+02 0.39285D+05 0.60000D+04 0.00000D+00                 <--- y0, a, b, sigmaa, and xeff for fg # 15 = HAROM
0.00000D+00 0.00000D+00 0.00000D+00 0.00000D+00 0.00000D+00                 <--- y0, a, b, sigmaa, and xeff for fg # 16 = CH3OH
0.23000D-01 0.32929D+02 0.38800D+05 0.28000D+04 0.00000D+00                 <--- y0, a, b, sigmaa, and xeff for fg # 17 = COXT
0.56200D+00 0.00000D+00 0.00000D+00 0.00000D+00 0.00000D+00                 <--- y0, a, b, sigmaa, and xeff for fg # 18 = CNV
0.10000D-01 0.00000D+00 0.00000D+00 0.00000D+00 0.00000D+00                 <--- y0, a, b, sigmaa, and xeff for fg # 19 = SORG
0.12116D-01 0.00000D+00 0.00000D+00 0.00000D+00 0.00000D+00                 <--- y0, a, b, sigmaa, and xeff for fg # 20 = HAL
0.50000D-02 0.29240D+02 0.24250D+05 0.15000D+04 0.00000D+00                 <--- y0, a, b, sigmaa, and xeff for fg # 21 = C2H4
0.00000D+00 0.29240D+02 0.24250D+05 0.15000D+04 0.00000D+00                 <--- y0, a, b, sigmaa, and xeff for fg # 22 = C3H6
0.15000D-01 0.29240D+02 0.24735D+05 0.10000D+04 0.00000D+00                 <--- y0, a, b, sigmaa, and xeff for fg # 23 = C4H8
0.50000D-02 0.29240D+02 0.24250D+05 0.15000D+04 0.00000D+00                 <--- y0, a, b, sigmaa, and xeff for fg # 24 = C2H6
0.00000D+00 0.29240D+02 0.24250D+05 0.15000D+04 0.00000D+00                 <--- y0, a, b, sigmaa, and xeff for fg # 25 = C3H8
0.25000B-01 0.29240D+02 0.24735D+05 0.10000D+04 0.00000D+00                 <--- y0, a, b, sigmaa, and xeff for fg # 26 = C4H10
0.00000D+00 0.00000D+00 0.00000D+00 0.00000D+00 0.00000D+00                 <--- y0, a, b, sigmaa, and xeff for fg # 27 = C2H2
            0.32236D+02 0.26675D+05 0.12500D+04                                         <--- a,b, and sigmaa for bond kinetics
6 0.8202D+00 0.8202D+00 0.3600D-01 0.1000D+01 0.4000D+01                        <--- jmax,psoft,ptotal,qtotal,sigma1,sigma2
0.130D+00 0.000D+00 0.000D+00 0.000D+00 0.000D+00 0.000D+00 0.000D+00 0.000D+00 0.000D+00 0.000D+00          <--- pdist( 1,1:10)
0.290D+00 0.170D-01 0.000D+00 0.000D+00 0.000D+00 0.000D+00 0.000D+00 0.000D+00 0.000D+00 0.000D+00          <--- pdist( 2,1:10)
0.310D+00 0.950D-01 0.200D-02 0.000D+00 0.000D+00 0.000D+00 0.000D+00 0.000D+00 0.000D+00 0.000D+00          <--- pdist( 3,1:10)
0.270D+00 0.190D+00 0.220D-01 0.000D+00 0.000D+00 0.000D+00 0.000D+00 0.000D+00 0.000D+00 0.000D+00          <--- pdist( 4,1:10)
0.000D+00 0.270D+00 0.700D-01 0.500D-02 0.000D+00 0.000D+00 0.000D+00 0.000D+00 0.000D+00 0.000D+00          <--- pdist( 5,1:10)
0.000D+00 0.233D+00 0.143D+00 0.200D-01 0.100D-02 0.000D+00 0.000D+00 0.000D+00 0.000D+00 0.000D+00          <--- pdist( 6,1:10)
0.000D+00 0.142D+00 0.207D+00 0.550D-01 0.500D-02 0.000D+00 0.000D+00 0.000D+00 0.000D+00 0.000D+00          <--- pdist( 7,1:10)
0.000D+00 0.530D-01 0.221D+00 0.109D+00 0.180D-01 0.100D-02 0.000D+00 0.000D+00 0.000D+00 0.000D+00          <--- pdist( 8,1:10)
0.000D+00 0.000D+00 0.180D+00 0.164D+00 0.450D-01 0.500D-02 0.000D+00 0.000D+00 0.000D+00 0.000D+00          <--- pdist( 9,1:10)
0.000D+00 0.000D+00 0.104D+00 0.195D+00 0.860D-01 0.150D-01 0.000D+00 0.000D+00 0.000D+00 0.000D+00          <--- pdist(10,1:10)
0.000D+00 0.000D+00 0.430D-01 0.184D+00 0.133D+00 0.360D-01 0.000D+00 0.000D+00 0.000D+00 0.000D+00          <--- pdist(11,1:10)
0.000D+00 0.000D+00 0.900D-02 0.138D+00 0.168D+00 0.690D-01 0.000D+00 0.000D+00 0.000D+00 0.000D+00          <--- pdist(12,1:10)
0.000D+00 0.000D+00 0.000D+00 0.128D+00 0.545D+00 0.874D+00 0.000D+00 0.000D+00 0.000D+00 0.000D+00          <--- pdist(13,1:10)
0.20D+00                                                                                <--- particle internal pressure drop
0.8320D+00  0.5300D-01  0.8900D-01  0.1600D-01  0.1000D-01                          <--- ultimate composition (daf)
File generated: Tue Apr 14 18:28:56 1992                                                        coal0.arg6
```

temperature, pressure, gas phase composition, flow rates, char consumption rates, particle diameter and burnout. Transport and thermodynamic properties are also available. The output files and their contents are discussed in the following sections.

Main Output File, FB1OUT

The main output file FB1OUT, given in Table 6.5, corresponds to the input data given in Tables 6.1 to 6.3. This file echos the input data, provides the values of the variables calculated from the input data, the effluent output data from the two-zone, zero-dimensional submodel, and the axial output from the one-dimensional submodel. Overall heat loss and cpu time are also reported at the end of each integration pass. The axial output consists of the axial distance (m), the solid and gas temperatures (K), and the mole percentage of H_2, CO_2, CO, CH_4, and H_2O. The results reported in Table 6.5 were obtained by executing the FBED-1 code on a SUN4/310 computer. The results may be slightly different on other computers, due to the differences in hardware and machine architecture.

Table 6.5 Main Output File, FB1OUT.

```
Simulation Started: Thu Jun  3 15:11:50 1993
************************************************************** FBED1D
************** BRIGHAM YOUNG UNIVERSITY SIMULATION OF ******* Vol. 2
**************** WELLMAN GALUSHA 10/30/82 TEST USING  ******* Page 68
********************** JETSON BITUMINOUS COAL ********************
************************************************************** 12/10/92
 ------------------------------------------------------------------------
 Zero-dimensional input parameters:
 ------------------------------------------------------------------------
 F          T--> do 0-d calculation only
 T          T--> all exit gases in equil. mainly for 0-d
 F          T--> do FREEBoard calculation using qfreeb
 F          T--> calculate heat loss with flowjs latent heat
 F          T--> use ASH composition to calculate CP
 F          T--> use usrx0 for x0 rather than SET model x0
 T          T--> use FG-DVC devolatilization submodel
 F          T--> compute tar cracking rates using FIXed Gaussian
 T          T--> echo input parameters to fb1out
 0.198E+01  DIAmeter of reactor CHamber, m
 0.208E+01  reactor CHamber axial LenGtH, m
```

```
0.102E+06  reactor PRESsure at bed top, pa
0.343E+03  Temperature of Wall at reactor TOP, K
0.287E+03  Temperature of Wall at reactor BOTtom, K
0.298E+03  Temperature of feed COAL, K
0.000E+00  heat loss in FREEBoard, watts
0.352E+00  FLOW rate of feed Coal, kg/s
0.948E+00  FLOW rate of Oxidizer in feed, kg/s
0.156E+00  FLOW rate of Steam in feed, kg/s
0.134E+00  FLOW rate of Jacket Steam, kg/s
0.800E+06  heat loss through reactor walls, J/s
0.000E+00  Tar Recycle Fraction
0.000E+00  Temperature of ReCycled TAR, K
0.100E+01  fractional char/coal conversion in 0-d
0.490E-01  PRoXimate ASH fraction, as received basis
0.491E+00  PRoXimate Fixed Carbon fraction, as received basis
0.671E-01  PRoXimate moisture fraction, as received basis
0.393E+00  PRoXimate Volatile fraction, as received basis
0.812E+00  DAF ultimate mass fraction of C in Feed Coal
0.505E-01  DAF ultimate mass fraction of H in Feed Coal
0.104E+00  DAF ultimate mass fraction of O in Feed Coal
0.170E-01  DAF ultimate mass fraction of N in Feed Coal
0.163E-01  DAF ultimate mass fraction of S in Feed Coal
0.170E+04  Melting Temperature of ASH, K
0.420E+00  weight fraction of SiO2  in ash
0.910E-02  weight fraction of CaO   in ash
0.199E+00  weight fraction of Al2O3 in ash
0.660E-02  weight fraction of MgO   in ash
0.127E-01  weight fraction of K2O   in ash
0.230E-02  weight fraction of Na2O  in ash
0.109E-01  weight fraction of TiO2  in ash
0.000E+00  weight fraction of MnO   in ash
0.852E-01  weight fraction of FeO   in ash
0.243E+00  weight fraction of Fe2O3 in ash
0.000E+00  weight fraction of Fe    in ash
0.200E-03  weight fraction of P2O5  in ash
0.000E+00  weight fraction of CaF2  in ash
0.108E-01  weight fraction of SO3   in ash
6          Id of Coal selected (Output)
0.156E+00  USeR supplied X0, used when lx0 is set to t
-------------------------------------------------------------------------
One-dimensional input parameters:
-------------------------------------------------------------------------
T          T--> Shell Progressive rather than AS model
F          T--> let TAR go to equilibrium
F          T--> use STIFF LSODE solver
T          T--> STOP when bottom of reactor reached
T          T--> print optional file OUTA
T          T--> print optional file OUTB
T          T--> print optional file OUTC
```

```
T           T--> print optional file OUTD
T           T--> print optional file OUTE
T           T--> print optional file OUTF
T           T--> print optional file OUTG
T           T--> print optional file OUTH
T           T--> print optional file OUTI
T           T--> print optional file OUTJ
1           LSODE parameter used to specify output
0.100E-01   step size for output, m
0.100E-02   maximum step size allowed in LSODE, m
0.100E-07   ABSolute TOLerance used in LSODE
0.100E-03   RELative TOLerance used in LSODE
0.217E-01   initial Particle Diameter, m
0.100E+00   swelling parameter, fraction
0.100E+01   heat of rxn partition
0.600E+00   Void Fraction in ASH zone
0.330E+00   Void Fraction in COAL zone
0.119E+04   apparent coal density, kg/m^3
0.136E+00   POROSity of coal
0.589E+03   Frequency Factor for CO2 gasification rxn., m/s K
0.589E+00   Frequency Factor for H2 gasification rxn., m/s K
0.589E+03   Frequency Factor for H2O gasification rxn., m/s K
0.230E+01   Frequency Factor for O2 oxidation rxn., m/s K
0.223E+09   Activation Energy for CO2 gasification rxn., J/kmol
0.223E+09   Activation Energy for H2 gasification rxn., J/kmol
0.223E+09   Activation Energy for H2O gasification rxn., J/kmol
0.923E+08   Activation Energy for O2 oxidation rxn., J/kmol
0.100E+01   particle area factor for internal burning
0.500E+00   developing Ash Porosity DIVided by Tortuosity
0.500E-01   ADjustable Factor for Solid to Gas HT coef.
0.100E+01   ADjustable Factor for devolatilization
0.100E+01   ADjustable Factor CO2 gasification reaction
0.100E+01   ADjustable Factor H2 gasification reaction
0.100E+01   ADjustable Factor H2O gasification reaction
0.100E+01   ADjustable Factor O2 oxidation reaction
0.100E+01   ADjustable Factor for Gas-to-Wall HT coefficient
0.100E+01   ADjustable Factor for Solid-to-Wall HT coefficient
0.120E+04   Temperature to SWiTCH to/from equilibrium
0.104E+06   Pressure at the BOTtOM of the gasifier, Pa
0.000E+00   Axial position at the BOTtOM of gasifier, m
F           T--> Execute the code in INTeractive mode
1           Number of down & upward integration passes before iterations
-------------------------------------------------------------------------
Calculated input parameters:
-------------------------------------------------------------------------
0.315E+03   Temperature of WALL used, K
0.373E+03   SATurated water Temp. at reactor pressure, K
0.244E+07   VAporization enthalpy of water at TW, J/kg
0.800E+06   heat loss through reactor walls, J/s
```

```
 0.794E+01  Avg. Atomic Weight of DAF feed coal, kg/kmol
 0.331E+08  Higher Heating Value of coal, J/kg
-0.899E+06  Heat of Formation of Coal, J/kg
-0.165E+03  SENsible enthalpy of Coal, j/kg
 0.594E+03  a in Cp(ash) = a + bT - ct^-2
 0.586E+00  b in Cp(ash) = a + bT - ct^-2
 0.000E+00  c in Cp(ash) = a + bT - ct^-2
 0.159E+04  liquid ash heat capacity, J/kg K
 0.230E+06  heat of melting for ash, J/kg
 ------------------------------------------------------------------------
 INPUT ECHO
 ----------
   lfreeb, ljkstm, lx0                              F    F    F
   burnout                                          1.0000
------------------------------------------------------------------------
   Blast Steam Temp., K          560.00             (548.33 F)
   Blast Oxydizer Temp., K       560.00             (548.33 F)
------------------------------------------------------------------------
   HHV OF DAF COAL, j/kg         0.330557E+08       (14211.4 Btu/lb)
   Freeboard heat loss, watts    0.000000E+00       (0.0000E+00 Btu/s)
------------------------------------------------------------------------
   Chamber diameter, m           1.9812             ( 6.4999 ft)
   Chamber length, m             2.0828             ( 6.8333 ft)
   Wall temp., K                 315.10             (107.51 F)
   Chamber Pressure, KPa         .10226E+03         (  1.0 atm)
   Inlet coal temp., K           298.00             ( 76.7 F)
------------------------------------------------------------------------
   Coal mass flow, kg/s          0.3524             ( 1.3984 t/hr)
   Oxidizer mass flow,kg/s       0.94810            ( 3.7623 t/hr)
   Steam mass flow, kg/s         0.15620            ( 0.6198 t/hr)
   Jacket steam flow, kg/s       0.13390            ( 0.5314 t/hr)
   Tar recycle wt. fraction      0.0000
------------------------------------------------------------------------
   Tsat, K                       373.39             (212.44 F)
   Enthalpy of Vap., j/kg        0.2438E+07         (0.1048E+04 Btu/lb)
   Wall heat loss, watts         0.8000E+06         (0.7588E+03 Btu/s)
------------------------------------------------------------------------
Proximate (ash, fc, H2O, VM)     0.0490  0.4908  0.0671  0.3931
Ultimate anal. (input-CHONS)     0.8125  0.0505  0.1037  0.0170  0.0163
------------------------------------------------------------------------
OUTPUT RESULTS:                  V* = 0.4817        x0 = 0.3008
---------------
   Exit temp., K                  959.44            (1267.32 F)
   Equilibrium temp., K          1344.87            (1961.09 F)
   Product tar flow, kg/s        0.0727             ( 0.2887 t/hr)
   Recycle tar flow, kg/s        0.0000             ( 0.0000 t/hr)
   Total tar flow, kg/s          0.0727             ( 0.2887 t/hr)
                  RAW GAS COMPOSITION (DRY)-->
   COMPONENT                                       (DRY) MOLE %
```

```
---------                                          ------------
     CO                                                 17.41
     CO2                                                11.08
     H2                                                 22.57
     CH4                                                 0.26
     C2H6                                                0.00
     H2S                                                 0.20
     INERTS (AR =  0.60% & N2 = 47.87%)                 48.47
     OTHERS                                              0.01
     (CHX =  0.00%, HCN =  0.00%, NH3 =  0.01%, etc. =  0.00%)
               RAW GAS COMPOSITION (WET)-->
COMPONENT                                          (WET) MOLE %
---------                                          ------------
     CO                                                 16.08
     CO2                                                10.23
     H2                                                 20.84
     CH4                                                 0.24
     C2H6                                                0.00
     H2O                                                 7.68
     H2S                                                 0.19
     INERTS (AR =  0.55% & N2 = 44.19%)                 44.75
     OTHERS                                              0.00
     (CHX =  0.00%, HCN =  0.00%, NH3 =  0.00%, etc. =  0.00%)

ZERO-D CPU TIME:   0 hours,  8 minutes, 44.380 seconds!

Simulation Results for downward integration pass #  1
```

Axial Pos.	ts (K)	tg (K)	mol% H2	mol% CO2	mol% CO	mol% CH4	mol% H2O
2.0828E+00	298.0	959.4	20.84	10.23	16.08	0.24	7.68
2.0800E+00	321.9	966.0	20.86	10.24	16.09	0.24	7.59
2.0700E+00	395.9	988.8	20.94	10.28	16.15	0.24	7.24
2.0600E+00	457.6	1010.1	21.02	10.32	16.22	0.24	6.88
2.0500E+00	510.0	1030.0	21.10	10.36	16.28	0.24	6.51
2.0400E+00	558.7	1049.3	21.19	10.40	16.35	0.24	6.13
2.0300E+00	603.7	1067.9	21.27	10.45	16.41	0.24	5.75
2.0200E+00	644.9	1083.5	21.32	10.47	16.45	0.24	5.56
2.0100E+00	674.9	1094.1	21.32	10.47	16.45	0.24	5.56
2.0000E+00	690.8	1101.2	21.32	10.47	16.45	0.24	5.56
1.9900E+00	702.0	1107.1	21.32	10.47	16.45	0.24	5.56
1.9800E+00	712.8	1112.8	21.32	10.47	16.45	0.24	5.56
1.9700E+00	724.6	1118.8	21.32	10.47	16.45	0.24	5.56
1.9600E+00	737.7	1125.4	21.32	10.47	16.45	0.24	5.56
1.9500E+00	751.0	1132.8	21.32	10.47	16.45	0.24	5.56
1.9400E+00	764.6	1141.0	21.32	10.47	16.45	0.24	5.56
1.9300E+00	778.0	1150.1	21.32	10.47	16.45	0.24	5.56
1.9200E+00	791.7	1159.9	21.32	10.47	16.45	0.24	5.56

```
1.9100E+00    805.3    1170.2   21.32     10.47     16.45     0.24      5.56
1.9000E+00    819.2    1181.1   21.32     10.47     16.45     0.24      5.56
1.8900E+00    833.1    1192.3   21.32     10.47     16.45     0.24      5.56
Switched to equilibrium calculations at z = 1.8825 where tg = 1200.07
1.8800E+00    848.2    1265.1   13.35      8.47     17.72     0.00     10.28
1.8700E+00    864.3    1279.4   13.09      8.44     17.71     0.00     10.40
1.8600E+00    881.1    1293.8   12.85      8.41     17.71     0.00     10.52
1.8500E+00    899.6    1308.2   12.61      8.37     17.71     0.00     10.62
...
...
...
1.0000E-01    387.8     388.0    0.00      0.00      0.00      0.00     23.15
9.0000E-02    387.8     388.0    0.00      0.00      0.00      0.00     23.15
8.0000E-02    387.9     388.1    0.00      0.00      0.00      0.00     23.15
7.0000E-02    388.0     388.2    0.00      0.00      0.00      0.00     23.15
6.0000E-02    388.0     388.2    0.00      0.00      0.00      0.00     23.15
5.0000E-02    388.1     388.3    0.00      0.00      0.00      0.00     23.15
4.0000E-02    388.2     388.4    0.00      0.00      0.00      0.00     23.15
3.0000E-02    388.2     388.4    0.00      0.00      0.00      0.00     23.15
2.0000E-02    388.3     388.5    0.00      0.00      0.00      0.00     23.15
1.0000E-02    388.3     388.6    0.00      0.00      0.00      0.00     23.15
0.0000E+00    388.4     388.6    0.00      0.00      0.00      0.00     23.15
-------------------------------------------------------------------------------

Overall Heat Loss =   0.2776E+06 J/s

TOTAL CPU TIME:   0 hours, 30 minutes, 19.870 seconds!

Simulation Results for upward integration pass #  1

Axial Pos.   ts (K)    tg (K)   mol% H2   mol% CO2   mol% CO   mol% CH4   mol% H2O
----------   ------    ------   -------   --------   -------   --------   --------
0.0000E+00    388.4     560.0    0.00      0.00       0.00      0.00      20.94
1.0000E-02    388.3     552.3    0.00      0.00       0.00      0.00      20.94
2.0000E-02    388.3     545.0    0.00      0.00       0.00      0.00      20.94
3.0000E-02    388.2     538.0    0.00      0.00       0.00      0.00      20.94
4.0000E-02    388.2     531.4    0.00      0.00       0.00      0.00      20.94
5.0000E-02    388.1     525.1    0.00      0.00       0.00      0.00      20.94
6.0000E-02    388.0     519.0    0.00      0.00       0.00      0.00      20.94
7.0000E-02    388.0     513.2    0.00      0.00       0.00      0.00      20.94
8.0000E-02    387.9     507.7    0.00      0.00       0.00      0.00      20.94
9.0000E-02    387.8     502.5    0.00      0.00       0.00      0.00      20.94
1.0000E-01    387.8     497.5    0.00      0.00       0.00      0.00      20.94
...
...
...
1.9000E+00    819.2    1202.7   15.60      6.24      24.51      0.00      5.45
Switched to non-equilibrium calculations at z = 1.9029 where tg = 1199.69
1.9100E+00    805.3    1193.9   15.64      6.22      24.48      0.08      5.51
```

```
1.9200E+00    791.7    1186.7   15.66      6.21      24.44      0.18      5.60
1.9300E+00    778.0    1180.3   15.66      6.19      24.39      0.29      5.70
1.9400E+00    764.6    1174.6   15.66      6.17      24.33      0.40      5.81
1.9500E+00    751.0    1169.6   15.66      6.15      24.27      0.51      5.93
1.9600E+00    737.7    1165.3   15.64      6.12      24.21      0.63      6.06
1.9700E+00    724.6    1161.3   15.62      6.10      24.15      0.74      6.19
1.9800E+00    712.8    1157.5   15.60      6.08      24.09      0.84      6.31
1.9900E+00    702.0    1153.3   15.57      6.06      24.03      0.94      6.43
2.0000E+00    690.8    1148.4   15.54      6.04      23.98      1.02      6.53
2.0100E+00    674.9    1141.1   15.52      6.03      23.93      1.08      6.61
2.0200E+00    644.9    1129.9   15.52      6.03      23.90      1.11      6.66
2.0300E+00    603.7    1113.3   15.48      6.01      23.84      1.11      6.87
2.0400E+00    558.7    1093.2   15.42      5.99      23.74      1.11      7.25
2.0500E+00    510.0    1072.6   15.36      5.97      23.65      1.11      7.63
2.0600E+00    457.6    1051.2   15.30      5.94      23.55      1.11      7.99
2.0700E+00    395.9    1028.7   15.24      5.92      23.46      1.10      8.35
2.0800E+00    321.9    1004.7   15.18      5.90      23.37      1.10      8.70
2.0828E+00    298.0     997.7   15.17      5.89      23.35      1.10      8.79

TOTAL CPU TIME:    0 hours, 38 minutes, 58.680 seconds!


Simulation Results for downward integration pass #  2
iteration =  1  yup(2) = -2.77381E+06  factor =  0.000000  y(3) = -2.77381E+06
hbound = F   lbound = F   fuppas = F

Axial Pos.   ts (K)    tg (K)  mol% H2  mol% CO2  mol% CO   mol% CH4  mol% H2O
----------   ------    ------  -------  --------  -------   --------  --------
2.0828E+00    298.0     997.7   15.17      5.89      23.35      1.10      8.79
2.0800E+00    322.1    1004.7   15.18      5.90      23.37      1.10      8.70
...
...
...
1.9600E+00    746.2    1183.8   15.52      6.03      23.89      1.12      6.69
1.9500E+00    760.8    1193.7   15.52      6.03      23.89      1.12      6.69
Switched to equilibrium calculations at z = 1.9427 where tg = 1200.41
1.9400E+00    773.2    1147.5   16.58      6.36      24.44      0.00      5.06
...
...
...
2.0000E-02    552.3     552.9    0.00      0.00       0.00      0.00     20.80
1.0000E-02    552.5     553.1    0.00      0.00       0.00      0.00     20.80
0.0000E+00    552.7     553.3    0.00      0.00       0.00      0.00     20.80
-------------------------------------------------------------------------------

Overall Heat Loss =   0.3580E+06 J/s

TOTAL CPU TIME:    1 hours,  2 minutes, 20.480 seconds!
```

```
Simulation Results for downward integration pass #  3
iteration =  2  yup(2) = -2.77381E+06  factor =  0.006709  y(3) = -2.75520E+06
hbound = F   lbound = T   fuppas = F

Axial Pos.   ts (K)    tg (K)  mol% H2  mol% CO2  mol% CO   mol% CH4  mol% H2O
----------   ------    ------  -------  --------  -------   --------  --------
2.0828E+00    298.0    1006.0   15.17      5.89     23.35      1.10      8.79
2.0800E+00    322.6    1013.1   15.18      5.90     23.37      1.10      8.70
...
...
...
1.9600E+00    750.3    1195.4   15.52      6.03     23.89      1.12      6.69
Switched to equilibrium calculations at z = 1.9539 where tg = 1200.62
1.9500E+00    762.3    1143.1   16.86      6.29     24.52      0.00      5.00
...
...
...
1.0000E-02    560.9     561.5    0.00      0.00      0.00      0.00     20.81
0.0000E+00    561.1     561.7    0.00      0.00      0.00      0.00     20.81
-------------------------------------------------------------------------------

Overall Heat Loss =   0.3483E+06 J/s

TOTAL CPU TIME:   1 hours, 25 minutes, 59.280 seconds!


Simulation Results for downward integration pass #  4
iteration =  3  yup(2) = -2.77381E+06  factor =  0.003354  y(3) = -2.76451E+06
hbound = T   lbound = T   fuppas = F

Axial Pos.   ts (K)    tg (K)  mol% H2  mol% CO2  mol% CO   mol% CH4  mol% H2O
----------   ------    ------  -------  --------  -------   --------  --------
2.0828E+00    298.0    1001.9   15.17      5.89     23.35      1.10      8.79
2.0800E+00    322.3    1008.9   15.18      5.90     23.37      1.10      8.70
...
...
...
1.9600E+00    748.3    1189.6   15.52      6.03     23.89      1.12      6.69
Switched to equilibrium calculations at z = 1.9500 where tg = 1200.18
1.9500E+00    763.2    1138.2   16.90      6.32     24.49      0.00      4.97
...
...
...
1.0000E-02    556.7     557.2    0.00      0.00      0.00      0.00     20.80
0.0000E+00    556.8     557.4    0.00      0.00      0.00      0.00     20.80
-------------------------------------------------------------------------------

Overall Heat Loss =   0.3530E+06 J/s
```

TOTAL CPU TIME: 1 hours, 50 minutes, 4.350 seconds!

Simulation Results for downward integration pass # 5
iteration = 4 yup(2) = -2.77381E+06 factor = 0.005032 y(3) = -2.75985E+06
hbound = T lbound = T fuppas = F

Axial Pos.	ts (K)	tg (K)	mol% H2	mol% CO2	mol% CO	mol% CH4	mol% H2O
2.0828E+00	298.0	1003.9	15.17	5.89	23.35	1.10	8.79
2.0800E+00	322.4	1011.0	15.18	5.90	23.37	1.10	8.70
...							
...							
1.9600E+00	749.3	1192.5	15.52	6.03	23.89	1.12	6.69
Switched to equilibrium calculations at z = 1.9512 where tg = 1200.41							
1.9500E+00	762.6	1140.8	16.88	6.31	24.51	0.00	4.98
...							
...							
2.0000E-02	558.7	559.2	0.00	0.00	0.00	0.00	20.81
1.0000E-02	558.9	559.4	0.00	0.00	0.00	0.00	20.81
0.0000E+00	559.0	559.6	0.00	0.00	0.00	0.00	20.81

Overall Heat Loss = 0.3506E+06 J/s

TOTAL CPU TIME: 2 hours, 13 minutes, 12.890 seconds!

Simulation Results for final upward integration pass

Axial Pos.	ts (K)	tg (K)	mol% H2	mol% CO2	mol% CO	mol% CH4	mol% H2O
0.0000E+00	559.0	560.0	0.00	0.00	0.00	0.00	20.94
1.0000E-02	558.9	559.8	0.00	0.00	0.00	0.00	20.94
2.0000E-02	558.7	559.6	0.00	0.00	0.00	0.00	20.94
3.0000E-02	558.5	559.4	0.00	0.00	0.00	0.00	20.94
4.0000E-02	558.3	559.2	0.00	0.00	0.00	0.00	20.94
5.0000E-02	558.1	559.0	0.00	0.00	0.00	0.00	20.94
6.0000E-02	557.9	558.8	0.00	0.00	0.00	0.00	20.94
7.0000E-02	557.7	558.6	0.00	0.00	0.00	0.00	20.94
8.0000E-02	557.6	558.4	0.00	0.00	0.00	0.00	20.94
9.0000E-02	557.4	558.2	0.00	0.00	0.00	0.00	20.94
1.0000E-01	557.2	558.0	0.00	0.00	0.00	0.00	20.94
1.1000E-01	557.0	557.8	0.00	0.00	0.00	0.00	20.94
1.2000E-01	556.8	557.6	0.00	0.00	0.00	0.00	20.94
1.3000E-01	556.6	557.4	0.00	0.00	0.00	0.00	20.94
1.4000E-01	556.5	557.2	0.00	0.00	0.00	0.00	20.94
1.5000E-01	556.3	557.0	0.00	0.00	0.00	0.00	20.94
1.6000E-01	556.1	556.8	0.00	0.00	0.00	0.00	20.94

1.7000E-01	555.9	556.7	0.00	0.00	0.00	0.00	20.94
1.8000E-01	555.7	556.5	0.00	0.00	0.00	0.00	20.94
1.9000E-01	555.5	556.3	0.00	0.00	0.00	0.00	20.94
2.0000E-01	555.4	556.1	0.00	0.00	0.00	0.00	20.94
2.1000E-01	555.2	555.9	0.00	0.00	0.00	0.00	20.94
2.2000E-01	555.0	555.7	0.00	0.00	0.00	0.00	20.94
2.3000E-01	554.8	555.5	0.00	0.00	0.00	0.00	20.94
2.4000E-01	554.6	555.3	0.00	0.00	0.00	0.00	20.94
2.5000E-01	554.5	555.1	0.00	0.00	0.00	0.00	20.94
2.6000E-01	554.3	555.0	0.00	0.00	0.00	0.00	20.94
2.7000E-01	554.1	554.8	0.00	0.00	0.00	0.00	20.94
2.8000E-01	553.9	554.6	0.00	0.00	0.00	0.00	20.94
2.9000E-01	553.7	554.4	0.00	0.00	0.00	0.00	20.94
3.0000E-01	553.6	554.2	0.00	0.00	0.00	0.00	20.94
3.1000E-01	553.4	554.0	0.00	0.00	0.00	0.00	20.94
3.2000E-01	553.2	553.9	0.00	0.00	0.00	0.00	20.94
3.3000E-01	553.0	553.7	0.00	0.00	0.00	0.00	20.94
3.4000E-01	552.9	553.5	0.00	0.00	0.00	0.00	20.94
3.5000E-01	552.7	553.3	0.00	0.00	0.00	0.00	20.94
3.6000E-01	552.5	553.1	0.00	0.00	0.00	0.00	20.94
3.7000E-01	552.3	553.0	0.00	0.00	0.00	0.00	20.94
3.8000E-01	552.2	552.8	0.00	0.00	0.00	0.00	20.94
3.9000E-01	552.0	552.6	0.00	0.00	0.00	0.00	20.94
4.0000E-01	551.8	552.4	0.00	0.00	0.00	0.00	20.94
4.1000E-01	551.6	552.2	0.00	0.00	0.00	0.00	20.94
4.2000E-01	551.5	552.1	0.00	0.00	0.00	0.00	20.94
4.3000E-01	551.3	551.9	0.00	0.00	0.00	0.00	20.94
4.4000E-01	551.1	551.7	0.00	0.00	0.00	0.00	20.94
4.5000E-01	550.9	551.5	0.00	0.00	0.00	0.00	20.94
4.6000E-01	550.8	551.4	0.00	0.00	0.00	0.00	20.94
4.7000E-01	550.6	551.2	0.00	0.00	0.00	0.00	20.94
4.8000E-01	550.4	551.0	0.00	0.00	0.00	0.00	20.94
4.9000E-01	550.3	550.8	0.00	0.00	0.00	0.00	20.94
5.0000E-01	550.1	550.7	0.00	0.00	0.00	0.00	20.94
5.1000E-01	549.9	550.5	0.00	0.00	0.00	0.00	20.94
5.2000E-01	549.7	550.3	0.00	0.00	0.00	0.00	20.94
5.3000E-01	549.6	550.1	0.00	0.00	0.00	0.00	20.94
5.4000E-01	549.4	550.0	0.00	0.00	0.00	0.00	20.94
5.5000E-01	549.2	549.8	0.00	0.00	0.00	0.00	20.94
5.6000E-01	549.1	549.6	0.00	0.00	0.00	0.00	20.94
5.7000E-01	548.9	549.5	0.00	0.00	0.00	0.00	20.94
5.8000E-01	548.8	549.3	0.00	0.00	0.00	0.00	20.94
5.9000E-01	555.3	549.3	0.00	0.00	0.00	0.00	20.94
6.0000E-01	839.5	556.7	0.00	0.00	0.00	0.00	20.94
6.1000E-01	1345.3	639.8	0.00	0.53	0.00	0.00	20.98
6.2000E-01	1390.4	785.0	0.00	1.59	0.00	0.00	21.06
6.3000E-01	1428.2	922.5	0.00	2.63	0.00	0.00	21.14
6.4000E-01	1461.8	1053.8	0.00	3.67	0.00	0.00	21.21
6.5000E-01	1492.5	1180.1	0.00	4.70	0.00	0.00	21.29

6.6000E-01	1521.2	1302.2	0.00	5.73	0.00	0.00	21.37
6.7000E-01	1548.7	1420.9	0.00	6.76	0.00	0.00	21.44
6.8000E-01	1575.3	1536.4	0.00	7.80	0.00	0.00	21.51
6.9000E-01	1601.3	1648.9	0.00	8.84	0.00	0.00	21.58
7.0000E-01	1626.7	1758.3	0.00	9.88	0.01	0.00	21.64
7.1000E-01	1651.3	1864.1	0.01	10.91	0.02	0.00	21.68
7.2000E-01	1674.7	1964.8	0.02	11.91	0.06	0.00	21.71
7.3000E-01	1696.6	2058.0	0.06	12.84	0.16	0.00	21.69
7.4000E-01	1704.2	2137.8	0.12	13.61	0.39	0.00	21.64
7.5000E-01	1704.6	2197.3	0.24	14.12	0.81	0.00	21.52
7.6000E-01	1704.2	2232.6	0.42	14.31	1.49	0.00	21.32
7.7000E-01	1703.0	2242.9	0.67	14.16	2.42	0.00	21.02
7.8000E-01	1694.7	2233.9	0.99	13.79	3.52	0.00	20.65
7.9000E-01	1685.5	2214.8	1.34	13.32	4.63	0.00	20.22
8.0000E-01	1676.2	2191.9	1.69	12.86	5.70	0.00	19.79
8.1000E-01	1667.4	2167.9	2.05	12.41	6.69	0.00	19.35
8.2000E-01	1659.0	2144.2	2.39	12.01	7.61	0.00	18.92
8.3000E-01	1651.1	2121.1	2.72	11.63	8.46	0.00	18.51
8.4000E-01	1643.8	2098.8	3.05	11.29	9.25	0.00	18.10
8.5000E-01	1636.9	2077.5	3.36	10.97	9.98	0.00	17.72
8.6000E-01	1630.4	2057.2	3.66	10.68	10.66	0.00	17.34
8.7000E-01	1624.2	2037.8	3.95	10.42	11.29	0.00	16.98
8.8000E-01	1618.5	2019.2	4.23	10.18	11.89	0.00	16.64
8.9000E-01	1613.0	2001.6	4.50	9.95	12.44	0.00	16.31
9.0000E-01	1607.8	1984.7	4.76	9.75	12.96	0.00	15.99
9.1000E-01	1602.9	1968.6	5.00	9.56	13.44	0.00	15.68
9.2000E-01	1598.2	1953.2	5.24	9.38	13.90	0.00	15.39
9.3000E-01	1593.7	1938.5	5.46	9.22	14.33	0.00	15.11
9.4000E-01	1589.4	1924.4	5.68	9.07	14.74	0.00	14.84
9.5000E-01	1585.3	1910.9	5.88	8.93	15.13	0.00	14.58
9.6000E-01	1581.3	1898.0	6.08	8.80	15.49	0.00	14.33
9.7000E-01	1577.5	1885.6	6.27	8.67	15.84	0.00	14.09
9.8000E-01	1573.8	1873.7	6.45	8.56	16.17	0.00	13.86
9.9000E-01	1570.2	1862.2	6.62	8.45	16.49	0.00	13.64
1.0000E+00	1566.7	1851.1	6.79	8.35	16.79	0.00	13.43
1.0100E+00	1563.3	1840.4	6.95	8.26	17.08	0.00	13.22
1.0200E+00	1560.0	1830.0	7.11	8.16	17.35	0.00	13.02
1.0300E+00	1556.8	1819.9	7.26	8.08	17.62	0.00	12.83
1.0400E+00	1553.6	1810.1	7.41	7.99	17.88	0.00	12.64
1.0500E+00	1550.5	1800.6	7.55	7.91	18.12	0.00	12.46
1.0600E+00	1547.5	1791.3	7.69	7.84	18.36	0.00	12.28
1.0700E+00	1544.5	1782.2	7.82	7.76	18.59	0.00	12.11
1.0800E+00	1541.6	1773.3	7.95	7.69	18.81	0.00	11.95
1.0900E+00	1538.7	1764.7	8.08	7.62	19.02	0.00	11.79
1.1000E+00	1535.9	1756.2	8.21	7.56	19.23	0.00	11.63
1.1100E+00	1533.1	1748.0	8.33	7.49	19.43	0.00	11.48
1.1200E+00	1530.3	1739.9	8.45	7.43	19.62	0.00	11.33
1.1300E+00	1527.6	1732.0	8.57	7.37	19.81	0.00	11.18
1.1400E+00	1524.9	1724.3	8.68	7.31	19.99	0.00	11.04

1.1500E+00	1522.3	1716.8	8.79	7.25	20.16	0.00	10.91
1.1600E+00	1519.7	1709.4	8.90	7.20	20.33	0.00	10.78
1.1700E+00	1517.2	1702.2	9.00	7.15	20.49	0.00	10.65
1.1800E+00	1514.6	1695.2	9.11	7.09	20.65	0.00	10.52
1.1900E+00	1512.1	1688.3	9.21	7.05	20.80	0.00	10.40
1.2000E+00	1509.7	1681.5	9.30	7.00	20.95	0.00	10.28
1.2100E+00	1507.2	1674.9	9.40	6.95	21.09	0.00	10.16
1.2200E+00	1504.8	1668.5	9.49	6.91	21.23	0.00	10.05
1.2300E+00	1502.5	1662.2	9.58	6.86	21.37	0.00	9.94
1.2400E+00	1500.1	1656.0	9.67	6.82	21.50	0.00	9.83
1.2500E+00	1497.8	1649.9	9.76	6.78	21.63	0.00	9.73
1.2600E+00	1495.5	1644.0	9.84	6.74	21.75	0.00	9.63
1.2700E+00	1493.2	1638.2	9.93	6.70	21.87	0.00	9.53
1.2800E+00	1491.0	1632.5	10.01	6.67	21.98	0.00	9.43
1.2900E+00	1488.8	1626.9	10.08	6.63	22.10	0.00	9.34
1.3000E+00	1486.6	1621.4	10.16	6.60	22.21	0.00	9.25
1.3100E+00	1484.4	1616.1	10.24	6.56	22.31	0.00	9.16
1.3200E+00	1482.2	1610.8	10.31	6.53	22.42	0.00	9.07
1.3300E+00	1480.1	1605.7	10.38	6.50	22.52	0.00	8.99
1.3400E+00	1477.9	1600.6	10.45	6.47	22.61	0.00	8.90
1.3500E+00	1475.8	1595.7	10.52	6.44	22.71	0.00	8.82
1.3600E+00	1473.8	1590.8	10.58	6.41	22.80	0.00	8.75
1.3700E+00	1471.7	1586.0	10.65	6.38	22.89	0.00	8.67
1.3800E+00	1469.6	1581.4	10.71	6.36	22.98	0.00	8.59
1.3900E+00	1467.6	1576.8	10.77	6.33	23.06	0.00	8.52
1.4000E+00	1465.6	1572.3	10.83	6.31	23.14	0.00	8.45
1.4100E+00	1463.6	1567.8	10.89	6.28	23.22	0.00	8.38
1.4200E+00	1461.6	1563.5	10.95	6.26	23.30	0.00	8.31
1.4300E+00	1459.6	1559.2	11.00	6.23	23.38	0.00	8.24
1.4400E+00	1457.6	1555.0	11.06	6.21	23.45	0.00	8.18
1.4500E+00	1455.7	1550.9	11.11	6.19	23.52	0.00	8.12
1.4600E+00	1453.7	1546.8	11.16	6.17	23.59	0.00	8.05
1.4700E+00	1451.8	1542.8	11.22	6.15	23.66	0.00	7.99
1.4800E+00	1449.8	1538.9	11.27	6.13	23.72	0.00	7.93
1.4900E+00	1447.9	1535.0	11.32	6.11	23.79	0.00	7.88
1.5000E+00	1445.9	1531.2	11.36	6.09	23.85	0.00	7.82
1.5100E+00	1443.9	1527.5	11.41	6.07	23.91	0.00	7.76
1.5200E+00	1441.9	1523.8	11.46	6.06	23.97	0.00	7.71
1.5300E+00	1439.8	1520.1	11.50	6.04	24.03	0.00	7.66
1.5400E+00	1437.7	1516.5	11.55	6.03	24.08	0.00	7.60
1.5500E+00	1435.6	1513.0	11.59	6.01	24.14	0.00	7.55
1.5600E+00	1433.3	1509.5	11.63	6.00	24.19	0.00	7.50
1.5700E+00	1431.0	1506.0	11.67	5.98	24.24	0.00	7.46
1.5800E+00	1428.5	1502.6	11.71	5.97	24.29	0.00	7.41
1.5900E+00	1425.8	1499.1	11.75	5.95	24.34	0.00	7.36
1.6000E+00	1422.9	1495.7	11.79	5.94	24.38	0.00	7.32
1.6100E+00	1419.7	1492.3	11.83	5.93	24.42	0.00	7.28
1.6200E+00	1416.1	1488.9	11.86	5.92	24.46	0.00	7.23
1.6300E+00	1412.1	1485.5	11.90	5.91	24.50	0.00	7.19

1.6400E+00	1407.6	1482.0	11.94	5.90	24.54	0.00	7.15
1.6500E+00	1402.3	1478.4	11.97	5.90	24.57	0.00	7.11
1.6600E+00	1396.2	1474.7	12.01	5.89	24.60	0.00	7.08
1.6700E+00	1389.0	1470.9	12.04	5.89	24.62	0.00	7.04
1.6800E+00	1380.5	1466.9	12.08	5.89	24.64	0.00	7.01
1.6900E+00	1370.3	1462.6	12.11	5.89	24.66	0.00	6.97
1.7000E+00	1358.1	1458.0	12.15	5.89	24.67	0.00	6.94
1.7100E+00	1343.1	1452.8	12.19	5.90	24.68	0.00	6.90
1.7200E+00	1324.8	1446.9	12.24	5.90	24.68	0.00	6.87
1.7300E+00	1302.1	1440.1	12.31	5.91	24.68	0.00	6.83
1.7400E+00	1273.8	1431.9	12.39	5.91	24.67	0.00	6.78
1.7500E+00	1239.0	1422.1	12.50	5.92	24.66	0.00	6.73
1.7600E+00	1198.5	1410.5	12.65	5.92	24.65	0.00	6.67
1.7700E+00	1155.5	1397.5	12.82	5.92	24.63	0.00	6.60
1.7800E+00	1113.7	1383.6	13.00	5.93	24.61	0.00	6.53
1.7900E+00	1074.6	1369.1	13.19	5.94	24.58	0.00	6.46
1.8000E+00	1038.0	1354.4	13.38	5.97	24.55	0.00	6.39
1.8100E+00	1004.0	1339.7	13.56	5.99	24.52	0.00	6.32
1.8200E+00	973.3	1325.1	13.73	6.03	24.49	0.00	6.25
1.8300E+00	946.6	1310.6	13.92	6.06	24.46	0.00	6.18
1.8400E+00	923.5	1296.2	14.10	6.10	24.44	0.00	6.10
1.8500E+00	903.5	1281.9	14.29	6.13	24.42	0.00	6.02
1.8600E+00	885.8	1267.6	14.49	6.17	24.40	0.00	5.94
1.8700E+00	869.7	1253.5	14.70	6.20	24.38	0.00	5.86
1.8800E+00	854.8	1239.4	14.92	6.24	24.37	0.00	5.77
1.8900E+00	840.6	1225.1	15.15	6.27	24.36	0.00	5.68
1.9000E+00	826.8	1210.4	15.40	6.29	24.37	0.00	5.57
Switched to non-equilibrium calculations at z = 1.9083 where tg = 1199.71							
1.9100E+00	813.3	1199.2	15.41	6.29	24.36	0.03	5.59
1.9200E+00	800.0	1191.7	15.41	6.27	24.33	0.12	5.68
1.9300E+00	786.8	1184.5	15.41	6.25	24.29	0.22	5.77
1.9400E+00	773.9	1177.5	15.40	6.24	24.24	0.32	5.86
1.9500E+00	762.6	1171.1	15.39	6.22	24.19	0.42	5.96
1.9600E+00	749.3	1166.5	15.37	6.20	24.12	0.53	6.08
1.9700E+00	734.3	1163.5	15.37	6.17	24.06	0.66	6.22
1.9800E+00	720.5	1160.8	15.35	6.15	23.99	0.78	6.36
1.9900E+00	708.2	1158.0	15.33	6.13	23.93	0.89	6.49
2.0000E+00	696.3	1154.5	15.30	6.10	23.87	0.99	6.62
2.0100E+00	681.6	1148.8	15.28	6.09	23.81	1.06	6.72
2.0200E+00	654.1	1138.8	15.27	6.08	23.78	1.10	6.78
2.0300E+00	612.9	1122.8	15.24	6.07	23.71	1.12	6.99
2.0400E+00	566.3	1102.8	15.18	6.04	23.61	1.12	7.37
2.0500E+00	515.8	1082.1	15.12	6.02	23.52	1.11	7.74
2.0600E+00	461.6	1060.6	15.06	6.00	23.42	1.11	8.10
2.0700E+00	398.3	1038.0	15.00	5.97	23.33	1.11	8.46
2.0800E+00	322.4	1013.7	14.95	5.95	23.25	1.10	8.80
2.0828E+00	298.0	1006.7	14.93	5.95	23.22	1.10	8.89

TOTAL CPU TIME: 2 hours, 21 minutes, 39.959 seconds!

```
TOTAL CPU TIME:   2 hours, 21 minutes, 40.020 seconds!

Simulation Completed: Thu Jun  3 17:34:14 1993
```

Output Files, OUTA through OUTJ

FBED-1 output also includes ten optional output files OUTA through OUTJ. These files are created when the logical flags louta through loutj are set to "true". The contents of these optional output files are listed in Table 6.6.

Table 6.6 Contents of Output Files OUTA trough OUTJ.

outa	outb	outc	outd	oute	outf	outg	outh	outi	outj
z	z	z	z	z	z	z	z	z	z
y(1)	tg	re	frco2	trco2	pd	hrxn1	hw	xgas(1)	ts
y(2)	pres	pr	frh2	trh2	pdu	hrxn2	hgw	xgas(2)	pd
y(3)	cpg	scco2	frh2o	trh2o	brnout	hrxn3	hsw	xgas(3)	pnd
y(4)	gk	sch2	fro2	tro2	rco2	hrxn4	hsg	xgas(4)	areap
ydot(1)	gmw	sch2o	arco2	rw	rh2	r1h1	hrs	xgas(5)	sk
ydot(2)	gvisc	sco2	arh2	verate(1)	rh2o	r2h2	hrv	xgas(6)	vsolid
ydot(3)	vgas	difco2	arh2o	verate(2)	ro2	r3h3	rskgk	xgas(7)	stime
ydot(4)	gtime	difh2	aro2	verate(3)	risum	r4h4	ergk	xgas(8)	solhr
fdafch	gashr	difh2o	crco2	verate(4)		smrihi	ersk	xgas(9)	
		difo2	crh2	verate(5)			qgw	xgas(10)	
			crh2o	zirihi			qsw	xgas(11)	
			cro2				qsg	xgas(12)	
								xgas(13)	
								xgas(14)	
								xgas(15)	

The output file OUTA contains the gas and solid mass flow rates (**y(1)** and **y(2)**), gas and solid energy flow rates (**y(3)** and **y(4)**), the derivatives of mass and energy flow rates for the gas and the solids (**ydot(1) - ydot(4)**), and the char mass flow rate on dry, ash-free basis (**fdafch**).

The output file OUTB contains the transport properties and a few predicted quantities for the gas phase. These values are the gas temperature (**tg**), the gas phase pressure (**pres**), the gas heat capacity (**cpg**), the gas mixture conductivity (**gk**), the gas mixture molecular weight (**gmw**), the gas mixture viscosity (**gvisc**), the gas velocity (**vgas**), the gas residence time (**gtime**), and the gas heating rate (**gashr**).

The output file OUTC contains Reynolds and Prandtl numbers for the gas, the Schmidt number for the gasification and oxidation agents CO_2, H_2, H_2O, and O_2 (**scco2, sch2, sch2o,** and **sco2**), and the diffusivities of the gasification and oxidation agents in the gas mixture (**difco2, difh2, difh2o,** and **difo2**).

The output file OUTD contains the film resistances for gasification and oxidation agents, (**frco2, frh2, frh2o,** and **fro2**), the ash resistances for gasification and oxidation agents (**arco2, arh2, arh2o,** and **aro2**), and the chemical resistances to gasification and oxidation (**crco2, crh2, crh2o,** and **cro2**).

The output file OUTE contains the total resistance to gasification and oxidation (**trco2, trh2, trh2o, and tro2**), the volumetric drying rate (**rw**), the volumetric heterogeneous elemental reaction rates for carbon, hydrogen, oxygen, nitrogen, and sulfur (**verate(1) - verate(5)**), and the energy term associated with mass exchange between solid and gas phases (**zirihi**).

The output file OUTF contains the overall particle diameter (**pd**), the unreacted core diameter (**pdu**), the dry ash-free particle burnout (**brnout**), the volumetric char consumption rates by the CO_2, H_2 and H_2O gasification reactions (**rco2, rh2** and **rh2o**), the volumetric char consumption rate by oxidation reaction (**ro2**), and the total volumetric char consumption rate by the gasification and oxidation reactions (**risum**).

The output file OUTG contains the net enthalpy production rate for the gasification and oxidation reactions (**hrxn1** is for the CO_2 gasification reaction, **hrxn2** is for the H_2 gasification reaction, **hrxn3** is for the H_2O gasification reaction, and **hrxn4** is for the oxidation reaction), the products of reaction rates

and enthalpy production rate for these reactions (**r1h1, r2h2, r3h3,** and **r4h4**), and the overall volumetric energy production from the gasification and oxidation reactions (**smrihi**).

The output file OUTH contains the bed-to-wall heat transfer coefficient (**hw**), the gas-to-wall heat transfer coefficient (**hgw**), the solid-to-wall heat transfer coefficient (**hsw**), the solid-to-gas heat transfer coefficient (**hsg**), the solid radiation coefficient (**hrs**), the void-to-void radiation coefficient (**hrv**), the ratio of the solid thermal conductivity to the gas mixture thermal conductivity (**rskgk**), the effective radial gas conductivity (**ergk**), the effective radial solid conductivity (**ersk**), the volumetric heat transfer from the gas to the wall (**qgw**), the volumetric heat transfer from the solid to the wall (**qsw**), and the volumetric heat transfer from the solid to the gas (**qsg**).

The output file OUTI gives the concentration in mole percent of the gas phase. The mole percentages for the first fifteen gas species in the FB1THM file are printed (**xgas(1) - xgas(15)**). The mole percentages listed in Table 6.6 are for AR, CO, CO_2, CH_4, C_2H_6, H_2, HCN, H_2O, H_2S, N_2, NH_3, NO, O_2, OH, and SO_2 respectively.

The final output file OUTJ provides the properties and the quantities related to the solid phase. These values are temperature of the solid (**ts**), the overall particle diameter (**pd**), the unreacted core diameter (**pdu**), the external surface area of the particle (**areap**), the thermal conductivity of the solid (**sk**), the solid velocity (**vsolid**), the solid phase residence time (**stime**), and the solid heating rate (**solhr**).

Other Output Files

Additional output files generated by FBED-1 are: 1) BALANC.OUT, which presents the overall mass, energy and elemental balance for the gasifier, 2) PDIA.OUT, which is essentially the same as OUTF except the headings are not printed and only the results of the final downward pass are printed, 3) CCONV.OUT, which prints the drying, tar and total devolatilization rates, gasification and oxidation rates and finally the dry, ash-free char flow rate for the

final downward pass, 4) COMPOS.OUT, which prints the composition of the first fifteen species for the final upward pass, and 5) TANDP.OUT, which prints the temperature and pressure profiles for the final upward integration pass. In addition, an optional file COMPAR.OUT is generated when the flag **lexpt** is .true.. These output files are then used to plot the comparison of the predicted and experimental results as well as the simulations results, as discussed in the next section.

Graphics

The output of the FBED-1 code is provided in a form suitable for use with popular spreadsheet packages. The user can use a spreadsheet package available at his/her site and generate the plots of the quantities of interest by importing the output files to the spreadsheet. In addition, two computer programs (PLOT1 and PLOT2), written in FORTRAN, are provided to be used with the DISSPLA graphics package. The first program generates the temperature, pressure, composition, char consumption and burnout profiles. The second program generates a plot that compares the available experimental data with the predictions. These comparisons include the feed gas properties (i.e., the temperature and the composition for the species of interest), the product gas properties, the temperature and pressure profiles, and some other quantities of interest, such as the burnout, the product tar flow rate and the wall heat loss. Figures 6.3 and 6.4 were generated using these two programs. The descriptions of the associated input files needed to run these plotting programs are provided in Appendix J. The procedure to compile and execute these programs is also explained in Appendix J.

Code Operation

FBED-1 is a "user-specialist" code that requires familiarity with the theory and structure of the code in order to be used correctly and efficiently. This section provides the guidelines for the new users. A thorough understanding of the

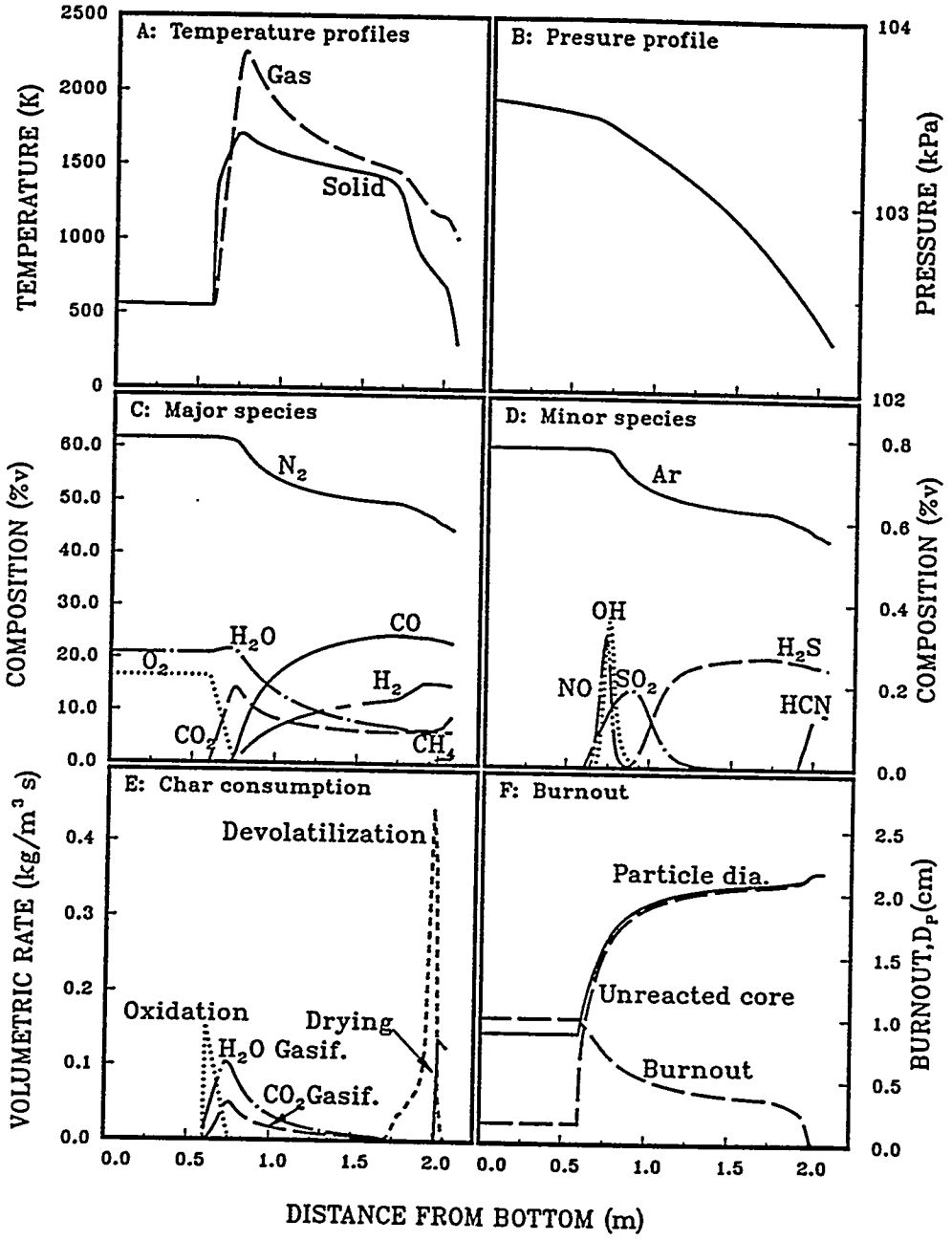

Figure 6.3. Plot generated by the program plot1 showing the predicted axial profiles.

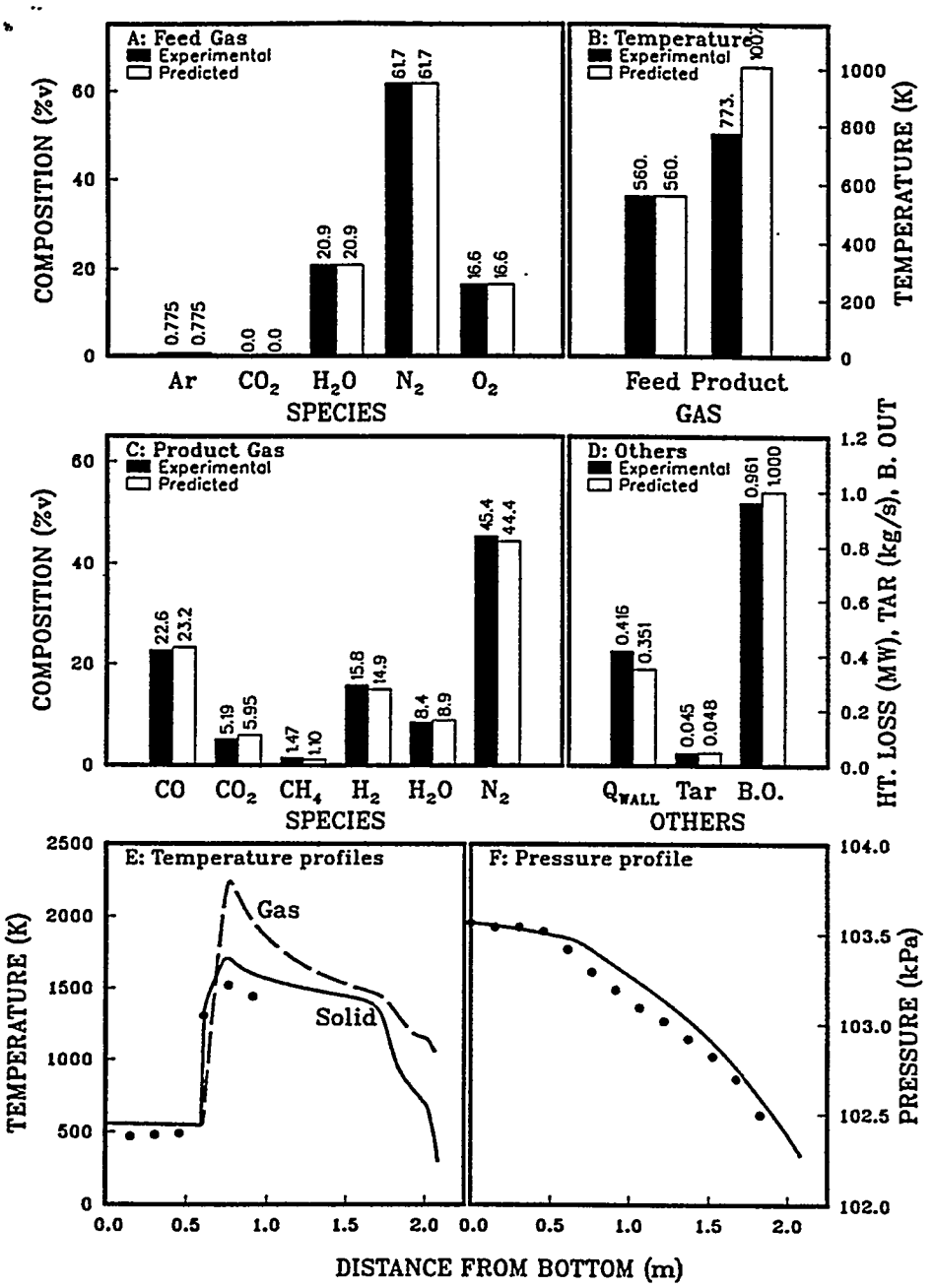

Figure 6.4. Plot generated by the program plot2 showing the comparison of the predicted and experimental data.

physics of the problem, assumptions, and numerical solution method is essential. Several iterations are required to obtain a converged solution. The iteration procedure is also discussed in this section.

Setting the Logical Variables

The various submodels and options provided in FBED-1 are exercised by the appropriate selection of the logical variables. Some of theses variables affect the operation of either zero-dimensional or one-dimensional portions of the model, whereas other variables affect the operation of both portions of the code. In addition to these logical variables, a few real variables are also needed for proper operation of the code. An example of such variables is **tswtch**, which governs the gas phase composition in the one-dimensional portion. A discussion of these variables is given below.

The flag **l0d** is used to run either zero-dimensioanl or one-dimensional model. When **l0d** is set to .true., the zero-dimensioanl, two-zone submodel is executed as a stand-alone model. The composition, and temperature of the product gas are computed and reported, along with the flow rates of the product gas and the product tar. When this flag is set to .false., these values serve as the initial guess for the one-dimensional model which is fully executed.

The flag **lgaseq** determines the gas phase chemistry submodel for the drying and devolatilization zone in the zero-dimensional portion. By setting this flag to .true., all the gases evolved in this zone are allowed to react to equilibrium with the gases from the equilibrium zone. When this flag is set to .false., all the gases but tar generated in the drying and devolatilization zone are considered to be non-reactive. Thus the product gas properties can be computed with either of these options, and their affect on the FBED-1 predictions can be studied.

The product gas temperature usually reported in the literature is at the gas off-take location and not at the top of the gasifier bed. In the freeboard, which is the space above the bed top, the gas stream losses some energy to the solid stream and the water jacket. If a reliable estimate of this energy loss is available, then the temperature drop in the freeboard zone for the gas stream can be computed. This

option is then exercised by setting **lfreeb** to .true.. If this information is not available or cannot be estimated, then the temperature of the product gas is assumed to be same as at the bed top. This is achieved by either setting **lfreeb** to .false. or assigning a value of zero to the variable **qfreeb.**

The logical flag **ljkstm** is used to estimate the wall heat loss, from the water jacket steam flow rate, for the zero-dimensional portion of the model. This option is exercised only if an estimate of the heat loss is not available. In case, neither an estimate of the wall heat loss nor jacket steam flow rate is available, the wall heat loss may also be computed from an overall heat transfer coefficient. This option is exercised by setting the flag **ljkstm** to .false., and assigning a value of zero to the variable **qwall.**

The flag **lashcp** provides the option to use either Kirov's correlation or Kopp-Neuman's formulation for the estimation of heat capacity of the ash.

The flag **ldvc**, perhaps the most important of all, selects the devolatilization submodel to be used in both the zero-dimensional and one-dimensional portions of the code. When this flag is set to .true., the FG-DVC submodel is used; otherwise the simpler FG-SET submodel is used.

The computation of the potential tar-forming fraction, when the FG-SET, submodel is used, is obtained either from the semiempirical correlation of Ko et al., (1988) or is specified by the user. If the flag **lx0** is set to .true. then the user specified value **usrx0** is used; otherwise Ko's correlation is used to determine the potential tar forming fraction.

The rate coefficients for the gas phase decomposition of tar may be determined by using a time dependent distribution for the activation energy. The time variation is approximated by keeping the activation energy function constant and changing the lower limit of the distribution function. This procedure is same as discussed for the FG-DVC submodel and the option can be exercised by setting the flag **lfixg** to .true.. When this flag is set to .false., the distribution function is kept constant throughout the decomposition process.

The flag **lsp** is used to select between the shell progressive and the ash segregation submodel. When **lsp** is set to .true., the oxidation and gasification of char is based on the shell progressive submodel, which takes into account the diffusion of the reactants and the products through the developing ash layer. Otherwise, the ash segregation submodel is used.

The variable **lstiff**, when set to .true., activates the stiff solver available in the LSODE package.

The gas phase chemistry in the one-dimensional portion of the code is governed by selecting an appropriate value of the variable **tswtch**. The gases are considered to be nonreactive when the gas temperature is below this value; otherwise full chemical equilibrium is assumed for the gas phase. The evolved tar in one-dimensional model can be either kept out of equilibrium, i.e., considered nonreactive, or allowed to react to complete equilibrium by setting the flag **ltareq** to .true..

The termination of the integration is exercised by assigning the axial position of the lower boundary to the variable **zbotom** and setting the flag **lstop** to .true.. Usually the variable **zbotom** is zero, but values less than zero may be specified to study the behavior of some coals that may need extended lengths of reaction zones for complete conversion. This option may be useful for design simulations when the gasifier's bed height is not known a priori. Required bed height may therefore be determined in an iterative manner.

Finally, the flags **louta** to **loutj** are used to invoke the printing of the optional output files.

Iteration Procedure

The nature of the governing equations for the FBED-1 requires an iterative solution. These equations are solved by a shooting method with split back and forth integration scheme, as discussed in chapter 5. The code can be executed in both an interactive and a noninteractive mode. When executed in a noninteractive mode, the values of the input parameters must be such that they lead to a solution

that is close to the final (converged) solution. The departure of the predicted feed gas temperature from the known boundary value is a measure of the closeness of the solution. Our simulation results suggest that the predicted feed gas temperature after the first iteration should not depart by more than 50 K from the input value. In case the difference is greater, a converged solution may be difficult to obtain.

The integration is started by obtaining an initial guess for the gas phase variables using the zero-dimensional submodel, FBED-0. Variables such as wall heat loss for the zero-dimensional portion (**qwall**), or the feed gas temperature may be changed to improve on the overall char conversion for the first downward integration pass. Once a reasonable burnout is obtained, the gas phase quantities are integrated from the bottom to the top of the reactor. This yields a new guess for the product gas properties. The complete set of differential equations is now integrated from the top to the bottom of the gasifier. This pass is treated as the first iteration pass, because the estimated product gas composition is more realistic. In the subsequent iterations, the product gas composition is held constant, but its enthalpy (and hence temperature) is varied until a converged solution is obtained. The enthalpy of the gas is lowered if the predicted temperature is higher than the input value and vice-versa. Once the solution is bracketed, a bisection techniques takes over to find the solution within the specified tolerance. It should be noted that the bracketing of the solution in a noninteractive mode may not always be possible, because high temperatures will be attained when the char conversion is not complete. This will mislead the iteration scheme, which will attempt to reduce the temperature by lowering the product gas enthalpy, resulting in even smaller char burnout. Thus the predicted feed gas temperature and the overall burnout must be closely monitored. If high feed gas temperature and less than adequate burnout are obtained, the user is urged to run the code in an interactive mode.

CHAPTER 7

IMPLEMENTATION GUIDE

Compiling, Linking, and Executing FBED-1 Code

This chapter discusses the implementation of fbed using the UNIX operating system. By replacing the commands used for compilation, linkage and execution, the procedure discussed in this chapter is also applicable to other computer systems. The UNIX "make" command is used to compile and link the subroutines which comprise the FBED-1 code.

The make file, called MAKEFBED, which is used to compile and link the FBED-1 code, is shown in Table 7.1. This file is specific to the Sun Computers, which invoke the compilation by the command f77. On a CONVEX machine this should be replaced by *fc*. The compilation and linking of the code is accomplished by invoking the *make* command. A successful execution of the *make* command will produce the executable code specified as *fbed1*. The code can then be executed by typing "fbed1." Selected results are printed to the screen to monitor the progress of simulation. The steps required for this procedure are as shown below. "%" represents the system's prompt; "al" is the name of our Sun computer.

```
al% make -f makefbed                    Generates the executable code fbed1.
f77 -g -sun4 -c  adjsty0.f
adjsty0.f:
        adjsty0:
f77 -g -sun4 -c  ashcp.f
ashcp.f:
        ashcp:
```

```
......
...... Similar messages for other routines.
......
f77 -g -sun4 -c  wrt0d.f
wrt0d.f:
        wrt0d:
Loading fbed1 ... done
```

The code can now be executed by typing fbed1. Parts of the typical output obtained on the monitor during the execution of the code are shown below.

```
al% fbed1

 Simulation Started: Thu Jun  3 15:11:50 1993
 Non-Interactive Run
 Coal input data will be read from: coal0.arg6
 Devolatilization will be based on FG-DVC submodel
 FBED0D: Iteration # 1
 FBED0D: Iteration # 2
 FBED0D: Iteration # 3
 FBED0D: Iteration # 4
 FBED0D: Iteration # 5
 FBED0D: Iteration # 6
 FBED0D converged with -->  Texit =  959.44
 ------------------------>  Teq   = 1344.87

 ZERO-D CPU TIME:   0 hours,  8 minutes, 45.530 seconds!


 Simulation Results for downward integration pass #  1

 Axial Pos.   ts (K)    tg (K)  mol% H2  mol% CO2  mol% CO   mol% CH4  mol% H2O
 ----------   ------    ------  -------  --------  -------   --------  --------
 2.0828E+00    298.0     959.4   20.84     10.23     16.08      0.24      7.68
 2.0800E+00    321.9     966.0   20.86     10.24     16.09      0.24      7.59
 ...
 ...
 ...
 1.9000E+00    819.2    1181.1   21.32     10.47     16.45      0.24      5.56
 1.8900E+00    833.1    1192.3   21.32     10.47     16.45      0.24      5.56
 Switched to equilibrium calculations at z = 1.8825 where tg = 1200.07
 1.8800E+00    848.2    1265.1   13.35      8.47     17.72      0.00     10.28
 1.8700E+00    864.3    1279.4   13.09      8.44     17.71      0.00     10.40
 ...
 ...
 ...
 1.0000E-02    388.3     388.6    0.00      0.00      0.00      0.00     23.15
```

```
0.0000E+00    388.4     388.6    0.00      0.00      0.00      0.00      23.15
-------------------------------------------------------------------------------

Overall Heat Loss =   0.2776E+06 J/s

TOTAL CPU TIME:   0 hours, 30 minutes, 19.870 seconds!

Simulation Results for upward integration pass #  1

Axial Pos.   ts (K)    tg (K)  mol% H2  mol% CO2  mol% CO   mol% CH4  mol% H2O
----------   ------    ------  -------  --------  -------   --------  --------
0.0000E+00    388.4     560.0    0.00      0.00      0.00      0.00      20.94
1.0000E-02    388.3     552.3    0.00      0.00      0.00      0.00      20.94
...
...
...
1.9000E+00    819.2    1202.7   15.60      6.24     24.51      0.00       5.45
Switched to non-equilibrium calculations at z = 1.9029 where tg = 1199.69
1.9100E+00    805.3    1193.9   15.64      6.22     24.48      0.08       5.51
1.9200E+00    791.7    1186.7   15.66      6.21     24.44      0.18       5.60
...
...
...
2.0800E+00    321.9    1004.7   15.18      5.90     23.37      1.10       8.70
2.0828E+00    298.0     997.7   15.17      5.89     23.35      1.10       8.79

TOTAL CPU TIME:   0 hours, 38 minutes, 58.680 seconds!


Simulation Results for downward integration pass #  2
iteration =  1  yup(2) = -2.77381E+06  factor =  0.000000  y(3) = -2.77381E+06
hbound = F   lbound = F   fuppas = F

Axial Pos.   ts (K)    tg (K)  mol% H2  mol% CO2  mol% CO   mol% CH4  mol% H2O
----------   ------    ------  -------  --------  -------   --------  --------
2.0828E+00    298.0     997.7   15.17      5.89     23.35      1.10       8.79
2.0800E+00    322.1    1004.7   15.18      5.90     23.37      1.10       8.70
...
...
...
1.9500E+00    760.8    1193.7   15.52      6.03     23.89      1.12       6.69
Switched to equilibrium calculations at z = 1.9427 where tg = 1200.41
1.9400E+00    773.2    1147.5   16.58      6.36     24.44      0.00       5.06
...
...
...
1.0000E-02    552.5     553.1    0.00      0.00      0.00      0.00      20.80
0.0000E+00    552.7     553.3    0.00      0.00      0.00      0.00      20.80
-------------------------------------------------------------------------------
```

```
Overall Heat Loss =   0.3580E+06 J/s

TOTAL CPU TIME:   1 hours,  2 minutes, 20.480 seconds!


Simulation Results for downward integration pass #  3
iteration =  2  yup(2) = -2.77381E+06  factor =  0.006709  y(3) = -2.75520E+06
hbound = F   lbound = T   fuppas = F

Axial Pos.   ts (K)    tg (K)  mol% H2  mol% CO2  mol% CO   mol% CH4  mol% H2O
----------   ------    ------  -------  --------  -------   --------  --------
2.0828E+00    298.0    1006.0   15.17      5.89     23.35      1.10      8.79
2.0800E+00    322.6    1013.1   15.18      5.90     23.37      1.10      8.70
...
...
...
1.9600E+00    750.3    1195.4   15.52      6.03     23.89      1.12      6.69
Switched to equilibrium calculations at z = 1.9539 where tg = 1200.62
1.9500E+00    762.3    1143.1   16.86      6.29     24.52      0.00      5.00
...
...
...
1.0000E-02    560.9     561.5    0.00      0.00      0.00      0.00     20.81
0.0000E+00    561.1     561.7    0.00      0.00      0.00      0.00     20.81
-------------------------------------------------------------------------------

Overall Heat Loss =   0.3483E+06 J/s

TOTAL CPU TIME:   1 hours, 25 minutes, 59.280 seconds!


Simulation Results for downward integration pass #  4
iteration =  3  yup(2) = -2.77381E+06  factor =  0.003354  y(3) = -2.76451E+06
hbound = T   lbound = T   fuppas = F

Axial Pos.   ts (K)    tg (K)  mol% H2  mol% CO2  mol% CO   mol% CH4  mol% H2O
----------   ------    ------  -------  --------  -------   --------  --------
2.0828E+00    298.0    1001.9   15.17      5.89     23.35      1.10      8.79
2.0800E+00    322.3    1008.9   15.18      5.90     23.37      1.10      8.70
...
...
...
1.9600E+00    748.3    1189.6   15.52      6.03     23.89      1.12      6.69
Switched to equilibrium calculations at z = 1.9500 where tg = 1200.18
1.9500E+00    763.2    1138.2   16.90      6.32     24.49      0.00      4.97
...
...
...
```

```
1.0000E-02    556.7     557.2     0.00      0.00      0.00      0.00      20.80
0.0000E+00    556.8     557.4     0.00      0.00      0.00      0.00      20.80
-------------------------------------------------------------------------------

Overall Heat Loss =   0.3530E+06 J/s

TOTAL CPU TIME:   1 hours, 50 minutes,  4.350 seconds!


Simulation Results for downward integration pass #  5
iteration =  4  yup(2) = -2.77381E+06  factor =  0.005032  y(3) = -2.75985E+06
hbound = T   lbound = T   fuppas = F

Axial Pos.   ts (K)    tg (K)  mol% H2  mol% CO2  mol% CO   mol% CH4  mol% H2O
----------   ------    ------  -------  --------  -------   --------  --------
2.0828E+00    298.0    1003.9   15.17      5.89     23.35      1.10      8.79
2.0800E+00    322.4    1011.0   15.18      5.90     23.37      1.10      8.70
...
...
1.9600E+00    749.3    1192.5   15.52      6.03     23.89      1.12      6.69
Switched to equilibrium calculations at z = 1.9512 where tg = 1200.41
1.9500E+00    762.6    1140.8   16.88      6.31     24.51      0.00      4.98
...
...
1.0000E-02    558.9     559.4    0.00      0.00      0.00      0.00      20.81
0.0000E+00    559.0     559.6    0.00      0.00      0.00      0.00      20.81
-------------------------------------------------------------------------------

Overall Heat Loss =   0.3506E+06 J/s

TOTAL CPU TIME:   2 hours, 13 minutes, 12.890 seconds!

Simulation Results for final upward integration pass

Axial Pos.   ts (K)    tg (K)  mol% H2  mol% CO2  mol% CO   mol% CH4  mol% H2O
----------   ------    ------  -------  --------  -------   --------  --------
0.0000E+00    559.0     560.0    0.00      0.00      0.00      0.00      20.94
1.0000E-02    558.9     559.8    0.00      0.00      0.00      0.00      20.94
...
...
...
1.9000E+00    826.8    1210.4   15.40      6.29     24.37      0.00      5.57
Switched to non-equilibrium calculations at z = 1.9083 where tg = 1199.71
1.9100E+00    813.3    1199.2   15.41      6.29     24.36      0.03      5.59
...
...
...
2.0800E+00    322.4    1013.7   14.95      5.95     23.25      1.10      8.80
2.0828E+00    298.0    1006.7   14.93      5.95     23.22      1.10      8.89
```

```
TOTAL CPU TIME:   2 hours, 21 minutes, 39.959 seconds!

TOTAL CPU TIME:   2 hours, 21 minutes, 40.020 seconds!

Simulation Completed: Thu Jun  3 17:34:14 1993
```

Table 7.1 Listing of the make file MAKEFBED

```
DEST        = /homes/ghani/fbed1

FFLAGS      = -g

LFLAGS      = -g

LIBS        =

LINKER      = f77

MAKEFILE    = makefbed

OBJS        = adjsty0.o \
              ashcp.o \
              ashh.o \
              avgatw.o \
              balanc.o \
              calc.o \
              coalin.o \
              convy.o \
              cnvyup.o \
              cputim.o \
              cree.o \
              cree0.o \
              ddzone.o \
              deltap.o \
              devol0.o \
              devol1.o \
              dlsodes.o \
              drying.o \
              drywet.o \
              echoin.o \
              elrate.o \
```

```
                eqexit.o \
                eqzone.o \
                exitt.o \
                f.o \
                f0.o \
                fup.o \
                fbed0d.o \
                fbed1d.o \
                fgdvc.o \
                fgset.o \
                freebd.o \
                gasin.o \
                gtemp.o \
                hschar.o \
                hcps.o \
                hdevol.o \
                hform.o \
                thtar.o \
                htcoef.o \
                hvh2o.o \
                ivalu0.o \
                ivalu1.o \
                iv1up.o \
                mtcoef.o \
                omegad.o \
                omegam.o \
                oxgas.o \
                pdpnd.o \
                ptemp.o \
                rtsfxg.o \
                readin.o \
                set.o \
                spece.o \
                t2geqz.o \
                tcrack.o \
                transp.o \
                ultcom.o \
                wrt0d.o

PROGRAM     = fbed1

SRCS        = adjsty0.f \
                ashcp.f \
                ashh.f \
                avgatw.f \
```

```
balanc.f \
calc.f \
coalin.f \
convy.f \
cnvyup.f \
cputim.f \
cree.f \
cree0.f \
ddzone.f \
deltap.f \
devol0.f \
devol1.f \
dlsodes.f \
drying.f \
drywet.f \
echoin.f \
elrate.f \
eqexit.f \
eqzone.f \
exitt.f \
f.f \
f0.f \
fup.f \
fbed0d.f \
fbed1d.f \
fgdvc.f \
fgset.f \
freebd.f \
gasin.f \
gtemp.f \
hschar.f \
hcps.f \
hdevol.f \
hform.f \
thtar.f \
htcoef.f \
hvh2o.f \
ivalu0.f \
ivalu1.f \
iv1up.f \
mtcoef.f \
omegad.f \
omegam.f \
oxgas.f \
pdpnd.f \
```

```
                ptemp.f \
                rtsfxg.f \
                readin.f \
                set.f \
                spece.f \
                t2geqz.f \
                tcrack.f \
                transp.f \
                ultcom.f \
                wrt0d.f

all:            $(PROGRAM)

$(PROGRAM): $(OBJS) $(LIBS)
            @echo -n "Loading $(PROGRAM) ... "
            @$(LINKER) $(LFLAGS) $(OBJS) $(LIBS) -o $(PROGRAM)
            @echo "done"

install:    $(PROGRAM)
            @echo Installing $(PROGRAM) in $(DEST)
            @install -s $(PROGRAM) $(DEST)

program:        $(PROGRAM)

update:           $(DEST)/$(PROGRAM)

$(DEST)/$(PROGRAM): $(SRCS) $(LIBS) $(HDRS) $(EXTHDRS)
            @make -f $(MAKEFILE) DEST=$(DEST) install
###
```

FORTRAN and Machine Incompatibilities

FBED-1 was developed on a SUN 4/310 running under the UNIX operating system. Significant efforts have been expended to make the code compatible with FORTRAN-77 standards. However, a few statements may be specific to the SUN architecture. For example, FBED-1 frequently calls a subroutine called CPUTIM, which uses a system-dependent utility to monitor the cpu time used in various sections of the code. On the non-unix machines, the function CPUTIM may need to be replaced by the corresponding utility available on

the host machine. Alternatively, the calls to the function CPUTIM may be commented out.

FBED-1 also uses calls to FLUSH, a UNIX utility, for flushing the contents of output buffers in a timely manner. These calls need to be replaced with calls to a similar utility available on the user's machine. Alternatively, they may be removed.

An ieee error trapping routine which is specific to the SUN system is also used in FBED-1. When compiled on a different system, statements relating to the SUN error trapping should be commented out. These statements are as follows:

```
C     external sample_handler
...
C     ieee = ieee_handler('set','common',sample_handler)
C     if (ieee.ne.0) print *, 'ieee_handler cannot set common '
...
C     integer function sample_handler(sig,code,sigcontext)
C     integer sig, code, sigcontext(5)
C     print *, 'ieee exception code ',loc(code),
C    &         ' occurred at pc ', sigcontext(4)
C     call abort
C     end
```

The error trapping routines can be activated when running in the debug mode on a SUN computer. To run in the debug mode, the UNIX "dbx" utility can be used. The error trapping is then activated by typing "catch FPE" at the dbx prompt and then executing the code.

CHAPTER 8

SAMPLE PROBLEM

In this chapter, a sample simulation of the atmospheric, air-blown, dry-ash Wellman-Galusha gasifier fired with the Jetson bituminous coal is presented and discussed. The input data for this case were presented in Tables 6.1 to 6.4.

Atmospheric Pressure, Air-Blown Gasification

The FBED-1 predictions for the atmospheric, air-blown, dry-ash Wellman-Galusha gasifier fired with the Jetson bituminous coal are shown in Figure 8.1. This case was selected because the experimental temperature profile show measurements in the ash zone. For other cases, either no or few data are available for the ash zone. The predicted profiles are shown for temperature, pressure, major and minor species composition, char consumption, and burnout. Both the solid and the gas temperatures show rapid change in the drying and devolatilization region. This is associated with the rapid addition of the devolatilized mass to the gas phase and the associated heat effects. In FBED-1, all coal conversion processes, namely drying, devolatilization, gasification and oxidation, are allowed to occur simultaneously. The results show that for atmospheric gasifiers, very little gasification occurs before devolatilization is complete, mainly due to the low solid temperatures. Oxidation and gasification reactions overlap in the region where oxygen is available. Due to high temperature in this zone, oxidation is dominant. The peak solid and gas temperatures occur when the oxygen becomes available to the char. The heat evolved due to the exothermic oxidation reaction causes the rapid heat-up of the gas stream. The temperatures drop sharply as soon as all char is

consumed and remain almost constant in the ash zone. CO and H_2 are not observed in the oxidation zone, due to chemical equilibrium in the gas phase, which causes all carbon and hydrogen to form CO_2 and H_2O. In the oxidation zone, H_2O concentration also shows some increase due to the reaction of char oxygen and hydrogen, which is assumed to be proportional to the overall char consumption rate. Char consumption by hydrogen gasification reaction is insignificant in comparison with CO_2 and H_2O gasification reactions. Increase in H_2O near the gasifier top is due to the release of moisture in the drying of feed coal. CH_4 appears only in the low temperature devolatilization zone, where the gas phase is assumed to be out of chemical equilibrium. Char sulfur is reacted to form H_2S in the oxygen free zone and is converted to SO_2 when the oxygen becomes available. NO and OH are observed only in the high temperature oxidation region. In addition, substantial amounts of HCN are observed in the product gas, with practically no NH_3 and NO. All of HCN is released in the devolatilization zone through HCN tight and extra-tight functional groups. The burnout profiles show rapid change in the devolatilization zone, followed by a gradual change in the gasification and oxidation zone. The particle size show a very rapid decrease in the oxidation zone, due to the high char consumption rates. Finally, the pressure profile shows a small drop in the ash zone, followed by a gradual change in the reactive zones of the gasifier. The small change in the ash zone is attributed to the higher bed void fraction offering little resistance to the gas flow.

Figure 8.2 presents the comparison of the FBED-1 predictions with the available data (Thimsen et al., 1984). The experimental data include the temperature and pressure profiles, and the product gas composition. Following Barriga and Essenhigh (1980), the experimental temperature profile is assumed to represent the solid temperature. The feed gas composition and temperatures are satisfied exactly. The product gas composition, the product tar flow rate, and the wall heat loss predicted by the model are in close agreement with the experimental data. The predicted pressure profile also shows good agreement with the experimental data. The predicted temperatures are slightly higher, but the trends in the devolatilization, gasification and oxidation zone are properly predicted.

The overall mass and energy balances close within 1%. The elemental mass balances close typically within 5%. Overall, the comparison between the experimental and the predicted values is good.

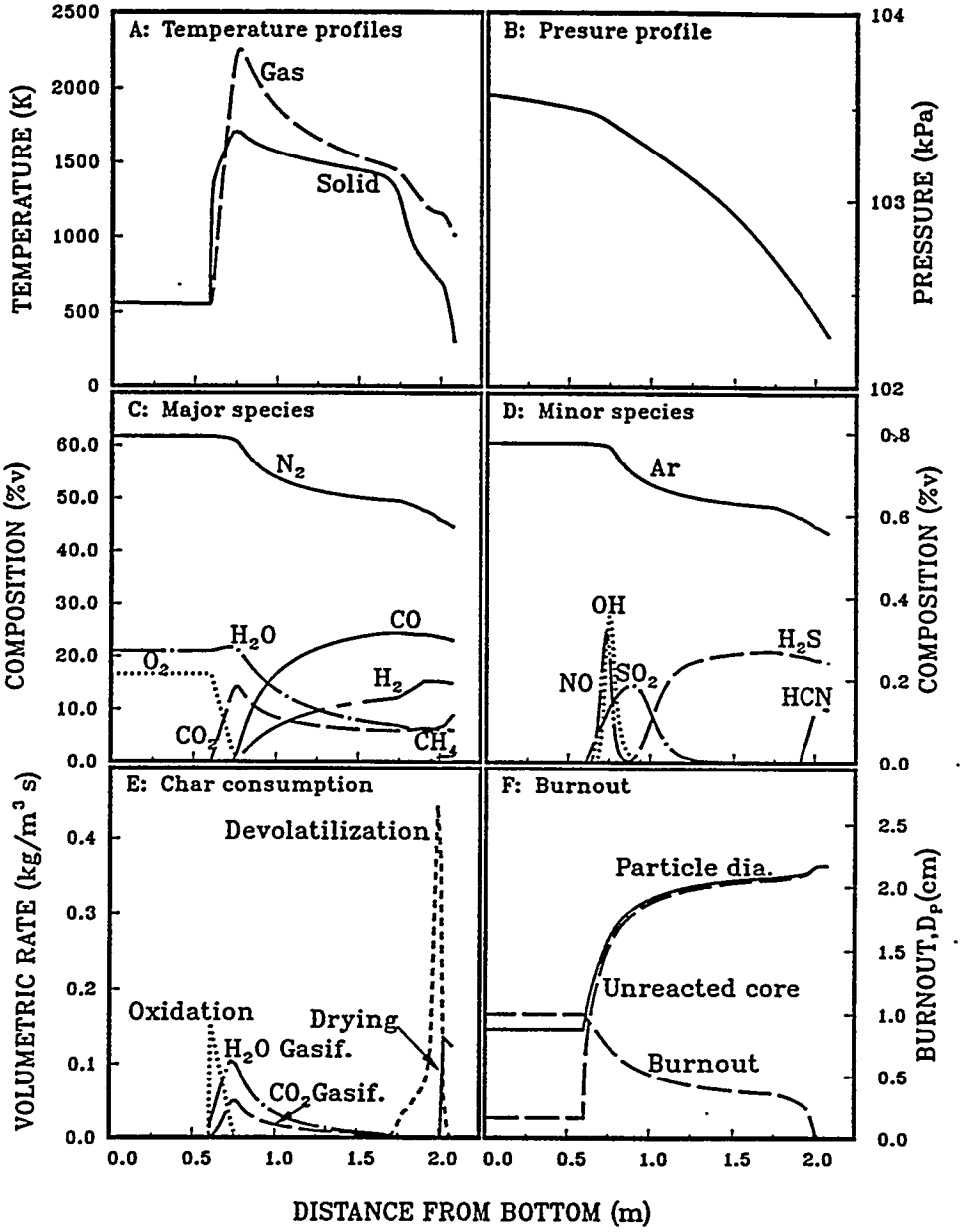

Figure 8.1. Predicted axial A) temperature, B) pressure, C) major species composition, D) minor species composition, E) volumetric char consumption rate, F) burnout and overall particle and unreacted core diameter in the atmospheric pressure, air-blown Wellman-Galusha gasifier fired with Jetson bituminous coal.

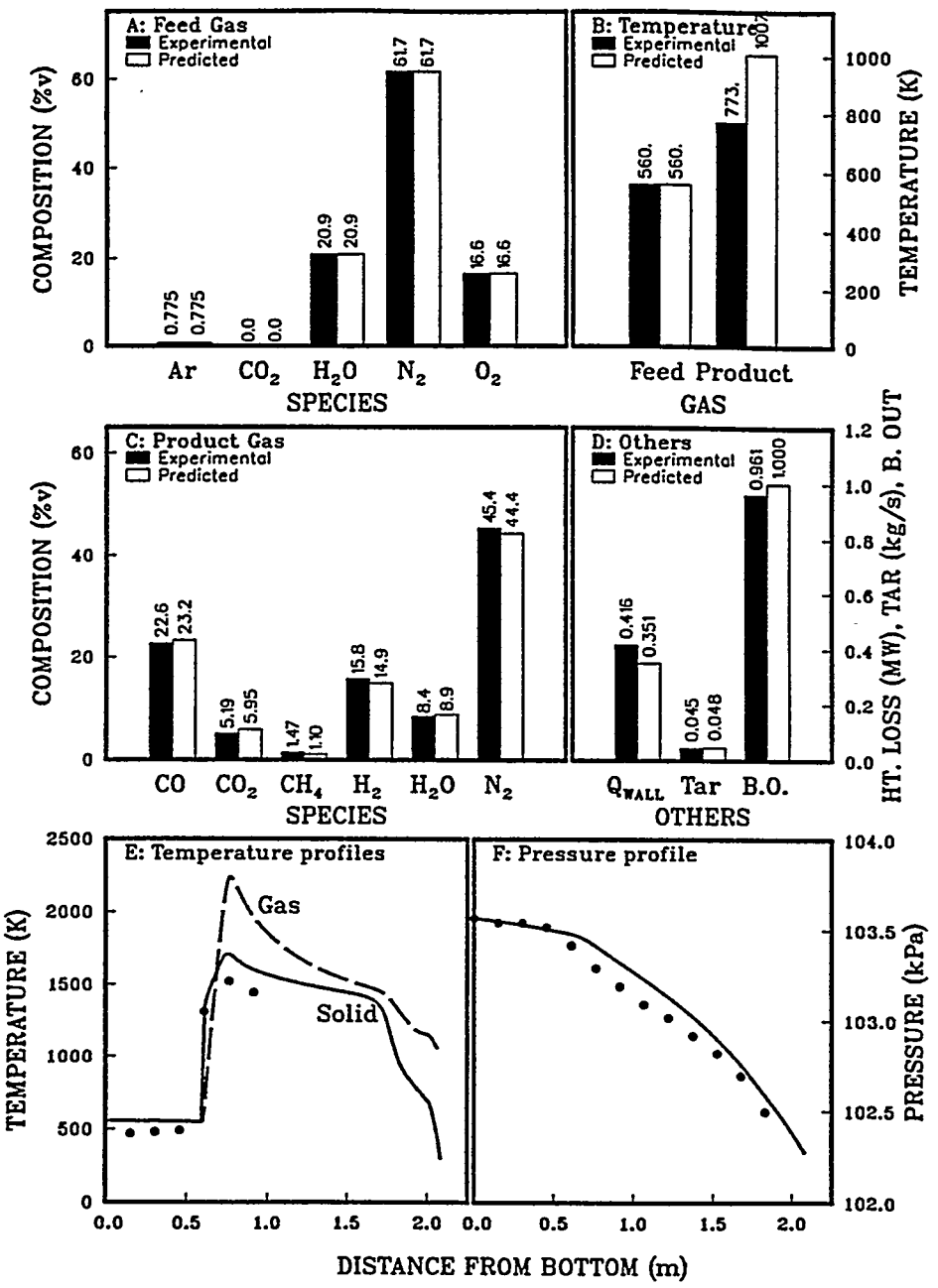

Figure 8.2. Comparison of FBED-1 predictions with experimental data for the gasification of the Jetson bituminuous coal in the atmospheric, air-blown, dry-ash Wellman-Galusha gasifier.

NOMENCLATURE

Symbol	Definition and Units
a	Mean atomic weight, *kg/kmol*
$a_{s,u}$	Number of ways to form a cluster with s bridges and u crosslinks
A	Arrhenius Pre-exponential factor, sec^{-1}
A	Cross sectional area of reactor, m^2
A	Particle surface area, m^2
A	Water wall surface area, m^2
C	Integration constant
C	Molar concentration of oxidizer or gasification agent, $kmol/m^3$
C_p	Specific heat, *j/kgK*
D	Diffusivity, m^2/s
D	Reactor diameter, m
d	Particle diameter, m
E	Activation Energy, *j/kmol*
F	Fraction of original carbon
$F(p,q)$	Fraction of sites in finite clusters
$F_n(p,q)$	Probability that a site is member of cluster of n sites
f	Aromaticity of coal used in the tar correlation of Ko et al. (1988)
f	Distribution function
f	Friction factor

G	Superficial gas mass flux, *kg/m²s*
G	Fraction of j-mer in mass bins, *kg/kg*
g	Acceleration due to gravity, 9.80665 *m/s²*
H	Convective heat capacity flux, *j/m²s*
h	Enthalpy, *j/kg*
h	Heat transfer coefficient, *watts/m²K*
ΔH	Reaction enthalpy, *j/kg*
Δh	Reaction enthalpy, *j/kg*
HHV	Higher heating value, *j/kg*
k	Arrhenius rate constant, *m/s or 1/s*
k	Thermal conductivity, *watts/mK*
L	Pressure parameter used in the tar correlation of Ko et al. (1988)
L	Reactor length, *m*
$\dot{m}$	Mass flow rate, *kg/s*
Mw	Molecular weight, *kg/s*
$\overline{M}_w$	Weight average molecular weight of the ash or slag, or particle molecular weight, *kg/kmol*
p	Number fraction of bridges in coal
P	Pressure, *KPa, Pa, or kg/m²*
P	Equilibrium vapor pressure of tar, *atm or KPa, or kg/m²*
Pe	Peclet number
Pr	Prantl number
q	Heat release for daf coal, *J/kg*
q	Number fraction of cross-links in coal
Q	Heat loss, *watts*
r	Volumetric reaction rate, *kg/m³s*
R	Universal gas constant, *j/kmolK*
Re	Reynold's number
s	Number of bridges
Sc	Schmidt number
t	Temperature, *℃*
t	Time, *s*
T	Temperature, *K*
u	Gas velocity, *m/s*

u	Number of crosslinks
U	Overall heat transfer coefficient, *watts/m^2K*
V	Volatile matter, *mass fraction*
V	Volume, *m^3*
VM	Volatile matter, *mass fraction*
w	Weight factor for Gausian quadrature
W	Mass flow rate, kg/s
W	Functional group mass fraction , *kg/kg*
x	Gas mole fraction
x	Mole fraction of ash constituents, *mole fraction*
x	Tar fraction, *mass fraction*
x	Tar parameter used in correlation of Ko et al. (1988)
x	Zero of Legendre polynomial
X	Crosslink efficiency, *(moles of crosslinks/mole of gas species formed)*(gm coal/mole of crosslink sites).*
y	functional group fraction, *mass fraction*
Y	Ultimate yield, *mass fraction*
z	Axial distance, *m*
z	Dummy variable representing the ratio of the Einstein temperature and T
α	Parameter used in tar correlation of Ko et al. (1988)
β	Parameter used in tar correlation of Ko et al. (1988)
ε	Bed void fraction, *void volume/bed volume*
ε	Emissivity
ε	Lennard-Jones parameter
Φ	Heat of combustion of elements, *J/kg*
Φ	Interaction parameter
ϕ	Packing parameter defined by Equation (10) in Table 3.5
ϕ	Porosity, *volume/volume*
η	Particle number density, *$1/m^3$*
κ	Ratio of solid conductivity and gas conductivity
λ	Stoichiometric coefficient for oxidation reaction, *mole/mole*

μ	Atomic weight, *kg/kmol*
μ	Viscosity, kg/ms
υ	Number of broken crosslinks
ν	Stoichiometric coefficient
ν	Stoichiometric coefficient to identify the number of moles of product gas per mole of oxidant, *mole/mole*
ρ	Density, kg/m^3
σ	Standard deviation of activation energy, *j/kmol*
σ	Stockmayer collision diameter, *Angstrom*
σ	Network coordination number
τ	Number of broken bridges
τ	Residence time of coal in the gasifier, *s*
Ω	Collision integral
Ω	Dry, ash-free mass fraction
ω	Functional group fraction or element fraction, *mass fraction*
ζ	Bed-to-wall heat transfer adjustable factor
ζ	Particle area factor to account for internal surface burning
ζ	Solid-to-gas heat transfer adjustable factor
ℓ	Boundary layer thickness, *m*
χ	Mole fraction tar in mass bin

Subscripts	*Definition*
a	Aromatic
a	Ash
ash	Ash
B	Labile bridge
BG	Blast gas
C	Carbon
c	Char
c	Coal

char	Char
co2	CO_2 gasification
devol	Devolatilization
e	Effective
e	Equilibrium
eff	Effective
exit	Exit
f	Formation
fb	Freeboard
FG	Functional group
g	Gas
gw	Gas-to-wall
H	Hydrogen
h2	H_2 gasification
h2o	H_2O gasification
i	Integer counter used to keep track of elements, species, or reactions
i	index for drying, devolatilization, gasification and oxidation reactions
i	index for tar monomer
i, k	index for functional groups
in	Entering control volume
j	index for elements C, H, O, N, and S
j	index for tar fraction
j	index for tar mass bin
L	Labile bridge
m	mass transport
moisture	Moisture
N	Nitrogen
n, m, h, j, k	Atomic stoichiometric coefficients
nonvolatile c	Carbon that is non-volatile
nonvolatile s	Sulfur that is non-volatile
O	Oxygen
o2	Oxidation
OH	Hydroxyl
out	Exiting control volume

p	Particle
S	Sulfur
s	Solid
sg	Solid-to-gas
sm	Solid measured (refers to the apparent density)
sw	Solid-to-wall
t	Tar
t	Total
tar	Tar
v	Volatiles
w	Wall
w	Water
x	Tar
z	axial
v	Volatiles

Superscripts	Definition
a	Axial
h	Thermal
m	Mass
o	Initial
o	Reference temperature
s	Sensible enthalpy
ultimate	Yield at large times
vap	Vaporization
∞	Infinity or ultimate

Operators	Definition
Δ	Difference

REFERENCES

Abramowitz, M. and Stegun, I. A., eds., Handbook of Mathematical Functions With Formulas, Graphs, and Mathematical Tables, 10th printing, National Bureau of Standards, Applied Mathematics Series, 55, U. S. Government Printing Office, Washington, D. C. (1972).

Anthony, D. B., Howard, J. B., Hottel, H. C. and Meissner, M. P., "Rapid Devolatilization of Pulverized Coal," 15th Symposium (International) on Combustion, The Combustion Institute, Pittsburgh, Pennsylvania, 1303 (1974).

Baxter, L. L., Condensed Phase Behavior in Combustion Environments, PhD Dissertation, Brigham Young University, Provo, Utah, 1987, see also Hedman, P. O., Smoot, L. D., Smith, P. J. and Blackham, A. U., "Entrained-flow Gasification at Elevated Pressure," Final Report, DOE/MC/22059-2570-Vol.1, DE88001070, Brigham Young University, Provo, Utah (1987).

Bird, R. B., Stewart, W. E. and Lightfoot, E. N., Transport Phenomena, John Wiley & Sons, New York (1960).

Bischoff, K. B., "A Note on Gas Dispersion in Packed Beds," Chem. Eng. Sci., 24, 607 (1962).

Brokaw, R. S., Ind. Eng. Chem. Process Design Develop., **8**, 240, (1969).

Carslaw, H. S. and Jaegar, J. C., Conduction of Heat in Solids, Oxford Press, London, England, 61 (1959).

Cho, Y. S., Modeling and Simulation of Lurgi-type Gasifiers, M. S. Thesis, Washington University, Saint Louis, Missouri (1980).

Computer Associates, CA-DISSPLA User's Manual, Release 11.0, Volume 1, Computer Associates International, Inc. Garden City, NY, (1989).

Crowe, C. T. and Smoot, L. D., "Multicomponent Conservation Equations," in Pulverized-Coal Combustion and Gasification, Smoot, L. D. and Pratt, D. T., editors, Plenum Press, New York (1979).

Denn, M., Wei, J., Yu, W., Cwiklinski, R., "Detailed Simulation of a Moving-Bed Gasifier, " Final Report, AP-2576, Research Project 1268-1, Electric Power Research Institute, Palo Alto, California (1982).

DeWasch, A. P. and Froment, G. F., "A Two-Dimensional Heterogeneous Model for Fixed Bed Catalytic Reactors," Chemical Engineering Science, 26, 629 (1971).

Dzhapbyev, K., Miropol'skii, A. L., and Mal'Kovskii, V. J., "Investigation of Unsteady Heat Transfer in a Packed Bed of Speheres Swept by Gas," Thermal Engineering, 33 (3), 159 (1986), translated from Teploenergetika, 33 (3), 70 (1986).

Elgin, D. C. and Perks, H. R., "Results of Trials of American Coals in Lurgi Pressure-Gasification Plant at Westfield, Scotland," Sixth Synthetic Pipeline Gas Symposium, Chicago, Illinois, October 18-20 (1974).

Ergun, S., "Fluid Flow Through Packed Columns," Chem. Eng. Prog., 48, 89 (1952).

Essenhigh, R. H., "Fundamentals of Coal Combustion," in Chemistry of Coal Utilization, Second Supplementary Volume, Elliott, M. A., editor, John Wiley & Sons, New York, 1153 (1981).

Field, M. A., "Rate of Combustion of Size-Graded Fractions of Char from a Low-Rank Coal Between 1200 K and 2000 K," Combustion and Flame, 13, 237 (1967).

Fisher, M.E. and Essam, J.W., *J. Math. Phys.*, 1961, 2, 609.

Froberg, R. W., "The Carbon-Oxygen Reaction: An Experimental Study of the Oxidation of Suspended Carbon Spheres," PhD Dissertation, The Pennsylvania State University, University Park, Pennsylvania (1967).

Froment, G. F. and Bischoff, K. B., Chemical Reactor Analysis and Design, John Wiley & Sons, New York (1979).

Goetz, G. J., Nsakala, N. Y., Patel, R. L. and LaO, T. C., "Combustion and Gasification Characteristics of Chars from Four Commercially Significant Coals of Different Rank," Final Report, Project 1654-6, Electric Power Research Institute, Palo Alto, California (1982).

Grant, D.M., Pugmire, R.J., Fletcher, T.H. and Kerstein, A.R., "Chemical Model of Coal Devolatilization using Percolation Lattice Statistics," Energy & Fuels, 3, 175 (1989).

Gray, D. D. and Stiles, J. M., "On the Consititutive Relation for Frictional Flow of Granular Materials," Topical Report DOE/MC/21353-2584, U. S. Department of Energy, Morgantown, West Virginia (1988).

Gupta, A. S. and Thodos, G., "Direct Analogy Between Mass and Heat Transfer to Beds of Spheres," AIChE J., 9, 751 (1963).

Hedman, P. O., Smoot, L. D., Smith, P. J. and Blackham, A. U. "Entrained-Flow Gasification at Elevated Pressure," DOE/MC/22059-2570, Combustion Laboratory, Chemical Engineering Department, Brigham Young University, Provo, Utah (1987).

Hindmarsh, A. C.: "ODEPACK, A Systematized Collection of ODE Solvers," in Scientific Computing (R. S. Stepleman, editor), Vol. 1. p. 55, IMACS Transactions on Scientific Computation, North-Holland, Amsterdam (1983).

Hobbs, M. L., Modeling Countercurrent Fixed-Bed Coal Gasification, PhD Dissertation, Brigham Young University, Provo, Utah (1990).

Hobbs, M. L., Radulovic, P. T., and Smoot, L. D., "Modeling Fixed-Bed Coal Gasifiers," AIChE J., 38, 681 (1992a).

Hobbs, M. L., Radulovic, P. T., and Smoot, L. D., "Predictions of effluent compositions for fixed-bed coal gasifiers," Fuel, 71, 1177 (1992b).

Johnson, J. L., "Fundamentals of Coal Gasification," in Chemistry of Coal Utilization, Second Supplementary Volume, M. A. Elliott, ed., John Wiley, New York (1981).

Kee, R. J., Rupley, F. M., and Miller, J. A., The Chemkin Thermodynamic Data Base, Report No. SAND87-8215B, Sandia National Laboratories, Livermore, CA, (1987).

Khan, M. R., "A Literature Survey and an Experimental Study of Coal Devolatilization at Mild and Severe Conditions: Influences of Heating Rate, Temperature, and Reactor Type on Products Yield and Composition," Fuel, 68, 1522 (1989).

Khanna, R. and Seinfeld, J. H., "Mathematical Modeling of Packed Bed Reactors: Numerical Solutions and Control Model Development," in Advances in Chemical Engineering edited by Wei, J., Anderson, J. L., Bischoff, K. B., Denn, M. M. and Seinfeld, J. H., 13, Academic Press, Inc., 113 (1987).

Kobayashi, H., Howard, J. B. and Sarofim, A. F., "Coal Devolatilization at High Temperatures," 16th Symposium (International) on Combustion, The Combustion Institute, Pittsburgh, Pennsylvania, 411 (1977).

Ko, G. H., Sanchez, D. M., Peters, W. A. and Howard, J. B., "Correlations for Effects of Coal Type and Pressure on Tar Yields from Rapid Devolatilization," 22nd Symposium (International) on Combustion , The Combustion Institute, Pittsburgh, Pennsylvania, 115 (1988).

Kunii, D. and Smith, J.M., "Heat Transfer Characteristics of Porous Rocks," AIChE J., 6, 71 (1960).

Kurylko, L., "The Unsteady and Steady Combustion of Carbon," PhD Dissertation, The Pennsylvania State University, University Park, Pennsylvania (1969).

Laidler, K. J. and Meiser, J. H., Physical Chemistry, The Benjamin/Cummings Publishing Compnay, Inc., Menlo Park, California (1982).

Laurendeau, N. M., "Heterogeneous Kinetics of Coal Char Gasification and Combustion," Prog. Energy Combust. Sci., 4, 221 (1978).

Lowry, H. H., Chemistry of Coal Utilization, Supplementary Volume, John Wiley & Sons, Inc., New York (1963).

Mayers, A. M., "The Rate of Reduction of Carbon Dioxide by Graphite," J. Am. Chem. Soc., 56, 70 (1934).

Merrick, D., "Mathematical Models of the Thermal Decomposition of Coal. 2. Specific Heats and Heats of Reaction," Fuel, 62, 540 (1983).

MeFayed, editor, Handbook of Powder Science and Technology, Van Nostrand Reinhold Company, New York (1984).

Mills, K. C. and Rhine, J. M., "The Measurement and Estimation of the Physical Properties of Slags Formed During Coal Gasification: 2. Properties relevant to heat transfer," Fuel, 68, 201 (1989).

Nsakala, N., Patel, R. L., Lao, T. C., "Combustion Characteristics of Coals for Industrial Applications," Final Technical Report for U. S. Department of Energy, Pittsburgh, Combustion Engineering Inc., Kreisinger Development Laboratory, Windsor, CT, DOE/PC/402067-5 (DE85010673) (1985).

Nuttall, H. E., Stoddart, W. G. and Chen, W. J., "Pyrolysis of Subituminous New Mexico Coal," Journal of Petroleum Technology, 418 (1979).

Park, K. Y. and Edgar, T. F., "Modeling of Early Cavity Growth for Underground Coal Gasification," Ind. Eng. Chem. Res., 26, 237 (1987).

Perry, R. H. and Chilton, C. H., eds., Chemical Engineers' Handbook, Fifth Edition, McGraw-Hill Book Company, New York (1973).

Pratt, D. T., "Multicomponent Equilibrium," in Pulverized-Coal Combustion and Gasification, eds. Smoot, L. D. and Pratt, D. T., Plenum Press, New York (1979).

Reid, R. C. and Sherwood, T. K., The Properties of Gases and Liquids, McGraw-Hill Book Company, New York (1966).

Rohsenow, W. M., Hartnett, J. P. and Ganic, E. N., Handbook of Heat Transfer Applications, McGraw-Hill, New York (1985).

Saxena, S. C., "Devolatilization and Combustion Characteristics of Coal Particles," Prog. Energy Combust. Sci., 16, 55 (1990).

Serio, M. A., Advanced Fuel Research, Inc., New Haven, Connecticut, personal communication, telefax (1989).

Serio, M. A., Hamblen, D. G., Markham, J. R. and Solomon, P. R., "Kinetics of Volatile Product Evolution in Coal Pyrolysis: Experiment and Theory," Energy & Fuels, 1, 138 (1987).

Smoot, L. D. and Smith, P. J., Pulverized-coal Combustion and Gasification (L. D. Smoot and D. T. Pratt, editors), Plenum Press, New York, 224 (1979).

Solomon, P. R., and Colket, M. B., "Coal Devolatilization," 17th Symposium (International) on Combustion, The Combustion Institute, Pittsburgh, Pennsylvania, 131 (1979).

Solomon, P. R. and Hamblen, D. G., "Pyrolysis," in Chemistry of Coal Conversion, ed. Schlosberg, R. H., Plenum Press, New York (1985).

Solomon, P. R., Hamblen, D. G., Carangelo, R. M., Serio, M. A. and Deshpande, G. Y., "General Model of Coal Devolatilization," Energy and Fuels, 2, 405 (1988).

Solomon, P. R., Hamblen, D. G., Zhen-Zhong Yu, and Serio, M. A., "Network models of coal thermal decomposition," Fuel, 69, 754 (1990).

Stull, D. R. and Prophet, H., JANAF Thermochemical Tables, Second Edition, National Bureau of Standards (1971).

Suuberg, E. M., Peters, W. A. and Howard, J. B., "Product Compositions and Formation Kinetics in Rapid Pyrolysis of Pulverized Coal--Implications for Combustion," 17th Symposium (International) on Combustion, The Combustion Institute, Pittsburgh, Pennsylvania, 177 (1979).

Thimsen, D., Maurer, R. E., Pooler, A. R., Pui, D. Y. H., Liu, B. Y. H. and Kittelson, D. B., "Fixed-Bed Gasification Research using U.S. Coals," 1-19, U.S. Bureau of Mines Contract H0222001 Final Report, (1984-1985).

Thorsness, C. B. and Kang, S. W., "Further Development of a General-Purpose, Packed-Bed Model for Analysis of Underground Coal Gasification Processes," Eleventh Annual Underground Coal Gasification Symposium, Denver, Colorado (1985).

Thorsness, C. B. and Kang, S. W., "A Method-of-line Approach to Solution of Packed-bed Flow Problems Related to Underground Coal Gasification

Processes," Tenth Annual Underground Coal Gasification Symposium, Williamsburg, Virginia (1984).

Walker, P. L., Rusinko, F., and Austin, L. G., Advances in Catalysis (D. D. Eley, P. W. Selwood and P. B. Weisz, Editors), XI, Academic Press Inc., New York, 134 (1959).

Wang, S. C. and Wen, C. Y., "Experimental Evaluation of Nonisothermal Solid-Gas Reaction Model," AIChE J., 18, 1231 (1972)

Yagi, S. and Kunii, D., "Studies on Heat Transfer Near Wall Surface in Packed Beds," AIChE J., 6, 97 (1960).

Yagi, S., Kunii, D. and Wakao, N., "Studies on Axial Effective Thermal Conductivities in Packed Beds," AIChE J., 6, 543 (1960).

Yagi, S. and Wakao, N., "Heat and Mass Transfer from Wall to Fluid in Packed Beds," AIChE J., 5, 79 (1959).

Yoon, H., Modeling and Analysis of Moving Bed Coal Gasifiers, PhD Dissertation, University of Delaware, Newark, Delaware (1978).

Yoon, H., Wei, J. and Denn, M. M., "A Model for Moving-bed Coal Gasification Reactors," AIChE J., 24, 885 (1978).

Young, L. L. and Finlayson, B. A., "Mathematical Methods of Monolith Catalytic Converter, Part I. Development of Model and Application of Orthogonal Collocation," AIChE J., 22, 331 (1976).

Yu, W., Dynamic Simulation of Moving Bed Coal Gasifiers, PhD Dissertation, University of Delaware, Newark, Delaware (1981).

APPENDIX A

Adjustment of Functional Group Composition

When the functional group composition data are not available for a given coal, its functional group composition must be estimated from the available data for the standard coals. The ultimate composition of the given coal and the standard coal may be close but not identical. In order to close the elemental mass balance, the initial functional group composition and the ultimate composition of a coal must match. Serio (1989; See Hobbs, 1990) recommended the following procedure to adjust the functional group composition of a standard coal to match the ultimate analysis of a given coal.

1. The elemental analysis and the functional group pools cannot be changed independently.

2. The compositions of aliphatic carbon and hydrogen are calculated by the amount of leftover carbon and hydrogen respectively.

3. The total amount of CH_4 and the fractions of CH_4-t and CH_4-xl are directly specified. The fraction of CH_4-l is determined by difference.

4. The total amount of CO_2 and the fractions of CO_2-t and CO_2-xl are directly specified. The fraction of CO_2-l is determined by difference.

5. The total amount of H_2O and the fraction of H_2O-t are directly specified. The fraction of H_2O-l is determined by difference.

6. The amounts of CO-l and CO-xt are specified. The amount of CO-t is determined from the amount of unspecified leftover oxygen. This implies that a higher oxygen content coal will have a higher amount of CO-t functional group.

7. The amounts of C_2H_4, C_2H_6, C_3H_6, C_3H_8, paraffins (C_4H_{10}) and olefins (C_4H_8) are directly specified.

8. The amounts of aromatic hydrogen and aromatic carbon are also directly specified.

9. The evolution of nitrogen occurs through NH_3 and HCN. The amounts of NH_3 and HCN-t are directly specified. The amount of HCN-l is determined by the difference.

10. The amount of organic sulfur functional group must be identical to the ultimate sulfur (dry, ash-free basis), since only one sulfur containing functional group is considered in the current formulation.

11. The order for the adjustment of nitrogen containing functional groups is HCN-l, HCN-t and finally NH_3.

12. The adjustment of oxygen containing functional groups is accomplished as follows. The CO-t functional group is adjusted initially, since this group is used for specifying leftover oxygen. If this group is not sufficient to adjust the oxygen content, the CO-t group will be set to zero, and other oxygen containing functional groups must be adjusted to match the reported ultimate oxygen content. The H_2O-l and H_2O-t functional groups are adjusted if the CO groups are insufficient to match the ultimate analysis. The water functional groups are chosen for adjustment rather than CO_2 groups, because CO_2 may be important in the crosslinking submodel. If further adjustment is required, CO-t, CO_2-l, CO_2-xl and CO_2-t functional groups are adjusted sequentially.

Following the above guidelines, the functional group composition for any given coal can be determined from the available data for the standard coals. These

data for eight standard coals are also included in this Appendix. This procedure is implemented through the subroutine ADJSTY0 in the fixed-bed code.

Table A.1: FG-DVC input data for Argonne Premium coal #1 (Zap Lignite, Beulah, N.D.)

```
27                                                                  <--- nfg (Number of Functional Groups)
0.74400D-02 0.29240D+02 0.17460D+05 0.15000D+04 0.20480D+03         <--- y0, a, b, sigmaa, and xeff for fg #  1 = CO2XL
0.33480D-01 0.29240D+02 0.22795D+05 0.20000D+04 0.20480D+03         <--- y0, a, b, sigmaa, and xeff for fg #  2 = CO2L
0.21080D-01 0.29646D+02 0.30070D+05 0.30000D+04 0.20480D+03         <--- y0, a, b, sigmaa, and xeff for fg #  3 = CO2T
0.44691D-01 0.29240D+02 0.22310D+05 0.27000D+04 0.00000D+00         <--- y0, a, b, sigmaa, and xeff for fg #  4 = H2OL
0.70229D-01 0.32929D+02 0.30070D+05 0.35000D+04 0.00000D+00         <--- y0, a, b, sigmaa, and xeff for fg #  5 = H2OT
0.18000D-01 0.29240D+02 0.23765D+05 0.30000D+04 0.00000D+00         <--- y0, a, b, sigmaa, and xeff for fg #  6 = COL
0.37139D-01 0.29240D+02 0.29100D+05 0.30000D+04 0.00000D+00         <--- y0, a, b, sigmaa, and xeff for fg #  7 = COT
0.38767D-02 0.31369D+02 0.29100D+05 0.15000D+04 0.00000D+00         <--- y0, a, b, sigmaa, and xeff for fg #  8 = HCNL
0.96296D-02 0.30482D+02 0.41225D+05 0.47500D+04 0.00000D+00         <--- y0, a, b, sigmaa, and xeff for fg #  9 = HCNT
0.00000D+00 0.28730D+02 0.26481D+05 0.30000D+04 0.00000D+00         <--- y0, a, b, sigmaa, and xeff for fg # 10 = NH3
0.17439D+00 0.00000D+00 0.00000D+00 0.00000D+00 0.00000D+00         <--- y0, a, b, sigmaa, and xeff for fg # 11 = CAL
0.00000D+00 0.00000D+00 0.00000D+00 0.00000D+00 0.00000D+00         <--- y0, a, b, sigmaa, and xeff for fg # 12 = CH4XL
0.10400D-01 0.31032D+02 0.27160D+05 0.25000D+04 0.10240D+03         <--- y0, a, b, sigmaa, and xeff for fg # 13 = CH4L
0.56000D-02 0.31725D+02 0.31040D+05 0.22000D+04 0.10240D+03         <--- y0, a, b, sigmaa, and xeff for fg # 14 = CH4T
0.16373D-01 0.33152D+02 0.39285D+05 0.60000D+04 0.00000D+00         <--- y0, a, b, sigmaa, and xeff for fg # 15 = HAROM
0.12769D-01 0.29240D+02 0.16005D+05 0.15000D+04 0.00000D+00         <--- y0, a, b, sigmaa, and xeff for fg # 16 = CH3OH
0.52500D-01 0.32929D+02 0.37830D+05 0.25000D+04 0.00000D+00         <--- y0, a, b, sigmaa, and xeff for fg # 17 = COXT
0.44000D+00 0.00000D+00 0.00000D+00 0.00000D+00 0.00000D+00         <--- y0, a, b, sigmaa, and xeff for fg # 18 = CNV
0.00000D+00 0.00000D+00 0.00000D+00 0.00000D+00 0.00000D+00         <--- y0, a, b, sigmaa, and xeff for fg # 19 = SORG
0.63999D-02 0.00000D+00 0.00000D+00 0.00000D+00 0.00000D+00         <--- y0, a, b, sigmaa, and xeff for fg # 20 = HAL
0.30000D-02 0.29240D+02 0.24250D+05 0.15000D+04 0.00000D+00         <--- y0, a, b, sigmaa, and xeff for fg # 21 = C2H4
0.00000D+00 0.29240D+02 0.24250D+05 0.15000D+04 0.00000D+00         <--- y0, a, b, sigmaa, and xeff for fg # 22 = C3H6
0.00000D+00 0.29240D+02 0.24250D+05 0.10000D+04 0.00000D+00         <--- y0, a, b, sigmaa, and xeff for fg # 23 = C4H8
0.30000D-02 0.29240D+02 0.24250D+05 0.25000D+04 0.00000D+00         <--- y0, a, b, sigmaa, and xeff for fg # 24 = C2H6
0.00000D+00 0.29240D+02 0.24250D+05 0.15000D+04 0.00000D+00         <--- y0, a, b, sigmaa, and xeff for fg # 25 = C3H8
0.30000D-01 0.29240D+02 0.24250D+05 0.10000D+04 0.00000D+00         <--- y0, a, b, sigmaa, and xeff for fg # 26 = C4H10
0.00000D+00 0.00000D+00 0.00000D+00 0.00000D+00 0.00000D+00         <--- y0, a, b, sigmaa, and xeff for fg # 27 = C2H2
            0.32236D+02 0.25220D+05 0.10000D+04                                 <--- a,b, and sigmaa for bond kinetics
6 0.5853D+00 0.9353D+00 0.6000D-01 0.1000D+01 0.4000D+01                  <--- jmax,psoft,ptotal,qtotal,sigma1,sigma2
0.130D+00 0.000D+00 0.000D+00 0.000D+00 0.000D+00 0.000D+00 0.000D+00 0.000D+00 0.000D+00 0.000D+00      <--- pdist( 1,1:10)
0.290D+00 0.170D-01 0.000D+00 0.000D+00 0.000D+00 0.000D+00 0.000D+00 0.000D+00 0.000D+00 0.000D+00      <--- pdist( 2,1:10)
0.310D+00 0.950D-01 0.200D-02 0.000D+00 0.000D+00 0.000D+00 0.000D+00 0.000D+00 0.000D+00 0.000D+00      <--- pdist( 3,1:10)
0.270D+00 0.190D+00 0.220D-01 0.000D+00 0.000D+00 0.000D+00 0.000D+00 0.000D+00 0.000D+00 0.000D+00      <--- pdist( 4,1:10)
0.000D+00 0.270D+00 0.700D-01 0.500D-02 0.000D+00 0.000D+00 0.000D+00 0.000D+00 0.000D+00 0.000D+00      <--- pdist( 5,1:10)
0.000D+00 0.233D+00 0.143D+00 0.200D-01 0.100D-02 0.000D+00 0.000D+00 0.000D+00 0.000D+00 0.000D+00      <--- pdist( 6,1:10)
0.000D+00 0.142D+00 0.207D+00 0.550D-01 0.500D-02 0.000D+00 0.000D+00 0.000D+00 0.000D+00 0.000D+00      <--- pdist( 7,1:10)
0.000D+00 0.530D-01 0.221D+00 0.109D+00 0.180D-01 0.100D-02 0.000D+00 0.000D+00 0.000D+00 0.000D+00      <--- pdist( 8,1:10)
0.000D+00 0.000D+00 0.180D+00 0.164D+00 0.450D-01 0.500D-02 0.000D+00 0.000D+00 0.000D+00 0.000D+00      <--- pdist( 9,1:10)
0.000D+00 0.000D+00 0.104D+00 0.195D+00 0.860D-01 0.150D-01 0.000D+00 0.000D+00 0.000D+00 0.000D+00      <--- pdist(10,1:10)
0.000D+00 0.000D+00 0.430D-01 0.184D+00 0.133D+00 0.360D-01 0.000D+00 0.000D+00 0.000D+00 0.000D+00      <--- pdist(11,1:10)
0.000D+00 0.000D+00 0.900D-02 0.138D+00 0.168D+00 0.690D-01 0.000D+00 0.000D+00 0.000D+00 0.000D+00      <--- pdist(12,1:10)
0.000D+00 0.000D+00 0.000D+00 0.128D+00 0.545D+00 0.874D+00 0.000D+00 0.000D+00 0.000D+00 0.000D+00      <--- pdist(13,1:10)
0.10D+02                                                                            <--- particle internal pressure drop
0.7300D+00  0.4800D-01  0.2150D+00  0.7000D-02  0.0000D+00                             <--- ultimate composition (daf)
File generated: Tue Apr 14 18:26:41 1992                                                            coal0.arg1
```

Table A.2: FG-DVC input data for Argonne Premium coal #2 (Wyodak-Anderson, Wyoming)

```
27                                                                                 <--- nfg (Number of Functional Groups)
0.54000D-02 0.29240D+02 0.17460D+05 0.15000D+04 0.20480D+03                        <--- y0, a, b, sigmaa, and xeff for fg #  1 = CO2XL
0.32940D-01 0.29240D+02 0.23280D+05 0.25000D+04 0.20480D+03                        <--- y0, a, b, sigmaa, and xeff for fg #  2 = CO2L
0.15660D-01 0.29646D+02 0.31040D+05 0.28000D+04 0.20480D+03                        <--- y0, a, b, sigmaa, and xeff for fg #  3 = CO2T
0.40248D-01 0.29240D+02 0.23522D+05 0.25000D+04 0.00000D+00                        <--- y0, a, b, sigmaa, and xeff for fg #  4 = H2OL
0.43992D-01 0.32929D+02 0.30070D+05 0.35000D+04 0.00000D+00                        <--- y0, a, b, sigmaa, and xeff for fg #  5 = H2OT
0.17000D-01 0.29240D+02 0.24008D+05 0.25000D+04 0.00000D+00                        <--- y0, a, b, sigmaa, and xeff for fg #  6 = COL
0.41982D-01 0.29240D+02 0.29342D+05 0.30000D+04 0.00000D+00                        <--- y0, a, b, sigmaa, and xeff for fg #  7 = COT
0.13410D-02 0.31369D+02 0.29100D+05 0.15000D+04 0.00000D+00                        <--- y0, a, b, sigmaa, and xeff for fg #  8 = HCNL
0.18296D-01 0.30482D+02 0.41225D+05 0.47500D+04 0.00000D+00                        <--- y0, a, b, sigmaa, and xeff for fg #  9 = HCNT
0.10000D-02 0.28730D+02 0.26481D+05 0.30000D+04 0.00000D+00                        <--- y0, a, b, sigmaa, and xeff for fg # 10 = NH3
0.88836D-01 0.00000D+00 0.00000D+00 0.00000D+00 0.00000D+00                        <--- y0, a, b, sigmaa, and xeff for fg # 11 = CAL
0.00000D+00 0.00000D+00 0.00000D+00 0.00000D+00 0.00000D+00                        <--- y0, a, b, sigmaa, and xeff for fg # 12 = CH4XL
0.12600D-01 0.31032D+02 0.27160D+05 0.22500D+04 0.10240D+03                        <--- y0, a, b, sigmaa, and xeff for fg # 13 = CH4L
0.84000D-02 0.31725D+02 0.31040D+05 0.20000D+04 0.10240D+03                        <--- y0, a, b, sigmaa, and xeff for fg # 14 = CH4T
0.11943D-01 0.33152D+02 0.39285D+05 0.60000D+04 0.00000D+00                        <--- y0, a, b, sigmaa, and xeff for fg # 15 = HAROM
0.93600D-02 0.29240D+02 0.16490D+05 0.15000D+04 0.00000D+00                        <--- y0, a, b, sigmaa, and xeff for fg # 16 = CH3OH
0.50000D-01 0.32929D+02 0.38558D+05 0.25000D+04 0.00000D+00                        <--- y0, a, b, sigmaa, and xeff for fg # 17 = COXT
0.52000D+00 0.00000D+00 0.00000D+00 0.00000D+00 0.00000D+00                        <--- y0, a, b, sigmaa, and xeff for fg # 18 = CNV
0.40000D-02 0.00000D+00 0.00000D+00 0.00000D+00 0.00000D+00                        <--- y0, a, b, sigmaa, and xeff for fg # 19 = SORG
0.15502D-01 0.00000D+00 0.00000D+00 0.00000D+00 0.00000D+00                        <--- y0, a, b, sigmaa, and xeff for fg # 20 = HAL
0.45000D-02 0.29240D+02 0.24250D+05 0.15000D+04 0.00000D+00                        <--- y0, a, b, sigmaa, and xeff for fg # 21 = C2H4
0.00000D+00 0.29240D+02 0.24250D+05 0.15000D+04 0.00000D+00                        <--- y0, a, b, sigmaa, and xeff for fg # 22 = C3H6
0.27700D-01 0.29240D+02 0.24250D+05 0.75000D+03 0.00000D+00                        <--- y0, a, b, sigmaa, and xeff for fg # 23 = C4H8
0.20000D-02 0.29240D+02 0.24250D+05 0.15000D+04 0.00000D+00                        <--- y0, a, b, sigmaa, and xeff for fg # 24 = C2H6
0.00000D+00 0.29240D+02 0.24250D+05 0.15000D+04 0.00000D+00                        <--- y0, a, b, sigmaa, and xeff for fg # 25 = C3H8
0.27300D-01 0.29240D+02 0.24250D+05 0.75000D+03 0.00000D+00                        <--- y0, a, b, sigmaa, and xeff for fg # 26 = C4H10
0.00000D+00 0.00000D+00 0.00000D+00 0.00000D+00 0.00000D+00                        <--- y0, a, b, sigmaa, and xeff for fg # 27 = C2H2
            0.32236D+02 0.25220D+05 0.10000D+04                                                   <--- a,b, and sigmaa for bond kinetics
6 0.7158D+00 0.9158D+00 0.4500D-01 0.1000D+01 0.4000D+01                                      <--- jmax,psoft,ptotal,qtotal,sigma1,sigma2
0.130D+00 0.000D+00 0.000D+00 0.000D+00 0.000D+00 0.000D+00 0.000D+00 0.000D+00 0.000D+00 0.000D+00        <--- pdist( 1,1:10)
0.290D+00 0.170D-01 0.000D+00 0.000D+00 0.000D+00 0.000D+00 0.000D+00 0.000D+00 0.000D+00 0.000D+00        <--- pdist( 2,1:10)
0.310D+00 0.950D-01 0.200D-02 0.000D+00 0.000D+00 0.000D+00 0.000D+00 0.000D+00 0.000D+00 0.000D+00        <--- pdist( 3,1:10)
0.270D+00 0.190D+00 0.220D-01 0.000D+00 0.000D+00 0.000D+00 0.000D+00 0.000D+00 0.000D+00 0.000D+00        <--- pdist( 4,1:10)
0.000D+00 0.270D+00 0.700D-01 0.500D-02 0.000D+00 0.000D+00 0.000D+00 0.000D+00 0.000D+00 0.000D+00        <--- pdist( 5,1:10)
0.000D+00 0.233D+00 0.143D+00 0.200D-01 0.100D-02 0.000D+00 0.000D+00 0.000D+00 0.000D+00 0.000D+00        <--- pdist( 6,1:10)
0.000D+00 0.142D+00 0.207D+00 0.550D-01 0.500D-02 0.000D+00 0.000D+00 0.000D+00 0.000D+00 0.000D+00        <--- pdist( 7,1:10)
0.000D+00 0.530D-01 0.221D+00 0.109D+00 0.180D-01 0.100D-02 0.000D+00 0.000D+00 0.000D+00 0.000D+00        <--- pdist( 8,1:10)
0.000D+00 0.000D+00 0.180D+00 0.164D+00 0.450D-01 0.500D-02 0.000D+00 0.000D+00 0.000D+00 0.000D+00        <--- pdist( 9,1:10)
0.000D+00 0.000D+00 0.104D+00 0.195D+00 0.860D-01 0.150D-01 0.000D+00 0.000D+00 0.000D+00 0.000D+00        <--- pdist(10,1:10)
0.000D+00 0.000D+00 0.430D-01 0.184D+00 0.133D+00 0.360D-01 0.000D+00 0.000D+00 0.000D+00 0.000D+00        <--- pdist(11,1:10)
0.000D+00 0.000D+00 0.900D-02 0.138D+00 0.168D+00 0.690D-01 0.000D+00 0.000D+00 0.000D+00 0.000D+00        <--- pdist(12,1:10)
0.000D+00 0.000D+00 0.000D+00 0.128D+00 0.545D+00 0.874D+00 0.000D+00 0.000D+00 0.000D+00 0.000D+00        <--- pdist(13,1:10)
0.10D+02                                                                                        <--- particle internal pressure drop
0.7500D+00  0.5400D-01  0.1810D+00  0.1100D-01  0.4000D-02                                        <--- ultimate composition (daf)
File generated: Tue Apr 14 18:27:48 1992                                                                      coal0.arg2
```

Table A.3: FG-DVC input data for Argonne Premium coal #3 (Illinois #6)

```
27                                                                                                  <--- nfg (Number of Functional Groups)
0.12000D-02 0.29240D+02 0.19885D+05 0.30000D+04 0.20480D+03                                         <--- y0, a, b, sigmaa, and xeff for fg #  1 = CO2XL
0.35000D-02 0.29240D+02 0.24008D+05 0.17500D+04 0.20480D+03                                         <--- y0, a, b, sigmaa, and xeff for fg #  2 = CO2L
0.53000D-02 0.29646D+02 0.31040D+05 0.27500D+04 0.20480D+03                                         <--- y0, a, b, sigmaa, and xeff for fg #  3 = CO2T
0.36025D-01 0.29240D+02 0.24250D+05 0.15000D+04 0.00000D+00                                         <--- y0, a, b, sigmaa, and xeff for fg #  4 = H2OL
0.67547D-01 0.32929D+02 0.31040D+05 0.28000D+04 0.00000D+00                                         <--- y0, a, b, sigmaa, and xeff for fg #  5 = H2OT
0.30000D-02 0.29240D+02 0.24250D+05 0.10000D+04 0.00000D+00                                         <--- y0, a, b, sigmaa, and xeff for fg #  6 = COL
0.23209D-01 0.29240D+02 0.29585D+05 0.20000D+04 0.00000D+00                                         <--- y0, a, b, sigmaa, and xeff for fg #  7 = COT
0.29386D-02 0.31369D+02 0.29100D+05 0.15000D+04 0.00000D+00                                         <--- y0, a, b, sigmaa, and xeff for fg #  8 = HCNL
0.24074D-01 0.30482D+02 0.41225D+05 0.47500D+04 0.00000D+00                                         <--- y0, a, b, sigmaa, and xeff for fg #  9 = HCNT
0.00000D+00 0.28730D+02 0.26481D+05 0.30000D+04 0.00000D+00                                         <--- y0, a, b, sigmaa, and xeff for fg # 10 = NH3
0.10507D+00 0.00000D+00 0.00000D+00 0.00000D+00 0.00000D+00                                         <--- y0, a, b, sigmaa, and xeff for fg # 11 = CAL
0.00000D+00 0.00000D+00 0.00000D+00 0.00000D+04 0.00000D+00                                         <--- y0, a, b, sigmaa, and xeff for fg # 12 = CH4XL
0.16340D-01 0.31032D+02 0.27160D+05 0.18000D+04 0.10240D+03                                         <--- y0, a, b, sigmaa, and xeff for fg # 13 = CH4L
0.21660D-01 0.31725D+02 0.31040D+05 0.22000D+04 0.10240D+03                                         <--- y0, a, b, sigmaa, and xeff for fg # 14 = CH4T
0.15433D-01 0.33152D+02 0.39285D+05 0.60000D+04 0.00000D+00                                         <--- y0, a, b, sigmaa, and xeff for fg # 15 = HAROM
0.90063D-02 0.29240D+02 0.17460D+05 0.18000D+04 0.00000D+00                                         <--- y0, a, b, sigmaa, and xeff for fg # 16 = CH3OH
0.32000D-01 0.32929D+02 0.38800D+05 0.30000D+04 0.00000D+00                                         <--- y0, a, b, sigmaa, and xeff for fg # 17 = COXT
0.55000D+00 0.00000D+00 0.00000D+00 0.00000D+00 0.00000D+00                                         <--- y0, a, b, sigmaa, and xeff for fg # 18 = CNV
0.22000D-01 0.00000D+00 0.00000D+00 0.00000D+00 0.00000D+00                                         <--- y0, a, b, sigmaa, and xeff for fg # 19 = SORG
0.16929D-02 0.00000D+00 0.00000D+00 0.00000D+00 0.00000D+00                                         <--- y0, a, b, sigmaa, and xeff for fg # 20 = HAL
0.40000D-02 0.29240D+02 0.24250D+05 0.15000D+04 0.00000D+00                                         <--- y0, a, b, sigmaa, and xeff for fg # 21 = C2H4
0.00000D+00 0.29240D+02 0.24250D+05 0.15000D+04 0.00000D+00                                         <--- y0, a, b, sigmaa, and xeff for fg # 22 = C3H6
0.27000D-01 0.29240D+02 0.24250D+05 0.15000D+04 0.00000D+00                                         <--- y0, a, b, sigmaa, and xeff for fg # 23 = C4H8
0.40000D-02 0.29240D+02 0.24250D+05 0.15000D+04 0.00000D+00                                         <--- y0, a, b, sigmaa, and xeff for fg # 24 = C2H6
0.00000D+00 0.29240D+02 0.24250D+05 0.15000D+04 0.00000D+00                                         <--- y0, a, b, sigmaa, and xeff for fg # 25 = C3H8
0.25000D-01 0.29240D+02 0.24250D+05 0.15000D+04 0.00000D+00                                         <--- y0, a, b, sigmaa, and xeff for fg # 26 = C4H10
0.00000D+00 0.00000D+00 0.00000D+00 0.00000D+00 0.00000D+00                                         <--- y0, a, b, sigmaa, and xeff for fg # 27 = C2H2
            0.32236D+02 0.25220D+05 0.75000D+03                                                                 <--- a,b, and sigmaa for bond kinetics
6 0.5968D+00 0.6568D+00 0.1000D+00 0.1000D+01 0.4000D+01                                                      <--- jmax,psoft,ptotal,qtotal,sigma1,sigma2
0.130D+00 0.000D+00 0.000D+00 0.000D+00 0.000D+00 0.000D+00 0.000D+00 0.000D+00 0.000D+00 0.000D+00 0.000D+00 <--- pdist( 1,1:10)
0.290D+00 0.170D-01 0.000D+00 0.000D+00 0.000D+00 0.000D+00 0.000D+00 0.000D+00 0.000D+00 0.000D+00 0.000D+00 <--- pdist( 2,1:10)
0.310D+00 0.950D-01 0.200D-02 0.000D+00 0.000D+00 0.000D+00 0.000D+00 0.000D+00 0.000D+00 0.000D+00 0.000D+00 <--- pdist( 3,1:10)
0.270D+00 0.190D+00 0.220D-01 0.000D+00 0.000D+00 0.000D+00 0.000D+00 0.000D+00 0.000D+00 0.000D+00 0.000D+00 <--- pdist( 4,1:10)
0.000D+00 0.270D+00 0.700D-01 0.500D-02 0.000D+00 0.000D+00 0.000D+00 0.000D+00 0.000D+00 0.000D+00 0.000D+00 <--- pdist( 5,1:10)
0.000D+00 0.233D+00 0.143D+00 0.200D-01 0.100D-02 0.000D+00 0.000D+00 0.000D+00 0.000D+00 0.000D+00 0.000D+00 <--- pdist( 6,1:10)
0.000D+00 0.142D+00 0.207D+00 0.550D-01 0.500D-02 0.000D+00 0.000D+00 0.000D+00 0.000D+00 0.000D+00 0.000D+00 <--- pdist( 7,1:10)
0.000D+00 0.530D-01 0.221D+00 0.109D+00 0.180D-01 0.100D-02 0.000D+00 0.000D+00 0.000D+00 0.000D+00 0.000D+00 <--- pdist( 8,1:10)
0.000D+00 0.000D+00 0.180D+00 0.164D+00 0.450D-01 0.500D-02 0.000D+00 0.000D+00 0.000D+00 0.000D+00 0.000D+00 <--- pdist( 9,1:10)
0.000D+00 0.000D+00 0.104D+00 0.195D+00 0.860D-01 0.150D-01 0.000D+00 0.000D+00 0.000D+00 0.000D+00 0.000D+00 <--- pdist(10,1:10)
0.000D+00 0.000D+00 0.430D-01 0.184D+00 0.133D+00 0.360D-01 0.000D+00 0.000D+00 0.000D+00 0.000D+00 0.000D+00 <--- pdist(11,1:10)
0.000D+00 0.000D+00 0.900D-02 0.138D+00 0.168D+00 0.690D-01 0.000D+00 0.000D+00 0.000D+00 0.000D+00 0.000D+00 <--- pdist(12,1:10)
0.000D+00 0.000D+00 0.000D+00 0.128D+00 0.545D+00 0.874D+00 0.000D+00 0.000D+00 0.000D+00 0.000D+00 0.000D+00 <--- pdist(13,1:10)
0.20D+00                                                                                                      <--- particle internal pressure drop
0.7770D+00  0.5000D-01  0.1370D+00  0.1400D-01  0.2200D-01                                                 <--- ultimate composition (daf)
File generated: Tue Apr 14 18:28:06 1992                                                                            coal0.arg3
```

Table A.4: FG-DVC input data for Argonne Premium coal #4 (Utah Blind Canyon)

```
27                                                                             <--- nfg (Number of Functional Groups)
0.96000D-03 0.29240D+02 0.20370D+05 0.40000D+04 0.20480D+03                    <--- y0, a, b, sigmaa, and xeff for fg #  1 = CO2XL
0.28800D-02 0.29240D+02 0.24250D+05 0.12500D+04 0.20480D+03                    <--- y0, a, b, sigmaa, and xeff for fg #  2 = CO2L
0.12160D-01 0.29646D+02 0.31040D+05 0.50000D+04 0.20480D+03                    <--- y0, a, b, sigmaa, and xeff for fg #  3 = CO2T
0.31122D-01 0.29240D+02 0.24250D+05 0.12500D+04 0.00000D+00                    <--- y0, a, b, sigmaa, and xeff for fg #  4 = H2OL
0.50778D-01 0.32929D+02 0.31040D+05 0.25000D+04 0.00000D+00                    <--- y0, a, b, sigmaa, and xeff for fg #  5 = H2OT
0.40000D-02 0.29240D+02 0.24250D+05 0.12500D+04 0.00000D+00                    <--- y0, a, b, sigmaa, and xeff for fg #  6 = COL
0.23377D-01 0.29240D+02 0.29585D+05 0.20000D+04 0.00000D+00                    <--- y0, a, b, sigmaa, and xeff for fg #  7 = COT
0.67976D-02 0.31369D+02 0.29100D+05 0.15000D+04 0.00000D+00                    <--- y0, a, b, sigmaa, and xeff for fg #  8 = HCNL
0.24074D-01 0.30482D+02 0.41225D+05 0.47500D+04 0.00000D+00                    <--- y0, a, b, sigmaa, and xeff for fg #  9 = HCNT
0.00000D+00 0.28730D+02 0.26481D+05 0.30000D+04 0.00000D+00                    <--- y0, a, b, sigmaa, and xeff for fg # 10 = NH3
0.13001D+00 0.00000D+00 0.00000D+00 0.00000D+00 0.00000D+00                    <--- y0, a, b, sigmaa, and xeff for fg # 11 = CAL
0.00000D+00 0.00000D+00 0.00000D+00 0.00000D+00 0.00000D+00                    <--- y0, a, b, sigmaa, and xeff for fg # 12 = CH4XL
0.16380D-01 0.31032D+02 0.27160D+05 0.15000D+04 0.10240D+03                    <--- y0, a, b, sigmaa, and xeff for fg # 13 = CH4L
0.25620D-01 0.31725D+02 0.31040D+05 0.22000D+04 0.10240D+03                    <--- y0, a, b, sigmaa, and xeff for fg # 14 = CH4T
0.15572D-01 0.33152D+02 0.39285D+05 0.60000D+04 0.00000D+00                    <--- y0, a, b, sigmaa, and xeff for fg # 15 = HAROM
0.00000D+00 0.00000D+00 0.00000D+00 0.00000D+00 0.00000D+00                    <--- y0, a, b, sigmaa, and xeff for fg # 16 = CH3OH
0.28000D-01 0.32929D+02 0.38800D+05 0.25000D+04 0.00000D+00                    <--- y0, a, b, sigmaa, and xeff for fg # 17 = COXT
0.55000D+00 0.00000D+00 0.00000D+00 0.00000D+00 0.00000D+00                    <--- y0, a, b, sigmaa, and xeff for fg # 18 = CNV
0.30000D-02 0.00000D+00 0.00000D+00 0.00000D+00 0.00000D+00                    <--- y0, a, b, sigmaa, and xeff for fg # 19 = SORG
0.11273D-01 0.00000D+00 0.00000D+00 0.00000D+00 0.00000D+00                    <--- y0, a, b, sigmaa, and xeff for fg # 20 = HAL
0.60000D-02 0.29240D+02 0.24250D+05 0.15000D+04 0.00000D+00                    <--- y0, a, b, sigmaa, and xeff for fg # 21 = C2H4
0.00000D+00 0.29240D+02 0.24250D+05 0.15000D+04 0.00000D+00                    <--- y0, a, b, sigmaa, and xeff for fg # 22 = C3H6
0.27000D-01 0.29240D+02 0.24492D+05 0.12000D+04 0.00000D+00                    <--- y0, a, b, sigmaa, and xeff for fg # 23 = C4H8
0.60000D-02 0.29240D+02 0.24250D+05 0.15000D+04 0.00000D+00                    <--- y0, a, b, sigmaa, and xeff for fg # 24 = C2H6
0.00000D+00 0.29240D+02 0.24250D+05 0.15000D+04 0.00000D+00                    <--- y0, a, b, sigmaa, and xeff for fg # 25 = C3H8
0.25000D-01 0.29240D+02 0.24492D+05 0.12000D+04 0.00000D+00                    <--- y0, a, b, sigmaa, and xeff for fg # 26 = C4H10
0.00000D+00 0.00000D+00 0.00000D+00 0.00000D+00 0.00000D+00                    <--- y0, a, b, sigmaa, and xeff for fg # 27 = C2H2
            0.32236D+02 0.26190D+05 0.12500D+04                                             <--- a,b, and sigmaa for bond kinetics
6 0.5835D+00 0.7735D+00 0.6000D-01 0.1000D+01 0.4000D+01                                <--- jmax,psoft,ptotal,qtotal,sigma1,sigma2
0.130D+00 0.000D+00 0.000D+00 0.000D+00 0.000D+00 0.000D+00 0.000D+00 0.000D+00 0.000D+00 0.000D+00          <--- pdist( 1,1:10)
0.290D+00 0.170D-01 0.000D+00 0.000D+00 0.000D+00 0.000D+00 0.000D+00 0.000D+00 0.000D+00 0.000D+00          <--- pdist( 2,1:10)
0.310D+00 0.950D-01 0.200D-02 0.000D+00 0.000D+00 0.000D+00 0.000D+00 0.000D+00 0.000D+00 0.000D+00          <--- pdist( 3,1:10)
0.270D+00 0.190D+00 0.220D-01 0.000D+00 0.000D+00 0.000D+00 0.000D+00 0.000D+00 0.000D+00 0.000D+00          <--- pdist( 4,1:10)
0.000D+00 0.270D+00 0.700D-01 0.500D-02 0.000D+00 0.000D+00 0.000D+00 0.000D+00 0.000D+00 0.000D+00          <--- pdist( 5,1:10)
0.000D+00 0.233D+00 0.143D+00 0.200D-01 0.100D-02 0.000D+00 0.000D+00 0.000D+00 0.000D+00 0.000D+00          <--- pdist( 6,1:10)
0.000D+00 0.142D+00 0.207D+00 0.550D-01 0.500D-02 0.000D+00 0.000D+00 0.000D+00 0.000D+00 0.000D+00          <--- pdist( 7,1:10)
0.000D+00 0.530D-01 0.221D+00 0.109D+00 0.180D-01 0.100D-02 0.000D+00 0.000D+00 0.000D+00 0.000D+00          <--- pdist( 8,1:10)
0.000D+00 0.000D+00 0.180D+00 0.164D+00 0.450D-01 0.500D-02 0.000D+00 0.000D+00 0.000D+00 0.000D+00          <--- pdist( 9,1:10)
0.000D+00 0.000D+00 0.104D+00 0.195D+00 0.860D-01 0.150D-01 0.000D+00 0.000D+00 0.000D+00 0.000D+00          <--- pdist(10,1:10)
0.000D+00 0.000D+00 0.430D-01 0.184D+00 0.133D+00 0.360D-01 0.000D+00 0.000D+00 0.000D+00 0.000D+00          <--- pdist(11,1:10)
0.000D+00 0.000D+00 0.900D-02 0.138D+00 0.168D+00 0.690D-01 0.000D+00 0.000D+00 0.000D+00 0.000D+00          <--- pdist(12,1:10)
0.000D+00 0.000D+00 0.000D+00 0.128D+00 0.545D+00 0.874D+00 0.000D+00 0.000D+00 0.000D+00 0.000D+00          <--- pdist(13,1:10)
0.20D+00                                                                                      <--- particle internal pressure drop
0.8070D+00  0.5800D-01  0.1160D+00  0.1600D-01  0.3000D-02                                         <--- ultimate composition (daf)
File generated: Tue Apr 14 18:28:24 1992                                                                     coal0.arg4
```

Table A.5: FG-DVC input data for Argonne Premium coal #5 (Upkana-Stokton, WV)

```
27                                                                                                  <--- nfg (Number of Functional Groups)
0.80000D-03 0.29240D+02 0.20612D+05 0.35000D+04 0.20480D+03                                         <--- y0, a, b, sigmaa, and xeff for fg #  1 = CO2XL
0.19000D-02 0.29240D+02 0.25220D+05 0.30000D+04 0.20480D+03                                         <--- y0, a, b, sigmaa, and xeff for fg #  2 = CO2L
0.73000D-02 0.29646D+02 0.31040D+05 0.32000D+04 0.20480D+03                                         <--- y0, a, b, sigmaa, and xeff for fg #  3 = CO2T
0.26264D-01 0.29240D+02 0.24735D+05 0.12500D+04 0.00000D+00                                         <--- y0, a, b, sigmaa, and xeff for fg #  4 = H2OL
0.48775D-01 0.32929D+02 0.31040D+05 0.25000D+04 0.00000D+00                                         <--- y0, a, b, sigmaa, and xeff for fg #  5 = H2OT
0.20000D-02 0.29240D+02 0.24735D+05 0.11000D+04 0.00000D+00                                         <--- y0, a, b, sigmaa, and xeff for fg #  6 = COL
0.13671D-01 0.29240D+02 0.29585D+05 0.16000D+04 0.00000D+00                                         <--- y0, a, b, sigmaa, and xeff for fg #  7 = COT
0.19827D-02 0.31369D+02 0.29100D+05 0.15000D+04 0.00000D+00                                         <--- y0, a, b, sigmaa, and xeff for fg #  8 = HCNL
0.28889D-01 0.30482D+02 0.41225D+05 0.47500D+04 0.00000D+00                                         <--- y0, a, b, sigmaa, and xeff for fg #  9 = HCNT
0.00000D+00 0.27813D+02 0.26481D+05 0.30000D+04 0.00000D+00                                         <--- y0, a, b, sigmaa, and xeff for fg # 10 = NH3
0.17701D+00 0.00000D+00 0.00000D+00 0.00000D+00 0.00000D+00                                         <--- y0, a, b, sigmaa, and xeff for fg # 11 = CAL
0.00000D+00 0.00000D+00 0.00000D+00 0.00000D+00 0.00000D+00                                         <--- y0, a, b, sigmaa, and xeff for fg # 12 = CH4XL
0.14850D-01 0.31032D+02 0.27160D+05 0.12000D+04 0.10240D+03                                         <--- y0, a, b, sigmaa, and xeff for fg # 13 = CH4L
0.30150D-01 0.31725D+02 0.31040D+05 0.22000D+04 0.10240D+03                                         <--- y0, a, b, sigmaa, and xeff for fg # 14 = CH4T
0.15648D-01 0.33152D+02 0.39285D+05 0.60000D+04 0.00000D+00                                         <--- y0, a, b, sigmaa, and xeff for fg # 15 = HAROM
0.00000D+00 0.00000D+00 0.00000D+00 0.00000D+00 0.00000D+00                                         <--- y0, a, b, sigmaa, and xeff for fg # 16 = CH3OH
0.30000D-01 0.32929D+02 0.38800D+05 0.30000D+04 0.00000D+00                                         <--- y0, a, b, sigmaa, and xeff for fg # 17 = COXT
0.55000D+00 0.00000D+00 0.00000D+00 0.00000D+00 0.00000D+00                                         <--- y0, a, b, sigmaa, and xeff for fg # 18 = CNV
0.50000D-02 0.00000D+00 0.00000D+00 0.00000D+00 0.00000D+00                                         <--- y0, a, b, sigmaa, and xeff for fg # 19 = SORG
0.10757D-01 0.00000D+00 0.00000D+00 0.00000D+00 0.00000D+00                                         <--- y0, a, b, sigmaa, and xeff for fg # 20 = HAL
0.30000D-02 0.29240D+02 0.24250D+05 0.15000D+04 0.00000D+00                                         <--- y0, a, b, sigmaa, and xeff for fg # 21 = C2H4
0.00000D+00 0.29240D+02 0.24250D+05 0.15000D+04 0.00000D+00                                         <--- y0, a, b, sigmaa, and xeff for fg # 22 = C3H6
0.10000D-01 0.29240D+02 0.24590D+05 0.10000D+04 0.00000D+00                                         <--- y0, a, b, sigmaa, and xeff for fg # 23 = C4H8
0.20000D-02 0.29240D+02 0.24250D+05 0.15000D+04 0.00000D+00                                         <--- y0, a, b, sigmaa, and xeff for fg # 24 = C2H6
0.00000D+00 0.29240D+02 0.24250D+05 0.15000D+04 0.00000D+00                                         <--- y0, a, b, sigmaa, and xeff for fg # 25 = C3H8
0.20000D-01 0.29240D+02 0.24590D+05 0.10000D+04 0.00000D+00                                         <--- y0, a, b, sigmaa, and xeff for fg # 26 = C4H10
0.00000D+00 0.00000D+00 0.00000D+00 0.00000D+00 0.00000D+00                                         <--- y0, a, b, sigmaa, and xeff for fg # 27 = C2H2
            0.32236D+02 0.26432D+05 0.10000D+04                                                                 <--- a,b, and sigmaa for bond kinetics
6 0.8357D+00 0.8357D+00 0.6000D-01 0.1000D+01 0.4000D+01                                                    <--- jmax,psoft,ptotal,qtotal,sigma1,sigma2
0.130D+00 0.000D+00 0.000D+00 0.000D+00 0.000D+00 0.000D+00 0.000D+00 0.000D+00 0.000D+00 0.000D+00                    <--- pdist( 1,1:10)
0.290D+00 0.170D-01 0.000D+00 0.000D+00 0.000D+00 0.000D+00 0.000D+00 0.000D+00 0.000D+00 0.000D+00                    <--- pdist( 2,1:10)
0.310D+00 0.950D-01 0.200D-02 0.000D+00 0.000D+00 0.000D+00 0.000D+00 0.000D+00 0.000D+00 0.000D+00                    <--- pdist( 3,1:10)
0.270D+00 0.190D+00 0.220D-01 0.000D+00 0.000D+00 0.000D+00 0.000D+00 0.000D+00 0.000D+00 0.000D+00                    <--- pdist( 4,1:10)
0.000D+00 0.270D+00 0.700D-01 0.500D-02 0.000D+00 0.000D+00 0.000D+00 0.000D+00 0.000D+00 0.000D+00                    <--- pdist( 5,1:10)
0.000D+00 0.233D+00 0.143D+00 0.200D-01 0.100D-02 0.000D+00 0.000D+00 0.000D+00 0.000D+00 0.000D+00                    <--- pdist( 6,1:10)
0.000D+00 0.142D+00 0.207D+00 0.550D-01 0.500D-02 0.000D+00 0.000D+00 0.000D+00 0.000D+00 0.000D+00                    <--- pdist( 7,1:10)
0.000D+00 0.530D-01 0.221D+00 0.109D+00 0.180D-01 0.100D-02 0.000D+00 0.000D+00 0.000D+00 0.000D+00                    <--- pdist( 8,1:10)
0.000D+00 0.000D+00 0.180D+00 0.164D+00 0.450D-01 0.500D-02 0.000D+00 0.000D+00 0.000D+00 0.000D+00                    <--- pdist( 9,1:10)
0.000D+00 0.000D+00 0.104D+00 0.195D+00 0.860D-01 0.150D-01 0.000D+00 0.000D+00 0.000D+00 0.000D+00                    <--- pdist(10,1:10)
0.000D+00 0.000D+00 0.430D-01 0.184D+00 0.133D+00 0.360D-01 0.000D+00 0.000D+00 0.000D+00 0.000D+00                    <--- pdist(11,1:10)
0.000D+00 0.000D+00 0.900D-02 0.138D+00 0.168D+00 0.690D-01 0.000D+00 0.000D+00 0.000D+00 0.000D+00                    <--- pdist(12,1:10)
0.000D+00 0.000D+00 0.000D+00 0.128D+00 0.545D+00 0.874D+00 0.000D+00 0.000D+00 0.000D+00 0.000D+00                    <--- pdist(13,1:10)
0.20D+00                                                                                                    <--- particle internal pressure drop
0.8260D+00  0.5300D-01  0.1000D+00  0.1600D-01  0.5000D-02                                                 <--- ultimate composition (daf)
File generated: Tue Apr 14 18:28:40 1992                                                                            coal0.arg5
```

Table A.6: FG-DVC input data for Argonne Premium coal #6 (Pittsburgh #8)

```
27                                                                 <--- nfg (Number of Functional Groups)
0.10000D-02 0.29240D+02 0.20855D+05 0.36000D+04 0.20480D+03        <--- y0, a, b, sigmaa, and xeff for fg #  1 = CO2XL
0.25000D-02 0.29240D+02 0.25705D+05 0.30000D+04 0.20480D+03        <--- y0, a, b, sigmaa, and xeff for fg #  2 = CO2L
0.65000D-02 0.29646D+02 0.31040D+05 0.25000D+04 0.20480D+03        <--- y0, a, b, sigmaa, and xeff for fg #  3 = CO2T
0.23040D-01 0.29240D+02 0.25220D+05 0.12500D+04 0.00000D+00        <--- y0, a, b, sigmaa, and xeff for fg #  4 = H2OL
0.42789D-01 0.32929D+02 0.31040D+05 0.25000D+04 0.00000D+00        <--- y0, a, b, sigmaa, and xeff for fg #  5 = H2OT
0.25000D-02 0.29240D+02 0.25220D+05 0.12500D+04 0.00000D+00        <--- y0, a, b, sigmaa, and xeff for fg #  6 = COL
0.15231D-01 0.29240D+02 0.29828D+05 0.19000D+04 0.00000D+00        <--- y0, a, b, sigmaa, and xeff for fg #  7 = COT
0.39087D-02 0.31369D+02 0.29100D+05 0.15000D+04 0.00000D+00        <--- y0, a, b, sigmaa, and xeff for fg #  8 = HCNL
0.26963D-01 0.30482D+02 0.41225D+05 0.47500D+04 0.00000D+00        <--- y0, a, b, sigmaa, and xeff for fg #  9 = HCNT
0.00000D+00 0.28730D+02 0.26481D+05 0.30000D+04 0.00000D+00        <--- y0, a, b, sigmaa, and xeff for fg # 10 = NH3
0.15687D+00 0.00000D+00 0.00000D+00 0.00000D+00 0.00000D+00        <--- y0, a, b, sigmaa, and xeff for fg # 11 = CAL
0.00000D+00 0.00000D+00 0.00000D+00 0.00000D+00 0.00000D+00        <--- y0, a, b, sigmaa, and xeff for fg # 12 = CH4XL
0.18000D-01 0.31032D+02 0.27160D+05 0.13000D+04 0.10240D+03        <--- y0, a, b, sigmaa, and xeff for fg # 13 = CH4L
0.32000D-01 0.31725D+02 0.31040D+05 0.22000D+04 0.10240D+03        <--- y0, a, b, sigmaa, and xeff for fg # 14 = CH4T
0.11587D-01 0.33152D+02 0.39285D+05 0.60000D+04 0.00000D+00        <--- y0, a, b, sigmaa, and xeff for fg # 15 = HAROM
0.00000D+00 0.00000D+00 0.00000D+00 0.00000D+00 0.00000D+00        <--- y0, a, b, sigmaa, and xeff for fg # 16 = CH3OH
0.23000D-01 0.32929D+02 0.38800D+05 0.28000D+04 0.00000D+00        <--- y0, a, b, sigmaa, and xeff for fg # 17 = COXT
0.56200D+00 0.00000D+00 0.00000D+00 0.00000D+00 0.00000D+00        <--- y0, a, b, sigmaa, and xeff for fg # 18 = CNV
0.10000D-01 0.00000D+00 0.00000D+00 0.00000D+00 0.00000D+00        <--- y0, a, b, sigmaa, and xeff for fg # 19 = SORG
0.12116D-01 0.00000D+00 0.00000D+00 0.00000D+00 0.00000D+00        <--- y0, a, b, sigmaa, and xeff for fg # 20 = HAL
0.50000D-02 0.29240D+02 0.24250D+05 0.15000D+04 0.00000D+00        <--- y0, a, b, sigmaa, and xeff for fg # 21 = C2H4
0.00000D+00 0.29240D+02 0.24250D+05 0.15000D+04 0.00000D+00        <--- y0, a, b, sigmaa, and xeff for fg # 22 = C3H6
0.15000D-01 0.29240D+02 0.24735D+05 0.10000D+04 0.00000D+00        <--- y0, a, b, sigmaa, and xeff for fg # 23 = C4H8
0.50000D-02 0.29240D+02 0.24250D+05 0.15000D+04 0.00000D+00        <--- y0, a, b, sigmaa, and xeff for fg # 24 = C2H6
0.00000D+00 0.29240D+02 0.24250D+05 0.15000D+04 0.00000D+00        <--- y0, a, b, sigmaa, and xeff for fg # 25 = C3H8
0.25000D-01 0.29240D+02 0.24735D+05 0.10000D+04 0.00000D+00        <--- y0, a, b, sigmaa, and xeff for fg # 26 = C4H10
0.00000D+00 0.00000D+00 0.00000D+00 0.00000D+00 0.00000D+00        <--- y0, a, b, sigmaa, and xeff for fg # 27 = C2H2
            0.32236D+02 0.26675D+05 0.12500D+04                          <--- a,b, and sigmaa for bond kinetics
6 0.8202D+00 0.8202D+00 0.3600D-01 0.1000D+01 0.4000D+01              <--- jmax,psoft,ptotal,qtotal,sigma1,sigma2
0.130D+00 0.000D+00 0.000D+00 0.000D+00 0.000D+00 0.000D+00 0.000D+00 0.000D+00 0.000D+00 0.000D+00   <--- pdist( 1,1:10)
0.290D+00 0.170D-01 0.000D+00 0.000D+00 0.000D+00 0.000D+00 0.000D+00 0.000D+00 0.000D+00 0.000D+00   <--- pdist( 2,1:10)
0.310D+00 0.950D-01 0.200D-02 0.000D+00 0.000D+00 0.000D+00 0.000D+00 0.000D+00 0.000D+00 0.000D+00   <--- pdist( 3,1:10)
0.270D+00 0.190D+00 0.220D-01 0.000D+00 0.000D+00 0.000D+00 0.000D+00 0.000D+00 0.000D+00 0.000D+00   <--- pdist( 4,1:10)
0.000D+00 0.270D+00 0.700D-01 0.500D-02 0.000D+00 0.000D+00 0.000D+00 0.000D+00 0.000D+00 0.000D+00   <--- pdist( 5,1:10)
0.000D+00 0.233D+00 0.143D+00 0.200D-01 0.100D-02 0.000D+00 0.000D+00 0.000D+00 0.000D+00 0.000D+00   <--- pdist( 6,1:10)
0.000D+00 0.142D+00 0.207D+00 0.550D-01 0.500D-02 0.000D+00 0.000D+00 0.000D+00 0.000D+00 0.000D+00   <--- pdist( 7,1:10)
0.000D+00 0.530D-01 0.221D+00 0.109D+00 0.180D-01 0.100D-02 0.000D+00 0.000D+00 0.000D+00 0.000D+00   <--- pdist( 8,1:10)
0.000D+00 0.000D+00 0.180D+00 0.164D+00 0.450D-01 0.500D-02 0.000D+00 0.000D+00 0.000D+00 0.000D+00   <--- pdist( 9,1:10)
0.000D+00 0.000D+00 0.104D+00 0.195D+00 0.860D-01 0.150D-01 0.000D+00 0.000D+00 0.000D+00 0.000D+00   <--- pdist(10,1:10)
0.000D+00 0.000D+00 0.430D-01 0.184D+00 0.133D+00 0.360D-01 0.000D+00 0.000D+00 0.000D+00 0.000D+00   <--- pdist(11,1:10)
0.000D+00 0.000D+00 0.900D-02 0.138D+00 0.168D+00 0.690D-01 0.000D+00 0.000D+00 0.000D+00 0.000D+00   <--- pdist(12,1:10)
0.000D+00 0.000D+00 0.000D+00 0.128D+00 0.545D+00 0.874D+00 0.000D+00 0.000D+00 0.000D+00 0.000D+00   <--- pdist(13,1:10)
0.20D+00                                                                                    <--- particle internal pressure drop
0.8320D+00  0.5300D-01  0.8900D-01  0.1600D-01  0.1000D-01                                  <--- ultimate composition (daf)
File generated: Tue Apr 14 18:28:56 1992                                                          coal0.arg6
```

Table A.7: FG-DVC input data for Argonne Premium coal #7 (Upper Freeport, PA)

```
27                                                                              <--- nfg (Number of Functional Groups)
0.50000D-03 0.29240D+02 0.21340D+05 0.20000D+04 0.20480D+03                     <--- y0, a, b, sigmaa, and xeff for fg #  1 = CO2XL
0.14000D-02 0.29240D+02 0.26190D+05 0.30000D+04 0.20480D+03                     <--- y0, a, b, sigmaa, and xeff for fg #  2 = CO2L
0.31000D-02 0.29646D+02 0.31040D+05 0.25000D+04 0.20480D+03                     <--- y0, a, b, sigmaa, and xeff for fg #  3 = CO2T
0.19300D-01 0.29240D+02 0.26675D+05 0.12500D+04 0.00000D+00                     <--- y0, a, b, sigmaa, and xeff for fg #  4 = H2OL
0.45034D-01 0.32929D+02 0.32980D+05 0.40000D+04 0.00000D+00                     <--- y0, a, b, sigmaa, and xeff for fg #  5 = H2OT
0.20000D-02 0.29240D+02 0.27160D+05 0.75000D+03 0.00000D+00                     <--- y0, a, b, sigmaa, and xeff for fg #  6 = COL
0.74604D-02 0.29240D+02 0.30555D+05 0.14000D+04 0.00000D+00                     <--- y0, a, b, sigmaa, and xeff for fg #  7 = COT
0.48681D-02 0.31369D+02 0.29100D+05 0.15000D+04 0.00000D+00                     <--- y0, a, b, sigmaa, and xeff for fg #  8 = HCNL
0.24074D-01 0.30482D+02 0.41225D+05 0.47500D+04 0.00000D+00                     <--- y0, a, b, sigmaa, and xeff for fg #  9 = HCNT
0.00000D+00 0.28730D+02 0.26481D+05 0.30000D+04 0.00000D+00                     <--- y0, a, b, sigmaa, and xeff for fg # 10 = NH3
0.19154D+00 0.00000D+00 0.00000D+00 0.00000D+00 0.00000D+00                     <--- y0, a, b, sigmaa, and xeff for fg # 11 = CAL
0.00000D+00 0.00000D+00 0.00000D+00 0.00000D+00 0.00000D+00                     <--- y0, a, b, sigmaa, and xeff for fg # 12 = CH4XL
0.19210D-01 0.31032D+02 0.27888D+05 0.80000D+03 0.10240D+03                     <--- y0, a, b, sigmaa, and xeff for fg # 13 = CH4L
0.37290D-01 0.31725D+02 0.31040D+05 0.20000D+04 0.10240D+03                     <--- y0, a, b, sigmaa, and xeff for fg # 14 = CH4T
0.11635D-01 0.33152D+02 0.39285D+05 0.60000D+04 0.00000D+00                     <--- y0, a, b, sigmaa, and xeff for fg # 15 = HAROM
0.00000D+00 0.00000D+00 0.00000D+00 0.00000D+00 0.00000D+00                     <--- y0, a, b, sigmaa, and xeff for fg # 16 = CH3OH
0.13700D-01 0.32929D+02 0.38800D+05 0.22500D+04 0.00000D+00                     <--- y0, a, b, sigmaa, and xeff for fg # 17 = COXT
0.56200D+00 0.00000D+00 0.00000D+00 0.00000D+00 0.00000D+00                     <--- y0, a, b, sigmaa, and xeff for fg # 18 = CNV
0.80000D-02 0.00000D+00 0.00000D+00 0.00000D+00 0.00000D+00                     <--- y0, a, b, sigmaa, and xeff for fg # 19 = SORG
0.58852D-02 0.00000D+00 0.00000D+00 0.00000D+00 0.00000D+00                     <--- y0, a, b, sigmaa, and xeff for fg # 20 = HAL
0.40000D-02 0.29240D+02 0.24250D+05 0.15000D+04 0.00000D+00                     <--- y0, a, b, sigmaa, and xeff for fg # 21 = C2H4
0.00000D+00 0.29240D+02 0.24250D+05 0.15000D+04 0.00000D+00                     <--- y0, a, b, sigmaa, and xeff for fg # 22 = C3H6
0.15000D-01 0.29240D+02 0.25705D+05 0.10000D+04 0.00000D+00                     <--- y0, a, b, sigmaa, and xeff for fg # 23 = C4H8
0.40000D-02 0.29240D+02 0.24250D+05 0.15000D+04 0.00000D+00                     <--- y0, a, b, sigmaa, and xeff for fg # 24 = C2H6
0.00000D+00 0.29240D+02 0.24250D+05 0.15000D+04 0.00000D+00                     <--- y0, a, b, sigmaa, and xeff for fg # 25 = C3H8
0.20000D-01 0.29240D+02 0.25705D+05 0.10000D+04 0.00000D+00                     <--- y0, a, b, sigmaa, and xeff for fg # 26 = C4H10
0.00000D+00 0.00000D+00 0.00000D+00 0.00000D+00 0.00000D+00                     <--- y0, a, b, sigmaa, and xeff for fg # 27 = C2H2
            0.32236D+02 0.27402D+05 0.12500D+04                                        <--- a,b, and sigmaa for bond kinetics
6 0.7683D+00 0.8683D+00 0.3000D-01 0.1000D+01 0.4000D+01                            <--- jmax,psoft,ptotal,qtotal,sigmal,sigma2
0.130D+00 0.000D+00 0.000D+00 0.000D+00 0.000D+00 0.000D+00 0.000D+00 0.000D+00 0.000D+00 0.000D+00     <--- pdist( 1,1:10)
0.290D+00 0.170D-01 0.000D+00 0.000D+00 0.000D+00 0.000D+00 0.000D+00 0.000D+00 0.000D+00 0.000D+00     <--- pdist( 2,1:10)
0.310D+00 0.950D-01 0.200D-02 0.000D+00 0.000D+00 0.000D+00 0.000D+00 0.000D+00 0.000D+00 0.000D+00     <--- pdist( 3,1:10)
0.270D+00 0.190D+00 0.220D-01 0.000D+00 0.000D+00 0.000D+00 0.000D+00 0.000D+00 0.000D+00 0.000D+00     <--- pdist( 4,1:10)
0.000D+00 0.270D+00 0.700D-01 0.500D-02 0.000D+00 0.000D+00 0.000D+00 0.000D+00 0.000D+00 0.000D+00     <--- pdist( 5,1:10)
0.000D+00 0.233D+00 0.143D+00 0.200D-01 0.100D-02 0.000D+00 0.000D+00 0.000D+00 0.000D+00 0.000D+00     <--- pdist( 6,1:10)
0.000D+00 0.142D+00 0.207D+00 0.550D-01 0.500D-02 0.000D+00 0.000D+00 0.000D+00 0.000D+00 0.000D+00     <--- pdist( 7,1:10)
0.000D+00 0.530D-01 0.221D+00 0.109D+00 0.180D-01 0.100D-02 0.000D+00 0.000D+00 0.000D+00 0.000D+00     <--- pdist( 8,1:10)
0.000D+00 0.000D+00 0.180D+00 0.164D+00 0.450D-01 0.500D-02 0.000D+00 0.000D+00 0.000D+00 0.000D+00     <--- pdist( 9,1:10)
0.000D+00 0.000D+00 0.104D+00 0.195D+00 0.860D-01 0.150D-01 0.000D+00 0.000D+00 0.000D+00 0.000D+00     <--- pdist(10,1:10)
0.000D+00 0.000D+00 0.430D-01 0.184D+00 0.133D+00 0.360D-01 0.000D+00 0.000D+00 0.000D+00 0.000D+00     <--- pdist(11,1:10)
0.000D+00 0.000D+00 0.900D-02 0.138D+00 0.168D+00 0.690D-01 0.000D+00 0.000D+00 0.000D+00 0.000D+00     <--- pdist(12,1:10)
0.000D+00 0.000D+00 0.000D+00 0.128D+00 0.545D+00 0.874D+00 0.000D+00 0.000D+00 0.000D+00 0.000D+00     <--- pdist(13,1:10)
0.20D+00                                                                                        <--- particle internal pressure drop
0.8560D+00  0.4700D-01  0.7400D-01  0.1500D-01  0.8000D-02                                        <--- ultimate composition (daf)
File generated: Tue Apr 14 18:29:11 1992                                                                  coal0.arg7
```

Table A.8: FG-DVC input data for Argonne Premium coal #8 (Pochahontes #3, VA)

```
27                                                                   <--- nfg (Number of Functional Groups)
0.60000D-03 0.29240D+02 0.22310D+05 0.25000D+04 0.40960D+03         <--- y0, a, b, sigmaa, and xeff for fg #  1 = CO2XL
0.78000D-03 0.29240D+02 0.27160D+05 0.25000D+04 0.40960D+03         <--- y0, a, b, sigmaa, and xeff for fg #  2 = CO2L
0.46200D-02 0.29646D+02 0.32495D+05 0.27000D+04 0.40960D+03         <--- y0, a, b, sigmaa, and xeff for fg #  3 = CO2T
0.51438D-02 0.29240D+02 0.27160D+05 0.12500D+04 0.00000D+00         <--- y0, a, b, sigmaa, and xeff for fg #  4 = H2OL
0.95527D-02 0.32929D+02 0.33950D+05 0.30000D+04 0.00000D+00         <--- y0, a, b, sigmaa, and xeff for fg #  5 = H2OT
0.15000D-02 0.29240D+02 0.28130D+05 0.12500D+04 0.00000D+00         <--- y0, a, b, sigmaa, and xeff for fg #  6 = COL
0.15336D-02 0.29240D+02 0.31040D+05 0.15000D+04 0.00000D+00         <--- y0, a, b, sigmaa, and xeff for fg #  7 = COT
0.19721D-02 0.31369D+02 0.29100D+05 0.15000D+04 0.00000D+00         <--- y0, a, b, sigmaa, and xeff for fg #  8 = HCNL
0.23111D-01 0.30482D+02 0.41225D+05 0.47500D+04 0.00000D+00         <--- y0, a, b, sigmaa, and xeff for fg #  9 = HCNT
0.00000D+00 0.28730D+02 0.26481D+05 0.30000D+04 0.00000D+00         <--- y0, a, b, sigmaa, and xeff for fg # 10 = NH3
0.27615D+00 0.00000D+00 0.00000D+00 0.00000D+00 0.00000D+00         <--- y0, a, b, sigmaa, and xeff for fg # 11 = CAL
0.00000D+00 0.00000D+00 0.00000D+00 0.00000D+00 0.00000D+00         <--- y0, a, b, sigmaa, and xeff for fg # 12 = CH4XL
0.15910D-01 0.31032D+02 0.28615D+05 0.75000D+03 0.20480D+03         <--- y0, a, b, sigmaa, and xeff for fg # 13 = CH4L
0.27090D-01 0.31725D+02 0.32010D+05 0.17000D+04 0.20480D+03         <--- y0, a, b, sigmaa, and xeff for fg # 14 = CH4T
0.11809D-01 0.33152D+02 0.39285D+05 0.60000D+04 0.00000D+00         <--- y0, a, b, sigmaa, and xeff for fg # 15 = HAROM
0.00000D+00 0.00000D+00 0.00000D+00 0.00000D+00 0.00000D+00         <--- y0, a, b, sigmaa, and xeff for fg # 16 = CH3OH
0.19000D-01 0.32929D+02 0.38800D+05 0.32000D+04 0.00000D+00         <--- y0, a, b, sigmaa, and xeff for fg # 17 = COXT
0.56200D+00 0.00000D+00 0.00000D+00 0.00000D+00 0.00000D+00         <--- y0, a, b, sigmaa, and xeff for fg # 18 = CNV
0.20000D-02 0.00000D+00 0.00000D+00 0.00000D+00 0.00000D+00         <--- y0, a, b, sigmaa, and xeff for fg # 19 = SORG
0.15232D-01 0.00000D+00 0.00000D+00 0.00000D+00 0.00000D+00         <--- y0, a, b, sigmaa, and xeff for fg # 20 = HAL
0.20000D-02 0.29240D+02 0.24250D+05 0.15000D+04 0.00000D+00         <--- y0, a, b, sigmaa, and xeff for fg # 21 = C2H4
0.00000D+00 0.29240D+02 0.24250D+05 0.15000D+04 0.00000D+00         <--- y0, a, b, sigmaa, and xeff for fg # 22 = C3H6
0.80000D-02 0.29240D+02 0.26675D+05 0.75000D+03 0.00000D+00         <--- y0, a, b, sigmaa, and xeff for fg # 23 = C4H8
0.20000D-02 0.29240D+02 0.24250D+05 0.15000D+04 0.00000D+00         <--- y0, a, b, sigmaa, and xeff for fg # 24 = C2H6
0.00000D+00 0.29240D+02 0.24250D+05 0.15000D+04 0.00000D+00         <--- y0, a, b, sigmaa, and xeff for fg # 25 = C3H8
0.10000D-01 0.29240D+02 0.26675D+05 0.75000D+03 0.00000D+00         <--- y0, a, b, sigmaa, and xeff for fg # 26 = C4H10
0.00000D+00 0.00000D+00 0.00000D+00 0.00000D+00 0.00000D+00         <--- y0, a, b, sigmaa, and xeff for fg # 27 = C2H2
            0.32236D+02 0.28130D+05 0.75000D+03                                  <--- a,b, and sigmaa for bond kinetics
5 0.9266D+00 0.9766D+00 0.3600D-01 0.1000D+01 0.4000D+01                 <--- jmax,psoft,ptotal,qtotal,sigma1,sigma2
0.300D-01 0.000D+00 0.000D+00 0.000D+00 0.000D+00 0.000D+00 0.000D+00 0.000D+00 0.000D+00 0.000D+00        <--- pdist( 1,1:10)
0.700D-01 0.100D-02 0.000D+00 0.000D+00 0.000D+00 0.000D+00 0.000D+00 0.000D+00 0.000D+00 0.000D+00        <--- pdist( 2,1:10)
0.110D+00 0.500D-02 0.000D+00 0.000D+00 0.000D+00 0.000D+00 0.000D+00 0.000D+00 0.000D+00 0.000D+00        <--- pdist( 3,1:10)
0.150D+00 0.140D-01 0.000D+00 0.000D+00 0.000D+00 0.000D+00 0.000D+00 0.000D+00 0.000D+00 0.000D+00        <--- pdist( 4,1:10)
0.190D+00 0.280D-01 0.100D-02 0.000D+00 0.000D+00 0.000D+00 0.000D+00 0.000D+00 0.000D+00 0.000D+00        <--- pdist( 5,1:10)
0.170D+00 0.500D-01 0.300D-02 0.000D+00 0.000D+00 0.000D+00 0.000D+00 0.000D+00 0.000D+00 0.000D+00        <--- pdist( 6,1:10)
0.130D+00 0.770D-01 0.700D-02 0.000D+00 0.000D+00 0.000D+00 0.000D+00 0.000D+00 0.000D+00 0.000D+00        <--- pdist( 7,1:10)
0.900D-01 0.102D+00 0.140D-01 0.100D-02 0.000D+00 0.000D+00 0.000D+00 0.000D+00 0.000D+00 0.000D+00        <--- pdist( 8,1:10)
0.600D-01 0.123D+00 0.250D-01 0.200D-02 0.000D+00 0.000D+00 0.000D+00 0.000D+00 0.000D+00 0.000D+00        <--- pdist( 9,1:10)
0.000D+00 0.134D+00 0.390D-01 0.400D-02 0.000D+00 0.000D+00 0.000D+00 0.000D+00 0.000D+00 0.000D+00        <--- pdist(10,1:10)
0.000D+00 0.130D+00 0.560D-01 0.700D-02 0.000D+00 0.000D+00 0.000D+00 0.000D+00 0.000D+00 0.000D+00        <--- pdist(11,1:10)
0.000D+00 0.114D+00 0.750D-01 0.130D-01 0.100D-02 0.000D+00 0.000D+00 0.000D+00 0.000D+00 0.000D+00        <--- pdist(12,1:10)
0.000D+00 0.223D+00 0.780D+00 0.974D+00 0.998D+00 0.000D+00 0.000D+00 0.000D+00 0.000D+00 0.000D+00        <--- pdist(13,1:10)
0.20D+00                                                                            <--- particle internal pressure drop
0.9110D+00  0.4400D-01  0.3000D-01  0.1300D-01  0.2000D-02                            <--- ultimate composition (daf)
File generated: Tue Apr 14 18:29:33 1992                                                              coal0.arg8
```

APPENDIX B

FG-SET DEVOLATILIZATION SUBMODEL

FG-SET Submodel Basis

The FG-SET devolatilization submodel is similar to FG-DVC submodel, which was presented in Chapter 4. In FG-SET, the evolution of light gases is based also on the functional groups. The major difference is in the computation of tar evolution, which is based on a quantity called potential tar-forming fraction, denoted by x^0; it represents the maximum possible tar yield. In the FG-SET formulation, the potential tar-forming fraction is calculated from the empirical correlation proposed by Ko et al., (1980). A provision is also provided for the user to specify the value of x^0 as input. Another difference between these two models is in the evaluation of rate coefficients. The FG-SET submodel also uses a distributed activation energy model for the calculation of rate coefficients but keeps the limits of normal distribution constant throughout the devolatilization process.

Figure B.1 shows a two-dimensional representation of this submodel. The dry, ash-free coal can be divided into various chemical functional groups, as shown in Figure B.1A. The X and Y dimensions represent the chemical functional group components (Solomon and Hamblen, 1985). The Y dimension is divided into

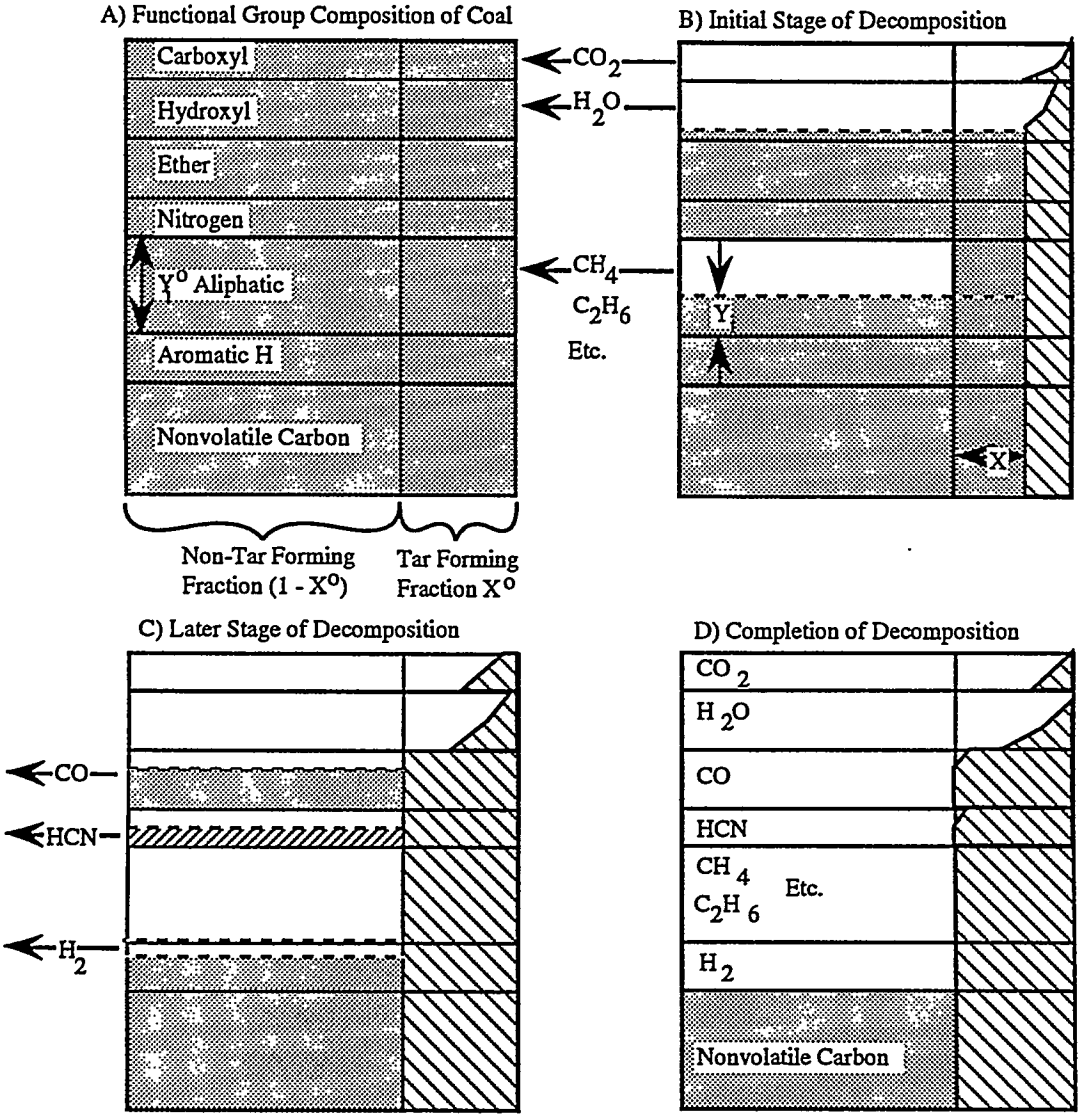

Figure B.1. Progress of thermal decomposition according to the functional group model: A) functional group composition of coal, B) initial state of decomposition, C) later stage of decomposition, D) completion of decomposition (after Solomon and Hamblen, 1985).

fractions according to the chemical composition of the coal. The X dimension represents non-tar-forming char, tar-forming char, i.e., instantaneous tar forming fraction x, and tar. The initial fraction of a particular functional group is represented by y_i^o, and the sum of y_i^o's equals 1. The initial functional group composition, y_i^o, for the formulation using nineteen functional groups, and the potential tar-forming fraction, x^o, for eight coals are given in Table B.1. The kinetic rate parameters can be either coal dependent or coal independent. The coal independent Arrhenius rate parameters for each functional group are also given in Table B.1 (from Solomon et al., 1988).

The evolution of each functional group into gas is represented by first order decay. The evolution of tar is also described by the first order decay of the dimension X, i.e., the tar forming fraction. It is assumed that light gases do not evolve from the tar functional groups at the solid temperature, i.e., within the solid (Solomon and Hamblen, 1985), but decompose to form light gases in the gas phase at gas temperature. The Arrhenius rate coefficients are determined using a distributed activation energy model. The differential equations for the FG-SET devolatilization submodel are, therefore, summarized as follows:

$$\frac{dW_{gas,i}}{dt} = k_i(T_s)(1 - x^0 + x)y_i + k_i(T_g)W_{Tar,i} \qquad \text{(B.1)}$$

$$\frac{dW_{Tar,i}}{dt} = k_x(T_s)W_{Tar,i} - k_i(T_g)W_{Tar,i} \qquad \text{(B.2)}$$

$$\frac{dW_{char,i}}{dt} = -k_i(T_s)(1 - x^0 + x)y_i - k_x(T_s)W_{Tar,i} \qquad \text{(B.3)}$$

$$\frac{dx}{dt} = -k_x(T_s)x \qquad \text{(B.4)}$$

Table B.1. Devolatilization kinetic parameters, functional group compositions, potential tar-forming fractions and ultimate analysis§.

Functional Groups (dry, ash free)	k_i^o, (s^{-1})	$\frac{E}{R}$, (K)	$\frac{\sigma}{R}$, (K)	Gillette y_i^o	IL #6 y_i^o	KY #9 y_i^o	ND Zap y_i^o	Pitt #8 y_i^o	Rose y_i^o	Utah y_i^o	Wyodak y_i^o
CO_2 extra loose	0.81E+13	22500	1500	0.018	0.022	0.000	0.065	0.000	0.035	0.003	0.028
CO_2 loose	0.65E+17	33850	1500	0.053	0.022	0.006	0.300	0.007	0.035	0.007	0.020
CO_2 tight	0.11E+16	38315	2000	0.028	0.030	0.005	0.005	0.005	0.030	0.017	0.021
H_2O loose	0.22E+19	30000	1500	0.031	0.045	0.011	0.061	0.012	0.051	0.025	0.030
H_2O tight	0.17E+14	32700	1500	0.031	0.000	0.011	0.033	0.012	0.051	0.020	0.022
CO ether loose	0.14E+19	40000	6000	0.080	0.060	0.050	0.060	0.050	0.055	0.025	0.050
CO ether tight	0.15E+16	40500	1500	0.043	0.063	0.026	0.044	0.021	0.013	0.034	0.055
HCN loose	0.17E+14	30000	1500	0.007	0.100	0.026	0.006	0.009	0.005	0.006	0.001
HCN tight	0.69E+13	42500	4750	0.015	0.016	0.009	0.012	0.023	0.015	0.024	0.018
NH3	0.12E+13	27300	3000	0.000	0.000	0.000	0.001	0.000	0.001	0.000	0.001
CH_x aliphatic	0.84E+15	30000	1500	0.158	0.081	0.183	0.095	0.207	0.127	0.188	0.152
CH_4 extra loose	0.84E+15	30000	1500	0.000	0.011	0.020	0.000	0.000	0.000	0.000	0.000
CH_4 loose	0.75E+14	30000	2000	0.026	0.011	0.015	0.016	0.020	0.022	0.022	0.017
CH_4 tight	0.34E+12	30000	2000	0.017	0.022	0.015	0.009	0.015	0.012	0.022	0.008
H aromatic	0.10E+15	40500	6000	0.012	0.016	0.012	0.017	0.013	0.013	0.017	0.013
CH_3OH	0.00E+00	NA	NA	0.000	0.000	0.000	0.000	0.000	0.000	0.000	0.000
CO extra tight	0.20E+14	45500	1500	0.031	0.000	0.020	0.090	0.020	0.000	0.040	0.043
C nonvolatile	0.00E+00	NA	NA	0.440	0.550	0.562	0.440	0.562	0.520	0.548	0.518
S organic	0.00E+00	NA	NA	0.005	0.038	0.024	0.011	0.024	0.012	0.003	0.004
Total	NA	NA	NA	1.000	1.000	1.000	1.000	1.000	1.000	1.000	1.000
Tar, x^o, pulverized	0.86E+15	27700	1500	0.200	0.430	0.430	0.160	0.430	0.160	0.430	0.160
Tar, x^o, TGA	0.86E+15	27700	1500	NA	NA	NA	0.040	0.110	0.060	NA	NA
Tar, x^o, SET 1 atm§	0.86E+15	27700	1500	0.071	0.116	0.270	0.043	0.270	0.098	0.270	0.160
Tar, x^o, SET 25 atm§	0.86E+15	27700	1500	0.067	0.092	0.168	0.031	0.168	0.082	0.168	0.117
Coal Type				subbit	bit	bit	lig	bit	subbit	bit	subbit
DAF Ultimate											
C				0.720	0.736	0.817	0.665	0.821	0.724	0.807	0.750
H				0.047	0.047	0.056	0.048	0.056	0.049	0.058	0.054
N				0.012	0.014	0.019	0.011	0.017	0.012	0.016	0.011
O				0.216	0.165	0.084	0.265	0.082	0.203	0.116	0.181
S (organic)				0.005	0.038	0.024	0.011	0.024	0.012	0.003	0.004

§Data that are not applicable or not available are represented by NA. Functional group data are from experimental measurements of Solomon and coworkers at Advanced Fuel Research Inc. (Serio, 1990, Solomon et al., 1988, Serio et al., 1987). Potential tar-forming fraction for pulverized coal applications and TGA measurements are from Serio et al. (1987). The semi-empirical model of Ko et al. (1988) was used to determine tar-forming fractions at 1 and 25 atmospheres.

Arrhenius Rate Constants

The rate constants for the evolution of char functional groups and tar-forming fraction are determined by using a distributed activation energy model. According to this model, coal is viewed as a composite material consisting of a large number of components which decompose at different rates. Following Anthony et al., (1974), a multiple reactions model for each functional group is used to determine the Arrhenius rate constants. Here it is assumed that the total volatile mass production from the *i-th* functional group is normally distributed with respect to activation energy in the same manner as the total potential volatile mass production at large times. The resulting equation is

$$k_i = \int_{-\infty}^{+\infty} k_i^o \exp\left(\frac{-E}{RT}\right) \frac{\exp\left[-\frac{1}{2}\left(\frac{E-\overline{E}_i}{\sigma_i}\right)\right]}{\sigma_i\sqrt{2\pi}} dE_i \qquad \text{(B.5)}$$

Equation B.5 is solved using a seven-point Gaussian-Legendre quadrature (Abramowitz and Stegun, 1972). The derivation of the distributed Arrhenius rate expression is discussed by Hobbs (1990). In the FG-SET submodel, options are provided to use either rank dependent or rank independent kinetic data. For the rank independent option, the frequency factors, k_i^o, mean activation energies, $\overline{E}_i$, and standard deviations of activation energies, σ_i, are given in Table B.1; they were obtained from Solomon et al., (1988).

Potential Tar-Forming Fraction

The potential tar-forming fraction, x^o, represents the maximum possible tar yield. However, competition from light gas evolution prevents maximum tar yield from being realized, as shown in Eqns. B.1 and B.2. The potential tar-forming

fraction can be adjusted to match experimentally determined tar yields, estimated from correlated experimental data (Khan, 1989, Ko et al., 1988 and Serio et al., 1987), predicted from simple ultimate yield models (Kobayashi et al., 1977), or predicted from coal-structure-dependent models (Solomon et al., 1988). The values for the potential tar-forming fraction can be chosen to match experimental tar yield data. The tar recirculated back to the oxidation and gasification zone can also be specified to match the reported tar recirculation rates. If tar yield data are not available, then the correlation of Ko et al., (1988) is recommended.

For comparison, the potential tar-forming fractions used in pulverized coal applications (Serio et al., 1987), experimental values obtained from TGA analysis, and calculated values at 1 and 25 atmospheres pressure from the semiempirical correlation of Ko et al., (1988) are given in Table B.1. The potential tar-forming fraction was calculated from the following equations (Ko et al., 1988):

$$x^{o} = 0.01[\alpha + \beta x_{tar}] \tag{B.6}$$

$$x_{tar} = \frac{(number\ of\ labile\ bridges)(abstractable\ hydrogen)}{(number\ of\ crosslinked\ bridges)} \tag{B.7}$$

$$number\ of\ labile\ bridges = \left[\frac{(1-f_a)(100\Omega_c)}{12}\right]^{1.8} \tag{B.8}$$

$$abstractable\ hydrogen = 100\left[\left(\frac{\Omega_H}{1}\right) - \left(\frac{\Omega_{OH}}{17}\right)\right] \tag{B.9}$$

$$number\ of\ crosslinked\ bridges = \begin{cases} 100\left(\frac{\Omega_O}{16} + \frac{\Omega_S}{32}\right) & \Omega_O > 0.035 \\ 100\left(\frac{0.035}{16} + \frac{\Omega_S}{32}\right) & \Omega_O > 0.035 \end{cases} \tag{B.10}$$

$$f_a = 0.830526 - 2.008147\Omega_c + 2.241218\Omega_c^2 \tag{B.11}$$

$$\Omega_{OH} = 0.332 - 0.35\Omega_c \tag{B.12}$$

$$\alpha = \begin{cases} 2 & x_{tar} < 15 \\ \dfrac{1}{\left(0.021533 + 0.028651 L_p\right)} - 36 & 15 \le x_{tar} \le \\ 11.24071 + 9.743707 L_p - 0.91326 L_p^2 & x_{tar} > 31 \end{cases} \tag{B.13}$$

$$\beta = \begin{cases} 0 & x_{tar} < 15 \\ 0.0508030 + 0.696487 L_p - 0.06959 L_p^2 & 15 \le x_{tar} \le 31 \\ 0 & x_{tar} > 31 \end{cases} \tag{B.14}$$

$$L_p = \begin{cases} -\log_{10} P + 1 & P \le 2.5 MPa \\ 2.5 & P > 2.5 MPa \end{cases} \tag{B.15}$$

where Ω_i represents the dry, mineral-matter-free weight fraction of the *i-th* component determined from the ultimate analysis, f_a represents the aromaticity of the coal, and Ω_{OH} represents the dry, mineral-matter-free hydroxyl group fraction. This semiempirical correlation has been used to correlate tar yields over pressures ranging from vacuum to 9 Mpa (about 90 atmospheres) and 37 coals ranging from lignites to anthracites, (Ko et al., 1988).

The potential tar-forming fractions determined for atmospheric, pulverized coal applications, TGA applications, and estimations based on the semiempirical tar model (SET model) of Ko et al. (1988) at 1 and 25 atmospheres are shown in Table B.1. The potential tar-forming fraction is smaller at high pressure due to mass transport effects, which are modeled empirically with the SET model. Also, the potential tar-forming fractions obtained from TGA experiments are smaller than the values using the SET model at atmospheric pressure. Mass transport through the coal bed, as well as secondary reactions with the hot char, may explain the

difference. The potential tar-forming fractions determined for pulverized coal applications are closer to the SET results at atmospheric pressure than to the SET results at high pressure or to the TGA results. Yet the values determined for pulverized coal applications are still higher than the atmospheric SET results. The largest difference between the potential tar-forming fraction determined for pulverized coal applications and the atmospheric SET predictions was for the N. D. Zap lignite, which differs by a factor of 2.7. The Wyodak subbituminous case was in good agreement. However, all values were considered inadequate for predicting tar yield for fixed-bed gasifiers. Quantitative comparisons are discussed further by Hobbs (1990).

The overall rates of evolution of light gases and tar from coal can then be determined by

$$r_i = \pm \rho^o_{sm}\left(1-\varepsilon^o\right)\left(1-\Omega^o_{ash}-\Omega^o_{moisture}\right)\frac{d\omega_{i,\,(char,\,tar,\,or\,gas)}}{dt} \qquad \text{(B.16)}$$

where ρ^o_{sm} is measured apparent density of the feed coal, ε^o is the bed void fraction of the gasifier top, Ω^o_{ash} and $\Omega^o_{moisture}$ are the proximate ash and moisture fractions of the feed coal, and $\omega_{i,\,(char,\,tar,\,or\,gas)}$ is the weight fraction of the *i-th* functional group in the char, tar, or gas. The time derivatives in Equation (B.16) are calculated by assuming that light volatile gases do not evolve from the gaseous tar:

$$\frac{d\omega_{i,gas}}{dt} = \left(1-x^o+x\right)k_i y_i \;\; and \;\; \frac{d\omega_{i,tar}}{dt} = k_x x y_i \qquad \text{(B.17)}$$

$$\frac{d\omega_{i,char}}{dt} = -\frac{d\omega_{i,gas}}{dt} - \frac{d\omega_{i,tar}}{dt} \qquad \text{(B.18)}$$

$\omega_{i,gas}$, $\omega_{i,tar}$, and $\omega_{i,char}$ represent the fractional amounts of a particular functional group that have evolved as light gas, tar or is remaining in the solid.

The volumetric devolatilization rate expressions $r_i^d\left(kg_i/m^3s\right)$ can be obtained by combining Equation B.17 and B.18 and by the use of the chain rule

$$r_i^d = \rho_{sm}^o\left(1-\varepsilon^o\right)\left(1-\Omega_{ash}^o-\Omega_{moisture}^o\right)\frac{d\omega_{i,char}}{dt} \tag{B.19}$$

$$\frac{d\omega_{i,char}}{dt} = \frac{d\left(1-x^o+x\right)y_i}{dt} = \left(1-x^o+x\right)\frac{dy_i}{dt} + y_i\frac{dx}{dt} \tag{B.20}$$

$$\frac{d\omega_{i,char}}{dt} = \left(1-x^o+x\right)\left(-k_i y_i\right) + y_i\left(-k_x x\right) \tag{B.21}$$

$$r_i^d = \rho_{sm}^o\left(1-\varepsilon^o\right)\left(1-\Omega_{ash}^o-\Omega_{moisture}^o\right)\left[\left(1-x^o+x\right)\left(k_i y_i\right) + y_i\left(k_x x\right)\right] \tag{B.22}$$

The volumetric devolatilization rate expressions $r_i^d\left(kg_i/m^3s\right)$ include mass loss due to both light gas evolution and tar evolution which is required by the continuity equations listed in Table 3.2. However, the tar continuity equations require the tar volumetric rate equations $r_{i,tar}^d\left(kg_i/m^3s\right)$, which are obtained similarly:

$$r_{i,tar}^d = \rho_{sm}^o\left(1-\varepsilon^o\right)\left(1-\Omega_{ash}^o-\Omega_{moisture}^o\right)k_x x y_i \tag{B.23}$$

Coupling between mass transport of oxidation and gasification products and devolatilization complicates the mathematical description of both devolatilization and char oxidation. The devolatilization rate expressions given by the above equations do not include resistance due to mass transport. Saxena (1990) concluded that heat and mass transport limitations in large coal particles are significant. In addition, simulations with purely kinetic devolatilization equations as formulated above result in unrealistically fast product evolution and extremely steep temperature gradient, indicating the importance of the transport effects in large coal particles. To account for the mass transport effects, resistances through the film and particle are added to

the Arrhenius rate expression as diffusional resistances, as shown by the following expression:

$$k_{i,x}^{effective} = \left(\frac{1}{k_{i,x}} + \frac{1}{k_m} + \frac{1}{k_{eff}} \right)^{-1} \qquad \text{(B.24)}$$

where $k_{i,x}^{effective}$, $k_{i,x}$, k_m and k_{eff} represent the effective devolatilization rate constant, the distributed Arrhenius rate constant for devolatilization, the film mass transport coefficient, and the effective mass transport coefficient for the particle. The resistance through the particle is a function of the particle burnout and is negligible at the beginning of devolatilization. The mass transfer resistances used herein for devolatilization are identical to the mass transfer resistances used in the oxidation and gasification submodel, as discussed in chapter 3.

Diffusional mass transport may not be an appropriate mode of transport for devolatilization. Jets of volatile gases suggest that convection may dominate mass transport for small particle devolatilization. However, diffusion may be important for devolatilization of large particles at typical heating rates found in fixed-bed reactors. Further research is needed to address mass transport during large particle devolatilization. Internal particle temperature gradients may be significant during devolatilization; but experimental evidence using thermocouples embedded into large coal particles during devolatilization indicates that thermal equilibrium is reached rapidly (Nuttall, 1979).

APPENDIX C

PREDICTION OF EFFLUENT COMPOSITIONS FOR FIXED-BED COAL GASIFIERS

Prediction of effluent compositions for fixed-bed coal gasifiers

Michael L. Hobbs*, Predrag T. Radulovic and L. Douglas Smoot
Advanced Combustion Engineering Research Center, Brigham Young University, Provo, UT 84602, USA
(Received 12 July 1991; revised 24 January 1992)

A two-zone, well-mixed, partial equilibrium model that provides efficient estimates of fixed bed coal gasifier effluent temperature, tar production and gas composition has been developed and evaluated. The model includes detailed treatment of devolatilization, partial equilibrium of volatile gases, treatment of a large number of gas-phase species, and estimation of tar production with potential for recirculation of effluent products. Predictions have been compared to measured effluent compositions from two large-scale fixed-bed reactors over a wide range of coal types and operating conditions. Model evaluation also includes determination of sensitivity of effluent temperature and composition to model options, model parameters and operational parameters. The model can be used separately or as part of a large process simulator since execution times are on the order of seconds using an engineering workstation. Furthermore, the predicted effluent compositions can provide useful initial estimates for one- or two-dimensional fixed-bed models.

(Keywords: coal; effluent; gasification)

A schematic diagram of a large-scale, fixed-bed gasifier is shown in *Figure 1*. Coal is fed to the top of the reactor and moves downward under gravity, countercurrent to the rising gas stream. The dry ash is removed at the bottom of the reactor. The feed gas is composed of air or oxygen and steam. Excess steam is supplied to the gasifier to control the ash temperature. *Figure 1* also shows the reactor divided into four zones: (1) drying; (2) devolatilization; (3) gasification; and (4) combustion. As the coal slowly descends, the hot gases produced in the gasification and combustion zones exchange energy with the cooler solid fuel. Water and volatile matter are released when the solid reaches a sufficiently high temperature. After drying and devolatilization, the char enters the gasification zone where carbon reacts with steam, carbon dioxide and hydrogen. Endothermic reactions in this zone produce carbon monoxide and hydrogen. The slightly exothermic reaction of hydrogen with carbon produces methane. Differentiation between the gasification zone and the combustion zone is based on the presence or absence of free oxygen. Heterogeneous combustion and gasification reactions can occur simultaneously in the combustion zone. Combustible gases such as carbon monoxide or hydrogen react with gaseous oxygen. Solid residence time in the drying, gasification and oxidation zones may be on the order of several hours. Residence time in the ash layer may be even longer depending on the thickness of this zone. Gas residence times are on the order of seconds.

Gumz[1] developed an equilibrium model for fixed-bed reactors. The effects of devolatilization, drying and sensible heat losses were not included in his model. Woodmansee[2] extended Gumz's equilibrium model to include sensible heat losses. Kosky and Floess[3] added devolatilization to the equilibrium model by assuming instantaneous devolatilization with yield based on proximate analysis and volatile composition based on the gas analysis of Loison and Chauvin[4]. Effluent temperature was calculated using overall energy balances. Compositions were calculated assuming water–gas shift equilibrium. Smoot and Smith[5] and more recently, Radulovic *et al.*[6] have reviewed fixed-bed models.

No major advancement has been made in predicting effluent temperatures and compositions in fixed-bed gasification in recent years. Even one- and two-dimensional, fixed-bed coal gasification models have failed to accurately predict effluent properties. An assessment of the fixed-bed models of Amundson and Arri[7], Yoon *et al.*[8], Desai and Wen[9], Stillman[10], Cho and Joseph[11], Yu and Denn[12], Earl and Islam[13], Thorsness and Kang[14], and Bhattacharya *et al.*[15] indicates common assumptions such as axially uniform gas/solid phase plug flow, uniform porosity, instantaneous devolatilization (with volatile yield from proximate analysis and compositions assumed to be constant), char oxidation parameters from small particle data, and little or no gas-phase chemistry. Recently, Hobbs[16] has relaxed most of these assumptions in a steady, one-dimensional model, while emphasizing the importance of devolatilization and gas-phase chemistry in the fixed-bed gasification processes.

An efficient two-zone, partial equilibrium model has been developed and is presented in this paper. The two-zone, fixed-bed model uses a coal-independent devolatilization submodel and a partial equilibrium gas-phase submodel to predict effluent temperatures and compositions. Effluent compositions can be determined for any number of species. Tar production can also be

*Current address: Sandia National Laboratories, PO Box 5800, Division 1512, Albuquerque, NM 87185, USA

0016-2361/92/101177-18

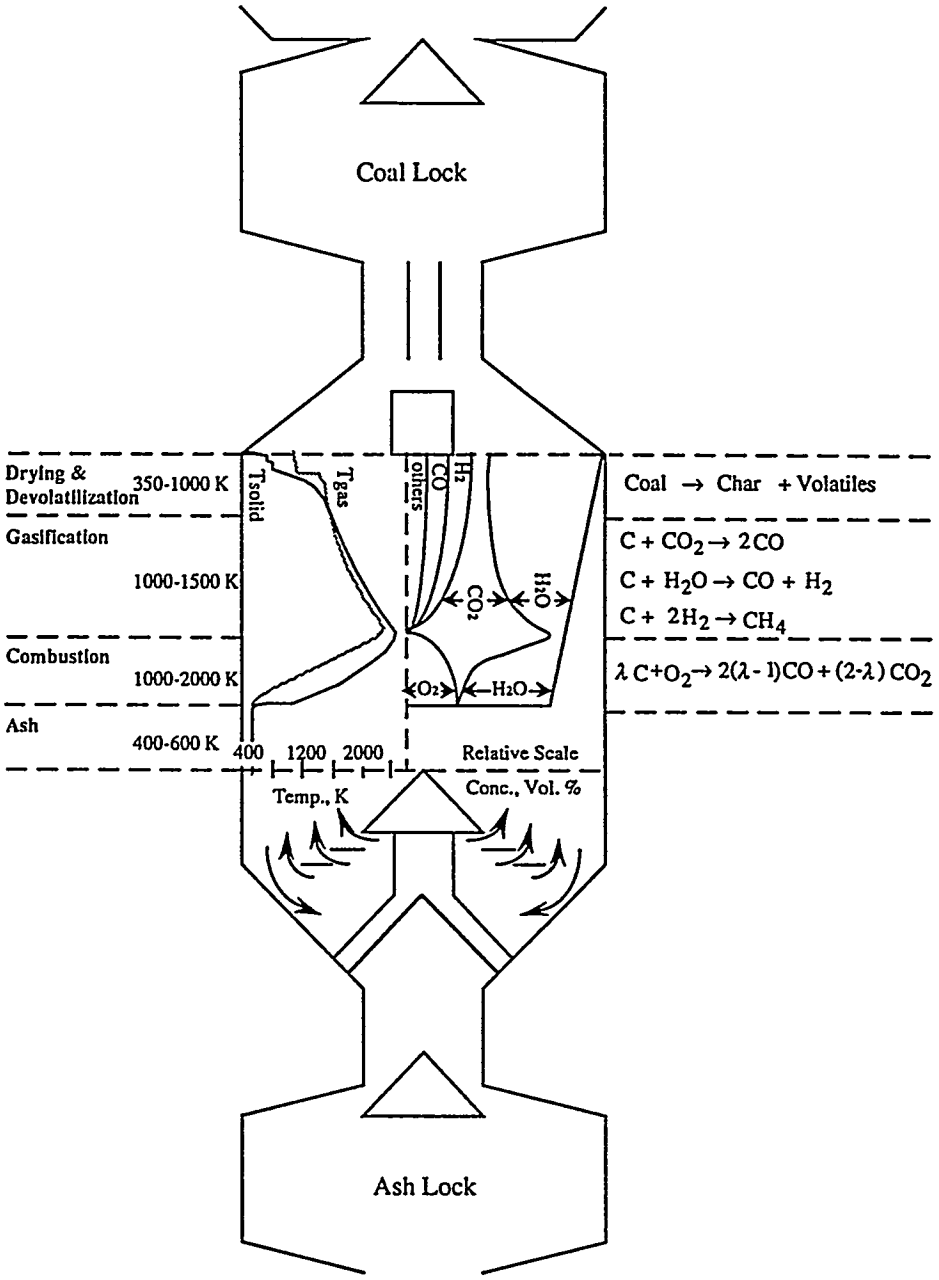

Figure 1 Schematic of large-scale, high pressure countercurrent fixed-bed gasifier. Temperature and concentration profiles are for illustration only

estimated and tar recycle can be taken into account. In many engineering applications, only effluent temperatures and compositions are of interest. For example, only effluent information is required from the gasifier in a comprehensive process simulation used for optimization of the overall coal conversion process. Also, since simulation of the gasifier is often only a small part of complete process calculations, computational time must be kept to a minimum. In such cases, the two-zone, partial equilibrium model is preferred to more complex and computationally demanding one- or two-dimensional models. Furthermore, this two-zone, partial equilibrium model can provide initial estimates for one- or two-dimensional models. Reliable initial estimates of fixed-bed reactor effluent temperatures and compositions have been found essential for solving the highly non-linear, fixed-bed equation set[16].

TWO-ZONE PARTIAL EQUILIBRIUM MODEL

Foundations and assumptions

Typical temperature and concentration profiles in a large-scale, fixed-bed gasifier are illustrated in *Figure 1*. Oxidation and gasification occur at relatively high temperatures compared to the cooler devolatilization zone. The temperature difference provides a natural division of the process into two zones. Higher temperatures in the oxidation/gasification section favour total equilibrium in the gas phase. Lower temperature

and short gas residence time in the devolatilization zone favour partial equilibrium.

The primary assumption for the two-zone, partial equilibrium model is that the oxidation/gasification zone and drying/devolatilization zone can be assigned different uniform temperatures, $T_{equilibrium}$ and T_{exit}, respectively. All gases are assumed to be in thermal equilibrium. Furthermore, the gases produced in the higher temperature oxidation/gasification zone are assumed to be in chemical equilibrium in this zone, but non-reactive in the lower temperature devolatilization/drying zone. The coal volatiles and water vapour produced in the lower temperature devolatilization zone are also assumed to be non-reactive in this zone. Coals are assumed to be composed of various percentages of chemical functional groups[17]. Reactor geometry, operational parameters, heat loss or overall heat transfer coefficient, coal properties, coal burnout and recycle tar fraction must be specified.

Energy balance

Control volumes for three equilibrium model options are shown in *Figure 2*. The one-zone models shown in *Figures 2a* and *2b* are included for comparison and show the evolution of the two-zone model. The energy balance around any control volume shown in *Figure 2* is:

$$\dot{m}_{s,in}h_{s,in}+\dot{m}_{g,in}h_{g,in}-\dot{m}_{s,out}h_{s,out}-\dot{m}_{g,out}h_{g,out}-Q=0 \quad (1)$$

where $\dot{m}$ is mass flow rate (kg s^{-1}), h is total enthalpy (J kg^{-1}) and Q is heat loss (J s^{-1}); the subscripts s, g, in and out refer to solid, gas, entering control volume and exiting control volume, respectively. The total equilibrium model shown in *Figure 2a* assumes complete reaction of the dry ash free coal by either devolatilization, gasification or oxidation. The total equilibrium model does not differentiate among mechanisms for these chemical processes as do the one- and two-zone partial equilibrium models. The only difference between the one- and two-zone partial equilibrium models relates to devolatilization and drying. The one-zone model assumes that drying and devolatilization occur in the same zone as oxidation and gasification. This assumption is relaxed in the two-zone partial equilibrium model of *Figure 2c*. Equation (1) can be solved by iteration as discussed in detail by Hobbs[16]. Computation time for the two-zone partial equilibrium model is less than 1 s on an engineering workstation.

The total enthalpy is composed of the enthalpy of formation and the sensible enthalpy:

$$h = h_f^o + h^s \quad (2)$$

where the superscript o refers to the reference temperature (298.15 K), and superscript s to sensible enthalpy from the reference temperature to the stream temperature. The heat of formation of coal, $h_{f,c}^o$, is based on the following coal reaction:

$$C_nH_mO_kS_jN_k+\left(n+\frac{m}{4}-\frac{h}{2}+j\right)O_2 \rightarrow nCO_2+\frac{m}{2}H_2O+\frac{k}{2}N_2+jSO_2 \quad (3)$$

The heat of formation of the coal can be obtained from the higher heating value of the coal (HHV, J kg^{-1}), which can be measured or estimated from the ultimate analysis with Dulong's formula[18]. The higher heating value is the negative of the heat of reaction (i.e. $HHV = -\Delta h_{reaction}$). Ash effects on the coal heat of formation are included via the experimentally determined HHV. The heat of formation of the coal is determined as the sum of the heats of formation of the products and the higher heating value of the coal:

$$h_{f,c}^o = \sum_{i=1}^{4} v_i h_{f,i}^o + HHV \quad (4)$$

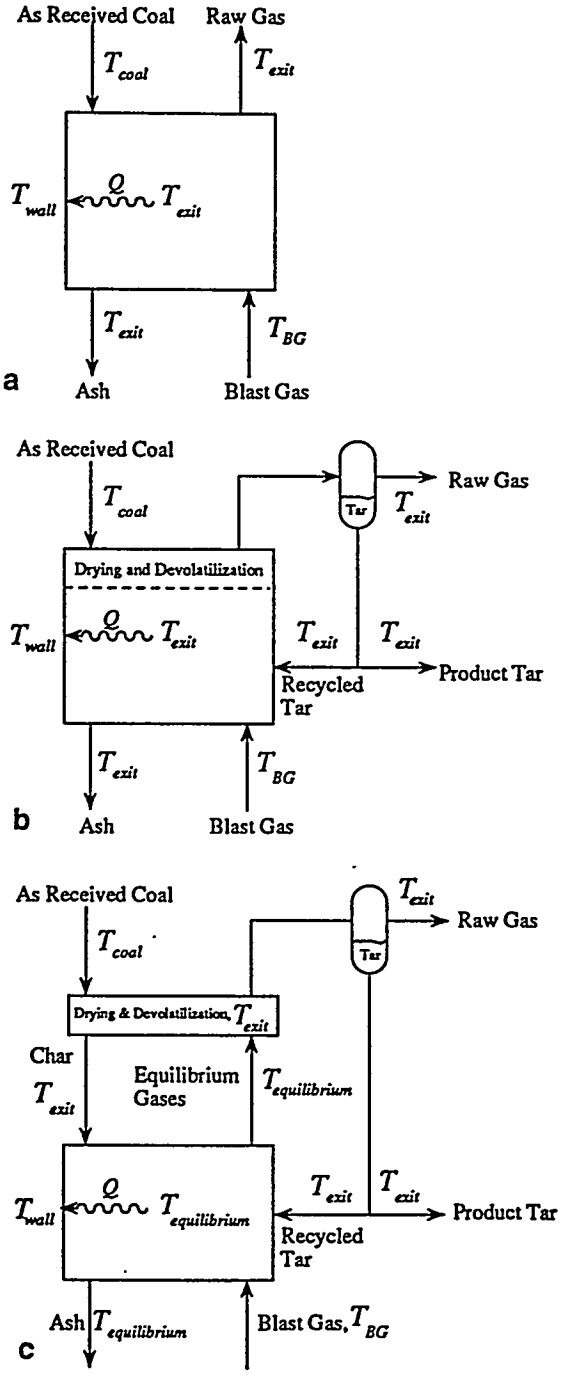

Figure 2 Control volume for (a) one-zone total equilibrium model; (b) one-zone partial equilibrium model; (c) two-zone partial equilibrium model

where v_i represents the stoichiometric coefficient for the ith product given in Equation (3) and i represents the formation of CO_2, H_2O, N_2 and SO_2. Error results in calculating the heat of formation of coal, which is a relatively small number, as the difference of two much larger numbers of limited accuracy[19]. Fortunately, the enthalpy of the feed coal is small in comparison to the feed gas enthalpy for dry-ash, fixed-bed gasifiers and has little influence on the equilibrium calculations.

The sensible enthalpy for the feed coal, h_c^s (J g^{-1}), can be determined using Merrick's enthalpy correlation evaluated at 298.15 K and the coal feed temperature[20].

$$h_c^s = \frac{R}{a}\left[380 g_o\left(\frac{380}{T}\right) + 3600 g_o\left(\frac{1800}{T}\right)\right] \quad (5)$$

$$g_o(z) = \frac{1}{\exp(z) - 1} \quad (6)$$

where R is the gas constant (8314.4 J kmol^{-1} K^{-1}), T is solid temperature (K), 380 and 1800 are characteristic Einstein temperatures and z is a dummy variable representing the ratio of the Einstein temperature and T. The mean atomic weight, a, may be defined as:

$$\frac{1}{a} = \sum_{i=1}^{5} \frac{\Omega_i}{\mu_i} \quad (7)$$

where μ_i and Ω_i represent the atomic weight and the dry ash free mass fraction, respectively, of carbon, hydrogen, oxygen, nitrogen and sulphur.

The specific heat of the ash, Cp_a (J kg^{-1} K^{-1}), can be determined from[20]:

$$Cp_a = 754 + 0.586t \quad (8)$$

where t is the ash temperature (°C). The Kopp–Neumann rule also gives reliable estimates of the ash heat capacity if the various constituents of the ash are known[21]. The heats of formation and sensible enthalpies for the feed gases are found with a generalized chemical equilibrium code[22] which uses polynomial fits of data in the JANAF thermochemical tables[23].

The final term to define in Equation (1) is the heat loss through the reactor wall, Q(W). This quantity can be calculated if the jacket steam and cooling water flow rates and temperatures are known, or by the following equation if the overall heat transfer coefficient, U (W m^{-2} K^{-1}), is known:

$$Q = UA(T_e - T_w) \quad (9)$$

where A is the water wall surface area and T_e and T_w represent the well mixed exit temperature and the wall temperature, respectively. Values for the overall heat transfer coefficient, U, range from 50 to 200 W m^{-2} K^{-1} which is in the forced convection regime. Calculations herein use measured heat loss based on jacket steam and cooling water flow rates.

Gas-phase chemistry

Partial equilibrium exists when certain reactions or species are in chemical equilibrium while other species concentrations are determined by other means such as no reaction, sometimes termed 'frozen'. In other words, partial equilibrium for the mixture is assumed if any species is considered to be out of equilibrium. The species concentration may be found by assuming full equilibrium, by using heterogeneous kinetics (devolatilization, gasification or oxidation), by using homogeneous gas-phase kinetics, or by 'freezing' the species to disallow further reaction. Most fixed-bed models in the literature have assumed the major gaseous species (CO, CO_2, H_2 and H_2O) to be in equilibrium, by the water-gas shift reaction, while neglecting all minor species.

The approach taken herein is to allow major species to be in partial equilibrium or full equilibrium depending on the zone. Minor species are not neglected, but taken to be in equilibrium. Gas temperature is determined by assuming all gas species to be in thermal equilibrium even though chemical equilibrium may not exist. The equilibrium composition and temperature is determined by Gibbs's free energy minimization[22], given total gas-phase static enthalpy, pressure and atomic composition. No account is made for secondary homogeneous chemistry, since little is yet known on this subject.

The gases produced in the hot oxidation/gasification zone are assumed to be in complete equilibrium at the oxidation/gasification zone temperature. However, when these gases are cooled to the temperature of the drying/devolatilization zone, the oxidation/gasification zone gases are not allowed to react further. Also, the coal volatile gases and coal moisture produced in the cooler devolatilization/drying zone can be assumed to be non-reactive in the gas phase. In countercurrent, fixed-bed gasifiers, the assumptions regarding non-reacting species may be justified by the low temperature of the drying/devolatilization zone which prevents further reactions of the volatile gases and coal moisture with the gases produced in the oxidation/gasification zone. However, the two-zone model also has the option to allow all gases in the drying/devolatilization zone to react to equilibrium, or to allow all gases but tar to react to equilibrium.

Devolatilization

Basis. Obtaining accurate coal volatiles yield and composition is important since as much as 40–60% of the dry ash free mass can be lost by devolatilization. Further, devolatilization products are carried off the top of the reactor by the countercurrent gas flow shortly after their release from the coal. Thus, specification of gas product composition depends upon the devolatilization model. The primary difference between the total equilibrium model and the partial equilibrium models is the addition of yield computations for coal volatile matter. Devolatilization is assumed to take place instantaneously with the yield and composition equal to the ultimate volatile yield and composition. Large solid particle residence time, compared to the time required for complete devolatilization, justifies this assumption when estimating fixed-bed effluent compositions.

The ultimate volatile composition, including coal gas, tar and chemically formed water yields, is predicted with a functional group (FG) model[17] and a semi-empirical tar (SET) formation model[24]. The devolatilization model uses coal-general devolatilization parameters. Also, the devolatilization submodel was used in a recently developed one-dimensional model[16].

The devolatilization submodel also predicts the amount and composition of the ultimate char fraction. Dulong's formula is used to calculate the heating value of the char which can be used to calculate the char heat of formation. Merrick's correlations[20] are used to

Table 1 Devolatilization kinetic parameters, functional group compositions, potential tar-forming fractions and ultimate analysis[a]

Functional groups (daf)	Kinetic parameters			Gillette	IL no. 6	KY no. 9	ND Zap	Pitt no. 8	Rose	Utah	Wyodak
	k_i° (s^{-1})	E_i/R (K)	σ_i/R (K)	y_i°	y_i°	y_i°	y_i°	y_i°	y_i°	y_i°	y_i°
CO_2 extra loose	0.81×10^{13}	22500	1500	0.018	0.022	0.000	0.065	0.000	0.035	0.003	0.028
CO_2 loose	0.65×10^{17}	33850	1500	0.053	0.022	0.006	0.300	0.007	0.035	0.007	0.020
CO_2 tight	0.11×10^{16}	38315	2000	0.028	0.030	0.005	0.005	0.005	0.030	0.017	0.021
H_2O loose	0.22×10^{19}	30000	1500	0.031	0.045	0.011	0.061	0.012	0.051	0.025	0.030
H_2O light	0.17×10^{14}	32700	1500	0.031	0.000	0.011	0.033	0.012	0.051	0.020	0.022
CO ether loose	0.14×10^{19}	40000	6000	0.080	0.060	0.050	0.060	0.050	0.055	0.025	0.050
CO ether tight	0.15×10^{16}	40500	1500	0.043	0.063	0.026	0.044	0.021	0.013	0.034	0.055
HCN loose	0.17×10^{14}	30000	1500	0.007	0.100	0.026	0.006	0.009	0.005	0.006	0.001
HCN tight	0.69×10^{13}	42500	4750	0.015	0.016	0.009	0.012	0.023	0.015	0.024	0.018
NH_3	0.12×10^{13}	27300	3000	0.000	0.000	0.000	0.001	0.000	0.001	0.000	0.001
CH_x aliphatic	0.84×10^{15}	30000	1500	0.158	0.081	0.183	0.095	0.207	0.127	0.188	0.152
CH_4 extra loose	0.84×10^{15}	30000	1500	0.000	0.011	0.020	0.000	0.000	0.000	0.000	0.000
CH_4 loose	0.75×10^{14}	30000	2000	0.026	0.011	0.015	0.016	0.020	0.022	0.022	0.017
CH_4 tight	0.34×10^{12}	30000	2000	0.017	0.022	0.015	0.009	0.015	0.012	0.022	0.008
H aromatic	0.10×10^{15}	40500	6000	0.012	0.016	0.012	0.017	0.013	0.013	0.017	0.013
CH_3OH	0.00	NA	NA	0.000	0.000	0.000	0.000	0.000	0.000	0.000	0.000
CO extra tight	0.20×10^{14}	45500	1500	0.031	0.000	0.020	0.090	0.020	0.000	0.040	0.043
C non-volatile	0.00	NA	NA	0.440	0.550	0.562	0.440	0.562	0.520	0.548	0.518
S organic	0.00	NA	NA	0.005	0.038	0.024	0.011	0.024	0.012	0.003	0.004
Total, Σy_i°	NA	NA	NA	1.000	1.000	1.000	1.000	1.000	1.000	1.000	1.000
Tar, x°, entrained	0.85×10^{15}[b]	27700[b]	1500[b]	0.200	0.430	0.430	0.160	0.430	0.160	0.430	0.160
Tar, x°, TGA	NA	NA	NA	NA	NA	NA	0.040	0.110	0.060	NA	NA
Tar, x°, SET 1 atm[a]	NA	NA	NA	0.071	0.116	0.270	0.043	0.270	0.098	0.270	0.160
Tar, x°, SET 25 atm[a]	NA	NA	NA	0.067	0.092	0.168	0.031	0.168	0.082	0.168	0.117
Coal type				Subbit.	Bit.	Bit.	Lig.	Bit.	Subbit.	Bit.	Subbit.
Ultimate analysis (wt% daf)											
C				0.720	0.736	0.817	0.665	0.821	0.724	0.807	0.750
H				0.047	0.047	0.056	0.048	0.056	0.049	0.058	0.054
N				0.012	0.014	0.019	0.011	0.017	0.012	0.016	0.011
O				0.216	0.165	0.084	0.265	0.082	0.203	0.116	0.181
S (organic)				0.005	0.038	0.024	0.011	0.024	0.012	0.003	0.004

[a]NA, data not applicable or not available. Functional group data are from experimental measurements of Solomon and co-workers[17,27,34]. Potential tar-forming fraction from small particle entrained-flow experiments and TGA experiments are from Serio *et al.*[27]. The semi-empirical tar model of Ko *et al.*[24] was used to determine tar-forming fractions at 1 and 25 atm (0.1 and 2.5 MPa, respectively)
[b]Kinetic parameters (k_i°, E/R and σ/R) are for tar formation

calculate the sensible enthalpy of the char. The tar fraction recirculated back to the oxidation/gasification zone is specified. Any recirculated tar is assumed to react to equilibrium with the other gases in this zone. The gases produced in the oxidation/gasification zone, and the coal volatiles and water vapour produced in the devolatilization/drying zone, can be assumed to be either non-reactive or reactive in the devolatilization/drying zone.

Ultimate composition. Dry ash free coal can be divided into various chemical functional groups as discussed by Solomon and Hamblen[25] and includes such species as carboxyl, hydroxyl, ether, etc. (see *Table 1*). The initial fraction of a particular functional group component is represented by y_i° and the sum of the y_i° values equals 1. The fraction of a functional group that can potentially form tar is represented by x°. The initial functional group components, y_i°, and the potential tar-forming fraction, x°, for eight coals are given in *Table 1*. The coal-independent Arrhenius rate parameters for each functional group are also given in *Table 1*.

The evolution of each functional group into the gas is represented by first-order decay, $(d/dt)y_i = -k_i y_i$. The evolution of tar is also described by first-order decay, $(d/dt)x = -k_x x$. Since the Arrhenius rate coefficients, k_i and k_x, are constant under isothermal conditions, y_i and x for volatile functional groups can be determined by integration:

$$y_i = y_i^\circ \exp(-k_i t) \quad \text{and} \quad x = x^\circ \exp(-k_x t)$$

Non-volatile functional group fractions are constant, $y_i = y_i^\circ$.

The fractional amounts of a particular functional group component that remain in the solid phase as char, or evolve as tar or gas, $\omega_{i,c}$, $\omega_{i,t}$ and $\omega_{i,g}$, can be determined by assuming that light gases do not evolve from the tar vapour[16,25]:

$$\omega_{i,c} = (1 - x^\circ + x)y_i \tag{10}$$

$$\omega_{i,t} = (x^\circ y_i^\circ - x y_i)\frac{k_x}{k_i + k_x} \tag{11}$$

$$\omega_{i,g} = (1 - x^\circ)(y_i^\circ - y_i) + \omega_{i,t}\left(\frac{k_i}{k_x}\right) \quad (12)$$

The ultimate volatile composition can then be determined by taking the limit of Equations (10) to (12) as time becomes large and by accounting for the Arrhenius rate constants of non-volatile functional groups being zero, to give:

$$\omega_{i,c}^\infty = \begin{cases} 0 & \text{for volatile functional groups} \\ (1 - x^\circ)y_i^\circ & \text{for non-volatile functional groups} \end{cases} \quad (13)$$

$$\omega_{i,t}^\infty = \begin{cases} x^\circ y_i^\circ\left(\dfrac{k_x}{k_i + k_x}\right) & \text{for volatile functional groups} \\ x^\circ y_i^\circ & \text{for non-volatile functional groups} \end{cases} \quad (14)$$

$$\omega_{i,g}^\infty = \begin{cases} (1-x^\circ)y_i^\circ + x^\circ y_i^\circ\left(\dfrac{k_i}{k_i + k_x}\right) & \text{for volatile functional groups} \\ 0 & \text{for non-volatile functional groups} \end{cases} \quad (15)$$

The ultimate char composition, $\omega_{i,c}^\infty$, predicted by the functional group model, is not a function of temperature when the potential tar-forming fraction, x°, is specified. However, the ultimate tar and gas compositions, $\omega_{i,t}^\infty$ and $\omega_{i,g}^\infty$, are functions of temperature even when x° is specified because of the temperature-dependent Arrhenius rate constants k_i and k_x.

Ultimate yields. The ultimate char, tar and gas yields, ω_c^∞, ω_t^∞, and ω_g^∞, are readily found from Equations (13) to (15) by summing over functional groups:

$$\omega_c^\infty = (1 - x^\circ) \sum_{i=\text{in}} y_i^\circ \quad (16)$$

$$\omega_t^\infty = x^\circ \sum_{i=\text{iv}} \frac{y_i^\circ k_x}{k_i + k_x} + x^\circ \sum_{i=\text{in}} y_i^\circ \quad (17)$$

$$\omega_g^\infty = (1 - x^\circ) \sum_{i=\text{iv}} y_i^\circ + x^\circ \sum_{i=\text{iv}} \frac{y_i^\circ k_i}{k_i + k_x} \quad (18)$$

where the subscripts iv and in refer to volatile and non-volatile functional groups, respectively. The ultimate volatiles yield, ω_v^∞, is by definition a sum of the tar and the gas ultimate yields, ω_t^∞ and ω_g^∞; thus, from Equations (17) and (18):

$$\omega_v^\infty = x^\circ + (1 - x^\circ) \sum_{i=\text{iv}} y_i^\circ \quad (19)$$

Potential tar-forming fraction. The potential tar-forming fraction, x°, represents the maximum possible tar yield. However, competition from light gas evolution prevents maximum tar yield from being realized, as shown in Equations (17) and (18). The potential tar-forming fraction can be: (1) determined from experimental tar yields; (2) estimated from correlated experimental data (e.g. Refs 24, 26, and 27); (3) predicted from simple ultimate yield models (e.g. Ref. 28); or (4) predicted from coal-structure-dependent models (e.g. Ref. 17). The potential tar-forming fraction from Ko *et al.*[24] is calculated from the following equations:

$$x^\circ = 0.01(\alpha + \beta x_{\text{tar}}) \quad (20)$$

$$x_{\text{tar}} = \frac{(\text{number of labile bridges})(\text{abstractable hydrogen})}{(\text{number of cross-linked bridges})} \quad (21)$$

where α and β are pressure-dependent correlations. The number of labile bridges is a function of the aromaticity of the coal; the abstractable hydrogen is determined from the difference in ultimate analysis hydrogen and the hydroxyl functional group content; and the number of cross-linked bridges is determined from the ultimate analysis oxygen and sulphur content. This semi-empirical correlation has been used to correlate tar yields over pressures ranging from vacuum to 9 MPa (~90 atm) for 37 coals ranging from lignites to anthracites[24].

The potential tar-forming fractions determined from entrained-flow experiments, TGA experiments, and estimations based on the semi-empirical tar model of Ko *et al.*[24] at 1 and 25 atm (0.1 and 2.5 MPa, respectively) are shown in *Table 1*. The potential tar-forming fraction is smaller at high pressure due to mass transport effects which are modelled empirically with the SET model. Also, the potential tar-forming fractions obtained from TGA experiments are smaller than the values using the SET model at atmospheric pressure. Mass transport through the coal bed as well as secondary reactions with the hot char may explain the difference. The potential tar-forming fractions determined from entrained-flow experiments are closer to the atmospheric SET results than to the high pressure SET results or to the TGA results. Yet, the measured entrained-flow values are still higher than the atmospheric SET results. The largest difference between the potential tar-forming fraction determined from entrained-flow experiments and the atmospheric SET predictions was for the N. D. Zap lignite, which differs by a factor of 3.7. Corresponding values for Wyodak subbituminous coal were in good agreement. However, all of these estimates were considered inadequate for predicting tar yield for fixed-bed gasifiers, when compared to measured values. For the simulations discussed in this paper, the potential tar-forming fraction was determined from the tar yields reported for commercial scale fixed-bed gasifers. The two-zone model discussed herein was used to determine the potential tar-forming fraction from experimental fixed-bed tar yields. The potential tar-forming fractions obtained from experimental fixed-bed data are closest to the values obtained with the semi-empirical correlation discussed above. However, the values from Ko *et al.*[24] are still higher, as discussed further.

Arrhenius rate constants. A multiple reactions model for each functional group (similar to that of Anthony *et al.*[28]) is used to distribute the Arrhenius rate constants. The total volatile mass production from the *i*th functional group is assumed to be normally distributed to activation energy in the same manner as the total potential volatile mass production at large times. Seven point Gaussian–Legendre quadrature was used to integrate the distributed rate equation[16,29]. Frequency factors, k_i°, mean activation energies, $\bar{E}_i$, and standard deviations of activation energies, σ_i, were obtained from Solomon *et al.*[17] and are given in *Table 1*. The rationale for using the distributed rate

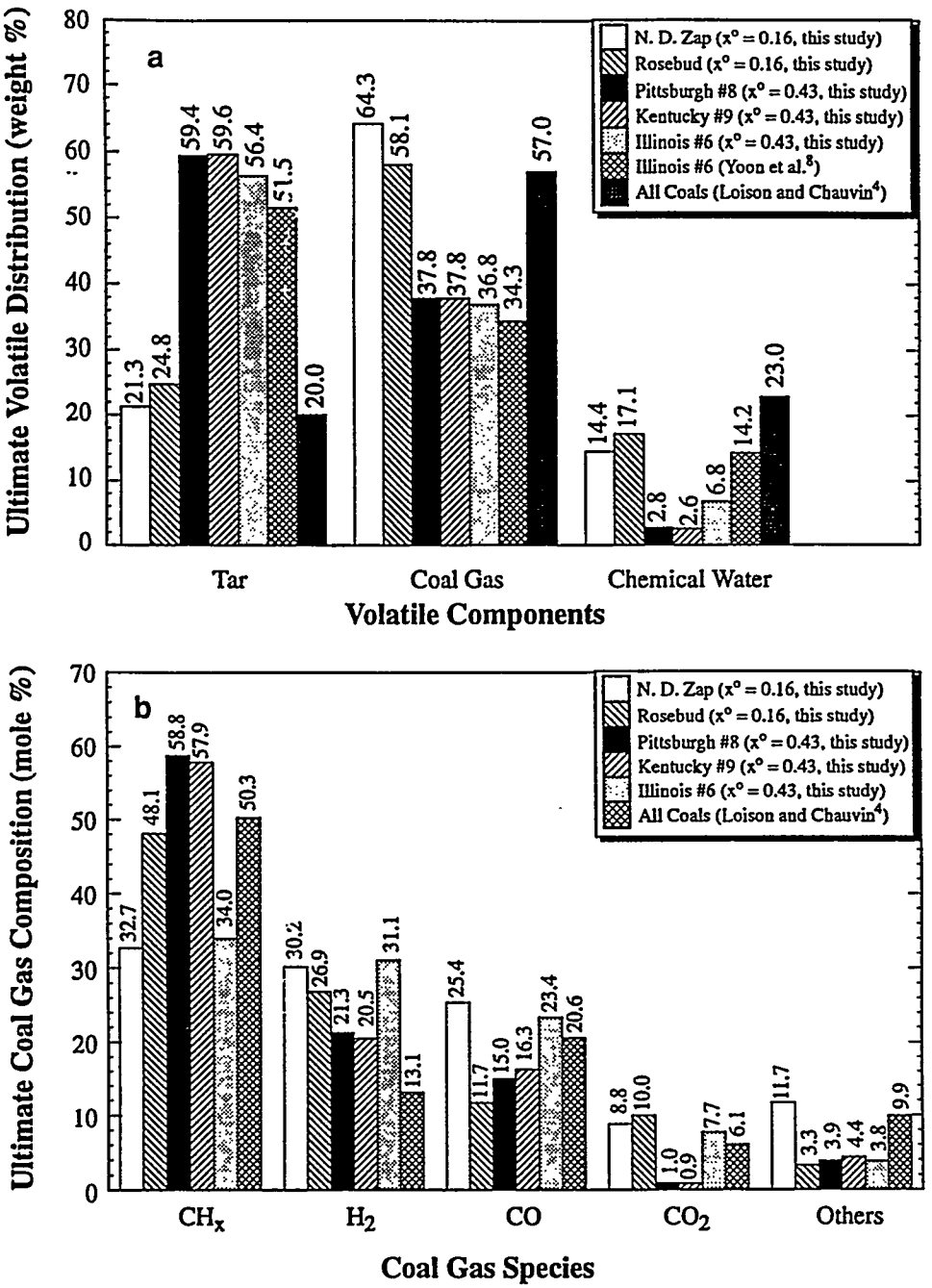

Figure 3 Comparison of predicted (a) ultimate coal volatiles distribution and (b) ultimate coal gas composition for various coals. Temperature is assumed to be 1000 K. Distributions from Loison and Chauvin[4] and Yoon *et al.*[8] at unspecified conditions are also shown

equation was to keep the functional group model consistent with the original development by Solomon *et al.*[17,25].

Oxidation and gasification

Oxidation and gasification are treated by specifying char burnout percentage following devolatilization. Temperature and composition sensitivity to specified burnout is discussed further in the sensitivity analysis. Complete burnout was specified for the predictions herein. Large solid residence times and high oxygen concentrations and temperatures in the oxidation/gasification zone often justify this assumption for fixed beds. If more information is needed on carbon conversion, a one- or two-dimensional model with kinetic rates for oxidation and gasification is required[16].

Freeboard

The freeboard is the void space directly above the coal bed. The sampling point for the offtake gas may be significantly downstream from the top of the coal bed. The two-zone model predicts the temperature at the top of the coal bed which is greater than the temperature at the higher sampling point due to heat loss in the

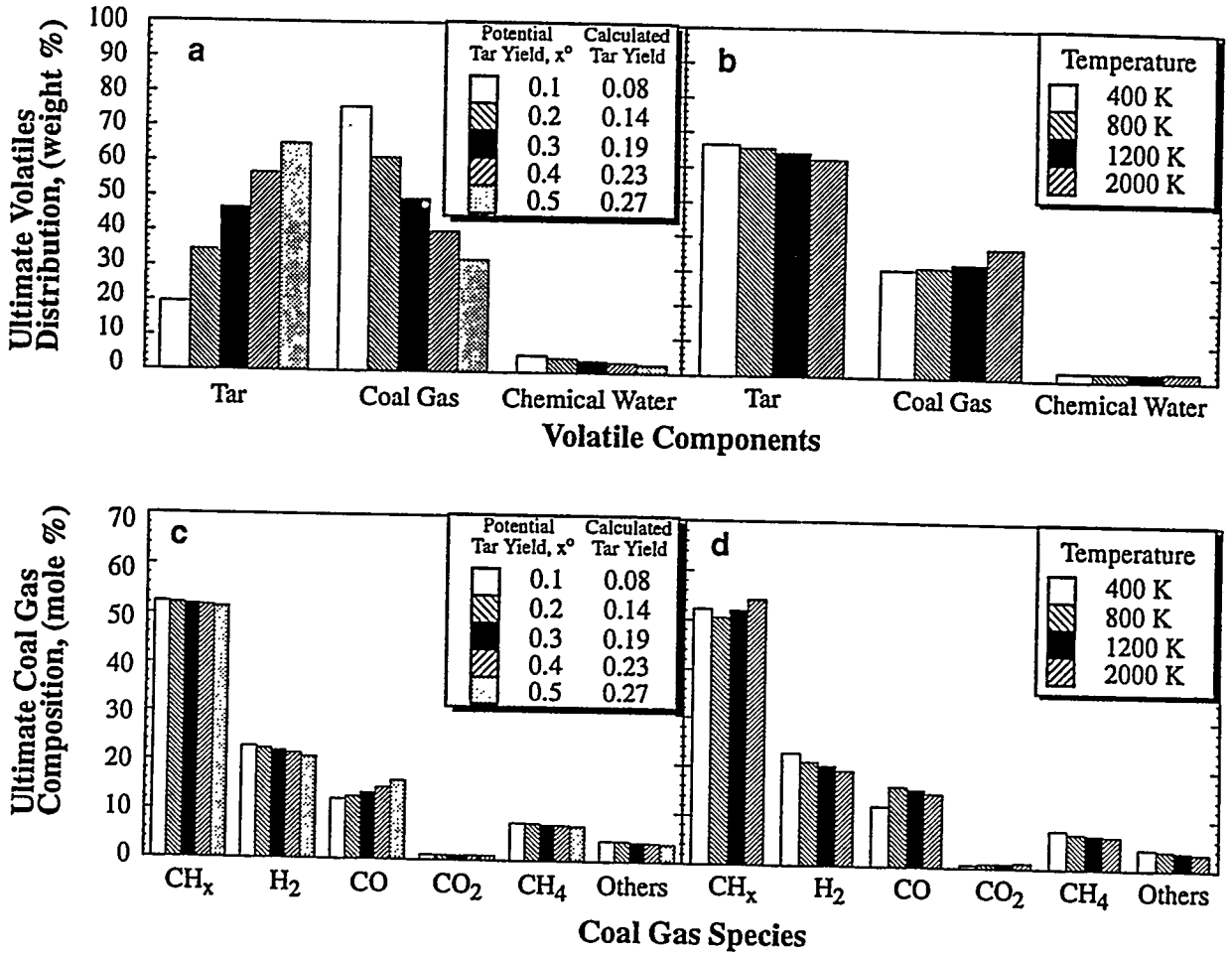

Figure 4 Predicted sensitivity of ultimate coal volatiles distribution to (a) potential tar-forming fraction and (b) temperature. Predicted sensitivity of ultimate coal gas composition to (c) potential tar-forming fraction and (d) temperature. Coal is assumed to be Pittsburgh no. 8. Temperature is assumed to be 1000 K for (a) and (c). Potential tar-forming fraction is assumed to be 0.5 for (b) and (d)

water-cooled freeboard. The freeboard temperature, T_{fg} (K), can be determined by doing a simple energy balance around the freeboard zone and accounting for heat loss in this section, Q_{fb}(W), as follows:

$$T_{fb} = T_{exit} + \frac{Q_{fb}}{\dot{m}_{gas} Cp_{gas}} \quad (22)$$

where T_{exit} is the exit temperature (K), $\dot{m}_{gas}$ is the exit gas mass flow rate (kg s^{-1}) and Cp_{gas} is the exit gas heat capacity (J kg^{-1} K^{-1}). The freeboard temperature is the temperature usually reported in the literature. For the air-fired Wellman-Galusha gasifier, the estimated temperature drop from the bed top to the sampling point is on the order of 10–20 K. Quantitative temperature comparisons were not attempted herein since: (1) the zero-dimensional assumption gives an average temperature in the drying/devolatilization zone which is significantly higher than the exit temperature; (2) there are no temperature measurements immediately above the bed and the freeboard heat loss was not predicted; and (3) measured temperature values are observed to scatter significantly and are lower than might be expected. However, qualitative comparisons are possible and are discussed.

SENSITIVITY ANALYSIS

Effluent product composition

Predicting accurate coal volatiles distribution and coal gas composition is important since as much as 40–60% of the dry ash free mass can be lost by devolatilization. The ultimate distribution of volatile matter into tar, water and coal gas is the final distribution, as time becomes large. The predicted ultimate coal volatile distribution and composition are primarily dependent on coal rank, temperature and potential tar-forming fraction.

Effects of coal rank. Comparisons of predicted ultimate volatile products distribution and ultimate coal gas composition for five of the coals listed in *Table 1* are shown in *Figure 3*. The predictions are from Equations (17), (18) and (19) at 1000 K. The temperature was chosen to be representative of the average temperature in the devolatilization zone. In addition, distributions often reported by other investigators are presented for comparison (e.g. the data of Loison and Chauvin[4], compiled from a wide range of coal types and assumed valid for all coals, as used by Yoon *et al.*[8], Kosky and Floess[3], Cho and Joseph[11], Yu and Denn[12]). The

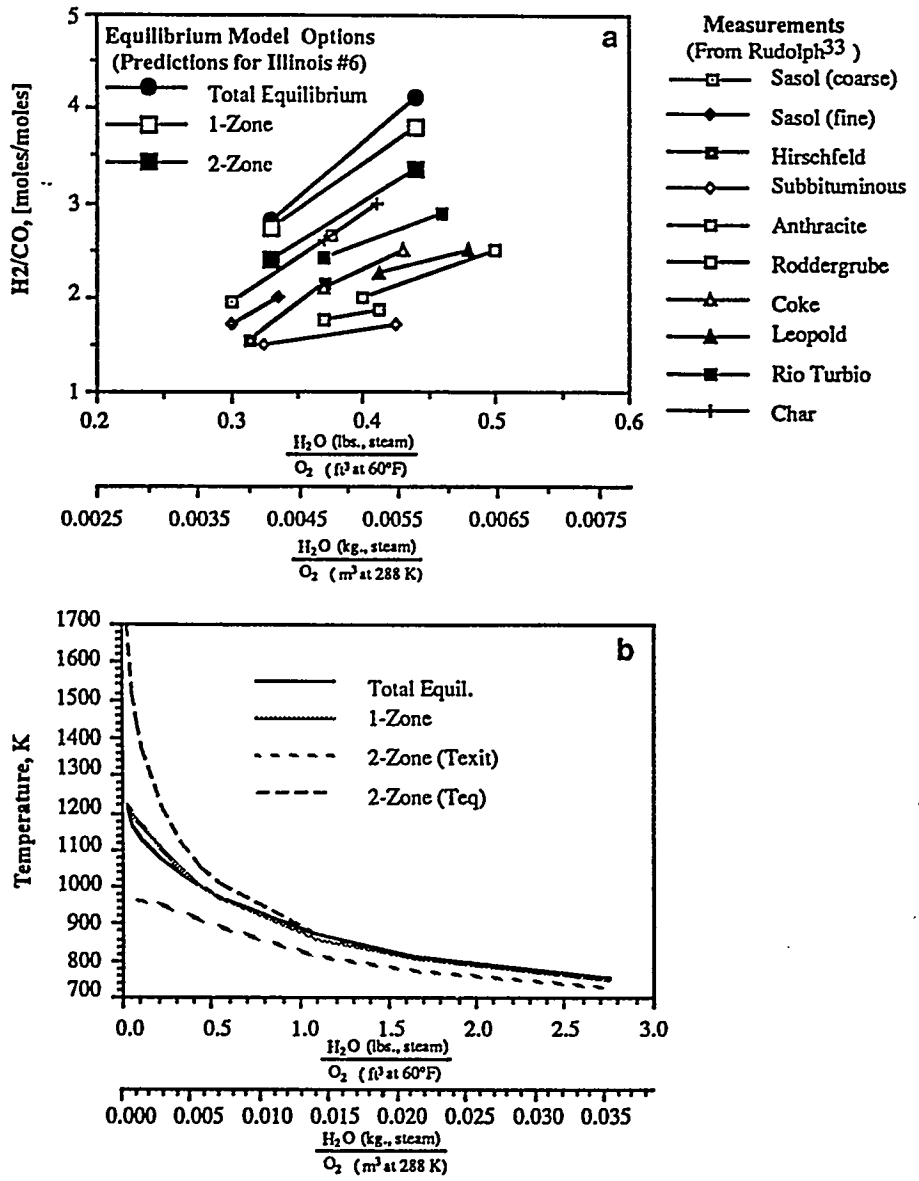

Figure 5 Temperature and composition sensitivity to steam-to-oxygen ratio. (a) Comparison of the effect of steam-to-oxygen feed ratio on hydrogen-to-carbon monoxide ratio for several fixed-bed test results and various equilibrium model options. Comparison is with Rudolph[33]. (b) Predicted temperature sensitivity to steam-to-oxygen ratio for various equilibrium model options using Illinois no. 6 in Westfield gasifier

ultimate volatiles distribution and ultimate coal gas composition strongly depend on coal rank. The lower ultimate tar yields for lignites and subbituminous coals are consistent with expected values. The lower tar yields may be caused by crosslinking associated with CH_4 and CO_2 evolution[17]. The distribution of Loison and Chauvin[4] should not be used for all coal types as is commonly assumed, but the ultimate coal volatiles distribution should be calculated for each coal rank. In fact, Yoon *et al.*[8] assumed a different coal volatiles distribution from the Loison and Chauvin distribution for the Illinois no. 6 case to get reasonable predictions. Yoon's volatiles distribution used for Illinois no. 6 is also given in *Figure 3a*.

Effects of temperature and tar fraction. Predicted sensitivities of ultimate coal volatile products distribution and ultimate coal gas composition for Pittsburgh no. 8 to temperature and potential tar-forming fraction are shown in *Figure 4*. The calculated tar yield is also shown. As much as 27% of the dry ash free mass of the coal may evolve as tar. In a fixed bed, the tar may also crack to form smaller light gas species or repolymerize to form char. The ultimate coal volatiles distribution is more sensitive to the potential tar-forming fraction than to the temperature. Furthermore, the ultimate coal gas composition is not very sensitive to either, which emphasizes the importance of predicting accurate volatile distributions into tar, coal gas and chemical water as opposed to the coal gas composition. The lack of sensitivity of the ultimate coal gas composition to the potential tar-forming fraction and temperature comes from competition between tar evolution and light gas evolution. When the tar rate constant, k_x, is significantly

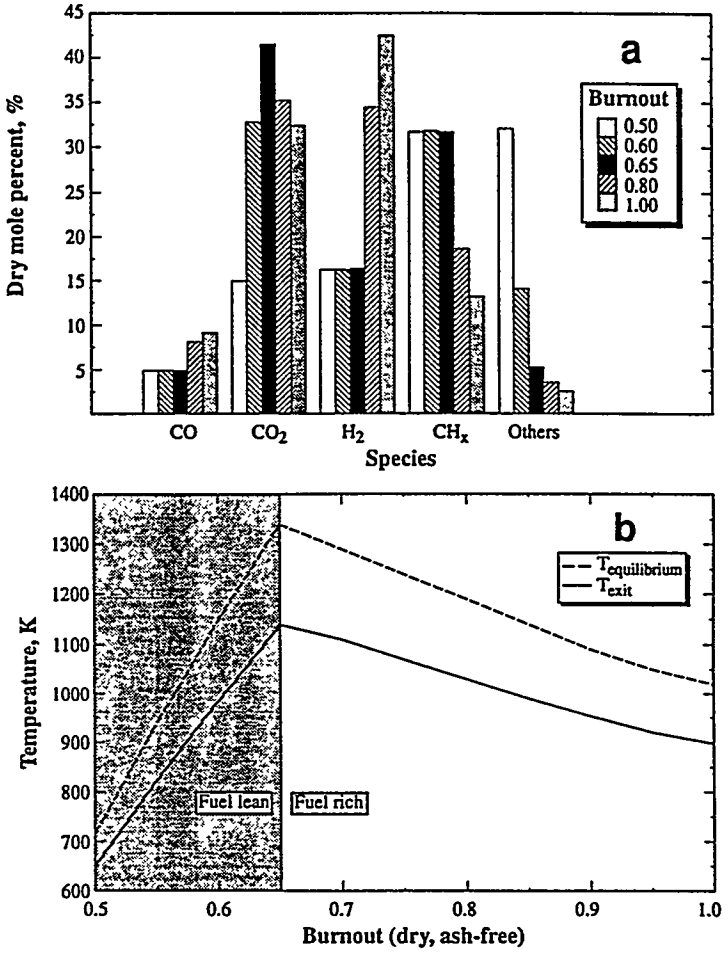

Figure 6 Influence of coal burnout on (a) effluent gas compositions and (b) equilibrium and exit temperature. Input parameters are from *Table 3* for gasification of Illinois no. 6 bituminous coal

smaller than the light gas rate constant, k_l, then the sensitivity of the ultimate coal gas composition to both temperature and potential tar-forming fraction is small, as seen from Equation (15). This conclusion is also supported by experimental data[30–32].

Effects of steam/oxygen ratio. The effects of the steam-to-oxygen ratio on the exit molar ratio of hydrogen-to-carbon monoxide are shown in *Figure 5a*. Data from Rudolph[33] are also shown for comparison. The operating conditions for the data of Rudolph were not given. Thus, quantitative agreement is not expected since the coals and operating conditions may not correspond. Qualitatively, all of the equilibrium model options predict the correct trend. While the two-zone model gives better quantitative values for the hydrogen-to-carbon monoxide ratio, the predicted values are higher than the measurements reported by Rudolph.

An implicit assumption in the ultimate volatiles prediction is that the composition of the tar is similar to that of the parent coal. This is a good assumption for high heating rates associated with entrained-bed reactors. However, Khan[26] has recently shown an increase in hydrogen-to-carbon ratio in tar derived from fixed-bed reactors compared to entrained-bed reactors. The higher hydrogen content in the tar may be caused by increased secondary reactions due to increased residence time or prolonged contact with char. The results of the sensitivity analysis and comparisons to measurements show that gaseous hydrogen is over-predicted. A possible explanation is the implicit assumption regarding the tar composition.

Effluent temperature

Effects of steam/oxygen ratio. The feed steam-to-oxygen ratio is often used to control ash temperature in a dry-ash, fixed-bed gasifier. Also, the steam-to-oxygen ratio affects the effluent temperature. The effects of the steam-to-oxygen ratio on the exit temperature using the three equilibrium model options for Illinois no. 6 coal, gasified in a commercial-scale Lurgi gasifier, are given in *Figure 5b*. As expected, the exit temperature decreases with increasing steam flow rate. The temperature of the equilibrium zone predicted by the two-zone model is also shown. The one-zone exit temperatures are bounded by the two-zone exit and equilibrium temperatures. As the steam flow rate is increased, the differences among model options decrease.

Effects of percentage burnout. The influence of burnout on the dry molar gas composition and temperature is shown in *Figure 6*. Burnout is defined as the weight

fraction (daf) of the organic matter in the raw coal that has reacted. The input conditions for *Figure 6* are for Illinois no. 6 gasified at Westfield, UK. As burnout declines, CO and H_2 steadily decrease and hydrocarbons increase while CO_2 reaches a maximum at 65% burnout. Temperature also reaches a maximum at this burnout level, where the gas-phase concentration is nearly stoichiometric. For fuel-rich operation, increasing burnout in the gasification/oxidation zone causes temperature to decrease. However, if burnout is small, the gas-phase becomes oxygen rich and increasing burnout causes the temperature of the oxidation zone to increase.

EXPERIMENTAL

Thirteen cases have been simulated by the two-zone model. The ultimate analyses of coals for the test cases were performed several years ago and do not correspond exactly to the ultimate analysis of the eight coals of similar rank with measured functional groups as listed in *Table 1*. The functional group composition must be consistent with the ultimate analysis to maintain elemental continuity. Both the measured ultimate analysis for the test coals (*Table 2*) and measured functional group compositions from similar coals (*Table 1*) were used to estimate the functional group composition of the test coals based on the method of Serio[34]. Functional groups with the highest experimental uncertainty were used to balance functional group compositions with the ultimate analysis. For example, the amount of CO-tight is based on the amount of leftover unspecified oxygen. Increasing the oxygen content of the coal will increase the amount of CO in this pool. The method of detailed chemical characterization of the coals is given by Hobbs[16]. *Table 2* lists the recommended values of the functional group composition and corresponding ultimate analysis for each of the 13 coals.

Lurgi data

Detailed experimental data on three high volatile bituminous coals and one subbituminous coal gasified in a high pressure, dry-ash, fixed-bed Lurgi gasifier in Westfield, UK, include flare-gas analysis and gas offtake temperature[35,36]. The four coals are Illinois no. 6 (greatest reserve for Eastern caking coals), Illinois no. 5 (equivalent to Kentucky no. 9), Pittsburgh no. 8 (major Eastern coal with a high swelling index), and Rosebud subbituminous (from Southern Montana). The properties of gasified Illinois no. 5 coal are taken to be those of

Table 2 Recommended functional group compositions, calculated potential tar-forming fractions, and ultimate analysis[a]

	Lurgi cases				Wellman-Galusha cases								
Functional groups (daf)	IL no. 6 y_i°	IL no. 5 y_i°	Pitt no. 8 y_i°	Rose y_i°	Absal y_i°	Benton y_i°	Elk y_i°	IL no. 6 y_i°	Jetson y_i°	Kemer y_i°	Leucite y_i°	Rose y_i°	Utah y_i°
CO_2 extra loose	0.022	0.000	0.000	0.035	0.028	0.065	0.000	0.022	0.000	0.028	0.028	0.035	0.003
CO_2 loose	0.022	0.006	0.007	0.035	0.020	0.030	0.006	0.022	0.006	0.020	0.020	0.035	0.007
CO_2 tight	0.030	0.005	0.005	0.030	0.021	0.005	0.005	0.030	0.005	0.021	0.021	0.030	0.017
H_2O loose	0.015	0.011	0.000	0.000	0.030	0.000	0.011	0.016	0.011	0.027	0.024	0.000	0.025
H_2O tight	0.000	0.011	0.004	0.051	0.022	0.027	0.011	0.000	0.011	0.022	0.022	0.040	0.020
CO ether loose	0.060	0.050	0.050	0.055	0.050	0.060	0.050	0.060	0.050	0.050	0.050	0.055	0.025
CO ether tight	0.000	0.037	0.000	0.000	0.043	0.000	0.044	0.000	0.059	0.000	0.000	0.000	0.036
HCN loose	0.013	0.021	0.007	0.010	0.000	0.005	0.022	0.011	0.025	0.003	0.016	0.005	0.000
HCN tight	0.016	0.009	0.023	0.015	0.013	0.013	0.009	0.016	0.009	0.018	0.018	0.015	0.022
NH_3	0.000	0.000	0.000	0.001	0.001	0.001	0.000	0.000	0.000	0.001	0.001	0.001	0.000
CH_x aliphatic	0.176	0.164	0.245	0.182	0.169	0.212	0.185	0.169	0.161	0.201	0.195	0.202	0.189
CH_4 extra loose	0.011	0.020	0.000	0.000	0.000	0.000	0.020	0.011	0.020	0.000	0.000	0.000	0.000
CH_4 loose	0.011	0.015	0.020	0.022	0.017	0.017	0.015	0.011	0.015	0.017	0.017	0.022	0.022
CH_4 tight	0.022	0.015	0.015	0.012	0.008	0.009	0.015	0.022	0.015	0.008	0.008	0.012	0.022
H aromatic	0.016	0.012	0.013	0.013	0.013	0.017	0.012	0.016	0.012	0.013	0.013	0.013	0.017
CH_3OH	0.000	0.000	0.000	0.000	0.000	0.000	0.000	0.000	0.000	0.000	0.000	0.000	0.000
CO extra tight	0.000	0.020	0.020	0.000	0.043	0.090	0.020	0.000	0.020	0.043	0.043	0.000	0.040
C non-volatile	0.552	0.565	0.562	0.522	0.518	0.440	0.565	0.552	0.565	0.518	0.518	0.522	0.548
S organic	0.035	0.039	0.029	0.017	0.004	0.009	0.009	0.042	0.016	0.010	0.006	0.013	0.006
Total	1.001	1.000	1.000	1.000	1.000	1.000	0.999	1.000	1.000	1.000	1.000	1.000	0.999
Calculated $x^{\circ a}$	0.177	0.168	0.168	0.110	0.137	0.227	0.270	0.270	0.222	0.219	0.167	0.150	0.270
Source coal for y_i°	IL no. 6	KY no. 9	Pitt no. 8	Rose	Wyo	Zap	KY no. 9	IL no. 6	KY no. 9	Wyo	Wyo	Rose	Utah
Coal type	Bit.	Bit.	Bit.	Subbit.	Subbit.	Lig.	Bit.	Bit.	Bit.	Subbit.	Subbit.	Subbit.	Bit.
Ultimate analysis (wt% daf)													
C	0.795	0.802	0.846	0.771	0.763	0.737	0.825	0.785	0.814	0.775	0.781	0.787	0.803
H	0.054	0.054	0.058	0.049	0.051	0.062	0.057	0.057	0.051	0.056	0.050	0.049	0.062
N	0.015	0.015	0.016	0.014	0.008	0.010	0.016	0.014	0.018	0.012	0.019	0.011	0.012
O	0.101	0.089	0.053	0.150	0.174	0.182	0.093	0.102	0.102	0.147	0.144	0.140	0.117
S (organic)	0.035	0.039	0.029	0.017	0.004	0.009	0.009	0.042	0.016	0.010	0.006	0.013	0.006

[a]Functional group compositions from *Table 1* were adjusted to match reported ultimate analysis using the criterion discussed by Hobbs[16]. The semi-empirical tar correlation of Ko *et al.*[24] was used to calculate x° at pressures listed in *Tables 3* and *4*

Table 3 Operating parameters and yield data for four coals in Lurgi gasifier simulations

	Illinois no. 6 (Bituminous)	Illinois no. 5[a] (Bituminous)	Pittsburgh no. 8 (Bituminous)	Rosebud (Subbituminous)
Proximate analysis (wt%)				
Ash	9.1	8.1	7.7	9.7
Fixed carbon	46.0	44.7	50.3	36.4
Moisture	10.2	11.9	4.6	24.7
Volatile	34.7	35.2	37.4	29.2
Ultimate analysis (wt%)				
Carbon	79.5	80.2	84.6	77.1
Hydrogen	5.4	5.4	5.8	4.9
Nitrogen	1.5	1.5	1.6	1.4
Sulphur	3.5	3.9	2.9	1.7
Oxygen	10.1	8.9	5.3	15.0
Operating parameters				
Chamber inside diameter (m)	2.74	2.74	2.74	2.74
Chamber length (m)	3.05	3.05	3.05	3.05
Chamber pressure (kPa)	2410	2450	2510	2560
Inlet coal temperature (K)	298	298	298	298
Feed gas temperature (K)	644	644	644	644
Wall temperature (K)	438	438	496	498
Coal mass flow (kg s^{-1})	1.67	1.80	1.02	2.23
Oxygen mass flow (kg s^{-1})	0.81	0.88	0.63	0.58
Steam mass flow (kg s^{-1})	4.20	4.04	3.29	2.80
Jacket steam mass flow (kg s^{-1})	0.89	0.73	0.66	0.31
Wall heat loss (MW)[b]	2.40	1.97	1.78	0.836
Predicted[c] T_{exit}, T_{equil} (K)	898, 1020	941, 1100	1040, 1110	728, 1020
Measured[d] T_{fb} (K)	863–895	879–908	911–928	635–664
x^o obtained from measured tar[e]	0.106	0.132	0.065	0.128
Measured tar data[f]				
Product tar (kg s^{-1})	0.070	0.107	0.054	0.123
Recycle tar (kg s^{-1})	0.058	0.068	0.000	0.046
Total tar (kg s^{-1})	0.128	0.175	0.054	0.169
Predicted dry gas yield (kg s^{-1})	3.13	3.26	2.07	2.92
Measured dry gas yield (kg s^{-1})	2.99	3.26	2.13	2.91
Predicted water yield (kg s^{-1})	3.39	3.28	2.74	2.39
Measured water yield (kg s^{-1})	3.53	3.18	2.64	2.18
Predicted CO yield (kg s^{-1})	0.392	0.605	0.262	0.487
Measured CO yield (kg s^{-1})	0.694	0.772	0.484	0.608
Predicted H_2 yield (kg s^{-1})	0.131	0.132	0.077	0.114
Measured H_2 yield (kg s^{-1})	0.113	0.122	0.081	0.119

[a]Illinois no. 5 is reported to be from the same basin as Kentucky no. 9, and they are taken to be equivalent coals
[b]Calculated from jacket steam flow rate (cooling water losses not reported)
[c]Predictions are from the two-zone model with light gases held out of equilibrium in the drying and devolatilization zone
[d]Measurements are from ref. 35
[e]Values obtained using the two-zone model to match measured tar data
[f]Values obtained with the two-zone model using the x^o value above

Kentucky no. 9 coal in *Table 1* since the two coals are reportedly from the same basin. The Illinois no. 6 coal has been used for comparison with predictions from several fixed-bed models (e.g. Refs 3, 8, 11, 12 and 37). Operational data for all four Lurgi cases are given in *Table 3*.

Wellman-Galusha data

The most extensive set of fixed-bed data was reported by Thimsen *et al.*[38]. These data have been compiled recently by Thimsen and Maurer[39]. Data for 17 coals (bituminous, subbituminous and lignite) peat and coke were reported. The data include gasifier operating conditions, coal properties, tar and water yield, ash and dust data, and gas composition. Some profile data for temperature and pressure were also reported as discussed further by Hobbs[16]. Of the 17 gasified coals, nine coals were chosen for simulation based on how well the coal gasified during the experimental test. The simulated coals are Absaloka/Robinson subbituminous C (from Powder River Basin, Montana), Benton lignite (from Arkansas), Elkhorn high volatile A bituminous (from Eastern Kentucky), Illinois no. 6 high volatile C bituminous (from the Illinois Basin), Jetson high volatile B bituminous (mined in Kentucky's Illinois Basin), Kemmerer subbituminous B (from Southwest Wyoming), Leucite Hills subbituminous A (from Sweetwater County, Wyoming), Rosebud subbituminous B (from the

Table 4 Operating parameters and yield data for nine coals in Wellman-Galusha gasifier simulations

	Absaloka (Subbitum.)	Benton (Lignite)	Elkhorn (Bituminous)	Illinois no. 6 (Bituminous)	Jetson (Bituminous)	Kemmerer (Subbitum.)	Leucite (Subbitum.)	Rosebud (Subbitum.)	Utah B.C. (Bituminous)
Proximate analysis (wt%)									
Ash	6.3	6.4	4.7	9.3	4.3	5.7	9.0	11.8	11.1
Fixed carbon	40.7	25.9	53.7	45.1	49.5	42.4	44.9	40.1	43.9
Moisture	23.5	32.8	4.6	10.3	6.3	16.8	17.4	21.3	6.1
Volatile	29.6	34.9	36.9	35.3	39.9	35.1	28.8	26.8	38.9
Ultimate analysis (wt%)									
Carbon	76.3	73.7	82.5	78.5	81.4	77.5	78.1	78.7	80.3
Hydrogen	5.1	6.2	5.7	5.7	5.1	5.6	5.0	4.9	6.2
Nitrogen	0.8	1.0	1.6	1.4	1.8	1.2	1.9	1.1	1.2
Sulphur	0.4	0.9	0.9	4.2	1.6	1.0	0.6	1.3	0.6
Oxygen	17.4	18.2	9.3	10.2	10.2	14.7	14.4	14.0	11.7
Operating parameters									
Chamber diameter (m)	1.98	1.98	1.98	1.98	1.98	1.98	1.98	1.98	1.98
Chamber length (m)	1.90	1.90	1.90	1.90	1.90	1.90	1.90	1.90	1.90
Chamber pressure (kPa)	101.3	101.3	101.3	101.3	101.3	101.3	101.3	101.3	101.3
Inlet coal temperature (K)	298	298	298	298	298	298	298	298	298
Feed gas temperature (K)	332	340	331	335	300	332	334	336	335
Wall temperature (K)	310	310	310	310	310	310	310	310	310
Coal mass flow ($kg\ s^{-1}$)	0.4201	0.7491	0.3243	0.3178	0.3524	0.2844	0.2928	0.1790	0.3373
Air mass flow ($kg\ s^{-1}$)	0.7637	0.9310	0.7889	0.7451	0.9481	0.5734	0.5323	0.3350	0.6730
Steam mass flow ($kg\ s^{-1}$)	0.1143	0.2312	0.1128	0.1347	0.1562	0.0881	0.0883	0.0500	0.1187
Jacket steam mass flow ($kg\ s^{-1}$)	0.0034	0.0510	0.0082	0.1257	0.1339	0.0030	0.0620	0.0174	0.0261
Wall heat loss (jacket steam) (MW)[a]	0.1554	0.2258	0.2602	0.6049	0.4159	0.1672	0.2907	0.1694	0.2947
Predicted[b] T_{exit}, T_{equil} (K)	872, 1360	723, 1340	1140, 1420	1000, 1260	1150, 1440	1010, 1400	801, 1120	929, 1310	980, 1230
Measured[c] T_{fb} (K)	579	432	711	729	699	646	544	501	699
x^o obtained measured tar[d]	0.0690	0.2093	0.1726	0.1910	0.1560	0.1175	0.0775	0.0730	0.1670
Measured tar yield ($kg\ s^{-1}$)[e]	0.0181	0.0832	0.0464	0.0435	0.0451	0.0230	0.0149	0.0079	0.0435
Predicted dry gas yield ($kg\ s^{-1}$)	1.09	1.39	1.09	1.01	1.28	0.807	0.784	0.470	0.970
Measured dry gas yield ($kg\ s^{-1}$)	1.09	1.39	1.10	1.00	1.25	0.813	0.780	0.469	0.962
Prediced water yield ($kg\ s^{-1}$)	0.159	0.390	0.074	0.114	0.120	0.0995	0.0876	0.0652	0.0779
Measured water yield ($kg\ s^{-1}$)	0.147	0.441	0.065	0.107	0.094	0.103	0.090	0.0607	0.0863
Predicted CO yield ($kg\ s^{-1}$)	0.286	0.271	0.258	0.155	0.253	0.185	0.189	0.0982	0.233
Measured CO yield ($kg\ s^{-1}$)	0.398	0.373	0.358	0.264	0.360	0.278	0.280	0.164	0.305
Predicted H_2 yield ($kg\ s^{-1}$)	0.0112	0.0167	0.0095	0.0092	0.0102	0.0076	0.0093	0.0044	0.0120
Measured H_2 yield ($kg\ s^{-1}$)	0.0166	0.0236	0.0167	0.0127	0.0181	0.0111	0.121	0.0064	0.0149
Reference 38[f]	12, 53	10, 55	9, 71	8, 68	2, 68	14, 49	4, 59	15, 50	13, 57

[a]Calculated from jacket steam and cooling water heat loss
[b]Predictions are from the two-zone model with light gases held out of equilibrium in the drying and devolatilization zone
[c]Measurements are from ref. 38
[d]Values obtained using the two-zone model to match measured tar data
[e]Values obtained with the two-zone model using the x^o value above
[f]Volume (bold) and page number

Powder River Basin, Montana), and Utah Blind Canyon high volatile B bituminous (from Central Utah). The recommended functional group compositions and corresponding ultimate analysis for each of these nine coals are listed in *Table 2*. Operational data for all nine Wellman-Galusha cases are given in *Table 4*.

MODEL COMPARISONS WITH DATA

Lurgi effluent predictions

Measured and predicted effluent compositions are shown in *Figures 7* and *8* for Illinois no. 6, Pittsburgh no. 8, Illinois no. 5, and Montana Rosebud coals. Measured and predicted tar yields and temperatures are given in *Table 3*. Complete burnout was assumed for all of the predictions in *Figures 7* and *8*. Heat loss was calculated based on the jacket steam flow rate; the potential tar-forming fraction, x^o, was determined from experimental tar yields. For the Lurgi cases, a portion of the tar was recycled back to the reactor and injected into the top of the reactor. For the simulations, the recycled tar fraction was chosen to match the measured tar recycle rate[35].

Tar. The predicted tar-forming fractions using the correlation of Ko *et al.*[24] are high for the three bituminous coals and slightly low for the subbituminous coal when compared to those obtained from experimental

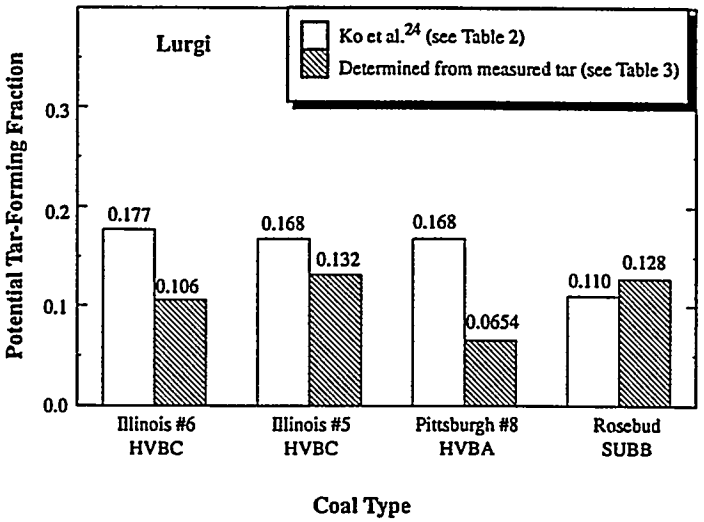

Figure 7 Potential tar-forming fractions calculated from the semi-empirical tar model of Ko *et al.*[24] and determined from experimental tar data[35]

data (see *Figure 7*). The correlation of Ko *et al.*[24] is reportedly good for coal particles smaller than 500 μm. Particle size effects may account for the observed discrepancy. More rigorous methods for tar prediction that depend on coal structure are being developed by Solomon *et al.*[17,40], Grant *et al.*[41] and Niksa[42].

Gas compositions. The measured effluent compositions and those predicted from the total equilibrium, one-zone partial equilibrium, and two-zone partial equilibrium models are shown in *Figure 8*. Both partial equilibrium models assume that the gases produced during drying and devolatilization are non-reactive. The Illinois no. 6 case also shows predictions from Yoon *et al.*'s[8] one-dimensional model, which are probably the best predictions of effluent composition in the literature. The two-zone model predictions are as good as these predictions and better than the one-zone model predictions. The predicted CH_x concentrations are high compared to measured values. The measured CH_x group was reported as CH_4. The predicted CH_x group consists of both CH_4 and other CH_x species which account for leftover aliphatic carbon and hydrogen in the functional group compositions. Predicted carbon monoxide concentrations for both one-zone models are low, although the partial equilibrium model predictions are closer to measured values. Carbon monoxide predictions from the two-zone model are closer to measured values. Other species are also predicted more closely to measured values with the two-zone partial equilibrium model.

Temperatures. Predicted exit temperatures using the partial equilibrium model, given in *Table 3*, were higher than the total equilibrium predictions for the bituminous coals. Since the gas phase exiting the reactor is fuel rich, separating tar out from the light gas species causes the gas mixture to become more fuel lean, thereby causing the exit temperature to increase slightly. This effect was more pronounced when comparing the total equilibrium model results to the two-zone partial equilibrium model.

The most interesting results are the Rosebud predictions. The one-zone models did not give reasonable exit temperature predictions or exit composition predictions for the Rosebud subbituminous coal case (see *Table 3* and *Figure 8*). The exit temperatures for the Rosebud one-zone equilibrium predictions were about 100 K higher than the two-zone model predictions. The energy required to dry the coal and heat up the feed coal causes the temperature in the drying/devolatilization zone to be lower. The predicted compositions for the Rosebud case with the two-zone partial equilibrium model are in close agreement with measured compositions. The improved agreement obtained by using the two-zone partial equilibrium model is attributed partially to dividing the process into two zones and also to using partial equilibrium in the gas phase rather than allowing the species to react to complete equilibrium.

Wellman-Galusha effluent predictions

Measured and predicted tar fractions and effluent compositions are shown in *Figures 9–11* for the nine coals. Predicted exit temperature and predicted equilibrium temperatures are given in *Table 4*. Complete burnout was assumed for all of the predictions in *Figures 9–11*. The heat loss was calculated from the jacket steam and cooling water flow rate; the potential tar-forming fraction, x°, was determined from experimental tar yields. For the Wellman-Galusha cases, tar was not recycled back to the reactor[38].

Tar. The potential tar-forming fractions for the Wellman-Galusha cases calculated with the correlation of Ko *et al.*[24] are compared with values determined from measurements in *Figure 9*. This correlation gives consistently high tar values for the Wellman-Galusha cases, although the trends seem to be predicted correctly. Quantifying tar yields from fixed-bed gasifier product gas streams is difficult. Liquid loadings are often underreported due to difficulties in collecting liquid droplets smaller than 1 μm in diameter[39].

Gas compositions. Measured effluent gas compositions from the atmospheric, air-blown Wellman-Galusha gasifier are shown in *Figures 10* and *11* for the nine coals with results from two sets of model predictions: (1) all gases in the drying and devolatilization zone are

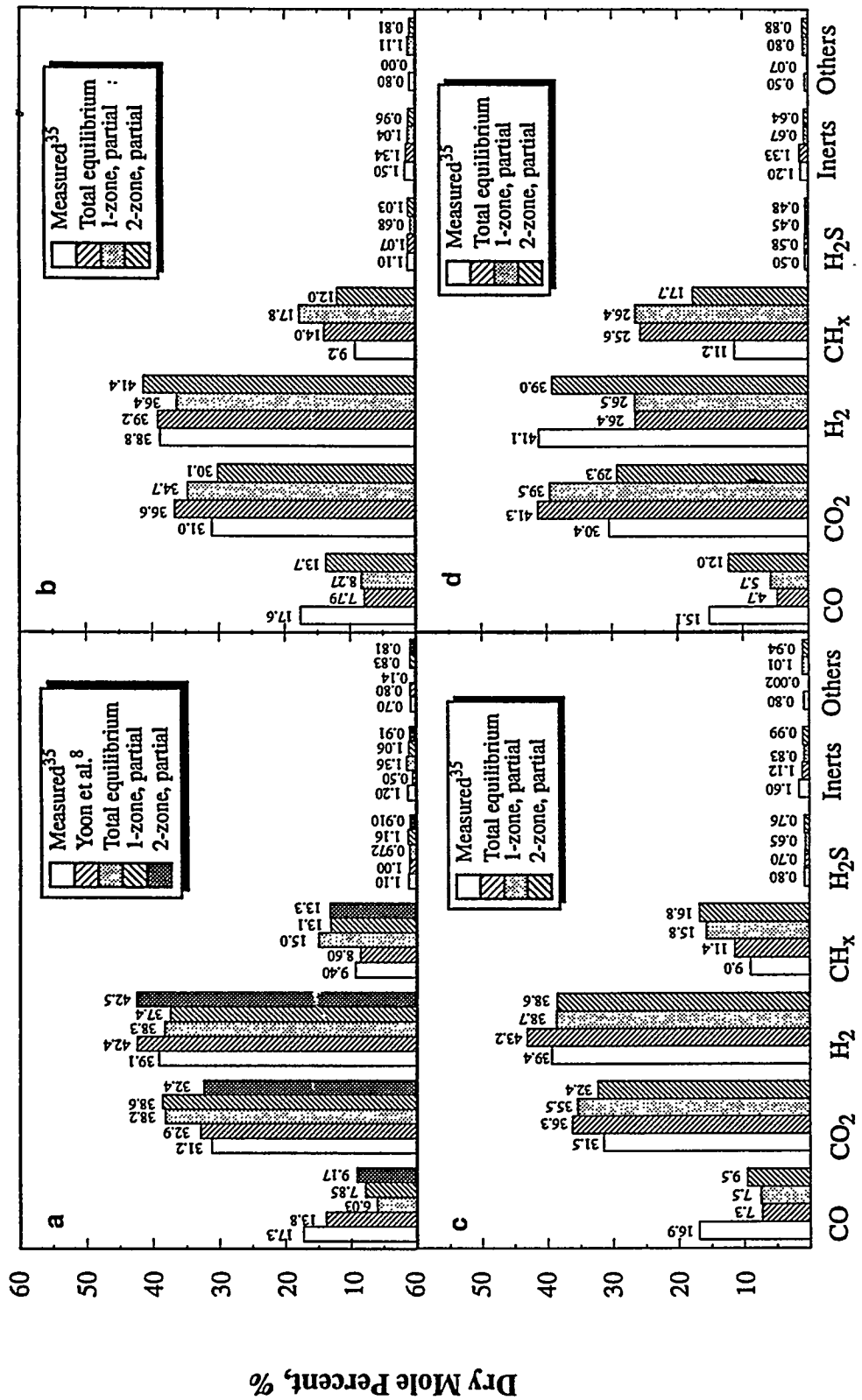

Figure 8 Predicted and measured effluent gas composition for Westfield Lurgi gasifier tests using coals: (a) Illinois no. 6; (b) Illinois no. 5; (c) Pittsburgh no. 8; (d) Montana Rosebud. Measurements are from Elgin and Perks[35]. Input parameters are from *Table 3*

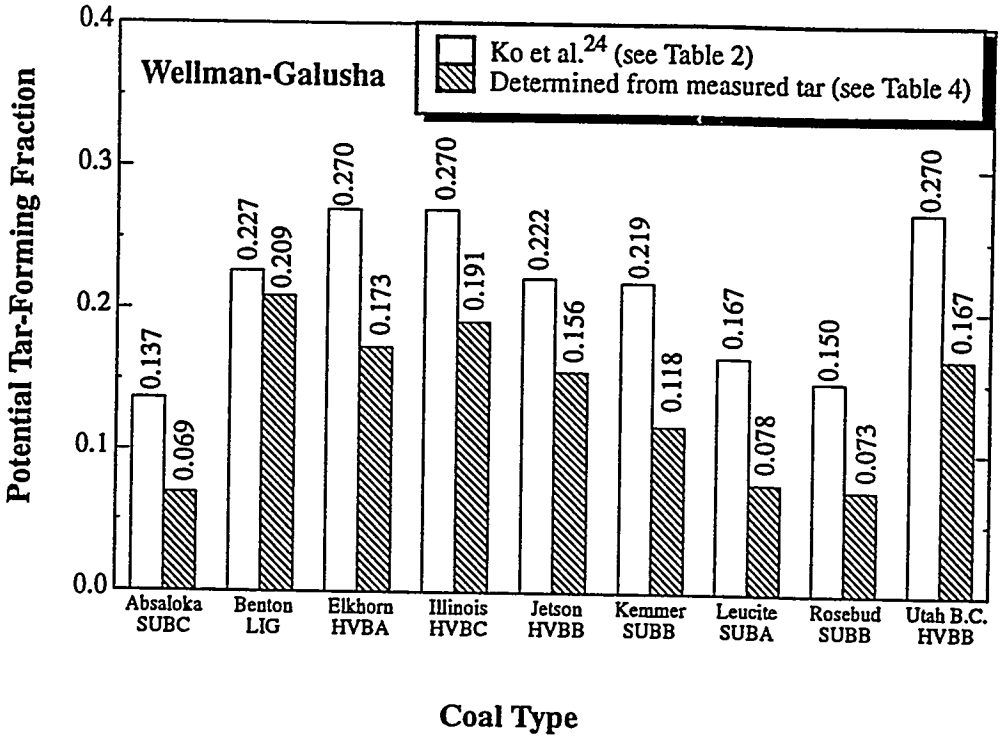

Figure 9 Potential tar-forming fractions calculated from the semi-empirical tar model of Ko *et al.*[24] and determined from experimental tar data[38]

non-reactive; and (2) all gases in the drying and devolatilization zone, except tar, are in chemical equilibrium. In general, predictions using either gas-phase assumption are acceptable; however, the assumption of non-reactive gases may give better results for low rank coals. For example, all of the subbituminous and lignite cases which assume complete equilibrium, predict high CO_2, low CO, and high H_2 effluent concentrations in comparison to the data. These concentration differences may be attributed to higher oxygen content in the lower rank coals. Also, the lower rank coals contain more moisture which results in lower exit temperatures favouring partial equilibrium.

Yields

Comparisons of predicted and measured dry gas yields, water yields, CO yields and H_2 yields are shown in *Tables 3* and *4*. In general, predictions of dry gas and water yields are acceptable. However, predicted CO yields are lower than measured values. Predicted CO values about 0.9 times measured values were also reported by Watkinson *et al.*[43]. Two factors are thought to relate to the observations that measured CO concentrations are consistently higher than predicted values, by about 3–10%. First, experimentally measured tar values were used in predictions. Yet, it has been noted that these tar values are thought to be low because of the difficulty in tar collection[39]. Carryover of coal fines could also add to the underestimate of the carbonaceous product. Thus actual tar values may have been somewhat higher, possibly closer to the predictions of Ko *et al.*[24]. As shown in *Figures 4a* and *4c*, higher values of tar yield lead to higher values of CO in the equilibrium mixture. Secondly, the equilibrium temperature, in zone 2, T_{exit}, is only a global temperature and is higher than the local exit temperature. The CO/CO_2 ratio is dependent on this calculated temperature. As T_{exit} declines, CO increases. This is shown in *Figure 8* by comparing one-zone and two-zone partial equilibrium values. For two-zone calculations, the equilibrium temperature is lower and the predicted CO is higher while the CO_2 is lower. Thus, higher tar yields and lower exit temperatures may explain the differences between observed CO and predicted CO percentages.

SUMMARY AND CONCLUSIONS

The two-zone partial equilibrium model uses a coal-general devolatilization submodel and a partial equilibrium gas-phase submodel to provide estimates of effluent temperature and composition for fixed-bed gasification and combustion. Effluent composition is determined for all the major species and a number of minor species. Tar production can be estimated, with some uncertainty, using a semi-empirical tar model and tar recycle is taken into account.

The key assumption for the two-zone model is that oxidation and gasification occur at relatively high temperatures compared to the cooler devolatilization and drying zones. The temperature difference provides a natural division of the process into two zones. High temperatures in the oxidation/gasification section favour total equilibrium in the gas phase. Lower temperature and small gas residence time in the devolatilization zone favour partial equilibrium. Limitations to the two-zone model are the need to specify burnout and uncertainty in wall heat loss.

The two-zone, partial equilibrium predictions show that the ultimate volatiles distribution and coal gas composition depend strongly on coal rank. The ultimate volatiles distribution is more sensitive to the potential

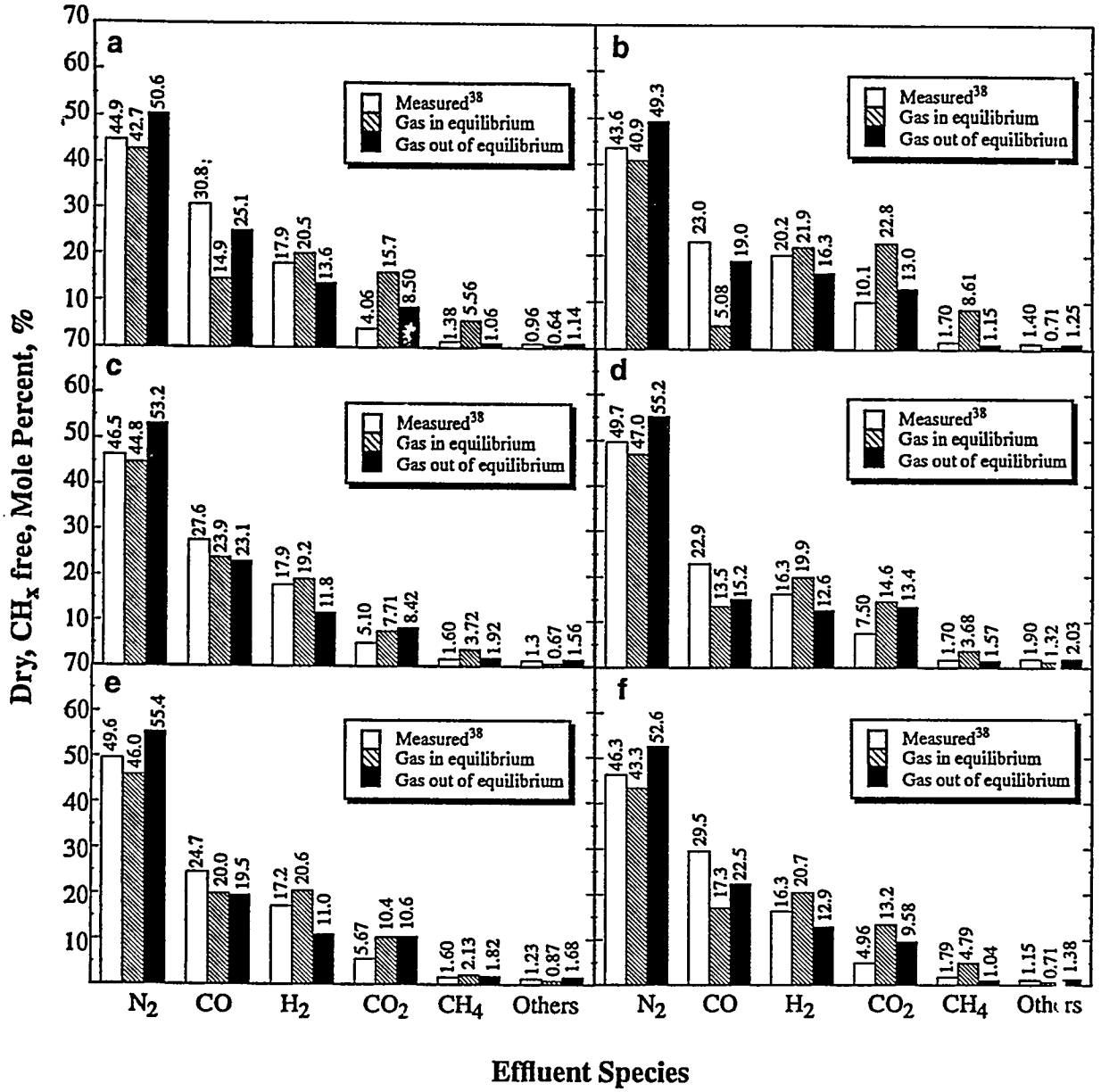

Figure 10 Predicted and measured effluent gas composition for Wellman-Galusha gasifier tests: (a) Absaloka/Robinson subbituminous; (b) Benton lignite; (c) Elkhorn bituminous; (d) Illinois no. 6 bituminous; (e) Jetson bituminous; (f) Kemmerer subbituminous. Input data are from *Tables 2* and *4*

tar-forming fraction than to the temperature. The coal gas composition is not very sensitive to either. This emphasizes the importance of predicting accurate volatiles distribution into tar, coal gas and chemical water.

Predicted fixed-bed effluent gas compositions compare reasonably well with experimental data for gasification of 13 coal types in two commercial-scale, fixed-bed gasifiers. However, the predicted tar yields from the correlation of Ko *et al.*[24] are high in comparison to the values measured in two commercial-scale, fixed-bed gasifiers. Part of the differences may be due to uncertainties in measurement of tar. More rigorous methods for predicting tar that depend on coal structure may improve these estimates.

The two-zone, partial equilibrium model may be preferred to more complex and computationally demanding one- or two-dimensional models when only effluent temperatures and composition are required and computational times must be minimized as in large process optimizations.

ACKNOWLEDGEMENTS

This work was sponsored principally by the US Department of Energy, Morgantown Energy Technol ›gy Center (Contract No. DE-AC21-86MC23075, Dr Richard Johnson, project officer) under subcont act from Advanced Fuel Research, Inc., East Hartford, Connecticut, and also in part by the Advanced

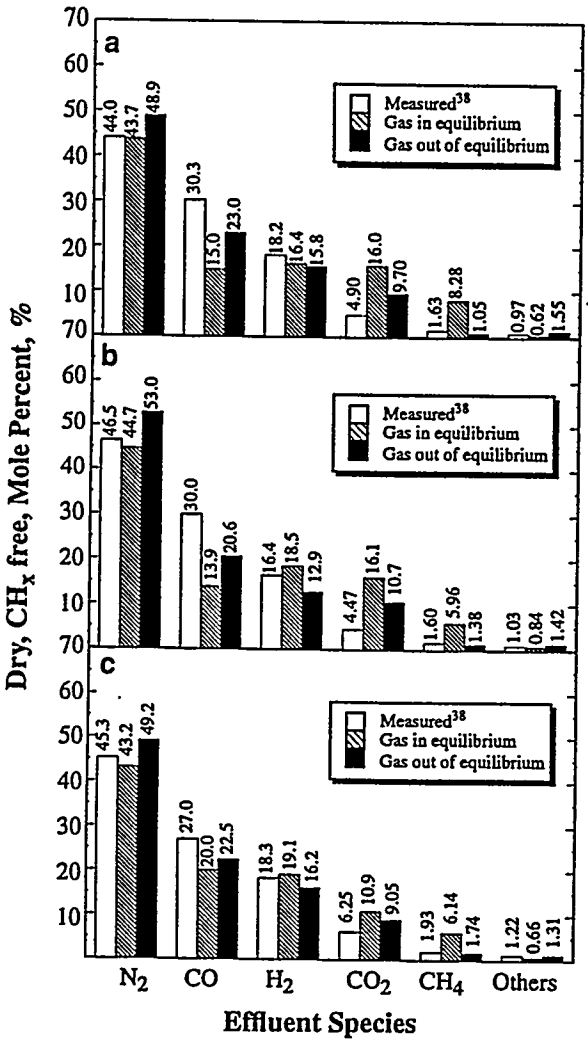

Figure 11 Predicted and measured effluent gas composition for Wellman-Galusha gasifier tests: (a) Leucite bituminous; (b) Rosebud subbituminous; (c) Utah Blind Canyon bituminous. Input data are from *Tables 2* and *4*

Combustion Engineering Research Center at Brigham Young University. Funds for this Center are received from the National Science Foundation's Engineering Centers Division (Dr Tapan Mukherjee, project officer), the State of Utah, and 25 industrial participants. Help from M. Usman Ghani is also acknowledged.

REFERENCES

1 Gumz, W. 'Gas Producers and Blast Furnaces', Wiley, New York, 1950
2 Woodmansee, E. E. *Energy Commun.* 1976, 2, 13
3 Kosky, P. G. and Floess, J. K. *Ind. Eng. Chem. Process Des. Dev.* 1980, 19, 586
4 Loison, R. and Chauvin, F. *Chem. Ind. (Paris)* 1964, 91, 269
5 Smott, L. D. and Smith, P. J. 'Coal Combustion and Gasification', Plenum Press, New York, 1985
6 Radulovic, P. T., Hobbs, M. L. and Smoot, L. D. *Prog. Energy Combust. Sci.* submitted
7 Amundson, N. R. and Arri, L. E. *AIChE J.* 1978, 24, 87
8 Yoon, H., Wei, J. and Denn, M. M. *AICHE J.* 1978, 24, 885
9 Desai, P. R. and Wen, C. Y. 'Computer Modeling of the MERC Fixed Bed Gasifier', MERC/CF-78/3, US Department of Energy, Morgantown, 1978
10 Stillman, R. *IBM J. Res. Dev.* 1979, 23, 240
11 Cho, Y. S. and Joseph, B. *Ind. Eng. Chem. Process Des. Dev.* 1981, 20, 314
12 Yu, W. and Denn, M. M. *Chem. Eng. Sci.* 1983, 38, 1467
13 Earl, W. B. and Islam, K. A. 'CHEMCA 85', Thirteenth Australian Chemical Engineering Conference, Institute of Engineers, Barton, Australia, 1985, p. 289
14 Thorsness, C. B. and Kang, S. W. 'A General-Purpose, Packed-Bed Model for Analysis of Underground Coal Gasification Processes', UCID-20731, Lawrence Livermore National Laboratory, University of California, Livermore, 1986
15 Bhattacharya, A., Salam, L., Dudukovic, M. P. and Joseph, B. *Ind. Eng. Chem. Process Des. Dev.* 1986, 25, 988
16 Hobbs, M. L. *PhD Dissertation* Brigham Young University, Provo, 1990 (see also Hobbs, M. L., Radulovic, P. T. and Smoot, L. D. *AIChE J.* in press)
17 Solomon, P. R., Hamblen, D. G., Carangelo, R. M., Serio, M. A. and Deshpande, G. Y. *Energy Fuels* 1988, 2, 405
18 Perry, R. H. and Chilton, C. H. (Eds), 'Chemical Engineering Handbook', 5th Edn, McGraw-Hill, New York, 1973
19 Johnson, J. L. in 'Chemistry of Coal Utilization' (Ed. M. A. Elliott) 2nd suppl. vol., John Wiley, New York, 1981
20 Merrick, D. *Fuel* 1983, 62, 540
21 Mills, K. C. and Rhine, J. M. *Fuel* 1989, 68, 201
22 Pratt, D. T. in 'Pulverized-Coal Combustion and Gasification' (Eds L. D. Smoot and D. T. Pratt), Plenum Press, New York, 1979
23 Stull, D. R. and Prophet, H. 'JANAF Thermochemical Tables', 2nd Edn, National Bureau of Standards, Washington, DC, 1971
24 Ko, G. H., Sanchez, D. M., Peters, W. A. and Howard, J. B. 'Twenty-Second Symposium (International) on Combustion', The Combustion Institute, Pittsburgh, 1988, p. 115
25 Solomon, P. R. and Hamblen, D. G. in 'Chemistry of Coal Conversion' (Ed. R. H. Schlosberg), Plenum Press, New York, 1985
26 Khan, M. R. *Fuel* 1989, 68, 1522
27 Serio, M. A., Hamblen, D. G., Markham, J. R. and Solomon, P. R. *Energy Fuels* 1987, 1, 138
28 Anthony, D. B., Howard, J. B., Hottel, H. C. and Meissner, M. P. 'Fifteenth Symposium (International) on Combustion', The Combustion Institute, Pittsburgh, 1974, p. 1303
29 Abramowitz, M. and Stegun, I. A. (Eds), 'Handbook of Mathematical Functions with Formulas Graphs, and Mathematical Tables', Applied Mathematics Series no. 55, National Bureau of Standards, US Government Printing Office, Washington, DC, 1972
30 Blair, D. W., Wendt, J. O. L. and Bartok, W. 'Sixteenth Symposium (International) on Combustion', The Combustion Institute, Pittsburgh, 1977, p. 475
31 Solomon, P. R. and Colket, M. B. 'Seventeenth Symposium (International) on Combustion', The Combustion Institute, Pittsburgh, 1979, p. 131
32 Suuberg, E. M., Peters, W. A. and Howard, J. B. 'Seventeenth Symposium (International) on Combustion', The Combustion Institute, Pittsburgh, 1979, p. 177
33 Rudolph, P. 'Fourth Synthetic Pipeline Gas Symposium', American Gas Institute, Chicago, 1972, p. 175
34 Serio, M. A. personal communication, Advanced Fuel Research, Inc., East Hartford, 1989
35 Elgin, D. C. and Perks, H. R. 'Sixth Synthetic Pipeline Gas Symposium', American Gas Institute, Chicago, 1974, p. 247
36 Elgin, D. C. and Perks, H. R. 'Fifth Synthetic Pipeline Gas Symposium', American Gas Institute, Chicago, 1973, p. 145
37 Kim, M. and Joseph, B. *Ind. Eng. Chem. Process Des. Dev.* 1983, 22, 212
38 Thimsen, D., Maurer, R. E., Pooler, A. R., Pui, D. Y. H., Liu, B. Y. H. and Kittelson, D. B. 'Fixed-Bed Gasification Research Using U.S. Coals', Vols 1–19, US Bureau of Mines Contract H0222001 Final Report, Houston, 1984–1985
39 Thimsen, D. P. and Maurer, R. E. 'Coal Devolatilization in a Moving-Bed Gasifier', GS-6797, Research Project 2524-14 Final Report, Electric Power Research Institute, Palo Alto, 1990
40 Solomon, P. R., Hamblen, D. G., Carangelo, R. M., Serio, M. A. and Deshpande, G. Y. *Fuel* 1990, 69, 754
41 Grant, D. M., Pugmire, R. J., Fletcher, T. H. and Kerstein, A. R. *Energy Fuels* 1989, 3, 175
42 Niksa, S. *AIChE J.* 1988, 34, 790
43 Watkinson, A. P., Lucas, J. P. and Lim, C. J. *Fuel* 1991, 70, 519

APPENDIX D

MODELING FIXED-BED COAL GASIFIERS

Reprinted from AICHE JOURNAL, MAY 1992

Modeling Fixed-Bed Coal Gasifiers

Michael L. Hobbs, Predrag T. Radulovic, and L. Douglas Smoot
Advanced Combustion Engineering Research Center, Brigham Young University, Provo, UT 84602

A one-dimensional model of countercurrent fixed-bed coal gasification has been developed, and results have been compared to experimental data from commercial-scale gasifiers. The steady-state model considers separate gas and solid temperatures, axially variable solid and gas flow rates, variable bed void fraction, coal drying, devolatilization based on chemical functional group composition, oxidation and gasification of char, and partial equilibrium in the gas phase. Generalized treatment of gas-phase chemistry and accounting for variable bed void fraction were necessary to predict realistic axial temperature and pressure profiles in an atmospheric fixed-bed gasifier. Model evaluation includes sensitivity of axial temperature profiles to model options, model parameters and operational parameters. Model predictions agree reasonably well with experimental temperature and pressure profile data for gasification of eight coal types ranging from lignite to bituminous. The relative importance of char oxidation resistances to bulk film diffusion, ash diffusion, and chemical reaction is identified.

Introduction

Fixed-bed systems are simple and reliable, have high thermal efficiency, and require minimal pretreatment of feed coal. Combustion and gasification of coal in fixed or slowly moving beds of packed coal particles are of substantial commercial interest. Such beds can be operated at high pressure, providing opportunity for increased power generation efficiency through combined cycle processes. Fixed beds are also a popular choice for mild gasification since, by their countercurrent nature, the liquids can be quickly removed before being altered by substantial reaction. The U.S. Clean Coal Technology demonstration program includes two fixed-bed gasifier processes undergoing commercial demonstration.

In a large-scale, fixed-bed gasifier, Figure 1, coal is fed to the top of the reactor and moves downward under gravity, countercurrent to the rising gas stream. The dry or slagging ash is removed at the bottom of the reactor. The feed gas is commonly composed of air or oxygen and steam. Excess steam is supplied to the gasifier to control the ash temperature. Figure 1 also shows the reactor divided into four overlapping zones: drying, devolatilization, gasification, and combustion. As the coal slowly descends, the hot gases produced in the gasification and combustion zones exchange energy with the colder solid. Water and subsequently volatile matter are released when the solid reaches sufficiently high temperatures. After drying and devolatilization, the char enters the gasification zone where carbon reacts with steam, carbon dioxide, and hydrogen. Endothermic reactions in this section produce carbon monoxide

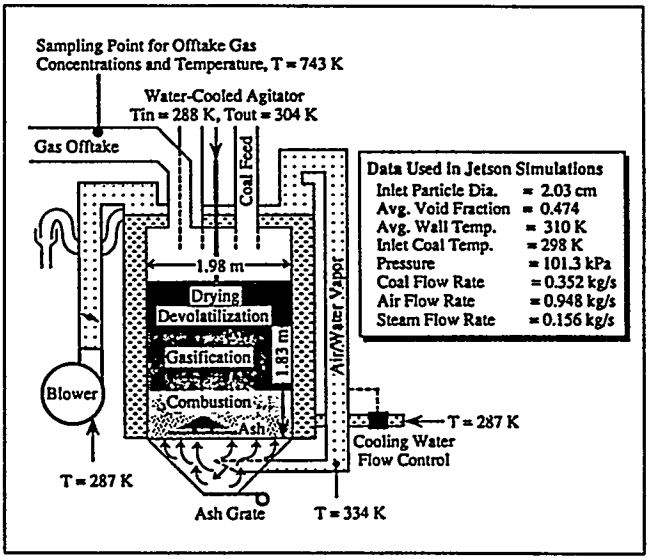

Figure 1. Typical atmospheric fixed-bed gasifier (Wellman-Galusha).

Temperatures are for gasification of Jetson coal blown with air. Configuration and data taken from Thimsen et al. (1984).

Correspondence concerning this article should be addressed to L. D. Smoot.
M. L. Hobbs is presently at the Sandia National Laboratories, P. O. Box 5800, Div. 1512, Albuquerque, NM 87185.

and hydrogen. The slightly exothermic reaction of hydrogen with carbon produces methane. Differentiation between the "gasification zone" and "combustion zone" is based on the presence or absence of free oxygen. Combustion and gasification reactions occur simultaneously in the "combustion zone." Combustible gases such as carbon monoxide or hydrogen may react with oxygen. The exothermic combustion reactions provide the necessary energy for the endothermic gasification reactions and drying. Blast gas, which is composed of steam and oxidant (air or oxygen), is preheated by the hot ash. Part of the process steam is produced by a water jacket surrounding the gasification chamber.

Solid residence times in the drying, gasification and oxidation zones may be on the order of several hours. Residence time in the ash layer may be even higher depending on the thickness of this zone. Large solid residence times indicate significant settling resulting in variable axial velocities. Gas residence times are on the order of seconds. Both solid and gas heating rates are most dramatic in the devolatilization and the oxidation zones. Typical solid heating rates are smaller than 10 K/s, while gas heating rates are up to 10,000 K/s.

Existing fixed-bed models in the open literature show that all fixed-bed models were qualitative until the late 1970s. At that time, Winslow (1976) presented a detailed model for underground coal gasification. Soon afterward, Amundson and Arri (1978), Yoon et al. (1978), Desai and Wen (1978), and Stillman (1979) presented detailed models of a fixed-bed gasifier. Cho and Joseph (1981) extended Yoon's model to include unequal gas-solid temperatures. Yoon's model was further extended by Kim and Joseph (1983) to account for transient effects. Yu et al. (1983) extended Yoon's model to two space dimensions. More recent models include the one-dimensional, steady-state model of Earl and Islam (1985) and the two-dimensional, transient models of Thorsness and Kang (1986) and Bhattacharya et al. (1986). Khanna and Seinfeld (1987) discussed recent advances in catalytic fixed-bed reactor models which have many of the features of coal gasification/combustion fixed-bed models discussed earlier. Smoot and Smith (1985), Hobbs (1990), and Radulovic et al. (1992) have reviewed fixed-bed modeling.

Previous fixed-bed models share common assumptions such as equal gas/solid temperatures, axially uniform gas/solid-phase plug flow, uniform bed porosity, instantaneous devolatilization (with percent volatiles from proximate analysis), combustion/gasification by shell progressive or ash segregation submodels, kinetic parameters from small particle data, and little or no gas-phase chemistry. The fixed-bed model discussed here eliminates most of these assumptions. The primary contribution of this article is the development and evaluation of an improved, comprehensive fixed-bed model that utilizes an advanced, coal-general devolatilization submodel.

One-Dimensional Fixed-Bed Model

Conservation equations

The conservation equations for mass and energy form the foundation of the model. The derivation of the two-phase conservation equations can be found in Crowe and Smoot (1979). The source terms in the continuity and energy equations are described by physical and chemical submodels. Input parameters are reactor dimensions, operating conditions, inlet solid and gas temperatures, pressure, concentrations, flow rates, and wall temperature. Calculated quantities include axial variation in gas temperature, solids temperature, pressure, species concentration, gas-flow rate, solid flow rate, and wall heat loss. Plug flow is assumed in both the solid and gas phases with variable axial velocities. Gas-phase pressure drop is calculated with the Ergun equation for packed beds (Ergun, 1952). An effective heat-transfer coefficient is used for heat loss to the wall, including both stagnant and dynamic contributions for convective and radiative transfer. Large coal particle devolatilization is allowed to occur simultaneously with char oxidation and gasification. Shell progressive or ash segregation, shrinking core char submodels describe oxidation and gasification. Chemical equilibrium is used to calculate gas concentrations and temperatures. Turbulence is not treated formally in the slowly moving bed with low gas velocities, but is included implicitly through model correlations such as the effective heat-transfer coefficient. Primary assumptions for the one-dimensional fixed-bed model include negligible aerodynamic drag, ideal gases, and particles locally isothermal throughout; one particle size and type exist in the feed coal. This model will be referred to as MBED-1D (moving-bed, one-dimensional) here. The reactor, however, is frequently referred to as a fixed-bed reactor because of the large difference in gas- and solid-phase residence times. Assumptions are discussed in detail by Hobbs (1990).

The conservation equations and boundary conditions for the one-dimensional, fixed-bed model are given in Table 1. These can be classified as gas and solid overall continuity, gas and solid energy equations, and gas and solid species or elemental continuity equations. The constitutive relations for solid flow have been proposed only recently, and no solution for these equations has been attempted (Gray and Stiles, 1988). Thus, only differential equations for continuity and energy are treated in the model described here.

The overall gas and solid species continuity equations are given in Eqs. 1 and 2 in Table 1. The gas and solid flow rates are represented by W_g (kg/s) and W_s (kg/s), respectively. The axial distance and cross-sectional areas are represented by z (m) and A (m^2), respectively. The volumetric reaction rate is represented by r_i ($kg/m^3 \cdot s$) where i depicts the different heterogeneous reactions such as drying, char oxidation, char gasification, and devolatilization. Reaction rates are written as the rate of mass addition to the gas phase per unit volume per unit time; thus, a positive rate indicates a source of mass for the gas phase and a sink for the particle phase.

The gas and solid energy equations are given by Eqs. 3 and 4 in Table 1. The total gas and solid enthalpies are represented by h_g (J/kg) and h_s (J/kg). The energy exchange between solid and gas is represented by Q_{sg} (W/m^3). Heat losses to the walls from the gas and solid phases are represented by Q_{gw} (W/m^3) and Q_{sw} (W/m^3), respectively. Calculation of Q_{sg}, Q_{gw}, and Q_{sw} will be discussed subsequently. The last term in the energy equation represents the energy exchange due to chemical reaction and accounts for mass loss from the particle phase and mass addition to the gas phase. This reaction term can be calculated by performing an energy balance around the particle/gas interface as discussed in detail by Hobbs (1990). The gaseous reactants are assumed to be at the gas temperature, and the reaction is assumed to take place at the solid temperature. A sample calculation associated with the term $r_i h_{ig}$ for the oxidation reaction is given by Hobbs (1990).

Table 1. Differential Equation Set and Boundary Conditions for MBED-1D

Overall Gas Species Continuity	$\frac{dW_g}{dz}=A\sum_{i=1}^{n}r_i$	(1)
Overall Solid Species Continuity	$\frac{dW_s}{dz}=-A\sum_{i=1}^{n}r_i$	(2)
Gas-Phase Energy	$\frac{dW_gh_g}{dz}=A\left(Q_{sg}-Q_{gw}+\sum_{i=1}^{n}r_ih_{ig}\right)$	(3)
Solid-Phase Energy	$\frac{dW_sh_s}{dz}=A\left(-Q_{sg}-Q_{sw}+\sum_{i=1}^{n}r_ih_{ig}\right)$	(4)
Solid Species Continuity		
Moisture	$\frac{dW_{\text{moisture}}}{dz}=-Ar_{\text{moisture}}$	(5)
Nonvolatile carbon	$\frac{dW_{\text{Nonvolatile C}}}{dz}=-Ar_{\text{Nonvolatile C}}$	(6)
Nonvolatile sulfur	$\frac{dW_{\text{Nonvolatile S}}}{dz}=-Ar_{\text{Nonvolatile S}}$	(7)
Organic functional groups	$dy_i/dz=-(1/u_s)k_iy_i$	(8-26)
Tar fraction	$dx/dz=-(1/u_s)k_xx$	(27)
Gas-Phase Elemental Continuity*	$\frac{dW_g\omega_j}{dz}=A\sum_{i=1}^{n}r_{ij}$	(28-32)
Gas-Phase Tar Species Continuity	$\frac{dW_{\text{tar}}}{dz}=A\sum_{i=1}^{n}r_{i,\text{tar}}$	(33)
Gas-Phase Tar Elemental Continuity*	$\frac{dW_{\text{tar}}\omega_{\text{tar},j}}{dz}=A\sum_{i=1}^{n}r_{ij}^{\text{tar}}$	(34-38)
Boundary Conditions		
Overall solid/gas species continuity	Feed coal/gas weight flow rate	
Solid/gas-phase energy	Feed coal/gas enthalpy or temperature	
Solid species continuity	Proximate and functional group analysis	
Gas-phase elemental and tar continuity	Feed gas and tar composition	

*j represents carbon, hydrogen, nitrogen, oxygen, and sulfur.

Auxiliary equations

Pressure Drop. The pressure drop in the reactor is calculated from Ergun's equation (Ergun, 1952) since Reynolds numbers are typically less than 500 in fixed-bed coal gasifiers. The small pressure drop in the reactor is sensitive to the bed void fraction, ϵ. Void fractions of the feed coal at the bed top and the product ash at the bed bottom were estimated based on coal and ash bulk and apparent density measurements. The void fraction was assumed to vary linearly from the top to the bottom of the bed. In two sets of independent measurements, Krishnudu et al. (1989) stopped coal bed reaction and measured bed void fraction along the bed length, which was shown to vary linearly from the top to the bottom of the bed. Subsequent comparisons with pressure drop measurements provide support for this approach.

Gas-Phase Chemistry. Gas temperature is determined by assuming all gas species to be in thermal equilibrium and partial or total chemical equilibrium. Gas-phase composition is determined by Gibbs free energy minimization. Solid temperature is determined from the solid enthalpy and the elemental composition of the coal. All gas-phase transport properties (such as conductivity, viscosity, and diffusivity) are considered to be functions of both temperature and composition. Partial equilibrium refers to a gaseous mixture where at least one species is held out of chemical equilibrium. Hobbs et al. (1992) investigated three options regarding equilibrium: total equilibrium, partial equilibrium where tar was held out of chemical equilibrium, and partial equilibrium where all gases in the drying and devolatilization zone were assumed to be nonreactive. Since gas-phase kinetic models for coal systems are complex, the one-dimensional fixed-bed model assumes partial equilibrium by holding tar out of chemical equilibrium.

Mass and Heat Transfer. Mass- and heat-transfer processes in fixed-bed gasifiers are affected by complex solids flow and chemical reactions. Coarsely crushed coal settles while undergoing heating, drying, devolatilization, gasification, and combustion. Coal particles change in diameter, shape, and porosity. Nonideal behavior may result from coal bridges, gas bubbles, and channels. Variable bed void fraction may also change heat- and mass-transport properties. Correlations for solid-to-gas heat-transfer coefficients are questionable, since they are typically obtained under ideal conditions. Mass transfer occurs by diffusion and convection. Heat transfer is by conduction, convection, and radiation in the gas and solid phases.

Several physical properties of the gas and particle phases are required to obtain mass- and heat-transfer coefficients needed to solve the differential equation set in Table 1. Chapman-Enskog theory has been used to calculate multicomponent gas mixture viscosity and diffusivity (Bird et al., 1960). Conventional gas species and mixture conductivity, viscosity, and diffusivity methods used here are documented by Hobbs (1990). The particle is assumed to swell linearly with the extent of devolatilization. Euken's formula is used to calculate the conductivity of individual gaseous species (Bird et al., 1960). Furthermore, the gaseous tar diffusivity is assumed to be 0.1 cm^2/s at standard temperature and pressure (Suuberg et al., 1979). The pressure and temperature dependences for the tar diffusivity are assumed to follow Chapman-Enskog theory. The JANAF tables were used to provide values for calculating gas-phase enthalpy, entropy and heat capacity (Stull and

Prophet, 1971). Dulong's formula (Perry and Chilton, 1973) was used for heating value of the char, Merrick's correlations (1983) were used for char enthalpy and heat capacity, and the Kopp-Neumann rule was used for ash heat capacity (Mills and Rhine, 1989).

The heat- and mass-transfer correlations used in the one-dimensional model are summarized in Table 2. Effective axial and radial conductivities are correlated by Yagi et al. (1960), Bischoff (1962), and Froment and Bischoff (1979), respectively. Both the axial and radial effective conductivities take into account molecular as well as turbulent contributions. The effective radial conductivities of the gas and solid phases, which account for radiation, are correlated by DeWasch and Froment (1971). The mass-transfer coefficient in Table 2 is used to calculate the film resistance and the effective particle resistance to mass transport.

The effective bed-to-wall heat-transfer coefficient as well as the gas- and solid-phase contributions are determined by the correlations suggested by DeWasch and Froment (1971). The heat transfer to the wall is treated by Yagi and Wakao (1959), Yagi and Kunii (1960), and Rohsenow et al. (1985). There are no direct experimental data available on the gas- and solid-phase contributions to the bed-to-wall heat transfer. The volumetric heat-transfer rate from solid to gas, Q_{sg} (J/m^3·s), can be written as:

$$Q_{sg}=\zeta h_{sg}\pi d_p^2\eta_p(T_s-T_g) \tag{1}$$

where ζ, h_{sg} (J/s·m^2·K), and η_p (1/m^3) represent deviations from nonreactive solid-to-gas heat transfer (ranges from 0.02 to 1.0), the nonreactive solid-to-gas heat-transfer coefficient (in Table 2), and the particle number density, respectively. The volumetric wall heat losses from the solid and gas phase, Q_{gw} and Q_{sw} (J/m^3·s), can be calculated as follows:

$$Q_{gw}=\frac{4h_w^g}{D}(T_g-T_{wall}) \tag{2}$$

Table 2. Heat- and Mass-Transport Correlations Used in MBED-1D

Bed-to-wall heat-transfer coefficient	$h_w=2.44k_r^0D^{-4/3}+0.033k_g\mathrm{PrRed}_p^{-1}$	(1)	Froment and Bischoff (1979)
Gas-to-wall heat-transfer coefficient	$h_w^g=h_wk_{rg}/(k_{rg}+k_{rs})$	(2)	DeWasch and Froment (1971)
Solid-to-wall heat-transfer coefficient	$h_w^s=h_wk_{rs}/(k_{rg}+k_{rs})$	(3)	DeWasch and Froment (1971)
Static effective radial conductivity	$k_r^0=k_g\epsilon\left(1+\frac{d_ph_{rv}}{k_g}\right)+\frac{k_g(1-\epsilon)}{\left(\frac{1}{\phi}+\frac{h_{rs}d_p}{k_g}\right)^{-1}+\frac{2}{3\kappa}}$	(4)	Froment and Bischoff (1979)
Gas effective radial conductivity	$k_{rg}=k_g\left\{\epsilon\left(1+\frac{d_ph_{rv}}{k_g}\right)+0.14\mathrm{PrRe}/\left[1+46\left(\frac{d_p}{D}\right)^2\right]\right\}$	(5)	Froment and Bischoff (1979)
Solid effective radial conductivity	$k_{rs}=k_g(1-\epsilon)/\left[\left(\frac{1}{\phi}+\frac{h_{rs}d_p}{k_s}\right)^{-1}+\frac{2}{3\kappa}\right]$	(6)	Froment and Bischoff (1979)
Solid conductivity	$k_s=(\rho_s^t/4{,}511)^{3.5}\sqrt{T_s}$	(7)	Merrick (1983)
Void-to-void radiation coefficient	$h_{rv}=2.27\times10^{-7}T_g^3/\left[1+\frac{\epsilon}{2(1-\epsilon)}\left(\frac{1-\epsilon'}{\epsilon'}\right)\right]$	(8)	Froment and Bischoff (1979)
Solid radiation coefficient	$h_{rs}=2.27\times10^{-7}\left(\frac{\epsilon'}{2-\epsilon}\right)T_s^3$	(9)	Froment and Bischoff (1979)
Packing parameter	$\phi=\begin{cases}\phi_2+(\phi_1-\phi_2)\frac{\epsilon-0.260}{0.476-0.260} & \text{if } \epsilon_1\ge\epsilon\ge\epsilon_2\\ \phi_1 & \text{if } \epsilon>\epsilon_1=0.476\\ \phi_2 & \text{if } \epsilon<\epsilon_2=0.260\end{cases}$	(10)	Kunii and Smith (1960)
Loose packing parameter (for ϵ_1)	$\phi_1=\frac{0.3525\left(\frac{\kappa-1}{\kappa}\right)^2}{\ln[\kappa-0.5431(\kappa-1)]-\frac{0.4569(\kappa-1)}{\kappa}}-\frac{2}{3\kappa}$	(11)	Kunii and Smith (1960)
Dense packing parameter (for ϵ_2)	$\phi_2=\frac{0.07217\left(\frac{\kappa-1}{\kappa}\right)^2}{\ln[\kappa-0.9250(\kappa-1)]-\frac{0.07498(\kappa-1)}{\kappa}}-\frac{2}{3\kappa}$	(12)	Kunii and Smith (1960)
Solid-to-gas heat-transfer coefficient	$h_{sg}=\frac{2.06Cp_gG}{\epsilon}\mathrm{Re}^{-0.575}\mathrm{Pr}^{-2/3}$	(13)	Gupta and Thodos (1963)
Mass-transfer coefficient	$k_m=\frac{2.06G}{\epsilon\rho_g}\mathrm{Re}^{-0.575}\mathrm{Sc}^{-2/3}$	(14)	Gupta and Thodos (1963)
Reynolds, Prandtl and Schmidt numbers	$\mathrm{Re}=d_pG/\mu_g$, $Pr=Cp_g\mu_g/k_g$, $\mathrm{Sc}_i=\mu_g/\rho_gD_{im}$	(15–17)	Definitions
Conductivity ratio	$\kappa=k_s/k_g$	(18)	Definitions
Bed void fraction	ϵ=void volume/bed volume	(19)	Definitions
Coal emissivity	$\epsilon'=0.85$	(20)	Perry and Chilton (1973)

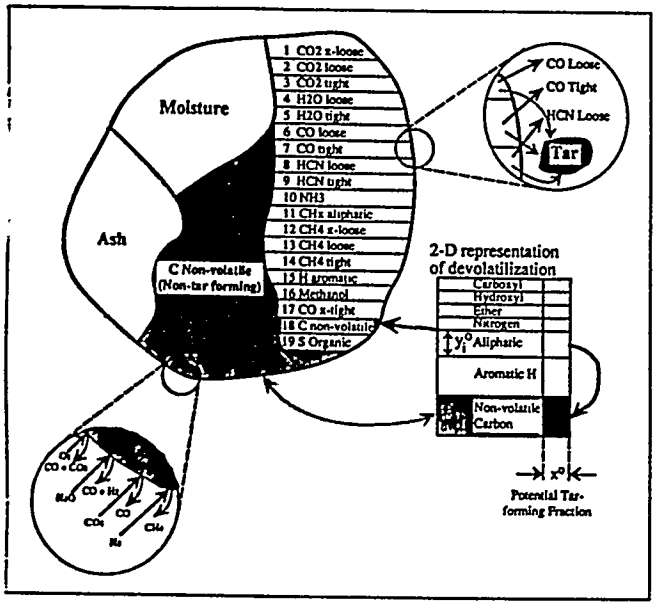

Figure 2. Coal particle with devolatilization model based on chemical functional groups (Solomon et al., 1988).

The potential tar-forming fraction of the nonvolatile carbon functional group evolves as tar. The nontar-forming C and S organic groups evolve via heterogeneous char oxidation or gasification.

$$Q_{sw}=\frac{4k_w^s}{D}(T_s-T_{wall}) \tag{3}$$

ne wall temperature can be varied from the bottom of the reactor to the top of the reactor.

Coal Drying and Devolatilization. Coal reaction source terms represent drying, devolatilization, char oxidation, and gasification. These chemical and physical processes in Figure 2 show a conceptual coal particle divided into various functional groups, including moisture and ash, which is taken to be inert. Drying is assumed to be diffusion-limited (Smoot and Smith, 1979):

$$r_w=k_{wm}(\rho_{wp}-\rho_{wg}) \tag{4}$$

Blowing effects have been neglected.

As shown in Figure 2, devolatilization is described by assuming that the organic portion of the coal particle is composed of various functional groups, such as carboxyl, hydroxyl, ether, and nitrogen. A functional group model (FG model) has been used to describe the devolatilization process (Serio et al., 1987; Solomon et al., 1988). The kinetics for functional group evolution are considered to be independent of the type of coal used.

Application of the functional group devolatilization model of Solomon et al. (1988), used here, is discussed in detail by Hobbs (1990). This section describes the devolatilization rate equations which appear as source terms in the continuity equations in Table 1. The change in functional group composition and tar fraction is obtained by Eqs. 8 through 27 in Table 1. The evolution of each functional group into the gas phase is represented by first-order decay. The equations representing this first-order decay are not truly solid species conservation equations; however, Eqs. 8 through 27 are used to keep track of the functional groups in the solid phase throughout the reactor. The values for Arrhenius rate coefficients, k_i and k_x, and the initial functional group compositions, y_i^o, can be found in Hobbs (1990) or Hobbs et al. (1992).

The mass rate of change of each reactive element in the gas phase is depicted by Eqs. 28 through 32 in Table 1. Gases such as argon are inert to reaction, and a differential equation is not required to track such gases. The sources for gas-phase elements are the heterogeneous oxidation, gasification and devolatilization reactions. The only gas-phase species that is tracked throughout the reactor is tar. Tar was either assumed to be nonreactive or to react to equilibrium in the gas phase.

Predicting accurate coal volatiles yield and composition is important since as much as 40–60% of the dry, ash-free mass can be lost by devolatilization. The coal particle in Figure 2 is divided into various chemical functional groups. The X and Y values represent the two-dimensional description of coal. The Y dimension is divided into fractions according to the chemical composition of the coal. The initial fraction of a particular functional group component is represented by y_i^o, and the sum of y_i^os equals 1. The evolution of each functional group into the gas is represented by the first-order decay of the Y dimension, $dy_i/dt=-k_iy_i$. The X dimension represents nontar-forming char, tar-forming char, and tar. The evolution of tar is represented by the first-order decay of the X dimension, $dx/dt=-k_xy_i$. The potential tar-forming fraction, x^o, was calculated with the semi-empirical correlation of Ko et al. (1988) as discussed by Hobbs et al. (1992). Values for y_i^ocan be found subsequently in Table 3. Normally distributed Arrhenius rate coefficients for 19 functional groups, k_i, and tar, k_x, were obtained from Solomon et al. (1988) for the organic functional groups in Figure 2.

The volumetric devolatilization rate expressions, r_i^d(kg/m^3·s) are derived by Hobbs (1990):

$$r_i^d=$$

$$\rho_{sm}^o(1-\epsilon^o)(1-\Omega_{ash}^o-\Omega_{moisture}^o)[(1-x^o+x)(k_iy_i)+y_i(k_xx)] \tag{5}$$

r_i^dincludes mass losses due to both light gas evolution and tar evolution, which are required by the continuity equations in Table 1. However, the tar continuity equations require the tar volumetric rate equations, $r_{i,tar}^d$ (kg/m^3·s), which are also found in Hobbs (1990):

$$r_{i,tar}^d=\rho_{sm}^o(1-\epsilon^o)(1-\Omega_{ash}^o-\Omega_{moisture}^o)k_xxy_i \tag{6}$$

Equations 5 and 6 do not explicitly include resistance due to mass transport. Saxena (1990) concludes that heat- and mass-transport limitations in large coal particles are significant. Coupling between mass transport of oxidation and gasification products and devolatilization complicates the mathematical description of both devolatilization and char oxidation. Simulations with the purely kinetic devolatilization equations as formulated above can result in unrealistically fast product evolution for large coal particles. To introduce mass transport effects, transport resistance through the film and particle is added to the Arrhenius rate expression as diffusional resistances:

Table 3. Functional Group Compositions, Calculated Potential Tar-Forming Fractions, and Ultimate Analysis*

Reactor** Functional Groups (Dry, Ash-Free)	Lurgi Rose y_i^0	WG Absal y_i^0	WG Benton y_i^0	WG Elk y_i^0	WG Jetson y_i^0	WG Kemer y_i^0	WG Leucite y_i^0	WG Rose y_i^0	WG Utah y_i^0
CO_2 extra loose	0.035	0.028	0.065	0.000	0.000	0.028	0.028	0.035	0.003
CO_2 loose	0.035	0.020	0.030	0.006	0.006	0.020	0.020	0.035	0.007
CO_2 tight	0.030	0.021	0.005	0.005	0.005	0.021	0.021	0.030	0.017
H_2O loose	0.000	0.030	0.000	0.011	0.011	0.027	0.024	0.000	0.025
H_2O tight	0.051	0.022	0.027	0.011	0.011	0.022	0.022	0.040	0.020
CO ether loose	0.055	0.050	0.060	0.050	0.050	0.050	0.050	0.055	0.025
CO ether tight	0.000	0.043	0.000	0.044	0.059	0.000	0.000	0.000	0.036
HCN loose	0.010	0.000	0.005	0.022	0.025	0.003	0.016	0.005	0.000
HCN tight	0.015	0.013	0.013	0.009	0.009	0.018	0.018	0.015	0.022
NH_3	0.001	0.001	0.001	0.000	0.000	0.001	0.001	0.001	0.000
CH_x aliphatic	0.182	0.169	0.212	0.185	0.161	0.201	0.195	0.202	0.189
CH_4 extra loose	0.000	0.000	0.000	0.020	0.020	0.000	0.000	0.000	0.000
CH_4 loose	0.022	0.017	0.017	0.015	0.015	0.017	0.017	0.022	0.022
CH_4 tight	0.012	0.008	0.009	0.015	0.015	0.008	0.008	0.012	0.022
H aromatic	0.013	0.013	0.017	0.012	0.012	0.013	0.013	0.013	0.017
CH_3OH	0.000	0.000	0.000	0.000	0.000	0.000	0.000	0.000	0.000
CO extra tight	0.000	0.043	0.090	0.020	0.020	0.043	0.043	0.000	0.040
C nonvolatile	0.522	0.518	0.440	0.565	0.565	0.518	0.518	0.522	0.548
S organic	0.017	0.004	0.009	0.009	0.016	0.010	0.006	0.013	0.006
Total	1.000	1.000	1.000	0.999	1.000	1.000	1.000	1.000	0.999
calculated x^{o}**	0.110	0.137	0.227	0.270	0.222	0.219	0.167	0.150	0.270
Coal type	Subbit	Subbit	Lig	Bit	Bit	Subbit	Subbit	Subbit	Bit
DAF ultimate									
C	0.771	0.763	0.737	0.825	0.814	0.775	0.781	0.787	0.803
H	0.049	0.051	0.062	0.057	0.051	0.056	0.050	0.049	0.062
N	0.014	0.008	0.010	0.016	0.018	0.012	0.019	0.011	0.012
O	0.150	0.174	0.182	0.093	0.102	0.147	0.144	0.140	0.117
S (organic)	0.017	0.004	0.009	0.009	0.016	0.010	0.006	0.013	0.006

*Functional group compositions were determined to match reported ultimate analysis using the criterion presented in Hobbs (1990). The semi-empirical correlation of Ko et al. (1988) was used to calculate x^o at pressures in Table 7.
**WG represents the atmospheric Wellman-Galusha Gasifier.

$$k_{i,x}^{\text{effective}} = \left(\frac{1}{k_{i,x}} + \frac{1}{k_m} + \frac{1}{k_{\text{eff}}}\right)^{-1} \tag{7}$$

where $k_{i,x}^{\text{effective}}$, $k_{i,x}$, k_m, and k_{eff} represent the effective devolatilization rate constant, the distributed Arrhenius devolatilization rate constant, the film mass-transport coefficient, and the effective internal mass-transport coefficient for the particle. The resistance through the particle is a function of the particle burnout and is negligible at the beginning of devolatilization. The mass-transfer resistances used here for devolatilization are identical to those used in the oxidation and gasification submodel and will be discussed in more detail in the following section.

Diffusional mass transport may not be an appropriate mode of transport for devolatilization. Jets of volatile gases suggest that convection may dominate mass transport for small-particle devolatilization. However, diffusion may be important for devolatilization of large particles at typical heating rates found in fixed-bed reactors. Internal particle temperature gradients may be significant during devolatilization (Phuoc and Mathur, 1991), but experimental evidence using thermocouples embedded into large coal particles during devolatilization indicates that thermal equilibrium is reached rapidly (for example, Nuttall et al., 1979).

Tar. Estimates of the tar production rate from a fixed-bed gasifier using the functional group devolatilization model have not been reliable (Hobbs, 1990). More recently, Solomon et al. (1988) and Fletcher et al. (1992) have developed network models of organic coal structure that lead to promising methods for estimating tar production rates. This new work, however, had not advanced to the point where it could be considered here. Ko et al. (1988) have published a correlation of a large quantity of tar production data, mostly on small coal particles. In our fixed-bed model, tar is either estimated from Ko et al. or provided from experimental data. In a separate study, we (Hobbs, et al., 1992) show that tar production estimated from Ko et al. was consistently higher than measured data for several coals in the Wellman-Galusha gasifier.

Oxidation and Gasification. Oxidation and gasification reactions consume the char that is assumed to be composed of nonvolatile functional groups. As shown in Figure 2, three gasification agents are considered: steam, carbon dioxide, and hydrogen. Light gases and tar competitively evolve, resulting in char. Both tar and char are treated as single species that have variable compositions depending on the location in the reactor.

The two most common char oxidation submodels used in fixed-bed coal gasification modeling are the Shell Progressive model (SP model) and the Ash Segregation model (AS model). The differences between the two models are in the description of the ash. The ash in the SP model remains intact. The oxidant is required to diffuse through the gas film boundary layer and the ash layer. The ash in the AS model is assumed to crumble and fall away from the char particle with the oxidant required to diffuse only through the gas film boundary layer. An ash layer may collect around the particle during oxidation as observed during the burning of large coal slabs (Park and Edgar, 1987).

The char oxidation/gasification submodels assume global reactions and depend on the external particle surface area. The SP or AS submodels are used to obtain the rates of char oxidation and gasification. Derivation of the rate equation for a single particle is given by Hobbs (1990):

$$r_i''^{,s} = \frac{A_p \nu_s M w_p C_{ig}}{\frac{1}{k_r \zeta} + \frac{1}{k_m} + \frac{1}{k_{eff}}} \tag{8}$$

The resistances in the denominator represent surface reaction, molecular diffusion through the gaseous film and diffusion through the ash layer. Equation 8 neglects the effects of diffusion-induced convective transport and assumes that the reactions are first order in oxidizer concentration. The validity of Eq. 8 has not been demonstrated for groups or packed beds of oxidizing particles. Values obtained for reaction order among various investigators vary between 0 and 1, with most investigators correlating their data on the basis of first order. Gray et al. (1974) explain the variation in terms of the controlling chemical reaction step: if adsorption is controlling, $n=1$, whereas if desorption controls, $n=0$, where n is the order of the reaction.

Equation 8 also explicitly neglects pore diffusion, in which case these effects are lumped into k_{eff}. The diffusional resistance through the ash layer is set to zero if the AS model is used. Oxidation and gasification kinetic rate constants are given in Table 4. Given the lack of more reliable steam-char reaction rate data, it has been assumed, based on the data of Walker (1959), Yoon (1978), Wen et al. (1982), Wen and Chaung (1979), and Blackwood (1959), that the steam gasification rate is the same as the carbon dioxide gasification rate: $A_{H_2O}=A_{CO_2}$, and $E_{H_2O}=E_{CO_2}$. Based on the same references, the hydrogen gasification rate is taken to be three orders of magnitude smaller than the carbon dioxide rate: $A_{H_2}=10^{-3}A_{CO_2}$ and $E_{H_2}=E_{CO_2}$. Although the parameters in Table 4 were derived from small-particle experimentation, the kinetic rate constants are assumed to be applicable to large-particle oxidation and gasification. Large-particle oxidation and gasification data are scarce. The model uses measured char oxidation rate data for various coals correlated to first-order kinetics, Table 4. Acceptable predictions can be obtained with these correlations without a precise knowledge of the mechanism or the intrinsic reaction order. This is particularly effective when correlated rates are for the same or similar coal of the appropriate size covering the appropriate temperature range. Use of this simpler expression makes the addition of important diffusional effects more straightforward.

Several studies have been done on large spherical carbon particles (for example, Froberg, 1967; Kurylko, 1969) and may not be applicable to coal. Mass transport, however, may dominate the oxidation and gasification processes. For example, diffusion through an ash layer was shown to be significant when predicting burning rates for large coal slabs (see Hobbs, 1990). For the slab, the film resistance was 10 orders of magnitude higher than the chemical resistance for oxidation using the parameters in Table 4. Similar results were obtained from the large particle rates of Froberg (1967) and Kurylko (1969). Although chemical rates for small particles may differ from large particle rates, film diffusion and internal diffusion dominate, at least for oxidation. Additional experimental data are needed to make this same conclusion for the gasification reactions.

The last resistance in the denominator of Eq. 8 can be determined using an effective mass-transfer coefficient (Thorsness and Kang, 1984):

$$\frac{1}{k_{eff}} = \frac{(1-F)d_p}{2D_{eff}} \tag{9}$$

Walker et al. (1959) and Laurendeau (1978) discuss methods for calculating effective diffusivities. Park and Edgar (1987) show the effect of a developing ash layer on the burning rate of a core sample of coal. The core burning rate can be predicted by using an effective diffusivity based on the molecular diffusivity multiplied by a constant ($D_{eff}=\phi D_{lm}$). The molecular diffusivity, D_{lm}, was calculated from Chapman-Enskog theory for gas mixtures (Bird et al., 1960). The constant, ϕ, is based on the porosity of the developing ash layer. Thorsness and Kang (1985) have used 0.35 for ϕ. Wang and Wen (1972) have measured porosity of a fire clay ash which varied from 0.4 to 0.8. Laurendeau (1978) shows that ϕ can be estimated by the ash porosity divided by the tortuosity, which was taken to be 2. Using Wang and Wen's values for the ash porosity (0.4 to 0.8), ϕ should range between 0.2 and 0.4. However, lower values of ash porosity were determined for ash originating

Table 4. Oxidation and Gasification Kinetic Rate Constants (after Hedman et al., 1987)*

		$k_r=A_rT\exp(-E_r/RT)$, m/s			
Reaction	Rank	A_r, m/s·K	E_r/R, K	Source of Data	Source of Correlation
$C+0.5\,O_2 \rightarrow CO$	All ranks*	2.30	11,100	Field et al. (1967)	Baxter (1987)**
	HVBA	1.03	9,010	Goetz et al. (1982)	Baxter (1987)
	HVBC	0.50	6,310	Goetz et al. (1982)	Baxter (1987)
	SUBC	10.4	11,200	Goetz et al. (1982)	Baxter (1987)
	Lignite A	1.22	10,300	Nsakala et al. (1985)	Nsakala et al. (1985)
$C+CO_2 \rightarrow 2\,CO$	All ranks*	589.0	26,800	Goetz et al. (1982)	This study†
	HVBA	1,160.0	31,200	Goetz et al. (1982)	Baxter (1987)
	HVBC	4,890.0	31.300	Goetz et al. (1982)	Baxter (1987)
	SUBC	6,190.0	28,900	Goetz et al. (1982)	Baxter (1987)
	Lignite A	3.42	15,600	Goetz et al. (1982)	Baxter (1987)

*Base case parameters used in sensitivity analysis.
**Baxter's (1987) rate constants were obtained by nonlinear analysis of Field et al. (1967) and Goetz (1982) data.
†The CO_2 rate constants for all ranks were obtained in this study by averaging Baxter's (1987) rate constants for four coal ranks.

from the Lurgi and Wellman-Galusha gasifiers (Hobbs, 1990). Porosities for these ashes ranged from 0.06 to 0.60, indicating a lower range for ϕ of 0.03 to 0.3 for fixed-bed gasifiers.

The single-particle model can be related to the bed by using particle number density and the unreacted core particle surface area. The particle diameter, unreacted core diameter, and number density for the SP model were obtained by mass balance, assuming spherical particles and constant solids density:

$$d_p = [(1-\Omega^o_{ash})d_u^3 + \Omega^o_{ash} d_o^3]^{1/3} \tag{10}$$

$$d_u = F^{1/3} d_o \tag{11}$$

$$\eta_p = \frac{6(1-\epsilon)}{\pi d_p^3} \tag{12}$$

The heterogeneous oxidation of carbon produces both CO and CO_2 as primary products as shown in the following reaction:

$$\lambda C + O_2 \rightarrow 2(\lambda-1)CO + (2-\lambda)CO_2, \quad 1 \le \lambda \le 2 \tag{13}$$

Carbon monoxide may be favored at higher temperatures, if CO is formed at carbon edges and CO_2 is formed at inorganic sites. Lower temperatures may favor CO_2 due to catalytic activity. The CO/CO_2 ratio has been correlated by Laurendeau (1978):

$$\frac{CO}{CO_2} = A\exp\left(-\frac{E}{RT}\right) = \frac{2(\lambda-1)}{(2-\lambda)} \tag{14}$$

where $A \approx 10^{2.5}$ and $E \approx 25$–38 kJ/mol for low pressures, and $A \approx 10^{3.5}$ and $E \approx 50$–80 kJ/mol at high pressures. The stoichiometric coefficient for Eq. 13 can be determined as a function of temperature from Eq. 14:

$$\lambda = \frac{2\left[A\exp\left(-\frac{E}{RT}\right)+1\right]}{A\exp\left(-\frac{E}{RT}\right)+2} \tag{15}$$

For oxidation, λ is equal to ν_s in Eq. 8. Values for λ at 500, 1,000, 1,500 and 2,000 K are 1.08, 1.78, 1.93, and 1.96, respectively, using Eq. 15 with the low-pressure parameters; 1.00, 1.06, 1.47, and 1.76, respectively, using the high-pressure parameters. Thus, CO is favored at higher temperatures.

Model equations, options and parameters

The one-dimensional fixed-bed model equations are summarized in Table 5. The 38 ordinary differential equations in Table 1 were solved simultaneously from the top to the bottom of the reactor with LSODE (Livermore Solver for Ordinary Differential Equations, Hindmarsh, 1983). Drying, devolatilization, combustion, and gasification are described by Eqs. 4, 5 and 8. The volumetric heat-transfer rates from solid to gas, solid to wall, and gas to wall are described by Eqs. 1, 2 and 3. The heat- and mass-transfer correlations are in Table 2.

Table 5. Summary of the One-Dimensional Fixed-Bed Model Equations

Basic Equations and Boundary Conditions	Reference
Overall gas species continuity	Table 1
Overall solid species continuity	Table 1
Gas-phase energy	Table 1
Solid-phase energy	Table 1
Solid species continuity	Table 1
Gas-phase elemental continuity	Table 1
Gas-phase tar species continuity	Table 1
Gas-phase tar elemental continuity	Table 1
Auxiliary Equations	**Reference**
Ash heat capacity	Mills and Rhine (1989)
Devolatilization rates	Eqs. 5 and 6
Diffusive radiation coefficients	Table 2
Drying rate	Eq. 4
Effective gas and solid conductivities	Table 2
Enthalpy exchange due to reaction	Hobbs (1990)
Formation enthalpies	Hobbs et al. (1992)
Gas conductivity, viscosity, and diffusivity	Bird, et al. (1960)
Gas-to-wall heat-transfer coefficient	Table 2
Mass-transfer coefficient	Table 2
Oxidation and gasification rates	Eq. 8
Particle diameter and surface area	Hobbs (1990)
Particle number density	Eq. 12
Pressure drop	Ergun (1952)
Reynolds, Prandl and Schmidt numbers	Table 2
Sensible enthalpies	Hobbs et al. (1992)
Solid conductivity	Table 2
Solid-to-gas heat-transfer coefficient	Table 2
Solid-to-wall heat-transfer coefficient	Table 2
Total enthalpies	Hobb et al. (1992)
Volumetric solid-to-gas heat-transfer rate	Eq. 1
Volumetric wall heat loss from gas	Eq. 2
Volumetric wall heat loss from solid	Eq. 3

Elemental reaction rates can be determined from reaction stoichiometry. The tar reaction rates can be determined from Eq. 6.

The one-dimensional fixed-bed model parameters and options are summarized in Table 6. Parameters that are difficult to obtain and subject to the most uncertainty include the solid-to-gas heat-transfer coefficient, effective diffusivity, and bed void fraction. It has been reported (Lowry, 1963) that the solid-to-gas heat-transfer coefficient typically ranges between 0.02 and 0.1 times that for a nonreacting fixed-bed system; this is discussed in detail in the sensitivity analysis. The effective diffusivity can be estimated from measured ash porosity. Bed void fraction for the feed coal can also be determined experimentally. However, the bed void fraction is not constant throughout the reactor. Values at the top and bottom of the reactor are required in the one-dimensional model.

Solution technique

The set of equations in Table 5 with boundary conditions describes a split boundary value problem. The term "split boundary" has been used to describe the partially known and unknown boundary conditions at both the top and the bottom of the moving-bed reactor. Although split boundary value problems have been solved satisfactorily for homogeneous models (equal solid and gas temperatures), heterogeneous models are more difficult to solve. For example, converged results from Cho's heterogeneous model (1980) indicate that the solid temperature is close to the gas temperature at the top

Table 6. Summary of One-Dimensional Fixed-Bed Model Parameters and Options

Parameter	Typical Value (Source)	Description
Devolatilization		
x^o	0.110–0.270 (Table 3)	Potential tar-forming fraction
k_f^o 1/s	0.81×10^{13} (CO_2 extra loose; Serio et al., 1987)	Functional group frequency factor
E_f/R, K	22,500 (CO_2 extra loose; Serio et al., 1987)	Functional group activation energy
k_x^o, 1/s	0.86×10^{15} (Tar; Serio et al., 1987)	Tar frequency factor
E_x/R, K	27,700 (Tar; Serio et al., 1987)	Tar activation energy
Oxidation/Gasification		
A_{CO_2}, m/s·K	589.0 (Table 4)	Gasification frequency factor
E_{CO_2}/R, K	26,800 (Table 4)	Gasification activation energy
A_{H_2}, m/s·K	0.589 (Table 4)	Gasification frequency factor
E_{H_2}/R, K	26,800 (Table 4)	Gasification activation energy
A_{H_2O}, m/s·K	589.0 (Table 4)	Gasification frequency factor
E_{H_2O}/R, K	26,800 (Table 4)	Gasification activation energy
A_{O_2}, m/sK	2.30 (Table 4)	Oxidation frequency factor
E_{O_2}/R, K	11,100 (Table 4)	Oxidation activation energy
Flow, Heat and Mass Transport		
ϵ'	0.85 (Table 2)	Coal emissivity
ϵ top	0.23–0.40 (Table 7)	Bed void at bed top
ϵ bottom	0.33–0.67 (Table 7)	Bed void at bed bottom
ζ	0.10 (Lowry, 1963)	Reactive/nonreactive heat-transfer coeff.
ϕ/τ^2	0.50 (Laurendeau, 1978)	Ash porosity divided by tortuosity squared
Operating Parameters		
Prox. & ult.	Table 7	Proximate and ultimate analysis
d_p, cm	1.27–3.63 (Table 7)	Particle diameter
D, m	1.98–2.74 (Table 7)	Reactor inside diameter
z, m	1.83–3.05 (Table 7)	Bed height
P, kPa	100–2,600 (Table 7)	Reactor pressure
T_{coal}, K	298 (Table 7)	Inlet coal temperature
T_{BG}, K	331–644 (Table 7)	Feed gas temperature
T_{wall}, K	310–498 (Table 7)	Wall temperature
m_c, kg/s	0.179–2.23 (Table 7)	Coal mass-flow rate
m_o, kg/s	0.335–0.948 (Table 7)	Oxidizer mass-flow rate
m_s, kg/s	0.0500–2.80 (Table 7)	Steam mass-flow rate
Model Options		
(1) AS or SP char submodel; (2) gas-phase tar reaction equilibrium option; (3) volatiles mass-transport option; (4) combustion product distribution.		

of the reactor, which was 1,050 K. However, the initial temperature of the solid at the top of the reactor was specified to be 370 K. In this study, iterative methods were used to satisfy temperature boundary conditions.

A two-zone, well-mixed, equilibrium-based, fixed-bed model (Hobbs et al., 1992) has been used here to provide an initial estimate of the effluent gas composition and temperature. However, the gas exit temperature predicted by the two-zone model is generally high due to the assumption that the devolatilization zone is at a single temperature. Likewise, the exit solid temperature is high due to the well-mixed assumption. Thus, after integrating from the top to the bottom of the reactor, the calculated feed gas temperature will be higher than the input feed gas temperature. Therefore, a new exit gas temperature must be estimated which is smaller than the temperature predicted by the two-zone model. This procedure can be repeated in an iterative manner until the calculated feed gas temperature is equal to the input feed gas temperature. In general, burnout should also be used as an iteration variable. However, burnout is typically high in fixed-bed gasifiers, and thus it was assumed to be unity for all calculations reported here and was not used as an iteration variable. Iterations using temperature converged to a burnout equal to unity. Typically, two to four iterations through the gasifier are required for convergence. Hobbs (1990) provides details on the computational algorithm. Calculation times for one sweep through the reactor using an engineering workstation for the two-zone model and one-dimensional model are on the order of seconds and minutes, respectively.

Parametric Analysis

The parametric sensitivity analysis was divided into three major categories: model options, model parameters, and operational parameters. Four model options were investigated: tar vapor reaction equilibrium, volatiles mass transport, char ash layer formation and combustion product distribution. Seven model parameters were also examined: solid-to-gas heat-transfer coefficient, effective diffusivity, bed-to-wall heat-transfer coefficient, potential tar-forming fraction, functional group composition, coal density, and oxidation and gasification kinetic parameters. Furthermore, eight operational parameters were examined: feed gas temperature, reactor pressure, coal mass flow rate, steam mass flow rate, air mass flow rate, proximate ash content of the feed coal, coal particle diameter, and bed void fraction.

The response to parametric changes in input parameters can be observed in various output parameters such as solid temperature, gas temperature, gas concentrations, and pressure drop. Solid temperature was chosen as the primary response variable for all the parametric simulations, since it is indicative of the extent of heterogeneous reaction. The base case for the parametric sensitivity simulations was gasification of Jetson bituminous coal in an air-blown Wellman-Galusha gasifier

Table 7. Operating Parameters for Lurgi and Wellman-Galusha Gasifiers

Gasifier* Coal Type	Lurgi Rosebud Subbitum.	WG Absaloka Subbitum.	WG Benton Lignite	WG Elkhorn Bituminous	WG Jetson Bituminous	WG Kemmerer Subbitum.	WG Leucite Subbitum.	WG Rosebud Subbitum.	WG Utah B.C. Bituminous
Proximate, wt. %									
Ash	9.7	6.3	6.4	4.7	4.3	5.7	9.0	11.8	11.1
Fixed carbon	36.4	40.7	25.9	53.7	49.5	42.4	44.9	40.1	43.9
Moisture	24.7	23.5	32.8	4.6	6.3	16.8	17.4	21.3	6.1
Volatile	9.2	29.6	34.9	36.9	39.9	35.1	28.8	26.8	38.9
Ultimate, wt. %									
Carbon	77.1	76.3	73.7	82.5	81.4	77.5	78.1	78.7	80.3
Hydrogen	4.9	5.1	6.2	5.7	5.1	5.6	5.0	4.9	6.2
Nitrogen	1.4	0.8	1.0	1.6	1.8	1.2	1.9	1.1	1.2
Sulfur	1.7	0.4	0.9	0.9	1.6	1.0	0.6	1.3	0.6
Oxygen	15.0	17.4	18.2	9.3	10.2	14.7	14.4	14.0	11.7
Operating Parameters									
Chamber inside dia., m	2.74	1.98	1.98	1.98	1.98	1.98	1.98	1.98	1.98
Bed Height, m	3.05	2.11	2.13	2.13	1.83	2.13	2.00	2.00	2.13
Chamber pres., kPa	2,560	101.3	101.3	101.3	101.3	101.3	101.3	101.3	101.3
Apparent density, kg/m³	1,270	1,260	1,200	1,300	1,190	1,260	1,310	1,310	1,220
Particle dia., cm	1.61	2.29	3.05	3.63	2.03	1.27	2.54	2.29	2.16
Void fraction at bed top**	0.40	0.36	0.25	0.35	0.33	0.30	0.32	0.23	0.33
Void fraction at bed bottom**	0.50	0.50	0.45	0.46	0.60	0.52	0.46	0.33	0.67
Inlet coal temp., K	298	298	298	298	298	298	298	298	298
Feed gas temp., K	644	332	340	331	334	332	334	336	335
Wall temp., K	498	310	310	310	310	310	310	310	310
Coal mass flow, kg/s	2.23	0.420	0.749	0.324	0.352	0.284	0.293	0.179	0.337
Air-mass flow, kg/s†	0.58	0.764	0.931	0.789	0.948	0.573	0.532	0.335	0.673
Steam mass flow, kg/s	2.80	0.114	0.231	0.113	0.156	0.0881	0.0883	0.050	0.119
Jacket steam mass flow, kg/s	0.31	0.0034	0.051	0.0082	0.134	0.0030	0.0620	0.0174	0.0261
Wall heat loss, MW‡	0.836	0.155	0.226	0.260	0.416	0.167	0.291	0.169	0.295
Wall heat loss, MW§	0.888	0.343	0.481	0.518	0.257	0.197	0.255	0.126	0.341
Reference¶		12 (53)	10 (55)	9 (71)	2 (68)	14 (49)	4 (59)	15 (50)	13 (57)

*WG represents the atmospheric Wellman-Galusha Gasifier.
**Estimated from measured bulk and apparent densities.
†Oxygen mass-flow rate for the Lurgi case, kg/s.
‡Heat loss calculated from reported jacket steam and cooling water heat loss.
§Heat loss calculated with the one-dimensional model (MBED-1D).
¶Volume (underlined) and page number (in parenthesis) of Thimsen et al. (1984).

(Thimsen et al., 1984). Operational data for the Jetson case are given in Table 7. Additional parameters required by the one-dimensional model for the base case (Jetson) are given in Table 3. The sensitivity of temperature to the solid-to-gas heat-transfer coefficient was completed for eight different cases, rather than just the Jetson case. Input parameters for these eight cases are also reported in Table 7.

Model options

Tar Vapor Chemistry. The one-dimensional, fixed-bed model has two options for treating tar vapor chemistry: 1. the tar is allowed to react in the gas phase to completion (chemical equilibrium assumption); or 2. the tar vapor is nonreactive (in thermal equilibrium, but "frozen" chemically). Condensed-phase tar remaining in the solid is considered as part of the char. If option 1 is chosen, all gases including tar are assumed to be in chemical equilibrium. If option 2 is chosen, all gases except for tar are assumed to be in chemical equilibrium.

The predicted sensitivity of the axial solid temperature profile to the tar gas-phase equilibrium assumption for gasification of Jetson bituminous coal in an atmospheric, air-blown, Wellman-Galusha gasifier is shown in Figure 3A. Use of the equilibrium assumption caused a small shift in the temperature peak toward the bottom of the reactor. This small effect can be explained by noting that gasifiers operate fuel-rich near the top of the gasifier. When the tar reacted to equilibrium in the drying and devolatilization zones, the gas phase became more fuel-rich, which caused the temperature to decrease slightly. The decrease in temperature in the devolatilization zone caused the devolatilization zone length to increase, which consequently caused the entire temperature profile to shift toward the reactor bottom. The transition between the devolatilization zone and the gasification zone was more gradual when the tar was allowed to react to equilibrium. Again, the gradual transition was caused by lower temperatures.

Volatiles Mass Transport. The predicted sensitivity of axial solid temperatures to the devolatilization mass transport (Eq. 7) for gasification of Jetson bituminous coal in an atmospheric, air-blown Wellman-Galusha gasifier is shown in Figure 3B. Inclusion of mass-transport resistance caused only a small effect on the solid temperature profile. The more rapid release of volatile matter near the reactor top caused the gas phase to become fuel-richer, which consequently caused the temperature of the devolatilization zone to decrease. The decreased temperature in the devolatilization zone caused the devolatilization zone length to increase, which caused the location of the maximum temperature to move toward the bottom of the reactor.

Char Ash Layer. The predicted sensitivity of axial solid temperature to the SP and AS ash assumptions for gasification

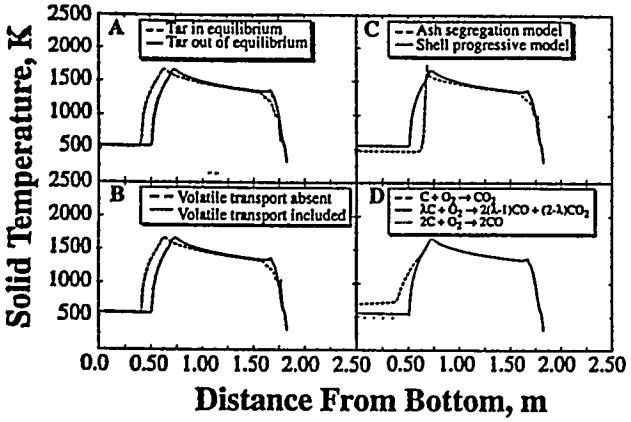

Figure 3. Predicted sensitivity of axial solid temperature to model options: A) tar gas-phase equilibrium assumption; B) volatile mass-transport assumption; C) char model ash assumption; and D) distribution of CO and CO_2 for the char oxidation reaction.

Simulation is for gasification of Jetson bituminous coal in an air-blown Wellman-Galusha gasifier. Input parameters are in Tables 3, 4, 7 and 8.

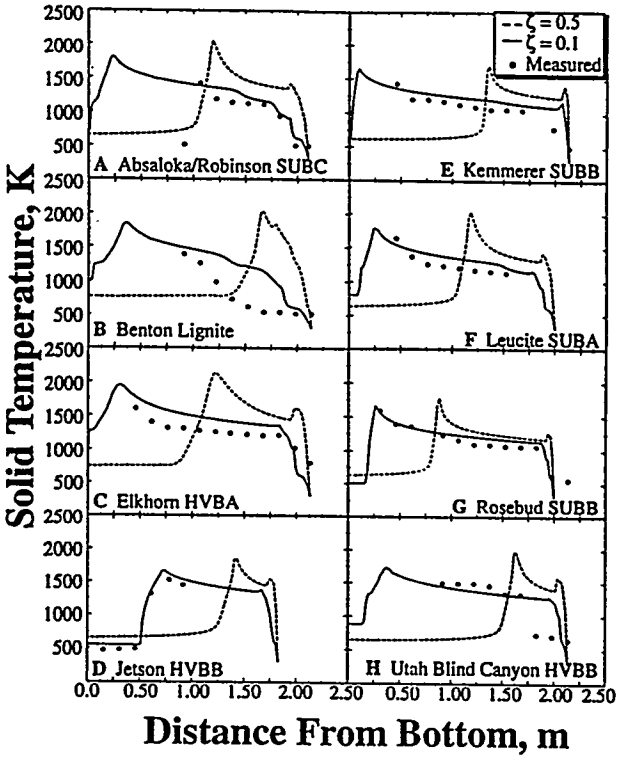

Figure 4. Predicted sensitivity of axial solid temperature to solid-to-gas heat-transfer correction factor, ζ, in an atmospheric pressure Wellman-Galusha gasifier fired with: A) Absaloka/Robinson subbituminous; B) Benton lignite; C) Elkhorn bituminous; D) Jetson bituminous; E) Kemmerer subbituminous, F) Leucite subbituminous; G) Rosebud subbituminous; and H) Utah Blind Canyon bituminous coals.

Measurements from Thimson et al. (1984). Input conditions are given in Tables 3, 4, 7 and 8.

of Jetson bituminous coal in an atmospheric air-blown Wellman-Galusha gasifier is shown in Figure 3C. Once again, relatively small differences are observed between the two options. The shape of the solid temperature profile using the AS model (no ash layer) was sharper than the broad peak predicted by the SP model. Also, the maximum temperature was higher when the AS model option was chosen. The two char models represent extremes in ash behavior, although the SP model may be closer to actual ash behavior. This observation is based on 1) comparing predicted temperature profiles to measured temperature profiles and 2) experimental observations of large-particle oxidation which show ash-layer accumulation (Park and Edgar, 1987). However, more specific data on oxidation of large particles in packed beds is required to confirm this suggestion.

Use of the AS submodel option resulted in an increased rate of carbon being added to the gas phase, which caused the gas phase to become fuel-richer. In the drying, devolatilization and gasification zones, a decrease in temperature was calculated. The combined effects of a shorter oxidation zone due to more rapid reaction and a lower devolatilization zone temperature caused the location of the maximum temperature to remain nearly unchanged.

Oxidation Product Distribution. Predicted sensitivity of axial solid temperature and gas concentration to the distribution of combustion products CO and CO_2 during gasification of Jetson bituminous coal in an atmospheric, air-blown Wellman-Galusha gasifier is shown in Figure 3D. Three assumptions are shown: 1) CO_2 as the sole primary combustion product; 2) CO as the sole primary combustion product; and 3) a distribution of CO_2 and CO combustion products that depends on solid temperature (Eq. 14). As expected, only the oxidation zone was affected by the combustion product distribution assumption. Different temperatures resulted from the energy exchange at the particle-to-gas interface due to reaction. Close agreement between the sole CO distribution and the combined CO/CO_2 distribution suggests that carbon monoxide may be assumed to be the primary product at typical combustion temperatures, which complements the findings of Laurendeau (1978).

Model parameters

Solid-to-Gas Heat-Transfer Coefficient. Effects of key model parameters that have not been reported experimentally and have a significant impact on the solid temperature profile were investigated. The solid-to-gas heat-transfer coefficient for a nonreacting system may be 10 to 50 times higher ($\zeta = 0.02$–0.1) than that for a reacting system (Lowry, 1963). Dzhaphyev et al. (1986) attribute the observed difference to unsteady heat transfer. Vigorous reactions as well as nonsphericity and transpiration cooling may also contribute to this difference. The solid temperature is sensitive to this ratio, ζ. Predicted sensitivity of axial solid temperature to ζ for the Wellman-Galusha cases is shown in Figure 4, where measured temperatures are also shown. None of the measured and predicted profiles correspond when ζ is greater than 0.1. All profiles in Figure 4

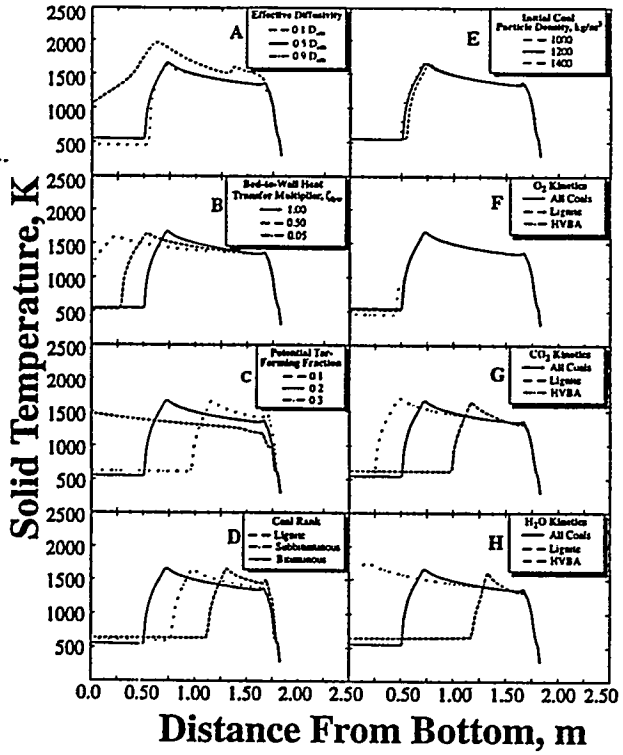

Figure 5. Predicted sensitivity of axial solid temperature to model parameters; A) effective diffusivity; B) bed-to-wall heat transfer; C) potential tar-forming fraction; D) coal rank; E) initial coal particle density; F) O_2-char oxidation kinetic parameters; G) CO_2-char gasification kinetic parameters; and H) H_2O-char gasification kinetics.

Input conditions are for atmospheric gasification of Jetson bituminous coal in an air-blown Wellman-Galusha gasifier. Input conditions are in Tables 3, 4, 7 and 8.

also show the importance of treating devolatilization as a kinetic process. The Benton lignite case with 33% moisture shows that the drying zone was about 0.5 m, thus discounting the common assumption of instantaneous drying.

Effective Diffusivity. The predicted sensitivity of the solid temperature to the effective diffusivity (Eq. 9) is shown in Figure 5A. The effective diffusivity affects the location of the maximum solid temperature, the magnitude of the maximum solid temperature, and the shape of the solid temperature profile. Lower values of ϕ (D_{eff}/D_{im}) cause the location of the maximum solid temperature to shift toward the bottom of the reactor and the size of the oxidation zone to increase, because the char oxidizes more slowly.

Bed-to-Wall Heat Transfer. The sensitivity of solid temperature to the bed-to-wall heat-transfer coefficient is shown in Figure 5B. For the calculations, h_w from Eq. 1 in Table 2 was multiplied by a constant, ζ_{hw}, to see the effect of lowering bed-to-wall heat transfer. Lower values of ζ_{hw} caused the solid temperature to decrease in the gasification and oxidation regions of the gasifier. The shift in location of the maximum solid temperature and the change in the shape of the curve were attributed to a redistribution of solid enthalpy.

Tar Fraction. Predicted sensitivity of solid temperature to the potential tar-forming fraction, x^o (maximum tar yield), for the base case is shown in Figure 5C. To provide a consistent method of calculating tar, a semi-empirical model of Ko et al. (1988) was used to predict tar yield. As x^o was increased, the ultimate volatile yield also increased and the corresponding ultimate char yield decreased, which resulted in a smaller gasification/oxidation zone. The shift in the location of the maximum solid temperature was attributed to the smaller oxidation and gasification zones.

Coal Rank. The predicted sensitivity of solid temperature to coal rank is shown in Figure 5D. Three different coal types were investigated: lignite, subbituminous, and bituminous coals. The solid temperature sensivity to rank may be attributed to the rank dependence of volatile matter (that is, lower-rank coals contain more volatile matter than higher rank coals). The increase in ultimate volatile yield and corresponding decrease in ultimate char yield resulted in a smaller gasification/oxidation zone.

Coal Density. During devolatilization, coal particles evolve tars and gases, and the density can decline. The particles can also soften and swell depending on coal rank. Thus, it is expected that solids density will decline during devolatilization. The rate equations for devolatilization (Eqs. 5 and 6) depend on initial coal density which is specified. However, rates of char reaction (with O_2, CO_2, H_2O, and H_2) depend on the char density, not on the original coal density. Further, the char density can change during oxidation (Smith, 1983). In this study, the solid density was taken to be constant throughout the bed at the initial coal density value. Sensitivity of solids density was tested by comparing temperature and pressure with different initial solids density values of 1,000–1,400 kg/m^3. Effects of solid density are shown in Figure 5E to be modest.

Oxidation and Gasification Kinetics. Sensitivity of solid temperature to oxidation and gasification parameters (Table 4) is shown in Figures 5F through 5H. The solid temperature was not sensitive to the H_2 gasification kinetics because of the slow reaction rate and is therefore not shown. The solid temperature, however, was sensitive to the O_2, CO_2 and H_2O gasification kinetic parameters as shown in Figures 5F and 5H. Differences among coals were small for oxygen rates, but large for CO_2 and H_2O rates, with faster rates shortening the gasification zone. This suggests that reliable gasification rates for specific coals are required to make reliable predictions.

Operational parameters

Sensitivity of solid temperature to operational parameters is shown in Figure 6. Operational parameters that can be changed readily are the feed gas temperature, the reactor pressure, the coal mass-flow rate, the steam mass-flow rate, and the air-mass-flow rate. Other operational parameters are not as easily modified during daily operation. Such parameters include the proximate ash content, coal particle diameter, and the bed void fraction. Coal selection or pretreatment such as washing or crushing may be necessary to change these parameters.

Feed Gas Temperature. The location and magnitude of the maximum solid temperature were substantially affected by feed gas temperature (Figure 6A). As expected, the maximum temperature decreased when feed gas temperature was lowered, while the location of the maximum temperature at steady operating conditions shifted toward the bottom of the reactor.

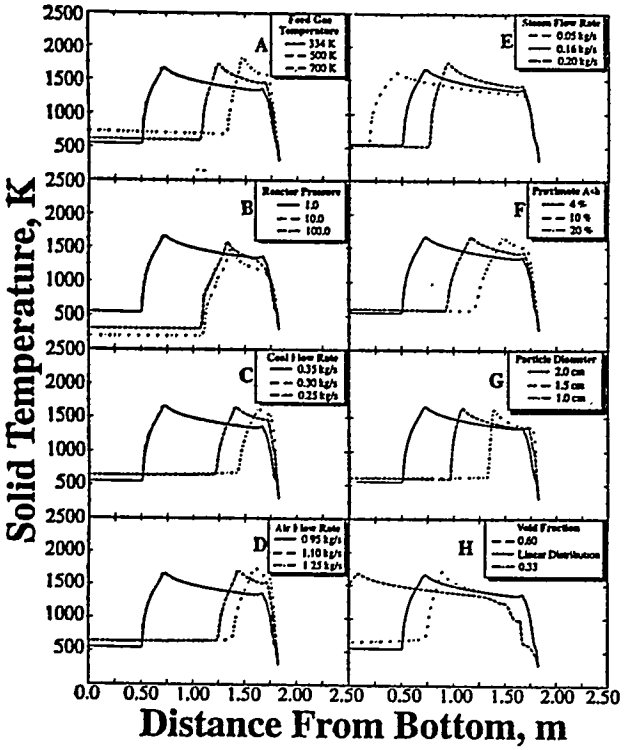

Figure 6. Predicted sensitivity of axial solid temperature to operational variables: A) feed gas temperature; B) reactor pressure; C) feed coal mass-flow rate; D) feed air-mass-flow rate; E) feed steam mass-flow rate; F) feed coal proximate ash content; G) feed coal mean particle diameter; and H) bed void fraction.

Input conditions are for atmospheric gasification of Jetson bituminous coal in an air-blown Wellman-Galusha gasifier. Input conditions are in Tables 3, 4, 7 and 8.

The lower feed gas temperature caused the effluent gas temperature to decrease. The lengths of the drying, the devolatilization, the gasification, and the oxidation zones were all increased, which caused the location of the maximum temperature to move toward the bottom of the reactor.

Reactor Pressure. The predicted sensitivity of solid temperature to reactor pressure is shown in Figure 6B. Increasing pressure at lower pressure levels caused the location of the maximum temperature to shift toward the top of the reactor. The change in temperature gradient in the oxidation zone of the high-pressure simulation was due to competition between the highly exothermic oxidation reaction and the endothermic steam gasification reaction. This effect was substantial in the high-pressure Lurgi case discussed subsequently. Once the solid temperature is sufficiently high for the oxidation reaction to begin, the rapid oxidation of carbon causes the solid temperature to increase dramatically. Once the temperature reaches about 1,000 K, the steam reaction begins. Although the steam reaction is not as fast as the oxidation reaction, the concentration of steam is significantly higher than the oxygen concentration. Thus, carbon consumption associated with the steam reaction approaches the carbon consumption associated with the oxidation reaction. The endothermic steam gasification reaction quenches the rapid increase in solid temperature and causes a sudden change in solid temperature, which was observed in the high-pressure case in Figure 6B.

When pressure is increased, the partial pressure of the water increases. Although the partial pressure of oxygen is also increased, the greater abundance of steam causes a substantial increase in the steam gasification reaction. The effect is to magnify the competition between the endothermic and exothermic reactions, producing a small peak shown subsequently in Figure 7A. Also, the diffusivity of water is greater than that of oxygen. Therefore, the steam gasification reaction is amplified at higher pressures.

Coal Flow Rate. The predicted sensitivity of solid temperature to coal mass-flow rate is shown in Figure 6C. All parameters in these simulations were held constant except for the coal mass-flow rate. The substantial shift in the location of the maximum temperature profile was attributed to a decrease in time required to consume all of the organic matter in the coal. The low coal mass-flow rates correspond to combustion occurring at the top of the gasifier. Thus, both combustion and gasification runs are depicted in Figure 6C.

Air Flow Rate. The predicted sensitivity of solid temperature to air-mass-flow rate is shown in Figure 6D. The influence of air-mass-flow rate was similar to that of coal mass flow rate. Again, the higher air-mass-flow rate corresponded to a combustion case. The shift in location of the maximum temperature was attributed to increased oxidation rates.

Steam Flow Rate. The predicted sensitivity of the solid temperature to the steam mass-flow rate is shown in Figure 6E. As the steam mass-flow rate was increased, both the lo-

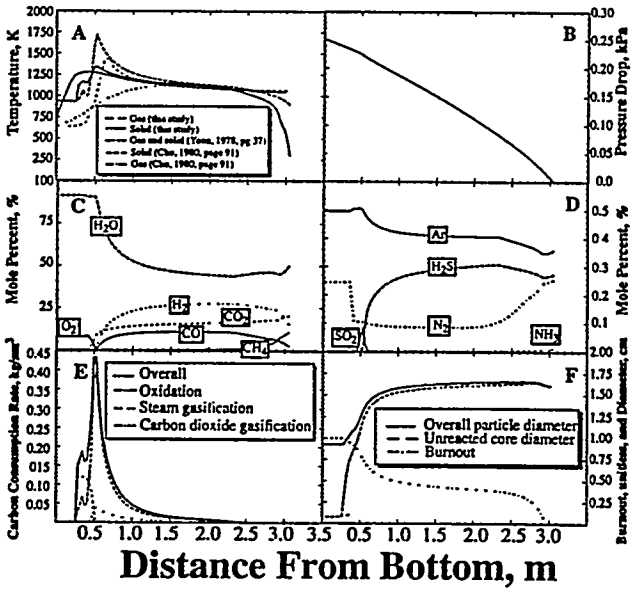

Figure 7. Predicted axial: A) temperature; B) pressure drop; C) major species concentration; D) minor species concentration; E) oxidation/gasification carbon consumption rate; F) burnout, overall and unreacted particle diameter in a high-pressure, oxygen-blown Lurgi gasifier fired with Rosebud subbituminous coal.

Input parameters are in Tables 3, 4, 7 and 8. Figure A shows results from the homogeneous model of Yoon (1979) and the heterogeneous model of Cho (1980).

cation and the magnitude of the maximum temperature were affected. Increasing feed steam caused the maximum temperature to decrease. The shift in the location of the maximum temperature is caused by lower exit temperatures associated with higher steam mass-flow rates. This operational parameter is used frequently to control the temperature to avoid significant ash melting.

Ash Content. The predicted sensitivity of solid temperature to proximate ash content of the feed coal is shown in Figure 6F. The shift in the location of the maximum solid temperature is analogous to the temperature shift caused by the coal mass-flow rate. Lower proximate ash content is equivalent to an increase in the coal mass-flow rate, which results in a larger gasification zone. Similar results were obtained when the proximate moisture content was changed.

Particle Diameter. The predicted sensitivity of solid temperature to feed coal particle diameter is shown in Figure 6G. Small particles heat up faster and react sooner than large particles. The increased solid temperature promotes all reactions, which are completed much earlier for the smaller particles than for the larger particles. Also, mass transport resistances are less for small particles than for large particles. Particle-size effects are approximately linear as shown in Figure 6G. The influence of a distribution of particle sizes is more difficult to determine. Heat- and mass-transport rates are affected significantly, and the bed void fraction may also change dramatically, as discussed in the following section. Wide particle-size distributions tend to decrease the bed void fraction (Fayed and Otten, 1984).

Void Fraction. The predicted sensitivity of solid temperature to bed void fraction is shown in Figure 6H. The void fraction significantly affects the particle number density, which in turn affects the overall bed consumption rate. Increasing void fraction causes a decrease in the overall bed reaction rate. Drying, devolatilization, gasification and oxidation rates are all decreased significantly when the void fraction is increased. Thus, all prominent reaction zones increase with increasing bed void fraction, and the location of the maximum temperature moves toward the bottom of the reactor.

Rapid increase in the solid temperature at the reactor top is due, for the most part, to the rising hot gases from the oxidation zone heating the descending coal particles. The solid heat capacity is reduced significantly by the release of the volatiles in the devolatilization zone making the solid temperature increase more rapidly. The gas temperature, at the same time, is reduced sharply due to the mixing with colder volatiles released from the solids.

Model parameters with the most uncertainty are the solid-to-gas heat-transfer coefficient and the effective diffusivity coefficient. Methods used for estimates of these parameters are summarized in Table 8. If experimental values are unavailable, the approach of Table 8 can be used with caution to estimate bed void fraction, ϵ, solid-to-gas heat-transfer ratio, ζ, and the ash porosity, ϕ, and consequently, the effective diffusivity.

Table 8. Procedures Used to Estimate Key Model Parameters

Parameter	Independent Calculation	Selection Procedure
Bed void fraction at coal inlet, ϵ_c, and ash outlet, ϵ_a	Void fractions can be measured or estimated from coal and ash properties. Typical values may range between 0.2 and 0.8 depending on particle distribution, sphericity and particle roughness.*	Bed void fraction is selected to match measured pressure profile. Initially, ϵ_c and ϵ_a are adjusted in equal increments; however, top or bottom void fractions are adjusted independently if the measured profile indicates a larger or smaller void fraction.
Solid-to-gas heat-transfer correction factor, ζ	Selection of ζ is based on experience with the sensitivity analysis shown in Figures 4 and 5. A value of 0.1 is recommended if no other data are available.	ζ is selected to match the location of the maximum measured temperature.
Effective diffusivity parameter, $\phi = \phi_a/\tau^2 \approx \phi_a/2$	ϕ can be measured or estimated from the ash porosity, ϕ_a. Ash porosities range from 0.06 to 0.60 for ash obtained from fixed-bed gasifiers (see Hobbs, 1990). An acceptable range for ϕ might be 0.02 to 0.5. A value of 0.5 is recommended if no other data are available.	ϕ can be selected to match the location of the maximum measured temperature. ϕ is usually adjusted after ζ is chosen. If adjusting ζ is insufficient to adjust the location of the maximum temperature, adjust ϕ.
SP or AS model option	Selection of the char model is based on experience with the sensitivity analysis as shown in Figure 3C. The SP model option is recommended if no other data are available.	The AS model can be chosen, if a discontinuity is observed in the measured pressure profile, if the oxidation zone is very small with a corresponding steep temperature gradient, or if burnout is high simultaneously with a large drying zone as is common for lignites with high moisture contents.

*Fayed and Otten (1984) discuss bed void fraction. For spherical particles, bed void fraction for close random packing ranges from 0.359 to 0.375; for hexagonal close packing, bed void fraction is 0.26. The effect of nonsphericity is to increase bed void fraction. For example, for a sphere with a sphericity of 1.0, it is 0.4; for a cube with sphericity 0.8, it is 0.5; and for a particle with sphericity of 0.2 it is 0.85.

Comparisons with Fixed-Bed Data

Selection of model variables

While effluent gas composition is predicted by MBED-1D, comparison of these predicted and measured values does not provide a strong evaluation of a generalized fixed-bed model. Once coal burnout is established, which is often near unity, and tar production is estimated (for example, Ko et al., 1988), effluent gas composition can be readily estimated without recourse to a generalized, fixed-bed model (Hobbs et al., 1992). Thus, evaluation of MBED-1 was performed by comparison with measured axial profiles of temperature and pressure in fixed beds. No data for composition profiles were located for this purpose, and experimental temperature and pressure profiles within laboratory or commercial-scale fixed-bed gasifiers are limited. Eight low-pressure, air-blown Wellman-Galusha cases (Thimsen et al., 1984) were simulated together with one high-pressure, oxygen-blown Lurgi gasifier case with Rosebud subbituminous coal. No measured profiles were available for the dry-ash Lurgi gasifier.

These simulations are also compared to predictions from other one-dimensional models. Measured and predicted solid temperatures for several operating conditions are also compared for some of the Wellman-Galusha tests. Comparisons of predicted and experimental temperature profiles have helped to determine recommended values of model parameters. Caution must be exercised, however, when making conclusions based on profiles from experimental fixed-bed data. Thimsen (1990) warns that temperature profiles for the Wellman-Galusha cases be used for qualitative comparisons only, since the temperature probe [1/2-in. (13-mm) schedule 40 304 SS pipe with six sheathed type-K thermocouples placed 6 in. (152 mm) apart] was retracted from the gasifier when any junction approached 1,600 K. Typically, the temperature probe was allowed 10 minutes to reach steady state (Thimsen et al., 1984). Furthermore, the temperature profiles may represent transient conditions if the probes were retracted early. The usual disadvantages related to intrusive probes may also cause problems in fixed-bed temperature measurements: physical processes may be altered by flow disturbances; catalytic perturbations may be caused by the probe; and radiation and/or conduction losses may be significant. The measured temperature profiles were assumed to be closer to the solid temperature following Barriga and Essenhigh (1980). Additional simulations predicted concentration profiles of major and minor species, carbon consumption rates due to oxidation and gasification, burnout, and particle diameter.

A solid-to-gas heat-transfer correction factor of 0.1 was used for all simulations. The effective diffusivity was assumed to equal 0.5 times the molecular diffusivity. The bed void distribution was assumed to vary linearly between the top and bottom of the bed, as supported by the data from Krishnudu et al. (1989). Bed void fractions were not measured directly for any of the cases. Void fractions of the feed coal at the bed top and the product ash at the bed bottom were estimated based on coal and ash bulk and apparent density measurements.

Wellman-Galusha dry-ash gasifier

Predicted axial variations in temperature and pressure profiles are compared to measurements for gasification of the eight coals in the Wellman-Galusha gasifier in Figures 8 and 9. Profile comparisons for both temperature and pressure are considered to be quite good for all, but the lignite case. Measurements for the Jetson case indicate the location of the maximum temperature. Predicted axial variations in temperature, pressure drop, gas concentration, oxidation/gasification carbon consumption rate, burnout, and particle diameter for atmospheric gasification of the Jetson bituminous coal are shown in Figure 10. This case is presented in detail since it was used as the base case in the sensitivity analysis. In the Jetson case, burnout (daf) was predicted to be unity as shown in Figure 10F. Thus, carbon is not available for oxidation in the ash zone. The ash zone temperature remains approximately 550 K. Carbon becomes available for oxidation approximately 0.5 m from the bottom of the reactor where oxidation begins. The highly exothermic oxidation reaction increases the solid temperature dramatically. The oxidation reaction occurs before the steam gasification reaction, as shown by the carbon consumption rates in Figure 10E. Once initiated, the endothermic steam gasification reaction causes the positive solid temperature gradient to decrease. This competition between exothermic and endothermic reactions describes the initial step in the temperature profile going from the ash zone to the oxidation zone.

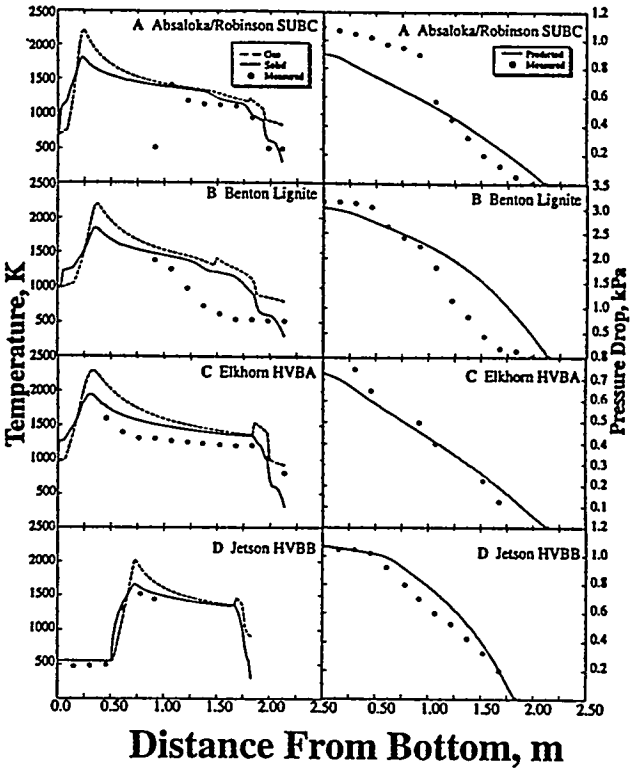

Figure 8. Predicted and measured axial variations in temperature and pressure drop during gasification of: A) Absaloka/Robinson subbituminous; B) Benton lignite; C) Elkhorn bituminous; and D) Jetson bituminous coals in an air-blown, atmospheric Wellman-Galusha gasifier.

Measurements are from Thimson et al. (1984). Input parameters are in Tables 3, 4, 7 and 8.

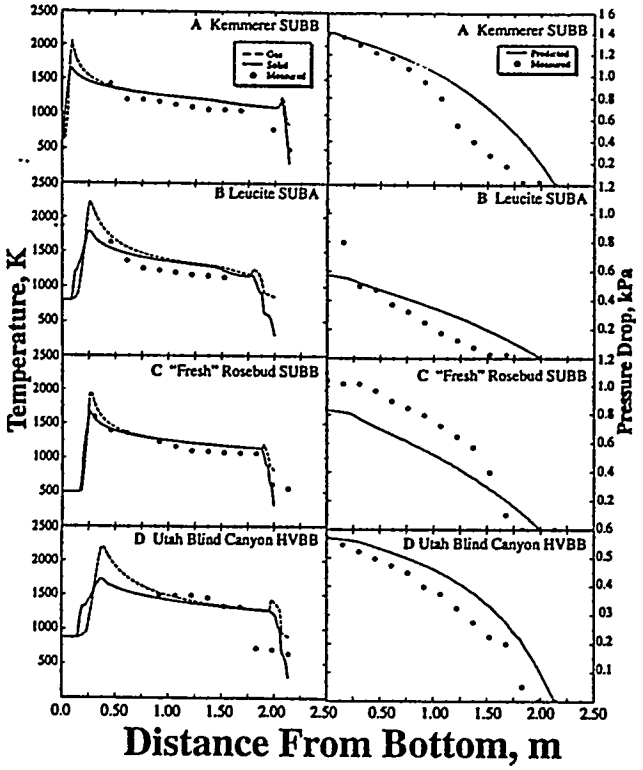

Figure 9. Predicted and measured axial variations in temperature and pressure drop during gasification of: A) Kemmerer subbituminous; B) Leucite subbituminous; C) "fresh" Rosebud subbituminous; and D) Utah Blind Canyon bituminous coals in an air-blown, atmospheric Wellman-Galusha gasifier.

Measurements are from Thimsen et al. (1984). Input parameters are in Tables 3, 4, 7 and 8.

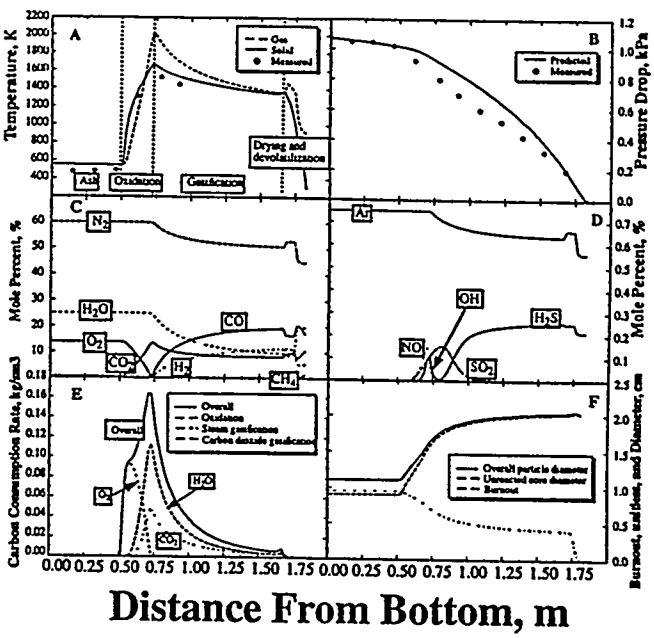

Figure 10. Predicted axial: A) temperature; B) pressure drop; C) major species concentration; D) minor species concentration; E) oxidation/gasification carbon consumption rate; and F) burnout, overall and unreacted particle diameter in an atmospheric air-blown Wellman-Galusha gasifier with Jetson bituminous coal.

Input parameters are in Tables 3, 4, 7 and 8. Measurements are from Thimsen et al. (1984, Vol. 2, p. K5).

The temperature is highest at the end of the oxidation zone and starts to decrease due to predominantly endothermic gasification reactions of carbon with steam and carbon dioxide in the gasification zone.

Steam gasification overlaps oxidation as shown in Figure 10E. For example, at 0.65 m from the reactor bottom, the carbon consumption rate due to steam gasification is approximately 0.05 $kg/s \cdot m^3$. At this location in the reactor, steam is reacting with carbon to produce hydrogen and carbon monoxide. However, no depletion of steam is observed in the concentration profile at this reactor location as shown in Figure 10C. Steam is being replenished by the homogeneous oxidation of hydrogen. Also, carbon monoxide produced from both oxidation and steam gasification is being oxidized in the presence of oxygen to produce carbon dioxide. Carbon dioxide reaches a maximum at the end of the oxidation zone and decreases in the gasification zone. In the gasification zone, carbon dioxide reacts heterogeneously with carbon to produce carbon monoxide. Carbon monoxide is not present in the gas phase until oxygen is depleted. As with carbon monoxide, hydrogen does not appear in the gas phase until oxygen is depleted. Although agreement between the predicted and measured pressure profiles was acceptable, the void distribution may not be linear throughout the reactor. For example, the measured pressure profile in Figure 10B indicated that the void fraction changed markedly near the ash zone.

The predicted increase in the particle diameter at the top of the reactor was due to coal particle swelling. Swelling was assumed to be proportional to the extent of devolatilization. For the Jetson case, the predicted particle diameter of the ash was about 1.1 cm. The measured geometric mean diameter of the ash was 1.02 cm as reported by Thimsen et al. (1984). The excess nitrogen and high temperatures caused the equilibrium quantities of NO and OH to form in the oxygen-rich, high-temperature zone of the reactor. These quantities decayed to zero as temperature decreased. Sulfur dioxide also formed in the presence of oxygen and was converted to H_2S in the colder, fuel-rich regions of the gasifier.

Several of the Wellman-Galusha experimental test cases included temperature profiles at different operating conditions. Predicted temperature profiles were compared to measurements for the Elkhorn, the Jetson, the Leucite Hills and the Utah Blind Canyon coals in Figure 11. A shift in the measured temperature profile due to changing reactant feed rates during gasification of Elkhorn bituminous coal is shown in Figure 11A. The predicted trends agreed with the direction of the measured temperature shifts in each case. From the sensitivity analysis, an increase in coal flow rate caused the location of the maximum temperature to move closer to the bottom of the reactor. In general, an increase in either the steam flow rate or air flow rate caused the location of the maximum temperature to move closer to the top of the reactor. In this

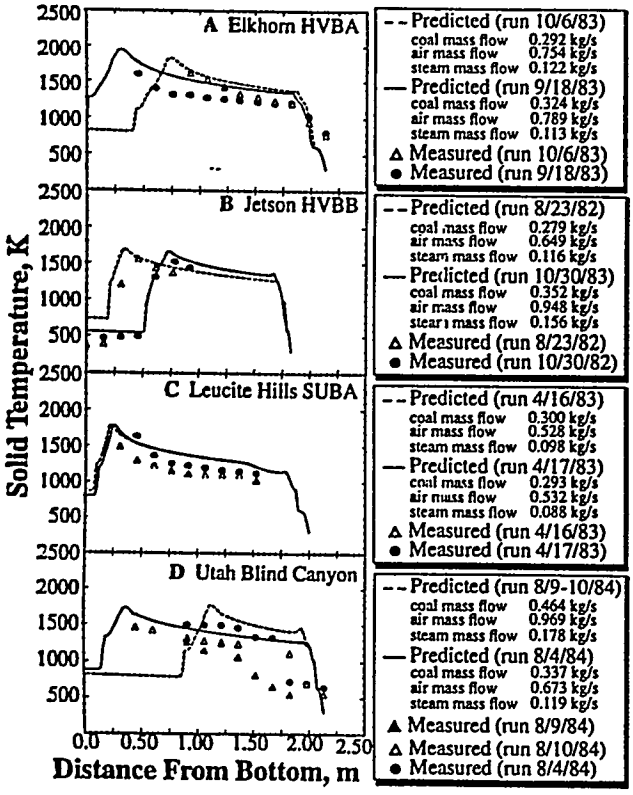

Figure 11. Measured temperature vs. predicted solid temperature for several operating conditions for gasification of: A) Elkhorn bituminous; B) Jetson bituminous; C) Leucite Hills subbituminous; and D) Utah Blind Canyon bituminous coals in an air-blown, low-pressure Wellman-Galusha gasifier.

Experimental data are in Thimsen et al. (1984). Input parameters are listed in the legend and in Tables 3, 4, 7 and 8.

case, the coal and the air flow rates were both increased, the steam flow rate was decreased, and the location of the maximum temperature moved toward the reactor bottom. Although the increased air flow rate should have caused the location of the maximum temperature to move toward the reactor top, changes in coal and steam flow rates were more significant for the Elkhorn case.

The effect of varying feed rates on the location of the maximum temperature is shown in Figure 11B for gasification of Jetson bituminous coal. The direction of the temperature shift was predicted adequately by the one-dimensional model. An increase in the coal, air and steam mass-flow rates caused the location of the maximum temperature to move toward the top of the reactor. For the Jetson case, the increase in steam and air mass-flow rates was more significant than the increase in the coal mass flow rate. Although the low-rank coals were more difficult to simulate, predictions from the one-dimensional model agreed with the experimental data for the Leucite Hills subbituminous coal as shown in Figure 11C. The increase in coal flow rate and decrease in steam flow rate caused the location of the maximum temperature to shift toward the bottom of the reactor for the Leucite Hills case. The Utah Blind Canyon case in Figure 11D also showed the effect of increased coal and gas throughputs. Trends in measured and predicted profiles do not agree for this case. However, the measurements were repeated on two separate days, but only one set of operational data was reported for this time period (Thimsen et al., 1984), possibly explaining variability in the data.

Lurgi dry-ash gasifier

Predicted axial temperature, pressure drop, gas concentration, carbon consumption rates due to oxidation and gasification, burnout, and particle diameter are shown in Figure 7 for the Lurgi gasifier fired with Rosebud subbituminous coal. The most obvious difference compared to results from the atmospheric air-blown gasifier was the absence of a carbon dioxide peak. The shape of the carbon dioxide profile was due to the low temperature of the solid in the gasification section, resulting from large quantities of steam in the feed gas stream. The temperature was low enough that the only significant heterogeneous reaction in this section of the gasifier was the steam gasification reaction. With only hydrogen and carbon monoxide being produced in the gasification section, the hydrogen and carbon monoxide profiles should have been similar. However, gas-phase reactions such as the water-gas-shift reaction produced a slight increase in carbon dioxide concentration.

Temperature predictions from two other one-dimensional models are also shown in Figure 7A. These cases were reported to be the Illinois #6 Westfield case (Yoon, 1978; Cho, 1980). However, the input conditions differed from those reported by Elgin and Perks (1974) and seemed to be closer to the Rosebud case. The source of Yoon's input data is uncertain. Also, Cho (1980) used the values provided by Yoon (1978). Yoon assumed equal solid and gas temperature, instantaneous devolatilization with a fixed composition, and gas-phase chemistry dominated by the water-gas-shift reaction. Cho essentially extended the model of Yoon to include separate solid and gas temperatures. The Yoon prediction was similar to the prediction made in our work. The shape of the solid temperature profile predicted by Cho is similar to the solid profile predicted here. Cho's gas temperature profile, however, does not correspond to the predictions by Yoon or this study. Cho's gas temperatures were less than the solid temperature in the oxidation zone. The gas temperature will be less when important gas-phase reactions are neglected. For example, steam gasification will produce H_2 and CO in the oxidation zone, and CO will be produced from oxidation. In the presence of oxygen, the homogeneous reactions of H_2 and CO with O_2 will react to produce H_2O, CO_2, and heat. These exothermic gas-phase reactions will cause a dramatic increase in gas temperature as shown in the predictions of this study.

Insights Into Fixed-Bed Gasification

Resistances to char oxidation and gasification

Chemical reaction resistance ($\propto 1/k_r\xi$), ash diffusion resistance ($\propto 1/k_{eff}$), and film diffusion resistance ($\propto 1/k_m$) illustrate the dominant chemical and physical processes occurring in fixed-bed reactors. Resistances for char oxidation and gasification of the base case are shown in Figure 12. Chemical resistances dominate at the top and bottom of the reactor for the oxidation and gasification reactions. The ash resistance was highest at the reactor bottom. At the top of the reactor,

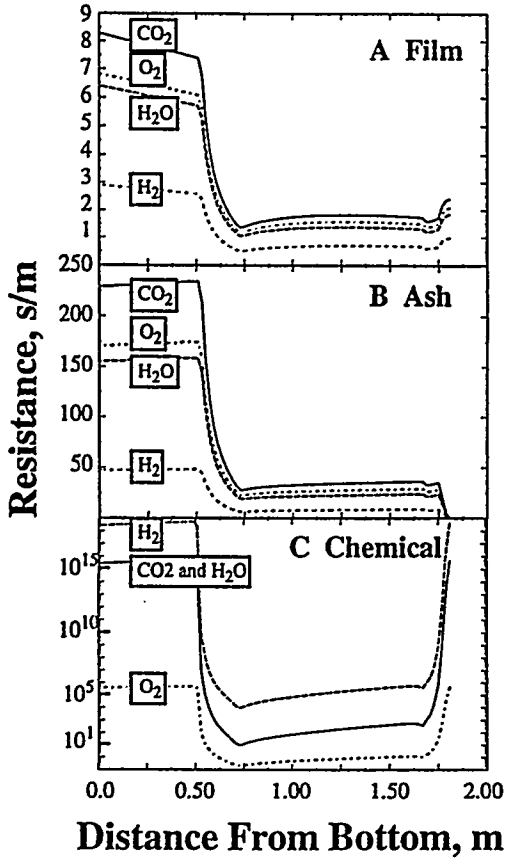

Figure 12. Resistances for char oxidation and gasification of Jetson coal in an atmospheric fixed-bed gasifier: A) film resistance; B) ash resistance; and C) chemical resistance to char oxidation and gasification reactions.

These plots correspond to the Jetson case in Figure 10.

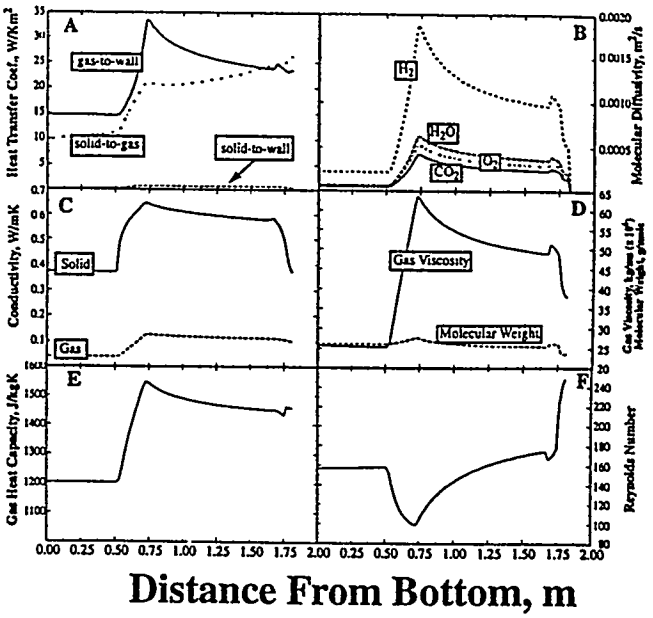

Figure 13. Predicted heat-transfer coefficients and transport properties for gasification of Jetson coal in an atmospheric Wellman-Galusha gasifier with air: A) heat-transfer coefficients; B) molecular diffusivities; C) solid and gas conductivities; D) gas viscosity and molecular weight; E) gas heat capacity; and F) Reynolds numbers.

These plots correspond to the Jetson case in Figure 10.

no ash layer was present. Once the ash layer was sufficiently thick, ash diffusion competed with the chemical reaction resistance in the gasification section of the gasifier as shown in Figures 12B and 12C. Although confidence in calculated mass-transfer coefficients was generally greater than confidence in chemical reaction coefficients, ash porosity was not measured throughout the reactor, and the effective ash diffusivity was difficult to predict.

Transport properties

Predicted heat-transfer and -transport coefficients for the base case are shown in Figure 13. Typical values for the overall bed-to-wall heat-transfer coefficient range from 15-35 $W/m^2 \cdot K$. The bed-to-wall heat-transfer coefficient can be divided into contributions from the gas-to-wall coefficient and solid-to-wall coefficient, as shown in Figure 13A. Over 95% of the heat loss to the wall for this case was due to the gas phase. The large heat transfer from the gas phase was caused by a high effective radial gas conductivity. The gas conductivity was dominated by a large dynamic contribution due to the high gas velocities. Gas Reynolds numbers throughout the reactor are shown in Figure 13F. The solid and gas conductivities are shown in Figure 13C. The solid conductivity was assumed to be proportional to the square root of solid temperature (Table 2, Eq. 7). The gas mixture conductivity was calculated from classical methods. Changes in gas conductivity, gas heat capacity, and gas viscosity were somewhat similar through the bed, all rising sharply with rapid increase in gas temperature, as shown in Figures 13C-13E.

Solid and gas residence time, velocity and heating rate

Solid residence time for the base case was on the order of hours as shown in Figure 14A. The corresponding gas residence time was on the order of seconds. The solid residence time increases in the ash zone due to significant settling resulting in variable axial velocity. Axial solid and gas velocities were shown in Figure 14B. Gas velocities were less than 3 m/s. Solid velocities were less than 0.1 mm/s. Solid velocity was affected by mass loss due to drying and devolatilization. The solid velocity decreases as heterogeneous oxidation and gasification reactions consumed the solid mass. With mass loss, the particle diameter decreased and the corresponding particle number density increased. Once all reactions were quenched, the solid velocity remained constant. Although mass addition to the gas phase contributed to increased gas velocity, temperature effects probably were more significant.

Gas and solid heating rates depend on the axial temperature profile and solid and gas residence times. Gas heating rates are approximately 4 orders of magnitude higher than the solid heating rate due to different residence times. Significant changes in heating rate occur at the oxidation temperature spike and

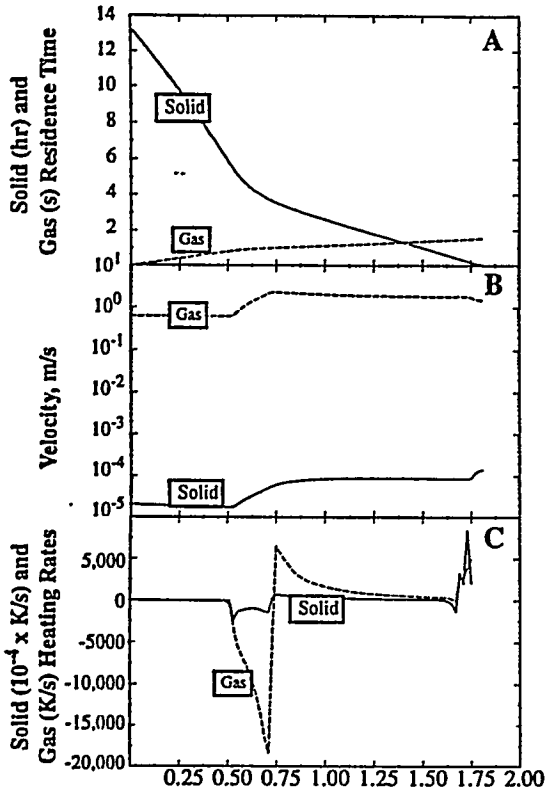

Figure 14. Predicted solid and gas: A) residence times; B) velocities; and C) heating rates during gasification of Jetson bituminous coal in an air-blown, atmospheric Wellman-Galusha gasifier.

These plots correspond to the Jetson case in Figure 10.

in the devolatilization zone where rapid heterogeneous reactions occur.

Summary and Conclusions

A generalized, one-dimensional fixed-bed gasification/combustion model (MBED-1D) has been formulated, solved numerically, evaluated through parametric sensitivity analysis, and compared with measured fixed-bed axial temperature and pressure profiles. Model advances and/or characteristics include separate gas and particle temperatures, simultaneous drying, coal devolatilization, char oxidation and gasification zones, generalized gas-phase chemistry, axially variable bed void fraction and gas/solid flow rates, and generalized, coal-independent rate-controlled devolatilization. Solution times on a midlevel computer workstation are only a few minutes.

Predictions from the MBED-1D are compared to temperature and pressure measurements from a commercial-scale Wellman-Galusha dry-ash gasifier. Predicted axial temperature and pressure profiles, using a common set of model parameters, compared well with the measured values for many coals. A suitable estimate of bed void distribution was shown to be necessary to predict the pressure drop throughout the reactor. A linear increase in bed void fraction from the top to the bottom of the reactor was found to be sufficient for most calculations. The void distribution dramatically influences volumetric reaction rates through the particle number density.

From temperature profile comparisons, higher coal feed rates or processes, which cause the gas phase to become fuel-richer, also cause the location of the maximum temperature to move toward the bottom of the reactor. Such processes include: cracking of tar in the gasification and devolatilization zones; increasing devolatilization rate by neglecting volatiles transport; and increasing the volatile content through changes in coal type, moisture content, or ash content. Devolatilization is not instantaneous, and volatile yield significantly affects the temperature profile and the location of the maximum temperature. Various dips and peaks in the axial temperature profile correspond to different functional groups that evolve at different temperatures. Furthermore, a dual temperature peak may result during high-pressure gasification as a result of competing endothermic and exothermic reactions. Oxidation and gasification do not occur in separate zones, but simultaneously in the reactor bed. Furthermore, results suggest that solid-to-gas heat transfer for reacting fixed beds is significantly smaller than for nonreacting fixed beds. Diffusional resistance of oxidizer through the ash layer during oxidation and gasification was predicted to be significant.

Important model parameters whose values are not well established were identified. These include the solid-to-gas heat-transfer coefficient, ash layer thickness and oxidizer diffusivity through the char-ash layer, and the variable bed void fraction. The effective diffusivity of oxidizer through the ash layer is a complex function of the developing ash porosity and tortuosity which is not likely to be constant throughout the reactor. Future research should include the effect of coal structure, mineral matter, devolatilization and bed burden on the effective diffusivity.

Acknowledgment

This work was sponsored principally by the U. S. Department of Energy, Morgantown Energy Technology Center (Contract No. DE-AC21-86MC23075) under subcontract from Advanced Fuel Research, Inc., East Hartford, and in part by the Advanced Combustion Engineering Research Center at Brigham Young University. Funds for this center are received from the National Science Foundation's Engineering Centers, the State of Utah, 25 industrial participants, and the U. S. Department of Energy. Help from Dr. M. Usman Ghani is also acknowledged. Helpful suggestions and comments by the reviewers are also acknowledged.

Notation

A = cross-sectional area of reactor, m^2
A = particle surface area, m^2
A = preexponential factor, m/s·K
A = water wall surface area, m^2
C = carbon
C = molar concentration of oxidizer or gasification agent, $kmol/m^3$
C_p = specific heat, J/kg·K
d = particle diameter, m
D = diffusivity, m^2/s
D = reactor diameter, m
E = activation energy, J/kmol
F = fraction of original carbon (Eq. 9), mass fraction
g = acceleration of gravity, 9.80665 m/s^2
G = superficial gas mass flux, $kg/m^2 \cdot s$
h = enthalpy, J/kg
h = heat-transfer coefficient, $W/m^2 \cdot K$

H = convective heat capacity flux, J/m²·s
H = hydrogen
k = rate and Arrhenius rate constant, m/s or 1/s
k = thermal conductivity, W/m·K
k = mass transport coefficient, m/s
L = reactor length, m
$\dot{m}$ = mass flow rate, kg/s
Mw = molecular weight, kg/kmol
N = nitrogen
O = oxygen
P = pressure, kPa, Pa
Pe = Peclet number (Table 2)
Pr = Prandtl number (Table 2)
Q = heat loss, W/m³
r = volumetric reaction rate, kg/m³·s
R = ideal gas constant, J/kmol·K
Re = Reynold's number (Table 2)
S = sulfur
Sc = Schmidt number (Table 2)
t = time, s
T = temperature, K
u = velocity, m/s
V = volatile matter, mass fraction
V = volume, m³
VM = volatile matter, mass fraction
W = mass-flow rate, kg/s
x = gas mole fraction
x = tar fraction, mass fraction
x = tar parameter used in correlation of Ko et al. (1988)
y = functional group fraction, mass fraction
z = axial distance, m

Greek letters

ϵ = bed void fraction, void vol./bed vol.
ϵ' = emissivity
ϕ = packing parameter defined by Eq. 10 in Table 2
ϕ = porosity, vol./vol.
η = particle number density, 1/m³
κ = ratio of solid conductivity and gas conductivity
λ = stoichiometric coefficient for oxidation reaction, mol/mol
μ = viscosity, kg/m·s
ν = stoichiometric coefficient, mol carbon/mol oxidant
ρ = density, kg/m³
Ω = dry, ash-free mass fraction
ω = functional group fraction or element fraction, mass fraction
ζ = bed-to-wall heat-transfer multiplier (for sensitivity analysis)
ζ = particle area factor to account for internal surface burning
ζ = reacting to nonreacting solid-to-gas heat-transfer ratio
τ = tortuosity

Subscripts

a = ash
BG = blast gas
c = char
c = coal
CO_2 = CO_2 gasification
e = effective
e = equilibrium
eff = effective
g = gas
gw = gas-to-wall
H_2 = H_2 gasification
H_2O = H_2O gasification
hw = heat transfer to the wall
i = index for elements, species, or reactions
j = index for solid species
m = mass transport
m = mixture
m = molecular
nonvol C = nonvolatile carbon
nonvol S = nonvolatile sulfur
o = initial
O_2 = oxidation
p = particle
r = radial
r = radiative
r = reaction
s = solid
s = steam
sg = solid-to-gas
sm = solid measured (refers to the apparent density)
sw = solid-to-wall
t = tar
t = total
u = unreacted core
v = void
v = volatiles
w = wall
w = water
x = tar
z = axial

Superscripts

a = axial thermal
d = devolatilization
g = gas
h = thermal
m = axial mass
o = initial
o = reference temperature
o = static
s = sensible enthalpy
s = solid
t = true
ultimate = yield at large times
∞ = infinity or ultimate

Literature Cited

Amundson, N. R., and L. E. Arri, "Char Gasification in a Countercurrent Reactor," *AIChE J.*, 24, 87 (1978).
Barriga, A., and R. H. Essenhigh, "A Mathematical Model of a Combustion Pot: Comparison of Theory and Experiment," Paper 80-WA/HT-32, ASME Meeting, Chicago (1980).
Baxter, L. L., personal communication, Brigham Young Univ., Provo (1987).
Bhattacharya, A., L. Salam, M. P. Dudukovic, and B. Joseph, "Experimental and Modeling Studies in Fixed-Bed Char Gasification," *Ind. Eng. Chem. Process Des. Dev.*, 25, 988 (1986).
Bird, R. B., W. E. Stewart, and E. N. Lightfoot, *Transport Phenomena*, Wiley, New York (1960).
Bischoff, K. B., "A Note on Gas Dispersion in Packed Beds," *Chem. Eng. Sci.*, 24, 607 (1962).
Blackwood, J. D., "The Reaction of Carbon with Hydrogen at High Pressure," *Aust. J. Chem.*, 12, 14 (1959).
Cho, Y. S., *Modeling and Simulation of Lurgi-type Gasifiers*, MS Thesis, Washington Univ., St. Louis, MO (1980).
Cho, Y. S., and B. Joseph, "Heterogeneous Model for Moving-Bed Coal Gasification Reactors," *Ind. Eng. Chem. Process Des. Dev*, 20, 314 (1981).
Crowe, C. T., and L. D. Smoot, "Multicomponents Conservation Equations," *Pulverized-Coal Combustion and Gasification*, L. D. Smoot and D. T. Pratt, eds., Plenum Press, New York (1979).
Desai, P. R., and C. Y. Wen, "Computer Modeling of the MERC Fixed Bed Gasifier," MERC/CR-78/3, U. S. Dept. of Energy, Morgantown, WV (1978).
DeWasch, A. P., and G. F. Froment, "A Two-Dimensional Heterogeneous Model for Fixed Bed Catalytic Reactors," *Chem. Eng. Sci.*, 26, 629 (1971).

Dzhapbyev, K., A. L. Miropol'skii, and V. J. Mal'kovskii, "Investigation of Unsteady Heat Transfer in a Packed Bed of Spheres Swept by Gas," *Thermal Eng.*, 33(3), 159 (1986); translated from *Teploenergetika*, 33(3), 70 (1986).
Earl, W. B., and K. A. Islam, "Steady-state Model of a Lurgi-type Coal Gasifier," *Innovation in the Process and Resource Industry, CHEMCA*, Proc. Australian Chem. Eng. Conf., Perth, Australia, Paper c2b, 289 (1985).
Elgin, D. C., and H. R. Perks, "Results of Trials of American Coals in Lurgi Pressure-Gasification Plant at Westfield, Scotland," *Synthetic Pipeline Gas Symp.*, Chicago (Oct. 18-20, 1974).
Ergun, S., "Fluid Flow Through Packed Columns," *Chem. Eng. Prog.*, 48, 89 (1952).
Fayed, M. E., and L. Otten, eds., *Handbook of Powder Science and Technology*, Van Nostrand Reinhold, New York (1984).
Field, M. A., D. W. Gill, B. B. Morgan, and P. G. W. Hawksley, *Combustion of Pulverized Coal*, The British Coal Utilization Res. Assoc., Leatherhead, England (1967).
Fletcher, T. F., A. R. Kerstein, R. J. Pugmire, M. S. Solem, and D. M. Grant, "A Chemical Percolation Model for Devolatilization: 3. Chemical Structure as a Function of Coal Type," *Energy and Fuels*, submitted (1992).
Froberg, R. W., *"The Carbon-Oxygen Reaction: an Experimental Study of the Oxidation of Suspended Carbon Spheres,"* PhD Diss., Pennsylvania State Univ., University Park (1967).
Froment, G. F., and K. B. Bischoff, *Chemical Reactor Analysis and Design*, Wiley, New York (1979).
Goetz, G. J., N. Y. Nsakala, R. L. Patel, and T. C. Lao, "Combustion and Gasification Characteristics of Chars from Four Commercially Significant Coals of Different Rank," final report 165-6, EPRI, Palo Alto, CA (1982).
Gray, D. D., and J. M. Stiles, "On the Constitutive Relation for Frictional Flow of Granular Materials," topical report DOE/MC/21353-2584, U. S. Dept. of Energy, Morgantown, WV (1988).
Gray, D., J. G. Cogoli, and R. H. Essenhigh, "Problems in Pulverized Coal and Char Combustion," *Adv. Chem. Ser.*, 131, 72, (1974).
Gupta, A. S., and G. Thodos, "Direct Analogy Between Mass and Heat Transfer to Beds of Spheres," *AIChE J.*, 9(6), 751 (1963).
Hedman, P. O., L. D. Smoot, P. J. Smith, and A. U. Blackham, "Entrained-Flow Gasification at Elevated Pressure," DOE/MC/22059-2570, Combustion Laboratory, Chemical Engineering Dept., Brigham Young Univ., Provo (1987).
Hindmarsh, A. C., "ODEPACK, A Systematized Collection of ODE Solvers," *Scientific Computing*, R. S. Stepleman, ed., Vol. 1, p. 55, IMACS Trans. on Scientific Computation, North-Holland, Amsterdam (1983).
Hobbs, M. L., *"Modeling Countercurrent Fixed-Bed Coal Gasification,"* PhD Diss., Brigham Young Univ., Provo (1990).
Hobbs, M. L., P. T. Radulovic, and L. D. Smoot, "Prediction of Effluent Temperatures and Compositions for Fixed-Bed Coal Gasifiers," *Fuel*, accepted (1992).
Khanna, R., and J. H. Seinfeld, "Mathematical Modeling of Packed Bed Reactors: Numerical Solutions and Control Model Development," *Advances in Chemical Engineering*, J. Wei, J. L. Anderson, K. B. Bischoff, M. M. Denn, and J. H. Seinfeld, eds., Vol. 13, p. 113, Academic Press (1987).
Kim, M., and B. Joseph, "Dynamic Behavior of Moving-Bed Coal Gasifiers," *Ind. Eng. Chem. Process Des. Dev.*, 22, 212 (1983).
Ko, G. H., D. M. Sanchez, W. A. Peters, and J. B. Howard, "Correlations for Effects of Coal Type and Pressure on Tar Yields from Rapid Devolatilization," *Symp. Int. on Combustion*, p. 115, The Combustion Institute, Pittsburgh (1988).
Krishnudu, T., B. Madhusudhan, S. N. Reddy, V. S. R. Sastry, K. S. Rao, and R. Vaidyeswaren, "Studies in a Moving Bed Pressure Gasifier: Prediction of Reaction Zones and Temperature Profile," *Ind. Eng. Chem. Res.*, 28, 438 (1989).
Kunii, D., and J. M. Smith, "Heat Transfer Characteristic of Porous Rocks," *AIChE J.*, 6(1), 71 (1960).
Kurylko, L., *"The Unsteady and Steady Combustion of Carbon,"* PhD Diss., The Pennsylvania State Univ., University Park (1969).
Laurendeau, N. M., "Heterogeneous Kinetics of Coal Char Gasification and Combustion," *Prog. Energy Combust. Sci.*, 4, 221 (1978).
Lowry, H. H., *Chemistry of Coal Utilization*, Supple. Vol. Wiley, New York (1963).
Merrick, D., "Mathematical Models of the Thermal Decomposition of Coal: 2. Specific Heats and Heats of Reaction," *Fuel*, 62, 540 (1983).
Mills, K. C., and J. M. Rhine, "The Measurement and Estimation of the Physical Properties of Slags Formed During Coal Gasification: 2. Properties Relevant to Heat Transfer," *Fuel*, 68, 201 (1989).
Nsakala, N., R. L. Patel, and T. C. Lao, "Combustion Characterization of Coals for Industrial Applications," Final Technical Report for U. S. Dept. of Energy, Pittsburgh, Combustion Engineering Inc., Kreisinger Development Laboratory, Winsor, CT, DOE/PC/402067-5 (DE85010673) (Mar. 1985).
Nuttall, H. E., W. G. Stoddart, and W. J. Chen, "Pyrolysis of Subbituminous New Mexico Coal," *J. of Petr. Tech.*, 31, 418 (1979).
Park, K. Y., and T. F. Edgar, "Modeling of Early Cavity Growth for Underground Coal Gasification," *Ind. Eng. Chem. Res.*, 26, 237 (1987).
Perry, R. H., and C. H. Chilton, eds., *Chemical Engineers' Handbook*, 5th ed., McGraw-Hill, New York (1973).
Phuoc, T. X., and M. P. Mathur, "Transient Heating of Coal Particles Undergoing Pyrolysis," *Combust. and Flame*, 85, 380 (1991).
Radulovic, P. T., M. L. Hobbs, and L. D. Smoot, "Fixed-Bed Coal Combustion and Gasification Review," *Prog. Energy Combust. Sci.*, submitted (1992).
Rohsenow, W. M., J. P. Hartnett, and E. N. Ganic, *Handbook of Heat Transfer Applications*, McGraw-Hill, New York (1985).
Saxena, S. C., "Devolatilization and Combustion Characteristics of Coal Particles," *Prog. Energy Combust. Sci.*, 16, 55 (1990).
Serio, M. A., D. G. Hamblen, J. R. Markham, and P. R. Solomon, "Kinetics of Volatile Product Evolution in Coal Pyrolysis: Experiment and Theory," *Energy & Fuels*, 1, 138 (1987).
Smith, I. W., "The Combustion Rates of Coal Chars: a Review," *Int. Symp. on Combustion*, p. 1045, The Combustion Institute, Pittsburgh (1983).
Smoot, L. D., and P. J. Smith, *Coal Combustion and Gasification*, Plenum Press, New York (1985).
Smoot, L. D., and P. J. Smith, *Pulverized-Coal Combustion and Gasification*, p. 224, L. D. Smoot and D. T. Pratt, eds., Plenum, Press, New York (1979).
Solomon, P. R., D. G. Hamblen, R. M. Carangelo, M. A. Serio, and G. Y. Deshpande, "General Model of Coal Devolatilization," *Energy and Fuels*, 2, 405 (1988).
Stillman, R., "Simulation of a Moving Bed Gasifier for a Western Coal," *IBM J. Res. Dev.*, 23, 240 (1979).
Stull, D. R., and H. Prophet, *JANAF Thermochemical Tables*, 2nd ed., National Bureau of Standards (1971).
Suuberg, E. M., W. A. Peters, and J. B. Howard, "Product Compositions and Formation Kinetics in Rapid Pyrolysis of Pulverized Coal—Implications for Combustion," *Int. Symp. on Combustion*, p. 177, The Combustion Institute, Pittsburgh (1979).
Thimsen, D., personal communications (1990).
Thimsen, D., R. E. Maurer, A. R. Pooler, D. Y. H. Pui, B. Y. H. Liu, and D. B. Kittelson, "Fixed-Bed Gasification Research using U. S. Coals," 1-19, U. S. Bureau of Mines Contract H0222001, final report (1984).
Thorsness, C. B., and S. W. Kang, "Further Development of a General-Purpose, Packed-Bed Model for Analysis of Underground Coal Gasification Processes," *Underground Coal Gasification Symp.*, Denver (1985).
Thorsness, C. B., and S. W. Kang, "A General-Purpose, Packed-Bed Model for Analysis of Underground Coal Gasification Processes," UCID-20731, Lawrence Livermore National Laboratory, Univ. of California, Berkeley (1986).
Thorsness, C. B., S. W. Kang, "A Method-of-line Approach to Solution of Packed-bed Flow Problems Related to Underground Coal Gasification Processes," *Underground Coal Gasification Symp.*, Williamsburg, VA (1984).
Walker, P. L., F. Rusinko, and L. G. Austin, *Advances in Catalysis*, p. 134, D. D. Eley, P. W. Selwood, and P. B. Weisz, eds., XI, Academic Press, New York (1959).
Wang, S. C., and C. Y. Wen, "Experimental Evaluation of Non-isothermal Solid-Gas Reaction Model," *AIChE J.*, 18(6), 1231 (1972).
Wen, C. Y., and T. Z. Chaung, "Entrainment Coal Gasification Modeling," *Ind. Eng. Chem. Process Des. Dev.*, 18(4), 684 (1979).
Wen, C. Y., H. Chen, and M. Onozaki, *User's Manual for Computer Simulation and Design of the Moving Bed Coal Gasifier*, final report

prepared for Morgantown Energy Technology Center, U. S. Dept. of Energy, DOE/MC/16474-1390, Morgantown, WV (1982).
Winslow, A. M., "Numerical Model of Coal Gasification in a Packed Bed," *Int. Symp. on Combustion*, p. 503, The Combustion Institute, Pittsburgh, (1976).
Yagi, S., and D. Kunii, "Studies on Heat Transfer Near Wall Surface in Packed Beds," *AIChE J.*, 6(1), 97 (1960).
Yagi, S., D. Kunii, and N. Wakao, "Studies on Axial Effective Thermal Conductivities in Packed Beds, *AIChE J.*, 6(4), 543 (1960).
Yagi, S., and N. Wakao, "Heat and Mass Transfer from Wall to Fluid in Packed Beds," *AIChE J.*, 5(1), 79 (1959).
Yoon, H., "Modeling and Analysis of Moving Bed Coal Gasifiers," PhD Diss., Univ. of Delaware, Newark (1978).
Yoon, H., J. Wei, and M. M. Denn, "A Model for Moving-bed Coal Gasification Reactors," *AIChE, J.*, 24(5), 885 (1978).
Yu, W., M. M. Denn, and J. Wei, "Radial Effects in Moving Bed Coal Gasifiers," *Chem. Eng. Sci.*, 38, 1467 (1983).

Manuscript received Aug. 9, 1991, and revision received Mar. 5, 1992.

APPENDIX E

NETWORK MODELS OF COAL THERMAL DECOMPOSITION

Network models of coal thermal decomposition

Peter R. Solomon, David G. Hamblen, Zhen-Zhong Yu and Michael A. Serio

Advanced Fuel Research, Inc., 87 Church Street, East Hartford, CT 06108, USA

(Received 24 July 1989; revised 2 February 1990)

Several groups have considered statistical network fragmentation models to describe coal thermal decomposition. In these models, the coal macromolecule is viewed as a collection of fused aromatic rings (monomers) linked by bridges. During thermal decomposition, existing bridges break and new bridges are formed. The parameters of the models are the geometry of the network, which is expressed as the number of attachments per monomer (the coordination number, $\sigma+1$), and the chemistry of bridge breaking and formation. Given $\sigma+1$ and the instantaneous number of unbroken and formed bridges, the molecular weight distribution can be predicted. The different groups have employed both Monte Carlo methods and percolation theory to describe the network statistics. The former approach has advantages in terms of describing both the depolymerization and crosslinking processes in coal decomposition, since it does not require a constant coordination number. The latter method provides closed form solutions and is computationally less demanding. The models differ in the geometry of the network, the chemistry of bridge breaking and bridge formation (crosslinking) and the mass transport assumptions. This paper considers for three such models: the mathematical schemes; the assumed network geometries; the assumed bond breaking and bond formation chemistries; and the mass transport assumptions. The predictions of three models were compared by comparing the oligomer populations as a function of the number of unbroken bridges per ring cluster. This paper also presents results from a new model which combines the geometry, chemistry and mass transport assumptions of the FG-DVC model with the mathematics of a modified percolation theory.

(Keywords: thermal decomposition; coal; modelling)

Many recent studies have proposed that coal can be thought of as having a macromolecular network structure to which concepts of crosslinked polymers can be applied[1–10]. These concepts have been employed to understand and model such properties of coal as: the insolubility; the equilibrium swelling and penetration of solvents; the viscoelastic properties; similarities between the parent coal and products of hydrogenolysis, or mild oxidation; crosslinking during char formation[11,12]; and the formation of coal tar in pyrolysis[13–17]. With the success of these concepts in describing coal properties, it appears logical to extend macromolecular network concepts to completely describe the thermal decomposition behaviour of coal.

A number of investigators have used statistical methods to predict how the network behaves when subjected to thermally induced bridge breaking, crosslinking, and mass transport processes[17–30]. Gavalas *et al.*[20] employed statistical methods to predict the release of monomers from a randomly connected network. The model of Niksa and Kerstein employed percolation theory in a model called DISARAY[28], which extended their previous model built on chain statistics[24,25]. Grant *et al.*[30] employed percolation theory in a model called chemical percolation devolatilization (CPD). Solomon *et al.*[21–23,27] used Monte Carlo methods in a network model called the depolymerization, vaporization, and crosslinking (DVC) model. This was an extension of their previous model for linear polymers[17,20]. The DVC model was recently combined with their functional group (FG) model[27,29] to produce the general FG-DVC pyrolysis model. This model is currently being applied to model the devolatilization behaviour of Argonne premium coals[31] and to predict the fluidity of coals[32]. Other statistical methods for network behaviour have been employed in the polymer literature[33–38].

In applying network models to coal thermal decomposition, one considers the coal to consist of aromatic ring clusters linked together by bridges in some geometry. The geometry is described by the degree of branching in the network. An unbranched linear network will have one bridge per ring cluster attaching it to the next cluster. Thus each cluster has two attachments and is said to have a coordination number ($\sigma+1$) of two. A highly branched 'fish net' would have two bridges per cluster, attaching it to the neighbouring four clusters and thus a coordination number of four. A branch point is considered to occur at any cluster connected to more than two neighbours (i.e. having more than two attachments).

When the coal is heated, the bridges can break and new bridges can form. Various statistical methods can be employed to predict the concentration of individual aromatic ring clusters (monomers) and linked clusters (oligomers of n clusters, 'n-mers') up to a totally linked network. By assigning an average or distribution of molecular weights to the monomers, the amounts of tar, extractables, liquids or char can then be defined from the distribution of oligomer sizes. The models vary in the assumed chemistry of bridge breaking and crosslinking,

0016-2361/90/060754-10

in the definition of tar, extracts, liquids, and char and in the statistical methods used.

In view of the importance of macromolecular network models to the accurate predictions of coal processing behaviour, this paper assesses the assumptions and limitations of the proposed models. It appears that the way one performs the statistics (Monte Carlo, percolation theory, or other statistical methods) makes little difference. For example, percolation theory methods were substituted for Monte Carlo calculations in the FG-DVC model, and comparable predictions were obtained for appropriately restricted cases. The important differences among models are in the assumptions for: the network geometry (i.e. the degree of branching or coordination number); the chemistry of bridge breaking; the chemistry of crosslink formation; hydrogen utilization; and mass transport. This paper compares the three most recent models (DISARAY, CPD, and FG-DVC) and considers how the assumed network properties relate to behaviours observed for coal.

MACROMOLECULAR NETWORKS

General properties of networks

Figures 1 and *2* present the networks employed in the FG-DVC Monte Carlo calculations and percolation theory, respectively. For the FG-DVC Monte Carlo calculation, linear oligomers of l clusters (shown as the horizontal chains of clusters) of a molecular weight distribution defined by M_{avg} and deviation, ΔM, are linked by m_0 'crosslinks' per monomer[26,29]. These 'crosslinks' are indicated by the vertical double lines as shown in *Figure 1*. The branch points in the network are defined to occur at those clusters where more than two attachments connect a cluster to another cluster. Unless the crosslink occurs at the end of the oligomer, it forms at least one branch point. The term 'crosslink' has previously been used to mean the extra bridges that can form a branch point, and this is the definition employed here[27,29]. During thermal decomposition, bridges break, new crosslinks are added and the molecular weight of the oligomers is calculated by randomly distributing these changes.

For the percolation theory, a Bethe lattice is employed[28,30,39]. Lattices are characterized by the coordination number, $(\sigma+1)$, which is the number of attachment sites for bridges per cluster and the probability, p, that an unbroken bridge occupies the site. *Figure 2* shows lattices at $p=1$ (i.e. all possible bridges occupied) for $\sigma+1=2.2$ and $\sigma+1=4$. The Bethe lattice has no loops, but it has been demonstrated that this lattice is a good approximation to a lattice of equivalent coordination number containing loops[39]. As shown in *Figure 2*, the $\sigma+1=2.2$ lattice has branch points every 5th cluster. This network is close to a linear polymer $\sigma+1=2$ which has no branch points. The $\sigma+1=4$ lattice is much more highly branched, having double branch points on each cluster (this would be the Bethe lattice analogue of the 'fish net'). For values of p less than 1, the bridges are randomly removed from the network. It is important to realize that the statistical distribution of unbroken bridges means that even when the average number of unbranched bridges per cluster is identical for the two networks in *Figure 2*, the $\sigma+1=4$ network can never look like the $\sigma+1=2.2$ network (except for the case $p=0$).

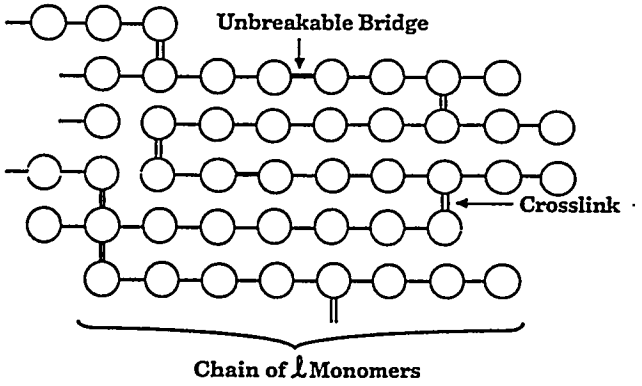

Figure 1 Macromolecular network used in Monte Carlo simulation

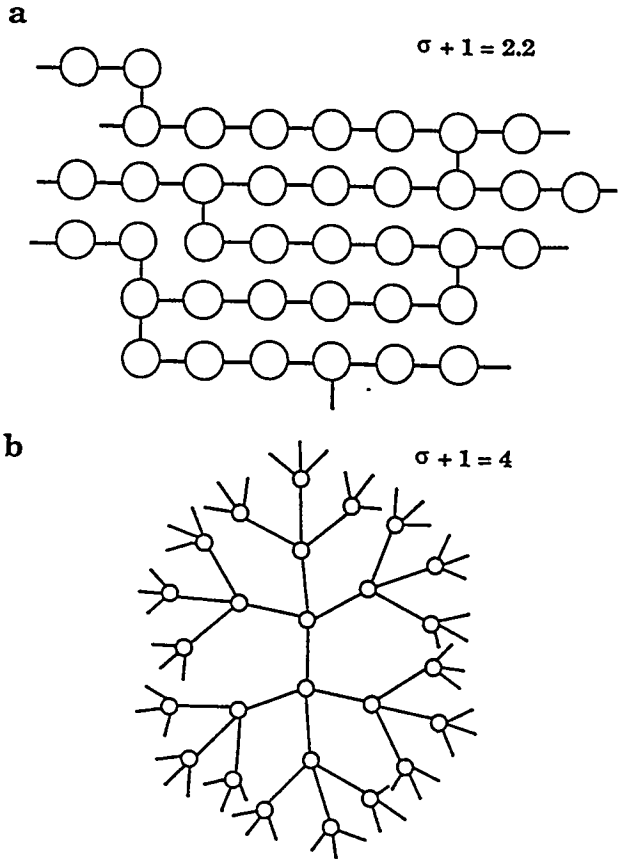

Figure 2 Bethe lattice for a, coordination number 2.2, $p=1$; b, coordination number 4, $p=1$

The loop free geometry of the Bethe lattice allows for the number of free oligomers to be analytically expressed as a function of $\sigma+1$ and the probability p of bonds being unbroken. This is the feature which makes the percolation theory so attractive from the standpoint of computer efficiency and for understanding the behaviour of networks under conditions of varying bridge populations. *Figure 3* shows calculations using percolation theory (for three values of $\sigma+1$) for the monomer, the sum of oligomers up to 3, up to 10, and the sum of all free oligomers as a function of the number of unbroken bridges per ring cluster α, where $\alpha=1/2p\,(\sigma+1)$. The 1/2 enters because $\sigma+1$ is the number of attachments per cluster, which is twice the number of bridges (i.e. each

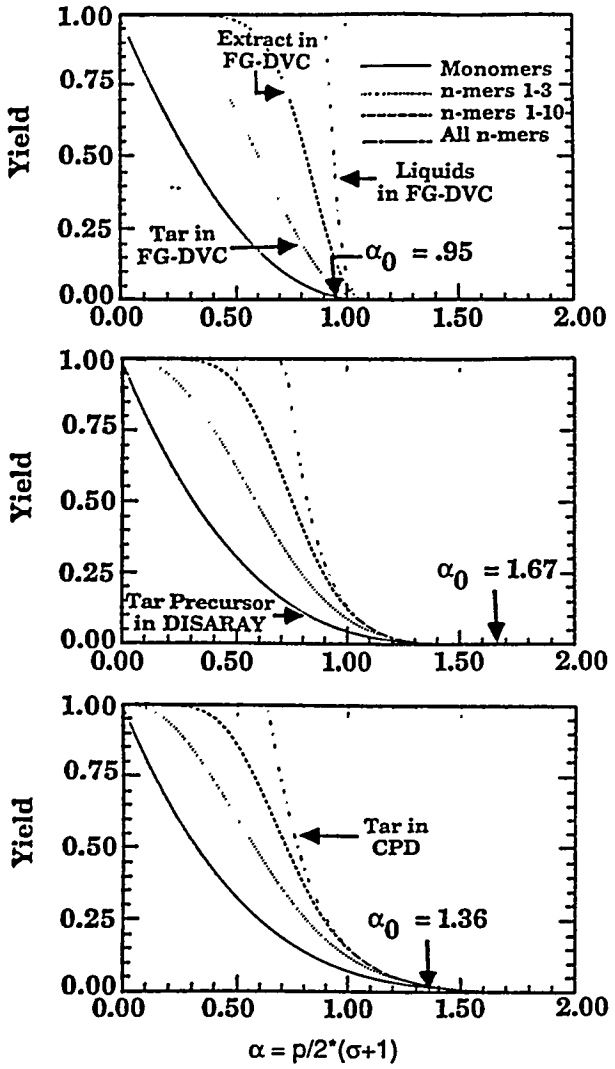

Figure 3 Percolation theory predictions for pyrolysis products (monomers, tar, extracts and total liquids) for three values of the coordination number ($\sigma+1$): a, $\sigma+1=2.2$; b, $\sigma+1=3.25$; c, $\sigma+1=4.6$

bridge forms two attachments). If $\sigma+1$ remains constant during pyrolysis, the molecular weight distribution is a single valued function of α. For ring clusters of molecular weight 300 amu, the sum of 1–3 *n*-mers corresponds roughly to the potential tar fraction (up to 900 amu), the sum of 1–10 *n*-mers corresponds to the extractable fraction (up to 3000 amu), and the sum of all oligomers corresponds to the liquids fraction (all free oligomers). It can be seen that, with increasing $\sigma+1$, more broken bridges are required to achieve equivalent fractions of free oligomers. Also, at a fixed value of α, the relative amounts of tar, extracts, and liquids vary with $\sigma+1$.

Network geometries representative of coal

The three important parameters of the network are the average ring cluster size M_{avg}, the coordination number ($\sigma+1$), and the starting probability of bridges being unbroken, p_0. To compare networks of different coordination numbers, it is convenient to use α and α_0 rather than p and p_0. The assumptions of DISARAY, CPD, and FG-DVC are considered below.

Ring cluster size. Ring cluster sizes have been estimated from n.m.r. alone[40], n.m.r. and FT-i.r.[41], mild degradation[42], and the molecular weight distribution of tar[15,16,29]. Based on these results, the average ring cluster size for coals with less than 90% carbon is expected to be between 2 and 3 aromatic rings or a total molecular weight per cluster, including peripheral groups, of 200–400 amu. DISARAY assumes a value of 1400 amu for the monomer which can split into two 700 amu tar fragments. CPD does not specify the monomer molecular weight. For coals with less than 90% carbon, FG-DVC employs a distribution of monomers with an M_{avg} of 256 amu.

Coordination number. Information on the coordination number comes from solvent swelling measurements and recent estimates made using n.m.r. of the number of non-peripheral group attachments to the cluster[40]. There is some controversy about the meaning of the measurements of the solvent swelling ratio. Network theories have, however, been applied[2–9] to relate the solvent swelling ratio, Q, and the average molecular weight of a cluster, M_{avg}, to the average molecular weight between branch points, M_c. The M_c determinations[2–9] suggest that there are between 4 and 8 repeating units (ring clusters) between branch points for coals with less than 90% carbon. (In this work the term crosslink has been used to indicate the bridge which makes a ring cluster into a branch point). This indicates a value for $\sigma+1$ between 2.13 and 2.25, since $\sigma+1$ is the average number of attachments per cluster (1 bridge makes two attachments). The n.m.r. data suggest that there are between 2 and 3 bridge or loop attachments per cluster (see Figure 8 of Ref. 40). This suggests $\sigma+1$ is between 2 and 3. Based on these two measurements, the coordination number for the starting coal for describing the break up of the network by bridge cleavage should be less than 3, and probably between 2.2 and 2.5. A different value of $\sigma+1$ might be appropriate for describing crosslinking (branch point formation at higher temperature). To model a high volatile bituminous coal, the different models used networks with $(\sigma+1)=3.25$ (DISARAY), 4.6 (CPD), and ≈ 2.1 (FG-DVC).

Initial bridge population, p_0. The starting macromolecular network for FG-DVC is chosen to match the measured extract yield and molecular weight between crosslinks by picking two parameters: the length of the linear oligomer chain, l; and the number of initial crosslinks (branch points) per monomer, m_0. First m_0 is picked such that $m_0 = M_{avg}/M_c$, where M_{avg} is the average ring cluster (monomer) molecular weight and M_c is the molecular weight between crosslinks determined from solvent swelling[2–9]. Then l is chosen so that when the molecule is randomly constructed, the weight per cent of oligomers less than 3000 amu matches the measured extract yield. There is the implicit assumption that the extract yield is due to the unpolymerized fraction of a homogeneous network. Polymethylenes or highly fluid macerals (e.g. exinites), which can be a significant portion of the extracts in coal, should really be treated as separate components but were not in the first version of the FG-DVC model. The initial value of α is approximately $((l-1)/l+m_0)$, which for the Pittsburgh seam coal modelled in Ref. 29 is $\alpha_0 \approx 0.95$. This initial value is indicated in *Figure 3a*. In DISARAY, p_0 is set equal to 1 ($\alpha_0 = 1.63$). This is illustrated in *Figure 3b*.

The starting macromolecular network in the CPD model is chosen by picking two parameters: the coordination number $\sigma+1$, picked to match the average number of all connections (including peripheral groups in addition to bridges and loop attachments) per ring determined by n.m.r.[30,40]; and p_0, the starting probability of unbroken bonds. For the high volatile bituminous coal simulated in Ref. 30, $\alpha_0 = 1/2\ p_0(\sigma+1) = 1.36$. This initial value is indicated in *Figure 3*.

PROCESSES CONTROLLING THE NETWORK DECOMPOSITION

This section considers the important processes in pyrolysis: bridge breaking, and hydrogen utilization: crosslinking (branch point formation): and the mass transport processes which control the distribution of oligomers into tar, extracts, liquids, and solids. The processes are summarized in *Figure 4*.

Bridge breaking and hydrogen utilization

Figure 4a summarizes the bridge breaking assumptions of the three models. Both the FG-DVC and CPD models assume similar (within a factor of 3) bridge breaking rates, $0.86\times10^{15}\ \exp-(55\,400/RT)\ s^{-1}$ for FG-DVC* and $2.6\times10^{15}\ \exp-(55\,400/RT)\ s^{-1}$ for CPD. Both models employ rank independent kinetics. The FG-DVC model rate was determined in experiments in which particle temperatures were directly measured[43]. The rate was recently confirmed within a factor of 2 by Fletcher *et al.*[44] in a second experiment to directly measure particle temperatures. The DISARAY model* assumes a bridge dissociation rate which can produce monomers of $6\times10^{8}\ \exp-(30\,000/RT)\ s^{-1}$. The monomers subsequently decompose at $1.4\times10^{7}\ \exp-(31\,000/RT)\ s^{-1}$ to form tar.

In DISARAY, all the initial bridges can break. In FG-DVC and CPD, there is a process for creating unbreakable bridges associated with the bridge breaking process. The FG-DVC model includes three kinds of bonds: labile bridges, 'unbreakable bridges' (which do not form branch points), and crosslinks (which do form branch points). The unbreakable bridges are represented by the heavy horizontal lines in *Figure 1*. For each broken labile bridge, FG-DVC requires that hydrogen be available to stabilize the free radicals. It is assumed that all the donatable hydrogen (aliphatic plus hydroaromatic) is located in the labile bridges, so that only half the labile bridges can break with the other half becoming unbreakable with the donation of their hydrogen (i.e. there is a 1:1 ratio between the occurrence of bridge breaking and the formation of additional 'unbreakable bridges'). In the FG-DVC model, crosslinks are also considered to be bridges which cannot be broken, but are not in the 'unbreakable bridges' pool. The weight fraction of the initial bridges in the chain of length l which are labile is given by the parameter W_B; the rest are assumed to be unbreakable bridges. W_B is a fitting parameter chosen to make the model fit the pyrolysis data.

In a similar manner, in CPD there are both unbreakable bridges with probability c_0 and labile bridges with probability L_0 ($L_0+c_0=p_0$). As pyrolysis proceeds, the labile bridges can break and react by two possible routes to form unbreakable 'char' bridges or broken bridges. CPD assumes a 0.9:1.0 ratio of broken bridge to char bridge formation. That assumption is almost identical to the 1:1 ratio used in FG-DVC. In

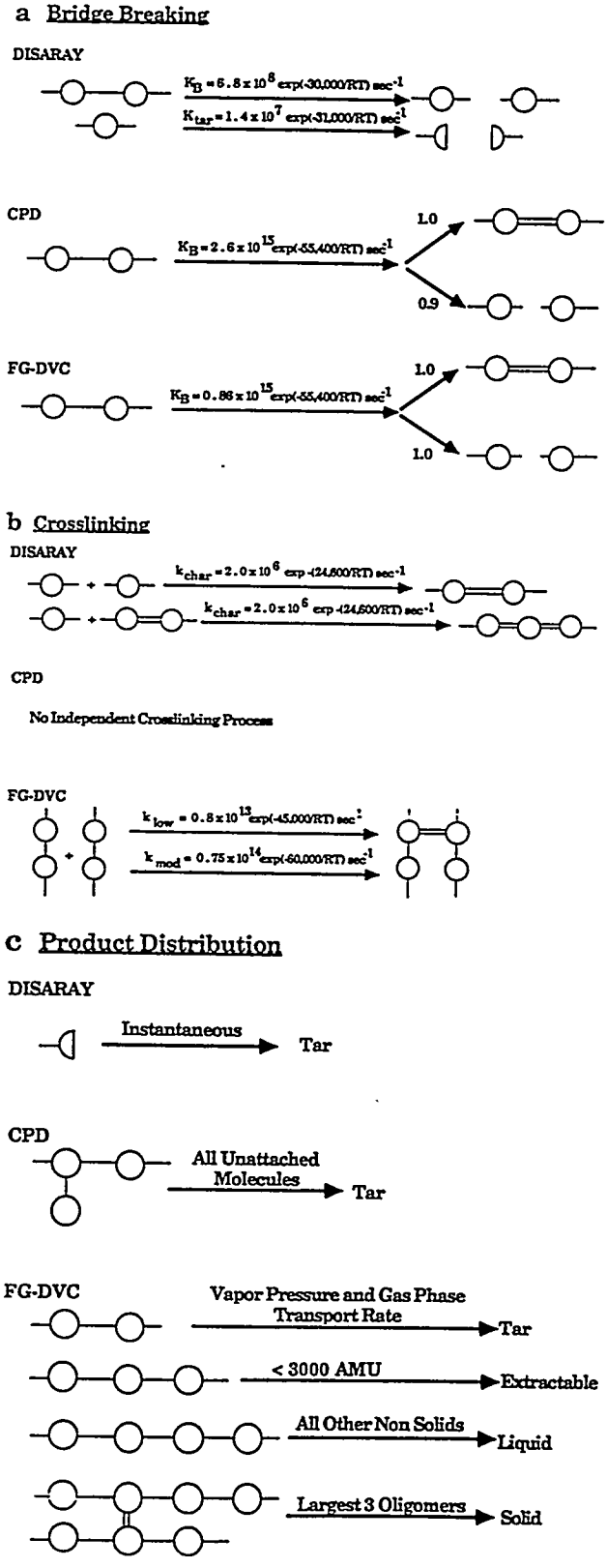

Figure 4 Summary of model assumptions for a, bridge breaking; b, crosslinking; c, product distribution

* Both FG-DVC and DISARAY employ distributed activation energy expressions. The rates quoted above are for the centre of the distribution

CPD there is no distinction between unbreakable bridges and crosslinks. A branch point occurs any place there are three or more attachments per cluster.

Crosslinking

The crosslinking (branch point forming) reactions are summarized in *Figure 4b*. CPD does not define any distinct crosslinking processes. Char forming reactions produce unbreakable bridges as a consequence of bridge breaking. These reactions form branch points (three or more attachments per cluster) randomly depending on the coordination number, $\sigma+1$ and probability, p.

DISARAY assumes char formation occurs at a rate $2\times10^6 \exp-(24\,600/RT)\ s^{-1}$. Char formation is assumed to occur by monomers attaching to the original lattice or to each other.

FG-DVC assumes two independent crosslinking reactions. These are the only reactions which can form branch points in the Monte Carlo formulation. One process occurs at low temperature (below that for bridge breaking) for low rank coals and is associated with CO_2 evolution[11,12,45]. Crosslinking also occurs at moderate temperatures, slightly higher than bridge breaking, and is associated with the evolution of CH_4. The model assumes one crosslink is formed for each CH_4 or CO_2 evolved[29]. The mechanistic basis for these assumptions has been discussed elsewhere[45].

Product distribution

The product distribution assumptions are summarized in *Figure 4c*. The identification of different size oligomers with tar, extracts, liquids, and solids is related to their molecular weight. The oligomers which can form tar are the lightest fraction. Tar formation is controlled in part by the vapour pressure of the components. This idea is supported by the observation that tar yields are strongly influenced by external pressure[29,46,47].

Only oligomers with molecular weights less than 1000 amu have sufficient vapour pressure to become gas at typical pyrolysis tempratures, so tar is roughly limited to <1000 amu[47–51]. The extract yield is controlled by the solubility of the oligomers. For coal fragments in pyridine this limit is roughly 3000 amu[47–49,52]. Larger fragments appear to be important to the fluid properties of coal[32].

In FG-DVC, the Monte Carlo calculation is employed to determine the molecular weight distribution in the decomposing char. Then, a mass transport equation is applied to determine the probability of the light n-mers evolving as tar. The transport equation assumes that a molecular weight dependent vapour pressure controls the appearance of these molecules in the gas phase and that they escape the coal particles by convective transport of the gas[29]. Tar is thus the light end of the molecular weight spectrum, i.e. those with sufficiently high vapour pressures. This produces tar with number average molecular weights of 300–400 amu and maximum weights of 800–1000 amu. Thus, in FG-DVC, tar is approximately the sum of 1–3 n-mers in *Figure 3a*. Extractable material is defined as all molecules up to 3000 amu (sum of 1–10 n-mers) and liquids are defined as all molecules not attached to the starting network. An alternative definition, which has been employed here, is to assume the largest three molecules constitute the solid, and all the rest are liquid.

In DISARAY, tar is defined as half the monomer, and the monomer is taken as 1400 amu. Consequently, the tar would be defined as some fraction of the monomer curve in *Figure 3b*. No transport equations are employed in CPD. Tar is defined as all molecules not attached to the infinite lattice. Thus tar is represented by the highest line in *Figure 3c*.

One advantage of the Monte Carlo method over the percolation theory is that, when tar is produced, molecules can be removed from the network. In percolation theory, there is no consistent way to remove molecules from the network and to allow the formation of new bridges such as the crosslinking events in FG-DVC. CPD avoids this problem by excluding any independent crosslinking which would reconnect oligomers. This presents the limitation that independent crosslinking and mass transport cannot be treated with the exact percolation theory expressions.

EXAMPLES OF MODEL CALCULATIONS

Formation of pyrolysis products

The evolution of the macromolecular network in the CPD model is illustrated in *Figure 5*. *Figure 5a* shows the percolation theory predictions for the total of

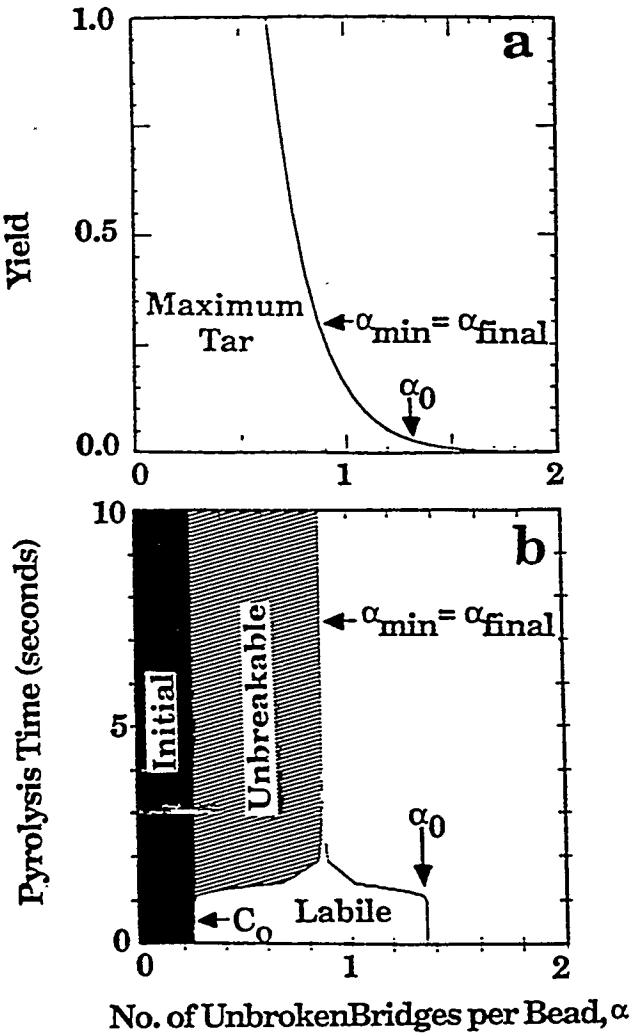

Figure 5 Tar yield for a bituminous coal predicted by the CPD model: a. tar yield versus α: b. variation in α with time. heating at 450°C s^{-1} to 936 K. The shaded areas show the relative amounts of the two types of crosslinks (initial: unbreakable bridge formation)

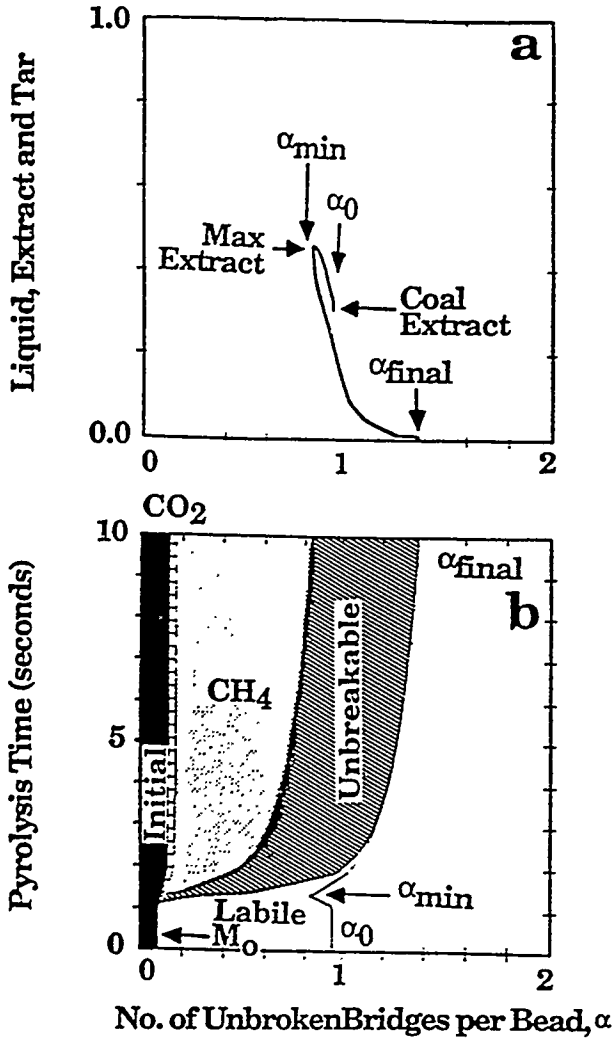

Figure 6 Extract yield for a bituminous coal predicted by the FG-DVC model: a, extract yield versus α: b, variation in α with time, heating at 450°C s^{-1} to 936 K. The shaded areas show the relative amounts of the three types of crosslinks (initial; crosslinks related to gas evolution; unbreakable bridge formation)

unattached oligomers (defined to be the tar) as a function of α. The coal is represented at $p_0=0.59$ or $\alpha_0=1/2p_0$ $(\sigma+1)=1.36$. During pyrolysis, the labile bridges form either broken bridges or unbreakable char bridges in the ratio 0.9 to 1.0. *Figure 5b* shows how α changes during pyrolysis. Pyrolysis proceeds until α_{min} is reached, and all the labile bridges are either broken or have formed unbreakable bridges. Thus

$$\alpha_{min}=1/2(\sigma+1)\ (c_0+(1.0/1.9)L_0)=0.83$$

and the change in α during pyrolysis was 0.53. Note that α can only decrease in the CPD model.

The evolution of the macromolecular network for FG-DVC computed using the Monte Carlo method for a bituminous coal is illustrated in *Figure 6*. *Figure 6a* shows the calculated extract yield as a function of α. The initial probability of unbroken bridges, α_0, starts out at close to 1.0 to produce the measured extract yield (30%). *Figure 6b* shows the computed value of α with its contributions from the initial crosslinks m_0, the conversion of labile bridges to broken bridges and unbreakable bridges and the added crosslinks related to gas evolution. For the bituminous coal, the added crosslinks are almost all due to CH_4 related processes. α goes back up in the FG-DVC model to resolidify the lattice. This is necessary to model fluidity effects[32].

Results of the FG-DVC model applied to a lignite are presented in *Figure 7*. For the lignite, the formation of low temperature crosslinks from CO_2 evolution prevents α from being reduced due to bridge breaking. Thus pyrolysis produces no additional extract yield. The thermosetting behaviour of the low rank coal, and the release of little tar or extracts is related to this low temperature crosslinking process.

Utilization of donatable hydrogen

As discussed above, W_B, the initial fraction of labile bridges, is a parameter of the FG-DVC model. This parameter is related to the fraction of donatable hydrogen by $H(d)=2/28\ W_B$, i.e. there are two donatable hydrogens per labile bridge. This parameter has a strong effect on α_{min} and hence the yield of tar, extracts, and liquids.

There are two ways to estimate the amount of hydrogen donated. During pyrolysis the donation of hydrogen converts two aliphatic or hydroaromatic

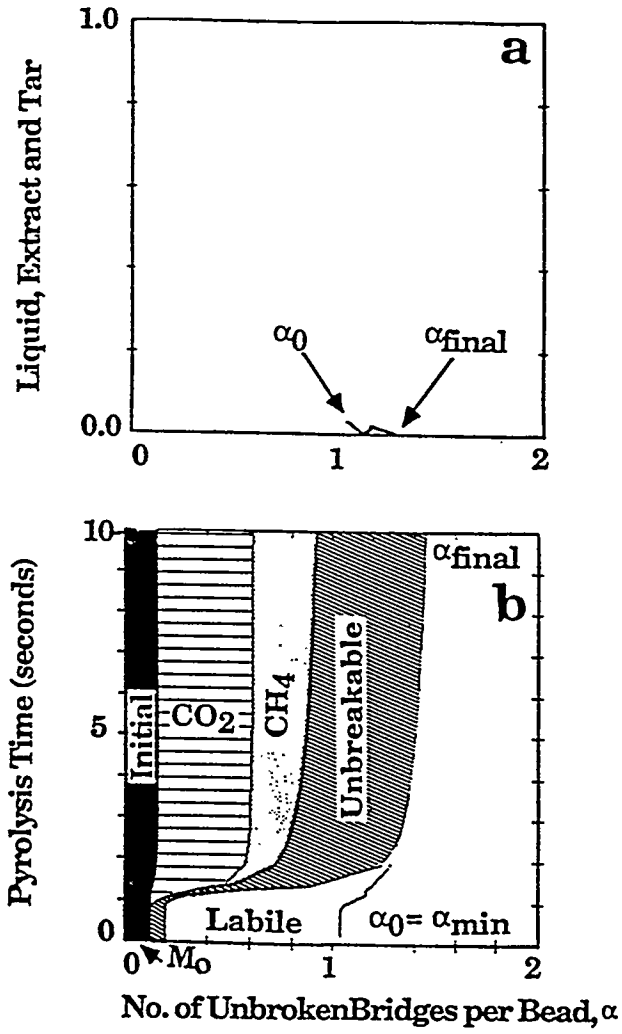

Figure 7 Extract yield for a lignite predicted by the FG-DVC model: a, extract yield versus α; b, variation in α with time, heaing at 450°C s^{-1} to 936 K. The shaded areas show the relative amounts of the three types of crosslinks (initial; crosslinks related to gas evolution; unbreakable bridge formation)

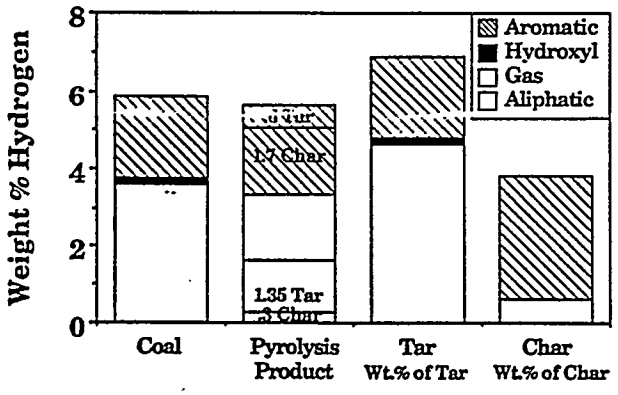

Figure 8 Distribution of hydrogen in coal and pyrolysis products. Pyrolysis produced approximately 53% char, 30% tar and 21% gas

hydrogens into a donated aliphatic hydrogen plus a newly formed aromatic hydrogen. The increase in aromatic hydrogen in the pyrolysis products, and the increase in aliphatic hydrogen in the tar, can both be measured using quantitative FT-i.r. analysis[53,54]. The results for a Pittsburgh seam coal are summarized in *Figure 8*. They show that the aromatic hydrogen in the total pyrolysis products increased from 2.1 to 2.4%, or an increase of 0.3% on a starting coal basis. This increased aromatic content is all in the char. The aromatic content in the tar remains about the same. The tar, which is approximately 30% of the starting coal, increases its aliphatic hydrogen content by about 1% or 0.3% on the starting coal basis. The two numbers are thus consistent; 0.6% aliphatic or hydroaromatic hydrogens in the coal are converted to 0.3% new aromatics plus 0.3% donated aliphatics. If it is assumed that a monomer has a molecular weight of 300 amu, then one breakable bridge per monomer with four aliphatic hydrogens is 1.33%. Half the bridges can break (0.67%) and the other half (0.67%) can donate half its hydrogen (0.34%), in reasonable agreement with the experimentally estimated value of 0.3% hydrogens actually donated. The value assumed[29] in FG-DVC for $H(d)$ for the Pittsburgh seam coal is 0.67%.

The value of $H(d)$ has implications for the CPD model. If there is only one labile bridge per monomer, then

$$\alpha_{min} = 1/2(\sigma+1)(c_0 + (1.0/1.9)L_0)$$
$$= 1/2(4.6)(0.37 + (1.0/1.9)0.22) = 1.11$$

rather than 0.83. In this case, the value of $\sigma+1$ would have to be reduced to match the data. Also, the average molecular weight for the unattached molecules is too high to be identified as tar. If a more reasonable definition of tar is used (e.g. the sum of oligomers up to 3), then $\sigma+1$ has to be reduced still further.

Comparison of Monte Carlo calculation with percolation theory

To further illustrate some of the differences between the FG-DVC Monte Carlo model and percolation theory calculations, the extract yield calculated for a case similar to that in *Figure 6a*, but with tar evolution not permitted, is plotted in *Figure 9* along with the predictions of percolation theory for several values of $\sigma+1$. The FG-DVC Monte Carlo prediction is not a single valued function of α. As pyrolysis proceeds, the increase in extract yield follows $\sigma+1 \approx 2.2$ while the decrease in extract yield follows $\sigma+1 \approx 4$.

It is important to know whether this result is an artefact of the Monte Carlo calculation or a real feature of pyrolysis. Based on what is known to happen in pyrolysis, the result does make sense. For a bituminous coal, the initial process occurring in pyrolysis is bridge breaking. This occurs by breaking bridges in the network described by $\sigma+1$ between 2.1 and 2.5. No crosslinking occurs initially as the solvent swelling ratio is observed to increase during this period[45]. Thus, the coordination number used in CPD, which includes all connections to the ring cluster (bridges, loops, and peripheral groups)[30,40], may not be appropriate to this phase of pyrolysis. Eventually crosslinks start forming, resulting in an increase in the coordination number and in α. There is evidence that crosslinks form at peripheral group sites so that the coordination number used in CPD (the sum of branches and peripheral groups) is appropriate for this phase of the process. Consequently, the network cannot adequately be described by one type of bridge site with a single coordination number. There are bridge sites for labile bridges and for crosslinks, each with their own coordination number. This observation motivated the development of a more general percolation theory model.

LATTICE MODEL WITH TWO BRIDGE BOND TYPES

Two-σ model

To deal with a structure with a time dependent coordination number, a Bethe lattice with two types of bridging bonds is considered, with coordination numbers and probabilities of occupation given by σ_1+1, p, and σ_2+1, q, for the two types, respectively. Such a lattice for $\sigma_1+1=\sigma_2+1=2$ is illustrated in *Figure 10*. The analysis can be carried through using the procedures described previously[30,39], but with extensions to deal with the extra variables. The equations are presented in Appendix A.

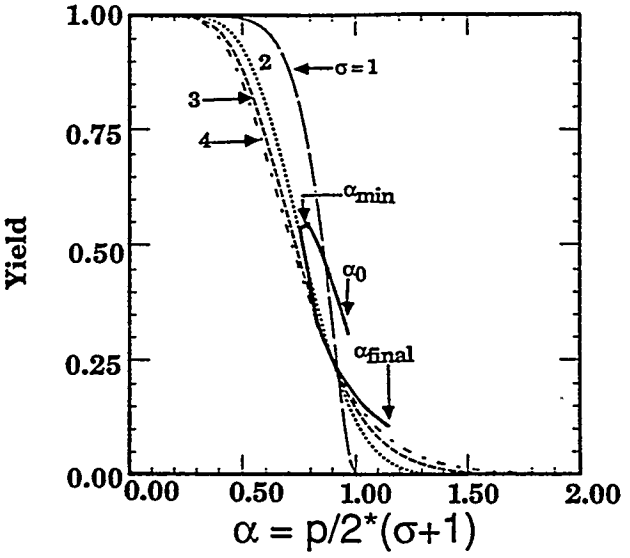

Figure 9 Comparison of extract yield predictions from FG-DVC model with percolation theory for $\sigma=1$, 2, 3 and 4. FG-DVC predictions are for Pittsburgh seam coal heated at 450°C s^{-1} to 936 K with no tar evolved

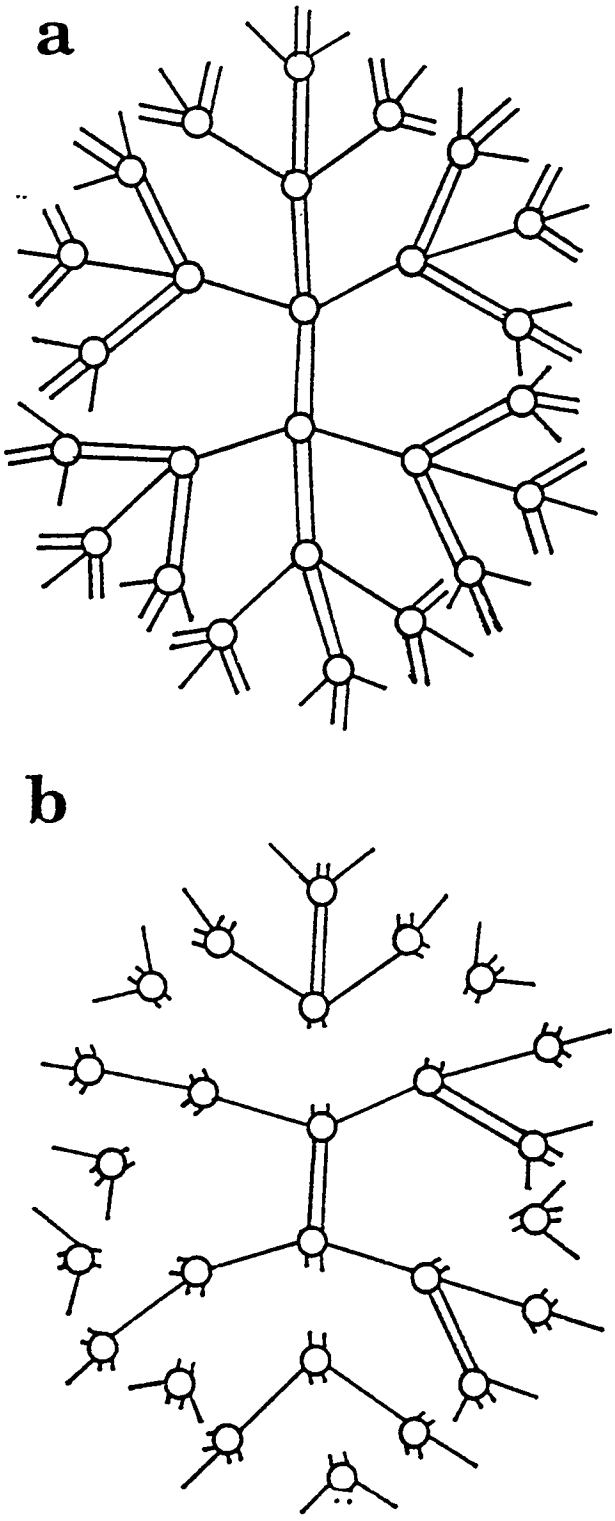

Figure 10 Bethe lattice for two-σ model with $\sigma_1=1$ (shown as single bonds) and $\sigma_2=1$ (shown as double bonds): a, fully linked case ($p=q=1$) is like one-σ model with $\sigma=3$; b, shown with most double bonds (representing the crosslinks) not yet formed to represent the starting coal. This lattice is like a one-σ model with $\sigma=1$, linear chains

Application of two-σ model

Figure 11 presents a comparison of the predictions for pyrolysis assuming the FG-DVC chemistry, using: the Monte Carlo calculation; the two-σ percolation calculations ($\sigma_1+1=2$, $\sigma_2+1=2$); and two cases of the one-σ percolation calculation ($\sigma+1=2.2$ and $\sigma+1=3.2$). The calculations are made under the assumption that no tar is evolved. The tar values in *Figure 11* are the sum of 1–3 n-mers remaining in the char. The Monte Carlo calculation in *Figure 11a* is matched best by the two-σ model if liquids are assumed to be the sum of the first 100 n-mers (i.e. up to 300 000 amu). The two-σ model has a reasonable value for the initial extract yield but predicts slightly more initial tar. Neither of the one-σ cases is a good match. Use of $\sigma+1=2.2$ is good at low temperature, but overpredicts the maximum values of extracts and liquids and resolidifies the network very abruptly at too low a temperature. Use of $\sigma+1=3.2$ does a much better job at predicting the maximum values of tar, extract and liquids, and resolidifies the network more slowly at a higher temperature, but the initial ratio of tar to extract is not consistent with that observed for coal and the rate of increase of n-mers is too slow. It thus appears that the two-σ model can be used instead of the Monte Carlo calculations when no tar is evolved, while one-σ calculations are less accurate.

The real test, however, is how well the models fit the data for coal. A comparison of tar yield is not a sufficient test since α_0 and $\Delta\alpha$ can always be selected in conjunction with the network geometry to fit the data. A critical test requires a careful comparison of how α_0 and $\alpha(t)$ match with measurement of functional group changes in the char (e.g. the transformation of hydrogen functional groups and bridges), solvent swelling behaviour (i.e. crosslink density), and the complete molecular weight distribution as reflected in the amounts of tar, extracts, and fluidity.

COMPARISON OF NETWORK MODELS

A summary of the processes predicted by the three recent network models, CPD, DISARAY and FG-DVC is presented in *Table 1*. All the models predict their primary objective, i.e. the variations in tar and gas yield with time and temperature. All three are capable of predicting

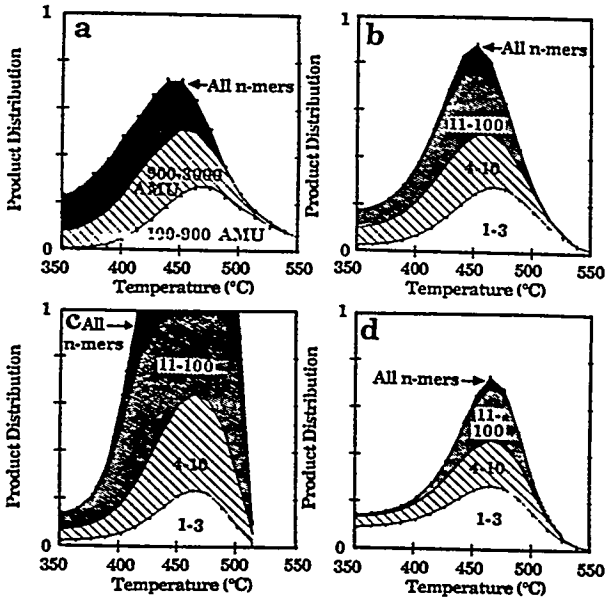

Figure 11 Comparison of distribution of n-mers for pyrolysis of upper Freeport coal at 3°C min^{-1}: a, Monte Carlo calculation; b, two-σ model ($\sigma_1=1$, $\sigma_2=1$); c, one-σ model ($\sigma=1.2$); d, one-σ model ($\sigma=2.2$)

Table 1 Comparison of network models

	CPD	DISARAY	FG-DVC Monte-Carlo or 2σ	Relevant model process
Tar yield versus time	Yes	Yes	Yes	Bond breaking
Extract yield versus time	No[a]	No	Yes	Bond breaking
Gas yield versus time	Yes	Yes	Yes	From peripheral groups
Tar yield versus heating rate	Not yet	Yes	Yes	Relative rates of bond breaking and crosslinking
Variation of tar molecular weight with heating rate	No	No	Yes	Relative rates of bond breaking and crosslinking
Molecular weight of tar	No	No	Yes	Mass transport limitation
Tar yields versus pressure	No	No	Yes	Mass transport limitation
Molecular weight versus pressure	No	No	Yes	Mass transport limitation
Solvent swelling of char	No	No	Yes	Crosslinking

[a] All oligomers are defined as tar

variations of tar yield with heating rate, but CPD has not yet done this. All three models are capable of predicting the complete molecular weight distributions of fragments, but only FG-DVC uses this information to predict the extract yield, the tar yield and the tar molecular weight distribution. DISARAY uses only the prediction for monomers (defined as tar precursor) and CPD uses only the prediction for all oligomers (defined as tar). In a recent paper[32], the total oligomer population computed by the FG-DVC model was used to predict coal fluidity behaviour. Only FG-DVC employs a mass transport equation which is necessary to predict tar molecular weights and the variations of yield and molecular weights with pressure. Only FG-DVC predicts the solvent swelling ratio, which is determined by the crosslink density in the char.

CONCLUSIONS

This paper examines the extension of macromolecular network concepts to describe coal thermal decomposition. The statistical methods (Monte Carlo calculations and percolation theories) and the classes of chemical reactions (labile bridge breaking, hydrogen utilization, crosslinking) and mass transport (vaporization and convection) employed by different researchers have been compared. The conclusion are as follows:

1. The application of macromolecular network concepts appears to be a very promising and versatile approach.
2. Monte Carlo methods for computing the network statistics are the most versatile, but are computationally demanding.
3. The use of percolation theory is computationally efficient and helps provide insight into network behaviour, but the use of a fixed coordination number may be inadequate to accurately describe coal thermal decomposition. The network appears to require a coordination number between 2.2 and 2.5 during labile bridge breaking and greater than 3 during crosslinking.
4. Alternatively, a more general percolation theory model for a network with two types of bridging bonds was developed, each with their own $\sigma+1$.
5. When the two-σ percolation model is applied using the FG-DVC chemistry to cases in which tar is not removed, it is much more flexible in matching the Monte Carlo calculations. The one-σ models either decompose at too low a temperature for large values of $\sigma+1$, or decompose too much and resolidify at too low a temperature for small values of $\sigma+1$. Applying percolation theory to cases where tar is removed requires additional approximations.
6. Of the three models compared (CPD, DISARAY, and FG-DVC), FG-DVC is the most complete in treating the molecular weight distribution of network fragments and the processes of vaporization and mass transport to define tar, the tar molecular weight distribution and the extract yield.
7. Of the three models, FG-DVC is the most closely related with the previous concepts of coal as a macromolecular network by requiring that the model predict the coal solvent swelling ratios and measured extract yields. The assumptions which define the parameters of the starting network are open to question and must be explored.
8. Future efforts should focus on identifying the chemistry for the processes of bridge breaking, low temperature crosslinking, moderate temperature crosslinking, and hydrogen utilization.

ACKNOWLEDGEMENTS

The authors acknowledge support for the work provided by the Morgantown Energy Technology Center of the Department of Energy under Contract No. DE-AC21-86MC23075.

REFERENCES

1 van Krevelen, D. W. in 'Coal', Elsevier, Amsterdam, The Netherlands, 1961
2 Green, T. K., Kovac, J. and Larsen, J. W. *Fuel* 1984, 63, 935
3 Brenner, D. *Fuel* 1985, 64, 167
4 Lucht, L. M. and Peppas, N. A. *Fuel* 1987, 66, 803
5 Lucht, L. M., Larsen, J. M. and Peppas, N. A. *Energy & Fuels* 1987, 1, 56
6 Larsen, J. W. *Am. Chem. Soc. Div. Fuel Chem. Prepr.* 1985, 30(4), 444
7 Green, T., Kovac, J., Brenner, D. and Larsen, J. in 'Coal Structure' (Ed. R. A. Meyers), Academic Press, NY, USA, 1982, p. 199
8 Hall, P. J., Marsh, H. and Thomas, K. M. *Fuel* 1988, 67, 863
9 Sanada, Y. and Honda, H. *Fuel* 1966, 45, 295
10 Suuberg, E. M., Yoshi, O. and Deevo, S. *Am. Chem. Soc. Div. Fuel Chem. Prepr.* 1988, 33(1), 387
11 Suuberg, E. M., Lee, D. and Larsen, J. W. *Fuel* 1985, 64, 1668
12 Suuberg, E. M., Unger, P. E. and Larsen, J. W. *Energy & Fuels* 1987, 1, 305
13 Brown, J. K., Dryden, I. G. C., Dunevein, D. H. *et al. J. Inst. Fuel* 1958, 31, 259

14 Orning, A. A. and Greifer, B. *Fuel* 1956, 35, 318
15 Solomon, P. R. and Hamblen, D. G. in 'Chemistry in Coal Conversion' (Ed. R. H. Schlosberg), Plenum Press, New York, USA, chapter 5, p. 121
16 Solomon, P. R. 'New Approaches in Coal Chemistry', ACS Symposium Series 169, ACS, Washington, DC, USA, 1981, p. 61
17 Solomon, P. R. and King, H. H. *Fuel* 1984, 63, 1302
18 Gavalas, G. R. in 'Coal Pyrolysis' Elsevier, NY, USA, 1982, p. 51
19 Gavalas, G. R., Cheong, P. H. and Jain, R. *Ind. Eng. Chem. Fundam.* 1981, 20, 122
20 Squire, K. R., Solomon, P. R., Carangelo, R. M. and DiTaranto, M. B. *Fuel* 1986, 65, 833
21 Squire, K. R., Solomon P. R., DiTaranto, M. B. and Carangelo, R. M. *Am. Chem. Soc. Div. Fuel Chem. Prepr.* 1985, 30(1), 386
22 Solomon, P. R., Squire, K R and Carangelo, R. M. 'Proc. Int. Conf. on Coal Science', Pergamon, Sydney, Australia, 1985, p. 945
23 Solomon, P. R. and Squire, K. R. *Am. Chem. Soc. Div. Fuel Chem. Prepr.* 1985, 30(4), 347
24 Niksa, S. and Kerstein, A. R. *Comb. and Flame* 1986, 66, 95
25 Niksa, S. *Comb. and Flame* 1986, 66, 111
26 Solomon, P. R., Hamblen, D. G., Deshpande, G. V. and Serio, M. A. 'Proc. Int. Coal Science Conference', Elsevier, NY, USA, 1987, p. 601
27 Solomon, P. R., Hamblen, D. G., Carangelo, R. M. *et al. Comb. and Flame* 1988, 71, 137
28 Niksa, S. and Kerstein, A. R. *Fuel* 1987, 66, 1389
29 Solomon, P. R., Hamblen, D. G., Carangelo, R. M. *et al. Energy & Fuels* 1988, 2, 405
30 Grant, D. M., Pugmire, R. J., Fletcher, T. H. and Kerstein, A. R. *Energy & Fuels* 1989, 3, 175
31 Serio, M. A., Solomon, P. R., Yu, Z. Z. *et al. Am. Chem. Soc. Div. Fuel Chem. Prepr.* 1988, 33(3), 91
32 Solomon, P. R., Best, P. E., Yu, Z. Z. and Deshpande, G. V. *Am. Chem. Soc. Div. Fuel Chem. Prepr.* 1989, 34(3), 895
33 Nielsen, L. E. in 'Mechanical Properties of Polymers and Composites', Volume 2, Marcel Dekker, Inc., NY, USA, 1974
34 Bartels, C. R., Crist, B., Felters, L. J. and Graessley, W. W. *Macromolecules* 1986, 19, 785
35 Nazem, F. F. *Fuel* 1980, 59, 851
36 Macosko, C. W. *Brit. Polymer Journ.* 1985, 17, 239
37 Flory, P. J. *J. Am. Chem. Soc.* 1941, 63, 3083, 3097; 'Principles of Polymer Chemistry', Cornell University Press, Ithaca, NY, USA, 1953, chapter 9
38 Stockmayer, W. H. *J. Chem. Phys.* 1943, 11, 45; 1944, 12, 125
39 Fisher, M. E. and Essam, J. W. *J. Math. Phys.* 1961, 2, 609
40 Solum, M., Pugmire, R. J. and Grant, D. M. *Energy & Fuels* 1989, 3, 40
41 Gerstein, B. C., Murphy, D. P. and Ryan, L. M. in 'Coal Structure' (Ed. R. A. Meyers), Academic Press, NY, USA, 1982, chapter 4, p. 87
42 Hooker, D. T. II, Lucht, L. M. and Peppas, N. A. *Ind. Eng. Chem. Fundam.* 1986, 25, 103
43 Solomon, P. R., Serio, M. A., Carangelo, R. M. and Markham, J. R. *Fuel* 1986, 65, 182
44 Fletcher, T. H. *Comb. Sci. and Tech.* 1989, 63, 87
45 Solomon, P. R., Serio, M. A., Deshpande, G. V. and Kroo, E. *Energy & Fuels* submitted for publication; Deshpande, G. V., Solomon, P. R. and Serio, M. A. *Am. Chem. Soc. Div. Fuel Chem. Prepr.* 1988, 33(2), 310
46 Unger, P. E. and Suuberg, E. M. '18th Symposium (Int) on Combustion', The Combustion Institute, Pittsburgh, PA, USA, 1981, p. 1203
47 Suuberg, E. M., Unger, P. E. and Lilly, W. D. *Fuel* 1985, 64, 956
48 Unger, P. E. and Suuberg, S. E. *Fuel* 1984, 63, 606
49 Oh, M. S., Peters, W. A. and Howard, J. B. *AIChE J.* 1989, 35(5), 775
50 Serio, M. A. *Ph.D. Thesis* Massachusetts Institute of Technology, Cambridge, MA, USA, 1984
51 Khan, M. R., Serio, M. A., Malhotra, R. and Solomon, P. R. *Am. Chem. Soc. Div. Fuel Chem. Prepr.* 1989, 34(4), 1054
52 Fong, W. S., Peters, W. A. and Howard, J. B. *Fuel* 1986, 65, 251
53 Solomon, P. R. and Carangelo, R. M. *Fuel* 1982, 61, 663
54 Solomon, P. R. and Carangelo, R. M. *Fuel* 1988, 67, 949

APPENDIX A

The probability $F_{s,u}(p, q)$, that a site is a member of a cluster of n sites with s type 1 bridges and u type 2 bridges is given by

$$F_{s,u}(p, q)=a_{s,u}p^s(1-p)^\tau q^u(1-q)^\nu \tag{1}$$

where

$$\begin{aligned} n&=u+s+1 \\ \tau&=(\sigma_1+1)n-2s \\ \nu&=(\sigma_2+1)n-2u \end{aligned} \tag{2}$$

τ and ν are the number of broken bridges of type 1 and 2, respectively, on the perimeter of the cluster, and $a_{s,u}$ is the number of different ways to form such a cluster. Following the procedure used by Fisher and Essam, an expression for the configuration coefficient can be derived

$$a_{s,u}=\frac{(\sigma_1+1)(\sigma_2+1)}{(s+\tau)(u+\nu)}\Gamma(s+\tau+1)\Gamma(u+\nu+1)(u+s+1) \tag{3}$$

where Γ is a gamma function. Note that for $u=0$ (no type 2 bonds), this reduces to the quantity nb_n in Ref. 30. To determine the probability, $F_n(p, q)$ that a given site is a member of a cluster of n sites, i.e. the fraction of n-mers, Equation (1) must be summed over all possible values of s and u that give an n-site cluster:

$$F_n(p, q)=\sum_{s=0}^{n-1} a_{s,u}p^s(1-p)^\tau q^u(1-q)^\nu \qquad u=n-s-1 \tag{4}$$

The total fraction of sites, $F(p, q)$ in finite clusters is the sum over all s and u

$$F(p, q)=\sum_{s=0}^{\infty}\sum_{u=0}^{\infty} F_{s,u}(p, q)=\left(\frac{1-p}{1-p^*}\right)^{\sigma_1+1}\left(\frac{1-q}{1-q^*}\right)^{\sigma_2+1} \tag{5}$$

where p^* and q^* are obtained by finding the least roots of

$$\begin{aligned} p^*(1-p^*)^{\sigma_1-1}(1-q^*)^{\sigma_2+1}-p(1-p)^{\sigma_1-1}(1-q)^{\sigma_2+1}&=0 \\ q^*(1-q^*)^{\sigma_2-1}(1-p^*)^{\sigma_1+1}-q(1-q)^{\sigma_2-1}(1-p)^{\sigma_1+1}&=0 \end{aligned} \tag{6}$$

The critical point at which an infinite lattice begins to form (i.e. $F(p, q)$ begins to decrease) becomes a critical curve which divides the p-q plane into two regions. Note that for $q=0$, the equations all reduce to the single σ case given in Ref. 30.

APPENDIX F

GENERAL MODEL OF COAL DEVOLATILIZATION

Reprinted from Journal of ENERGY & FUELS, 1988, 2, 405.

General Model of Coal Devolatilization†

P. R. Solomon,* D. G. Hamblen, R. M. Carangelo, M. A. Serio, and G. V. Deshpande

Advanced Fuel Research, Inc., 87 Church Street, East Hartford, Connecticut 06108

Received December 21, 1987. Revised Manuscript Received April 21, 1988

A general model for coal devolatilization, which combines a functional group model for gas evolution and a statistical model for tar formation, has been presented. The tar formation model includes depolymerization, cross-linking, external transport, and internal transport. The cross-linking is related to the evolutions of CO_2 and CH_4, with one cross-link formed per molecule evolved. The model predictions compare favorably with a variety of data for the devolatilization of Pittsburgh Seam coal and North Dakota (Beulah) lignite, including volatile yields, extract yields, cross-link densities, and tar molecular weight distributions. The variations with pressure, devolatilization temperature, rank, and heating rate were accurately predicted. Comparison of the model with several sets of data employing alternative assumptions on transport suggests that assuming that the particle is well mixed (i.e. the surface concentration of tar molecules is the same as the bulk) overpredicts the transport rate. For 50-μm particles, assuming that the internal-transport limitation dominates (i.e. neglecting the external transport) provides a good fit to the data. The rank dependence of tar formation, extract yields, cross-linking, and viscosity appears to be explained by the rank dependence of CO_2 yields and its associated cross-linking. High CO_2 yields in low-rank coals produce rapid cross-linking at low temperatures and hence thermosetting behavior, low tar yields, low extract yields, loss of solvent-swelling properties, and high viscosities. The relative importance of cross-linking compared to bond breaking is, however, sensitive to heating rate, and this effect is predicted by the model. Areas for improving the model include (1) refinement of the internal and external transport assumptions, (2) accounting for hydroaromatic structures and bridge structures besides ethylene, and (3) including polymethylene "guest" molecules.

Introduction

Coal devolatilization is a process in which coal is transformed at elevated temperatures to produce gases, tar, and char. (Tar is defined as the room-temperature condensibles formed during coal devolatilization.) The combined chemical and physical processes in devolatilization have been reviewed by a number of investigators.[1-6] Gas formation can often be related to the thermal decomposition of specific functional groups in the coal and can be predicted with reasonable accuracy by models employing first-order reactions with ultimate yields.[5-15] On the other hand, tar and char formation are more complicated, and success in mechanistic modeling of tar formation has been more limited.

Predicting tar formation is, however, important for several reasons. Tar is a major volatile product (up to 40% of the DAF coal weight for some bituminous coals). Tar yields vary substantially depending on reactor conditions

*To whom correspondence is to be addressed

†Presented at the Symposium on Coal Pyrolysis: Mechanisms and Modeling, 194th National Meeting of the American Chemical Society, New Orleans, LA, August 31–September 4, 1987.

(1) Howard, J. B.; Peters, W. A.; Serio, M. A. "Coal Devolatilization Information for Reactor Modeling"; Final Report on EPRI Project No. 986-5, 1981.
(2) Howard, J. B. In *Chemistry of Coal Utilization*; Elliott, M. A., Ed.; Wiley: New York, 1981; Chapter 12, p 665.
(3) Gavalas, G. R. *Coal Pyrolysis*; Elsevier: Amsterdam, The Netherlands, 1981.
(4) Suuberg, E. M. In *Chemistry of Coal Conversion*; Schlosberg, R. H., Ed.; Plenum: New York, 1985; Chapter 4.
(5) Solomon, P. R.; Hamblen, D. G. In *Chemistry of Coal Conversion*; Schlosberg, R. H., Ed.; Plenum: New York, 1985; Chapter 5, p 121.
(6) Serio, M. A.; Hamblen, D. G.; Markham, J. R.; Solomon, P. R. *Energy Fuels* 1987, *1*, 138.
(7) Suuberg, E. M.; Peters, W. A.; Howard, J. B. *Seventeenth Symposium (International) on Combustion*; The Combustion Institute: Pittsburgh, PA, 1979; p 117.
(8) Juntgen, H.; van Heek, K. H. *Fuel Process. Technol.* 1979, *2*, 261.
(9) Weimer, R. F.; Ngan, D. Y. *Prepr. Pap.—Am. Chem. Soc., Div. Fuel Chem.* 1979, *24*(3), 129.
(10) Campbell, J. H. *Fuel* 1978, *57*, 217.
(11) Solomon, P. R.; Colket, M. B. *Seventeenth Symposium (International) on Combustion*; The Combustion Institute: Pittsburgh, PA, 1979; p 131.

0887-0624/88/2502-0405$01.50/0

(pressure, heating rate, final temperature, bed geometry, particle size, etc.). In combustion or gasification, tar is often the volatile product of highest initial yield and thus controls ignition and flame stability. It is a precursor to soot, which is important to radiative heat transfer. The process of tar formation is linked to the char viscosity[16-19] and the subsequent physical and chemical structure of the char and so is important to char swelling and reactivity. Also, because tar molecules are sometimes minimally disturbed coal molecular fragments, primary tars provide important clues to the structure of the parent coal.[5,6,20]

It is generally agreed that the tar formation includes the following steps: (1) depolymerization by rupture of weaker bridges in the coal macromolecule to release smaller fragments that make up the "metaplast";[3,5,7,16,21-33] (2) repolymerization (cross-linking) of metaplast molecules;[3,5,7,16,21-33] (3) transport of lighter molecules away from the surface of the coal particles by combined vaporization and gas phase diffusion;[23,32] (4) internal transport of lighter molecules to the surface of the coal particles by convection and diffusion in the pores of nonsoftening coals[24,27,34,35] and liquid-phase or bubble transport in softening coals.[17,36-38] Char is formed from the unreleased or recondensed fragments. Varying amounts of loosely bound "guest" molecules, usually associated with the extractable material, are also released in devolatilization.

The complexity of proposed devolatilization models varies substantially. They can be divided into four categories. The simplest are the "weight loss models" employing a single rate,[6,22,39-42] two rates,[39,43] multiple parallel rates, or distributed rates.[9,22] These models do not account for the variations in tar yield with reaction conditions, and a number of "tar formation models" incorporating retrogressive char-forming reactions and mass transport have been proposed that account for such variations.[16,21-33,37,44-49] A recent innovation has been the description of the decomposition and repolymerization of the macromolecular network by using statistical methods.[28,29,44-46,50,51]

Most of the above models do not consider the evolution of gas species, which have been treated in a number of "species evolution/functional group models" as parallel first-order reactions.[5-13] More complicated "comprehensive chemical models" also describe the composition of the char and tar.[3,5,6,11-13,33,48,49,51]

The level of detail required in a model depends on its application. In the modeling of combustion and gasification, the simple "weight loss models" have often been employed. However, to predict the variations in yield with reactor conditions, the more complicated "tar formation models" must be used. A case can also be made for employing "species evolution/functional group models" or "comprehensive chemical models". For example, in predicting the energy released from combustion of the volatiles, it is important to know that for low-rank coals a high percentage of the volatiles may be noncombustible H_2O and CO_2. For a North Dakota lignite, the total of these two components can be as high as 35% of the rapidly released volatiles which are important for ignition.[6] In addition, the swelling, particle agglomeration properties, char reactivity, and char fragmentation are functions of the char composition. Soot formation (which can dominate radiative energy transport) is controlled by the tar amount.

In the modeling of liquefaction and mild gasification, knowledge of the chemical makeup and molecular weight distribution of the soluble and volatile products is essential, requiring the more complete "comprehensive chemical models".

This paper presents a "comprehensive chemical model" for coal devolatilization that considers the evolution of gas, tar, char, and guest molecules. The model is general in its applicability to bituminous coals, subbituminous coals,

(12) Solomon, P. R.; Hamblen, D. G.; Carangelo, R. M.; Krause, J. L. *Nineteenth Symposium (International) on Combustion*; The Combustion Institute: Pittsburgh, PA, 1982; p 1139.
(13) Solomon, P. R.; Serio, M. A.; Carangelo, R. M.; Markham, J. R. *Fuel* 1986, *65*, 182.
(14) Xu, W.-C.; Tomita, A. *Fuel* 1987, *66*, 627.
(15) Juntgen, H. *Fuel* 1984, *63*, 731.
(16) Fong, W. S.; Peters, W. A.; Howard, J. B. *Fuel* 1986, *65*, 251.
(17) Oh, M. S.; Peters, W. A.; Howard, J. B. *Proceedings of the 1983 International Conference on Coal Science*; Center for Conference Management: Pittsburgh, PA, 1983; p 483.
(18) Fong, W. S.; Khalil, Y. F.; Peters, W. A.; Howard, J. B. *Fuel* 1986, *65*, 195.
(19) Van Krevelen, D. W. *Properties of Polymers*; Elsevier: Amsterdam, 1976.
(20) Solomon, P. R. *New Approaches in Coal Chemistry*; ACS Symposium Series 169; American Chemical Society: Washington, DC, 1981; pp 61–71.
(21) van Krevelen, D. W.; Schuyer, J. *Coal Science*; Elsevier: Amsterdam, 1957.
(22) Anthony, D. B.; Howard, J. B.; Hottel, H. C.; Meissner, H. P. *Fifteenth Symposium (International) on Combustion*; The Combustion Institute: Pittsburgh, PA, 1974; p 1303.
(23) Unger, P. E.; Suuberg, E. M. *Eighteenth Symposium (International) on Combustion*; The Combustion Institute: Pittsburgh, PA, 1981; p 1203.
(24) Russel, W. B.; Saville, D. A.; Greene, M. I. *AIChE J.* 1979, *25*, 65.
(25) James, R. K.; Mills, A. F. *Lett. Heat Mass Transfer* 1976, *3*, 1.
(26) Lewellen, P. C. S.M. Thesis, Department of Chemical Engineering, MIT, 1975.
(27) Chen, L. W.; Wen, C. Y. *Prepr. Pap.—Am. Chem. Soc., Div. Fuel Chem.* 1979, *24*(3), p 141.
(28) Niksa, S.; Kerstein, A. R. *Combust. Flame* 1986, *66*, 95.
(29) Niksa, S. *Combust. Flame* 1986, *66*, 111.
(30) Solomon, P. R.; Squire, K. R.; Carangelo, R. M. *Proceedings of the International Conference on Coal Science*; Pergamon: Sydney, Australia, 1985; p 945.
(31) Solomon, P. R.; Squire, K. R. *Prepr. Pap.—Am. Chem. Soc., Div. Fuel Chem.* 1985, *30*(4), 347.
(32) Suuberg, E. M.; Unger, P. E.; Lilly, W. D. *Fuel* 1985, *64*, 956.
(33) Solomon, P. R.; Hamblen, D. G.; Carangelo, R. M.; Serio, M. A.; Deshpande, G. V. *Prepr. Pap.—Am. Chem. Soc., Div. Fuel Chem.* 1987, *32*(3), 83.
(34) Gavalas, G. R.; Wilks, K. A. *AIChE J.* 1980, *26*, 201.
(35) Simons, G. A. *Prog. Energy Combust. Sci.* 1983, *9*, 269.
(36) Suuberg, E. M.; Sezen, Y. *Proceedings of the International Conference on Coal Science*; Pergamon: Sydney, Australia, 1985; p 913.
(37) Melia, P. F.; Bowman, C. T. *Combust. Sci. Technol.* 1983, *31*, 195; Paper presented at the Western States Section of the Combustion Institute, Salt Lake City, UT, 1982.
(38) Oh, M. S. Sc.D. Thesis, Department of Chemical Engineering, MIT, Cambridge, MA, 1985.
(39) Kobayashi, H.; Howard, J. B.; Sarofim, A. F. *Sixteenth Symposium (International) on Combustion*; The Combustion Institute: Pittsburgh, PA, 1977; p 411. Kobayashi, H. Ph.D. Thesis, Department of Mechanical Engineering, MIT, Cambridge, MA. 1976.
(40) Niksa, S.; Heyd, L. E.; Russel, W. B.; Saville, D. A. *Twentieth Symposium (International) on Combustion*; The Combustion Institute: Pittsburgh, PA, 1984; p 1445.
(41) Badzioch, S.; Hawksley, P. G. W. *Ind. Eng. Chem. Process Des. Dev.* 1970, *9*, 521.
(42) Maloney, D. J.; Jenkins, R. G. *Twentieth Symposium (International) on Combustion*; The Combustion Institute: Pittsburgh, PA, 1984; p 1435.
(43) Witte, A. B.; Gat, N. Presented at the DOE Direct Utilization AR&TD Contractor's Meeting, Pittsburgh, PA, 1983.
(44) Solomon, P. R.; King, H. H. *Fuel* 1984, *63*, 1302.
(45) Solomon, P. R.; Squire, K. R.; Carangelo, R. M. *Prepr. Pap.—Am. Chem. Soc., Div. Fuel Chem.* 1984, *29*(1), 10.
(46) Squire, K. R.; Solomon, P. R.; Carangelo, R. M.; DiTaranto, M. B. *Fuel* 1986, *65*, 833.
(47) Squire, K. R.; Solomon, P. R.; DiTaranto, M. B.; Carangelo, R. M. *Prepr. Pap.—Am. Chem. Soc., Div. Fuel Chem.* 1985, *30*(1), 386.
(48) Gavalas, G. R.; Cheong, P. H.; Jain, R. *Ind. Eng. Chem. Fundam.* 1981, *20*, 113.
(49) Gavalas, G. R.; Cheong, P. H.; Jain, R. *Ind. Eng. Chem. Fundam.* 1981, *20*, 122.
(50) Solomon, P. R.; Hamblen, D. G.; Carangelo, R. M.; Serio, M. A.; Deshpande, G. V. *Combust. Flame* 1988, *71*, 137.
(51) Solomon, P. R.; Hamblen, D. G.; Deshpande, G. V.; Serio, M. A. *Coal Sci. Technol.* 1987, *11*, 601.

and lignites (employing rank-independent kinetic parameters), in its application to reactors of widely differing heating rates (0.05 to 20000 °C/s), and in its ability to predict the variations in tar yield with reactor conditions.

Two previously developed models, a functional group (FG) model[5,6,11-13] (a "species evolution/functional group model") and a depolymerization–vaporization–cross-linking (DVC) model[30,31,44-47] (a "tar formation model") have been combined as subroutines of what is now called the "FG–DVC" model.[33,50,51] The DVC subroutine is employed to determine the yield of tar and the molecular weight distribution of the tar and char. The FG subroutine is used to describe the gas evolution and the elemental and functional group compositions of the tar and char. Cross-linking in the DVC subroutine is computed by assuming that this event is correlated with CO_2 and CH_4 evolutions predicted in the FG subroutine. The dependence of the yield of rapidly released CO_2 (which is related to coal rank or weathering) is the factor that controls the thermosetting or thermoplastic behavior of coals.

The combined FG–DVC model was described in two previous publications,[50,51] and comparisons were made to a limited set of data. In this paper, a description of internal transport has been added to the model. The model equations are presented, and comparisons are made to a wider set of data. The paper also includes a discussion of the assumptions, approximations, and exceptions to the model and a sensitivity analysis for the parameters of the DVC subroutine. The model describes the processes of (1) depolymerization and hydrogen consumption, (2) cross-linking, (3) external transport, (4) internal transport, (5) gas formation for all principal species, (6) tar composition, and (7) char composition.

The work presented here is limited to dilute phase reactions of small coal particles where internal temperature gradients can be neglected. Secondary gas phase reactions have been discussed elsewhere,[6] and reactions of pyrolysis products with a char bed and large particle effects have not yet been included. Only reactions involving C, H, and O are discussed here.

A number of coal composition parameters and reactor parameters (pressure, particle time–temperature profile) are required to predict the pyrolysis behavior. A substantial reduction in the number of parameters that must be measured for each coal is made by the use of rank-independent kinetic rates. These parameters have already been determined for a wide variety of coals and reactors. This simplification is a good first approximation to describe the kinetics of individual evolved species and the functional group decompositions.[5,6,49,52-55] The properties predicted as a function of time, include the following: for tar, molecular weight distribution, elemental and functional group composition, and yield; for char, molecular weight distribution, elemental and functional group composition, yield, cross-link density, and extract yield; for gas, yields of individual light gas species. Results are presented for a Pittsburgh Seam bituminous coal and a North Dakota lignite.

Experimental Section

Coals Examined. The two coals described in this paper are a Pittsburgh Seam bituminous coal and a North Dakota (Beulah, Zap) lignite. Samples of the Pittsburgh Seam coal were obtained from the Pittsburgh Energy Technology Center and the Argonne National Laboratory premium coal sample collection. Samples of the North Dakota (Beulah, Zap) lignite were obtained from the University of North Dakota Energy Research Center and the Argonne National Laboratory premium coal sample collection. Data on the premium samples are presented in ref 56, and data on the other two samples, in ref. 6. The FG–DVC model was also compared to data on Pittsburgh coal samples from ref 7, 16, and 22, and characterizations of these samples are presented therein.

Coal Characterization. The cross-link density was estimated by using the volumetric swelling technique developed by Larsen and co-workers.[57-59] Pyridine extract yields were obtained by using a Soxhlet apparatus. Molecular weight distributions of tars were obtained at SRI International on the field-ionization mass spectrometry (FIMS) apparatus described by St. John et al.[60] Tar samples were collected from the pyrolysis apparatus and vaporized from a heated probe into the FIMS apparatus. In addition, coal samples were pyrolyzed directly in the FIMS apparatus.

Apparatus. Pyrolysis experiments were performed in several apparatuses that have been described previously including a heated-grid pyrolyzer,[5,12] a heated-tube reactor,[6,13] and a thermogravimetric analyzer with analysis of evolved products by Fourier transform infrared (FT-IR) spectroscopy (TG-FTIR).[6,61]

General Model

Any general model of a process as complicated as coal devolatilization must of course be a gross approximation. However, there are many general trends that have been observed in devolatilization. The trick in developing a model is to pick a set of first approximations that best match the majority of these trends. There will of course be exceptions to the trends. These exceptions can be treated as perturbations to the first-order approximation. Differences in models occur because of the subjective choice of what is a general trend and what is an exception. The following discussion presents the authors' view of the general trends and the exceptions.

General Trends in Devolatilization. The general model of coal pyrolysis is based on a number of observations that have been previously made concerning coal pyrolysis. These are as follows: (i) Pyrolysis species kinetics are insensitive to rank.[5,6,11-13,52-55] (ii) Species amounts vary with coal rank and can be correlated with the coal's functional group compositions.[5,6,14,15,48,49,52] The evolution of each species can be correlated with the change in the corresponding functional group composition in the char.[5,6,52] (iii) The primary tar composition is similar (except for a higher concentration of methyl groups) to that of the parent coal for bituminous coals and rapidly heated low-rank coal.[5,20,45,62-64] (iv) Tar yields are controlled by the amount of donatable hydrogen and how efficiently it is used.[5,6,20,46] (v) Cross-linking correlates with CO_2 and CH_4 evolution.[50,51]

The general outline of devolatilization based on these observations was presented by Solomon and Hamblen[5] and Serio et al.[6] Figure 1 (adapted from ref 6) presents a hypothetical picture of the coal's or char's organic structure at successive stages of devolatilization. The figure represents (a) the raw coal, (b) the formation of tar and light

(52) Solomon, P. R.; Hamblen, D. G. *Prog. Energy Combust. Sci.* 1983, *9*, 323.
(53) Xu, W. C.; Tomita, A. *Fuel* 1987, *66*, 632.
(54) Agarwal, P. K. *Fuel* 1985, *64*, 870.
(55) Agarwal, P. K.; Agnew, J. B.; Ravindran, N.; Weimann, R. *Fuel* 1987, *66*, 1097.
(56) Vorres, K. S. *Prepr. Pap.–Am. Chem. Soc., Div. Fuel Chem.* 1987, *32*(4), 221.
(57) Green, T. K.; Kovac, J.; Larsen, J. W. *Fuel* 1984, *63*, 935.
(58) Green, T. K.; Kovac, J.; Larsen, J. W. In *Coal Structure*; Meyers, R. A., Ed.; Academic: New York, 1982.
(59) Suuberg, E. M.; Lee, D.; Larsen, J. W. *Fuel* 1985, *64*, 1668.
(60) St. John, G. A.; Butrill, S. E., Jr.; Anbar, M. *ACS Symp. Ser.* 1978. *No. 71*, 223.
(61) Carangelo, R. M.; Solomon, P. R.; Gerson, D. J. *Fuel* 1987, *66*, 960.
(62) Solomon, P. R.; Colket, M. B. *Fuel* 1978, *57*, 748.
(63) Brown, J. K.; Dryden, I. G. C.; Dunevein, D. H.; Joy, W. K.; Pankhurst, K. S. *J. Inst. Fuel* 1958, *31*, 259.
(64) Orning, A. A.; Greifer, B. *Fuel* 1956, *35*, 318.

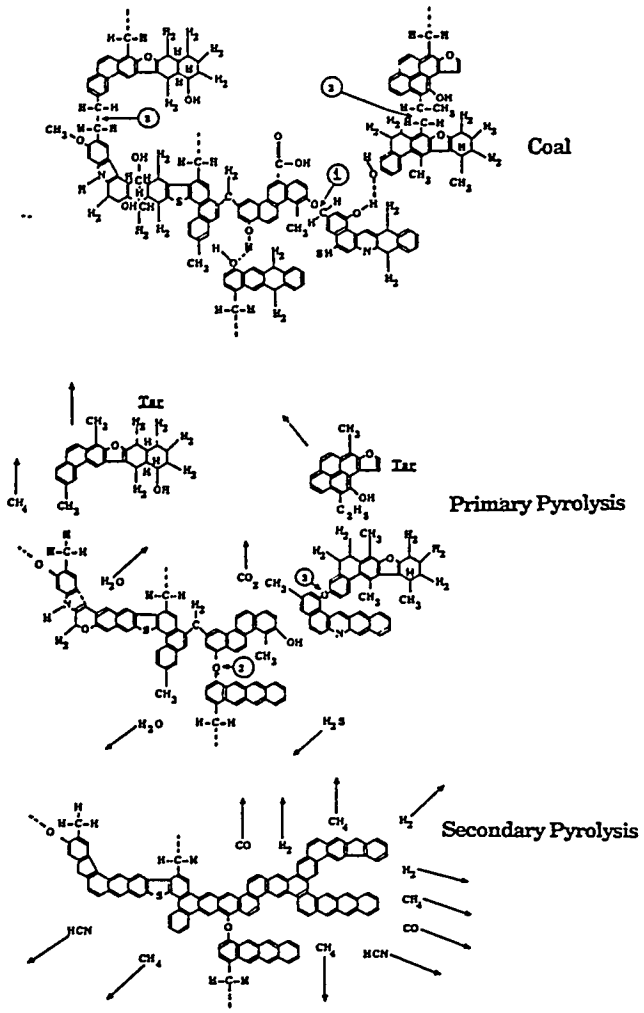

Figure 1. Hypothetical coal molecule during stages of pyrolysis. Adapted from ref 6.

hydrocarbons during primary pyrolysis, and (c) char condensation and cross-linking during secondary pyrolysis. The hypothetical structure in Figure 1a represents the chemical and functional group compositions for a Pittsburgh Seam bituminous coal as discussed by Solomon.[20] It consists of aromatic and hydroaromatic clusters linked by aliphatic bridges. During pyrolysis, the weakest bridges, labeled 1 and 2 in Figure 1a, can break producing molecular fragments (depolymerization). The fragments abstract hydrogen from the hydroaromatics or aliphatics, thus increasing the aromatic hydrogen concentration. These fragments will be released as tar if they are small enough to vaporize under typical pyrolysis conditions and do not undergo retrograde reactions before escaping from the particle. The two lightest fragments are labeled tar. The other two fragments are shown to have repolymerized, producing a molecule that is too large to vaporize.

The other events during primary pyrolysis are the decomposition of functional groups to release CO_2, light aliphatic gases, and some CH_4 and H_2O. The release of CH_4, CO_2, and H_2O may produce cross-linking, CH_4 by a substitution reaction in which the attachment of a larger molecule releases the methyl group, CO_2 by condensation after a radical is formed on the ring when a carboxyl is removed, and H_2O by the condensation of two OH groups to produce an ether link (labeled 3 in Figure 1b). The cross-linking is important to determine the release of tar and the viscoelastic properties of the char.

The end of primary pyrolysis occurs when the donatable hydrogens from hydroaromatic or aliphatic portion of the coal are depleted. During secondary pyrolysis (Figure 1c) there is additional methane evolution (from methyl groups), HCN from ring nitrogen compounds, CO from ether links, and H_2 from ring condensation. These general concepts are incorporated into the combined FG–DVC model.

Exceptions to the General Trends. a. Polymethylene. The major exception to the trends described above is the presence of varying amounts (typically 0–9%, but in some cases as high as 18%) of long-chain aliphatics (polymethylenes). These have recently been reported in pyrolysis products by Nelson[65] and by Calkins and coworkers[66–69] and references quoted therein. The chains appear alone and attached to aromatic nucleii.[65] During devolatilization, the smaller molecules may be released without bond breaking and the heavier molecules with bond breaking to contribute to the tar. The presence of these polymethylenes makes the tar more aliphatic than the parent coal. Further cracking of this material under more severe devolatilization conditions produces ethylene, propylene, and butadiene from which the concentration of polymethylenes may be determined.[68] Presently, the polymethylenes are included in the FG model as part of the aliphatic functional group pool, which is assumed to decompose to produce gas products, not tar. If the amount of heavy polymethylenes is determined, these can be computed as a separate functional group pool with an appropriate release rate and added to the tar. The modeling of polymethylene evolution will be the subject of a subsequent publication.

b. Tar/Coal Similarities. The general model assumed, as a first approximation, that tar is derived from material of the same average composition as that of the parent coal. The model predicts that the tar is richer than the parent coal in methyl groups (due to hydrogen stabilization) and poorer in the rapidly removed functional groups. Evidence for this assumption is the similarities in elemental composition, infrared spectra and NMR spectra[5,20,45,62–64] between the primary tar and parent coal observed for bituminous coals. It was, however, noted[5,45,70] that the infrared spectrum for a lignite tar was significantly different from that of the parent coal. The tar is much richer in aliphatic groups and poorer in oxygen functional groups. Freihaut et al. have recently reported a systematic increase in the tar hydrogen concentration with decreasing rank that suggests a similar trend.[71]

There are at least two reasons for this variation with rank. One reason is the influence of the polymethylene groups. As noted by Calkins,[68] the concentration of polymethylenes increases with decreasing rank (~4% for high volatile bituminous coals compared to ~8% for lignites). In addition, the tar yield decreases with decreasing rank (~6% for the North Dakota lignite compared to 30% for the Pittsburgh Seam bituminous coal). The relative contribution of the polymethylenes to the tar is therefore increased with decreasing rank. This will lead to a higher aliphatic content and lower oxygen content for the low-rank coal tar. This effect can be treated in the FG–DVC model by the addition of polymethylenes to the tar as discussed above.

(65) Nelson, P. F. *Fuel* 1987, *66*, 1264.
(66) Calkins, W. H.; Hagaman, E.; Zeldes, H. *Fuel* 1984, *63*, 1113.
(67) Calkins, W. H.; Tyler, R. J. *Fuel* 1984, *63*, 1119.
(68) Calkins, W. H. *Fuel* 1985, *63*, 1125.
(69) Calkins, W. H.; Hovsepian, B. K.; Drykacz, G. R.; Bloomquist, C. A. A.; Ruscic, L. *Fuel* 1984, *63*, 1226.
(70) Solomon, P. R. *Coal Structure*; Advances in Chemistry Series 192; American Chemical Society: Washington, DC, 1981; p 7.
(71) Freihaut, J. D.; Proscia, W. M.; Seery, D. J. Presented at the 194th National Meeting of the American Chemical Society, New Orleans, LA, Aug 31–Sept 4, 1987.

A second reason for differences in structure between the tar and parent coal is that the extensive cross-linking in low-rank coals is related to the carboxyl group concentration, which increases with decreasing rank. This cross-linking will thus selectively repolymerize the fragments rich in oxygen, while those poorer in oxygen are more likely to be released as tar. This effect has not as yet been included in the model.

It is interesting to note an exception to the above observations. At very high heating rates, the North Dakota (Beulah, Zap) lignite is observed to melt and swell and produce a higher yield of tar that resembles the parent coal.[13,30,31] The high heating rate appears to reduce the effect of cross-linking, leading to higher oxygen concentrations in the tar and to increase yields. Both effects enhance the resemblance to the parent coal.

c. Variations of Kinetic Rates with Rank. While the model assumes rank-independent kinetic rates, there is a systematic variation of rate with rank. As reported by Solomon and Hamblen,[52] the variation between a lignite and bituminous coal results in a 50–75 °C difference in the peak evolution temperature for most species (at a heating rate of 30 K/min). Systematic rank variations in the rate constants can be added to the model if increased accuracy is desired.

d. Macerals. Individual macerals are not considered in this model. The influence of the maceral concentration is assumed to occur through its effect on the average elemental and functional group composition. If details on macerals are desired, then each maceral must be treated as a distinct molecular population with its own functional group composition and molecular weight distribution.

e. Physical Properties of Molecular Fragments. The general model has assumed that the vaporization and solubility of the molecular fragments are functions of molecular weight alone. Both properties are expected to depend on functional group composition. Such effects can be included as corrections to the vaporization law and solubility assumptions.

Depolymerization–Vaporization–Cross-Linking (DVC) Subroutine Formulation. The DVC model has been described in a number of publications.[30,31,44-47,50,51] It predicts the tar yield, the tar molecular weight distribution, the char yield, the char molecular weight distribution, the extract yield, and the cross-link density. The model had its beginning in a study of polymers representative of structural features found in coal.[44] The objective of that study was to develop an understanding of coal pyrolysis by studying a simpler, more easily interpretable system. The polymers were studied in a series of pyrolysis experiments in which tar amounts and molecular weights were measured. The theory which was developed describes the combined effects of (1) *depolymerization and hydrogen consumption*, (2) cross-linking, and (3) *external transport*. Recently, an expression to describe (4) *internal transport* has been added to the model.[33] These processes, which are described below, are incorporated into a computer code that employs a Monte Carlo method for performing the statistical analysis.

Process 1. Depolymerization and Hydrogen Consumption. Bond cleavage in coal is likely to be very complicated, including homolytic cleavage, ipso substitution,[46] and hydrogen-transfer-induced bond-scission reactions[72] for a variety of bond types. However, it has been observed that tar evolution is consistent with a narrow distribution of activation energies,[5,6,12] which allows consideration in the model of a single type of bridge (while acknowledging that other types may be present). Also, the rate for tar formation from coal, k_{tar},[6,13] is in good agreement with the rate determined for the breaking of ethylene bridges between naphthalene rings, k_B. This kinetic rate, k_B,[46] employs an activation energy that is in agreement with resonance-stabilization calculations[73,74] and an overall rate that agrees with previous measurements on model compounds.[75] In view of these observations, a single type of bond (ethylene) undergoing homolytic cleavage is assumed for coal as a simple approximation of the complicated behavior.

Bond cleavage is accompanied by the consumption of donatable hydrogens, H(al), to cap free radicals, along with corresponding carbon–carbon double-bond formation at the donor site. In the polymers that were studied, the ethylene bridges were identified as a source of donatable hydrogen with the formation of a double bond between the bridge carbons.[46,47] The double-bond formation was assumed to remove a breakable bond. It should be noted that hydroaromatic groups are also a source of donatable hydrogen with aromatization of the ring. However, for simplicity, the DVC model assumes all the coal's donatable hydrogens, whether in bridges or in hydroaromatic rings, are in bridges, i.e., $H(\text{al}) = (2/28)W_B$. This approximation will produce some error in tar yield since a broken bond in a hydroaromatic ring will not be as effective as a broken bond in a bridge in fragmentating the coal. But this effect will be compensated for, since H(al) is a parameter that is determined for each coal from a selected pyrolysis experiment. H(al) could, in principle, be determined by FT-IR or NMR, but not with sufficient accuracy.

The equation describing the disappearance of labile bridges in the char, W_B (char), due to bond breaking and hydrogen donation is

$$dW_B/dt = -2k_B W_B \quad (1)$$

The value for k_B is taken as the previously determined k_{tar}.[6] The rate of decrease of labile bridges is twice the rate of bond breaking since for each broken bond, an additional labile bridge is converted to a nonlabile bridge with the donation of hydrogen. By assuming that all the donatable hydrogens are in the labile bridges, the consumption of labile bridges and donatable hydrogens occur simultaneously. The redistribution of hydrogen creates source and loss terms, $dW_i(\text{DVC})/dt$, in the equations for the char functional groups W_i(char), as will be discussed with the FG part of the model (see eq 7).

Equation 1 only describes the loss due to bond breaking and hydrogen donation. The loss of labile bridges due to evolution with the tar is computed in the Monte Carlo calculation by using the transport equations (eq 3 and 4) discussed below.

Process 2. Cross-Linking. Cross-linking reactions are important in describing the rank and heating rate dependence of the tar molecular weight distributions and yields. While cross-linking reactions were originally included in the DVC model, using adjustable parameters for the rate and amount,[30,31,46] work has recently been performed to define the reactions that cause cross-linking.[33,50,51] Under the assumption that the cross-linking reactions may also

(72) McMillen, D. F.; Malhotra, R.; Hum, G. P.; Chang, S. J. *Energy Fuels* 1987, *1*, 193.

(73) Stein, S. E. *New Approaches in Coal Chemistry*; Blaustein, B. D., Bockrath, B. C., Friedman, S., Eds.; ACS Symposium Series 169; American Chemical Society: Washingtin, DC, 1981; p 208.

(74) Stein, S. E. "Multistep Bond Breaking and Making Processes of Relevance to Thermal Coal Chemistry"; Annual Report for GRI Contract No. 5081-261-0556; Accession No. GRI-81/0147, 1983.

(75) Stein, S. E.; Robauch, D. A.; Alfieri, A. D.; Miller, R. E. *J. Am. Chem. Soc.* 1982, *104*, 6567.

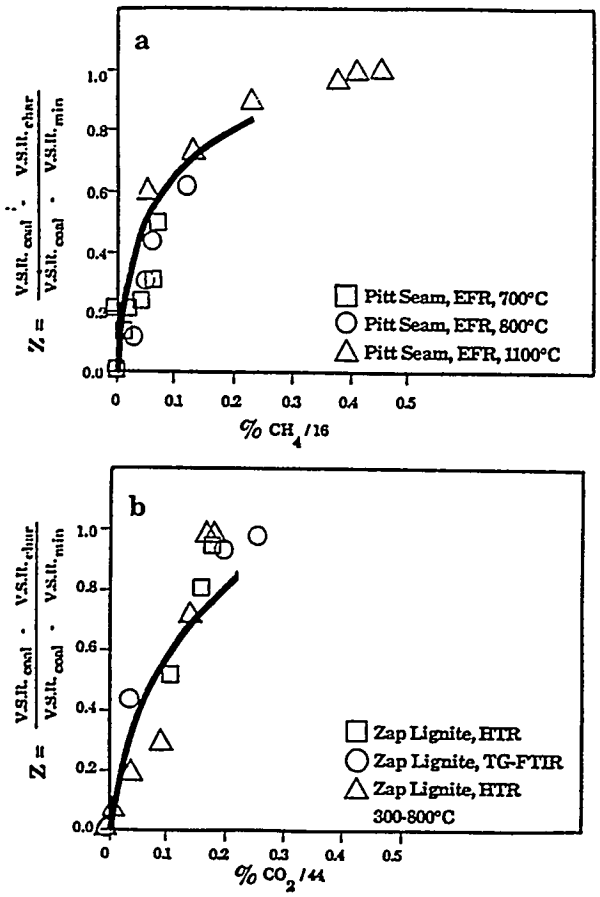

Figure 2. Measured and calculated normalized volumetric swelling ratio (VSR) for coal and chars: (a) Pittsburgh Seam bituminous coal plotted against the methane yield; (b) Zap North Dakota lignite plotted against the CO_2 yield. VSR_{min} is the value achieved when crosslinking is complete. The chars were prepared in an entrained-flow reactor (EFR), a heated-tube reactor (HTR), and a thermogravimetric analyzer with evolved product analysis by FT-IR (TG-FTIR) as described in ref 61.

release gas species, the molecular weight between cross-links (or cross-link density) measured by solvent swelling was correlated with the observed evolution of all the major gas species during pyrolysis. Likely candidates were CO_2 formation from carboxyl groups or methane formation from methyl groups. Suuberg et al.[59] also noted that cross-linking in low-rank coals is correlated with CO_2 evolution. Both CO_2- and CH_4-forming reactions may leave behind free radicals that can be stabilized by cross-linking. Condensation of hydroxyl groups to form water and an ether link is also a possible reaction.

For a series of chars, the reduction in the volumetric swelling ratio in pyridine was compared with CO_2 evolution for a North Dakota (Beulah) lignite and CH_4 evolution for a Pittsburgh Seam bituminous coal.[50] The results are presented in Figure 2. The abscissa (parameter Z), which is the change in the volumetric swelling ratio (VSR) between coal and char divided by the maximum change, is given by

$$Z = (VSR_{coal} - VSR_{char})/(VSR_{coal} - VSR_{min})$$

Z is 0 for coal and 1 for fully cross-linked char. Since the lignite reaches maximum cross-linking before the start of methane evolution and the Pittsburgh Seam bituminous coal evolves little CO_2, correlations can be made separately between cross-linking and CO_2 evolution in the lignite and cross-linking and CH_4 evolution in the Pittsburgh seam bituminous coal. On a molar basis, the evolution of CO_2 from the lignite and the evolution of CH_4 from the bituminous coal appear to have similar effects on the volumetric swelling ratio. The results suggest that one cross-link is formed for each CO_2 or CH_4 molecule evolved. No correlation was observed between the volumetric swelling ratio and tar yield for either coal. A correlation with water yield appears valid for the North Dakota (Beulah) lignite but not for the Pittsburgh Seam bituminous coal.

It therefore appears that a correlation exists between gas evolution and cross-linking which permits the rates for cross-linking and the number of cross-link sites to be related to rates and yields for gas evolution. The model assumes the following expression for the rate of increase of the number of cross-links per gram of coal, m

$$\frac{dm}{dt} = N_0\left[\frac{dW_{CO_2}(gas)/dt}{44} + \frac{dW_{CH_4}(gas)/dt}{16}\right] \quad (2)$$

where the rates, dW_i/dt, of evolution per gram of coal of CO_2 and CH_4 are calculated in the FG subroutine. N_0 is Avogadro's number.

Again, a caution should be added that the reactions which have been assumed must be a gross simplification of a very complicated set of chemical reactions. This is especially true for the cross-links occurring during methane formation, during which time there is extensive bond breaking and cross-linking accompanying tar formation. The inaccuracy in the description of this higher temperature cross-linking event is one of the present weaknesses in the model.

Process 3. External Transport. The external transport of tars from the particle surface to the bulk gas by vaporization and diffusion through a gas boundary layer as in the original DVC model[44-47,50,51] is described with the model of Unger and Suuberg.[23] However, in the current paper, the modified expression for the vapor pressure law of Suuberg et al.[32] is now used to replace that in the model of Unger and Suuberg. The rate of evolution per gram of coal, $(dn_j/dt)_{ET}$, of oligomers of molecular weight M_j is given by

$$(dn_j/dt)_{ET} = (3/r_0^3\rho)rD_j\mathcal{X}^s_j\,(P_j/RT) \quad (3)$$

where r is the particle radius assumed to shrink with the cubic root of its mass r_0 is the initial particle radius, ρ is the particle density, $\mathcal{X}^s_j$ is the mole fraction of species of molecular weight M_j in the metaplast at the surface of the particle, P_j is the vapor pressure for oligomers of molecular weight M_j (given by Suuberg et al.[32]), D_j is the gas-phase diffusivity of species of molecular weight M_j,[38] R is the gas constant, and T is the particle temperature.

In the previous work, it was assumed that the surface mole fraction, $\mathcal{X}^s_j$, was the same as that in the bulk, $\mathcal{X}^b_j$. That is, mass transport to the surface was not a limiting factor.

Process 4. Internal Transport. When comparing the predictions of the model to available data assuming $\mathcal{X}^s_j = \mathcal{X}^b_j$ it was found that tar yields were overpredicted when devolatilization occurred at low temperatures. This was observed for either low-heating-rate experiments[6] or experiments with rapid heating to relatively low temperatures.[16] As discussed in the Results, it appears that the lower yields were the result of the additional transport limitations within the particle.

For softening coals, the internal transport mechanisms include (i) the transport of tar molecules through the liquid to the surface, (ii) the transit of bubbles containing tar from the interior of the particle to the surface, (iii) the transport of tars within the liquid to the bubbles, and (iv)

the stirring action of the bubble evolution. For nonsoftening coals, transport occurs by (v) convection and diffusion within the pores.

Mechanism i was treated by Suuberg and Sezen.[36] The unknown factor is the diffusion coefficient of the tar molecules in the liquid. The detailed modeling of mechanisms ii and iii has been undertaken by several investigators.[4,26,37,38] Calculations for mechanism v have also been published.[24,25,34,35] The models are complicated and require many assumptions. A common feature of mechanisms iii and v is that tars are transported out of the particle with the light devolatilization products that exit the coal via bubbles or pores. In ref 33, the upper limit for this process was calculated. This limit, which occurs when the tars achieve their equilibrium vapor pressure in the evolving gases, can be computed with few assumptions. In this case, the rate of transport per gram of coal, $(dn_j/dt)_{IT}$, for tar component j is proportional to the volume of gases evolved, dV/dt. That is

$$(dn_j/dt) = P_j \mathcal{X}^b_j (dV/dt)(1/RT)$$

The volume of gases is proportional to the number of gas molecules and the temperature. It is inversely proportional to the pressure within the particle, $P_0 + \Delta P$ where P_0 is the ambient pressure and ΔP is the average pressure difference between the surface and the particle's interior. Then

$$dV/dt = \sum_i (dn_i/dt)_{gas} \left(\frac{RT}{P_0 + \Delta P} \right)$$

where $\sum_i (dn_i/dt)_{gas}$ is the rate of production per gram of coal of gas components i summed over all gas and light tar species. For gas molecules, dn_j/dt is taken as the rate of production given by the FG model. For light tar molecules, dn_j/dt is taken as the total amount transported out of the particle as tar computed in the previous time step. For computational efficiency, the sum has been limited to molecular weights less than 300 amu, since this accounts for over 90% of the volume. Combining the two equations with this approximation gives

$$(dn_j/dt)_{IT} = P_j \mathcal{X}^b_j \sum_{i<300} (dn_i/dt)_{gas} \left[\frac{1}{P_0 + \Delta P} \right] \quad (4)$$

ΔP is used as an adjustable parameter that varies with the coal and experimental conditions. For the highly fluid Pittsburgh Seam bituminous coal, in cases where P_0 is 1 atm or greater, we have considered the upper limit to this rate where $P_0 \gg \Delta P$. Then all the terms in eq 4 can be determined by the combined FG–DVC model. This limit coincides with assumptions recently used by Niksa in his FLASHKIN model for Pittsburgh Seam bituminous coal.[76]

While $\Delta P = 0$ appears to be a good approximation for fluid coals at one atmosphere or more, $\Delta P > 0$ is expected for some coals and situations. ΔP is proportional to the coal's viscosity and so will become important for less fluid coals. ΔP is also important when P_0 is small, when particles are large, and when the heating rates are very high.

Two possibilities have been considered for combining the internal and external transportation. In an earlier publication,[33] the internal-transport term and external-transport term (with $\mathcal{X}^s_j = \mathcal{X}^b_j$) were assumed to be in series. Then the transport was controlled by the smaller term. The internal-transport term was the smaller for all pyrolysis cases that were considered and so it dominated. *In fact, calculations performed by neglecting the external transport limitation where almost identical with those made by assuming the two terms to be in series.*

Alternatively, a case can be made that the total transport should be the sum of eq 3 and 4. The reasoning is that internal transport assumes the tars to be in equilibrium with the escaping light gases. It is more likely that this mechanism will transport the tars to the ambient gas than to the surface. In this case, the mechanism considered in eq 4 transports the tars away from the surface in parallel with the surface vaporization and gas diffusion considered in eq 3.

If the two terms are taken in parallel, it is again obvious that $\mathcal{X}^s_j = \mathcal{X}^b_j$ is a bad assumption. Since we did not have a good method to determine $\mathcal{X}^s_j$, calculations were made by assuming that the external-transport term can be neglected, i.e.

$$(dn_i/dt)_{tot} = (dn_i/dt)_{IT}$$

This provides an excellent fit to the data for 50-μm-diameter particles.

Therefore, for either parallel or series combinations of the transport terms, it appears best to neglect the external transport. It is likely that the external transport term will be increasingly important for smaller particles, but this will require better knowledge of the liquid-phase diffusion coefficient (mechanism i), and the stirring action of bubbles (mechanism iv). The relative importance of the various internal- and external-transport mechanisms is the subject of ongoing research.

Schematic Representation of DVC Model. In the current DVC model, the parent coal is represented as a two-dimensional network of monomers (condensed ring clusters) linked by strong and weak bridges as shown in Figure 3a. The monomers are linked to form unbranched oligomers of length "l" by breakable and nonbreakable bridges (shown as horizontal single or double lines, respectively, in Figure 3a). The monomers are represented by circles with molecular weights shown in each circle. The molecular weight distribution of the monomers is assumed to be Gaussian and is described by two parameters, M_{av} (mean) and σ (standard deviation). The breakable bridges (assumed to be ethylene) are represented by single lines, the unbreakable bridges by double lines. "m_0" cross-links per monomer are added (as vertical double lines in Figure 3a) to connect the oligomers of length l so that the molecular weight between cross-links, M_c, corresponds to the value reported in the literature[77] for coals of similar rank. The cross-links form the branch points in the macromolecule. Unconnected "guest" molecules (the extract yield) are obtained by choosing the value of l. A large value of l will mean that a completely connected macromolecule will be formed when even a small number of cross-links are added, leaving no extractable material. For smaller values of l some of the oligomers will be unattached after the cross-links are added, and these are the guest molecules. The number of ethylene bridges, W_B, (two donatable hydrogens per bridge) is chosen to obtain the appropriate value for total donatable hydrogen (i.e., to fit a selected laboratory pyrolysis experiment). The remainder are nonbreakable bridges whose carbons are counted with the aromatic carbons.

The parameters M_c, l, M_{av}, and σ determine the molecular weight distribution of oligomers in the starting coal molecule. A histogram showing the distribution created

(76) Niksa, S. Presented at the Western States Section/The Combustion Institute, Spring Meeting, Salt Lake City, UT, March 1988; Paper 88-4.

(77) Nelson, J. R. *Fuel* 1983, *62*, 112.

Table I. Coal Structure Parameters for DVC Subroutine

parameter	symbol	parameter determination: fixed	coal specific, determined	adjustable	dependent[b]	parameter values: Pittsburgh Seam	Zap lignite
Concentrations							
wt fraction of labile bridges	W_B		from tar yield in a pyrolysis expt			0.094	0.082
wt fraction of nuclei (ring clusters)[a]	W_N		from FG model			0.562	0.440
wt fraction of peripheral groups (sources of gases)[b]	W_P				by difference	0.344	0.478
total						1.000	1.000
Structure Parameters							
wt fraction of donatable hydrogens[b]	H(al)				$(2/28)W_B$	0.0067	0.0059
oligomer length (no. of monomers/oligomer)	l		from extract yield			7	10
molecular wt between cross-links	M_c		from solvent swelling (lit. values)			2900	1400
no. of initial cross-link sites per monomer[b]	m_0				M_{av}/M_c	0.088	0.183
no. of potential CO_2 cross-link sites per monomer	$m(CO_2)$		from FG model			0.070	0.582
no. of potential CH_4 cross-link sites per monomer	$m(CH_4)$		from FG model			1.063	0.875
Molecular Weights							
mol wt of labile bridges	M_L	28				28	28
mol wt of monomers	M_{av} (σ)		from FIMS or NMR			256 (250)	256 (250)
mol wt of nonlabile bridges	M_{NL}	26				26	26
mol wt of pyridine solubles	M_{PS}	3000				3000	3000
Other							
internal pressure, atm	ΔP			for each coal, particle, size, and reaction rate		0–0.2	1–10

[a] Carbon in aromatic rings plus nonlabile bridges. [b] Dependent parameters are calculated from the independent parameters.

by randomly picking monomers to form oligomers of length l and randomly cross-linking them to achieve an average molecular weight between cross-links, M_c, is presented at the right of Figure 3a. The distribution is divided into a pyridine-soluble portion below 3000 amu (light shading) and a pyridine-insoluble portion above 3000 amu (dark shading).

Figure 3b shows the molecule during pyrolysis. The rates for bond breaking and cross-linking are from the FG model and are the same for all coals and all experiments. Some bonds have broken, other bonds have been converted to unbreakable bonds by the abstraction of hydrogen to stabilize the free radicals, and new cross-links have been formed. To determine the change of state of the computer molecules during a time step, the number of cross-links formed is determined by using the FG subroutine and passed to the DVC subroutine. These cross-links are distributed randomly throughout the char, assuming that the cross-linking probability is proportional to the molecular weight of the monomer. Then the DVC subroutine breaks the appropriate number of bridging bonds and calculates the quantity of tar evolved for this time step by using the internal and external transport equations. The result is the coal molecule representation and the molecular weight distributions shown in Figure 3b. The lighter "tar molecules", which leave the particle according to the transport equations, are shown as crosshatched. A fraction of the donatable hydrogen is used to stabilize the free radicals formed by bridge breaking, creating two new methyl groups per bridge and the same fraction of breakable bridges is converted into (unbreakable) double bonds.

Figure 3c shows the final char, which is highly cross-linked with unbreakable bonds and has no remaining donatable hydrogen. The histogram now shows only tar and pyridine-insoluble fractions. The extractables have been eliminated by tar formation and cross-linking.

The output of the DVC subroutine is the molecular weight distribution in the coal, its time-dependent transformation during devolatilization, and the evolution of tar determined by the transport of the lighter components.

Selection of DVC Parameters. The DVC composition parameters employed for a Pittsburgh Seam coal and North Dakota lignite are summarized in Table I. The FG composition parameters and the kinetic parameters, which are fixed for all coals and experiments, are presented in Table II. In Table I, there are 11 independent composition parameters. Three parameters are fixed, the molecular weight of the labile bridges, M_L, the nonlabile bridges, M_{NL}, and the pyridine-extractable limit, M_{PS}.

Eight parameters are coal specific (i.e., fixed for each coal, for all conditions) and must be determined by some measurement. M_c and l are determined experimentally for each coal by the measured molecular weight between cross-links and the pyridine extract yield, respectively. The weight fraction of carbon in nucleii and nonbreakable bridges, W_N, is obtained from the FG model and is equal to the amount of nonvolatile carbon. This value is, in

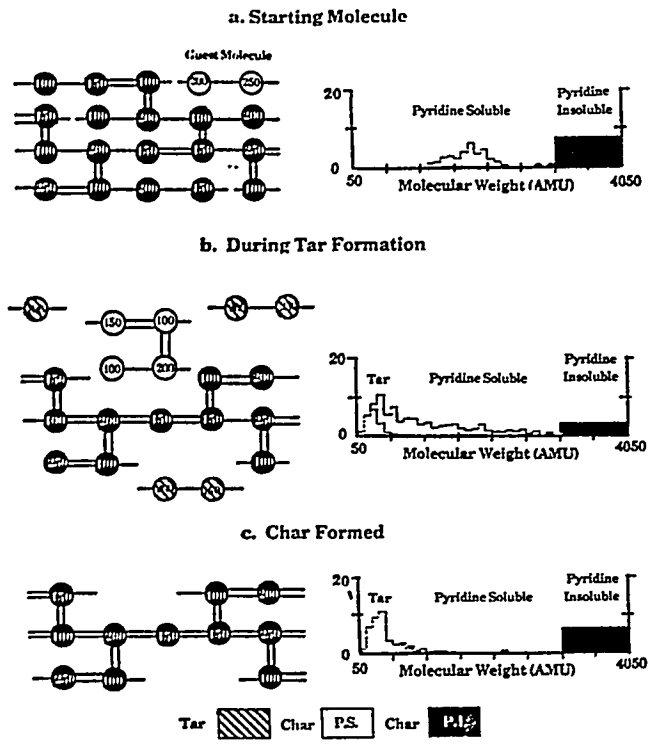

Figure 3. Representation of coal molecule in the DVC simulation and corresponding molecular weight distribution. In the molecule, the circles represent monomers (ring clusters and peripheral groups). The molecular weight shown by the numbers is the molecular weight of the monomer including the attached bridges. The single-line bridges are breakable and can donate hydrogen. The Double-line bridges are unbreakable and do not donate hydrogen. The molecular weight distribution of the coal, tar, and chars are shown as a histogram at the right. The histogram is divided into tar and char with pyridine-soluble and pyridine-insoluble fractions. The area under the histogram corresponds to the weight percent of the oligomers.

principle, determined for each coal for a single pyrolysis experiment. In practice, several experiments are performed. The number of potential cross-link sites, $m(CO_2)$ and $m(CH_4)$, are proportional to the total yield of CO_2 and the total yield of CH_4, respectively. W_B, M_{av}, and σ are determined by using the model to fit selected pyrolysis experiments. The value of W_B is adjustable to fit the tar yield or total volatile yield from one or two selected experiments. In principle, W_B could be measured by FT-IR or NMR but not with sufficient accuracy for this highly sensitive parameter. The values of M_{av} and σ are chosen based on FIMS analysis of the coal. M_{av} can be determined from the average cluster size determined by NMR.[78,79] The value of 256 chosen for both the lignite and bituminous coal is in reasonable agreement with these reported by Solum, et al.,[79] 290 for Zap and 300 for the Pittsburgh Seam coal.

One parameter, ΔP, is adjustable and can vary with each type of experiment. For fluid coals at pressures above one atmosphere, $\Delta P \approx 0$. For low external pressures, less fluid coals, large particles, or high heating rates, $\Delta P > 0$.

There are three dependent parameters that are computed from the other parameters: the weight fraction of peripheral groups, W_p; the donatable hydrogen, H(al); and the number of initial cross-link sites per monomer, m_0.

Functional Group (FG) Model Formulation. The Functional Group (FG) model has been described in a number of publications.[5,6,11-13] It permits the detailed prediction of the composition of volatile species (gas yield, tar yield, and tar functional group and elemental composition) and of char (elemental and functional group composition). It employs coal-independent rates for the decomposition of individual assumed functional groups in the coal and char to produce gas species. The ultimate yields of each gas species are related to the coal's functional group composition. Tar evolution is a parallel process which competes for all the functional groups in the coal. In the original FG model, the potential tar forming fraction of the coal, X^0, was an input parameter that was adjusted for each coal and type of experiment. In the combined FG–DVC model, the DVC subroutine provides this parameter.

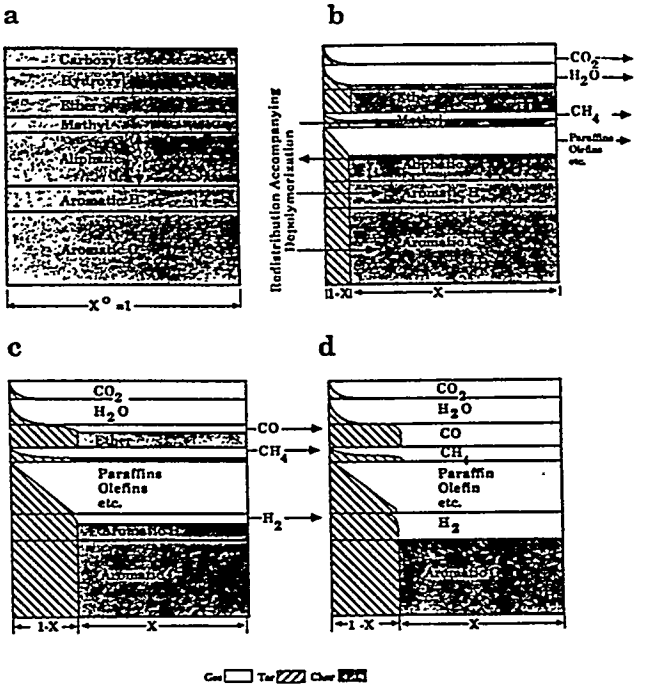

Figure 4. Schematic representation of functional group (FG) model: (a) Initial Coal Composition; (b) composition during tar formation; (c) composition after completion of tar formation; (d) composition after completion of devolatilization.

Schematic Representation of FG Model. The mathematical description of the functional group pyrolysis model has been presented previously.[5,6,11-13] The evolution of tar and light-gas species provides two competing mechanisms for removal of a functional group from the coal: evolution as a part of a tar molecule and evolution as a distinct gas species. This process is shown schematically in Figure 4. To model these two paths, with one path yielding a product that is similar in composition to the parent coal, the coal is represented as a rectangular area with X and Y dimensions. As shown in Figure 4a, the Y dimension is divided into fractions according to the chemical composition of the coal. Y_i^0 represents the initial fraction of a particular component (carboxyl, aromatic hydrogen, etc.), and the sum of the Y_i^0's equal 1. The evolution of each component into the gas (carboxyl into CO_2, aromatic hydrogen into H_2, etc.) is represented by the first-order diminishing of the Y_i dimension, $dY_i/dt = -k_iY_i$.

The X dimension is divided into char, X, and tar, $(1 - X)$; initially $X = 1$. The evolution of the tar is represented by the decreasing of the X dimension, dX/dt, computed in the DVC subroutine as

$$dX/dt = -\sum_j (dn_j/dt)_{tot} M_j$$

(78) Gerstein, B. C.; Murphy, P. D.; Ryan, L. M. *Coal Structure*; Meyers, R. A., Ed.; Academic Press: New York, 1982; Chapter 4.

(79) Solum, M. A.; Pugmire, R. J.; Grant, D. M.; Wolfenden, W. R., submitted for publication in *Energy Fuels*.

Table II. Kinetic Rate Coefficients and Species Composition Parameters for FG Subroutine

composition params	gas	primary functional group source	rate eq[a]	Pittsburgh No. 8 bituminous coal	North Dakota Zap lignite
C				0.821	0.665
H				0.056	0.048
N				0.017	0.011
S(org)				0.024	0.011
O				0.082	0.265
total				1.000	1.000
Y_1^0	CO_2 extra loose	carboxyl	$k_1 = 0.81E+13 \exp(-(22500 \pm 1500)/T)$	0.000	0.065
Y_2^0	CO_2 loose	carboxyl	$k_2 = 0.65E+17 \exp(-(33850 \pm 1500)/T)$	0.007	0.030
Y_3^0	CO_2 tight		$k_3 = 0.11E+16 \exp(-(38315 \pm 2000)/T)$	0.005	0.005
Y_4^0	H_2O loose	hydroxyl	$k_4 = 0.22E+19 \exp(-(30000 \pm 1500)/T)$	0.012	0.062
Y_5^0	H_2O tight	hydroxyl	$k_5 = 0.17E+14 \exp(-(32700 \pm 1500)/T)$	0.012	0.033
Y_6^0	CO ether loose		$k_6 = 0.14E+19 \exp(-(40000 \pm 6000)/T)$	0.050	0.060
Y_7^0	CO ether tight	ether O	$k_7 = 0.15E+16 \exp(-(40500 \pm 1500)/T)$	0.021	0.038
Y_8^0	HCN loose		$k_8 = 0.17E+14 \exp(-(30000 \pm 1500)/T)$	0.009	0.007
Y_9^0	HCN tight		$k_9 = 0.69E+13 \exp(-(42500 \pm 4750)/T)$	0.023	0.013
Y_{10}^0	NH_3		$k_{10} = 0.12E+13 \exp(-(27300 \pm 3000)/T)$	0.000	0.001
Y_{11}^0	CH_x aliphatic	H(al)	$k_{11} = 0.84E+15 \exp(-(30000 \pm 1500)/T)$	0.207	0.102
Y_{12}^0	methane extra loose	methoxy	$k_{12} = 0.84E+15 \exp(-(30000 \pm 1500)/T)$	0.000	0.000
Y_{13}^0	methane loose	methyl	$k_{13} = 0.75E+14 \exp(-(30000 \pm 2000)/T)$	0.020	0.017
Y_{14}^0	methane tight	methyl	$k_{14} = 0.34E+12 \exp(-(30000 \pm 2000)/T)$	0.015	0.009
Y_{15}^0	H aromatic	H(ar)	$k_{15} = 0.10E+15 \exp(-(40500 \pm 6000)/T)$	0.013	0.017
Y_{16}^0	methanol		$k_{16} = 0$	0.000	0.000
Y_{17}^0	CO extra tight	ether O	$k_{17} = 0.20E+14 \exp(-(45500 \pm 1500)/T)$	0.020	0.090
Y_{18}^0	C nonvolatile	C(ar)	$k_{18} = 0$	0.562	0.440
Y_{19}^0	S organic			0.024	0.011
total				1.000	1.000
X^0	tar		$k_B = k_T = 0.86E+15 \exp(-(27700 \pm 1500)/T)$		

[a]The rate equation is of the form $k_n = k_0 \exp(-(E/R \pm \sigma/R)/T)$, with k_0 in s^{-1}, E/R in K, and σ/R in K. σ designates the spread in activation energies in a Gaussian distribution. The notation for k_0 is defined as follows: 0.81E+13 is equivalent to 0.81×10^{13} etc.

The fractional amount of a particular functional group component in the char is

$$W_i(\text{char}) = XY_i$$

and the amounts in the gas and tar may be obtained by integration with respect to time starting from $t = 0$.

Secondary reactions such as further decomposition of aliphatic species to form olefins, acetylene, and soot modify the basic equations. Some of these have been described elsewhere.[6] These types of secondary reactions are not considered in the current paper.

Figure 4a shows the initial state of the coal. Values for Y_i^0 are obtained from elemental analysis and FT-IR analysis of the raw coal or from analysis of the products of one or two selected pyrolysis experiments. Figure 4b shows the initial stage of devolatilization, during which the most volatile components, H_2O, CO (loose), and CO_2 evolve from the hydroxyl, ether-loose, and carboxyl groups, respectively, along with aliphatics and tar. At a later stage (Figure 4c) CO (tight), HCN and H_2 are evolved from the ether-tight, ring nitrogen, and aromatic hydrogen groups. Figure 4d shows the final state of the char, tar, and gas.

The evolution of gas and the composition of the char and tar are then described mathematically as follows.

Process 5. Gas Formation. The evolution of each gas species is assumed to be a first-order reaction

$$dW_i(\text{gas})/dt = k_i W_i(\text{char}) = k_i X Y_i \qquad (5)$$

where, $dW_i(\text{gas})/dt$ is the rate of evolution of speices i into the gas phase, k_i is a distributed rate for species i and W_i(char) is the functional group source remaining in the char. The concept of the distributed rate was introduced by Pitt[80] and subsequently employed by Rennhack[81] and Anthony et al.[22] to describe weight loss. Hanbaba et al.,[82] van Heek et al.,[83] Weimer and Ngan,[9] and Solomon et al.[12] employed distributed rates for individual species. In the FG subroutine, k_i is given by an Arrhenius expression $k_i = k_i^0 \exp(-(E_i \pm \sigma_i)/RT)$, where $\pm\sigma_i$ indicates that a Gaussian distribution is employed to describe the product sources, $W_i(E_i)$, as a function of the activation energies E_i.[5,9,12,22] $W_i(E_i) = (W_i^0/\sigma_i(2\pi)^{1/2}) \exp(-(E_i - E_i^0)^2/2\sigma_i^2)$. E_i^0 is the average activation energy, and σ_i is the width of the Gaussian distribution.

Note that W_i(char) also is decreased by its evolution with the tar.

Process 6. Tar Formation. The tar composition is tracked by summing the functional group contributions evolved with the tar. The rate of evolution of each contribution is

$$dW_i(\text{tar})/dt = -(dX/dt)Y_i \qquad (6)$$

where $dW_i(\text{tar})/dt$ is the rate of evolution of each functional group component with the tar.

Process 7. Char Formation. The change in the ith char pool, W_i(char), is computed by summing the losses to the gas and tar and the redistributions determined in the DVC subroutine

$$dW_i(\text{char})/dt = -dW_i(\text{gas})/dt - dW_i(\text{tar})/dt + dW_i(\text{DVC})/dt \qquad (7)$$

where $dW_i(\text{DVC})/dt$ includes the source and loss terms from the DVC model, given by $(30/28)k_B W_B$, $(2/28)k_B W_B$,

(80) Pitt, G. J. *Fuel* 1962, *41*, 267.

(81) Rennhack, R. *Brennst.-Chem.* 1964, *45*, 300.

(82) Hanbaba, P.; Juntgen, H.; Peters, W. *Brennst.-Chem.* 1968, *49* 368.

(83) Van Heek, K. H.; Juntgen, H.; Peters, W. *Ber. Bunsen-Ges. Phys Chem.* 1967, *71*, 113.

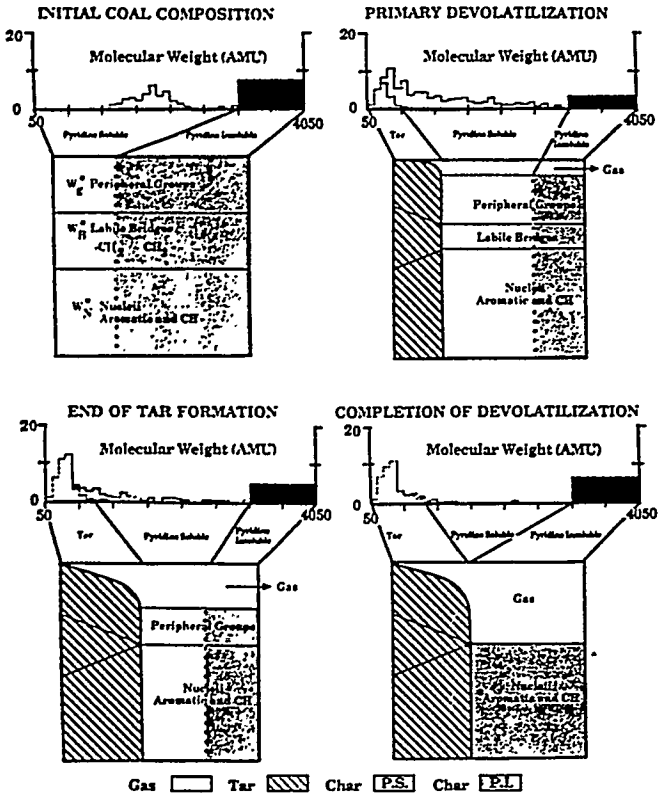

Figure 5. Schematic representation of the FG–DVC model combining the DVC and FG subroutines. The FG subroutine is illustrated for a single gas species only. The area under the histogram corresponds to the weight percent of the oligomers.

$(24/28)k_B W_B$, and $-2k_B W_B$ for methyl, aromatic H, aromatic C, and labile bridge functional groups, respectively.

The general rates and specific composition parameters for Pittsburgh Seam coal and North Dakota lignite are presented in Table II.

Schematic and Execution of FG–DVC Model. Figure 5 presents a schematic of the linked model for a simple case of only one gas species. The combined model connects the upper (DVC portion) and lower (FG portion) parts of Figure 5a–d. The model is initiated by specifying the functional group composition parameters (W_B, W_N, and, in this case, only one gas species parameter, W_p) and the coal structure parameters (starting oligomer length, l, number of added cross-links per monomer, m_0, and the monomer molecular weight distribution parameters, M_{av} and σ). The starting molecular weight distribution of oligomers is presented at the top of Figure 5a. The monomers are assumed to have the average elemental and functional group composition given by the FG parameters. The functional groups are divided into pyridine-soluble and pyridine-insoluble parts. Each computer simulation considers coal to consist of a network made from 2100–2400 monomers.

Once the starting distribution of oligomers in the coal is established, it is then subjected to a time–temperature profile made up of a series of isothermal time steps. Each time step is chosen so the temperature rise in each step does not exceed a fixed maximum. During each step, the gas yields, elemental composition, and functional group composition are computed by using the FG subroutine. The CO_2 and CH_4 yields are used to determine the number of new cross-links to be randomly added to the molecule. The molecular weight distribution, the escape of tar molecules, and the redistribution of hydrogens and carbons from the labile groups is computed with the DVC subroutine. Figure 5b illustrates tar formation simultaneous with gas formation. The labile bridges are either evolved with the tar, converted to methyl groups (and thus added to the peripheral groups), or converted to unbreakable bridges (and thus added to aromatic C and H groups). Tar formation is complete (Figure 5c) when all the labile bridges are consumed. Devolatilization is completed (Figure 5d) when all volatile functional groups (in this case the single gas species represented as peripheral groups) are removed from the char.

The model has been programmed in Fortran 77 and runs on the Sun Microsystems 3/260 and 3/50 computers. Run times on a Sun 3/260 are between 83 and 550 s/simulation for 2100–2400 monomers. A streamlined version of the code designed to run as a subroutine in a comprehensive combustion or gasification reactor simulation employs from 400 to 800 monomers and requires approximately 10 s/simulation for the pyrolysis of a single particle.

Summary of FG Subroutine Assumptions. (a) Light-gas species are formed from the decomposition of specific functional groups with rate coefficients that depend on the functional group but are independent of coal rank. The evolution rate is first order in the remaining functional group concentration in the char. The rates follow an Arrhenius expression with a Gaussian distribution of activation energies.[5,12,22]

(b) Simultaneous with the production of light-gas species is the thermal cleavage of bridge structures in the coal to release molecular fragments of the coal, which consist of a representative sampling of the functional group ensemble. These fragments may be transported out of the coal particle to form tar. The instantaneous tar yield is given by the DVC subroutine.

(c) Under conditions where pyrolysis products remain hot (such as an entrained-flow reactor), pyrolysis of the functional groups in the tar continues at the same rates used for functional groups in the char (e.g., the rate for methane formation from methyl groups in tar is the same as from methyl groups in the char).

Summary of DVC Subroutine Assumptions. (d) The oligomer length, l, the number of cross-links per monomer, m_0, and the fraction of labile bridges, W_B, are parameters of the model, chosen to be consistent with the coal's measured extract yield, cross-link density, and volatile yield in selected calibration experiments.

(e) The molecular weight distribution is adjusted so that the model predictions fit the observed molecular weight distribution for that coal, measured by pyrolysis of the coal (in vacuum at 3 °C/min to 500 °C) in a FIMS apparatus.[60] Molecular weights 106, 156, 206, 256, 306, 356, and 406 (which are aromatic one-ring through seven-ring compounds with two methyl substituents) are considered as representative of typical monomer molecular weights.

(f) During pyrolysis, the breakable bonds are assumed to rupture randomly at a rate $k_B = k_{tar}$, described by an Arrhenius expression with a Gaussian distribution of sources as a function of activation energies. Each rupture creates two free radicals that consume two donatable hydrogens to form two new methyl groups and convert two more donatable hydrogens to two aromatic CH groups. Oxymethylene bridges, which may be important for low-rank coals, have not been modeled although a second class of labile bridges could easily be added.

(g) All the donatable hydrogens are assumed to be located in the labile bridges. Two donatable hydrogens are available at each bridge. The consumption of the donatable hydrogen converts the bridge into an unbreakable bridge by the formation of a double bond. The unbreakable bridges are included in the aromatic hydrogen and

aromatic carbon functional groups.

(h) Tar formation continues until all the donatable hydrogens are consumed.

(i) During pyrolysis, additional unbreakable cross-links are added at a rate determined by the evolution of CH_4 and CO_2. One cross-link is created for each evolved molecule. The rates of CH_4 and CO_2 evolution are given by the FG subroutine.

(j) The cross-links are distributed randomly, with the probability of attachment on any one monomer being proportional to the molecular weight of the monomer.

(k) Tar molecules are assumed to vaporize from the surface of the coal particle (or into bubbles) with a molecular weight and temperature dependence based on the vapor pressure correlation of Suuberg et al.[32] The external-transport model is based on the surface-evaporation model of Unger and Suuberg.[23]

(l) To describe internal transport, a simple empirical expression (eq 4) is used to describe both bubble transport in softening coals and convective transport through pores in nonsoftening coals. The tar is assumed to be transported at its equilibrium vapor pressure in the light-gas species. The pressure increase that drives the transport within the particle, ΔP, is between 0 and 0.2 atm for the bituminous coal and between 0 and 10 atm for the lignite, depending on the experimental conditions.

(m) Extractable material (in boiling pyridine) in the char is assumed to consist of all molecules less than 3000 amu. This limit can be adjusted depending on the solvent and extraction conditions.

(n) The molecular weight between cross-links, M_c, is computed to be the total molecular weight of the computer molecule divided by the total number of cross-links. This assumption will underestimate M_c since broken bridges are not considered.

Results

The model predictions have been compared to the results obtained from a number of experiments on the pyrolysis of a Pittsburgh Seam coal[6,7,16,22] and a North Dakota (Beulah, Zap) lignite.[6,51] The coal composition and kinetic parameters are presented in Tables I and II. It should be noted that different samples of Pittsburgh seam coal from different sources were employed. While the elemental compositions were similar, extract yields varied depending on the sample source. The oligomer length in Table I was chosen to fit an extract yield of 30% for the Pittsburgh Seam coal and 1% for the lignite. Comparisons are considered for gas yields, tar yields, tar molecular weight distributions, extract yields, and volumetric swelling ratios.

Volatile Yields. Extensive comparisons of the FG model with gas yields have been presented previously for high- and low-heating-rate devolatilization experiments.[5,6,11-13] The evolution of gases for the combined model is similar to results of the FG model and will not be repeated here. There is good agreement between the measured and predicted results. The functional group parameters and the kinetic rates used for this work for the Pittsburgh Seam coal and North Dakota (Zap) lignite are principally those determined previously and published in ref 6. The methane parameters for the Pittsburgh Seam coal were, however, adjusted (methane X-L = 0.0, methane-L = 0.02, methane-T = 0.015, unchanged) to better match yields of refs. 5–7 (see Figure 20c in ref 6). Also note that the CH_x– aliphatic rate in ref 6 applies to the observed gas species (paraffins, olefins, C_2H_6, C_2H_4) only. The aliphatic material in the labile bridge part of the aliphatic groups is assumed to be made up of bridges that volatilize only when attached to a tar molecule (i.e., $k_i = 0$). Also,

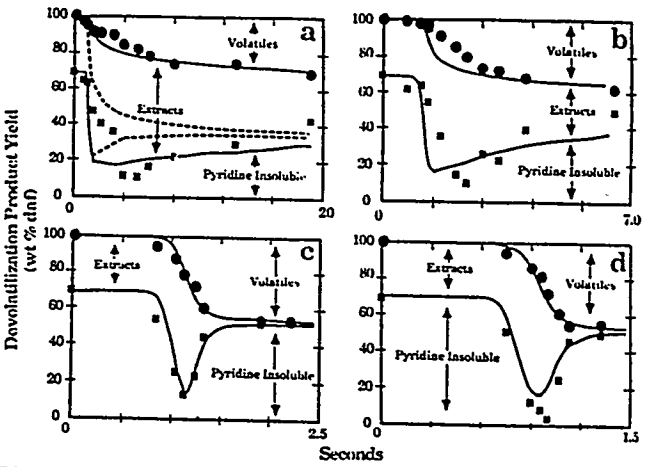

Figure 6. Comparison of FG–DVC model predictions with the data of Fong et al.[16] (symbols) for Pittsburgh Seam coal: (a) 813 K at 470 K/s; (b) 858 K at 446 K/s; (c) 992 K at 514 K/s; (d) 1018 K at 640 K/s. P = 0.85 atm. The solid line assumes transport by eq 4 (ΔP = 0 atm) and no external transport. The dashed line in part a shows the predicted yield assuming $\mathcal{K}^s_j = \mathcal{K}^b_j$ in eq 3 and no internal-transport limitations.

the rate for CO_2(loose) has been adjusted to improve the predictions of the change in tar molecular weight distributions and yield with heating rate. The predictions of gas yield due to this change have not been changed noticeably. The predicted values of X^0 from the DVC subroutine vary with heating rate and final temperature and are in good agreement with the values of X^0 used in the original FG model.

Extract Yields. Figure 6 compares the FG–DVC predictions to the data of Fong et al.[16] on total volatile yield and extract yield as a function of temperature in pyrolysis at 0.85 atm. The experiments were performed in a heated-grid apparatus at heating rates of approximately 500 °C/s, with variable holding times and rapid cooldown. The predictions at the two higher temperatures (Figures 6c,d) are in excellent agreement with the data.

The initial predictions for the two lower temperature cases, which neglected interal-transport limitations, were not good. The dashed line in Figure 6a shows the predicted yield in the absence of internal transport limitations (i.e., $(dn_i/dt)_{IT} = 0$ and with $\mathcal{K}^s_j = \mathcal{K}^b_j$ in eq 3). The predicted ultimate yield is clearly too high. The data suggest that the low yields are not a result of unbroken bonds (which would result from a lower bond breaking rate, k_B), since the extract yields at low temperatures are equivalent to those at the higher temperatures. The coal molecule thus appears to be well decomposed, the low yields resulting from poor transport out of the coal. This suggested an additional transport limitation in getting molecules to the surface, so $\mathcal{K}^s_j = \mathcal{K}^b_j$ appears to be a bad assumption.

Equation 4 was employed for the internal-transport rate, and surface evaporation by eq 3 was assumed to be unimportant ($\mathcal{K}^s_j = 0$). Then, W_B had to be slightly readjusted from 0.096 in ref 50 to 0.094 to match the 1018 K case. This new value of W_B was used for subsequent cases. The predictions with this assumption are the solid lines in Figure 6. The internal-transport limitation is most important when pyrolysis occurs at low temperatures and $\sum_{light} dn_i/dt$ in eq 4 is small.

There still is a discrepancy between the prediction and the data at early times for the two lower temperature cases (Figure 6a,b). While it is possible that the rate k_b for bond breaking is too high, adjustment of this rate alone would significantly lower the extractable yield, since the lower depolymerization rate is closer to the methane cross-linking

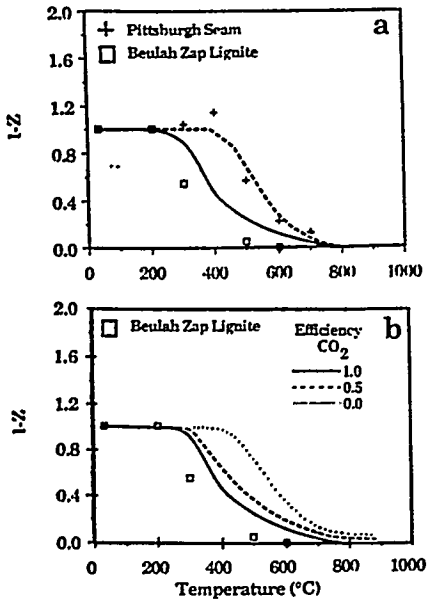

Figure 7. (a) Comparison of measured and predicted normalized volumetric swelling ratio as a function of temperature. The solid line is the prediction of Beulah lignite; the dashed line is for Pittsburgh Seam coal. The cross-link efficiency of CO_2 is 1.0. (b) Effect of cross-link efficiency of CO_2 on the normalized volumetric swelling ratio profile with temperature. For parts a and b the heating rate is 0.5 °C/s. $\Delta P = 0$ atm.

rate. In addition, both the methane and depolymerization rates appear to be in good agreement with the data at even lower temperatures.[6] Another possibility is that the coal particles heat more slowly than the nominal temperatures given by Fong et al.[16] Such an effect could be caused by having some clumps of particle that would heat more slowly than isolated particles, by reduction in the convective heat transfer due to the volatile evolution (blowing effect) or by endothermic tar forming reactions. A firm conclusion as to the source of this remaining discrepancy cannot be drawn without further investigation.

It is also seen in Figure 6a,b that the cross-linking rate is higher than predicted. This can be due to other crosslinking events not considered. These possibilities are currently under investigation.

Cross-Link Density. To examine the effect of coal rank on cross-linking, the volumetric swelling ratios (VSR) for North Dakota (Beulah, Zap) lignite and Pittsburgh Seam bituminous coal were measured as a function of temperature at 0.5 °C/s. The VSR can be related to the cross-link density.[77] The swelling data are plotted in Figure 7a as $1 - Z$, where Z is the change in VSR between coal and char normalized by the maximum change. For coal, Z is 0 and for completely cross-linked char, Z is 1. While the weight loss profiles of the two samples look similar at 0.5 °C/s, the swelling behaviors in Figure 7a are quite different. The Pittsburgh Seam coal starts to cross-link during tar evolution, and the Beulah lignite cross-links well before tar evolution. Similar results have been reported by Suuberg et al.,[59] who also suggested a correlation between cross-linking in lignites and CO_2 evolution. The coals that undergo early cross-linking are less fluid, produce less tar, and produce lower molecular weight tar compared with coals that do not experience early cross-linking.[30,31,44]

As discussed previously, under the assumption that the cross-linking reactions may also release gas species, the VSR was correlated with the observed evolution of gas species during pyrolysis. Correlations presented in Figure 2 show that on a molar basis, the evolution of CO_2 from the lignite and CH_4 from the bituminous coal appear to have similar effects on the VSR. Reactions that form these gases, leave behind free radicals that can be stabilized by cross-linking.

Assuming that one cross-link is formed for each CO_2 or CH_4 evolved from the char, the FG–DVC model predictions are presented as the lines in Figures 2 and 7a. The agreement between theory and experiment is good except that the increase in $1 - Z$ for the Pittsburgh Seam coal in Figure 7a is not predicted. This may be related to the restrictions of assumption n (see summary of DVC subroutine assumptions). The predictions in Figure 2a are different from those originally presented in ref 50. In ref 50, the value used for VSR_{min} was not appropriate for the fully cross-linked molecule. This error has now been corrected.

In Figure 7b, the effect of varying the CO_2 cross-linking efficiency is considered. The figure shows cases calculated for the lignite assuming 0, 0.5, and 1.0 cross-links are formed per CO_2 evolved. Varying this assumption has a major effect on the early cross-linking of the lignite. Assuming that the cross-linking efficiency per CO_2 is 1.0 gives the best agreement with the data.

The difference in crosslinking behavior between the two coals is manifested in several areas. At low heating rates, the Pittsburgh Seam chars soften; the Beulah, Zap chars do not. This is in agreement with the high predicted maximum extract yields in the Pittsburgh char (70%) compared to the low extract yields in the Beulah, Zap lignite (7%). The measured values are 71%[16] and ~6%, respectively. The predicted yield of tar plus aliphatic gases at 1 atm, 0.5 °C/s to 900 °C, of 26% is in good agreement with the measured value of 28% for the Pittsburgh Seam coal. The predicted value of 11% (for $\Delta P = 10$ atm) is in good agreement with the measured value of 10% for the Beulah, Zap lignite.

Molecular Weight Distribution. A sensitive test of the general model is the ability to predict the tar molecular weight distribution and its variations with rank, pressure, and heating rate. The input to the model is the distribution of monomer molecular weights. The tar, which consists of oligomers, has a different distribution from the monomer distribution and is controlled by the relative effects of bond breaking, cross-linking, and transport. The tar molecular weight distribution is not highly sensitive to the choice of M_{av} and σ. For Pittsburgh Seam coal, the average monomer was assumed to be a three-ring compound ($M_{av} = 256$) and a fairly broad distribution ($\sigma = 250$) was chosen. The same values appeared to work for the lignite. These are in reasonable agreement with the measured values of ~300 reported by Solum et al.[79] for both coals.

Figure 8c,d show results for the Pittsburgh Seam bituminous coal and the Beulah, Zap lignite pyrolyzed in the FIMS apparatus. The data have been summed over 50 amu intervals. While the Pittsburgh bituminous coal shows a peak intensity at about 400 amu, the lignite peak is at 100 amu. The predicted average tar molecular weight distributions are in good agreement with FIMS data as shown in Figure 8a,b. Since both tar distributions are from the same monomer distribution, the enhanced drop off in amplitude with increased molecular weight for the lignite compared to the bituminous coal must be due to early cross-linking and transport effects in the lignite.

Pressure Effects. The predicted effect of pressure on the tar molecular weight distribution is illustrated in Figure 9a,b. Pressure enters the model through the transport eq 3 and 4. The internal-transport rate (eq 4), which is assumed to dominate, is inversely proportional to the am-

Table III. Comparison of Measured and Predicted Yields for Pittsburgh Seam Bituminous Coal (ΔP = 0 atm)

experiment	heating rate, °C/s	P_0, atm	final temp, °C	max yield of tar + aliphatic gases, %		total max volatiles, wt %	
				measd	predicted	measd	predicted
TG-FTIR	0.5	1.0	600	25	29	35	37
entrained flow	5000	1.0	700	36	37	43	43
heated grid	640	0.85	745		40	47	47

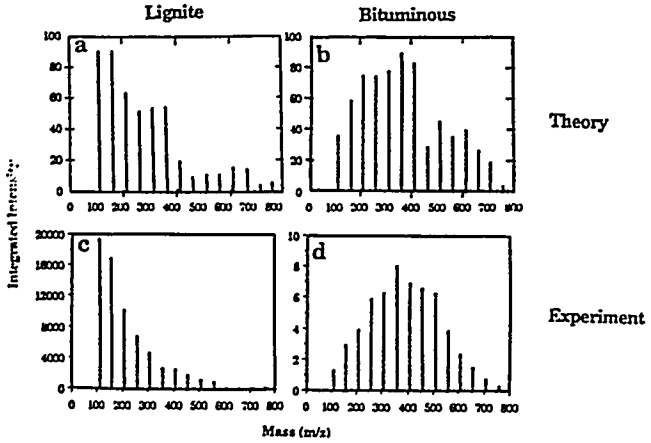

Figure 8. Comparison of measured and predicted tar molecular weight distributions for lignite and bituminous coals. The experiments are performed by pyrolysis of coal samples in a FIMS apparatus. Intensities have been summed over 50 amu intervals. For part a ΔP = 10 atm, and for part b ΔP = 0.0 atm.

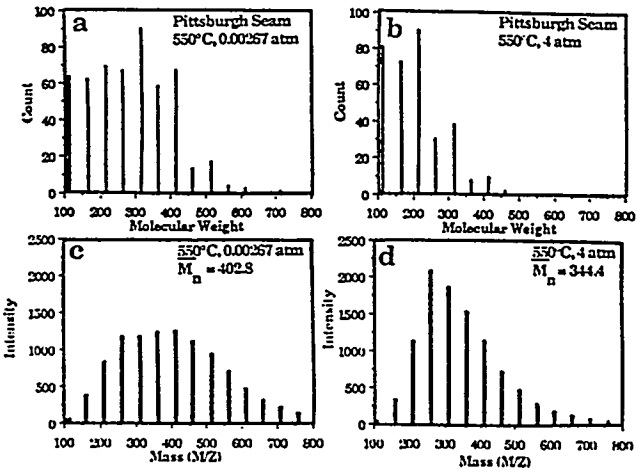

Figure 9. Comparison of predicted (a and b) and measured (c and d) tar molecular weight distribution for pyrolysis of a Pittsburgh Seam coal in a heat-grid apparatus at a heating rate of 500 °C/s to 550 °C. Parts a and c compare the prediction and the measurement at 0.00267 atm. Parts b and d compare the prediction and measurement at 4.0 atm. ΔP = 0.2 atm.

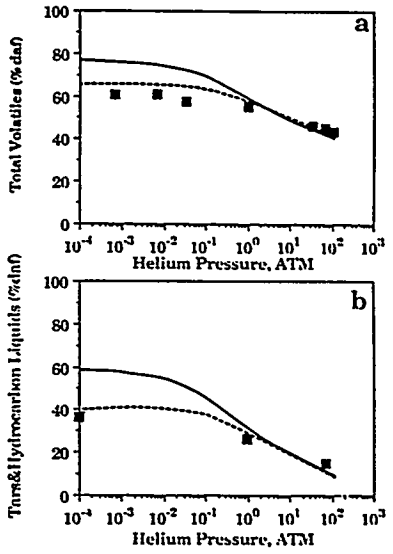

Figure 10. Comparison of measured and predicted volatile yield for a Pittsburgh Seam bituminous coal; (a) total volatiles, data of Anthony et al.;[22] (b) tars and hydrocarbon liquids, data of Suuberg et al.[7] The solid line assumes ΔP = 0 atm; the dashed line assumes ΔP = 0.2 atm.

bient pressure P_0. The reduced transport rate reduces the evolution rate of the heavier molecules. Therefore, the average molecular weight and vaporization "cutoff" decrease with increasing pressure. The trends are in agreement with observed tar molecular weight distributions shown in Figure 9c,d. The spectra are for previously formed tar that has been collected and analyzed in a FIMS apparatus.[60] The low values of intensity between 100 and 200 mass units are believed to be due to loss of these components due to their higher volatility.

Pressure effects on yields have also been examined. Figure 10 compares the predicted and measured pressure dependence on yield for a Pittsburgh Seam coal. Figure 10a compares the prediction to the total volatile yield data of Anthony et al.[22] while Figure 10b compares the prediction to the tar plus liquids data of Suuberg et al.[7] The agreement between theory and experiment is good at 1 atm and above, but the theory with ΔP = 0 (solid line) overpredicts the yields at low pressure. Below 1 atm, it is expected that ΔP within the particle will become important compared to the ambient pressure, P_0. The dashed lines, which agree with the data, were obtained by assuming ΔP = 0.2 atm, which is physically reasonable.

Heating-Rate Effects. It is well-known that the heating rate can affect the amount of volatiles produced.[29,76,84-86] Heating rate can also affect the melting and swelling behavior of low-rank coals.[13] Considering the mechanisms proposed for pyrolysis (including those in this paper), it is the relative rates of competing processes for tar formation (e.g., bond breaking, cross-linking, and mass transport) that provide the heating-rate effects. The relative rates of these processes change with temperature, and it is the heating rate that determines the temperature at which the controlling reactions occur. So it is really the temperature of tar formation and not the heating rate per se which is important.

Consider first the effects of heating rate on the yields of a Pittsburgh Seam bituminous coal. Table III summarizes the results for three experiments[16,87,88] in which the heating rate varied from 0.5 to 5000 °C/s and in which the final temperature reached is sufficiently high for tar

(84) Gibbins-Matham, J.; Kandiyoti, R. *Prepr. Pap.—Am. Chem. Soc., Div. Fuel Chem.* 1987, *32*(4), 318.
(85) Freihaut, J. D.; Seery, D. J. *Prepr. Pap.—Am. Chem. Soc., Div. Fuel Chem.* 1983, *28*(4), 265.
(86) Serio, M. A.; Peters, W. A.; Sawada, K.; Howard, J. B. *Prepr. Pap.—Am. Chem. Soc., Div. Fuel Chem.* 1984, *29*(2), 65.
(87) Serio, M. A.; Solomon, P. R.; Carangelo, R. M. *Prepr. Pap.—Am. Chem. Soc., Div. Fuel Chem.* 1988, *33*(2), 295.
(88) Solomon, P. R.; Hamblen, D. G.; Serio, M. A.; Smoot, L. D.; Brewster, S. "Measurement and Modeling of Advanced Coal Conversion"; First Annual Report for U.S. METC Contract No. DE-AC21-86MC23075, 1987.

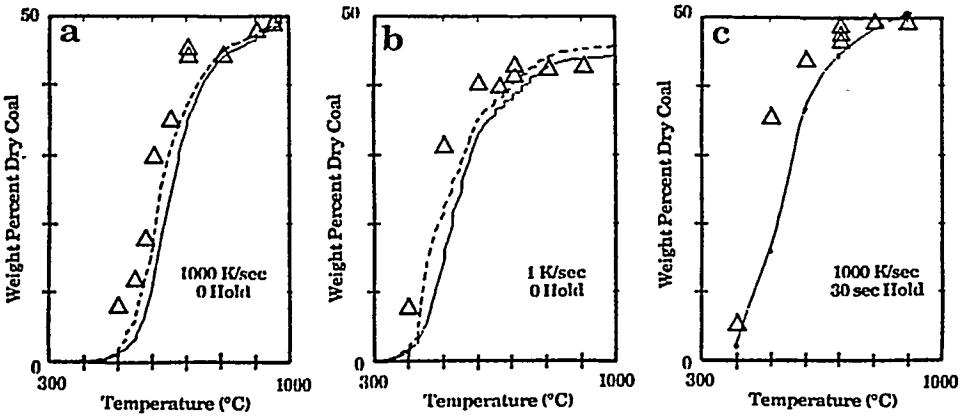

Figure 11. Comparison of FG-DVC model predictions with the data of Gibbins-Matham and Kandiyoti[83] (symbols) for Pittsburgh Seam coal: (a) 1000 K/s, zero hold; (b) 1 K/s, zero hold; (c) 1000 K/s, 30-s hold. $P = 1.18$ atm. Transport is by eq 4 ($\Delta P = 0$) and no external-transport limitation. The dashed line assumes no transport limitations for molecules whose vapor pressure exceeds $P_0 + \Delta P$.

formation to be completed during the heating period. As can be seen, the predicted and measured volatile yields increased by about 10% from low to high heating rates. As can also be seen, the increase in yield results from the increase in tar plus aliphatic gases. Examination of the rates in the model shows that the major contribution to the variation in yield is the internal-transport rate relative to the bond-breaking rate. At low temperatures, internal transport severely limits the evolution of the heavier molecules, resulting in smaller tar molecules and inefficient use of the donatable hydrogens.

A set of data showing the effect of heating rate on yield for the Argonne Pittsburgh Seam coal was recently reported by Gibbins-Matham and Kandiyoti.[84] Data were obtained in a wire-grid apparatus at 1 and 1000 °C/s with no holding time and at 1000 °C/s with a 30-s hold. These data (triangles) are compared to predictions of the model in Figure 11. For all three cases, the theory predicts the correct pyrolysis final yields, the correct yield variation with heating rate, and the correct temperature shift with heating rate.

The predicted yields, however, occur at temperatures from 20 to 80 °C higher than the comparable experimental yields. At this time, the reason for the discrepancy is not clear. One possible reason is the assumptions used for the internal transport limitations. Calculations were made assuming that molecules for which $P_j \geq P_0 + \Delta P$ evolve as they are produced, while only heavier molecules evolve as described in eq 4. The predicted curves (dashed lines in Figure 11) are 20–40 °C lower than in the original calculation. Alternatively, the vapor pressure may not be accurately described by the expression of Suuberg et al.[32] Oh[38] compared a number of correlations for the tar vapor pressure. At 1000 °C, the expression of Suuberg et al.[32] gave vapor pressures from 1–2 orders of magnitude lower than other published expression.[89,90] Calculations using the expression for aliphatic molecules of Maiorella[89] gave predictions at about 40 °C lower temperatures, in better agreement with the data of Gibbons-Matham and Kandiyoti. The simulation, however, required a lower value of W_B (0.060) to compensate for the higher volatility. Predictions using the same assumptions failed to match those of Fong et al.[16] in Figure 6 with regard to the temperature of evolution and the amount of extract produced. Possible refinements of the internal-transport model are being considered.

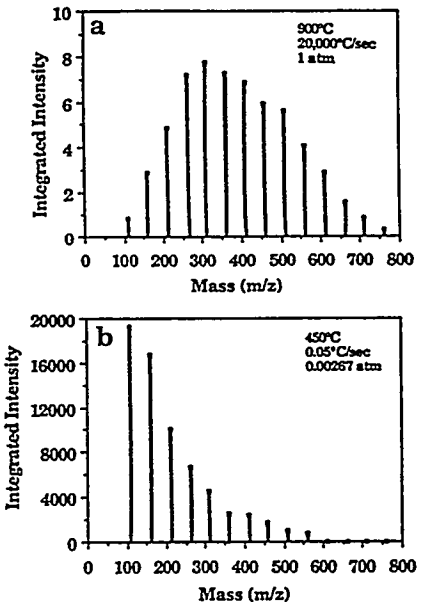

Figure 12. Comparison of FIMS spectra of tars of Beulah Zap lignite formed at (a) high heating rate (20000 °C/s) and (b) low heating rate (0.05 °C/s).

Another possible explanation for the discrepancy is the accuracy of the reported pyrolysis temperature, which has been notoriously variable among investigators. Other Pittsburgh Seam coal data (not shown) for Niksa et al.[40] under the same conditions as Figure 11c (1000 °C/s, 30-s hold) and from Oh[38] and Suuberg et al.[7] for the same conditions as Figure 11a (1000 °C/s, zero hold) show substantial variations in temperature compared to the results of Gibbons-Matham and Kandiyoti.[84] The theoretical predictions would lie within the scatter of the several data sets. Work is in progress to resolve this question.

Low-rank coals also exhibit heating-rates effects. It has been found that Beulah lignite chars soften and exhibit bubble formation at high heating rates (~20000 °C/s).[13] Under these conditions, molecular weight distribution of tars of Beulah lignite look like that of a bituminous coal.[30,31] The infrared spectrum of the tar is also closer in appearance to that of the parent coal.[31] The mass spectra of the tars formed at high heating rate (20000 °C/s) and low heating rate (0.05 °C/s) are shown in parts a and b of Figure 12, respectively. The low values of intensity between 100 and 200 mass units in Figure 12b are believed

(89) Maiorella, B. L. B.S. Thesis, Department of Chemical Engineering, MIT, Cambridge, MA, 1975.
(90) Grey, J. A.; Brady, A. J.; Cunningham, J. R.; Freeman, J. R.; Wilson, G. M. *Ind. Eng. Chem. Process Des. Dev.* 1983, *22*, 410.

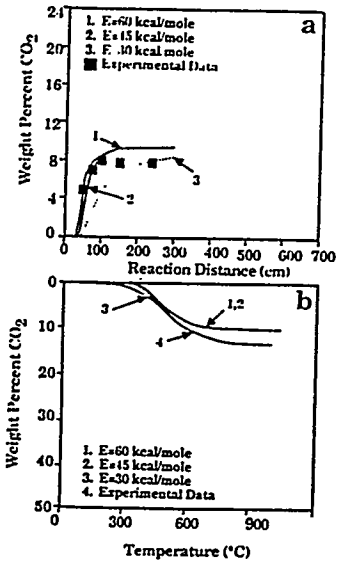

Figure 13. Comparison of CO_2 evolution data from North Dakota lignite for low-heating-rate (0.5 °C/s) and high-heating-rate (20000 °C/s) experiments with model predictions for different values of activation energy for CO_2 (extra loose) in the FG–DVC Model: (a) heated-tube-reactor experiments;[6] (b) TG-FTIR experiments.[6]

to be due to loss of these components due to their high volatility. The molecular weight distribution of the tars is very sensitive to the heating rate. The effect is attributed to the higher rate of depolymerization reactions relative to cross-linking reactions at high temperatures, as discussed in the sensitivity section.

The FG–DVC model, assuming the internal-mass-transport limitations, was used to simulate the low heating rate (0.05 °C/s) and high heating rate (20000 °C/s) pyrolysis of Beulah lignite. The activation energy for CO_2 (extra loose) in the FG subroutine was reduced from 60 to 45 kcal/mol in order to make it lower than the activation energy for bond breaking (55 kcal/mol). This was done since measurements of the rate of cross-linking at high heating rates suggested that the relative rate of bond-breaking and cross-linking reactions associated with CO_2 evolution is increased with increasing temperature.[91] This change in the activation energy makes only a slight change in the CO_2 evolution profiles for high-heating-rate (20000 °C/s) and low-heating rate (0.5 °C/s) predictions. The CO_2 gas evolution profiles are compared to the data in Figure 13a,b for high-heating-rate (20000 °C/s) and low-heating-rate (0.5 °C/s) experiments with Beulah lignite using activation energies of 60, 45, and 30 kcal/mol. When the activation energy for CO_2 (extra loose) evolution was reduced to 45 kcal/mol, acceptable fits to the gas evolution data were still obtained. However, at 30 kcal/mol, the high-heating-rate CO_2 evolution profile was quite different and did not agree with the experimental data.

The model, with internal-mass-transport limitations included, was used to simulate the tar molecular weight distributions with $\Delta P = 0$ atm for Beulah lignite for high heating rate (20000 °C/s) in Figure 14a,b. The simulations were done for both the original activation energy (60 kcal/mol) and altered activation energy (45 kcal/mol) for CO_2 (extra loose) evolution. The tar molecular weight distributions (for $\Delta P = 0$ atm) at high heating rates (Figure 14a,b) show the observed high values of the tar molecular weight at high heating rate (Figure 12a). The lower activation energy case (Figure 14a) exhibits more high molecular weight molecules and gives a higher tar yield (10%)

(91) Deshpande, G. V.; Solomon, P. R.; Serio, M. A. *Prepr. Pap.—Am. Chem. Soc., Div. Fuel Chem.* 1988, *33*(2), 310.

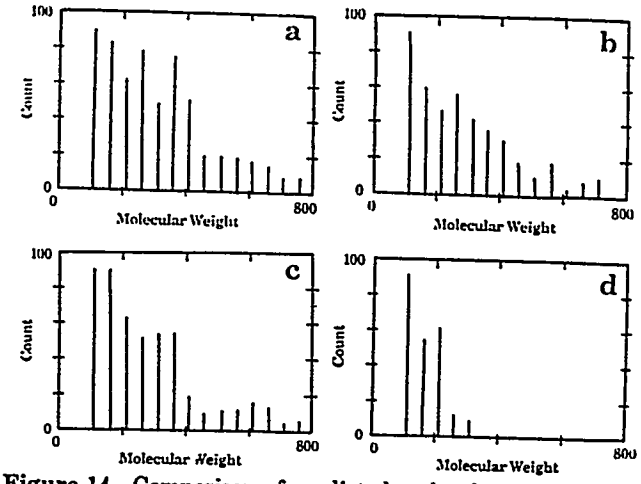

Figure 14. Comparison of predicted molecular weight distribution of tars of Beulah lignite for (a and b) high heating rate (20000 °C/s) and (c and d) low heating rate (0.05 °C/s). In parts a, c, and d the CO_2 activation energy is 45 kcal/mol and in part b it is 60 kcal/mol. In parts a–c $\Delta P = 0$ atm, and in part d $\Delta P = 10$ atm.

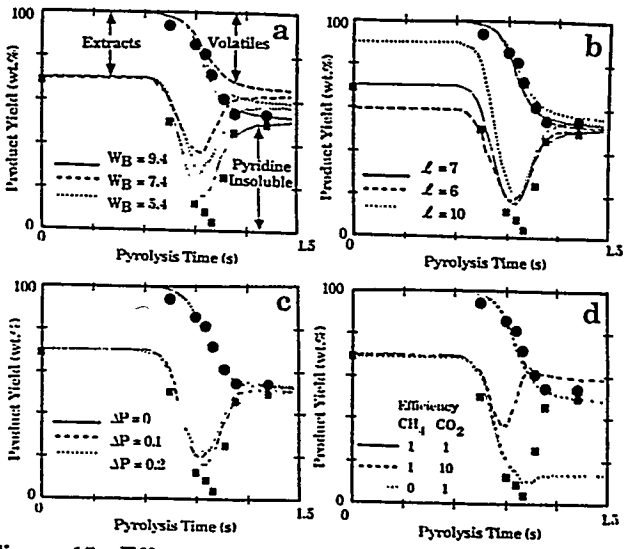

Figure 15. Effect on product yields of (a) fraction of labile bridges, W_B, (b) oligomer length, l, (c) internal pressure difference, ΔP, and (d) cross-linking efficiency. Data were taken from Fong et al.[16] for Pittsburgh Seam bituminous coal (1018 K at 640 K/s, $P = 0.85$ atm); $\Delta P = 0$ atm.

than the high activation energy case (8%) (Figure 14b). The low-heating-rate (0.05 °C/s) case ($\Delta P = 0$) (Figure 14c) exhibits lower molecular weights consistent with Figure 12b. At high heating rates, where cross-linking reactions are curbed and the lignite melts, ΔP is likely to be low. At low heating rate, due to the higher extent of cross-linking before tar evolution, the coal is less fluid, and hence ΔP (which is related to viscosity of the solid/liquid mixture) is likely to be higher. A simulation for the slow-heating-rate case with $\Delta P = 10$ atm is shown in Figure 14d. The measured molecular weight distribution in Figure 12b appears to be intermediate between the $\Delta P = 0$ and $\Delta P = 10$ atm cases.

Sensitivity Analysis. This section considers the sensitivity of the FG–DVC model to variations in the DVC parameters. The FG parameter sensitivities have been considered elsewhere.[52]

(a) Variations in W_B. The number of labile bridges is the most important parameter in determining tar yield. The value of W_B for the Pittsburgh Seam coal was reduced from its value of 9.4 to 7.4 and 5.4. The results in Figure 15a were calculated for the case considered in Figure 6d.

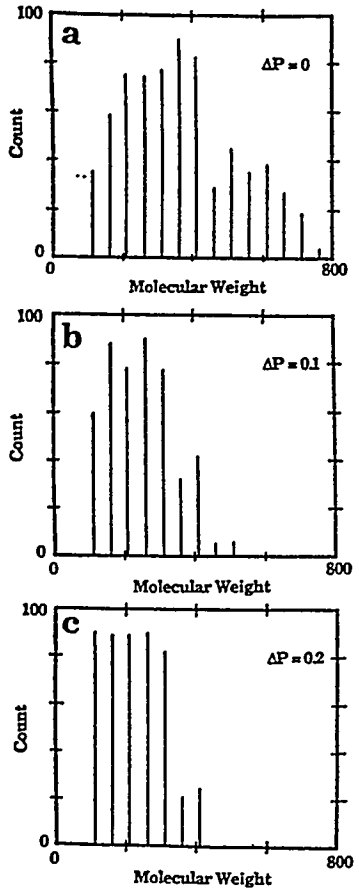

Figure 16. Effect of ΔP on tar molecular weight distribution for Pittsburgh Seam bituminous coal heated to 723 K at 0.05 K/s. $P = 0.00267$ atm.

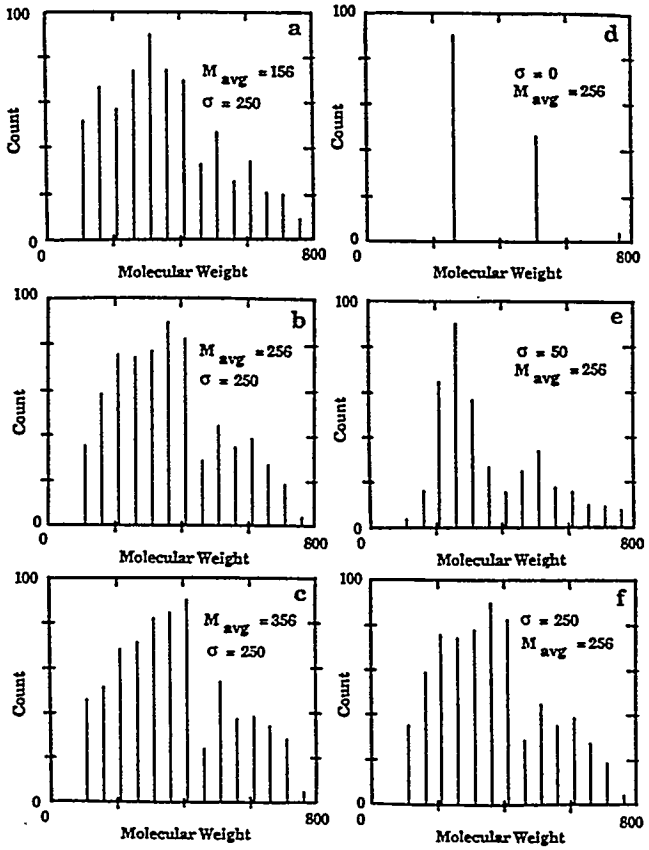

Figure 17. (a–c) Effect of M_{av} on the shape of the tar spectrum and (d–f) effect of σ on the shape of the tar spectrum. The heating rate is 0.05 °C/s to 450 °C, $P = 0.00267$ atm, and $\Delta P = 0$ atm.

The reduction in W_B reduces the tar yield, the total volatile yield, and the extract yield. Higher values of W_B could not be considered because the molecule already contained the maximum number of labile bridges. This is a limitation in the model as it is currently formulated since all the donatable hydrogens are assumed to be in bridges.

(b) Variations in l. The parameter l affects mainly the extract yield in the raw coal. Figure 15b demonstrates variations in l from 6 to 10 around the base value of 7. The initial extract yield varies substantially while there is only a minor effect on the tar yield, total volatile yield, and extract yield at elevated temperature.

(c) Variations in ΔP. The effect of variations in ΔP on the overall yield are considered in Figure 10. There is no effect at 1 atm pressure and above but a strong effect at lower ambient pressures. Figure 15c confirms that ΔP has little effect on the tar yield or the total volatile yield for pyrolysis at 1 atm pressure. Only the extract yield is slightly affected.

Figure 16 illustrates the effect on the molecular weight distribution for three values of ΔP for pyrolysis in vacuum ($P_0 \simeq 0$). The yield of higher molecular weight tars present for $\Delta P = 0$ is lower for $\Delta P = 0.1$ atm and eliminated for $\Delta P = 0.2$ atm. The total tar yields are 39%, 21%, and 17% for $\Delta P = 0$, 0.1, and 0.2 atm respectively. The tar molecular weight distribution for $\Delta P = 0$ atm gives the best match to Figure 9c, but $\Delta P = 0.1$–0.2 atm provides the best match to the yield.

The variation of ΔP in the tar molecular weight distribution for lignite is discussed with reference to Figure 13.

(d) Variations in $m(CO_2)$ and $m(CH_4)$. Variations in $m(CO_2)$ were considered for the lignite in the discussion accompanying Figure 7. Variations in both $m(CO_2)$ and $m(CH_4)$ are considered in Figure 15d. These have a major effect on the yields. Increasing $m(CO_2)$ from 1 to 10 reduces the extract and volatile yields while reducing $m(CH_4)$ from 1 to 0 prevents the repolymerization of the extract.

(e) Variations in M_c. Variations in the M_c values were made. These chiefly affect the extract yield, requiring an adjustment in l. They have little effect on the subsequent cross-linking in the coal. The reason for this can be seen in Table I. The initial value of M_c consistent with the literature required only 0.09 and 0.18 cross-link/monomer for the bituminous coal and lignite, respectively. The total number of cross-links added during pyrolysis are 0.49 and 0.89, respectively. The added number of cross-links is thus much larger than that in the raw coal and, consequently, dominates the char's behavior.

(f) Variations in M_{av} and σ. Figure 17a–c illustrates the effects of variations in M_{av}. Varying M_{av} changes the shape of the tar spectrum, but not drastically. The shape is still dominated by the transport properties (e.g., see Figure 16). The effect on the tar yield is also modest, giving values of 45%, 44%, and 42% for M_{av} values of 156, 256, and 356, respectively.

A similar lack of sensitivity of the molecular weight distribution to M_{av} was exhibited for the lignite for both high-heating-rate (~20 000 °C/s) and low-heating-rate (0.05 °C/s) cases (not shown).

The effect of variations in σ is illustrated in Figure 17d–f. $\sigma = 250$ fills in the spectrum in a more realistic fashion and is more aesthetically pleasing than the two smaller values of σ. The effect on the total tar yield is minor with yields of 41%, 46%, and 45% for $\sigma = 0$, 50, and 250, respectively.

(g) Variations in W_N. This parameter, which is taken from the FG model, controls the split between tar, char, and gas.

Table IV. Summary of Sensitivity Analysis[a]

	W_N	W_B	l	M_c	$m(CO_2)$	$m(CH_4)$	M_{av}	σ	ΔP
tar molecular weight	W	W	W	W	S	W	M	M	S
tar yield	S	S	W	W	S	M	W	W	S
char extract yield	W	S	W	W	S	S	W	W	M
coal extract yield	W	W	S	M	W	W	W	W	W
char solvent-swelling ratio	W	W	W	S	S	S	W	W	W
coal solvent-swelling ratio	W	W	W	W	W	W	W	W	W

[a] Key: W = weak or none; M = moderate; S = strong.

(h) Vaporization Law. The results are sensitive to the choice of the tar vapor pressure correlation. Higher vapor pressures result in faster tar evolution and higher yields as discussed in reference to Figure 11.

A summary of the sensitivity analysis is presented in Table IV. The concentration of labile bridges W_B and the CO_2 cross-linking parameter $m(CO_2)$ are the most important parameters in determining yields.

Conclusions

A general FG–DVC model for coal devolatilization, which combines a functional group model for gas evolution and a statistical model for tar formation, has been presented. The tar formation model includes depolymerization, cross-linking, external transport and internal transport. The cross-linking is related to the evolutions of CO_2 and CH_4, with one cross-link formed per molecule evolved. The predictions of the tar formation model are made by using Monte Carlo calculation methods. Predictions take between 10 s and 10 min (depending on coal rank, experimental conditions, and accuracy required) on a Sun 3/260 computer.

The FG–DVC model predictions compare favorably with a variety of data for the devolatilization of Pittsburgh Seam coal and North Dakota (Beulah) lignite, including volatile yields, extract yields, cross-link densities, and tar molecular weight distributions. The variations with pressure, devolatilization temperature, rank, and heating rate were accurately predicted. Comparison of the model with several sets of data employing alternative assumptions on transport suggests assuming that the particle is well mixed (i.e. the surface concentration of tar molecules is the same as the bulk) overpredicts the transport rate. For 50-μm particles, assuming that the internal-transport limitation dominates (i.e. neglecting the external transport) provides a good fit to the data. This is consistent with assuming (a) that the internal- and external-transport mechanisms act in series or (b) that they act in parallel but liquid-phase diffusion of tar molecules to the surface is very small and so the external transport term can be neglected.

The rank dependence of tar formation, extract yields, cross-linking, and viscosity appears to be explained by the rank dependence of CO_2 yields. The high CO_2 yields in low-rank coals produce rapid cross-linking at low temperatures and hence low tar yields, low extract yields, loss of solvent-swelling properties, and high viscosities. The relative importance of cross-linking compared to bond breaking is, however, sensitive to heating rate, and this effect is predicted by the FG–DVC model. The predicted cross-linking associated with methane evolution appears to match the observed cross-linking in high-rank coals (which evolve little CO_2).

The model has eight coal structure parameters that must be determined for each coal from selected laboratory experiments. Once determined, these remain fixed for all experiments. The model also contains one adjustable parameter, ΔP, the internal pressure difference that drives the volatiles out of the particle. A sensitivity analysis shows that the volatile yield is most sensitive to the fraction of labile bridges, W_B, the cross-linking parameters $m(CO_2)$ and $m(CH_4)$, and, in some cases (low-rank coals, low pressure), to ΔP. The monomer molecular weight distribution parameters, M_{av} and σ, have only a weak effect on yields and tar molecular weight distributions. The initial molecular weight between cross-links, M_c, and the initial oligomer length, l, affect the coal's solvent-swelling ratio and extract yield but have little effect on the subsequent pyrolysis behavior.

The model currently has several deficiencies. There is no model for estimating liquid-phase diffusion of tar molecules, which may be important for very small particles. The calculation of the average molecular weight between cross-links neglects the effect of labile bridge rupture. The assumption that all the donatable hydrogen is in bridges may be restrictive for some high hydrogen coals. The model presented here has neglected polymethylene in coal and the effect of other types of weak bonds besides ethylene bridges. There are some discrepancies between the predictions and reported temperatures of pyrolysis experiments. It is unclear at this time whether this is due to errors in the reported temperatures or in the transport predictions. Many of these deficiencies require only minor modifications to the model and are currently being addressed.

Acknowledgment. This work was supported under DOE Contracts DE-AC21-85MC22050, DE-AC21-84MC21004, DE-AC21-86MC23075, and DE-FG22-85PC80910. We express our thanks to Professor Eric Suuberg for many helpful discussions on transport properties and to Dr. Zhen Zhong Yu for assistance with the model calculations.

APPENDIX G

A CHARACTERIZATION METHOD AND MODEL FOR PREDICTING COAL CONVERSION BEHAVIOUR

A characterization method and model for predicting coal conversion behaviour

Peter R. Solomon, David G. Hamblen, Michael A. Serio, Zhen-Zhong Yu and Sylvie Charpenay

Advanced Fuel Research Inc., 87 Church Street, East Hartford, CT 06108, USA

(Received 15 April 1991; revised 1 April 1992)

This paper considers the development of a predictive macromolecular network decomposition model for coal conversion which is based on a variety of modern analytical techniques for coal characterization. Six concepts which are the foundation of the functional group–depolymerization–vaporization–cross-linking (FG–DVC) model are considered: (1) The decomposition of functional group sources in the coal yields the light gas species in thermal decomposition. The amount and evolution kinetics can be measured by t.g.–FT–i.r., the functional group changes by FT–i.r. and n.m.r. (2) The decomposition of a macromolecular network yields tar and metaplast. The amount and kinetics of the tar evolution can be measured by t.g.–FT–i.r. and the molecular weight by f.i.m.s. The kinetics of metaplast formation and destruction can be determined by solvent extraction, by Gieseler plastometer measurements and by proton magnetic resonance thermal analysis (p.m.r.t.a.). (3) The molecular weight distribution of the metaplast depends on the network coordination number (average number of attachments on aromatic ring clusters). The coordination number can be determined by solvent swelling and n.m.r. (4) The network decomposition is controlled by bridge breaking. The number of bridges broken is limited by the available donatable hydrogen. (5) The network solidification is controlled by cross-linking. The changing cross-link density can be measured by solvent swelling and n.m.r. Cross-linking appears to occur with evolution of both CO_2 (before bridge breaking) and CH_4 (after bridge breaking). Thus low-rank coals (which evolve much CO_2) cross-link before bridge breaking and are thus thermosetting. High-volatile bituminous coals (which form little CO_2) undergo significant bridge breaking before cross-linking and become highly fluid. Weathering, which increases the CO_2 yield, causes increased cross-linking and lowers fluidity. (6) The evolution of tar is controlled by mass transport in which the tar molecules evaporate into the light gas or tar species and are carried out of the coal at rates proportional to their vapour pressure and the volume of light species. High pressures reduce the volume of light species and hence reduce the yield of heavy molecules with low vapour pressures. These changes can be studied with f.i.m.s. The paper describes how the coal kinetic and composition parameters are obtained by t.g.–FT–i.r., solvent swelling, solvent extraction and Gieseler plastometer data. The model is compared with a variety of experimental data in which heating rate, temperature and pressure are all varied. There is good agreement with theory for most of the data available from the authors' laboratory and in the literature.

(Keywords: characterization; coal; conversion)

The question addressed by this paper is: can coal science be predictive? More specifically, is it possible to accurately predict the way a coal behaves in a coal conversion process, given coal characteristics which can be measured in the laboratory. For example, *Figure 1* illustrates the behaviour of coal in combustion. The left-hand side shows a picture of a coal burning in a reactor after injection into the centre of a hot air stream. The processes that occur are illustrated on the right-hand side: the heating of the coal, softening, devolatilization, swelling, the ignition of the volatiles, the formation of soot, the burning of the volatiles, the ignition of the char, the combustion of the char, and finally the fragmentation of the char which determines the ultimate distribution of the ash particles. Can one qualitatively predict pyrolysis yields, swelling, soot formation, char reactivity, etc.?

As a second example, consider coal in a liquefaction process. The important step is the fragmentation of the coal macromolecule into small pieces. As shown in *Figure 2*, that fragmentation takes place very quickly for a bituminous coal. The coal dissolves into the solvent, and the subsequent reactions between the solvent and the coal are all liquid–liquid phase interactions, which can occur very rapidly. In a lignite, this fragmentation process is prevented by low-temperature cross-linking. Thus for a lignite there is no quick solubilization of the coal, and most of the reaction takes place between the solvent and a solid cross-linked residue. Can one predict macromolecular fragmentation and cross-linking?

The research conducted during the last 10 years suggests that many of the steps discussed above can be accurately predicted. The concept used in the authors' laboratory is to employ a set of characterization procedures to determine the kinetic and composition parameters for a general predictive model. Five experiments define these parameters. The most important is t.g.–FT–i.r., thermogravimetry (t.g.) with analysis of the evolved product by Fourier transform infrared (FT i.r.) spectroscopy[1]. This allows determination of

0016-2361 93 04 0469-20

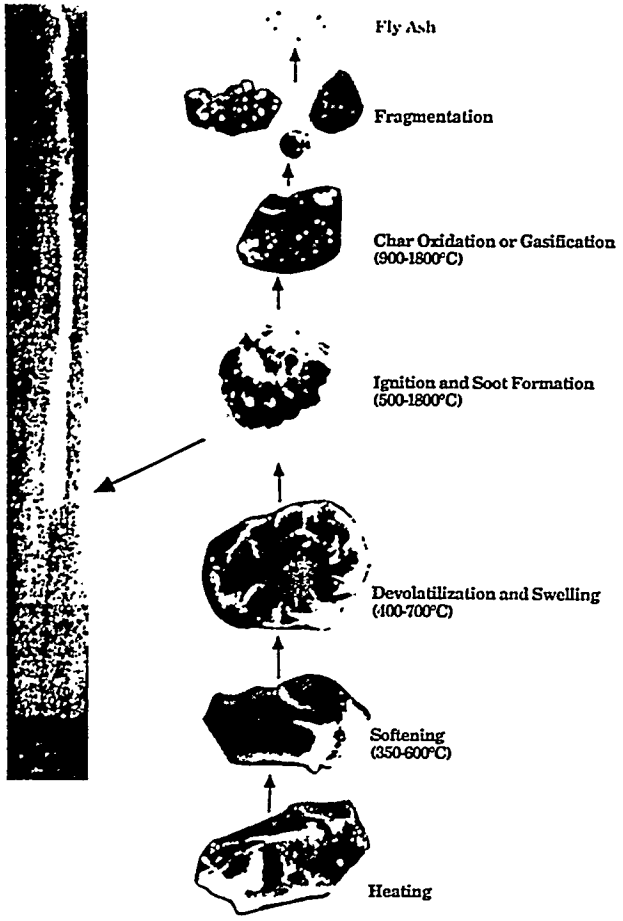

Figure 1 Processes in coal combustion

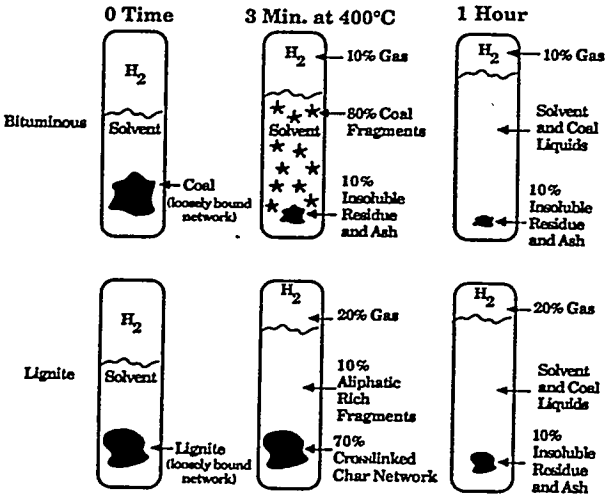

Figure 2 Processes in coal liquefaction

the amount of volatiles, their composition, the kinetics of their evolution, the reactivity of the char, and also the moisture and ash contents of the coal. Also measured are the solvent swelling ratio[2,3], the extract yield, and the fluidity in a Gieseler plastometer[4], to which are added nuclear magnetic resonance (n.m.r.)[5] and field ionization mass spectrometry (f.i.m.s.) data[6]. These experiments determine the macromolecular network parameters for the model.

The model is called FG–DVC[7,8]. The letters FG stand for functional group, and DVC for depolymerization, vaporization and cross-linking. The FG model considers certain functional groups in the coal which lead to the formation of the light gas species[9–12]. At the same time, the DVC model describes the overall depolymerization of the macromolecular network which combines bridge breaking and cross-linking to produce fragments of the coal macromolecule[13–15]. These fragments are then subjected to transport behaviour, specifically the vaporization of the lightest fragments to form tar. The fragmentation process provides a second mechanism for the removal of functional groups from the coal. The model, whose parameters are determined in the laboratory at moderate temperatures and atmospheric pressure, can then be used to extrapolate from the laboratory conditions to predict pyrolysis and combustion in high-temperature reactions, or liquefaction at high pressure. Recently, extrapolation of the kinetics and reactions to low-temperature geological transformations in coal beds has been explored[16].

The model for coal thermal decomposition has six basic concepts:

- functional groups (decompose to produce light gases)
- macromolecular network (decomposes to produce tar and metaplast)
- network coordination number (determines fragment molecular weight distribution)
- bridge breaking (limited by hydrogen availability)
- cross-linking (related to gas evolution)
- mass transport of tar (evaporation of network fragments into light gases and tars).

The first concept is that light gases are formed by the decomposition of certain functional groups in the coal. For example, methyl groups can detach and pick up a hydrogen to form methane, carboxyl groups can lead to the formation of CO_2, etc.[9–12,17–20]. The second concept is that coal consists of a macromolecular network[2,3,7,13–15,21–36]. This network is made up of fused aromatic ring clusters (which are described by their molecular weight) linked by bridges, some of which are relatively weak. There are some unattached parts of the network which can be extracted. Sometimes there is also a second polymethylene component[37–41]. When heated, this network decomposes to produce smaller fragments. The lightest of the fragments evaporate to produce tar[7,42], and the heavier fragments form the metaplast. These heavier molecules are the primary liquid fragments in liquefaction or the fragments that make coal fluid[8,43].

The third concept is that one of the most important properties of the network is its coordination number. The coordination number describes the geometry of the network by specifying how many possible attachments there are per aromatic ring cluster[31–36]. For example, a linear polymer chain has a coordination number of 2, because each fused aromatic ring has two possible attachments to link it in the chain. On the other hand, a 'fishnet' has a coordination number of 4, because there are four possible attachments at each ring cluster. The coordination number controls the molecular weight distribution of the network fragments at a given extent of decomposition. The extent of decomposition is specified by the probability that the possible attachments

exist. For example, for 20% of broken bridges, a linear chain is totally fragmented, while a 'fishnet' will have some holes but is almost totally connected. In describing the network, a cross-link site is defined to occur at a ring cluster where there are more than two possible attachments. The coordination number is thus related to the density of cross-link sites. With no possible cross-links between chains, the coordination number is 2. With increasing density of cross-link sites, the coordination number increases.

The other important property of the network is the fraction of possible attachments that actually exist. During thermal decomposition, this fraction is determined by the rates of bridge breaking and cross-linking[7,15,44–47]. The factors which control how many of the bridges can break are the rate constant and the amount of hydrogen that can be donated from the coal to stabilize the free radicals that form when the bridges break[10].

A competitive process with the bridge breaking is the retrogressive process of cross-linking. Cross-linking reactions appear to be related to the evolution of certain gases[7,15,44,47]. Specifically, for low-rank coals, cross-linking at low temperature (before bridge breaking) seems to be related to the evolution of carbon dioxide (or possibly water). For coals of all ranks, a higher-temperature cross-linking event (following bridge breaking) seems to be related to the evolution of methane. At high temperatures, the evolution of hydrogen is also related to cross-linking in the form of aromatic ring condensation reactions.

The final concept is that the tar evolution is controlled by mass transport. Bridge breaking and cross-linking produce fragments with a molecular weight distribution. The lightest fragments can leave the coal melt by evaporation into the light gas and tar species[7,42]. The heavier fragments remain, forming the metaplast, which controls the coal's fluidity.

The remainder of the paper describes how these concepts are incorporated into a practical predictive model. The next section considers the FG–DVC model in detail. It discusses each of the six concepts and the evidence for each assumption. The following two sections consider the experiments used to obtain the model parameters and compare predictions of the model with a variety of experimental data. A summary and conclusions complete the paper.

COAL PYROLYSIS MODEL

Functional group decomposition model

Figure 3 illustrates the phenomena in coal thermal decomposition considered in the functional group model. The diagrams are not meant to describe the exact structure of coal or the exact chemistry of pyrolysis, but rather to illustrate the kinds of structure considered and the classes of phenomena that can occur. The important processes are the decomposition or detachment of the individual functional groups to form the light gases and the competitive decomposition of the macromolecular network to form fragments, the lightest of which can evaporate as tar.

Figure 3a shows a representative part of a Pittsburgh Seam coal macromolecule. The structure is based on measurements of the aromatic ring cluster size, the functional group composition and the elemental composition[48]. The molecule consists of several fused

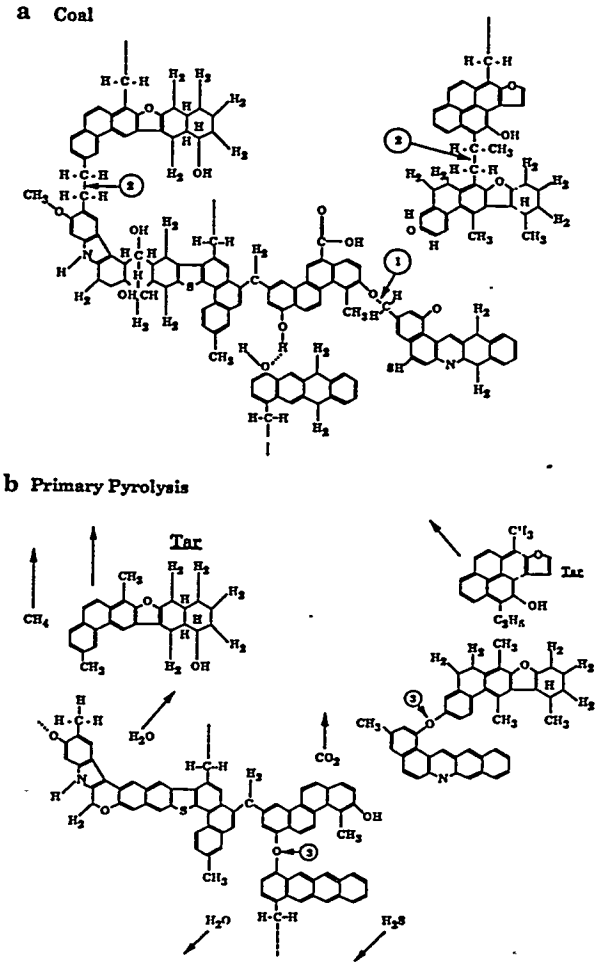

Figure 3 Hypothetical model of Pittsburgh seam coal: (a) original coal; (b) during pyrolysis. From ref. 12

aromatic ring clusters linked by labile bridges. The ring clusters have various functional groups attached to them. When the coal is heated, two things happen to the functional groups. The first is that certain functional groups can detach to form light gases. The second is that fragmentation of the network, and removal of light fragments as tar, can cause the same type of functional group to be removed as part of the tar. So there are two parallel processes for the volatilization of the functional groups.

The way the coal behaves during pyrolysis is illustrated in *Figure 3b*. The carbon–carbon aliphatic bridge in the upper left-hand corner of the molecule (labelled 2 in *Figure 3a*) has broken and picked up hydrogen to form two methyl groups. The hydrogen is assumed to come from hydroaromatic or aliphatic portions of the coal. For example, the hydroaromatic ring in the lower right-hand portion of the coal molecule of *Figure 3a* has lost two hydrogens to become an aromatic ring in *Figure 3b*. This process creates a fragment which is light enough to evolve as tar. There is also independent detachment of functional groups to form light gases. The carboxyl group in the middle of *Figure 3a* is shown as carbon dioxide evolving in *Figure 3b*. Methyl groups have detached to form methane, there has been a condensation of hydroxyl groups to form water and an ether link (labelled 3), mercaptans detach to form H_2S, etc.

The evidence for this description is as follows. (1) For bituminous coals and low-rank coals heated rapidly, the tar is strikingly similar in elemental and functional group composition to the parent coal[9,10,48–50]. The tar appears to consist of representative fragments of the parent coal macromolecule. In contradiction to this result, however, is the observation that tar produced from low-rank coals at low heating rates appears to be significantly different in composition from the coal[51] and is probably dominated by polymethylenes. (2) There is a correlation between the decrease in the functional group sources in the char and the evolution of specific gases[9–12]. (3) There is a systematic variation in functional group composition with rank, and this variation is correlated with the evolved gas composition.

Macromolecular network decomposition model

The concept of a macromolecular network decomposition model is illustrated in *Figure 4*, which recently appeared in a paper by Grant and co-workers[36]. The figure represents aromatic ring clusters with four possible attachments to their neighbours, arranged in a 'fishnet' type of network (a network with a coordination number of 4). *Figure 4a* illustrates what happens when 20% of the possible attachments are broken. As can be seen, only three fragments are created, shown by the clusters with boxes around them. The breaking of 20% of the bridges produces very little fragmentation of the network. On the other hand, consider (*Figure 4b*) what happens when 45% of the bridges are broken. Now there is a much higher concentration of fragments and the fragments have a molecular weight distribution from monomers up to heptamers (consisting of seven fused ring clusters linked together). The lightest of these fragments – monomers, dimers, and trimers – can evaporate into the light gas species and are removed from the coal particles as tar.

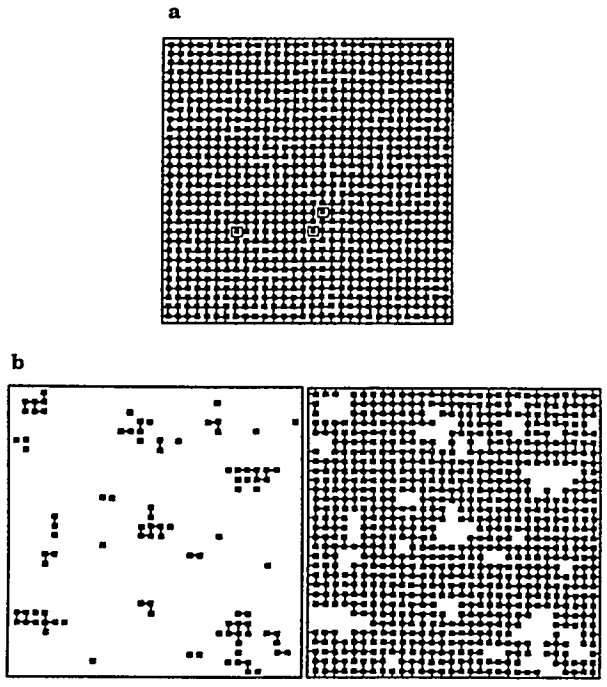

Figure 4 Macromolecular network decomposition model using Monte Carlo calculations for coordination number of 4: (a) 20% broken bridges; (b) 45% broken bridges (from ref. 36)

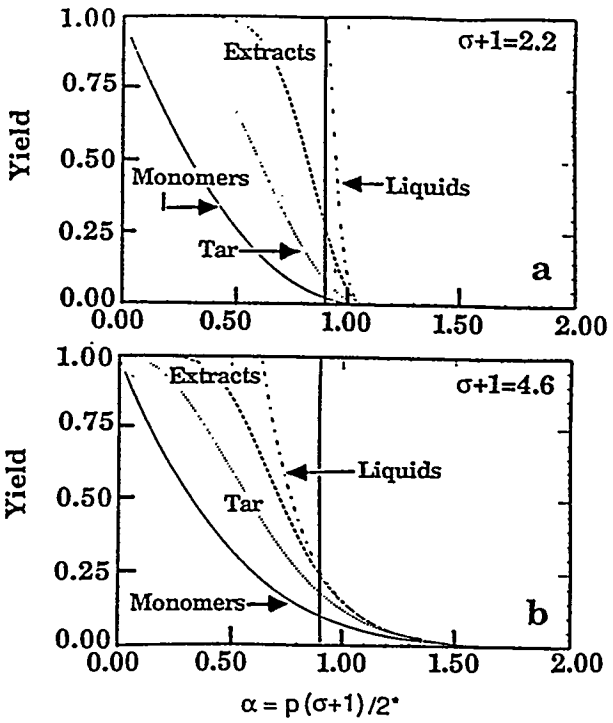

Figure 5 Percolation theory predictions for pyrolysis products for coordination numbers of 2.2 and 4.6

The heavier fragments make up the metaplast. The lightest of these can be extracted using a solvent, while others are too heavy to be extracted. The presence of a sufficiently large fraction of these fragments is what makes these materials fluid.

Network coordination number

The importance of the network coordination number is illustrated in *Figures 4* and *5*. In *Figure 4a* with 20% of the bridges broken in a 'fishnet', only a small number of fragments are produced, and they are all monomers. On the other hand, if 20% of the bridges in the linear chain are broken, 100% of the material becomes fragments and there will be many dimers, trimers, etc. Thus the molecular weight distribution of the fragments depends very strongly on the coordination number.

In *Figure 4*, the molecular distribution was computed using Monte Carlo calculations in which a representative network is set up in computer memory and the fragment molecular weight distribution is calculated after the broken bridges are randomly distributed. Alternatively, a technique called percolation theory allows a closed-form analytical solution of the molecular weight distribution as a function of the number of actual attachments per ring cluster.

Figure 5 shows percolation theory calculations for networks with two different coordination numbers: (a) 2.2 and (b) 4.6. The variable σ is one less than the coordination number. The figure shows the calculated yield distributions of: (1) monomers; (2) up to trimers (i.e. monomer, dimer, trimer) representative of what might be evolved as tar for a ring cluster size of 300 daltons; (3) n-mers up to 10, representative of extractable material; and (4) all n-mers, representative of liquids. These are plotted as a function of α, which is the average number of bridges per fused aromatic ring, and is equal

to the probability p that a bridge is occupied multiplied by the coordination number of the network divided by 2: $\alpha = p(\sigma + 1)/2$. As can be seen, there is a very different distribution of fragments, depending on the coordination number. For example, at $\alpha = 0.9$, the network with coordination number 4.6 has most of the fragments in the tar, with only a small number of n-mers between 3 and 10 and almost no n-mers above 10. On the other hand, for a network with a coordination number of 2.2 at $\alpha = 0.9$, there is a smaller number of monomers and a somewhat smaller concentration of tar, but a much higher concentration of n-mers up to 10, and a 100% yield of all n-mers. In other words, for 0.9 bridges per cluster, most of the molecules have decomposed to produce fragments of one size or another.

The DVC model was originally implemented using a Monte Carlo solution method, which allows an arbitrary network geometry. Percolation theory, however, offers significant benefits in computational speed and reproducibility, at the cost of restricting the network geometries.

As will be seen below, in the Monte Carlo version of the model, the starting network is represented by linear chains of monomers (6–12 aromatic clusters) with some cross-linking which ties the chains together. Thus the starting network has a coordination number between 2 (straight chains) and ≥ 3 (fully cross-linked). As pyrolysis proceeds, the linear chain bridges are broken, and cross-links are formed. Thus the coordination number, or degree of branching, increases with extent of pyrolysis. The conventional percolation theory models of coal decomposition do not model this feature. With conventional percolation theory, one can make any identification of the various chemical bonds with the percolation lattice bonds, so that the probability of a bond being occupied tracks the chemistry, but the occupied bonds must be randomly distributed within the lattice. The structure cannot be converted from 'chain-like' to 'fishnet-like'.

The DVC model predicts, and experiments confirm, that there are different kinds of bonds (bridges and cross-links), which have different coordination numbers, and independent probabilities of being broken. To take advantage of the benefits of percolation theory, percolation theory on a Bethe lattice (one with no loops) has been extended to use two independent sub-networks, as illustrated in *Figure 6*[32]. In the figure, double lines represent one of the bond types, while single lines represent the other. As can be seen by comparing *Figures 6a* and *6b*, this lattice has the desired feature of modelling a transition from chain-like structures (a) to fishnet structures (b). The mathematics of this '2-σ' percolation theory follows closely that of the standard theory[32]. The results obtained from the '2-σ' percolation theory agree well with those obtained from the original Monte Carlo calculations, as will be discussed under Comparison of theory and experiment.

Bridge breaking and hydrogen utilization

There are two questions with respect to bridge breaking: what is the bridge breaking rate, and how many bridges break? Pyrolysis rates have been reviewed by a number of authors[10,52–54]. One of the problems over the last two decades is the very wide variation in the reported rates for either weight loss or tar evolution in pyrolysis.

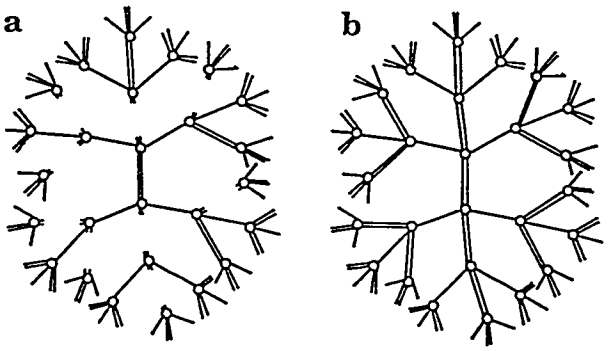

Figure 6 Bethe lattice for two-σ model with $\sigma_1 = \sigma_2 = 1$ (shown as single bonds): (a) with most double bonds representing the crosslinks not yet formed to represent the starting coal, the lattice is like a one-σ model with $\sigma = 1$, linear chains; (b) fully linked case ($p = q = 1$) is like a one-σ model with $\sigma = 3$

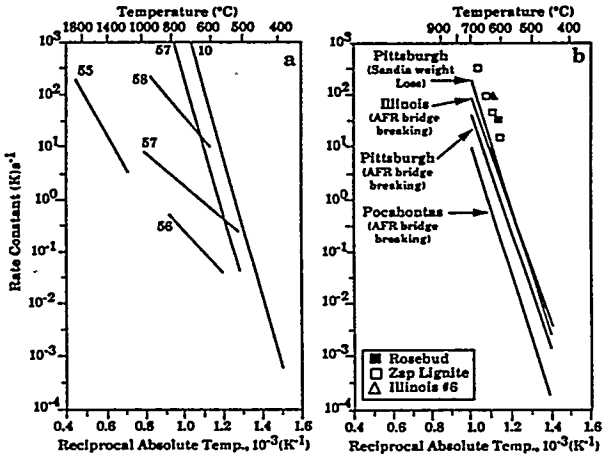

Figure 7 Kinetic rate constants for weight loss or bridge breaking: (a) extremes of published rates from experiments in which particle temperatures were not directly measured; (b) more recent rates from experiments in which particle temperatures were measured

Figure 7a presents several of the extremes in rates reported before 1985 for high-heating-rate experiments[10,55–58]. At 800°C there is a variation of almost four orders of magnitude in the reported rate constants. An analysis of the data shows that this sort of variation in kinetics cannot be attributed to variations in coal type, because investigators who tested more than one coal type found that the variation in kinetic rates among coals is typically within a factor of 10. So there has to be another explanation for such a wide variety of reported rates. The answer appears to lie in the estimation of the coal particle temperature[53,54,59–62]. Almost none of the experiments involved direct measurement of the particle temperature. For entrained-flow reactor experiments, the temperature is usually calculated, and the calculation depends critically on the rate of mixing of the preheated gases with the coal stream. An error by a factor of 2 in the heating rate can lead to errors of hundreds of degrees celsius in the estimate of particle temperature during pyrolysis. For heated-grid experiments, temperature is measured with a thermocouple and it is inferred that the thermocouple temperature is the same as the coal particle temperature. Recent reviews of experiments for Pittsburgh Seam coal heated at 1000 K s^{-1} show a wide variation

in pyrolysis temperatures, suggesting that this is not a good assumption[60,63].

Since 1985, several experiments have been performed in which coal particle temperatures were measured during pyrolysis[12,53,61,62,64]. Careful experiments have also been performed at several low heating rates where the thermocouple temperature is a good measure of the coal particle temperature[65,66]. As can be seen from *Figure 7b*, the data are much more tightly grouped. There is a systematic variation with coal rank and the kinetic rate constants appear to have an activation energy between 190 and 230 kJ mol^{-1}. This is the magnitude expected for the kind of labile bridges depicted in *Figure 3*[14,67].

Besides the kinetic rate for bridge breaking, one needs to know the number of bridges that can be broken. The number depends on the amount of hydrogen that is available to stabilize the free radicals formed when bridges break. To understand why the hydrogen utilization controls the amount of tar and its hydrogen concentration, consider the following example. Assume that every time a bridge is broken, two hydrogens are used to stabilize the free radicals, and that two radicals are assumed to be stabilized per tar molecule. If the tar is made up of large fragments, the utilization of hydrogen per unit weight of tar is very efficient. On the other hand, if the tar consists of small molecules, the utilization of hydrogen is much less efficient. A sample calculation was made for 0.3 wt% hydrogen in the coal available for donation to the tar. For an average molecular weight of 100 u (atomic mass units, or daltons), 15 wt% tar is produced. The amount of additional hydrogen in the tar is 2 wt%. On the other hand, at an average molecular weight of 300 u the yield is up to 45 wt%, while the additional hydrogen per unit mass is only 0.7 wt%. The average molecular weight of the tar is affected by cross-linking, pressure, heating rate and bed geometry.

Cross-linking

During pyrolysis, another important process occurs besides bridge breaking. This is cross-linking, in which new bonds are formed between the fused aromatic ring clusters. One way of measuring the cross-link density is through solvent swelling[2,3], in which a solvent (e.g. pyridine) is used to swell the char or coal[7,15,44–47]. To understand how solvent swelling indicates the cross-link density, consider the analogy of an air mattress, which is stitched in long rows along its length. When the mattress is inflated there are several connected small tubes instead of one big round tube. The small tubes have a smaller volume than one large tube and the volume can be used to infer the limiting circumference of the tubes. In a similar manner, the addition of the solvent to a coal indicates the circumference of linked molecules that make a loop to limit the swelling. Since it is cross-links (more than two attachments per cluster) that allow loops to be formed, the amount of swelling indicates the average molecular weight between cross-links.

Figure 8 shows the solvent swelling ratio as a function of the char temperature for coals of several ranks. Chars were produced by heating to the indicated temperatures at 30 K min^{-1} in an inert atmosphere and then cooling. These chars were subjected to solvent swelling experiments to determine the ratio of the volume of swollen material to the unswollen volume. Coals have solvent swelling ratios as high as 2.7. As char is formed,

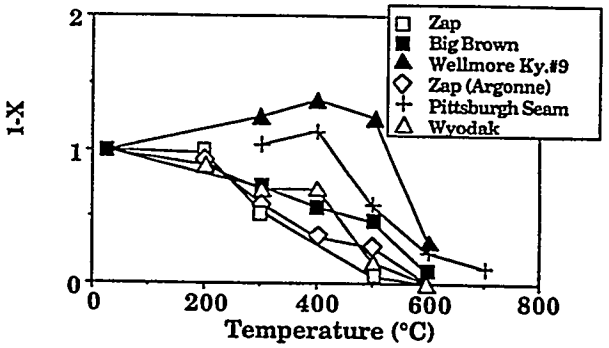

Figure 8 Solvent swelling ratios for coals of different rank at a series of final pyrolysis temperatures; heating rate 30 K min^{-1}. From ref. 47

new cross-links reduce the swelling ratio to unity. The solvent swelling ratio in *Figure 8* is normalized: the parameter X is the difference in solvent swelling ratio between the coal and the char, divided by the maximum difference that can be achieved. This normalization allows different coals with different initial solvent swelling ratios to be compared conveniently. If $X = 0$, the material swells the same as coal; if $X = 1$, it is fully cross-linked.

There is a wide variation in behaviour, depending on rank. This rank-dependence of the cross-linking behaviour was first noted by Suuberg *et al.*[44], who tested a lignite and a bituminous coal and found the same sort of difference as shown here. For the lowest-rank coal, Zap lignite, at temperatures as low as 200°C the char starts to undergo cross-linking, losing most of its solvent swelling properties by 400°C. However, it is between 400 and 500°C that most of the weight loss occurs. Thus for a low-rank coal, the cross-linking occurs well in advance of bridge breaking.

For higher-rank coals, the cross-linking event is delayed relative to bridge breaking. For a highly softening bituminous coal (e.g. Pittsburgh Seam, or Kentucky No. 9) the material swells even more as it is heated into the region of pyrolysis, and loses its solvent swelling properties only after most of the weight loss has occurred. There is thus a very strong rank-dependence of cross-linking behaviour. Low-rank coals cross-link early, before bridge breaking, while high-rank coals undergo cross-linking after most of the bridge breaking has taken place.

The results of solvent swelling experiments are not unambiguous, because the solvent swelling ratio depends on two things: the cross-link density and the solvent interaction parameter. This parameter can change with the functional group composition of the coal. Since the functional group composition will change as the coal pyrolyses, the change in solvent swelling ratio could be due to the change in functional group composition, not to cross-linking. However, estimation of the likely change in solvent swelling ratio with functional group composition indicates that the drastic change from 2.7 typical of coal to 1 for char is not likely to be due to the small changes in functional group composition during low-temperature pyrolysis[47].

Another way of investigating the cross-link density is by nuclear magnetic resonance (n.m.r.). Results of work in collaboration with the University of Utah[68] are shown

in *Figure 9*. The n.m.r. experiments used cross-polarization with magic angle spinning and dipolar dephasing (CP–MAS–DD)[5]. Dipolar dephasing allows determination of the functional-group form of the carbon atoms studied. When all the different kinds of bonds are considered, it is possible to determine an average molecular weight for the ring clusters and also the average number of attachments per ring cluster. In *Figure 9*, the average number of attachments is compared with the solvent swelling data for Pittsburgh Seam bituminous coal and a North Dakota lignite. The average number of attachments determined by n.m.r. is normalized to determine an index that can be compared with $1 - X$. *Figure 9a* presents the results for the lignite. Although there are differences in cross-link density determined by n.m.r. and by solvent swelling ratio, both techniques show that the material starts to cross-link at a reasonably low temperature, 573–673 K, and is almost completely cross-linked by 773 K. In contrast, for the Pittsburgh Seam coal shown in *Figure 9b*, the char has not undergone any cross-linking by 673 K and is not fully cross-linked even at 873 K.

To develop an understanding of the chemistry of cross-linking, an attempt was made to determine whether the addition of cross-links could be correlated with any other observation, specifically the evolution of gases. In

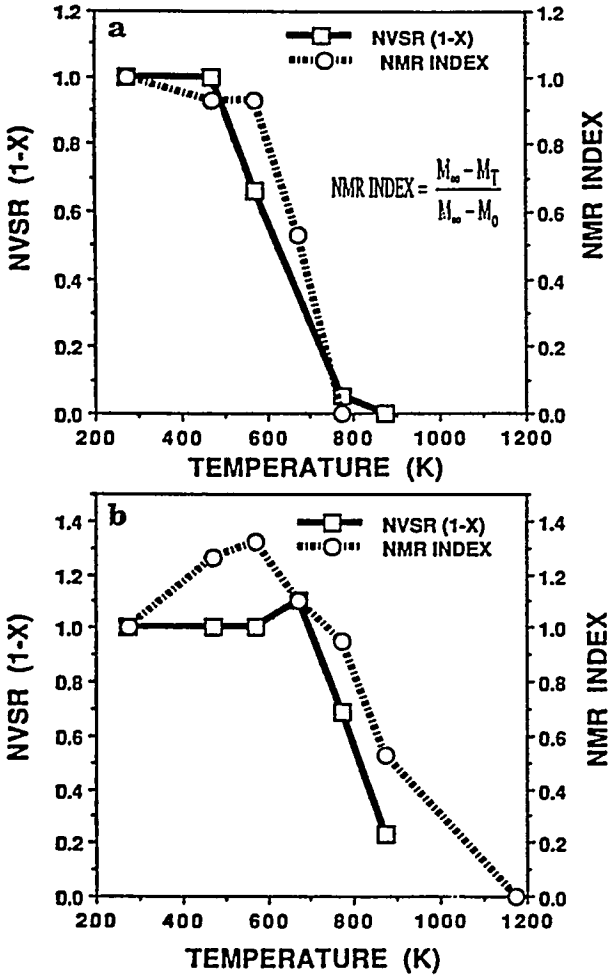

Figure 9 Comparison of n.m.r. and swelling data for (a) Zap lignite, (b) Pittsburgh No. 8 coal

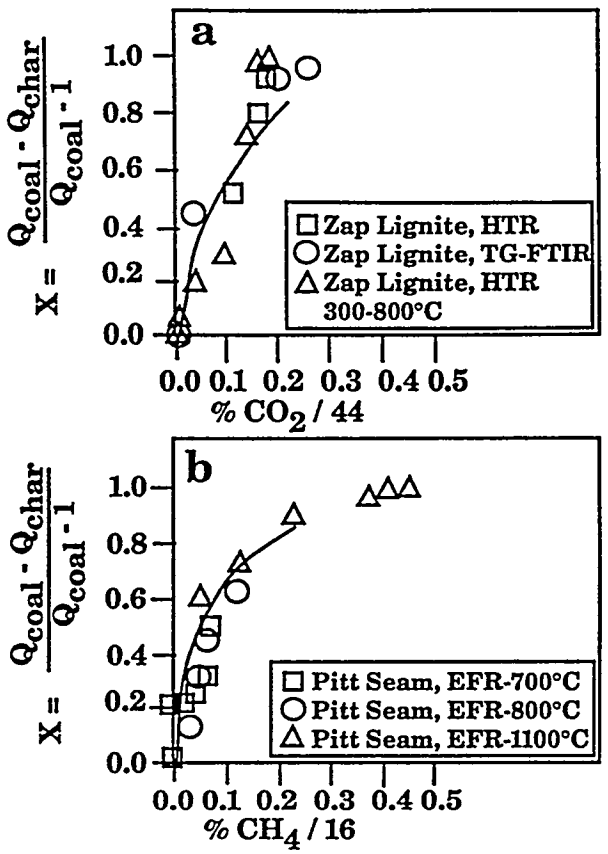

Figure 10 Measured and calculated normalized volumetric swelling ratios for coal and chars: (a) Zap lignite vs. CO_2 yield; (b) Pittsburgh Seam bituminous coal vs. CH_4 yield. Chars prepared in an entrained-flow reactor (EFR), a heated-tube reactor (HTR), and a thermogravimetric analyser with evolved product analysis by FT–i.r. (t.g.–FT–i.r.) as described in ref. 7

their initial work, Suuberg *et al.*[44] noted that the one gas species which correlated with the early creation of cross-linking in lignite was CO_2. *Figure 10* shows the results obtained in the authors' laboratory. *Figure 10a* presents the parameter X as a function of CO_2 yield divided by 44 so that it is on a molecular basis. For a wide variety of experiments (some at high and some at low heating rates) there is a very reasonable correlation between the loss of swelling and the appearance of CO_2 in pyrolysis. For all the low-rank coals studied, there appears to be a good correlation between the appearance of cross-links and the appearance of CO_2. The line shown in *Figure 10a* is from the FG–DVC model, where one cross-link is assumed for each molecule of CO_2 evolved.

For a higher-rank coal, which does not produce significant yields of CO_2, a different correlation is observed. *Figure 10b* compares the normalized solvent swelling ratio for a Pittsburgh Seam coal with the evolution of methane divided by 16. There is a good correlation between these two parameters for chars produced at different temperatures at high heating rates. The line in *Figure 10b* is from the FG–DVC model, where it is assumed that one cross-link is formed for each methane molecule evolved.

The correlation of the loss of swelling with other parameters was examined, but the correlation for CO_2 and methane was found to be the best. There was a

correlation for low-rank coals between the formation of cross-links and water evolution, but not quite as good as for CO_2. There was no good correlation for high-rank coals between cross-linking and tar evolution. Cross-linking correlated with hydrogen evolution is also expected at higher temperatures, as ring condensation by hydrogen elimination occurs. However, this phenomenon has not been studied.

Three sets of results illustrating the phenomena of bridge breaking and cross-linking are presented in *Figure 11*. *Figure 11a* shows the proton magnetic resonance thermal analysis (p.m.r.t.a.) results obtained at CSIRO[69–71]. This technique, which measures the relaxation time for protons, can distinguish between protons attached to mobile molecules (which are free to rotate) and those attached to a rigid lattice. The higher the concentration of mobile protons, the lower the value of the parameter M_{2T}. The data, obtained at 4 K s^{-1}, were provided by Dr R. Sakurovs (personal communication). The decrease in M_{2T} at low temperatures appears to be associated with melting, the sharp drop above 400°C is due to bridge breaking, and the sharp increase above 440°C is due to cross-linking.

Figure 11b shows fluidity data measured with a Gieseler plastometer for the same coal at a similar heating rate (3 K s^{-1})[4]. While the fluidity below 400°C is probably due to melting, above 400°C bridge breaking becomes important, and above 440°C cross-linking resolidifies the network.

Figure 11c presents data[72] on the extract yield from chars produced at a high heating rate, 640 K s^{-1}. The maximum extract yield occurs at a much higher temperature than for the other two experiments, owing to the high heating rate. The increase in extract yield is due to bridge breaking, and the decrease to cross-linking.

Transport

The above discussion shows how bridge breaking and cross-linking can fragment the macromolecular network and allow small pieces to be formed. The evolution of tar is controlled by the formation of these small fragments and their transport out of the metaplast. In the FG–DVC model, a very simple transport process has been assumed. The assumption is that the fragments reach their equilibrium vapour pressure in the light gas species and are removed from the metaplast by convective transport in the light gas species[7]. In a highly fluid coal, the expulsion of the light gases occurs by bubble transport. In a low-rank thermosetting coal, the transport of the light gas species is through the pores. In either case, the degree to which the tar molecules are transported depends on the volume of light species that evolve and the vapour pressure of the molecule. The low-molecular-weight species that have high vapour pressure are therefore easily transported, whereas heavy species are not. The result is that the tar from a bituminous coal pyrolysed at $\leqslant 1$ atm consists of molecules up to ~ 800 u. As the pressure is increased, the volume of the light gases is reduced and those marginal heavy products that were previously transported at 1 atm can no longer be transported. Thus, as the pressure is increased, the average molecular weight of the tar is reduced. The amount of tar is also reduced, because of the reduced efficiency of hydrogen utilization. As the pressure is decreased below 1 atm, the molecular weights and tar amounts increase. There is a minimum pressure ΔP, which is believed to be the internal pressure within the particles. ΔP is an adjustable parameter, depending on the coal and heating rate, and has a minimum value of 0.2 for fluid coals.

For low-rank coals, low-temperature cross-linking increases the effective coordination number of the

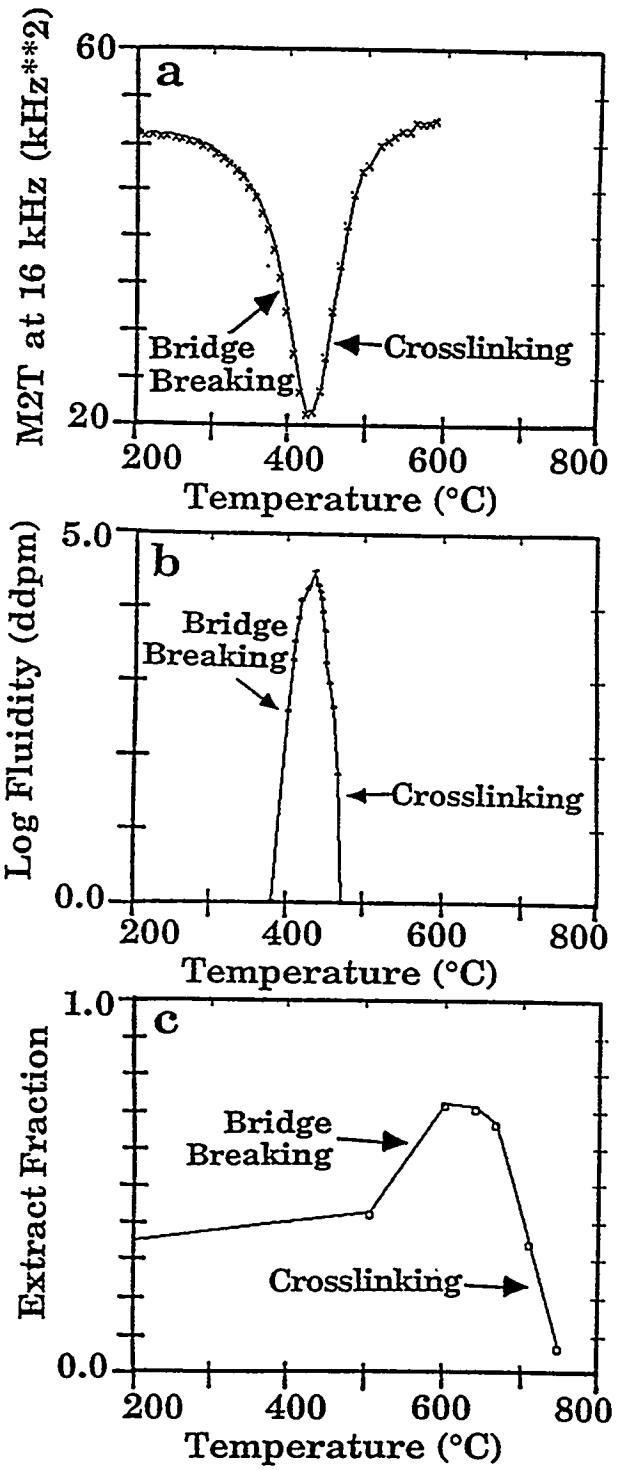

Figure 11 Results illustrating bridge breaking and cross-linking for Pittsburgh Seam coal: (a) p.m.r.t.a. at 4 K s^{-1} (R. Sakurovs, personal communication); (b) Gieseler fluidity at 3 K s^{-1} (data from Commercial Testing and Engineering Co.); (c) extract yield at 640 K s^{-1} (ref. 72)

network, and only small molecules are produced. The yields are low, and pressure has little influence on the yield or molecular weight distribution.

Summary of the FG–DVC model

Figure 12 summarizes the FG–DVC model. In *Figure 12a*, an assumed macromolecular network is presented. In the Monte Carlo version of the model, each piece of this network is actually described in the computer memory. The description of the network contains the molecular weights of the aromatic ring clusters (shown as the numbers in the circles) and the cross-linking density (shown by the vertical double line). The potential numbers of labile bridges (related to the donatable hydrogen) are indicated by the single horizontal lines, while the unbreakable bridges are indicated by double horizontal lines. The starting molecule is constructed from linear chains of a certain length l (typically between 6 and 12 aromatic ring clusters) connected by the appropriate number of cross-links, which together with the monomer molecular weight defines the molecular weight between cross-links M_c. When this is done, a certain number of the chains may be unattached to the rest of the macromolecular network. These are the guest molecules whose molecular weight is <3000 u and would be pyridine-soluble. The length of the chains l is adjusted to obtain the proper amount of pyridine-solubles. The number of cross-links is chosen to obtain a coordination number that yields the right ratio of tar to heavier fragments (e.g. extracts and liquids) in the metaplast.

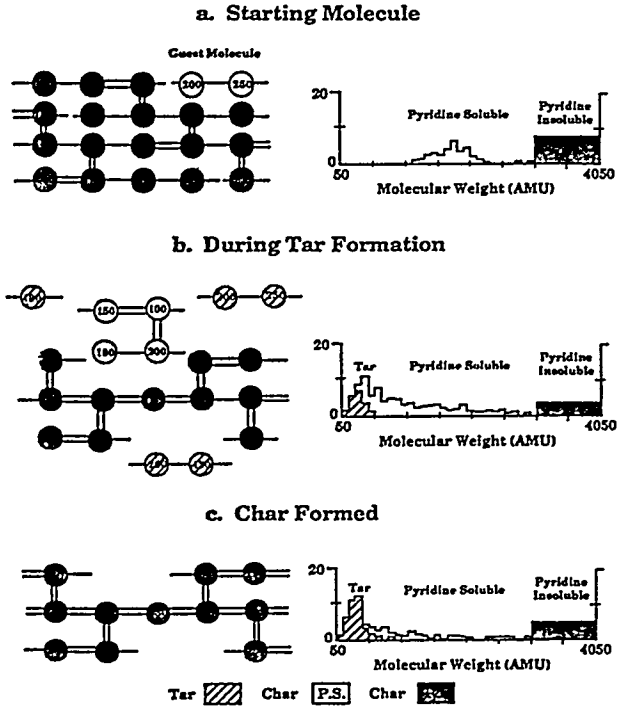

Figure 12 Representation of coal molecule in the DVC simulation and corresponding molecular weight distribution (from ref. 7). Circles represent monomers (ring clusters and peripheral groups); numbers denote the molecular weight of the monomer including attached bridges. Single-line bridges are breakable and can donate hydrogen; double-line bridges are unbreakable and do not donate hydrogen. Histograms show molecular weight distribution of the coal, tar and char; pyridine-soluble and -insoluble fractions of coal and char are differentiated; the area under the histogram corresponds to the weight per cent of the oligomers

The number of labile bridges (amount of donatable hydrogen, H_{al}) is chosen to obtain the proper tar yield in the t.g.–FT–i.r. experiments. Thus the model has three parameters, l, M_c and H_{al}, two of which are independently adjustable to obtain the correct tar, extract yield and viscosity.

Figure 12b considers what happens during pyrolysis. As the temperature increases, some of the weak bridges (single horizontal lines) can break according to the bridge breaking rate. The hydrogen limitation is accomplished by requiring that for each bridge that is broken, another one of the labile bridges becomes an unbreakable bridge as its hydrogen is used to stabilize the free radicals generated by the broken bridges. Thus for each broken bridge, two of the labile bridges are consumed. The broken bridges and new unbreakable bridges (horizontal double lines) are distributed randomly.

In the model, the cross-linking is assumed to correlate with CO_2 and CH_4 evolution. The evolution of these species is determined from the functional-group part of the model: one cross-link is inserted randomly for each CO_2 and each methane molecule evolved. If bridge breaking predominates over cross-linking, the macromolecular network is broken up into smaller fragments. On the right-hand side of *Figure 12b*, the molecular weight distribution that results from the bridge breaking and cross-linking events is shown. Molecules of <3000 u are greater in number, the lightest molecules escape as tar, and the rest of the network is described as pyridine-insoluble.

Figure 12c shows the network at the conclusion of the pyrolysis process. When all the labile bridges are consumed, the decomposition of the network is complete. All of the network is completely connected by unbreakable bridges, and is highly cross-linked. All the previously loose fragments have been incorporated into the network by cross-linking or have escaped as tar.

ANALYSIS OF COMPOSITION AND KINETIC PARAMETERS

In this section, the laboratory characterization to determine the model parameters is considered. Analysis by t.g.–FT–i.r. is used to determine kinetic rates and functional group compositions. Solvent swelling, solvent extraction, and fluidity measurements in a Gieseler plastometer are used to obtain information on the molecular weight distribution of the metaplast and hence determine the network parameters. N.m.r. and f.i.m.s. are used to determine the molecular weight of the ring clusters.

T.g.–FT–i.r.

Apparatus and procedure. The instrument used, a Bomem TG/plus, comprises a DuPont 951 t.g.a., a hardware interface (including a furnace power supply), an Infrared Analysis 16-pass gas cell with transfer optics, a Michelson MB series FT–i.r. spectrometer (resolution 4 cm^{-1}, detector MCT), and a PC-AT compatible computer. The cell is connected without restrictions to the sample area and helium sweep gas is used to bring evolved products from the t.g.a. directly into the gas cell. The infrared spectra quantitatively track the composition of the volatiles as a function of time.

The most difficult volatiles to analyse are the tars which condense at room temperature. In the TG/plus, the rapid

cooling from the high-thermal-conductivity helium sweep gas causes these products to form an aerosol fine enough to follow the gas through the analysis cell. The aerosol is also sufficiently fine as to cause little scattering of the infrared beam and it thus appears as though the tar were in the gas phase.

As an example of the analysis procedure, the pyrolysis and oxidation of a bituminous coal is described. More detail can be found in ref. 1. *Figure 13a* illustrates the weight loss from this sample and the temperature history. A 25 mg sample of Pittsburgh Seam coal, loaded in the sample basket of the DuPont 951, is heated at 30 K min^{-1} in the He sweep gas, first to 150°C to dry, then to 900°C for pyrolysis. After cooling, a small flow of O_2 is added to the furnace at 57 min and the temperature is ramped to 900°C for oxidation.

During this procedure, infrared spectra are obtained once every 40 s. As discussed previously[1], the spectra show absorption bands for CO, CO_2, CH_4, H_2O, SO_2, COS, C_2H_4, HCl and NH_3. Unfortunately, H_2 evolution is not directly determined by this technique, but can be determined by a second experiment in which the volatiles are oxidized. The spectra above 400°C also show aliphatic, aromatic, hydroxyl, carbonyl and ether bands from tar. The evolutions of gases derived from the i.r. absorbance spectra are obtained by a quantitative analysis program using a database of calibration spectra for different compounds. The routine decides which regions of each calibration spectrum to use for best quantitation with least interference. A correlation between the sample spectrum and the reference spectrum is performed to determine gas amounts. A database of integration windows is also available for tracking functional group absorption. Tar quantitation is discussed in ref. 1. The routine is fast enough for the product analysis to be performed and displayed every 40 s during the actual experiment.

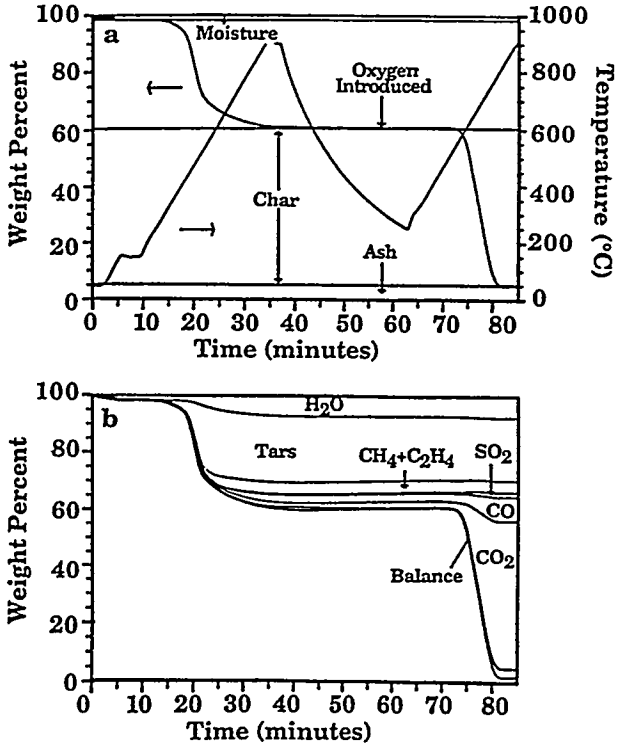

Figure 13 Thermogram and quantitative breakdown of evolved gases for Pittsburgh Seam coal

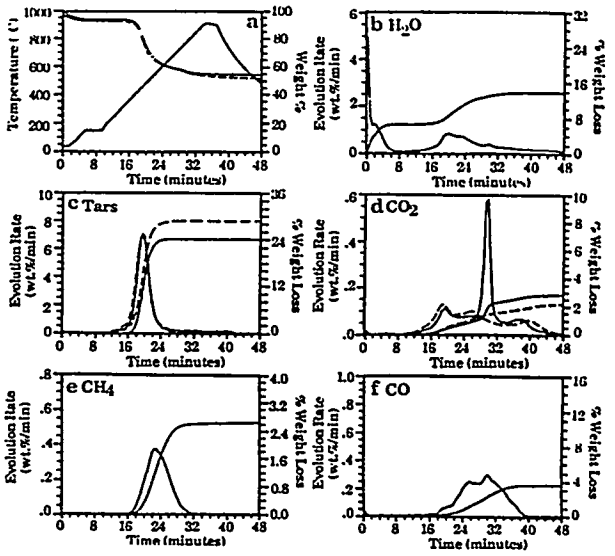

Figure 14 T.g.–FT–i.r. analysis of raw and demineralized Illinois No. 6 coal during pyrolysis: (a) weight loss (——), sum of evolved products (– – –) and temperature profile; (b) H_2O evolution rate and integral; (c) tar evolution rate and integral for raw coal (——) and demineralized coal (– – –); (d) CO_2 evolution rate and integral for raw coal (——) and demineralized coal (– – –); (e) CH_4 evolution rate and integral; (f) CO evolution rate and integral; all weight losses are on the as-received basis

Figure 13b illustrates the integral of the evolution curves to obtain cumulative evolved product amounts. Because the data are quantitative, the sum of these curves matches the weight loss as determined by the t.g.a. Discrepancies occur because of components such as H_2 which cannot be seen by i.r.

Determination of FG–DVC model parameters. The kinetic and composition parameters for the FG–DVC model are obtained from the TG/plus pyrolysis cycle. The pyrolysis cycle for Illinois No. 6 coal (Argonne premium sample) is presented in *Figure 14*. *Figure 14a* shows the weight loss and temperature profile; the dashed line is the sum of species (tar, CH_4, H_2O, CO_2, CO, SO_2, NH_3, C_2H_4 and COS). The sum of species is within a few per cent of the weight loss.

The water evolution (*Figure 14b*) consists of a low-temperature moisture peak followed by a pyrolysis peak. To fit the wide pyrolysis peak by the FG submodel, three sources are used for H_2O. Each source evolves according to

$$dW_i/dt = k_i W_i(\text{char}) \quad (1)$$

where W_i is the gas species and W_i(char) is the amount of the functional group source remaining in the char. The rate constant k_i is given by an Arrhenius expression of the form

$$k_i = A_i \exp((-E_i \pm \sigma_i)/RT) \quad (2)$$

where A_i is the pre-exponential factor, E_i the activation energy and σ_i the distribution in activation energies. Two sources are used for CH_4 and three for CO and CO_2. A single source is used for H_2, but the kinetic rates have not been finalized. Note the elimination of the calcite

CO_2 evolution peak (*Figure 14d*) and the increase in tar (*Figure 14c*) for the demineralized coal.

To obtain the model parameters, the model is fitted to the TG/plus data at three heating rates (3, 30 and 100 K min^{-1}). When there are multiple sources for a given species and the sources have overlapping peaks, the determination of parameters is not unique and some rules must be assumed. Based on chemical arguments, A_i is restricted between 10^{12} and 10^{15} s^{-1}. Also, the pre-exponential factor for a given species pool is assumed rank-invariant. This assumption is based on the observed rank variation of the evolution curves. With increasing coal rank, the leading edges and the early peaks (extra-loose or loose pools) shift to higher temperatures, while the trailing edges (tight or extra-tight pools) remain at the same temperature. An example of this is shown for water for five coals in *Figure 15a*[16]. Ignoring the moisture release at low temperature, the figure shows a systematic increase with rank of the temperature T_{max} of the peak evolution rate. An interesting speculation is that the shift in the evolution curve with rank is due to natural pyrolysis over geological time. With increasing ageing temperature and time, the maturation process gradually evolves the loosely bound functional groups, while leaving the tightly bonded groups intact. Thus there is an increase in T_{max} with rank.

The shift can be simulated by pyrolysing a species described by a distribution of activation energies (equation (2)) up to different bed temperatures in order to represent natural ageing. An example is shown in *Figure 15b*. Starting with the evolution profile for Zap lignite, the coal is assumed to pyrolyse at 10 K Ma^{-1} up to temperatures of 60, 120, 150 and 180°C. The resulting geologically aged sample is simulated using the TG/plus temperature profile and the predicted results are plotted. The curves for geological ageing at 120, 150 and 180°C are similar to the actual TG/plus evolution curves shown in *Figure 15a* for Illinois No. 6, Pittsburgh No. 8 and Upper Freeport coals respectively. Thus, in the FG–DVC model, the pre-exponential factor is assumed to be constant as rank increases, and the activation energy of the pool is increased with increasing coal rank to fit the data. It is found that the activation energy of tight pools generally changes with rank much less than does that of the loose pools.

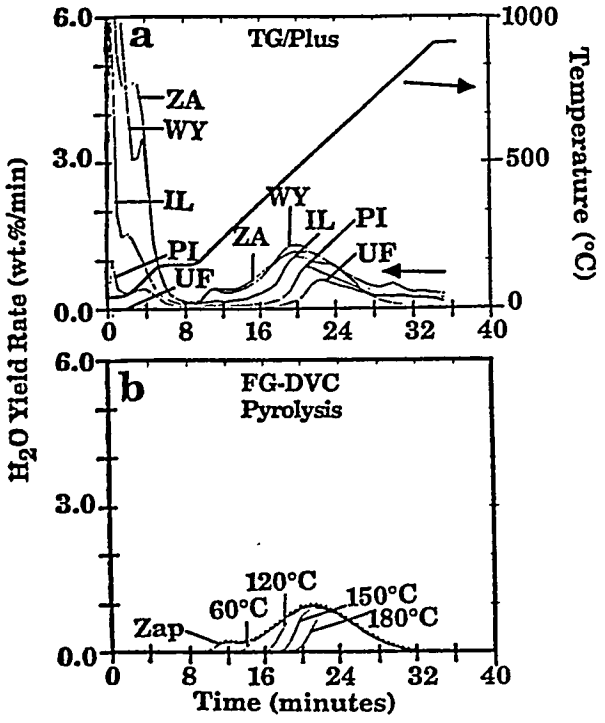

Figure 15 Evolution of H_2O from five Argonne premium coals: (a) pyrolysed at 30 K min^{-1}; (b) predicted by FG–DVC for slow pyrolysis (geological ageing) at different temperatures. ZA, Beulah Zap lignite; WY, Wyodak Anderson subbituminous; IL, Illinois No. 6 hvb; PI, Pittsburgh No. 8 hvb; UF, Upper Freeport mvb

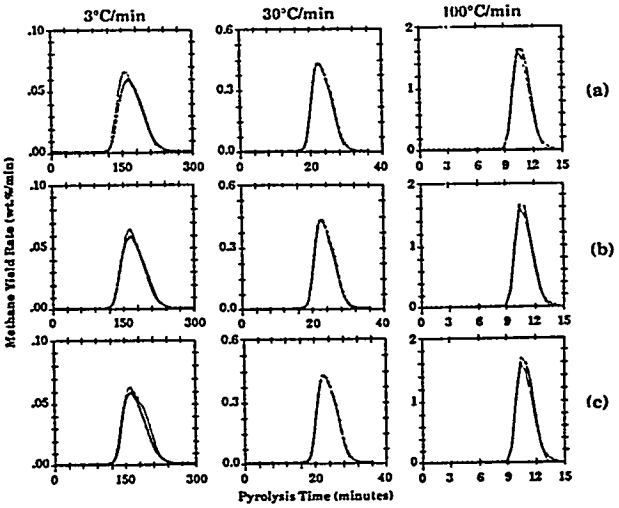

Figure 16 Kinetic analysis for CH_4 evolution at three heating rates for Pittsburgh Seam coal: comparison of theory (——) and experiment (·—·). E_{CH4} (kJ mol^{-1}): (a) 193 (L), 226 (T); (b) 234 (L), 268 (T); (c) 276 (L), 310 (T)

The amounts of the functional group pools and kinetic parameters are obtained by comparing the data from the t.g.–FT–i.r. with the model at heating rates of 3, 30 and 100 K min^{-1}. The resolution of the hydrocarbon evolution into paraffins, olefins, ethane, ethylene, propane and propylene and the determination of H_2 evolution is done in other experiments if required. *Figure 16* compares the theory and experiment for methane evolution from the Pittsburgh Seam coal at three heating rates and for three sets of E_i, A_i and σ_i values, where E_i was specified and A_i and σ_i were adjusted to obtain the kinetic rate that fits the data at 30 K min^{-1}. The kinetic parameters are then derived from this analysis, the kinetic rate being known within a factor of ~2. The agreement between the theory and experiment in *Figure 16* is best for $E_{CH4(L)} = 234$ and $E_{CH4(T)} = 268$ kJ mol^{-1}. In the determination of kinetic parameters, uncertainties arise from the fact that each gas evolution is represented by several pools, which gives more degrees of freedom to the choice of parameters. Based on such analysis it is determined that E can be specified to within ±20 kJ mol^{-1}. Once E is fixed, then A is determined to within a factor of 2, and σ to ±1.3 kJ mol^{-1}. On the other hand, if A is chosen based on chemical arguments, then E is determined by the data to within ±2 kJ mol^{-1}.

These curve-fitting procedures have been applied to the eight Argonne premium coals according to the rules cited above (i.e. frequency factor between 10^{12} and 10^{15} s^{-1} and constant for a given gas species pool, independent of coal rank). Results for E, A and σ for bridge breaking and the evolution of methane (two

Table 1 Kinetic data for major functional group pools in Argonne premium coals

Group-pool[a]; A (s^{-1})	Values of E R (K) (upper figure) and σ R (K) (lower figure)[b] Beulah Zap lignite	Wyodak Anderson subbit.	Illinois No. 6 hvb	Blind Canyon hvb	Lewiston Stockton hvb	Pittsburgh No. 8 hvb	Upper Freeport mvb	Pocahontas No. 3 lvb
CO_2-XL	18000	18000	20500	21000	21250	21500	22000	23000
5.0×10^{12}	1500	1500	3000	4000	3500	3600	2000	2500
CO_2-L	23500	24000	24750	25000	26000	26500	27000	28000
5.0×10^{12}	2000	2500	1750	1250	3000	3000	3000	2500
CO_2-T	31000	32000	32000	32000	32000	32000	32000	33500
7.5×10^{12}	3000	2800	2750	5000	3200	2500	2500	2700
CO-L	24500	24750	25000	25000	25500	26000	28000	29000
5.0×10^{12}	3000	2500	1000	1250	1100	1250	750	1250
CO-T	30000	30250	30500	30500	30500	30750	31500	32000
5.0×10^{12}	3000	3000	2000	2000	1600	1900	1400	1500
CO-XT	39000	39750	40000	40000	40000	40000	40000	40000
2.0×10^{14}	2500	2500	3000	2500	3000	2800	2250	3200
CH_4-L	28000	28000	28000	28000	28000	28000	28750	29500
3.0×10^{13}	2500	2250	1800	1500	1200	1300	800	750
CH_4-T	32000	32000	32000	32000	32000	32000	32000	33000
6.0×10^{13}	2200	2000	2200	2200	2200	2200	2000	1700
H_2O-XL	16500	17000	18000	0	0	0	0	0
5.0×10^{12}	1500	1500	1800	0	0	0	0	0
H_2O-L	23000	24250	25000	25000	25500	26000	27500	28000
5.0×10^{12}	2700	2500	1500	1250	1250	1250	1250	1250
H_2O-T	31000	31000	32000	32000	32000	32000	34000	35000
2.0×10^{14}	3500	3500	2800	2500	2500	2500	4000	3000
Tar-BB	26000	26000	26000	27000	27250	27500	28250	29000
1.0×10^{14}	1000	1000	750	1250	1000	1250	1250	750

[a]BB, bridge breaking; L, loose; T, tight; XL, extra-loose; XT, extra-tight
[b]R is the gas constant

pools), CO (three pools), CO_2 (three pools) and H_2O (three pools) are presented in *Table 1*. These Arrhenius parameters do not represent fundamental kinetics, but have been found to give good predictions at the three heating rates investigated. In addition, as shown in the next section, these parameters appear to give reasonable predictions at high heating rates. The values for H_2 are not yet finalized and are not presented. There is a systematic increase in activation energy with increasing rank. The variation in activation energy is maximum for the loose pool and decreases as the activation energy increases. The amounts for these pools are presented in *Figure 17*, which shows a systematic variation with rank. Oxygenated species – CO, CO_2 and H_2O – decrease with increasing rank. Methane increases with increasing rank.

Solvent swelling, extraction and n.m.r.

Solvent swelling and extraction data for the Argonne premium coals are presented in *Table 2*. As discussed above, the extract yield is used to determine the length of the chains (Monte Carlo) or the starting bond probabilities (percolation) used in the model. There appears to be some problem in this approach for the highest-rank coals (Pocahontas and Upper Freeport). The swelling and extract yields for these coals in pyridine appear to be limited by weak cross-linking (other than hydrogen bonding) forces which are not eliminated by pyridine.

The solvent swelling ratio has been used to determine the cross-link density[2,3,24–29]. The various theories and

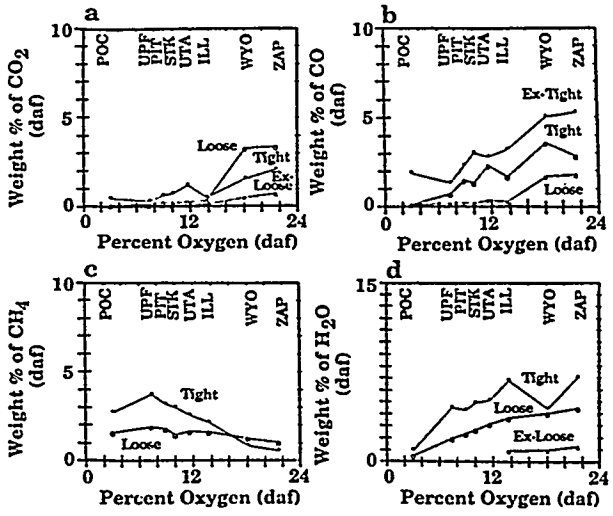

Figure 17 Amounts of four gases released for functional group pools of the eight Argonne premium coals, as a function of the oxygen content of the coal. POC, Pocahontas No. 3; UPF, Upper Freeport; PIT, Pittsburgh No. 8; STK, Lewiston-Stockton; UTA, Blind Canyon; ILL, Illinois No. 6; WYO, Wyodak Anderson; ZAP, Beulah Zap

values for the solvent interaction parameter[24–29] suggest that there are between four and eight ring clusters between cross-links, indicating a value of $\sigma + 1$ between 2.13 and 2.25[32]. N.m.r. results of Solum *et al.*[5] for the number of bridges and loops suggest a value of $\sigma + 1$ of between 2 and 3, so a value in the neighbourhood of 2.5

Table 2 Extract yields and volumetric swelling ratio (VSR) for Argonne premium coals

Coal	Pyridine extract (wt% daf)	VSR (vacuum-dried)
Beulah Zap	5.4	2.7
Wyodak Anderson	10.7	2.7
Lewiston-Stockton	18.3	2.3
Blind Canyon	22.5	2.7
Pittsburgh No. 8	27.7	2.3
Illinois No. 6	35.7	2.5
Pocahontas No. 3	1.0	1.1
Upper Freeport	10.4	1.3

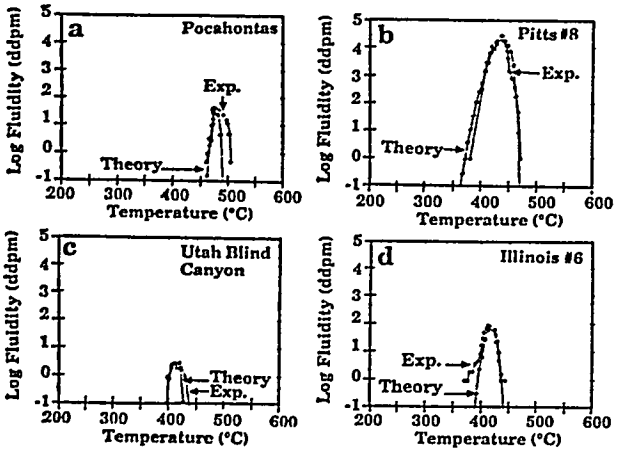

Figure 18 Measured and predicted Gieseler fluidities of four Argonne premium coals, from ref. 77

seems reasonable. However, the uncertainty in the coordination number determined by n.m.r. is too large for use in the model. The cross-link density is instead considered as an adjustable parameter used to fit the fluidity data.

Gieseler fluidity

As discussed above, the cross-link density controls the effective coordination number of the network and hence the molecular weight distribution and amount of the fragments. For bituminous coals, it is the initial cross-link density that is important, since few new cross-links are formed before pyrolysis. A recent theory for fluidity was developed based on the liquid fraction in the coal computed by the FG–DVC model[8,43]. Measurements of the tar and the fluidity thus provide a constraint on the molecular weight distribution of the fragments and hence on the cross-link density. *Figure 18* presents a comparison of theory and experiment for four of the Argonne coals with the kinetic parameters fitted from t.g.–FT–i.r. data. The fitting procedure for fluidity and tar determines a unique combination of the cross-link density and donatable hydrogen.

Monomer molecular weight distribution

The molecular weight distribution of the monomers is chosen based on the ring cluster size determined by n.m.r.[5] and the results of the model checked with f.i.m.s. data[6].

COMPARISON OF THEORY AND EXPERIMENT

Volatiles evolution

A good test of the validity of using the t.g.–FT–i.r. method over a range of low heating rates to obtain kinetic parameters is the ability to use the kinetic parameters to extrapolate to high heating rate conditions. *Figure 19a* presents results for Illinois No. 6 coal using the complete FG–DVC model and the most recent kinetic and composition parameters derived from the TG/plus[65]. The data were obtained in the heated-tube reactor, where FT–i.r. emission and transmission measurements of coal particle temperatures determined the heating rate to be $>2 \times 10^4$ K s^{-1}. The predicted rates of evolution for each species are in good agreement with the observed rates except for water, for which moisture sometimes creates measurement errors.

The sensitivity of the predictions to the assumed kinetic rates has been considered by running cases with rates at a factor of 10 lower and higher. Such a change produces a ± 65 K shift in the curves or a variation of ± 5 cm in the position on the x-axis. The results thus suggest a knowledge of the kinetic rates at these high heating rates to within a factor of 10. On the other hand, the accuracy of the temperature measurements is estimated to be ± 25 K.

Char

A number of char characteristics can be measured and compared with the model. These include fluidity (already discussed in the previous section), functional group composition, cross-link density, p.m.r.t.a., and extract yield. These are discussed below.

Functional group composition. The functional group composition can be determined by FT–i.r.[73–76] or CP–MAS n.m.r. with dipolar dephasing[5]. Chars were prepared by heating Pittsburgh Seam coal to temperatures of 200, 300, 400, 500 and 600°C at 30 K s^{-1} and were

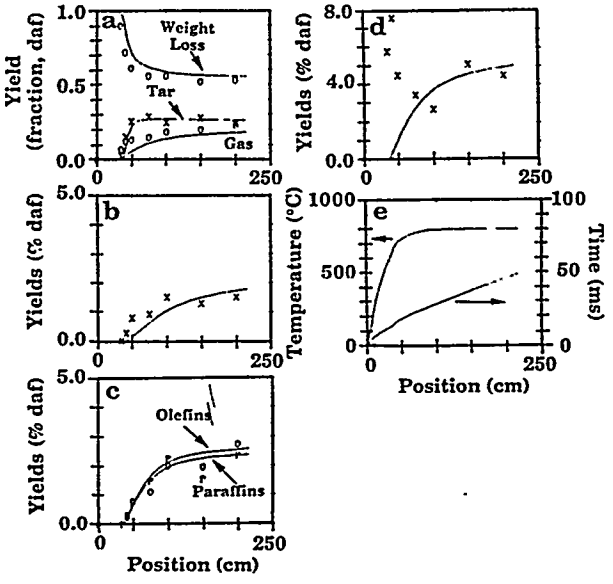

Figure 19 Predictions of the FG–DVC model for Illinois No. 6 coal pyrolysed in the heated-tube reactor: (a) weight loss, tar and gas; (b) methane; (c) olefins and paraffins; (d) water; (e) time and temperature as a function of position. Data points are from ref. 53

characterized[68]. *Figure 20* compares the theory with n.m.r. and FT i.r. measurements. The fractions of aliphatic and aromatic carbons are compared in *Figure 20a*, and aliphatic, aromatic, methyl and hydroxyl hydrogens in *Figure 20b*. *Figures 20b* and *20d* compare the n.m.r. and FT–i.r. measurements for the same quantities (except that methyl and aliphatic hydrogen are lumped together in the latter). The tar (*Figure 21a*) and methane (*Figure 21b*) yield rates are presented for comparison. Although there are some discrepancies between the theory and experiment in the magnitudes of the quantities (the FT–i.r. quantities are the less well predicted), the theory matches the data for the temperatures at which variations occur to within ± 20 K or the kinetic rate to within a factor of 2. The experimental uncertainty in the temperature is ± 10 K. The model predictions are thus in good agreement with the data.

Cross-link density. The application of the volumetric swelling ratio to obtain the changing cross-link density in the char was discussed in the section dealing with the FG–DVC model. Comparison with theory was discussed in ref. 7. *Figure 21c* compares the theory and experiment on the cross-link density as determined by the solvent swelling ratio for the set of chars of *Figures 20* and *21a,b*. The agreement is good except for the increase in $1 - X$, which is not predicted. *Figure 22* compares the theory and experiment for two coals. The theory predicts the early cross-linking in Zap lignite (related to CO_2 evolution), not seen for the bituminous coal. The agreement between theory and experiment is good, except that as in *Figure 21c* the increase in $1 - X$ for the Pittsburgh Seam coal is not predicted.

The n.m.r. data also provide a direct measurement of the number of attachments per cluster[5] (see *Figure 9*). *Figure 23* presents data[68] for the total number of attachments (which includes peripheral groups, bridges and loops), and only bridges and loops (B & L) as a function of final temperature for Pittsburgh Seam coal

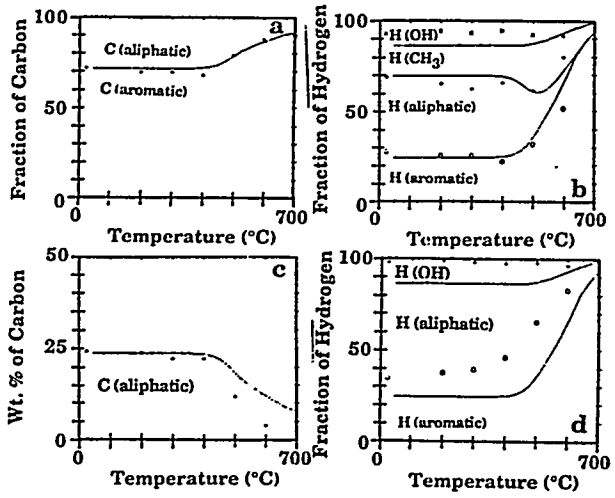

Figure 20 Comparison of measured (points) and predicted (——) functional group composition of char from Pittsburgh Seam coal pyrolysed at 30 K min^{-1} to the indicated temperatures: (a) carbon distribution by n.m.r.; (b) hydrogen distribution by n.m.r.; (c) aliphatic carbon by FT–i.r.; (d) hydrogen distribution by FT–i.r. Data from ref. 68

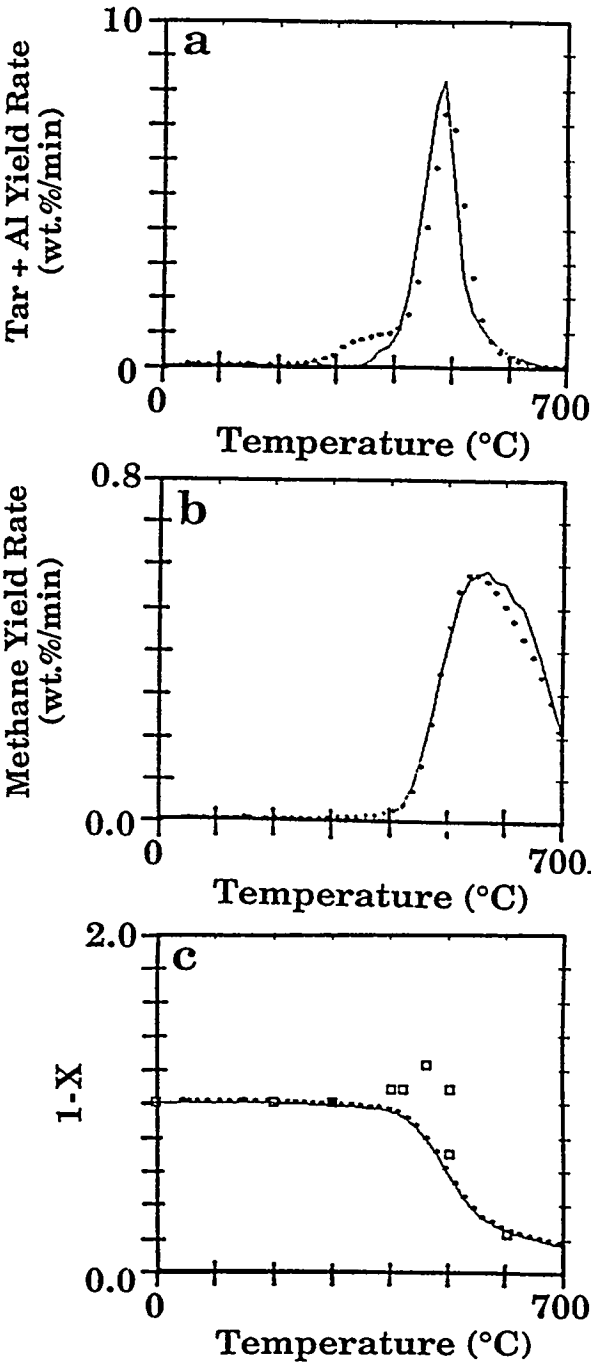

Figure 21 Comparison of measured (points) and predicted (——) pyrolysis behaviour of Pittsburgh Seam coal heated at 30 K min^{-1} to the indicated temperatures: (a) tar yield rate; (b) methane yield rate; (c) solvent swelling ratio

heated at 30 K min^{-1} to the indicated temperature. These are the same chars as in *Figures 20* and *21*. The FG–DVC model predicts the number of B & L. This quantity (~ 2 for coal) is the coordination number, suggesting that coal is quite chain-like. There is little change in B & L up to 400°C, but an increase at 500°C and above, where cross-linking related to methane evolution is believed to occur.

Notice that the total number of attachments changes very little. This would be reasonable if the methane

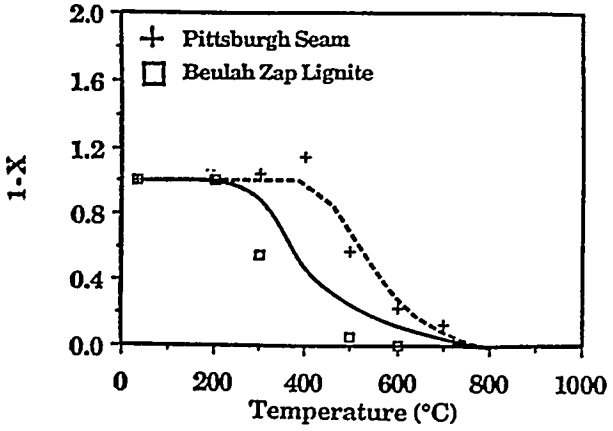

Figure 22 Comparison of measured (points) and predicted (-----, ---) normalized volumetric swelling ratio as a function of pyrolysis temperature for a lignite and a bituminous coal

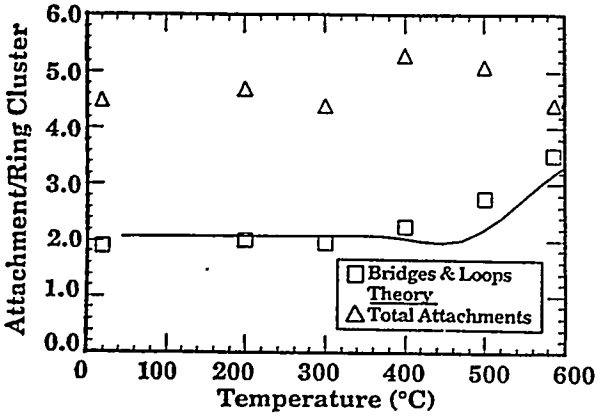

Figure 23 Comparison of theory with n.m.r. data for attachments to ring clusters (data from University of Utah)

peripheral groups were replaced by bridges in substitution reactions. This is believed to be the reason for the correlation between methane evolution and cross-linking.

P.m.r.t.a. Proton magnetic resonance thermal analysis (p.m.r.t.a.) is used at CSIRO as an alternative to fluidity measurements. The measurement of proton mobility can distinguish protons on molecules free to rotate from protons on a rigid lattice. The molecule's ability to rotate depends on its freedom from the network (i.e. it must be unattached or attached at only one place) and on the mobility of free molecules to rotate (which depends on the temperature). From the measured M_{2T} values, a 'mobile' liquid fraction can be defined by the expression (R. Sakurovs, personal communication):

$$\text{Liquid fraction} = \frac{M_{2T}(\text{room temperature}) - M_{2T}(T)}{M_{2T}(\text{room temperature})} \quad (3)$$

At sufficiently high temperature, when the free molecules have sufficient energy to rotate, this quantity should be equal to the FG–DVC liquid fraction. *Figures 24a* and *24d* compare the measured and predicted liquid fraction using both the Monte Carlo and percolation models. As expected, the theory and experiment do not agree at low temperature where the material is solid and the molecules are not free to rotate. However, there is good agreement on the softening temperature, peak fluidity temperature and solidification temperature, which are predicted to within ±20 K (a factor of 2 in rate). The liquid amounts in the two theories are defined differently and so the absolute amounts do not agree. Also shown in *Figures 24b, c, e* and *f* are comparisons of both theories and experiment for the fluidity and tar evolution curves for the same coal at a similar heating rate. The agreement between the data and both theories is good.

Extract yields. Figure 25 compares the FG–DVC predictions with the data of Fong *et al.*[72] on total volatiles yield and extract yield as a function of temperature in pyrolysis at 0.85 atm. The experiment was performed in a heated-grid apparatus at heating rates of 470 K s^{-1} to 814 K (*Figure 25a*) and 640 K s^{-1} to 1018 K (*Figure 25b*), with variable holding times and rapid cooldown. The predictions in *Figure 25* are in reasonable agreement with the data. The temperatures at which the extract yield increases owing to bridge breaking and decreases owing to cross-linking are predicted to within ±30 K. This is well within the accuracy of the experiment. The predicted extract yields are not as high as the measured yields. However, such high yields of extracts have not been duplicated by others, and it is possible that the extracted fraction also contains some colloidal material.

Weathering. Oxidation of Pittsburgh Seam coal was performed at 80°C for 10, 20 and 62 d. In the model, the loss of fluidity with increasing oxygen concentration is related to the increase in CO_2 evolution and hence to increases in low-temperature cross-linking. To determine the CO_2 evolution, measurements were made in the t.g.–FT–i.r.[77]. *Figure 26a* shows that the low-temperature CO_2 evolution significantly increased after 10 d of oxidation, becoming comparable with that for Illinois No. 6 coal. After 20 d, the early CO_2 evolution

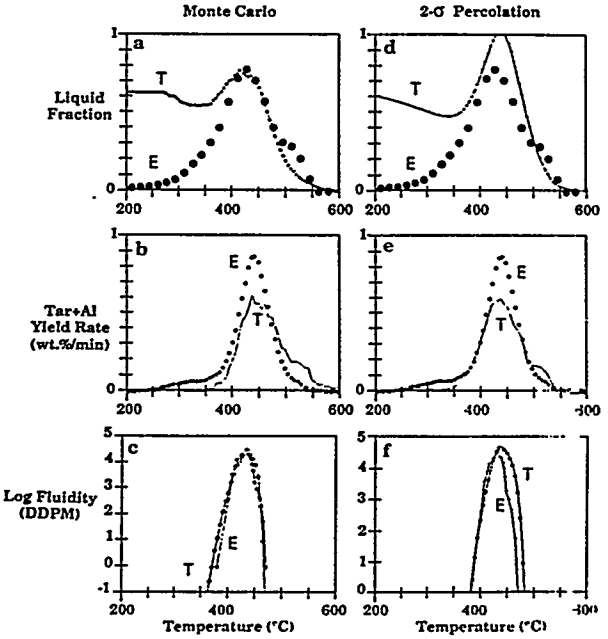

Figure 24 Comparison of Monte Carlo and 2-σ percolation theory for liquid fraction, tar yield rate and Gieseler fluidity for Pittsburgh No. 8 bituminous coal pyrolysed at 3 K min^{-1}. T, theory; E, experimental data

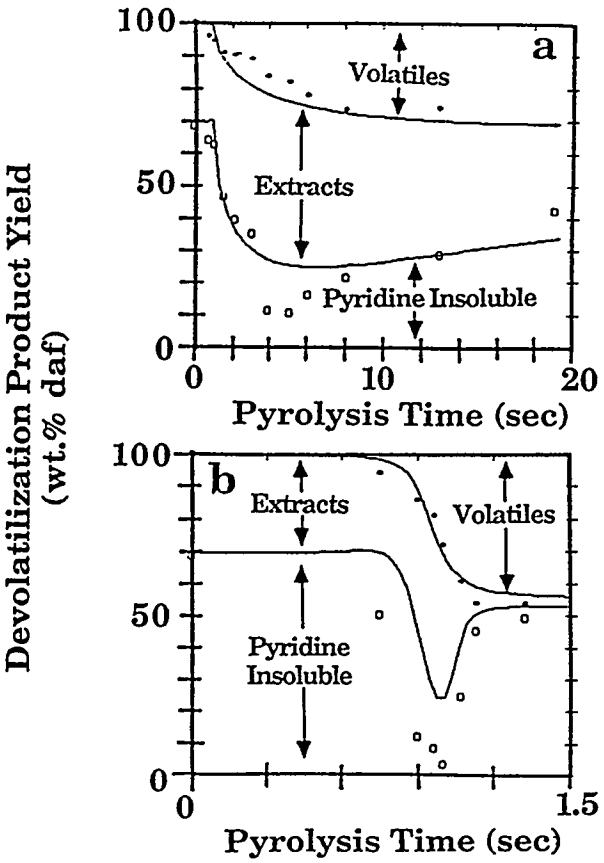

Figure 25 Comparison of FG-DVC model predictions (——) with the data of ref. 72 (points) for Pittsburgh Seam coal: (a) 813 K, 470 K s^{-1}; (b) 1018 K, 640 K s^{-1}; $P = 0.85$ atm. The predictions assume transport by equation (4) ($\Delta P = 0$ atm) and no external transport

was greater than that for Utah bituminous coal. After 3 months at 110°C the CO_2 evolution was comparable with that of a lignite. When these increased CO_2 yields were incorporated in the simulation for the oxidized Pittsburgh Seam coal's fluidity, the maximum fluidity was reduced. The predicted maximum fluidity is compared in *Figure 26b* with the measurements of Wu *et al.*[78] for comparable coal and oxidation treatment. The agreement is quite reasonable.

Predicted molecular weight distribution. The dominant factors determining the char's properties are the starting cross-link density and low-temperature cross-linking behaviour. To illustrate the differences between plastic and non-plastic coals, *Figure 27* compares the predicted molecular weight distribution of macromolecular network fragments in the char and tar for Zap lignite and Pittsburgh Seam bituminous coal. The bituminous coal (*Figure 27a*) exhibits substantial fragmentation of tar precursors with molecular weights of 300 to 900 daltons (*n*-mers 1–3), extracts or pyridine solubles with molecular weights of 1200 to 3000 daltons (*n*-mers 4–10), and liquids with molecular weights of 3300 to 30000 daltons (*n*-mers 11–100). On the other hand, the initial cross-link density in the lignite, and the subsequent increase due to CO_2-related cross-linking, allow only minimal fragmentation producing only small molecules (*Figure 27b*). (Note the factor of 10 scale difference between the bituminous coal and the lignite.) These predictions of the model are related to the extract yields, p.m.r.t.a. analysis, fluidity and tar yields. Bituminous coals have high extract yields, high fluidity and high tar yields; lignites have low values of these quantities. The chief difference is the cross-link density.

Tar

Molecular weight distribution. The tar is evolved from the lightest fractions of the metaplast and depends on the metaplast distribution and the transport. For the bituminous coal, the upper molecular weight is limited only by the vapour pressure of the large molecules. For

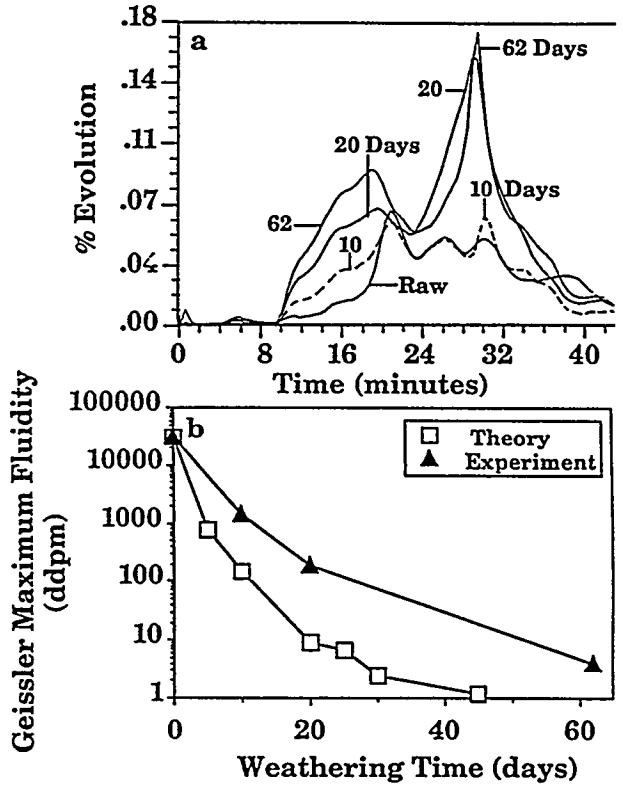

Figure 26 Reduction in Gieseler fluidity due to weathering of Pittsburgh Seam coal by oxidation at 80°C for the number of days shown: (a) CO_2 evolution of raw and weathered coal; (b) predicted and measured fluidity (measurements from ref. 78)

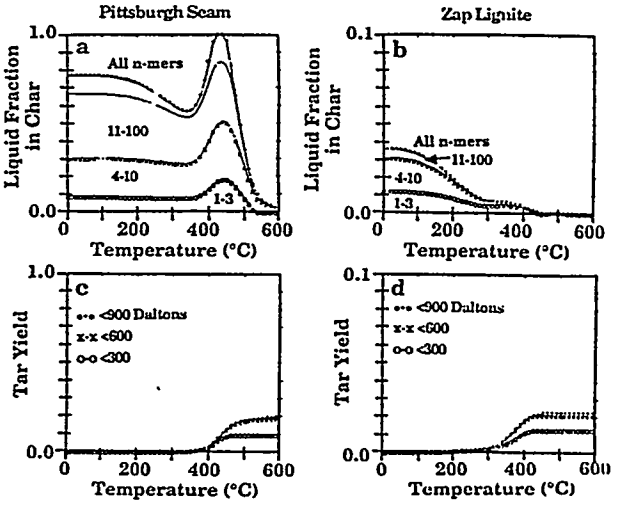

Figure 27 Predicted molecular weight distribution of macromolecular network fragments in char and tar for a bituminous coal and a lignite

the lignite, the metaplast distribution limits the amount and molecular weight distribution. *Figures 28c* and *28d* show measurements for the Beulah Zap lignite and the Pittsburgh Seam bituminous coal pyrolysed in the f.i.m.s. apparatus, in which the tar is ionized immediately upon evolution and is directly transported to the mass spectrometer, so the spectra are a good indicator of the tar molecular weight distribution. The data have been summed over 50 u intervals. Whereas the Pittsburgh bituminous coal shows a peak intensity at ~400 u the lignite peak is at 100 u. The predicted average tar molecular weight distributions are in good agreement with f.i.m.s. data, as shown in *Figures 28a* and *28b*. In the FG–DVC model, the same monomer distribution is used for both the lignite and bituminous coal. Thus the greater fall in amplitude with increasing molecular weight for the lignite than for the bituminous coal must be due to early cross-linking and transport effects in the lignite.

Pressure effects. The predicted effect of pressure on the tar molecular weight distribution is illustrated in *Figures 29a* and *29b*. Pressure enters the model through the transport assumption. The internal transport rate is inversely proportional to the ambient pressure. The reduced transport rate reduces the evolution rate of the heavier molecules. Therefore the average molecular weight and vaporization 'cutoff' decrease with increasing pressure. The amount of tar also decreases because of the inefficient use of the available hydrogen in stabilizing small tar molecules. The predicted trends are in reasonable agreement with the observed tar molecular weight distributions shown in *Figures 29c* and *29d*. The spectra are for previously formed tars analysed by f.i.m.s.[6]. The low intensities between 100 and 200 u are believed to be due to loss of these components as a result of their higher volatility.

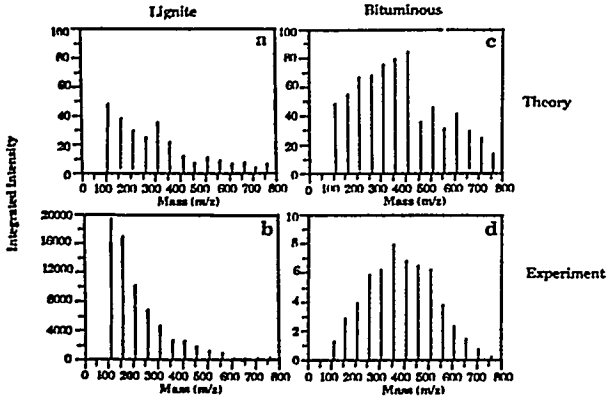

Figure 28 Comparison of measured and predicted tar molecular weight distributions for Zap lignite and Pittsburgh Seam bituminous coal pyrolysed in an f.i.m.s. apparatus. Intensities are summed over 50 u intervals

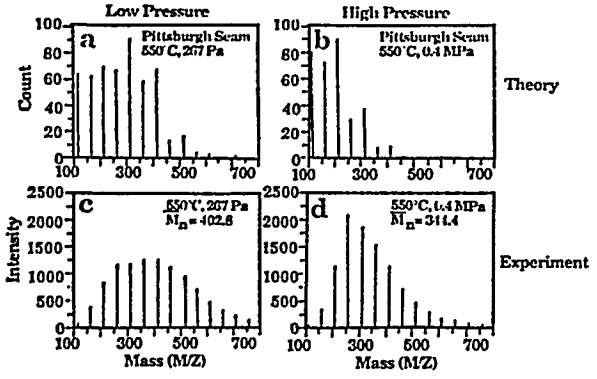

Figure 29 Comparison of predicted (a, b) and measured (c, d) tar molecular weight distributions for Pittsburgh Seam coal pyrolysed in a heated-grid apparatus at 500 K s^{-1}; $\Delta P = 0.2$ atm

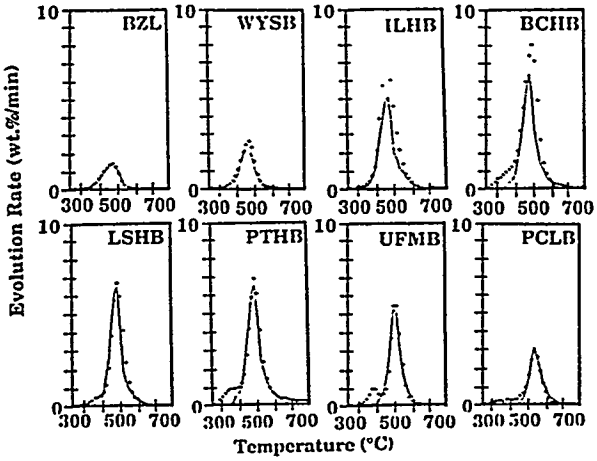

Figure 30 Comparison of measured (points) and predicted (——) t.g.–FT–i.r. analysis of tar evolution for the eight Argonne premium coals. BZL, Beulah Zap lignite; WYSB, Wyodak Anderson subbituminous; ILHB, Illinois No. 6 hvb; BCHB, Blind Canyon hvb; LSHB, Lewiston-Stockton hvb; PTHB, Pittsburgh No. 8 hvb; UFMB, Upper Freeport mvb; PCLB, Pocahontas No. 3 lvb

Yield. The evolution rates measured with t.g.–FT–i.r. are compared in *Figure 30* with the predicted values as a function of temperature for the eight Argonne premium coals. These are the data used in establishing the kinetic rates, so the agreement between the theory and experiments is within the ± 10 K accuracy of the experiment. However, the low-temperature evolution of guest molecules (see peaks and shoulders between 300 and 400°C for Blind Canyon, Lewiston Stockton, Pittsburgh and Upper Freeport) is not well predicted in the standard model. Improvements to predict this early peak have been published elsewhere[8].

Network parameters

As discussed under 'Summary of the FG–DVC model', there are three network parameters l, M_c and H_{al} which are adjusted to fit the laboratory characterization data (t.g.–FT–i.r. tar yield, extract yield and Gieseler fluidity). Whether or not these parameters have any physical or chemical meaning or whether they are only adjustable curve-fitting parameters remains to be seen. To address this question, it is useful to examine their dependence on rank. *Figure 31* shows the adjustable network parameters as functions of the oxygen content of the coal. The oligomer length l and the molecular weight between crosslinks M_c increase smoothly with rank. The concentration of available hydrogen H_{al} for ring stabilization has a maximum for the high-volatile bituminous coals.

Figure 32a compares the predicted extract yield required to obtain the correct Gieseler fluidity and the

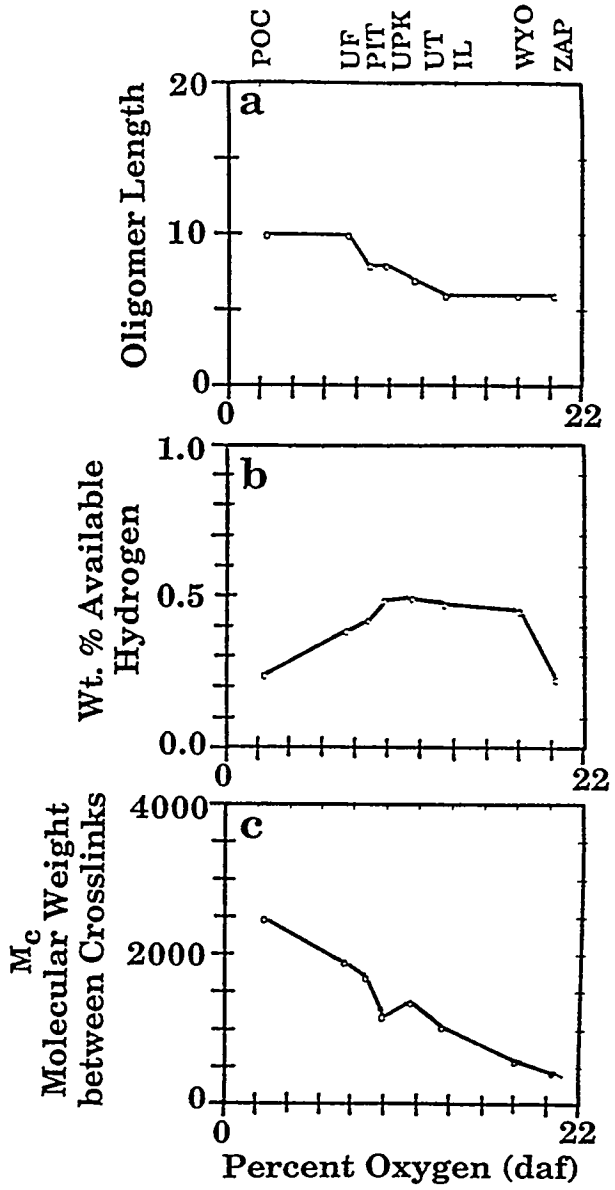

Figure 31 Network parameters for Monte Carlo version of FG-DVC model for the eight Argonne premium coals, as a function of the oxygen content of the coal. The order of the coals is the same as in *Figure 17*

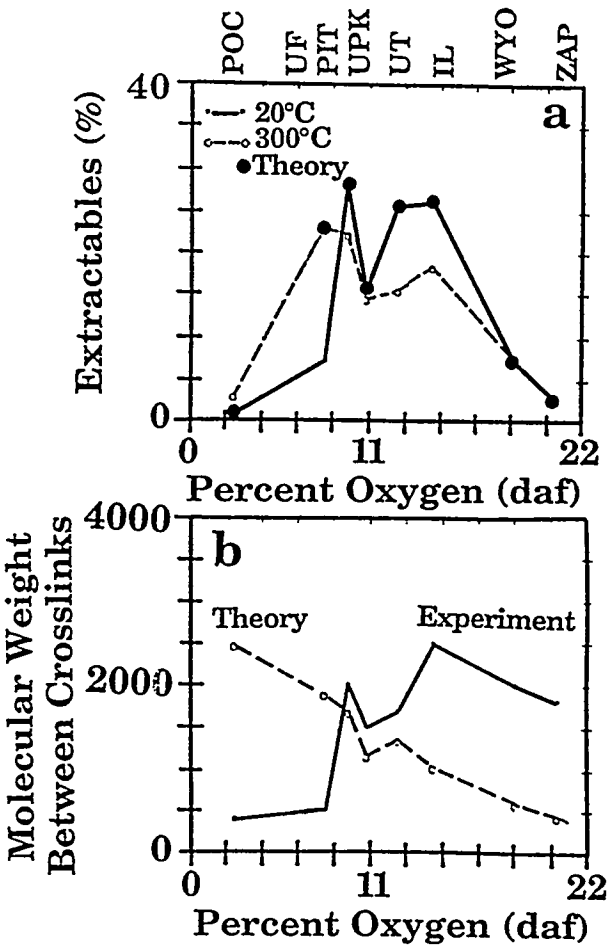

Figure 32 Comparison of experimental and theoretical parameters for the eight Argonne premium coals, as a function of the oxygen content of the coal. The order of the coals is the same as in *Figure 17*

measured extract yield. The model requires a higher extract yield for Upper Freeport and Pocahontas coals than the measured yield. The problem is that there may be an additional kind of weak cross-link for high-rank coals, which affects the solvent extraction experiments at low temperature but not the Gieseler fluidity. Such weak cross-linking could be the aromatic–aromatic interactions suggested by Larsen[79]. When the Upper Freeport coal is heated to 300°C and then cooled, the solvent swelling ratio increases from 1.32 to 2.13 and the extract yield from 10.4 to 21 wt%, suggesting that this treatment may loosen some of these weak bonds irreversibly.

Figure 32b compares the predicted and estimated (from solvent swelling experiments) molecular weight between cross-links. The cross-link density for the bituminous coals is within the range of measured values. However, the model requires a high molecular weight between crosslinks for Pocahontas and Upper Freeport, whereas the solvent swelling ratios would indicate a low M_c. This discrepancy probably has the same cause as discussed above for the solvent extract. The predicted M_c values for the low-rank coals are much lower than those derived from solvent swelling experiments. There are two possible explanations. First, the theories for deriving M_c from solvent swelling are highly controversial. Second, the predicted values are not well-defined, because of the lack of Gieseler fluidity data and the presence of polymethylenes in the extracts of low-rank coals which are unrelated to unattached macromolecular network fragments considered in the model. These discrepancies cannot be resolved without further study.

SUMMARY AND CONCLUSIONS

The paper poses the question: can coal science be predictive? The answer is 'yes' for coal thermal decomposition in particles small enough to be isothermal. It is possible to construct a model based on reasonable assumptions to predict almost all of the observed behaviour. The model has only one parameter (the internal pressure in the transport submodel) which is adjusted for the process conditions. All other model parameters of the coal are fixed for each coal, and are

based on simple laboratory experiments. The model has composition and kinetic parameters to describe the evolution of each individual gas species. These can be determined in t.g.–FT–i.r. experiments and exhibit a systematic variation with rank. There are three network parameters in the Monte Carlo version of the model: the chain length l, the molecular weight between cross-links M_c, and the available donatable hydrogen H_{al}. A similar set of network parameters is used in the percolation theory. They are adjusted to fit the t.g.–FT–i.r. tar yields, extract yields and fluidity. These also exhibit a systematic variation with rank.

The paper explores the six concepts that are the foundation of the FG–DVC model:

1. **The thermal decomposition of functional group sources in the coal yields the light gas species.** The amount and evolution kinetics can be measured by t.g.–FT–i.r., and the functional group changes by FT–i.r. and n.m.r. (CP–MAS–DD). There is good agreement between the model and the results of these measurements on Pittsburgh Seam coal heated at 30 K min^{-1} and for gas evolution for a lignite and Illinois No. 6 bituminous coal at 30 K min^{-1} and 2×10^4 K s^{-1}.
2. **The decomposition of a macromolecular network yields tar and metaplast.** The amount and kinetics of the tar evolution can be measured by t.g.–FT–i.r. and the molecular weight by f.i.m.s. The kinetics of metaplast formation and destruction can be measured by solvent extraction, Gieseler plastometry and proton magnetic resonance thermal analysis (p.m.r.t.a.). Reasonable agreement has been demonstrated for the solvent extract of Pittsburgh Seam coal pyrolysed at 30 K min^{-1} and 640 K s^{-1}. Good agreement is shown for four of the Argonne premium coal samples for Gieseler fluidity, and for one coal by p.m.t.r.a.
3. **The molecular weight distribution of the metaplast depends on the network coordination number.** The coordination number can be determined by solvent swelling and n.m.r. (CP–MAS–DD).
4. **The network decomposition is controlled by bridge breaking, and the amount of bridge breaking is limited by the available donatable hydrogen H_{al}.**
5. **The network solidification is controlled by cross-linking.** The changing cross-link density can be measured by solvent swelling and n.m.r. (CP–MAS–DD). Cross-linking appears to occur with evolution of both CO_2 (before bridge breaking) and CH_4 (after bridge breaking). Thus low-rank coals (which form much CO_2) cross-link before bridge breaking and are thus thermosetting. High-volatile bituminous coals (which form little CO_2) undergo significant bridge breaking before cross-linking and become highly fluid. Weathering, which increases the CO_2 yield, causes increased cross-linking and lowers fluidity. There is good agreement between the predicted and measured cross-link densities and fluidities in the FG–DVC model in which cross-links are correlated with CO_2 and CH_4 gas evolution.
6. **The evolution of tar is controlled by mass transport in which the tar molecules evaporate into the light gas species and are carried out of the coal at rates proportional to their vapour pressure and the volume of light gases.** High pressure reduces the volume of light gases and hence reduces the yield of heavy molecules with low vapour pressure. These changes can be studied with f.i.m.s. The changes in tar yield and molecular weight distribution with pressure have been accurately predicted using the vapour pressure law of Suuberg and co-workers.

Although the experimental results and the model are consistent with the suggested processes, the chemical reactions for bridge breaking, cross-linking and functional group decomposition are not defined in detail. Also there are only sparse data to validate the transport assumption, and the internal pressure in the particle is an adjustable parameter of the model.

ACKNOWLEDGEMENTS

The authors wish to acknowledge the following organizations for their support over the last 10 years: US Department of Energy, Morgantown Energy Technology Center; US Department of Energy, Pittsburgh Energy Technology Center; National Science Foundation; and Gas Research Institute. The authors also wish to acknowledge the extensive contribution from many co-authors who have collaborated in this work: Robert Carangelo, James Markham, Philip Best, Erik Kroo, Yan Ping Zhang, Rosemary Bassilakis, Marie DiTaranto, Girish Deshpande, Po-Liang Chien, H. H. King, Tom Squires and Kevin Squire, who worked at Advanced Fuel Research, Inc.; Meredith Colket from United Technologies Research Center; Douglas Smoot and Scott Brewster from Brigham Young University; Eric Suuberg from Brown University; Ronald Pugmire, David Grant and Mark Solum from the University of Utah; Donald McMillen and Ripudaman Malhotra from SRI International; Rashid Khan from Texaco; Tom Fletcher from Sandia National Laboratory; Leo Lynch and Richard Sakurovs from CSIRO; Bernie Gerstein from Iowa State University; Jean Whelan from Woods Hole Oceanographic Institute; Harold Schobert and Caroline Burgess at Penn State University; Garry Vail, Fred Baudais, Michel Baillargeon and Daniel Gravel from Bomem, Inc.; and Dennis Gerson from IBM Instruments.

REFERENCES

1 Solomon, P. R., Serio, M. A., Carangelo, R. M., Bassilakis, R., Gravel, D., Baillargeon, M., Baudais, F. and Vail, G. *Energy Fuels* 1990, 4, 319
2 Green, T. K., Kovac, J. and Larsen, J. W. *Fuel* 1984, 63, 935
3 Green, T. K., Kovac, J. and Larsen, J. W. In 'Coal Structure' (ed. R. A. Meyers), Academic Press, New York, 1982, p. 199
4 Gieseler plastometer data were supplied by Mr George Engelke of Commercial Testing and Engineering Company
5 Solum, M. A., Pugmire, R. J. and Grant, D. M. *Energy Fuels* 1989, 3, 187
6 St John, G. A., Butrill, S. E. Jr and Anbar, M. *Am. Chem. Soc. Symp. Ser.* 1978, 71, 223
7 Solomon, P. R., Hamblen, D. G., Carangelo, R. M., Serio, M. A. and Deshpande, G. V. *Energy Fuels* 1988, 2, 405
8 Solomon, P. R., Serio, M. A., Hamblen, D. G., Yu, Z. Z. and Charpenay, S. *Am. Chem. Soc. Div. Fuel Chem. Preprints* 1990, Charpenay, S. *Am. Chem. Soc. Div. Fuel Chem. Preprints* 1990, 35(2), 479
9 Solomon, P. R. *Am. Chem. Soc. Adv. Chem. Ser.* 1981, 192, 95
10 Solomon, P. R. and Hamblen, D. G. In 'Chemistry of Coal Conversion' (ed. R. H. Schlosberg), Plenum Press, New York, 1985, pp. 121–251
11 Solomon, P. R., Hamblen, D. G., Carangelo, R. M. and Krause, J. L. In Nineteenth Symp. (Int.) Combustion, Combustion Institute, Pittsburgh, 1982, p. 1139

12 Serio, M. A., Hamblen, D. G., Markham, J. R. and Solomon, P. R. *Energy Fuels* 1987, 1, 138
13 Solomon, P. R. and King, H. H. *Fuel* 1984, 63, 1302
14 Squire, K. R., Carangelo, R. M., DiTaranto, M. B. and Solomon, P. R. *Fuel* 1986, 65, 833
15 Solomon, P. R., Hamblen, D. G., Carangelo, R. M., Serio, M. A. and Deshpande, G. V. *Combust. Flame* 1988, 71, 137
16 Solomon, P. R., Serio, M. A., Carangelo, R. M., Bassilakis, R., Yu, Z. Z., Charpenay, S. and Whelan, J. *J. Anal. Appl. Pyrol.* 1991, 19, 1
17 Suuberg, E. M., Peters, W. A. and Howard, J. B. In 'Seventeenth Symp. (Int.) Combustion', Combustion Institute, Pittsburgh, 1979, p. 117
18 Gavalas, G. R., Cheong, P. H. and Jain, R. *Ind. Eng. Chem. Fundam.* 1981, 20, 113
19 Gavalas, G. R., Cheong, P. H. and Jain, R. *Ind. Eng. Chem. Fundam.* 1981, 20, 122
20 Xu, W. C. and Tomita, A. *Fuel* 1987, 66, 627
21 Van Krevelen, D. W. 'Coal', Elsevier, Amsterdam, 1961
22 Solomon, P. R., Squire, K. R. and Carangelo, R. M. In Int. Conf. Coal Science, Pergamon, Sydney, 1985, p. 945
23 Brenner, D. *Fuel* 1985, 64, 167
24 Lucht, L. M. and Peppas, N. A. *Fuel* 1987, 66, 803
25 Lucht, L. M., Larsen, J. M. and Peppas, N. A. *Energy Fuels* 1987, 1, 56
26 Larsen, J. W. *Am. Chem. Soc. Div. Fuel Chem. Preprints* 1985, 30(4), 444
27 Green, T., Kovac, J., Brenner, D. and Larsen, J. In 'Coal Structure' (ed. R. A. Meyers), Academic Press, New York, 1982, p. 199
28 Hall, P. J., Marsh, H. and Thomas, K. M. *Fuel* 1988, 67, 863
29 Sanada, Y. and Honda, H. *Fuel* 1966, 45, 295
30 Suuberg, E. M., Yoshi, O. and Deevo, S. *Am. Chem. Soc. Div. Fuel Chem. Preprints* 1988, 33(1), 387
31 Gavalas, G. R. In 'Coal Pyrolysis', Elsevier, Amsterdam, 1982, p. 51
32 Solomon, P. R., Hamblen, D. G., Yu, Z. Z. and Serio, M. A. *Fuel* 1990, 69, 754
33 Niksa, S. and Kerstein, A. R. *Combust. Flame* 1986, 66, 95
34 Niksa, S. *Combust. Flame* 1986, 66, 111
35 Niksa, S. and Kerstein, A. R. *Fuel* 1987, 66, 1389
36 Grant, D. M., Pugmire, R. J., Fletcher, T. H. and Kerstein, A. R. *Energy Fuels* 1989, 3, 175
37 Nelson, P. F. *Fuel* 1987, 66, 1264
38 Calkins, W. H., Hagaman, E. and Zeldes, H. *Fuel* 1984, 63, 1113
39 Calkins, W. H. and Tyler, R. J. *Fuel* 1984, 63, 1119
40 Calkins, W. H. *Fuel* 1985, 64, 1125
41 Calkins, W. H., Hovsepian, B. K., Drykacz, G. R., Bloomquist, C. A. A. and Ruscic, L. *Fuel* 1984, 63, 1226
42 Niksa, S. *AIChE J.* 1988, 34, 790
43 Solomon, P. R., Best, P. E., Yu, Z. Z. and Deshpande, G. V. *Am. Chem. Soc. Div. Fuel Chem. Preprints* 1989, 34(3), 895
44 Suuberg, E. M., Lee, D. and Larsen, J. W. *Fuel* 1985, 64, 1668
45 Suuberg, E. M., Unger, P. E. and Larsen, J. W. *Energy Fuels* 1987, 1, 305
46 Bockrath, B. C., Illig, E. G. and Eassell-Bridger, W. D. *Energy Fuels* 1987, 1, 227
47 Solomon, P. R., Serio, M. A., Deshpande, G. V. and Kroo, E. *Energy Fuels* 1990, 4, 42
48 Solomon, P. R. *Am. Chem. Soc. Symp. Ser.* 1981, 169, 61
49 Brown, J. K., Dryden, I. G. C., Dunevein, D. H., Joy, W. K. and Pankhurst, K. S. *J. Inst. Fuel* 1958, 31, 259
50 Orning, A. A. and Greifer, B. *Fuel* 1956, 35, 318
51 Freihaut, J. D., Proscia, W. M. and Seery, D. J. *Energy Fuels* 1989, 3, 692
52 Anthony, D. B. and Howard, J. B. *AIChE J.* 1976, 22, 625
53 Solomon, P. R., Serio, M. A., Carangelo, R. M. and Markham, J. R. *Fuel* 1986, 65, 182
54 Solomon, P. R. and Serio, M. A. In 'Fundamentals of the Physical-Chemistry of Pulverized Coal Combustion' (ed. J. Lahaye and G. Prado), Martinus Nijhoff, 1987, p. 126
55 Kobayashi, H., Howard, J. B. and Sarofim, A. F. In Sixteenth Symp. (Int.) Combustion, Combustion Institute, Pittsburgh, 1977, p. 411
56 Solomon, P. R. and Colket, M. B. In Seventeenth Symp. (Int.) Combustion, Combustion Institute, Pittsburgh, 1979, p. 131
57 Anthony, D. B., Howard, J. B., Hottel, H. C. and Meissner, H. P. In Fifteenth Symp. (Int.) Combustion, Combustion Institute, Pittsburgh, 1974, p. 1303
58 Badzioch, S. and Hawksley, P. G. *Ind. Eng. Chem. Process Des. Dev.* 1970, 9, 521
59 Solomon, P. R., Fletcher, T. H. and Pugmire, R. J. *Fuel* in press
60 Solomon, P. R., Serio, M. A. and Suuberg, E. M. *Prog. Energy Combust. Sci.* 1992, 18, 133
61 Fletcher, T. H. *Combust. Flame* 1989, 78, 223
62 Fletcher, T. H. *Combust. Sci. Technol.* 1989, 63, 89
63 Freihaut, J. D. and Proscia, W. M. *Energy Fuels* 1989, 3, 625
64 Solomon, P. R., Serio, M. A. and Markham, J. R. In Proc. Int. Conf. Coal Science, Tokyo, 1989, p. 575
65 Serio, M. A., Solomon, P. R., Charpenay, S., Yu, Z. Z. and Bassilakis, R. *Am. Chem. Soc. Div. Fuel Chem. Preprints* 1990, 35(3), 808
66 Burnham, A. K., Oh, M. S., Crawford, R. W. and Samoun, A. M. *Energy Fuels* 1989, 3, 42
67 Stein, S. E., Robauch, D. A., Alfieri, A. D. and Miller, R. E. *J. Am. Chem. Soc.* 1982, 104, 6567
68 Solomon, P. R., Charpenay, S., Yu, Z. Z., Serio, M. A., Kroo, E., Solum, M. S. and Pugmire, R. J. In Proc. Int. Conf. Coal Science, Newcastle upon Tyne, 1991, p. 484
69 Lynch, L. J., Sakurovs, R., Webster, D. S. and Redlich, P. J. *Fuel* 1988, 67, 1036
70 Lynch, L. J., Webster, D. S., Sakurovs, R., Barton, W. A. and Maher, T. P. *Fuel* 1988, 67, 579
71 Barton, W. A. and Lynch, L. J. *Energy Fuels* 1989, 3, 402
72 Fong, W. S., Peters, W. A. and Howard, J. B. *Fuel* 1986, 65, 251
73 Sobkowwiak, M., Riesser, B., Given, R. and Painter, P. *Fuel* 1984, 63, 1245
74 Riesser, B., Starsinic, M., Squires, E., Davis, A. and Painter, P. *Fuel* 1984, 63, 1253
75 Solomon, P. R. and Carangelo, R. M. *Fuel* 1988, 67, 949
76 Solomon, P. R. and Carangelo, R. M. *Fuel* 1982, 61, 663
77 Solomon, P. R., Best, P. E., Yu, Z. Z. and Charpenay, S. *Energy Fuels* 1992, 6, 143
78 Wu, M. M., Robbins, G. A., Winschel, R. A. and Burke, F. P. *Energy Fuels* 1988, 2, 150
79 Larsen, J. W. *Am. Chem. Soc. Div. Fuel Chem. Preprints* 1988, 33(1), 400

APPENDIX H

FBED-1 SUBROUTINES

Subroutine Name	Description
ADJSTY0	Adjusts the functional group composition of the selected standard coal to match the ultimate composition of the feed coal.
ASHCP	Initializes the coefficients for the polynomial expression for the ash heat capacity based on either Kopp-Neumann rule or Kirov's expression.
ASHH	Computes the total enthalpy of ash.
AVGATW	Computes the average atomic weight based on the ultimate composition.
BALANC	Computes the overall mass, energy, and elemental balance for the gasifier.
CALC	This routine is the part of the CREE equilibrium subroutines library. It constructs the Newton-Raphson derivative matrix

	for equilibrium solution and solves it using pivotal Gaussian reduction.
COALIN	Reads the input data for the devolatilization submodel.
CONVY	Converts the dependent variables to the quantities of interest, such as total gas enthalpy to gas temperature, total solid enthalpy to solid temperature etc.
CNVYUP	Counterpart of CONVY during the upward integration pass.
CPUTIM	Tracks the total CPU time since the start of the execution.
CREE	Calculates chemical equilibrium composition for the gas phase.
CREE0	Part of the CREE equilibrium subroutines library. Reads and initializes the elemental and species input data and computes various parameters used in the chemical equilibrium calculations.
DDZONE	Computes the ultimate yields and composition of gas, tar and char in the drying and devolatilization zone of the zero-dimensional submodel.
DELTAP	Calculates the pressure drop based on Ergun's equation for packed beds.
DEVOL0	Computes the devolatilization rates for the zero-dimensional submodel.
DEVOL1	Computes the devolatilization rates for the one-dimensional portion of the model.

DLSODES	This is the Lawrence Livermore Solver for the Ordinary Differential Equations. It includes the sparse solver as well as the regular version. The auxiliary routines needed for LSODE or LSODES reside in the file `dlsodes.f`.
DRYING	Computes the rate of evaporation of moisture and the heat of vaporization.
ECHOIN	Echos the input data and writes the derived quantities to the output file fb1out.
ELRATE	Converts the volumetric evolution rates to elemental basis.
EQZONE	Computes the composition and temperature of the streams, leaving the equilibrium zone of the zero-dimensional submodel.
EQEXIT	Computes the temperature of the drying and devolatilization zone, assuming full chemical and thermal equilibrium.
EXITT	Computes the temperature of the drying and devolatilization zone, keeping the devolatilized gases out of equilibrium.
F	Constructs the derivatives of the dependent variables for the downward integration pass.
F0	Constructs the derivatives for the dependent variables for the zero-dimensional portion of the model.
FUP	Constructs the derivatives of the dependent variables for the upward integration pass.
FBED0D	Provides the initial estimates for the effluent gas and tar streams to be used as initial guess to convert the split boundary value problem to an initial value problem.

FBED1D	The main program to predict detailed axial profiles for fixed-bed gasification and combustion.
FGDVC	Computes the devolatilization rates based on the FG-DVC submodel developed by AFR. This subroutine calls RTS, which computes the kinetic rate of devolatilization and PERCVAP, which computes the tar evolution from the char. These and other FG-DVC auxiliary routines are lumped in the file `fgdvc.f`.
FGSET	Computes the devolatilization rates based on the FG-SET submodel.
FREEBD	Calculates the heat exchange between the gas and the solid phase in the free board zone.
GASIN	Computes the composition and the temperature of the blast gas entering the gasifier.
GTEMP	Calculates the temperature of the gas phase given the enthalpy and composition.
HSCHAR	Computes the sensible enthalpy of char based on Merrick's correlation.
HCPS	Part of the CREE equilibrium subroutines library. Calculates the heat capacity, enthalpy and entropy of the gaseous species, as well as of the gas mixture.
HDEVOL	Calculates the heat of devolatilization associated with tar and gas evolution from the char matrix.
HFORM	Calculates the heat of formation of char or coal.

THTAR	Computes the total enthalpy of tar.
HTCOEF	Calculates the heat transfer coefficients for solid-to-gas, solid-to-wall, and gas-to-wall.
HVH2O	Computes the heat of vaporization of moisture at the solid temperature.
IVALU0	Initializes the dependent variables for the zero-dimensional portion of the model.
IVALU1	Initializes the dependent variables for the downward integration pass of the one-dimensional model.
IV1UP	Initializes the dependent variables for the upward integration pass of the one-dimensional model.
MTCOEF	Calculates the mass transfer coefficients.
OMEGAD	Computes the collision integral for diffusivity.
OMEGAM	Computes the collision integral for viscosity.
OXGAS	Calculates the oxidation and gasification rates and associated heat exchange effects.
PDPND	Computes the particle diameter and particle number density.
PTEMP	Calculates the solid temperature given the solid composition and enthalpy.
RTSFXG	Calculates the kinetic rates for devolatilization, assuming that Gaussian remains fixed in shape.

READIN	Reads the input data for the fixed-bed model and computes basis parameters for later use.
SET	Computes the potential tar forming fraction based on Ko's correlation.
SPECE	Part of the CREE equilibrium subroutine library. This subroutine calls CALC to compute the corrections to chemical species and temperature.
T2GEQZ	Calculates the gas phase decomposition of tar to yield gas in equilibrium zone of the the zero-dimensional portion.
TCRACK	Calculates the gas phase decomposition of tar to yield gas.
TRANSP	Calculates the transport properties of the gaseous species and the gas mixture.
ULTCOM	Computes the ultimate composition given the functional group composition of char or tar.
WRT0D	Prints the results of the zero-dimensional portion of the code to the output file `fb1out`.

APPENDIX I

CODE VARIABLES

A partial listing of variables used in FBED-1 is included in this appendix. Variables used within the LSODE routines are not included. Most of the FBED-1 subroutines contain a list of code variables at the beginning. Units are included where appropriate. Also, uppercase letters are used to show how the code variable name was chosen (e.g., diach DIAmeter of reactor CHamber, m).

Variables	Description and Units
a(i)	ln of the pre-exponential factor for ith functional group and bond-breaking kinetics.
a(i,j)	composition of ith element in jth functional group
absth2	amount of ABSTactable H2
abstol	ABSolute TOLerance used in LSODE
acpash	coefficient A for heat CaPacity of ASH, (J/kg K)
adfco2	ADjustable Factor for CO2 gasification reaction
adfdev	ADjustable Factor for DEVolatilization rates
adfh2	ADjustable Factor for H2 gasification reaction
adfh2o	ADjustable Factor for H2O gasification reaction
adfhgw	ADjustable Factor for Heat transfer between Gas and Wall
adfhsg	ADjustable Factor for Heat transfer between Solid and Gas
adfhsw	ADjustable Factor for Heat transfer between Solid and Wall
adfo2	ADjustable Factor for oxidation reaction
alamda(i)	LAMbDA (Carbon stoichiometric coefficient for the oxidation reaction) at ith output point
alpha	coefficient ALPHA in Ko's correlation for x0
apd(i)	Particle Diameter at the ith output point, m

apdivt	Ash Porosity DIVided by Tortuosity, dimensionless
apnd(i)	Particle Number Density at ith output point, #/m^3
arbot(i)	Ar composition in feed gas stream (BOTtom) in ith pass, %
arc(i)	Arrhenius Rate Cons. for ith functional group or tar, 1/s
arco2	Ash Resistance for CO2, s/m
arsco2	Ash ReSistance for CO2, s/m
arco2(i)	Rate of CO2 gasification reaction at ith output point, s/m
area	cross sectional AREA of reactor chamber, m^2
areap	external Particle surface AREA, m^2
arh2	Ash Resistance for H2, s/m
arsh2	Ash ReSistance for H2, s/m
arh2(i)	Rate of H2 gasification reaction at ith output point, s/m
arh2o	Ash Resistance for H2O, s/m
arsh2o	Ash ReSistance for H2O, s/m
arh2o(i)	Rate of H2O gasification reaction at ith output point, s/m
arisum(i)	SUM of gasification and oxidation reactions at ith output point, kg/m^3 s
aro2	Ash Resistance for O2, s/m
arso2	Ash ReSistance for O2, s/m
aro2(i)	Rate of Oxidation reaction at ith output point, s/m
arw(i)	Rate of water vaporization at ith output point, kg/m^3 s
arwhw(i)	Rate of heat release due to Water vaporization at ith output point, J/m^3 s
ashcom(i)	name of ith ASH COMponent
ashh	ASH entHalpy (total) at the tash, J/kg
ashres(i)	ASH RESistance for the ith species or pseduo-species tar
asmrd(i)	SuMmed (total) rate of Devol. at ith output point, kg/m^3 s
asrdhd(i)	product of Summed Rate of Devolatilization and Heat of Devolatiliztion at ith output point, J/m^3 s
asrihi(i)	product of the Summed gasification and oxidation Rates and corresponding Heats of reactions at ith output point, J/m^3 s
asub	species name
atedot(i,j)	Tar Evolution rate for jth functional group at ith output point, kg/kg (initial char) s
atol	Absoltue TOLerance
atomwt	mean ATOMic WeighT of char, kg/kg-atom
ats(i)	Temperature of Solid at ith output point, K
atwth	ATomic Weight of Hydrogen, kg/kg-atom
atwto	ATomic Weight of Oxygen, kg/kg-atom
averat(i,j)	Volumetric Elemental evolution RATe for jth element at ith output point, kg/m^3 s
avgatw	AVeraGe ATomic Weight, (kg/kg-atom)
awash(i)	Atomic Weight of ith ASH component
awchar	Atomic Weight of CHAR, kg/kmol
awfc	Atomic Weight of Feed Coal, kg/kmol
awgdot(i,j)	jth gas functional group's evolution rate at ith output point, kg/s
awtar	Atomic Weight of TAR, kg/kmol or kg-atom
axpos(i)	aXial position at ith output point, m

azrihi(i)	product of zi and Heat of reaction for the oxidation and gasification reactions at ith output point, J/m^3 s
b(i)	Activation energy divided by R for ith functional group and bond-breaking kinetics, K
b0(i)	atom number for reactant mixture, kmol i/kg mixture
basis	specifies whether ash composition is on mass or molar basis
bcpash	coefficient B for heat CaPacity of ASH, (J/kg K^2)
beta	effective length between centers of neighboring solid particles divided by equivalent diameter of the particles
beta	coefficient BETA in Ko's correlation for x0
bf0(i)	atom number for Feed stream 0, kmol (atom i)/kg
bf1(i)	atom number for Feed stream 1, kmol (atom i)/kg
bout0d	Burn OUT for 0-dimensionl submodel
brnbot(i)	predicted BuRN OUT (at BOTtom) in ith pass
brnout	BuRN OUT for 1-dimensional model
ccpash	coefficient C for heat CaPacity of ASH, (J K/kg)
cfrac	instantaneous FRACtion of organic matter in daf coal
cg	molar Concentration of Gas , kmol/m^3
cgco2	molar CO2 Concentration in Gas, kmol(co2)/m^3
cgh2	molar H2 Concentration in Gas, kmol(h2)/m^3
cgh2o	molar H2O Concentration in Gas, kmol(h2o)/m^3
cgo2	molar O2 Concentration in Gas, kmol(o2)/m^3
ch4top(i)	CH4 composition in exit gas stream (at TOP) in ith pass, %
chlgh	reactor CHamber LenGtH, m
chrtot	TOTal instantaneous CHaR functional groups
chvol	reactor CHamber VOLume, m^3
co2bot(i)	CO2 composition in feed gas stream (BOTtom) in ith pass, %
co2crc	Chemical Rate Constant for CO2 gasification, m/s
co2top(i)	CO2 composition in exit gas stream (at TOP) in ith pass, %
cotop(i)	CO composition in exit gas stream (at TOP) in ith pass, %
cp(i)	non-dimensional heat CaPacity of species i
cpa(i)	heat CaPacity cofficient A for ith ash component, (J/kg K)
cpb(i)	heat CaPacity cofficient B for ith ash component, (J/kg K^2)
cpc(i)	heat CaPacity cofficient C for ith ash component, (J K/kg)
cpg	heat CaPacity of gas mixture, (J/kg K)
cph2ol	heat CaPacity of Liquid H2O, J/kg K
cplash	heat CaPacity of Liquid ASH, (J/kg K)
cpliq(i)	heat CaPacity of ith LIQuid ASH component
cpsout	heat CaPacity of OUTgoing Solids from the eq. zone, J/kg K
cpsum	non-dimensional heat CaPacity of gaseous mixture
crco2	Chemical Resistance for CO2, s/m
crh2	Chemical Resistance for H2, s/m
crh2o	Chemical Resistance for H2O, s/m
cro2	Chemical Resistance for O2, s/m
dafcrg	initial DAF ChaRGe of feed coal, kg/m^3
datafl	name of selected (or user specified) DATA FiLe
dateid	DATE IDentification stamp
delab	Binary polar contribution parameter for species a and b
deltap	particle over pressure, FG-DVC parameter, atm

```
deltap      axial pressure gradient, Pa/m
deltat      Difference between texit and free board temperature, (K)
deltat      Tolerance for the feed gas stream temperature, K
dendaf      true DENsity of DAF char, kg/m^3
diach       DIAmeter of CHamber, m
difco2      molecular DIFfusivity OF CO2, m^2/s
diffim(i)   DIFFusivity of ith species in the gas Mixture, m^2/s
difh2o      molecular DIFfusivity of H2O, m^2/s
difo2       molecular DIFfusivity OF O2, m^2/s
distnc       DISTaNCe between the feed coal and standard coals on h/c vs o/c
plot.
dvdone      logical variable indicating if DeVolatilization is DONE
dwttot      TOTal rate of change of the Tar forming fraction
eco2        activation Energy for CO2 gasification reaction, J/kmol
effdif(i)   Effective DIFfusivity of ith species,  m^2/s
eh2         activation Energy for H2 gasification reaction, J/kmol
eh2o        activation Energy for H2O gasification reaction, J/kmol
elatwt      ELements ATomic WeighT in the order C,H,O,N,S, kg/kg-atom
elemnt      ELEMeNt's names
emiss       solid EMISSivity
eo2         activation Energy for O2 oxidation reaction, J/kmol
eqgflo      EQuilibrium Gas FLOw rate (doesn't include tar), kg/s
er          Equivalence Ratio i. e., fuel-to-oxidizer ratio
ergk        Effective Radial conductivity of gas, J/m s K
ersk        Effective Radial conductivity of Solid, J/m s K
factor      Value of adjustment/correction FACTOR gas enthalpy at top
fcall       logical variable indicating the First CALL to routine
fcelmi      Flow rate of Char ELements In, kg/s
fcelmo      Flow rate of Char ELements Out, kg/s
fchar       Flow rate of CHAR, kg/s
fchrhi      Flow rate of Char entHalpy In, J/kg
fchrho      Flow rate of Char entHalpy Out, J/kg
fdafch      Flow rate of DAF CHar, kg/s
fdaffc      Flow rate of DAF Feed Coal, kg/s
fdvgas(i)   ith species molar Flow rate in DeVolatilized gas, kmol/s
ffco2       Frequency Factor for CO2 gasification reaction, m/s K
ffh2        Frequency Factor for H2 gasification reactio, m/s K
ffh2o       Frequency Factor for H2O gasification reaction, m/s K
ffo2        Frequency Factor for O2 oxidation  reaction, m/s K
fgchar(i)   fraction of ith Functional Group in CHAR
fgelc(j,i)  ELemental Compostion of jth element in ith Functional Group
fgelmi      Flow rate of Gas ELements In, kg/s
fgelmo      Flow rate of Gas ELements Out, kg/s
fghin       Flow rate of Gas entHalpy IN, J/kg
fghout      Flow rate of Gas entHalpy OUT, J/kg
fgmw(i)     Molecular Weight of ith Functional Group, kg/kmol
fgname(i)   NAME of ith Functional Group
flmres(i)   FiLM RESistance for the ith species or pseduo-species tar
floar       FLow rate of ARgon, kg/s
```

floash	FLOw rate of ASH, kg/s
flochr	FLOw rate of CHar, kg/s
flogas	Flow rate of gases including tar, kg/s
flogeq	FLOw rate of gases in EQuilibrium zone, kg/s
flogin	FLOw rate of total Gas IN, kg/s
floh2o	FLOw rate of slurry H2O (coal moisture), kg/s
flotar	FLOw rate of TAR, kg/s
flotgg	Flow rate of tar Generated Gases, kg/s
flowc	FLOW rate of feed Coal, kg/s
flowo	FLOW rate of Oxidizer in feed, air or oxygen, kg/s
flows	FLOW rate of Steam in feed, kg/s
fmax	Value of the function for bisection method at xmax
fmid	Value of the function for bisection method at xmid
fmin	Value of the function for bisection method at xmin
fmoist	Flow rate of MOISTure in coal, kg/s
frco2	Film Resistance for CO2, s/m
frctar	Flow rate of ReCycled TAR, kg/s
frh2	Film Resistance for H2, s/m
frh2o	Film Resistance for H2O, s/m
fro2	Film Resistance for O2, s/m
fsolid	Flow rate of SOLID (fdafch+fmoist+floash)
fsout	Flow rate of OUTgoing Solids from the eq. zone, kg/s
fsuba	aromaticity of the coal, parameter of Ko's correlation
fsyngs	Flow rate of SYSnthesis GaS, kg/s
ftelmi	Flow rate of Tar ELements In, kg/s
ftelmo	Flow rate of Tar ELements Out, kg/s
fthin	Flow rate of Tar entHalpy IN, J/kg
fthout	Flow rate of Tar entHalpy OUT, J/kg
fts	enthalpy Function computed at Temperature of Solid
fuppas	logical specifying Final Upward PASS
gamma	PARTICLE SWELLING PARAMETER
gasden	GAS mixture's DENsity, (kg/m^3)
gasflo	FLOW rate of Oxidizer in feed, air or oxygen, kg/s
gashr	Gas's Heating rate, K/s
gastmp(i,j)	GAS TeMPeraturure in ith integration pass at jth point, K
gasvel	GAS superficial VELocity, m/s
gelflo	light gases ELemental FLOw rate, kg/s
gk	Gas thermal conductivity, J/smK
gmflux	Gas superficial Mass FLUX, kg/s m^2
gmw	Gas mixture Molecular Weight
gtime	Gas residence TIME, s
gvisc	Gas VISCosity, kg/m s
h0(i)	molar enthalpy of species i, J/kmol(specie i)
h0(i)	non-dimensional entHalpy of species i
h0sum	non-dimensional heat CaPacity of gaseous mixture
h2crc	Chemical Rate Constant for H2 gasification, m/s
h2cstd	Hydrogen to Carbon ratio of standard coals
h2obot(i)	H2O composition in feed gas stream (BOTtom) in ith pass, %
h2ocrc	Chemical Rate Constant for H2O gasification, m/s

```
h2omw       Molecular Weight of H2O, kg/kmol
h2otop(i)   H2O composition in exit gas stream (at TOP) in ith pass, %
h2top(i)    H2 composition in exit gas stream (at TOP) in ith pass, %
hash        total entHalpy of ASH, J/kg
hashtc      total entHalpy of ASH at TCoal, J/kg
hashtx      total entHalpy of ASH at TeXit, J/kg
hbound      logical specifying Higher BOUND in bisection method obtained
hchar       total entHalpy of CHAR, J/kg
hchin       entHalpy of CHar of the INcoming stream to eq. zone, J/kg
hdev        Heat of DEVolatilization,
hdevi       contribution to the Heat of DEVOLatilization by ith light gaseous
            species or the pseudospecies tar
heq         entHalpy of gases in EQuilibrium zone, J/kg
hf0         entHalpy of Feed stream 0 (air or oxygen), J/kg
hf1         enthalpy of Feed stream 1 (steam), J/kg
hfash       Heat of Formation of ASH, J/kg
hfchar      Heat of Formation of CHAR, J/kg
hffc        Heat of Formation of Feed Coal, J/kg
hfh2o       Heat of Formation of H2O, J/kg
hfh2ol      Heat of Formation of Liquid H2O, J/kg
hgin        Total entHalpy flow rate of Gas IN, J/kg
hgtop       entHalpy of Gas at gasifier TOP, J/kg
hh2o        total entHalpy of H2O, J/kg
hhv         Higher Heating Value of Coal, J/kg
hlh2o       Latent Heat of vaporization of H2O, J/kg
hmash       Heat of fusion (Melting) of ASH, J/kg
hmax        MAXimum step size for LSODE integration package
hmoist      total entHalpy of moisture at tcoal, J/kg
hrctar      entHalpy of ReCycled TAR, J/kg
hrg         entHalpy of Gas stream at gasifier top excluding tar, J/kg
hrs         Radiation coefficient for Solid, j/m^2sK
hrv         Void to void Radiative Heat transfer coeff., J/m^2sK
hrxn1       total enthalpy production for:  C + CO2 --> 2CO, J/kg
hrxn2       total enthalpy production for:  C + 2H2 --> CH4, J/kg
hrxn3       total enthalpy production for:  C + H2O --> H2 + CO, J/kg
hrxn4       total enthalpy production for:  C + O2 --> CO + CO2, J/kg
hs          entHAlpy of Solid, J/kg
hsfc        Sensible entHalpy of Feed Coal, J/kg
hsg         Heat transfer coefficient for Solid-to-Gas, J/sm^2K
hsub0       specific enthalpy of the gaseous mixture, [J/kg]
htar        entHalpy of Tar, J/kg
htaro       total entHalpy of TAR in the outlet stream, J/kg
htloss      HeaT LOSS through reactor walls, J/s or watts
htref       entHalpy of char at REFerence Temperature (298.15 K), J/kg
htsatl      sensible entHalpy of SATurated liquid h2o, J/kg
hvap        Heat of Vaoprization of H2O at temperature T, J/kg
hvapts      Heat of Vaoprization of H2O at temperature TSat, J/kg
hw          overall Heat Transfer to Wall, J/m^2sK
icnv        Index on Non-Voltile carbon functional group
```

idcoal	IDentification number of COAL
iel	Index on ELements
ifg	Index on Functional Groups
ihcps	index for calculations of some/all thermodynamic properties = 0, computes heat capacity only = 1, computes heat capacity and enthalpies only = 2, computes heat capacities, enthalpies and entropies
ila	eLement Identification number for Argon
ilc	eLement Identification number for Carbon
ilh	eLement Identification number for Hydrogen
iln	eLement Identification number for Nitrogen
ilo	eLement Identification number for Oxygen
ils	eLement Identification number for Sulfur
ind	local INDex
indx(i)	mapping INDeX between functional groups & gaseous species
indx15(i)	mapping INDeX between functional groups & gaseous species, when the problem is setup for 15 gaseous species
indx1d	INDeX pointer for species flow rates in the 1-D portion
indx22(i)	mapping INDeX between functional groups & gaseous species, when the problem is setup for 22 gaseous species
indxup	INDeX pointerfor species flow rates in UPward integration
intrac	logical flag specifying INTeRACtive simulation
iopt	Indicator specifiying OPTional inputs are used for LSODE
iout	Index on OUTput points
ipass	index on Integration PASS
isorg	Index on ORGanic Sulfur functional group
itask	LSODE parameter specifing one-step/multi-step output
itol	LSODE parameter specifing mix of tolerances
itratn	number of downward integration passes before ITRATioNs
iwork	Integer WORK array used by LSODE
ix	Index for eXperimental data
kinvis	KINemetic VIScosity of gas, m^2/s
lambda	Carbon stoicheometic coef for oxidation reaction
lashcp	Logical selecting Kirov or Kopp-Neumann rule for ASH CP
lbound	logical specifyinh Lower BOUND in bisection method obtained
ldebug	logical variable to turn on DEBUGging in equilibrium routines
ldvc	Logical variable to select between fg-DVC and fg-set model
lexpt	Logical specifying availability of EXPerimenTal data
lfinsh	Logical vraible to FINiSH integration
lfixg	Logical selecting FIXed or variable Gaussian for devol. rates
lfreeb	Logical variable to perform FREEBoard calculation using qfreeb
lgaseq	Logical variable to keep all exit gases but tar in equil in 0-D
liw	declared Length of array IWork for LSODE
ljkstm	Logical prompting wall heat loss calculations using JacKet STeaM
lnoeq	Logical variable prompting to perform NOn-EQuilibrium cals.
lrw	declared Length of array RWork for LSODE
lstiff	Logical variable specifies the use of STIFF LSODE solver
ltareq	Logical indicating if TAR is to be kept in EQuilibrium
lua	Logical variable prompting use of ua in heat loss calc.

lup	Logical variable setting upward integration
lx0	Logical variable to use usrx0 for x0 rather than SET model x0
lzerod	Logical flag to indicate call from ZERO-Dimensional part
maxel	MAXimum number of ELements
maxfg	Maximum number of Functional Groups
maxits	MAXimum number of ITerationS
maxsp	MAXimum number of SPecies set in parameter statement
mf	Method Flag for LSODE
mnashc	Maximum Number of ASH Components
mneq0d	Maximum Number for EQuations for 0-Dimensional submodel
mneq1d	Maximum Number for EQuations for 1-Dimensional simulations
mout	Maximum number of OUTput points
mpass	Maximum number of integration PASSes
mtc(i)	Mass transfer Coefficient for the ith species, m/s
mwh2o	Molecular Weight of H2O, kg/kmol
mxolig	MaXimum number of OLIGomers
n2bot(i)	N2 composition in feed gas stream (BOTtom) in ith pass, %
n2top(i)	N2 composition in exit gas stream (at TOP) in ith pass, %
nalabil	Number of LABILe bridges
narrow	logical specifying NARROW range of bisection method variable
nashc	Number of ASH Components
natoms(j,i)	Number of ATOMS of jth elememt in ith functional group
nbars	Number of BARS in output plot
nbins	Number of tar mass BINS
ncatom(i)	Number of Carbon ATOMs in ith functional group
ncoals	Number of standard COALS
ndat	Number of DATa points for output plot
ndebug	DEBUG print flag used in equilibrium routines
ndelt	iNdex to override DELtaT
ndpass	Number of Downward integration PASS
nelem	Number of ELEMents
neq	Number of EQuations
neq0d	Number of EQuations for 0-Dimensional submodel
neqdev	Number of EQuations for DEVolatilization submodel
nequp	Number of EQuations for UPward integration pass
nfac	iNdex to override correction FACtor in bisection method
nfg	Number of Functional Groups
nhatom(i)	Number of Hydrogen ATOMs in ith functional group
nlm	Number of eLeMents
nnatom(i)	Number of Nitrogen ATOMs in ith functional group
noatom(i)	Number of Oxygen ATOMs in ith functional group
nolig	Number of OLIGomers
nout	Number of OUTput points in downward integration pass
ns	Number of gaseous Species
nsatom(i)	Number of Sulfur ATOMs in ith functional group
nspc	Number of SPeCies listed for output plot
ntpass	Number of Total integration PASSes
nup	Number of output points in UPward integration pass
nupass	logical variable indicating a NU integration pass

nxlink	Number of X-LINKs, parameter of Ko's correlation
nxtrld	Number of eXTRa equations for 1-Dimensional portion
o2bot(i)	O2 composition in feed gas stream (BOTtom) in ith pass, %
o2crc	Chemical Rate Constant for O2 (oxidation) reaction, m/s
o2cstd	Oxygen to Carbon ratio of standard coals
oh	OH group fraction, dry, mineral-free basis, (Ko's correlation)
omegad	Diffusion collision integral, dimensionless
omegam	Viscosity collision integral, dimensionless
p	Presure, Pa
p,p0,p1	values of temperature (independent variable) in secant method following Burden and Faires's nomenclature.
pa	pressure used in equilibrium routines, n/m^2 or pa
patm	Pressure in ATMospheres, atm
pbar	Pressure in BARs, bar
pbotom	Pressure at the BOTtom of the gasifier, Pa
pc	Critical Pressure of H2O, bar
pd	Particle Diameter, m
pdash(i)	ASH Particle Diameter (at BOTtom) in ith pass, m
pdist(i,j)	Probability Distribution function for jth tar in ith mass bin, kg i/kg j-mer
phi	coefficients for heat of combustion of elements C,H,O,N,S
phi	bed packing parameter
phico2	carbon stoichiometic coefficient for CO2 gasificaton rxn.
phih2	carbon stoichiometic coefficient for H2 gasification rxn.
phih2o	carbon stoichiometic coefficient for H2O gasificaton rxn.
phio2	carbon stoichiometic coefficient for O2 oxidation rxn.
pi	constant PI
pnd	Particle Number Density, 1/m^3
poros	POROuSity of coal
pr	PRandtl number
pred	REDuced Pressure
pres	reactor PRESsure at bed top, Pa
press	PRESSure, pa
presur	PRESsURe, Pa
presur(i,j)	gasifer PRESsURe in ith integration pass at jth point, Pa
psoft	number fraction of labile bridges
ptff	Potential Tar Forming Fraction
ptotal	number fraction of total bridges
q0,q1	values of the function in secant method following Burden and Faires's nomenclature.
qfreeb	heat loss in FREEBoard, watts
qgw	volumetric heat transfer rate from Gas to the Wall, J/m^3 s
qsg	volumetric heat transfer rate from Solid to Gas, J/m^3 s
qsw	volumetric heat transfer rate from Solid to the Wall, J/m^3 s
qtotal	number fraction of cross-links
qw	volumetric heat transfer rate to the Wall, J/m^3 s
qwalld(i)	1-D WALL heat loss in ith integration pass, J/s
qwall	heat LOSS through walls, J/s
r	Universal gas constant, J/kg-mole K

rco2	volumetric CO2 gasification rate, kg/m^3 s
rdev(i)	total (tar & gas) volumetric Devolatilization Rate, kg(i)/m^3 s
rdevol	Rate of DEVOLatilization of light gaseous species or pseudospecies tar
rdgas(i)	Rate of Devolatilization of ith GAS functional group, kg/m^3 s
rdtar(i)	Rate of Devolatilization of ith TAR functional group, kg/m^3 s
re	REynold number
reltol	RELative TOLerance used in LSODE
rgasin	INverse of universal GAS constant, kmol K/J
rh2	volumetric H2 gasification rate, kg/m^3 s
rh2o	volumetric H2O gasification rate, kg/m^3 s
rhog	gas density, kg/m^3
risum	SUM of oxidation and gasfication rates, kg/m^3 s
ro2	volumetric O2 gasification rate, kg/m^3 s
rskgk	Ratio of Solid conductivity to Gas conductivity
rtol	Relative TOLerance
rw	volumetric moisture evaporation rate, kg(H2O)/m^3 s
rwhw	volumetric energy production from evaporation, J/m^3 s
rwork	Real WORK array used by LSODE
s0(i)	non-dimensional entropy of species i
s0sum	non-dimensional entropy of gaseous mixture
s2(i)	mole number of species i, kmol i/kg gas
sc(i)	SChmidt number for the ith species
scco2	SChmidt number for CO2
sch2	SChmidt number for H2
sch2o	SChmidt number for H2O
sco2	SChmidt number for O2
schar	Sum of CHAR functional groups in devolatilized char
sgas	Sum of devolatilized light GAS functional groups
sigma1	percolation submodel parameter
sigma2	percolation submodel parameter
sigmaa(i)	Standard deviation divided by R for ith functional group and bond-breaking kinetics, K
sk	Solid thermal conductivity, J/smK
sm	reciprocal of mixture molecular weight, kmol/kg
small	A SMALL constant
smrd	Summed rate of DEvolatilzation, kg /m^3 s
smrdhd	Sum rate of Heat Release due to DEvolatilzation , J/m^3 s
smrihi	volumetric energy production from char ox/gas, j/m^3_s
smw(i)	Species i's Molecular Weight, kg/kmol
solhr	SOLid's Heating rate, K/s
soltmp(i,j)	SOLid TeMPeraturure in ith integration pass at jth point, K
spcmg0(i)	mole numbers for the mixed gas stream, kmol(species i)/kg
specf0(i)	mole numbers for Feed stream 0, kmol(specie)/kg
specf1(i)	mole numbers for Feed stream 1, kmol(specie)/kg
specm(i)	SPEciec i's Molar flow rate, kmol/s
srgk	Static Radial Gas conductivity, J/smK
srk	Static Radial conductivity, J/smK
srsk	Static Radial Solid conductivity, J/smK

star	Sum of devolatilized TAR functional groups
stdfls	names of STanDard coals input data FiLeS
stime	Solid residence TIME, s
sum	array of elemental SUMs in adjusted functional groups
sumash	SUM of the ASH composition
sumcfg	instantaneous SUM of Char Functional GRoup fraction
switch	logical variable indicating SWTICH from/to eq. calc.
t	Temperature, K
t	independet variable, i.e., time for 0-d portion, sec
t2g(i)	Tar's ith functional group decomposed to Gas
tarin	TAR IN rate to the eq. zone, kg/s
tartop(i)	TAR flow rate in exit gas stream (top) in ith pass, kg/s
tash	Temperature of ASH (K)
tc	Critical Temperature of H2O, K
tcoal	Temperature of feed COAL, K
tcrtar	Temperature of ReCycled Tar, K
tdd	Temperature in the Drying and Devolatilization zone, K
telmin	Total flow rate of ELeMents IN, kg/s
telmot	Total flow rate of ELeMents OuT, kg/s
teq	Temperature in the EQuilibrium zone, K
texit	Temperature of the EXIT gaseous stream from D&D zone, K
tf0	Temperature of Feed stream 0 (air or oxygen), K
tf1	Temperature of Feed stream 1 (steam), K
tfb	Temperature in Free Board, K
tfbold	Temperature in Free Board computed in previous iteration, K
tfilm	Temperature of Film, K
tg	Temperature of Gas, K
tgasin	Total flow rate of GAS IN, kg/s
tgbot(i)	Temperature of the feed gas stream (BOTtom) in ith pass, K
tgin	Temperature of Gas IN, K
tgtop(i)	Temperature of the exit GAS stream (at TOP) in ith pass, K
thloss	Total entHalpy flow LOSS, J/kg
tinfnt	Time at INFiNiTy, s
tk	Temperature of the gaseous mixture [K]
tmash	Temperature (Melting) of ASH, (K)
tmax	MAXimum temperature for the applicability range, K
tmin	MINimum temperature for the applicability range, K
tol	TOlerance
toldi	Temperature in one step OLDer Iteration, K
tothin	TOTal entHalpy flow rate IN, J/kg
tothot	TOTal entHalpy flow rate OuT, J/kg
totin	TOTal mass flow rate In, kg/s
totkg	TOTal mass flow rate, kg/s
totkm	TOTal molar flow rate of product gases, (kmol/s)
totlos	TOTal LOSt mass flow rate, kg/s
totmol	TOTal molar flow rate, kmol/s
totout	TOTal mass flow rate OUT, kg/s
tott2g	TOTal Tar decomposed to Gas
tottar	TOTal flow rate of TAR, kg/s

trco2	Total Resistance for CO2, s/m
trctar	Temperature of ReCycle TAR, K
trdev(i)	Total Rate of DEV. of light gases and tar
trdgas	Total Rate of Devolatilization of light GASes
trdtar	Total Rate of Devolatilization of TAR
tred	REDuced temperature
tref	REFerence Temperature, K
trf	Tar Recycle Fraction, only used if l0d = t
trh2	Total Resistance for H2, s/m
trh2o	Total Resistance for H2O, s/m
tro2	Total Resistance for O2, s/m
ts	Temperature of Solid, K
ts0d	Solid Temp. in 0-D's drying and devolatilization zone, K
tsat	Saturation Temperature of H2O at pressure p, K
tsolid	local SOLID Temperature, K
tsolin	Total flow rate of SOLIDS IN, kg/s
tsolot	Total flow rate of SOLIDS OuT, kg/s
tsout	Temperature of OUTgoing Solids from the eq. zone, K
tstar	Reduced temperature, dimensionless
tswtch	Temperature at which SWiTCH is made to non-equil. cals., K
ttarin	Total flow rate of TAR IN, kg/s
twall	WALL Temperature, K
tzero	Time ZERO at start of integration, s
ua	u multiplied by wall surface area, J/s K
udafch	Ultimate composition of DAF CHar, mass fract. [C,H,O,N,S]
udaffc	Ultimate DAF composition of Feed Coal
udaft	Ultimate DAF composition of Tar
ulcomp	ULtimate COMPosition, dry ash-free basis
ultdaf	ULTimate Dry, Ash-Free composition order must be C,H,O,N,S
ulttgg	Ult. composition of Tar Generated Gas (for balance purpose)
verate(i)	net Volumetric Evolution RATE for ith element, kg(i)/m^3 s
vf	bed Void Fraction = (bed vol.-particle vol.)/bed vol.
vgas	Velocity of GAS stream, m/s
vinf	ultimate (at INFinite time) Voltile yield
vsolid	Velocity of SOLID stream, m/s
vsubt	instantaneous volatiles yield
watrmw	Molecular Weight of WATeR, kg/kmol
wchar(i)	Weight fraction of Ith CHAR functional group
wgas(i)	Weight fraction of Ith GAS functional group
wtar(i)	Weight fraction of Ith TAR functional group
wtash	array containing the composition of ash [fraction]
xgas(i)	mole fraction of ith species in the GASeous mixture, (%m)
x0	Potential tar forming fraction (input for fgset submodel)
x0pred	Potential tar forming fraction, PREDicited in FG-DVC
xeff	cross-link efficiency for the functional groups
xgasin(i)	mole fraction of ith species in GAS IN
xhyd	fraction of HYDrogen in unadjusted functional groups
xmax	Higher value of independent variable for bisection method
xmfash(i)	normalized Molar composition of ith ASH component

xmid	mid value of independent value for the bisection method
xmin	lower value of independent variable for bisection method
xntrgn	fraction of NiTRoGeN in unadjusted functional groups
xoxygn	fraction of OXYGeN in unadjusted functional groups
xsurf	water mole fraction at particle surface
xtar	qunatity XTAR used in the Ko's correlation for x0
y0	adjusted functional group composition of feed coal
y0	functional group composition of standard coal
ydot	Vector of derivatives of the dependent variables
ynoneq(i)	NON-EQuilibrium mass flow rate of ith gas species, kg/s
ysav	local array to SAVe the initialized Y's
yup	vector of dependent variables for upward integration pass
z	coefficients for the calculation of thermodynamic properties
zbotom	axial position at the BOTtOM of the gasifier, m
zeta	particle area factor to account for internal burning
zi	heat of reaction partition, if zi =1 HRNX to particle
zirihi	heat of reaction assigned to solid, J/m^3 s (Not active in code)

APPENDIX J

FBED-1 GRAPHICS

FBED-1 code produces output in standard ASCII files. These files can be used in conjunction with any popular graphics package to plot the quantities of interest. In addition, two FORTRAN programs written for the DISSPLA graphics package are also distributed with the FBED-1 code. This Appendix includes the input files to setup these plots, and the procedure to compile, execute and print the plots. The reader is referred to the DISSPLA user's manual (Computer Associates, 1989) for the description of the subroutines.

The programs PLOT1 and PLOT2 generate the plots shown in Figures 6.1 and 6.2. The corresponding input files to set up these plots are PLOT1.DIM and PLOT2.DIM, as shown in Tables J.1 and J.2, respectively. These files contain the information regarding the names of the files containing the FBED-1 output data, as well as sizes and the locations of the subplots. All input data in these files are explained as well. The output of these programs is PLOT1.POP and PLOT2.POP respectively. These output files are in a device independent format and can be viewed or plotted on various output devices using a script program called POPOUT. The programs needed to run this script file are also distributed with the FBED-1 code. However, it is pointed out that the DISSPLA graphics package in our Research Center (ACERC, BYU) is available on a SUN computer, and some

Table J.1 Input file plot1.dim for the program plot1

```
'cconv.out'           DATFILE1
'pdia.out'            DATFILE2
'compos.out'          DATFILE3
'tandp.out'           DATFILE4
8.50,11.0             XPAGE,YPAGE
2.75,2.75             XSIZE,YSIZE
0.0,0.5,2.25          XS,XI,XF
1.50,2.00             XORIGN(1),YORIGN(1)
0.0,0.10,0.495        YS(1),YI(1),YF(1)
4.30,2.00             XORIGN(2),YORIGN(2)
0.0,0.5,2.95          YS(2),YI(2),YF(2)
1.50,4.80             XORIGN(3),YORIGN(3)
0.0,10.0,69.9         YS(3),YI(3),YF(3)
4.30,4.80             XORIGN(4),YORIGN(4)
0.0,0.2,0.895         YS(4),YI(4),YF(4)
1.50,7.60             XORIGN(5),YORIGN(5)
0.0,500.0,2500.0      YS(5),YI(5),YF(5)
4.30,7.60             XORIGN(6),YORIGN(6)
102.0,1.0,104.0       YS(6),YI(6),YF(6)
0.0,0.5,2.7           YS2,YI2,YF2
1.225,0.15            X AND Y COORDINATES FOR DRYING RATE CURVE LABEL
1,1.75,0.15,2.0,0.092867 COORDINATES FOR THE ARROW FOR DRYING RATE CURVE
0.70,0.40             X AND Y COORDINATES FOR DEVOLATILIZATIONOLATILIZATION RATE
0.125,0.16            X AND Y COORDINATES FOR OXIDATION RATE CURVE LABEL
0.975,0.05            X AND Y COORDINATES FOR CO2 GASIFICATION RATE CURVE LABEL
1,1.20,0.045,1.00,0.01729 COORDINATES FOR THE ARROW FOR CO2 GASIFICATION CURVE
0.70,0.11             X AND Y COORDINATES FOR FOR H2O GASIFICATION CURVE LABEL
0,1.00,0.20           X AND Y COORDINATES FOR FOR H2 GASIFICATION CURVE LABEL
1.00,0.55             X AND Y COORDINATES FOR BURNOUT PROFILE LABEL
0.80,2.10             X AND Y COORDINATES FOR PARTICLE DIAMETER PROFILE LABEL
0.725,1.15            X AND Y COORDINATES FOR UNREACTED CORE DIAMETER PROFILE LAB
1.0,55.0              X AND Y COORDINATES FOR N2 COMPOSITION PROFILE LABEL
0.725,22.5            X AND Y COORDINATES FOR H2O COMPOSITION PROFILE LABEL
0.20,17.5             X AND Y COORDINATES FOR O2 COMPOSITION PROFILE LABEL
0.40,3.5              X AND Y COORDINATES FOR CO2 COMPOSITION PROFILE LABEL
1.60,14.5             X AND Y COORDINATES FOR H2 COMPOSITION PROFILE LABEL
1.7,25.5              X AND Y COORDINATES FOR CO COMPOSITION PROFILE LABEL
1.85,2.50             X AND Y COORDINATES FOR CH4 COMPOSITION PROFILE LABEL
1.0,0.70              X AND Y COORDINATES FOR AR COMPOSITION PROFILE LABEL
0.65,0.365            X AND Y COORDINATES FOR OH COMPOSITION PROFILE LABEL
0.45,0.175            X AND Y COORDINATES FOR NO COMPOSITION PROFILE LABEL
1.775,0.285           X AND Y COORDINATES FOR H2S COMPOSITION PROFILE LABEL
0.8,0.20              X AND Y COORDINATES FOR SO2 COMPOSITION PROFILE LABEL
1.80,0.145            X AND Y COORDINATES FOR HCN COMPOSITION PROFILE LABEL
0.90,2050.0           X AND Y COORDINATES FOR GAS TEMPERATURE CURVE LABEL
1.25,1300.0           X AND Y COORDINATES FOR SOLID TEMPERATURE CURVE LABEL
```

Table J.2 Input data file plot2.dim for the program plot2

```
'compar.out'          INPUT DATAFILE DFILE1
'tandp.out'           INPUT DATAFILE DFILE5
'tdata.jetp68'        EXPERIMENTAL TEMPERATURE DATA FILE TDATAF
'pdata.jetp68'        EXPERIMENTAL PRESSURE DATA FILES PDATAF
8.50,11.0             XPAGE,YPAGE
1.50,7.95             XORIGN(1),YORIGN(1)
3.50,2.50             XSIZE(1),YSIZE(1)
0.0,1.0,6.0           XS(1),XI(1),XF(1)
0.0,20.0,75.0         YS(1),YI(1),YF(1)
5.05,7.95             XORIGN(2),YORIGN(2)
2.00,2.50             XSIZE(2),YSIZE(2)
0.0,1.0,3.0           XS(2),XI(2),XF(2)
0.0,200.0,1150.0      YS(2),YI(2),YF(2)
1.50,4.85             XORIGN(3),YORIGN(3)
3.50,2.50             XSIZE(3),YSIZE(3)
0.0,1.0,7.0           XS(3),XI(3),XF(3)
0.0,20.0,65.0         YS(3),YI(3),YF(3)
5.05,4.85             XORIGN(4),YORIGN(4)
2.00,2.50             XSIZE(4),YSIZE(4)
0.0,1.0,4.0           XS(4),XI(4),XF(4)
0.0,0.20,1.199        YS(4),YI(4),YF(4)
1.50,1.50             XORIGN(5),YORIGN(5)
2.75,2.75             XSIZE(5),YSIZE(5)
0.0,0.5,2.25          XS(5),XI(5),XF(5)
0.0,500.0,2500.0      YS(5),YI(5),YF(5)
4.30,1.50             XORIGN(6),YORIGN(6)
2.75,2.75             XSIZE(6),YSIZE(6)
0.0,0.5,2.25          XS(6),XI(6),XF(6)
102.0,0.5,104.0       YS(6),YI(6),YF(6)
0.90,2050.0           X AND Y COORDINATES FOR GAS TEMPERATURE CURVE LABEL
1.25,1300.0           X AND Y COORDINATES FOR SOLID TEMPERATURE CURVE LABEL
```

changes might be necessary to run this script file on a different platform. The user should consult with the system's manager for help, if needed.

Compilation, Execution and Viewing/Printing of the Program PLOT1

In our center, the DISSPLA graphics package is installed on a computer named hodg. The plotting routines reside in the subdirectory jetp68. The symbol ">>" is the system prompt. The procedure to compile and execute the program is as follows:

Step 1: Compile the program plot1.

```
[hodg:3]mag-jetp68>> f77 -c plot1.f

plot1.f:
 MAIN plot1:
        setenv:
        dashdd:
        mydash:
```

Step 2: Link and generate the executable code plot1.

```
[hodg:4]mag-jetp68>> dis77link -o plot1 plot1.o
```

Step 3: Execute plot1 to generate the device independent file plot1.pop

```
[hodg:5]mag-jetp68>> plot1

 END OF DISSPLA 11.0 9003, DRIVERS 9003 -- 27291 VECTORS IN 1
 PLOTS.
 RUN ON 3/4/93 USING SERIAL NUMBER 7380 AT BRIGHAM YOUNG
 UNIVERSITY
 PROPRIETARY SOFTWARE PRODUCT OF COMPUTER ASSOCIATES, INC.
 2391 VIRTUAL STORAGE REFERENCES; 8 READS; 0 WRITES.
STOP: all done happy camper
```

Step 4: Run the script file to view the plot1.pop on a X-Windows environment.

```
[hodg:6]mag-jetp68>> popout

Choose your output device
     x) X window
     h) HP Laserjet III Si
```

```
     c) Color Printer
     t) Tektronix terminal
     p) PostScript file (no printing)

x

What is the metafile (popfile) to be printed? plot1.pop
What display will you be using? (Ex: hodg)
hodg

Creating output...
<<<<< Plot is displayed on the monitor. >>>>>
rm: remove popfile? y
```

Step 5: run the script file to generate the postscript file plot1.ps.

```
[hodg:7]mag-jetp68>> popout


Choose your output device
     x) X window
     h) HP Laserjet III Si
     c) Color Printer
     t) Tektronix terminal
     p) PostScript file (no printing)

p

Do you want the output in landscape (l) or portrait (p) ?
p

What is the metafile (popfile) to be printed?
plot1.pop
Creating output...
rm: remove popfile? y
```

Step 6: Print the file plot1.ps using the appropriate print command.

Other output devices supported by this script file are an HP Laserjet III Si printer, a color printer, and Tektronix terminal.

The second program plot2 can also be executed in a similar manner, by replacing plot1 with plot2 in the above commands.

USER'S FORUM

If you have any comments concerning your experiences using FBED-1, please foward them to:

Dr. Andrew M. Eaton
ACERC Software Specialist
75 Crabtree Building
Brigham Young University
Provo, UT 84602
Phone: (801) 378-5008
E-mail: ame@homer.et.byu.edu

You are also invited to submit your comments concerning the clarity, accuracy, and usefulness of this manual. Constructive critical comments are most welcome and will help us continue our efforts to generate quality user documentation. Please list the page number for questions and comments. Use other side if necessary.

From:

Name_____ Title_____

Company_____ Date_____

Address and Phone No._____

August 20, 1993

FBED-1 Code Installation Instructions

We have executed the FBED-1 code on our Sun 4/310 and Silicon Graphics workstations and made sample runs. The code runs properly. We have copied all the files, including the sample input and the sample output files on the enclosed tapes. The files can be recovered as follows:

% mkdir FBED1
% cd FBED1
% tar -xvf /dev/rst8 (please use the appropriate device name for the magnetic tape drive on your workstation)

Next the sample output files, **fb1out, outa - outj, balanc.out, cconv.out, compar.out, compos.out and pdia.out,** should be moved to a subdirectory **outfiles** as follows:

% mkdir outfiles
% mv *out* outfiles

The sample case is for Wellman-Galusha gasifier fired with Jetson bituminous coal and may be run while in FBED1 directory simply by typing:
% fbed1

The new output files, **fb1out, outa - outj, balanc.out, cconv.out, compar.out, compos.out and pdia.out,** will be generated and may be compared with our results in the subdirectory **outfiles.** We also recommend that you recompile the code and rerun the sample case and again compare the results with the earlier ones. The code may be recompiled by first removing all object (with extension o) files, and then by typing:

% make -f makefbed

After successful compilation, linking and loading, the sample case can be run as before by typing:
% fbed1

The tape also includes two plotting programs for the DISSPLA package. The executable files on the tape are for SUN computer and can be run following the procedure outlined in **Appendix J** of the **FBED-1 User's Manual.** Please make the appropriate changes , if needed, for running these programs on a Silicon Graphics machine.

If you need any further assistance, please call Dr. Predrag T. Radulovic at (801) 378-3097 or Dr. M. Usman Ghani at (801) 378-6074.